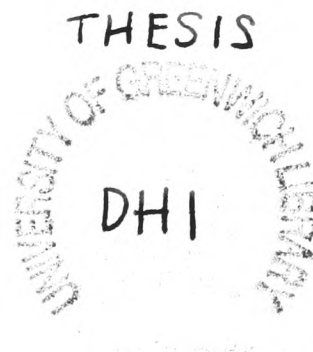# Development and Application of Low Reynolds Number Turbulence Models for Air-Cooled Electronics

Kulvir Kaur Dhinsa

Ph.D.

November 2006

Development and Application of Low Reynolds Number Turbulence Models for Air-Cooled
Electronics

Kulvir Kaur Dhinsa

Centre for Numerical Modelling and Process Analysis

School of Computing and Mathematical Sciences

the University of Greenwich

London, United Kingdom.

A thesis submitted in partial fulfilment of the requirements of the

University of Greenwich for the degree of Doctor of Philosophy.

This research programme has been carried out in collaboration with:

Flomerics Ltd.

and

the Engineering and Physical Sciences Research Council (EPSRC)

through the PRIME Faraday organisation as an Industrial Case Award.

November 2006

ABSTRACT

Semiconductors are at the heart of electronic devices such as computers, mobile phones, avionics systems, telecommunication racks, etc. Power dissipation from semiconductor devices is continuing to increase due to the growth in the number of transistors on the silicon chip as predicted by Moore's Law. Thermal management techniques, used to dissipate this power, are becoming more and more challenging to design. Air cooling of electronic components is the preferred method for many designs where the air flow is characterised as being in the laminar-to-turbulent transitional region.

Over the last fifteen years there has been a dramatic take-up of Computational Fluid Dynamics (CFD) technology in the electronics industry to simulate the airflow and temperatures in electronic systems. These codes solve the Reynolds Averaged Navier-Stokes (RANS) equations for momentum and turbulence. RANS models are popular as they are much quicker to solve than time-dependent models such as Large Eddy Simulation (LES) or Direct Numerical Simulation (DNS).

At present the majority of thermal design engineers use the standard $k - \varepsilon$ model which is a high Reynolds number model. This is because there is limited knowledge on the benefit of using low Reynolds number models in the electronics cooling industry. This Ph.D. investigated and developed low Reynolds number models for use in electronics cooling CFD calculations. Nine turbulence models were implemented and validated in the in-house CFD code PHYSICA. This includes three zero-equation, two single equation, and four zonal models. All of these models are described in the public literature except the following two models which were developed in this study:

- AUTO_CAP: This zero-equation model automates the existing LVEL_CAP model available within the commercial CFD code FLOTHERM.

- $k\varepsilon / kl$: This zonal model uses a new approach to blend the $k - l$ model used at the wall with the $k - \varepsilon$ model used to predict the bulk airflow.

Validation of these turbulence models was undertaken on eight different test cases. This included the detailed experimental work undertaken by Meinders. Results show that the $k\varepsilon / kl$ model provides the most accurate flow predictions. For prediction of temperature there was no clear favourite. This was probably due to the use of the universal log-law function in this study. A generalised wall function may be more appropriate.

Results from this research have been disseminated through a total of nine peer-reviewed conference and journal publications, evidence of the interest the topic of this investigation generates amongst electronic packaging engineers.

ACKNOWLEDGEMENTS

TABLE OF CONTENTS

Roman Letters

A	Area	m^2
C_d	Model constant	0.1643
C_p	Specific heat capacity	$J.kg^{-1}.K^{-1}$
$C_{1\varepsilon}$	Model constant	1.44
$C_{2\varepsilon}$	Model constant	1.92
C_μ	Model constant (Wolfshtein & $k-\varepsilon$)	0.09
	Model constant ($k\varepsilon/kl$)	0.5478
$CD_{k\omega}$	Cross diffusion term	
D	Maximum local length scale	m
D_h	Hydraulic diameter	m
E	Energy	$J \equiv N.m$
	Integration constant, smooth walls	9.0
F	Force	$N \equiv kg.m.s^{-2}$
F_1	Blending function	
F_2	Blending function	
G	Generation term	s^{-2}
H	Step height	m
	Cube height	m
L	Characteristic length	m
	Distance to nearest wall	m
L_m	Mixing length	m
M	Measurement points	
Pe	Peclet number	
Pr	Prandtl number	
P_k	Production term	
$\widetilde{P_k}$	Production limiter	
Q	Power	$W \equiv J.s^{-1}$
Re	Reynolds number	
Re_{k-l}	Turbulent Reynolds number $k\varepsilon/kl$ model	
R_k	Model constant	6.0

R_t^* ....Turbulent Reynolds number

R_w .... Model constant..2.7

R_β .... Model constant..8.0

S ....Source term

................SST strain rate..s^{-1}

................Mean rate-of-strain tensor..s^{-1}

................Pitch of cubes..m

T .... Temperature..°C

U .... Chacteristic velocity..$m.s^{-1}$

................In-cell value of velocity..$m.s^{-1}$

U_r .... Resultant velocity..$m.s^{-1}$

V ....Local speed..$m.s^{-1}$

$\bar{V}$ ....Average velocity..$m.s^{-1}$

Vol .... Volume..m^3

X_r ....Reattachment length.. m

a_1 ....Model constant..0.31

b .... 1/2 distance between plates................................m

f ....Fanning friction factor

f_1 ....Damping function

f_2 ....Smoothing function

f_μ ....Damping function

h .... Cuboid height..m

................Channel height.. m

................Heat transfer coefficient................................$W.m^{-2}.K^{-1}$

i .... Internal energy..$J.kg^{-1}$

................Turbulence intensity.. %

k .... Turbulent kinetic energy................................$m^2.s^{-2}$

................Thermal conductivity................................$W.m^{-1}.K^{-1}$

l_ε ....Dissipation length.. m

l_μ ....Turbulent mixing length................................ m

$\dot{m}$ .... Mass flow rate..$kg.s^{-1}$

$\mathbf{n}$ .... Outward normal vector

n .... Total number of cells

p ....Pressure..$Pa \equiv N.m^{-2}$

q .... Heat flux..$W.m^{-2}$

$\underline{q}$ .... Flow rate..$m^3.s^{-1}$

s ....Skin friction factor

t .... Time..s

$\mathbf{u}$ .... Velocity vector...m.s^{-1}

u, v, w .... Velocity components..m.s^{-1}

u', v', w' ....Fluctuating velocity components...m.s^{-1}

w ....Channel width..m

x .... Distance, direction x-axis.. m

y ....Distance, direction y-axis...................................... m

y^* ....Turbulent Reynolds number

z .... Distance, direction z-axis...m

Greek Letters

Φ .... Dissipation function

Γ ....Diffusion coefficient

Ω_{ij} .... Mean rate-of-rotation tensor...s^{-1}

α ....Thermal expansion coefficient.....................................K^{-1}

................Model constant (LVEL)..0.0769251

................Closure coefficient ($k - \omega$)

................Model constant ($k\varepsilon / kl$) 5.3

α_0 ....Model constant ($k - \omega$) 0.1

α_1 ....Model constant.. 5/9

α_2 ....Model constant..0.44

α^* ....Closure coeffient

α_0^* ....Model constant 0.025

β ....Model constant ($k - \omega$) 0.075

................$k\varepsilon - LVEL$ step function

................Model constant ($k\varepsilon / kl$) 0.0198

β_1 .... Model constant..0.075

β_2 ....Model constant..0.0828

β^* ....Closure coefficient ($k - \omega$)

................Model constant (SST) 0.09

β_{i1} .... Model constant...0.075

β_{i2} ....Model constant...0.0828

δ ....Boundary layer thickness...m

................Centre-to-face distance.. m

ε .... Turblent dissipation rate................................... m^2.s^{-3}

ϕ .... Solved variable/quantity

κ ....von Karman constant

μ ....Dynamic viscosity..kg.m^{-1}.s^{-1}

ν .... Kinematic viscosity...m^2.s^{-1}

ρ ....Density...kg.m^{-3}

σ_k ....Model constant (Wolfshtein, $k-\varepsilon$ & $k\varepsilon/kl$).................. 1.0

..................Model constant ($k-\omega$)... 2.0

σ_{k1} ....Model constant (SST)... 0.85

..................Model constant (SST_V).. 1.176

σ_{k2} ....Model constant..1.0

σ_ε ....Model constant...1.3

σ_ω .... Model constant...2.0

$\sigma_{\omega1}$ .... Model constant (SST)... 0.5

..................Model constant (SST_V).. 2.0

$\sigma_{\omega2}$ .... Model constant (SST) 0.856

..................Model constant (SST_V) 1.168

τ .... Shear stress.. N.m^{-2}

ω ....Specific dissipation rate..s^{-1}

Sub-scripts

A ....Region A

B ....Region B

E ....Control volume to the east

N ....Control volume to the north

P ....Current cell

S ....Control volume to the south

W ....Control volume to the west

b .... Bulk value

calculated ...... Calculated value

crit ....Critical

e ....Face between the current and east control volumes

face ....Face value

fd ....Fully developed

i .... Cell number

in .... Inlet value

k .... Turbulent kinetic energy

l .... Laminar value

measured ...... Measured value

mom ....Momentum

new ....New value

nw ....Near-wall

previous ....Previous value

REF ....Reference

t .... Turbulent value

t_max .... Turbulent maximum

w .... Wall value

.... Face between the current and west control volumes

ε .... Turbulent dissipation rate

ϕ .... Solved variable

ω .... Specific dissipation rate

∞ .... Freestream value

Super-scripts

$+$ .... Dimensionless quantity

Mathematical Operators

∂ .... Partial differential

$\Delta \equiv grad$ .... Gradient, rate of change

$\nabla \equiv div$ .... Divergence

Σ .... Summation

$\sqrt{}$ .... Square Root

INTRODUCTION

The research reported in this thesis was financially supported by the Engineering and Physical Sciences Research Council (EPSRC) through the PRIME Faraday Partnership as a Ph.D. Industrial Case Award. The industrial partner was Flomerics Limited, a leading UK software house, who produce the Computational Fluid Dynamics (CFD) code FLOTHERM. This code is used by many electronics design engineers around the world to predict and optimise the thermal behaviour of electronic systems.

The research presented throughout this thesis has an industrial focus geared towards the development of a new transitional turbulence model specifically designed for the cooling of electronic components. This chapter discusses the motivation behind the Ph.D., electronic systems and thermal management, the layout of the thesis, and a summary of the original techniques and findings from the research.

1.1 Project Motivation

Electronic products are built up around Printed Circuit Boards (PCBs) that contain many electronic components (memory chips, CPU chips, resistors, etc). During the operation of a product (e.g. a Laptop) these cluttered geometries emit excessive heat that must be extracted otherwise the product will become too hot and result in failure. With the ever-increasing demand for extra power driven by higher frequencies (i.e. greater than 1GHz) and product miniaturisation (smaller computers, PDAs, intelligent devices, etc) thermal requirements of products are becoming ever more important.

Heat is conducted away from the chip through the PCB by conduction and radiation but for many cases this is not sufficient to ensure safe working temperatures. Air cooling can also be used to help remove heat. This is aided by fans which force cooler air around the hot electronic components. The rate at which heat is removed by air cooling is dependent on the characteristics of the flow and whether it is laminar or turbulent.

- Laminar Flow: When this flow of air moves across the component in smooth horizontal layers, sheared only by the viscosity of the air, then the flow is referred to as laminar flow (represented by a low Reynolds number $Re < 2000$).

- Turbulent Flow: If unsteady eddies exist throughout the flow then it is classified as turbulent flow (high Reynolds number $Re > 4000$).

- Transitional Flow: Typically a transition region exists between the laminar and turbulent flow regimes. This transitional region is recognised to be the dominant flow region for air cooling of electronics. $\left(2000 \leq Re \leq 4000\right)$.

The boundary layer close to the surface of the component is very important, as this is where the heat is extracted and then carried away by the rest of the airflow. The rate of heat transfer taking place in this thermal boundary layer is strongly dependent on the nature of the airflow in this region (Laminar, Transitional, Turbulent).

The increasing importance of thermal design in electronics and the growth of the market has resulted in a number of thermal experts entering this field. They are using design software tools such as FLOTHERM (Flomerics Ltd.) to solve the governing equations of fluid flow (including turbulence) and heat transfer and hence predict the effects of a new design on temperature. Consequently, these software users are becoming more aware of various aspects of CFD technology, in particular, a number of recent technical papers have pointed to current turbulence models as a limiting factor in the quality of the results predicted. This has generated substantial interest in the community for research into new turbulence models that, when integrated into a CFD framework, can more accurately predict both the flow behaviour over heated surfaces and the rate of heat transfer from electronic system components.

The aim of this Ph.D. is to investigate and develop turbulence modelling capabilities to provide the most appropriate model(s) for low Reynolds number transitional flows encountered in electronics applications. The model should also have the ability to be integrated within a commercial CFD code such as FLOTHERM and to be used by thermal design engineers. In this context the model should also address the following commercial constraints:

- Relevant for congested domains which experience a mix of low and high aspect ratio geometries frequently found in electronic applications (see Figure 1.1)

- Low computational and data storage expense to allow electronic thermal design engineers to adopt the model within an industrial environment

- Robust giving acceptable accuracy and numerical stability
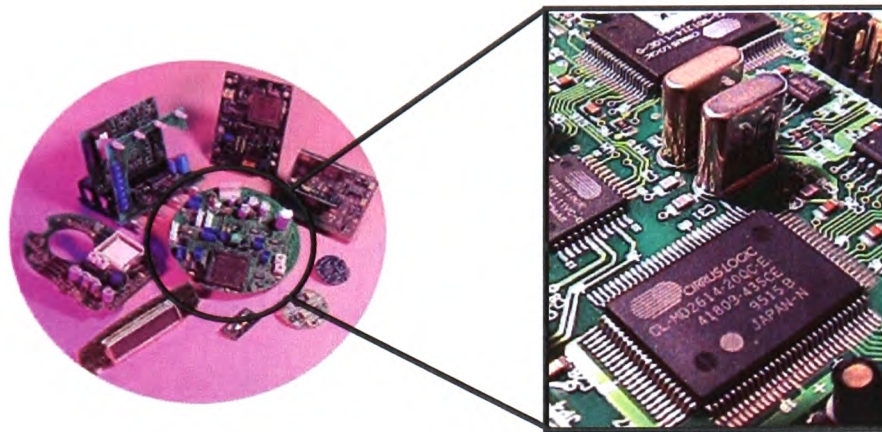
Figure 1.1 Mixed low/high aspect ratio geometries

The above aim was achieved through the following objectives:

- Undertake a literature review of turbulence modelling and low Reynolds number models as their suitability for thermal management of electronic systems

- Review CFD technology and capabilities using the commercial software codes FLOTHERM[1] and PHOENICS[2] along with the in-house code PHYSICA[3]

- Investigate the use of zonal turbulence models. Develop a zonal model to accurately capture the flow phenomena at the walls and within the bulk region

- Incorporate the above turbulence models into the CFD code PHYSICA

- Validate these turbulence models against published numerical benchmarks and experimental data

- Publish and disseminate the results from this research at conferences and in journal articles.

Dissemination of the results from this project will greatly benefit the wider scientific community in helping understand key phenomena taking place in this flow regime and its effect on heat extraction and help educate the electronics cooling community to the difficulties associated with the accurate prediction of turbulent flows. Such models may also be useful for other industrial flow problems operating within this type of regime.

1.2 Thermal Management of Electronics

As electronic products become faster and incorporate greater functionality, they are also reducing in size and weight, with continuing pressures for cost and time-to-market reductions. Thermal issues are critical at all levels of the electronic product hierarchy, from the chip to the system. The miniaturisation of the system is resulting in increasing volumetric heat generation rates and surface heat fluxes in many products.

It has been reported by the US Air Force Avionics Integrity Program that the major cause of electronic failure is the over heating of an appliance. This is illustrated in Figure 1.2.
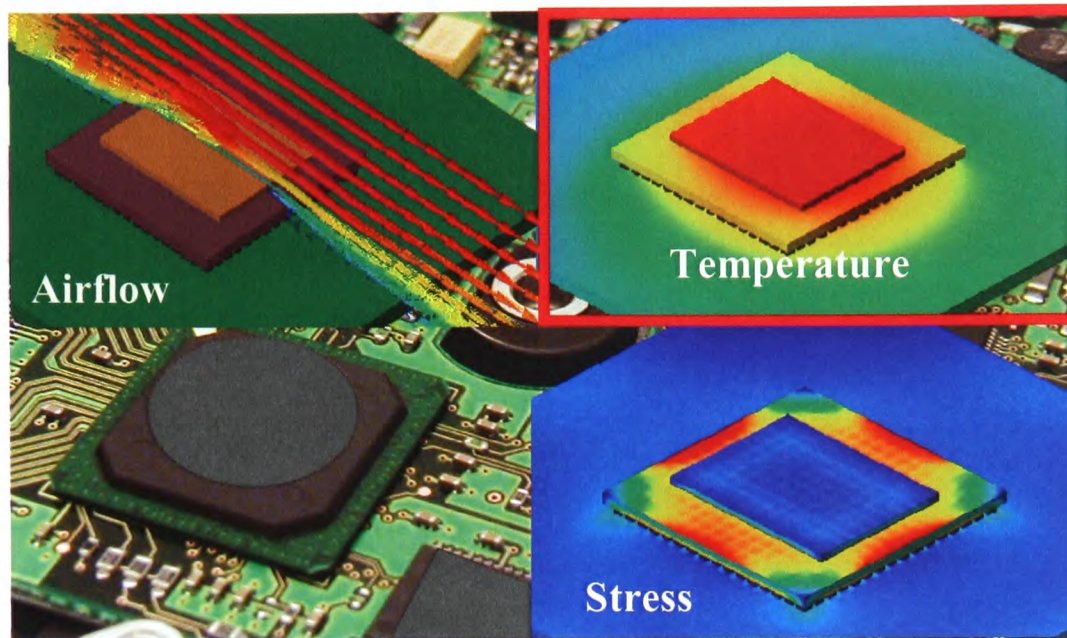
Major causes of electronic failure:
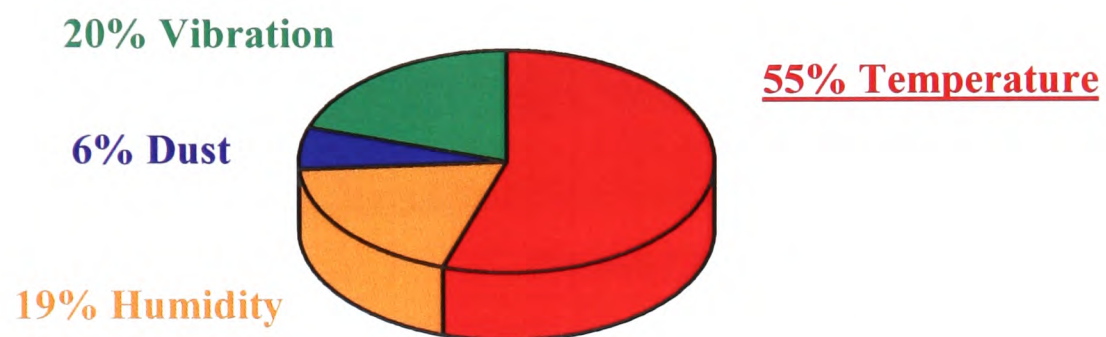
Figure 1.2 Major causes of electronic failure identified by the US Air Force Avionics Integrity Program

Why is temperature such a problem? Consider a component assembly which is constructed of several different materials, illustrated in Figure 1.3.
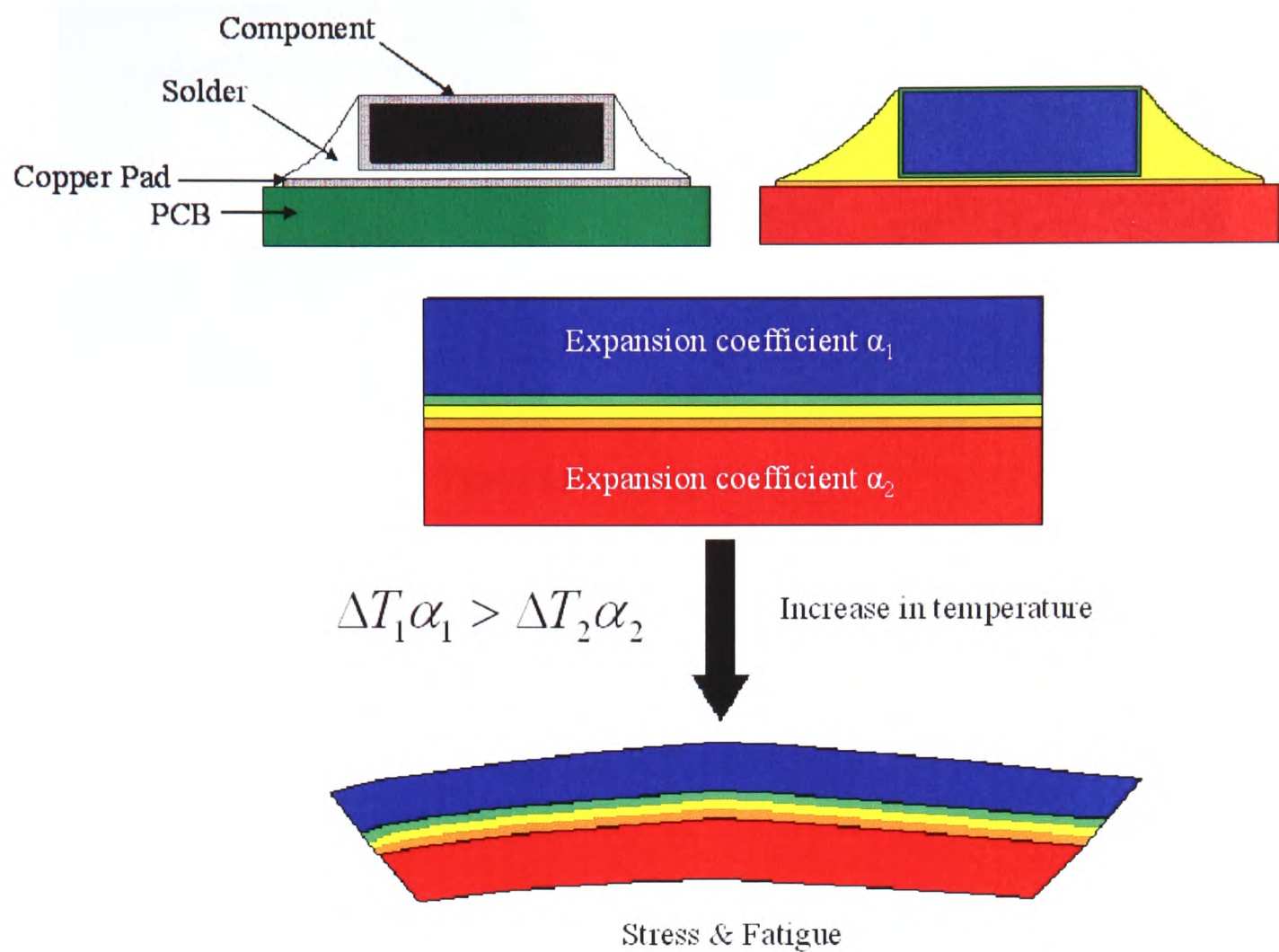
Figure 1.3 Coefficient of thermal expansion mismatch

Each material within the assembly has a different rate of thermal expansion, hence coefficient of thermal expansion (CTE) mismatch. Therefore as this material assembly runs through a thermal cycle uneven expansion will take place causing stress in the materials. The greater the temperature change (ΔT) the higher the stress that can result due to the CTE mismatch. High stresses can cause fatigue induce cracks and lead to material failure. One particular area of concern in electronic systems is the solder joints between the semiconductor package and the PCB. Figure 1.4 shows a typical solder joint that has failed due to temperature cycling.
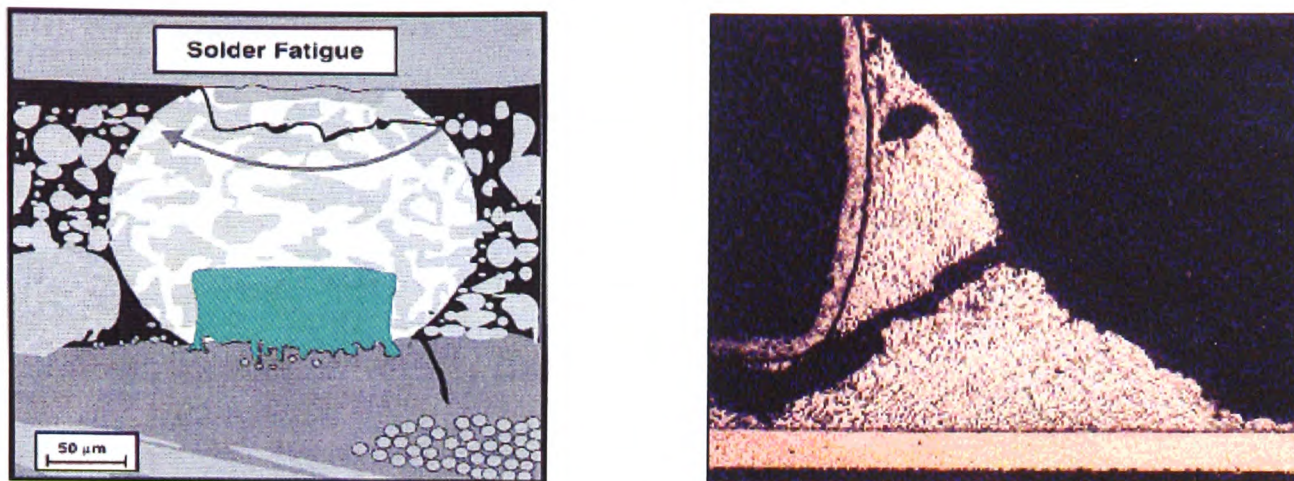
Figure 1.4 Solder joint fatigue

The ultimate goal of thermal management is to keep components at or below their maximum operating temperature to guarantee performance and reliability while dissipating power to a local ambient. However as the density of circuits increase, so does the need to develop more effective methods of thermal management.

1.2.1 Trends in the Electronics Industry

In today's electronic products, total system dissipated power levels are increasing with the introduction of every new design. Increases in power levels combined with the market expectation of reduced package size leads to thermal issues that, if uncontrolled, can significantly reduce the product life expectance.

In 1965, Gordon Moore (co-founder of Intel) observed an exponential growth in the number of transistors per integrated circuit. Moore's predictions suggest that on average computer performance doubles every 18-24 months. Moore's observations seem to have turned into reality, but what is to be expected if this trend continues?
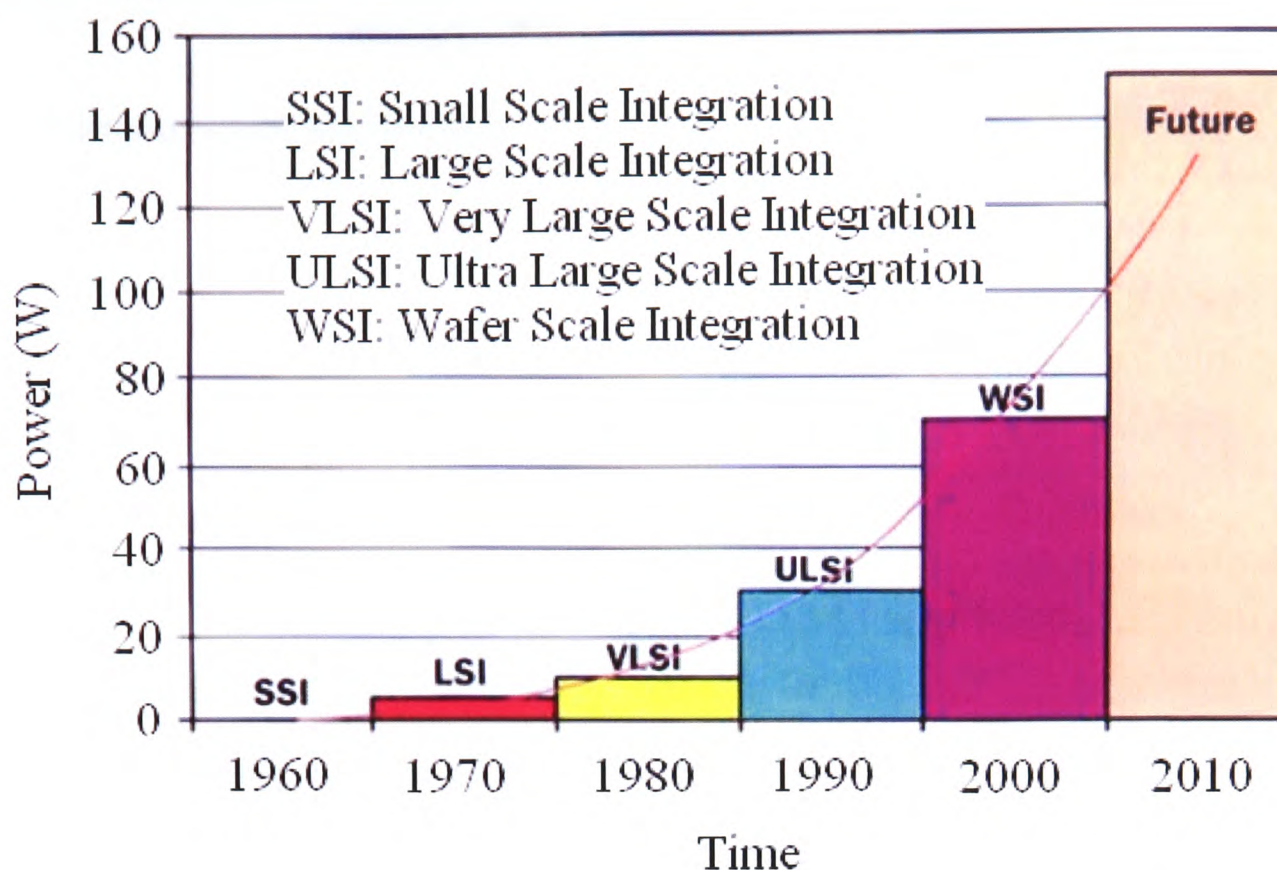
Figure 1.5 Timeline plot of device technology with respect to power predictions[4]

From Figure 1.5 it is clear that there is nothing in the timeline projections to suggest that device or system level power dissipation is on the decline, nor is power dissipation likely to reach a plateau in coming years. Therefore in answer to this question thermal design engineers could be routinely dealing with chip powers of 130W or more by 2010. This has motivated the introduction of new cooling techniques such as liquid and evaporative cooling.

Market demands for electronics products of superior quality and performance, yet miniaturised as much as possible. Clearly electronics products are evolving rapidly bringing complex problems associated with cooling the equipment. Some of the key industrial trends have been summarised in Figure 1.6.

Miniaturisation of electronic circuitry	
Faster product performance	Greater functionality

Outcome: Increase of power density	

Reduce cost	Reduce lead time

Outcome: Exploitation of thermal management software	
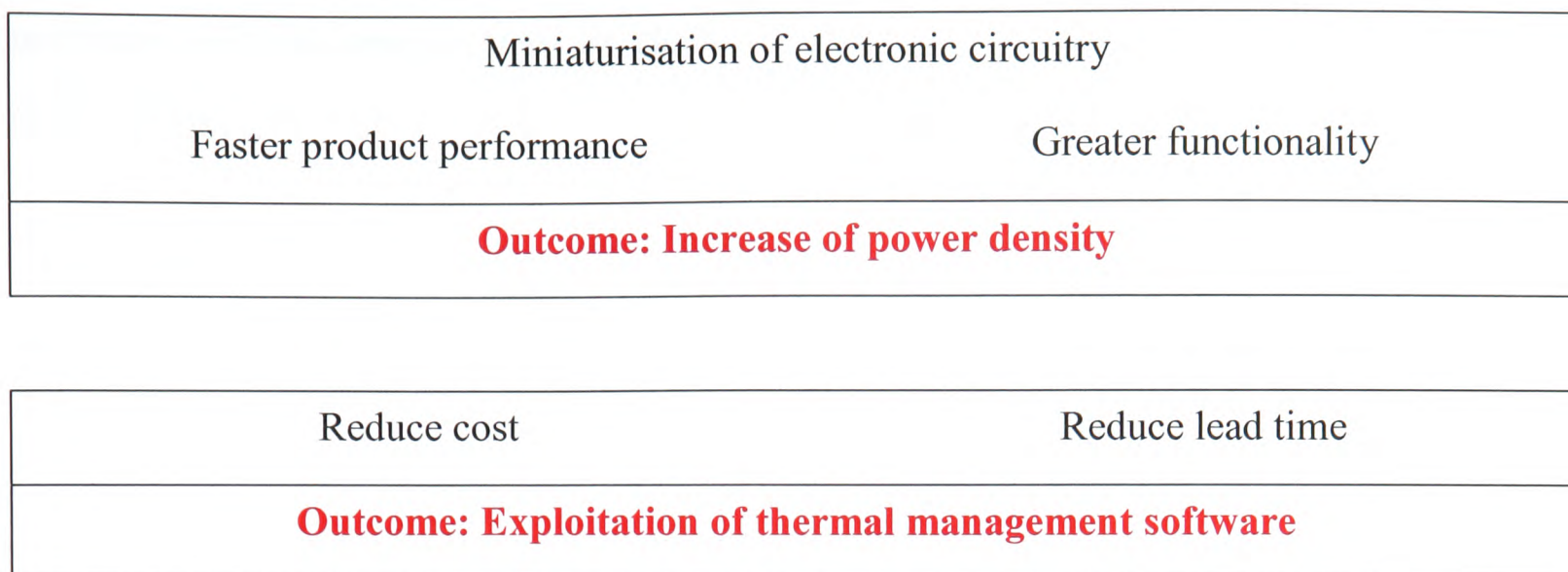
Figure 1.6 Industrial trends in the electronics industry

These latter two trends only magnify the problems facing thermal design engineers and prompt the use of sophisticated cooling techniques. As a result, thermal considerations (cooling) need to be considered early in the design, affecting component selection, PCB logout etc. Consequently electronic engineers are becoming increasingly "thermally-aware."

1.2.2 Cooling of Electronics

A common rule of thumb is that every 10°C reduction in the junction temperature of a semiconductor will double the life expectancy of that semiconductor – clearly then it is of interest to keep the junction temperature as cool as is practically possible.

There are three main cooling strategies for electronics: air cooled (natural and forced convection), liquid cooled, and fluid phase change. Air cooled natural convection methods are usually used for low powered applications, whereas forced convection techniques are used for higher powered applications. Liquid cooling and fluid phase change methods are then used for significantly higher powered applications where forced convection systems are unable to sufficiently dissipate the heat generated.

The preferred method of cooling electronics is air induced as it is cheap, simple, safe and reliable. However the limits of air cooling are fast being approached in some applications. To continue with the use of this cooling technique for as long as possible it has become extremely important to develop accurate methods of predicting the airflow structures within the system environment. Inevitably this will lead to greater accuracy when considering the

prediction of heat transfer from an electronic package. Therefore air cooling of electronic applications is the focus of this work.

Understanding the nature of the airflow around electronic components and how it affects the transfer of heat from them is very important from a product design perspective. If the heat removed is insufficient, then the temperature of the component will exceed the manufacturer's specifications and the components reliability may be compromised.

Commercially available CFD software for electronics cooling applications often include pre-programmed components such as printed circuit boards, fans, vents, and heat sinks which make the design process easier, allowing engineers to carry out numerous design scenarios in a short space of time.[5]

1.2.3 Role of CFD within Electronic Applications

Thermal design engineers within the electronics community regularly use CFD to predict the temperatures in new designs of electronic systems such as computers, telecommunication racks, etc. These software tools numerically solve the governing equations of fluid flow and heat transfer to predict the air velocity throughout the system, and the temperatures within the components. Turbulence in the airflow is important as it influences the airflow structures formed around a component and hence the amount of heat extracted.

There are two principal benefits from the use of CFD analysis. Firstly, CFD can reduce development time and expense by allowing a design to be tested, improved, and optimised prior to the creation of physical prototypes. Depending on the application, CFD may be able to completely replace prototype testing. Secondly, CFD offers an enhanced understanding of the physical phenomena. For example, flow path visualisation allows for the identification of recirculation regions, helping to explain the causes of high component temperatures.

In electronics cooling applications the flow regime is often in a stage of transition between laminar and turbulent flow due to the low velocities, small length scales and flow obstructions encountered within the system environment. Commercially accessible general purpose CFD procedures often neglect transition entirely and classify flows as either laminar or fully turbulent. Clearly the drawback of such an assumption means that modelling errors are likely

to occur, this in turn will lead onto inaccuracies in the prediction of the heat transfer phenomena.

It has now become a necessity for electronics cooling CFD vendors to understand and develop modelling techniques for transitional flow regions. CFD users are becoming aware of this and other deficiencies as their need for accuracy increases. As the majority of industrial CFD analysis is performed on desktop computers this constrains the development of any new turbulence model, hence accuracy at low computational cost is considered a "must have."

The cost of rectifying mistakes increases by roughly an order of magnitude at each major design phase, providing incentive for the use (and hence the development) of virtual prototyping tools as both time and money are saved. This has been illustrated in Figure 1.7.
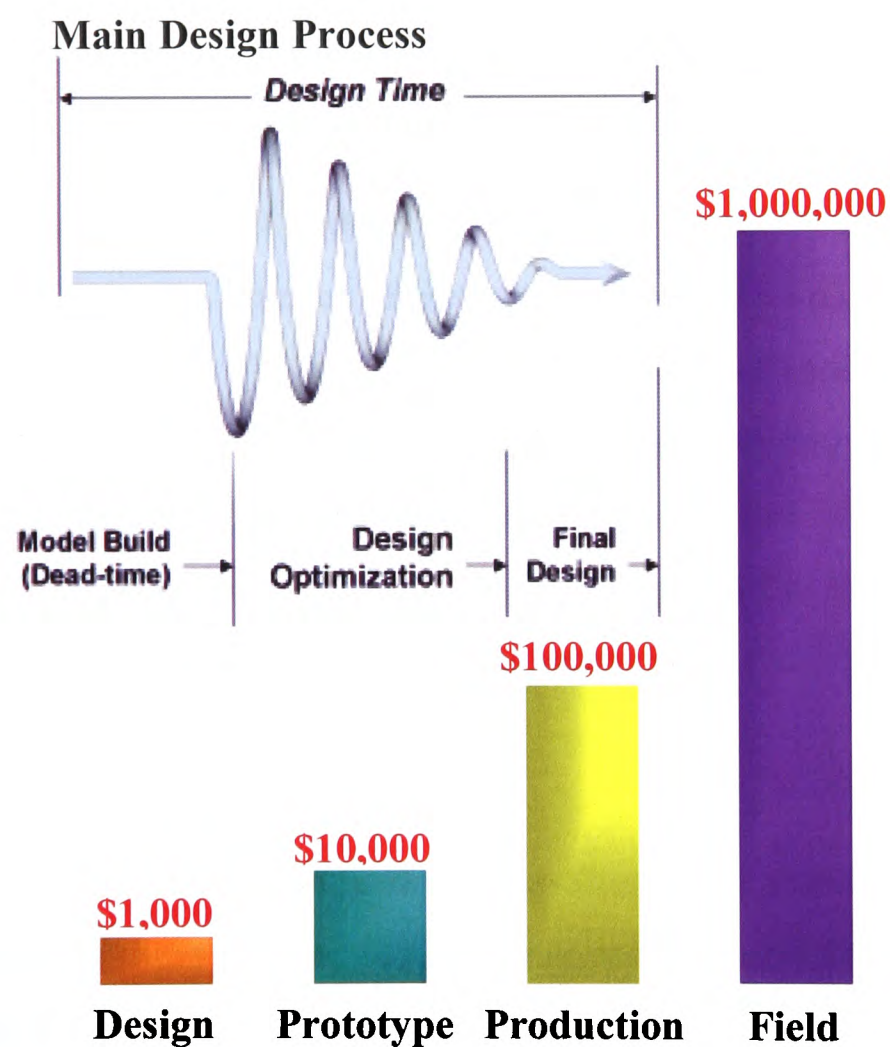
Figure 1.7 Product design cycle cost assessment[6]

Although CFD software is not cheap, (annual licenses average $20,000), the technical insights gained are invaluable. A wide range of modelling scenarios can be assessed within a very short time frame reducing both overall costs and time-to-market. There are, of course,

limitations to the application of CFD, and research is being done to overcome them. The primary limitation of interest to this Ph.D. study is in the area of turbulent flow.

1.3 Layout of Thesis

The rest of this thesis consists of nine chapters. These detail the background to the research and the implementation and development of low Reynolds number turbulence models and their validation.

Chapter 2 provides a literature review which discussed previous modelling and experimental work undertaken on electronic cooling and low Reynolds number turbulence modelling. This is followed by Chapter 3 which provides a summary on the theory behind CFD. Chapter 4 details the theory of turbulence and provides material on RANS turbulence models such as the zero-, one-, and two-equation models, as well as the classical log-law wall function which was used in this research.

Chapter 5 compares the three CFD codes: FLOTHERM, PHOENICS and PHYSICA. This comparison was undertaken on a number of test case geometries using the standard turbulence models which were available in PHYSICA these being the $k-\varepsilon$ and $k-\omega$ models. This is followed by Chapter 6 which compares the above three codes on two test geometries for zero and one-equations models. These models were implemented into PHYSICA as part of this Ph.D. Chapter 7 compares FLOTHERM and PHYSICA against the Martinuzzi test data for a high Reynolds number flow three-dimensional geometry. Both the LVEL and standard $k-\varepsilon$ models were compared.

Chapter 8 discusses zonal models such as the Shear-Stress Transport (SST), $k\varepsilon - LVEL$, and the $k\varepsilon/kl$ model. Each of these models was implemented into PHYSICA as part of the Ph.D. Also discussed is the role of the blending function which merges the two turbulence models at locations where the regions change from high to low Reynolds number. A novel approach was developed as part of this Ph.D. to merge the $k-l$ and $k-\varepsilon$ models into the $k\varepsilon/kl$ hybrid model. Also proposed are some novel blending methods for the $k\varepsilon - LVEL$ model currently used in FLOTHERM.

Chapter 9 validates a selection of models that were considered most appropriate for electronics cooling against the Meinders experimental data for low Reynolds number airflow over a single and an array of cubes. Chapter 10 provides conclusions to this Ph.D. study and suggestions for further work.

The thesis also contains five appendices, which provide a full description of each test case plus other details on CFD and turbulence modelling.

1.4 Original Techniques and Findings

The research performed during the course of this project has allowed for a thorough review of turbulence models suitable for the low Reynolds number regime encountered in electronic cooling applications.

The author has independently implemented and performed critical testing on a total of nine RANS turbulence models, two of which are novel, within the structure of the University of Greenwich CFD code PHYSICA Version 2.12.

The first new model that was developed in the research is the parameter-free zero-equation model, termed AUTO_CAP. This new model is an alternative to the LVEL_CAP (Revised Algebraic) model available within FLOTHERM Versions 3.2-6.1. The proposed model automates the calculation of the characteristic length and velocity scales which would otherwise be required to be specified by the user of the code.

The second newly-developed model was a zonal model, termed the two-layer hybrid $k\varepsilon/kl$ turbulence model. This was developed to satisfy the particular demands imposed by the electronics cooling sector. This model incorporates a novel technique which matches the values of k, ε, and v_t at the interface, ensuring a smooth transition between the turbulence models used near the wall and within the bulk flow.

Further to the development of two new turbulence models, modifications are also suggested to the zonal $k\varepsilon - LVEL$ model available within FLOTHERM. The current structure of the model experiences too fast a transition between the turbulence models. The novel modifications suggested ensures a smoother shift between the models.

All of the implemented turbulence models were validated against both numerical benchmarks and experimental data. These validations demonstrate the advantages and disadvantages of all the models. Both of the new models resulting from this Ph.D. are suitable for use in CFD calculations for airflow cooling of electronic systems and satisfy the original aim of the project and requirements of the industrial partner.

1.5 Dissemination of Research

The results from this Ph.D. study have been published in a number of peer-reviewed publications and presented at international conferences. The list of journal and conference papers published at the time of completion of this Ph.D. thesis are:

1. Dhinsa, K., Bailey, C., Pericleous, K. *Investigation into the Performance of Turbulence Models for Fluid Flow and Heat Transfer Phenomena in Electronic Applications*, IEEE Transactions on Components and Packaging Technologies, Vol. 28, No. 4, pp. 686-699, Pub. IEEE (2005)

2. Dhinsa, K., Bailey, C., Pericleous, K., *Turbulence Modelling for Electronic Cooling: A Review*, 7th International Symposium on Electronics Materials and Packaging (EMAP-2005), Tokyo, Japan, pp. 275-281, Pub. IEEE (2005)

3. Dhinsa, K., Bailey, C., Pericleous, K., *Turbulence Modelling and its Impact on CFD Predictions For Electronic Components*, 9th Intersociety Conference on Thermal, Mechanics and Thermomechanical Phenomena in Electronic Systems (ITherm-2004), Las Vegas, USA, pp. 487-494, Pub. IEEE (2004)

4. Dhinsa, K., Bailey, C., Pericleous, K., *Low Reynolds Number Turbulence Models for Accurate Thermal Simulations of Electronic Components*, 5th International Conference in Thermal and Mechanical Simulation and Experiments in Microelectronics and Microsystems (EUROSIME-2004), Brussels, Belgium, pp. 483-490, Pub. IEEE (2004)

5. Dhinsa, K., Bailey, C., Pericleous, K., *Investigation into the Performance of Turbulence Models for Fluid Flow and Heat Transfer Phenomena in Electronic Applications*, 20th Annual IEEE Semiconductor Thermal Measurement and Management Symposium (SEMITHERM-2004), San Jose, USA, pp. 278-285, Pub. IEEE (2004)

6. Dhinsa, K., Bailey, C., Pericleous, K., *Turbulence Modelling for Thermal Management of Electronic Systems*, 12th Association for Computational Mechanics in Engineering (ACME), Cardiff University, UK, Session 5b (2004)

7. Dhinsa, K., Bailey, C., Pericleous, K., *Accuracy of Turbulence Models and CFD for Thermal Characterisation of Electronic Systems*, 5th Electronics Packaging Technology Conference (EPTC-2003), Singapore, pp. 507-512, Pub. IEEE (2003)

8. Dhinsa, K., Bailey, C., Pericleous, K., *Turbulence Modelling and its Effects on Electronic Systems*, 4th International Symposium on Turbulence, Heat & Mass Transfer (ICHMT), Antalya, Turkey, pp. 1163-1170, (2003)

9. Dhinsa, K., Bailey, C., Pericleous, K., Parry, J., Dyson, J., Bornoff, R., *Airflow Predictions For Cooling Electronic Systems*, Proc. Postgraduate Research Conference in Electronics, Photonics, Communications & Software (PREP), Exeter University, UK, pp. 117, (2003)

A literature review has been conducted of relevant experimental and numerical work for electronic cooling applications. The turbulence models highlighted for study together with applied near-wall treatment have also been discussed.

2.1 Experimental Cases

A range of two- and three-dimensional experimental configurations were considered as relevant test cases for the validation of turbulence model implementation and the cooling of electronic components.

The two-dimensional configurations consist of Poiseuille flow between parallel plates and the classic backward facing step. The three-dimensional group consists of both low and high Reynolds number single cube configurations, and a matrix of cubes.

2.1.1 Two-Dimensional Experimental Cases

A classic, and simple, test case is Poiseuille flow between parallel plates. This problem can be solved analytically assuming that velocity is a function of (x) along the channel, and u is the only velocity component. Many commercial CFD software developers use this test case as an initial validation of both turbulence models and wall functions.[7, 8, 9] This case study is considered relevant to practical electronic applications as it represents flow in a passage (e.g. between the back side of a PCB and the equipment casing) or between the fins of a heat sink.

Due to the popularity of this case many standard transport phenomena textbooks also state the analytical solution of the expected velocity profiles for such a case.[10, 11, 12]

The natural progression from Poiseuille flow between parallel plates would be the consideration of a backward facing step or a rib. Flow separation, recirculation and subsequent reattachment are among the fundamental problems in fluid mechanics; both of

these cases include these conditions which frequently occur in engineering applications such as electronics cooling. Of the two cases the backward facing step seems to be a more popular configuration to evaluate the performance of turbulence models due to the extensive experimental and numerical work conducted. Attention will be given to this configuration as the validation of implemented turbulence models is a key focus within the current work.

The experimental work of Vogel and Eaton[13] is a popular dataset within the literature. They stated that the most important factor in determining the reattachment length is the state of the upstream boundary layer. Eaton and Johnson,[14] and Kim et al.[15] indicate that the reattachment length, which is weakly influenced by the Reynolds number,[16] lies in the range 7.0 ± 1.0 times the step height, and this range is universally accepted. The simulation work of Nallasamy and Chen[17] shows that the reattachment point predicted by the standard high Reynolds number $k - \varepsilon$ turbulence model lies in the range of $5.8 - 6.1$ step heights. However it is well known that the standard $k - \varepsilon$ model under predicts the reattachment length by approximately 20-25%. This has been widely discussed since the 1980-81 AFOSR-HTTM Stanford Conference on Complex Turbulent Flows.[18]

2.1.2 Three-Dimensional Experimental Cases

Turbulent flow around and heat transfer to, or from, bluff bodies can be found in various practical engineering applications. For the purpose of this study the focus is electronic cooling applications. Entire international conferences are dedicated to the problem of thermal management of electronic applications. For instance SEMI-THERM, ITHERM, EuroSimE, and EUROTHERM, therefore the interest in understanding the formation of vortex structures and how these influence the heat transfer mechanism is increasing.

The literature review conducted by Schofield and Logan[19] in 1990 further discusses two-dimensional flow observations and considers flow over three-dimensional obstacles but draws the readers attention to the fact that relatively little published data of three-dimensional flow over components exist and thus all proposed flow patterns reported in their work are based on flow visualisation studies. They further conclude that there is insufficient evidence to fully evaluate the effect of Reynolds number on the number and position of vortices in geometrically similar flow fields.

In 1992 Martinuzzi et al.[20, 21, 22, 23] attempted to fill the experimental gap by analysing the three-dimensional configuration of flow over a cube in a fully developed channel flow using Laser Doppler Anemometry (LDA). Martinuzzi provides a detailed description of the general flow features around a single wall-mounted cube. The observations include the identification of the horseshoe vortex system which is responsible for creating a downwash on the front face of the cube and the region of reversed flow in front of the cube. Furthermore, there is a separation of the flow on the sharp leading top and side edges of the cube, and an arch-shaped wake recirculation zone in the lee of the cube. These flow features are also observed for a configuration of multiple cubes. AbuOmar and Martinuzzi[24] recently reported that three-dimensional bluff body flows still receive less attention than two-dimensional cases.

To build on Martinuzzi's work, Meinders in 1998, introduced heat transfer calculations for a similar, but low Reynolds number configuration. Meinders research focuses on the experimental approach to the accurate analysis of the local convective heat transfer in idealised models of electronic PCBs. One of the major goals of this research was to provide accurate and reliable experimental heat transfer and flow field data for benchmarking commercial and in-house CFD codes with particular attention given to the benchmarking of turbulence models employed for the thermal design of PCBs.

The investigation was primarily focussed on the flow structures and the turbulent heat transfer in flows over surface-mounted obstacles in a turbulent channel flow. Four test configurations were considered: Single Cube, Array of Nine Cubes, Tandem of Two Cubes and Matrix of Cubes. For the current work undertaken two of the four cases stated above have been selected for investigation based on their relevance to electronic applications. The reader is referred to the references provided for further details on the Array of Nine Cubes[25, 26, 27, 28, 29, 30, 31] and the Tandem of Two Cubes[32, 33, 34] which will not be discussed further.

An isolated wall-mounted cube can be considered as the most basic representation of a sparsely populated PCB. A densely populated board, allowing the study of the interaction between components can be represented by configurations of multiple cubes. These Meinders configurations are considered to be the most realistic of the four test cases to investigate in this project.

For the single cube configuration Meinders[35, 36] concluded that the shear layers on the top and side faces of the cube reattached on these faces, contrary to the conclusions made by Martinuzzi for his higher Reynolds number case. Also a difference was observed in the downstream reattachment length, Meinders observed a larger reattachment length than that noted by Martinuzzi. Meinders also states that the local flow structures had a significant effect on the local convective heat transfer from the cube.

The matrix of cubes investigated by Meinders[37, 38, 39, 40] is an idealised representation of an actual PCB. The quality of this experimental dataset is believed to be high and therefore has served as a reference dataset for the validation of numerical simulations on three occasions at ERCOFTAC workshops held at Delft University of Technology,[41] the University of Manchester[42] and Helsinki University of Technology.[43]

The general flow features that emerge for this configuration are similar to those observed for the single cube. Meinders notes that like the single cube case, distinct vortex structures were only observed close to the obstacle, while the core region above the cubes remained almost undisturbed.

The heat transfer was measured at one powered cube in the spatially periodic matrix, while all other cubes remained unpowered. Heat convected away from the hot cube recirculates in the vortices causing local vortex temperatures to rise. The increased temperature levels prevent beneficial cooling close to the cube's surface. This again suggests that the accurate prediction of the vortex formation is considered key for the accurate prediction of the heat transfer coefficient. Hence for the present work the range (zero-, one- and two-equation) of turbulence models investigated will be closely monitored to determine which model overall produces the most accurate predictions.

Due to the extensive use of this dataset and the well documented case specifications this configuration has been the focus of the current work and is thought of as the ultimate test for the range of turbulence models investigated.

More recently Eveloy and co-workers [44, 45, 46, 47, 48, 49, 50, 51, 52] have conducted experimental work of actual components placed on PCBs. Their work has concentrated on arrays of Plastic Quad Flat Packs (PQFPs).

The main conclusion to be drawn from Eveloy's work was that compared to the gathered experimental data the turbulence models which showed the most promise were the one-equation Spalart-Allmaras model[53] and the hybrid two-layer SST formulation[54] as implemented in the FLUENT CFD code. As the test configuration is extremely flat, a PCB containing a number of PQFPs, little evidence of recirculating vortices would be present. The Spalart-Allmaras model was originally designed for the accurate prediction of flow over an airfoil and would therefore be expected to perform well for the considered geometry. The SST model was also originally designed for aeronautics applications. However it is not clear how these models are implemented in FLUENT so the above description is only relevant to the models presented in the publications stated.[53, 54]

Although this work is probably the most realistic representation of a PCB it should be noted that limited information has been published with regards to the experimental configuration therefore reconstruction of these models is not possible. One would naturally turn to Eveloy's[55] Ph.D. thesis for guidance but the work has been restricted from public access.

Further to the experimental data access limitations this work does not consider the mixture of low and high aspect ratio geometries which are frequently found within electronic systems. This is an important aspect for the current work.

Benchmark data from other fields of science may be relevant for electronics also from the point of view of turbulence. Examples include the low Reynolds number flow in steel making tundish containers,[56] the flow of air around buildings (especially low Reynolds number wind tunnel studies).[57]

2.2 Numerical Work

This section explores the numerical work which has been conducted on the relevant experimental configurations discussed in the previous section. This section identifies relevant turbulence models used to predict the cooling of electronic applications.

Most of the flow situations in the cooling of electronic products lie in the transitional regime. At present most of the community use turbulence models that are most suited to high

Reynolds numbers such as the standard $k - \varepsilon$ model. The use of these models results in errors in the predicted flow and turbulent viscosity fields, which both influence heat transfer. Other models such as Large Eddy Simulation (LES) have proved to be more accurate than the $k - \varepsilon$ model, but they require excessive computing time and resources – a serious limitation for the design engineer. Alternative low Reynolds number versions of the famous $k - \varepsilon$ model and the similar $k - \omega$ model have proved more successful in transitional flows, especially where the presence of many solid obstacles prevents the flow from developing fully. At present these models have not been seriously investigated for use in simulating electronic cooling.

The backward facing step configuration is a testing case study to assess the performance accuracy of turbulence models. Much numerical work has been done on this case study including that of Heyerichs and Pollard[58] who examine the performance of a range of $k - \varepsilon$ and $k - \omega$ type turbulence models and wall function implementations against the experimental work of Vogel and Eaton.[13] This paper concludes that from the range of turbulence models tested the Wilcox $k - \omega$[59, 60] model produced the most accurate results when compared against the experimental data. Later Wilcox[61] himself also reaches this conclusion from the smaller number of models he examined.

Menter[54, 62] concentrates further on variants of Wilcox's $k - \omega$ model and concludes that compared to the experimental work of Driver and Seegmiller[63] the $k - \omega$ based models all perform significantly better than the standard Launder and Spalding $k - \varepsilon$[64] model. The SST model was reported to predict the reattachment length most accurately. Menter's colleagues, Vieser et al.[65] draw similar conclusions for a study conducted later where an enhanced wall function treatment is applied.

Consistently Wilcox's $k - \omega$ model and the SST model have shown good agreement with the backward facing step configuration. Therefore both of these models will be investigated further in the current work.

Martinuzzi's high Reynolds number single cube configuration is a popular case; it has served as a reference dataset for the Workshop on Large Eddy Simulation of Flows Past Bluff Bodies held in Germany[66] and for the validation of numerical simulations at an ERCOFTAC workshop held at Delft University of Technology.[41]

The numerical work performed at the ERCOFTAC workshop was divided into five groups depending on the complexity of the turbulence model employed. The turbulence model range included standard high Reynolds number $k - \varepsilon$ with wall functions, low Reynolds number single- and two-layer $k - \varepsilon$ models, low Reynolds number $k - \omega$ and its variant SST, standard and modified Second-Moment (Reynolds-stress) Closure (SMC) with wall functions, low Reynolds number algebraic and differential SMC and LES solutions.

It was concluded that usually the standard $k - \varepsilon$ model predicts too small a recirculation in front of the cube and too large a separation region behind it. Surprisingly, the solutions presented showed the reattachment length behind the cube to be within reasonable accuracy of the experiments. The two-layer models produced marginal improvements of the flow pattern around the cube but with too large reattachment length behind the cube. In comparison the SST model predicted a much too long recirculation behind the cube. Generally the LES solutions were superior to the RANS models, especially in the wake of the cube, but it was reported that the simulation time for LES was around 600 times greater than for the RANS computations with wall functions.

Some interesting conclusions were drawn for this high Reynolds number test case by Breuer et al.[67] Comparisons were made between four RANS two-equation models and LES with two subgrid-scale models. In general the LES results compared better to the experiments than the RANS models. The standard $k - \varepsilon$ model and the ReNormalisation Group (RNG) predict poor separation results for the top face of the cube. Rodi's[68] two-layer model is the only RANS approach in better agreement with the experimental data for this face. The length of the recirculation region behind the cube is highly over predicted by all RANS models. Both LES solutions show better agreement with the measurements.

The more recent work conducted by Krajnović and Davidson[69, 70] also favours the LES approach for this configuration. They conclude that unsteadiness in the wake of the cube means that only transient models would be successful for such a case.

Based on the conclusions reached at the ERCOFTAC workshop and the observations of Breuer et al. the two-layer approach seems a sensible method to adopt for the current work since it keeps the advantages of the RANS models as they are much more cost effective in terms of run time than the unsteady LES approach.

Little published numerical work exists for Meinders single cube configuration. However as mentioned earlier the matrix of cubes has been used many times as a reference dataset for ERCOFTAC workshops and is considered to be well documented.

The key conclusions which emerged from the combined ERCOFTAC workshops were that Direct Numerical Simulation (DNS) and LES solutions for the velocity profiles were in excellent agreement with the experiments. The Reynolds stresses are also well predicted by these approaches.

As expected the steady-state RANS calculations were not as accurate as the time-dependent simulations. The RANS models predicted the streamwise mean velocity profiles reasonably well particularly in front of the cube, though inferior to DNS and LES. No conclusive difference in the quality of predictions by low and high Reynolds number RANS models was identified; this indicated the insensitivity of results to the near-wall treatment.

More recently Zhong and Tucker[71, 72] have conducted numerical studies on this matrix configuration for zonal RANS/LES turbulence models. These models apply the RANS model at the near-wall region and are proposed to circumvent the large expense of pure LES. Zhong and Tucker compare their proposed zonal model with the experimental data and the RANS predictions of Rautaheimo and Siikonen.[73] They conclude that the proposed hybrid RANS/LES scheme performs well, is effective at improving the predicted heat transfer from the cube and zonal results are comparable to the LES predictions.

Tucker has continued his interest in zonal RANS/LES turbulence models. Tucker and Davidson[74] published numerical work for the performance of zonal $k-l$ based RANS/LES approaches applied to plane and ribbed channel flows which have already been highlighted as relevant to electronic cooling applications.

The study concludes that for a periodic ribbed channel the zonal LES predictions are found to be significantly more accurate than those for an established two-equation RANS model and also LES. Although improvements are acknowledged by these time-accurate models in comparison to purely RANS-based models the computational expense is greatly increased. As commercial CFD code users in an industrial environment can not afford these increases in

computational time unfortunately these time-dependent models await further progress in computing power to allow simulation times to be comparable to those experienced by RANS-based simulations.

The conclusions reached by Zhong and Tucker, and Tucker and Davidson strengthen the argument that zonal turbulence modelling is an interesting area to further pursue as a compromise between pure single RANS models and the time intensive approaches of LES and DNS.

Eveloy et al.[48] have already identified a possible candidate model for electronic applications. From their experimental study which evaluates the predictive capability of turbulence models suited to the analysis of electronic component heat transfer the SST model agreed well with the gathered experimental data for a board containing a number of flat-pack type packages. The SST model has made its way into most industrial, commercial and many research-based CFD codes and therefore seems an interesting turbulence model to investigate.

Menter et al.[75] (originator of the SST model) have also developed a zonal model based on the Detached Eddy Simulation (DES) proposed by Spalart et al.[76] The SST-DES model has been shown to provide better flow recovery after an obstacle in comparison to the pure RANS SST model. However while an improved flow recovery could be computed with this zonal DES formulation due to the large computational expense incurred this approach, together with other such DES models, is not yet possible for electronic applications.

2.2.1 Summary of Recommended Turbulence Models

The LES approach is clearly the most favoured in the literature with regards to performance accuracy. However the increase in computational expense in comparison to RANS-based models is considered impractical for the constraints facing electronic design engineers using commercial CFD software tools. Therefore some form of alternative calculation method must be explored. From the relevant numerical work discussed in the previous section a range of RANS-based turbulence models relevant for electronic cooling applications can be determined for further investigation within the structure of the current work.

Wilcox's $k-\omega$ model and the SST model have been reported to agree well with the backward facing step configuration and they were found to be suitable for low Reynolds number flows.[56] Therefore both of these models will be investigated further in the current work.

Based on the conclusions reached at the ERCOFTAC workshop for Martinuzzi's single cube configuration and the observations of Breuer et al. the two-layer approach seems a reasonable method to investigate as an alternative to the fully time-dependent calculation procedures currently available. The conclusions drawn by Zhong and Tucker, and Tucker and Davidson regarding Meinders matrix configuration further reinforce the argument that zonal turbulence modelling is an attractive area to explore.

Eveloy et al. highlight the Spalart-Allmaras and SST models to be promising models for electronic applications. Therefore this has prompted the implementation of the SST model but not the Spalart-Allmaras model due to the ambiguous specification of the trip function. As noted by the original model developers:[77]

"The boundary layer is "tripped". We use this word to mean that transition in the real flow is imposed by an actual trip, or that it is natural but its location is known. On no account should the model be trusted to predict the transition location. The responsibility of choosing transition points rests with the user of this turbulence model, whether through an educated guess or a separate prediction method."

The specification of this user-defined trip point goes against the objectives of this research project i.e. a fully automated turbulence model, and will therefore not be discussed further. Note that a trip point was not prescribed in Eveloy's work and is not used within the FLUENT implementation.

2.2.2 Near-Wall Treatment

Wall functions are widely used in commercial CFD software tools as they offer a significant saving in computational expense compared to techniques which abandon the use of wall functions within the structure of their mathematical derivation e.g. low Reynolds number formulations.

The focus of the current research is to capture the bulk flow features, hence investigation of alternative wall function formulations is considered outside the scope of this work. Nevertheless some attention must be given to the application and development of wall functions. If not otherwise stated it has been assumed within the numerical work reviewed that the standard log-law wall functions have been applied as these have been most widely used for industrial flows. These assume that close to a solid wall the velocity and temperature profiles can be described by universal logarithmic profiles for these quantities. It is also assumed that in this region the turbulence is in a state of local equilibrium. This standard log-law wall function technique will be discussed in further detail in Chapter 4.

The limitations of the existing wall function approach were recognised from the earliest days of turbulent flow CFD. A number of attempts have been made to generalise wall functions for non-equilibrium flows. However these schemes did not even come close to the popularity of the standard log-law wall function approach adopted within commercial CFD codes. One of the first attempts was proposed by Launder and Spalding.[64] They suggested that the wall shear stress, τ_w, in the temperature log-law should be replaced by the turbulent kinetic energy, k.

The poor performance of wall functions were brought to the focus of researchers again in the 1990s by Heyerichs and Pollard[58] who compare the performance of six low Reynolds number turbulence models and three wall function treatments. No definitive conclusions about the superiority of any one wall function was made, expect for the general comment that wall functions are unsuitable for complex flows where the assumptions used in their derivation are not valid.

Recent developments in wall function strategies have been suggested by Craft et al.[78, 79, 80, 81] to circumvent the inabilities of existing wall function techniques. Craft argues that since existing wall functions are based on assumed near-wall profiles of velocity, turbulence parameters and temperature they are unsuitable for complex, non-equilibrium flows. Craft proposes that instead of assuming profiles for the dependent variables, these quantities should be determined by solving boundary-layer-type transport equations across an embedded grid situated within the near-wall cell.

While computational costs have been noted to increase by up to 60% in comparison to standard wall functions, Craft states that the results show a clear improvement in reproducing low Reynolds number predictions over standard wall function treatment. The new wall function method does not suffer from the slow convergence problems of a full low Reynolds number model treatment which requires a fine mesh near to the wall. Subgrid values of velocity, turbulence parameters and temperature are saved per iteration so the overall storage requirements of the new wall function are roughly equal to those of a full low Reynolds number model.

Utyuzhnikov[82, 83, 84] has also proposed improvements to the standard wall function method. He notes that the main disadvantage of the standard log-law wall functions is the dependence on the mesh point closest to a wall where the wall functions are applied; problems arise if the first cell adjacent to the wall is placed in the viscous sub-layer. Utyuzhnikov suggests that a method of boundary layer transfer is used.

It is noted that the current study employs the standard log-law wall functions as this approach is considered to be universally employed within the majority of commercial CFD software tools currently on the market. The implementation of the more complex wall functions mentioned within this literature review were considered to be outside the scope of the current work and will therefore not be expanded upon.

COMPUTATIONAL FLUID DYNAMICS

CFD software codes work by dividing the region of interest, the air flow over a heat dissipating electronic component or a car for example, into a large number of cells or control volumes. In each cell the Partial Differential Equations (PDEs) describing fluid flow (the Navier-Stokes equations) and temperature are discretised into algebraic equations that relate the pressure, velocity, temperature and other variables, such as species concentrations, to the values in the neighbouring cells. These equations are then solved numerically yielding a prediction of the transported quantities across the whole domain.

3.1 Conservation Principles

The motion of a fluid in three-dimensions is described by a system of five PDEs: mass conservation, x-, y-, and z-momentum equations and the energy equation.

The mass balance of a fluid element can be stated as:

Rate of increase of mass in fluid element = Net rate of flow of mass into fluid element

The conservation of mass, or continuity equation, in three-dimensional space is stated in equation (3.1) for a compressible fluid.

$$\frac{\partial \rho}{\partial t} + div(\rho \mathbf{u}) = 0 \qquad (3.1)$$

For an incompressible fluid equation (3.1) simply reduces to the form stated in equation (3.2) as the density is constant.

$$div\, \mathbf{u} = 0 \qquad (3.2)$$

The momentum equations are based on Newton's second law of motion which states:

Rate of increase of momentum of fluid particle = Sum of forces on fluid particle

The types of forces acting upon the fluid element are surface and body forces. Surface forces include pressure and viscous forces whereas body forces represent the gravity, electromagnetic forces etc. Within CFD calculations the surface forces are generally expressed as separate terms within the momentum equations whereas the body forces are incorporated within the momentum source terms.

The x-, y- and z-components of the momentum equation are found by setting the rate of change of x-, y- and z-momentum of the fluid particle equal to the total force in the x-, y-, and z-direction on the element due to surface stresses plus the rate of increase of x-, y- and z-momentum due to sources. The three components of the momentum equation have been stated in equations (3.3)-(3.5).

$$\rho \frac{Du}{Dt} = \frac{\partial\left(-p + \tau_{xx}\right)}{\partial x} + \frac{\partial \tau_{yx}}{\partial y} + \frac{\partial \tau_{zx}}{\partial y} + S_{Mx} \tag{3.3}$$

$$\rho \frac{Dv}{Dt} = \frac{\partial \tau_{xy}}{\partial x} + \frac{\partial\left(-p + \tau_{yy}\right)}{\partial y} + \frac{\partial \tau_{zy}}{\partial z} + S_{My} \tag{3.4}$$

$$\rho \frac{Dw}{Dt} = \frac{\partial \tau_{xz}}{\partial x} + \frac{\partial \tau_{yz}}{\partial y} + \frac{\partial\left(-p + \tau_{zz}\right)}{\partial z} + S_{Mz} \tag{3.5}$$

It is noted that if the value of a property per unit mass be denoted by ϕ then the substantial derivative of ϕ with respect to time is represented by $D\phi/Dt$ a definition of which is stated in equation (3.6).

$$\frac{D\phi}{Dt} = \frac{\partial \phi}{\partial t} + u\frac{\partial \phi}{\partial x} + v\frac{\partial \phi}{\partial y} + w\frac{\partial \phi}{\partial z} = \frac{\partial \phi}{\partial t} + \mathbf{u} \cdot grad\phi \tag{3.6}$$

The energy equation originates from the first law of thermodynamics which can be expressed as:

$$\begin{matrix} \textit{Rate of increase} & & \textit{Net rate of} & & \textit{Net rate of work} \\ \textit{of energy of} & = & \textit{heat added to} & + & \textit{done on} \\ \textit{fluid particle} & & \textit{fluid particle} & & \textit{fluid particle} \end{matrix}$$

The total rate of work done per unit volume on a fluid particle by surface stresses is stated in equation (3.7).

$$-div(p\mathbf{u}) + \left[\frac{\partial(u\tau_{xx})}{\partial x} + \frac{\partial(u\tau_{yx})}{\partial y} + \frac{\partial(u\tau_{zx})}{\partial z} + \frac{\partial(v\tau_{xy})}{\partial x} + \frac{\partial(v\tau_{yy})}{\partial y} \right.$$
$$\left. + \frac{\partial(v\tau_{zy})}{\partial z} + \frac{\partial(w\tau_{xz})}{\partial x} + \frac{\partial(w\tau_{yz})}{\partial y} + \frac{\partial(w\tau_{zz})}{\partial z} \right]$$

$$(3.7)$$

Fourier's law of heat conduction relates the heat flux to the local temperature gradient and has been used to define the rate of heat addition to the fluid particle due to heat conduction stated in the following expression:

$$div(k\ grad\ T)$$

$$(3.8)$$

The energy equation, stated in equation (3.9), can now be constructed by summing the net rate of work done on the fluid particle (3.7), the net rate of heat addition to the fluid (3.8) and the rate of increase of energy due to sources.

$$\rho \frac{DE}{Dt} = -div(p\mathbf{u}) + \left[\frac{\partial(u\tau_{xx})}{\partial x} + \frac{\partial(u\tau_{yx})}{\partial y} + \frac{\partial(u\tau_{zx})}{\partial z} + \frac{\partial(v\tau_{xy})}{\partial x} \right.$$
$$\left. + \frac{\partial(v\tau_{yy})}{\partial y} + \frac{\partial(v\tau_{zy})}{\partial z} + \frac{\partial(w\tau_{xz})}{\partial x} + \frac{\partial(w\tau_{yz})}{\partial y} + \frac{\partial(w\tau_{zz})}{\partial z} \right]$$
$$+ div(k\ grad\ T) + S_E$$

$$(3.9)$$

The specific energy E of a fluid is often defined as the sum of the internal energy i, kinetic energy $\frac{1}{2}(u^2 + v^2 + w^2)$ and gravitational potential energy. The gravitational force is regarded as a body force and can therefore be included within the source term.

Normally the energy equation is expressed in terms of the internal energy i or the temperature T. Equation (3.10) is the internal energy equation.

$$\rho \frac{Di}{Dt} = -p \ div \ \mathbf{u} + div\left(k \ grad \ T\right) + \tau_{xx}\frac{\partial u}{\partial x} + \tau_{yx}\frac{\partial u}{\partial y} + \tau_{zx}\frac{\partial u}{\partial z} + \tau_{xy}\frac{\partial v}{\partial x}$$
$$+ \tau_{yy}\frac{\partial v}{\partial y} + \tau_{zy}\frac{\partial v}{\partial z} + \tau_{xz}\frac{\partial w}{\partial x} + \tau_{yz}\frac{\partial w}{\partial y} + \tau_{zz}\frac{\partial w}{\partial z} + S_i$$

(3.10)

For the purposes of the current work the internal energy equation expressed in equation (3.10) is converted into the temperature equation for incompressible flow i.e. $div \ \mathbf{u} = 0$ using the relationship $i = C_p T$ and is stated in equation (3.11).

$$\rho \ C_p \frac{DT}{Dt} = div\left(k \ grad \ T\right) + \tau_{xx}\frac{\partial u}{\partial x} + \tau_{yx}\frac{\partial u}{\partial y} + \tau_{zx}\frac{\partial u}{\partial z} + \tau_{xy}\frac{\partial v}{\partial x}$$
$$+ \tau_{yy}\frac{\partial v}{\partial y} + \tau_{zy}\frac{\partial v}{\partial z} + \tau_{xz}\frac{\partial w}{\partial x} + \tau_{yz}\frac{\partial w}{\partial y} + \tau_{zz}\frac{\partial w}{\partial z} + S_i$$

(3.11)

3.1.1 Navier-Stokes Equations

The viscous stress components τ_{ij} which appear in the governing equations for momentum and energy transfer are unknown quantities. Using Newton's law of viscosity approximations can be made for the viscous stresses as a function of the local deformation rate, the nine viscous stress components are stated in equation (3.12) for incompressible fluids, hence $div \ \mathbf{u} = 0$.

$$\tau_{xx} = 2\mu\frac{\partial u}{\partial x} \quad \tau_{yy} = 2\mu\frac{\partial v}{\partial y} \quad \tau_{zz} = 2\mu\frac{\partial w}{\partial z}$$
$$\tau_{xy} = \tau_{yx} = \mu\left(\frac{\partial u}{\partial y} + \frac{\partial v}{\partial x}\right) \quad \tau_{xz} = \tau_{zx} = \mu\left(\frac{\partial u}{\partial z} + \frac{\partial w}{\partial x}\right) \quad \tau_{yz} = \tau_{zy} = \mu\left(\frac{\partial v}{\partial z} + \frac{\partial w}{\partial y}\right)$$

(3.12)

Substitution of equation (3.12) into the x-, y- and z-momentum equations (3.3), (3.4) and (3.5) respectively and the internal energy equation (3.10) and after some simplification leads to the Navier-Stokes equations (3.13)-(3.16) written in their most useful form for the development of the finite volume method.

$$\rho \frac{Du}{Dt} = -\frac{\partial p}{\partial x} + div\left(\mu\ grad\ u\right) + S_{Mx} \qquad (3.13)$$

$$\rho \frac{Dv}{Dt} = -\frac{\partial p}{\partial y} + div\left(\mu\ grad\ v\right) + S_{My} \qquad (3.14)$$

$$\rho \frac{Dw}{Dt} = -\frac{\partial p}{\partial z} + div\left(\mu\ grad\ w\right) + S_{Mz} \qquad (3.15)$$

$$\rho \frac{Di}{Dt} = -p\ div\ \mathbf{u} + div\left(k\ grad\ T\right) + \Phi + S_i \qquad (3.16)$$

The dissipation function, Φ stated in equation (3.17) for incompressible fluids, which appears in the internal energy equation represents all the effects due to the viscous stresses.

$$\Phi = \mu\left\{2\left[\left(\frac{\partial u}{\partial x}\right)^2 + \left(\frac{\partial v}{\partial y}\right)^2 + \left(\frac{\partial w}{\partial z}\right)^2\right] + \left(\frac{\partial u}{\partial y} + \frac{\partial v}{\partial x}\right)^2 \right.$$
$$\left. + \left(\frac{\partial u}{\partial z} + \frac{\partial w}{\partial x}\right)^2 + \left(\frac{\partial v}{\partial z} + \frac{\partial w}{\partial y}\right)^2\right\} \qquad (3.17)$$

An explanation of the derivation of both the conservation and Navier-Stokes equations can be found in Patankar[85] and more recently Versteeg and Malalasekera[86] as well as many texts related to the introduction to CFD and will therefore not be repeated here.

3.1.2 General Conservation Equation

All the dependent variables of interest obey a generalised conservation principle. If the dependent variable is denoted by ϕ, the general differential equation therefore takes the form of equation (3.18).

$$\frac{\partial(\rho\phi)}{\partial t} + div\left(\rho\phi\mathbf{u}\right) = div\left(\Gamma\ grad\ \phi\right) + S_\phi \qquad (3.18)$$

Transient term + Convection term = Diffusion term + Source term

The quantities of the diffusion coefficient, Γ, and the source term, S_ϕ, are specific to a particular definition of ϕ.

Noting that all the relevant differential equations for heat and mass transfer, fluid flow, turbulence and related phenomena can be thought of as variations of the general ϕ equation is an important time-saving step as now we need only concern ourselves with the numerical solution of equation (3.18). Hence CFD software developers need only write a general sequence of instructions for solving equation (3.18) for different meanings of ϕ along with appropriate expressions for Γ and S_ϕ, and suitable initial and/or boundary conditions.

The set of differential equations described by the general equation could, in theory, be solved for a given flow problem by using methods from calculus. However, in reality, these equations are too difficult to solve analytically. In the past engineers would make further approximations and simplifications to the equation set until they had a group of equations that could be solved. Nowadays high speed computers are used to solve approximations to the equations using a variety of techniques such as the finite difference, finite volume, finite element, and spectral methods. For the purposes of the current work the finite volume method will be adopted.

3.2 Discretisation Concept

The starting point for the numerical solution of the above general conservation equation is its transformation into a set of algebraic equations that can be solved easily using direct or iterative solvers. Consider the two dimensional mesh illustrated in Figure 3.1.
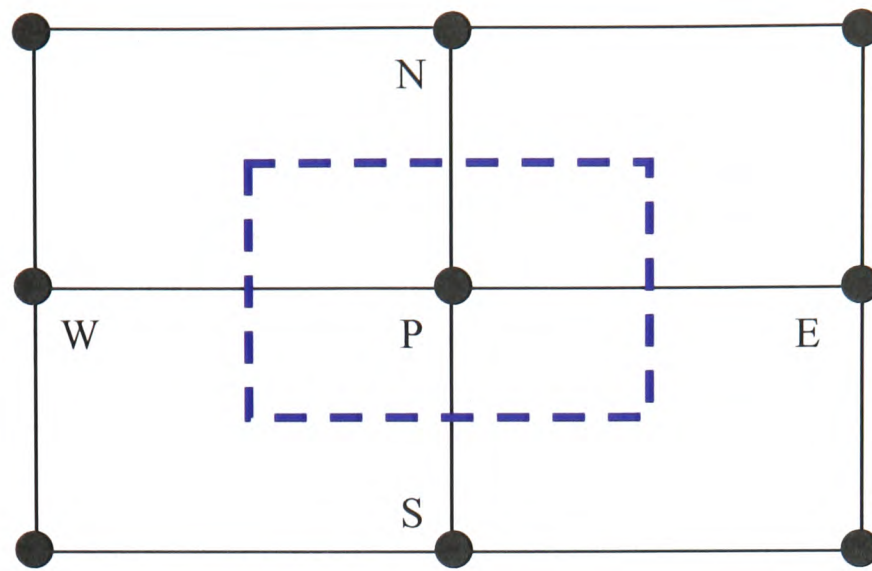
Figure 3.1 Control volume around point P showing neighbour nodes

Here we have a computational stencil containing five nodes P, N, E, S, and W. A control volume is established around node P and it is over this control volume that the general conservation equation is integrated. For given variables of velocity, pressure, mass, and temperature different formats of control volume can be set-up. These formats are dependent on the actual variable being solved and also on whether the computational mesh is structured or unstructured.

The first step in the discretisation process is to integrate the partial differential equation over the control volume for the variable being solved. The discretised general equation is given by:

$$\int_{CV} \frac{\partial(\rho\phi)}{\partial t} dV + \int_A \mathbf{n} \cdot (\rho\phi\mathbf{u}) \, dA = \int_A \mathbf{n} \cdot (\Gamma \, grad \, \phi) \, dA + \int_{CV} S_\phi \, dV \qquad (3.19)$$

Where CV is the control volume and A is the cross-sectional area of the control volume face. The velocity components and the outward normal vector to the boundary are given by $\mathbf{u}$ and $\mathbf{n}$. It is clear from the above integration that we need to approximate the convection and diffusion terms at the boundaries of the control volume and the transient and source terms across the whole control volume.

Numerous techniques can be used to approximate the above integrals depending on whether the mesh is structured or unstructured (see Patankar[85] and Versteeg and Malalasekera[86]). The final set of equations resulting from these approximations are represented by:

$$a_P \phi_P = \sum_{i=1}^{n} a_i \phi_i + S_\phi \qquad\qquad (3.20)$$

Where a_P and a_i are the coefficients containing the transient, convection and diffusion contributions. Suitable approximations and schemes are used for the convection (i.e. upwind, hybrid, etc) and diffusions (i.e. harmonic mean, etc). The term S_ϕ contains source term contributions which are dependent on the variable being solved. The above algebraic equations are suitable for solution by computers.

In CFD we have a set of algebraic equations for the velocity variables $(u, v \text{ and } w)$, the temperature (T) and mass continuity. These are highly coupled systems which are solved using numerical techniques such as the SIMPLE algorithm (see Patankar[85] and Versteeg and Malalasekera[86]).

It should be noted that for structured meshes the control volumes are staggered where the velocity control volumes are located differently to those used for pressure and temperature. For unstructured meshes the control volumes are co-located and techniques such as Rhie and Chow[87] are used to approximate fluxes at control volumes and this avoids the need for a staggered system.

In summary discretisation makes it possible to replace the governing partial differential equations with algebraic equations which can be solved numerically using computers.

3.3 Differencing Schemes for Convection

The purpose of a differencing scheme is to evaluate the face value of ϕ which is required to be substituted within the discretised transport equations.

The general form of a differencing scheme is expressed in equation (3.21)

$$\phi_{face} = \phi_{i-1} + 0.5B \left(\phi_{i-1} - \phi_{i-2} \right) \qquad\qquad (3.21)$$

where B is a function of r, defined in equation (3.22).

$$r = \frac{\left(\phi_i - \phi_{i-1}\right)}{\left(\phi_{i-1} - \phi_{i-2}\right)} \qquad (3.22)$$

For electronics cooling applications the differencing schemes used are generally first order accurate schemes which are both robust and stable and therefore do not significantly increase the computational effort.

3.3.1 First Order Upwind Scheme

This is the simplest numerical scheme where it is assumed that the value of ϕ at the face is the same as the cell centred value in the cell upstream of the face, illustrated in Figure 3.2. Using equations (3.21) and (3.22) it can be shown that $\phi_e = \phi_P$ given that $B(r) = 0$.
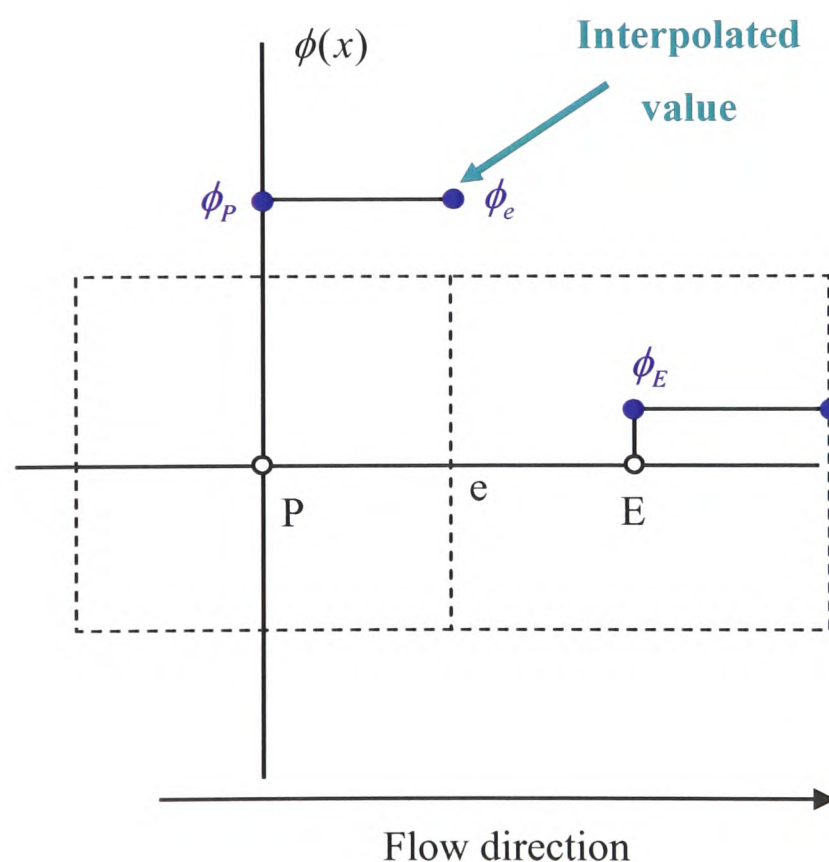
Figure 3.2 Upwind differencing scheme

The main advantages are that it is easy to implement and that it results in very stable calculations, but it's also very diffusive. Gradients in the flow field tend to be smeared out. However this is often the best scheme to start calculations with.

3.3.2 Central Differencing Scheme

The value of ϕ at the cell face is determined by linear interpolation between the cell centred values, illustrated in Figure 3.3. Using equations (3.21) and (3.22) it can be shown that $\phi_e = 0.5\phi_P + 0.5\phi_E$, given that $B(r) = r$. This scheme is more accurate than the first order upwind scheme, but leads to oscillations in the solution or divergence if the local Peclet number is greater than two. (see Patankar[85]).
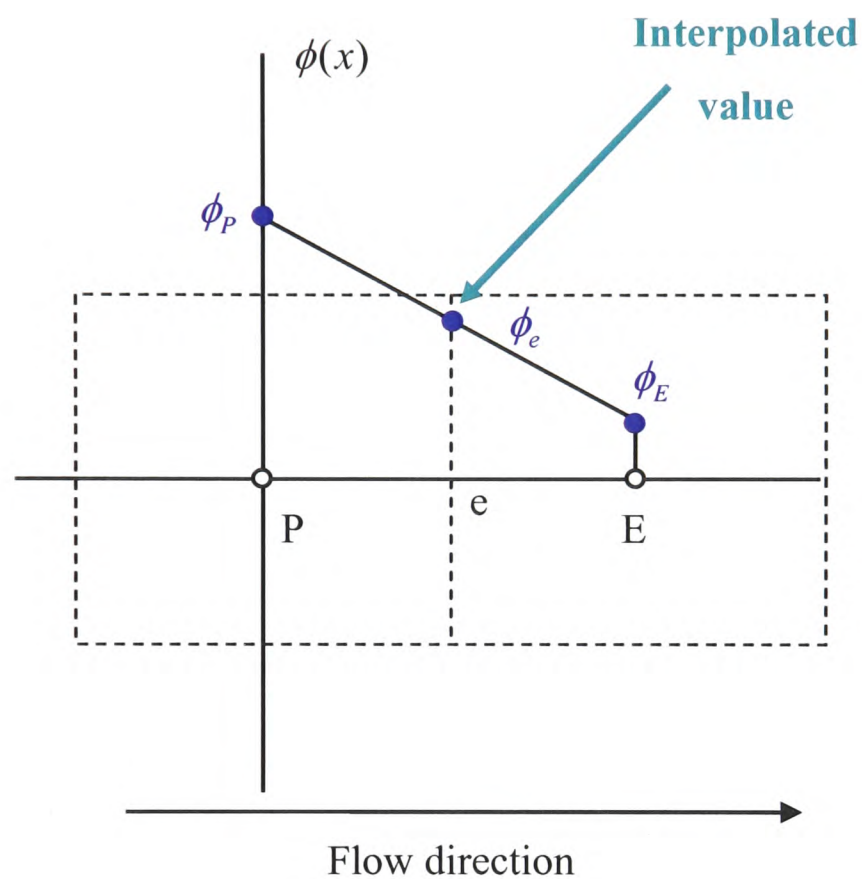
Figure 3.3 Central differencing scheme

The Peclet number is the ratio between convective and diffusive transport and has been defined in equation (3.23).

$$Pe = \frac{\rho u L C_p}{k} \qquad (3.23)$$

When the cell Peclet number is greater than two it is common to switch to the upwind scheme. Such an approach is termed the hybrid differencing scheme.

The accuracy of the upwind and hybrid schemes is only first order in terms of the Taylor series truncation error shown below. As these schemes only use the constant and ignore the first derivative and consecutive terms.

$$\phi(x_e) = \phi(x_P) + \frac{\phi'(x_P)}{1!}(x_e - x_P) + \frac{\phi''(x_P)}{2!}(x_e - x_P)^2 + ... + \frac{\phi^n(x_P)}{n!}(x_e - x_P)^n + ...$$

The use of upwind quantities ensures that these first order schemes are very stable but are prone to numerical diffusion errors which can only be minimised by considering higher order schemes. The second order accurate central differencing scheme, as an alternative to the first order schemes, trends to be unstable as the flow direction is not taken into account. Therefore higher order schemes which preserve upwinding for stability and account for the flow direction have also been developed.

3.3.3 QUICK Differencing Scheme

The higher order Quadratic Upwind Interpolation for Convective Kinetics (QUICK)[88] scheme fits a quadratic curve through two upstream nodes and one downstream node to determine the value of ϕ at the cell face, illustrated in Figure 3.4. Equations (3.21) and (3.22) can be shown to equate to equation (3.24) for the east face, given that $B(r) = 0.5\left[(1+K)r + (1-K)\right]$ where $K = 0.5$.

$$\phi_e = \frac{6}{8}\phi_P + \frac{3}{8}\phi_E - \frac{1}{8}\phi_W \tag{3.24}$$
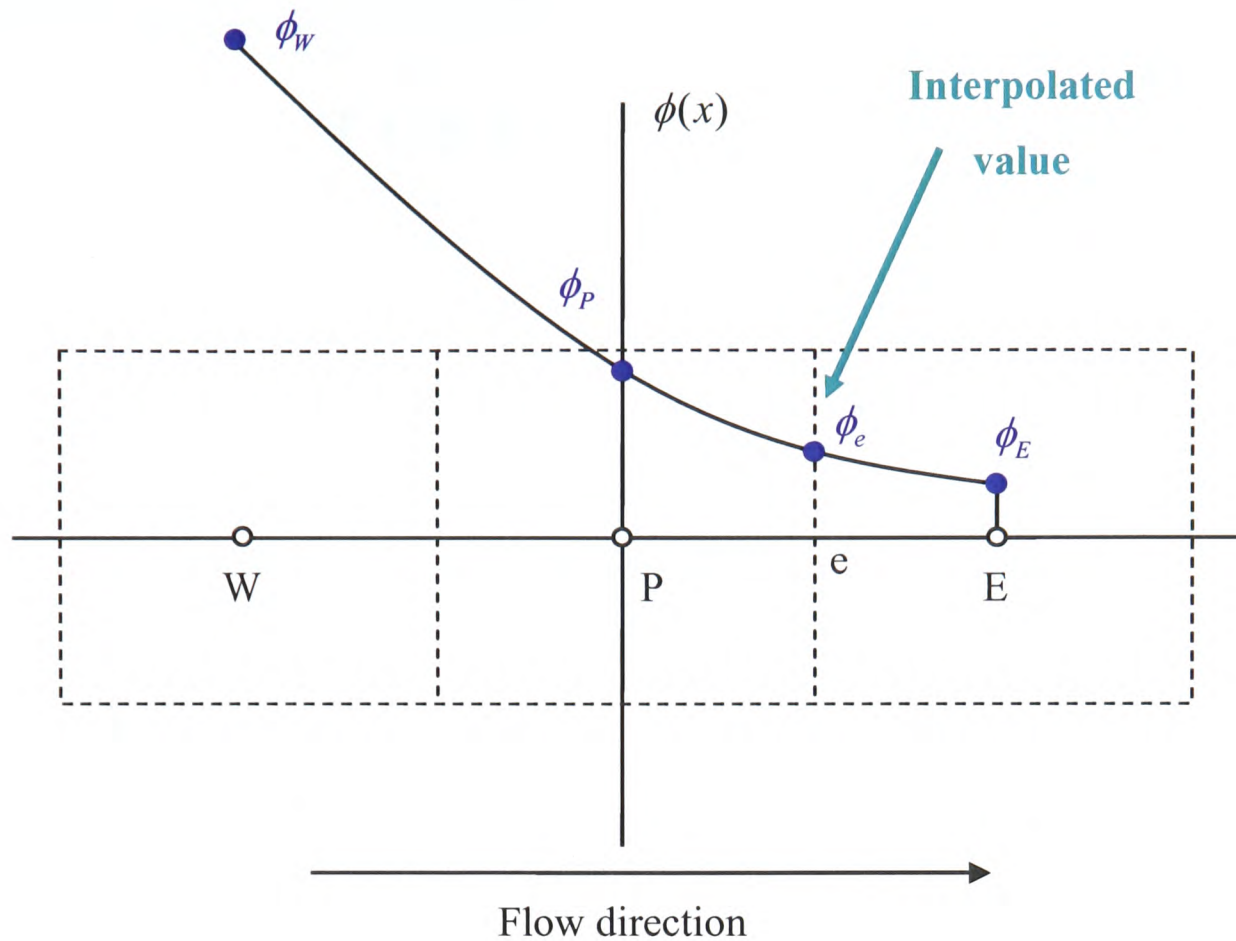
Figure 3.4 QUICK differencing scheme

QUICK does take the second order derivative of the Taylor series into account, but ignores the third order derivative. This scheme is then considered third order accurate. It is an accurate scheme, but in regions with strong gradients, overshoots and undershoots can occur. This can lead to stability problems in the calculation.

To help stabilise QUICK a bounded version is available, termed Sharp and Monotonic Algorithm for Realistic Transport (SMART).[89] The B function for this scheme is $B(r) = \max\left[0, \min\left(2r, 0.75r + 0.25, 4\right)\right]$.

Higher order schemes such as QUICK, SMART and Monotonic Upwind Scheme for Conservation Laws (MUSCL)[90] which approximate the face value of ϕ based upon a greater number of neighbour points reduce smearing and are considered to be outside the scope of the current work as they tend to experience poor convergence and are not as robust as the first order schemes.

TURBULENT FLOW MODELLING

Turbulence is one of the key issues in tackling engineering flow problems. As powerful computers and accurate numerical methods are now available for solving the flow equations, and since engineering flow applications nearly always involve turbulence effects, the reliability of CFD analysis depends increasingly on the performance of the turbulence models. From an industry perspective an ideal model should introduce the minimum amount of complexity while capturing the essence of the relevant physics. For turbulence models to be effective tools in general purpose CFD codes they must have a wide applicability, be accurate, simple and economical to run. There are a range of turbulence models currently available from the basic zero-equation model to more complex higher order models.

4.1 Theory of Turbulence: A Review

At high velocities fluids become unstable and break down into a highly chaotic state known as turbulence. Fully developed turbulent motion is characterised by entangled eddies of various sizes. The largest eddies break down into smaller eddies which, in succession, break down into even smaller eddies. This process is known as energy cascade and transfers kinetic energy from the mean flow to progressively smaller scales of motion. At the smallest scales (known as the Kolmogrov scales) of turbulent motion the kinetic energy is transformed to heat by means of viscous dissipation, thus turbulent flow is dissipative in nature. Furthermore if there is no continuous external source of energy to ensure the continued generation of the turbulent motion, the motion will eventually decay.

In the early 1500's Leonardo da Vinci had already realised that a bird flies according to mathematical principles and drew clearly the turbulent eddying motion of air generated by bird flight.

Reynolds studied turbulence experimentally in 1895 at Manchester University and observed that above a certain critical velocity, orderly water flow in a duct developed random

fluctuations. Over a hundred years later the ideas contained in his paper remain central to current turbulent research and are widely used in the study of practical flows.

The Reynolds number, stated in equation (4.1), is a dimensionless quantity used to determine if turbulence exists within a flow field. It is a measure of the relative importance of fluid inertia to viscous forces.

$$\mathrm{Re} = \frac{\rho U L}{\mu} \qquad (4.1)$$

The parameters U and L are characteristic speed and length scales for the flow respectively. The choice of U and L is somewhat arbitrary and there may not be single values that characterise all the important features of an entire flow field. A good choice for U and L is usually one that characterises the region showing the strongest shear flow, i.e. where viscous forces would be expected to have the most influence.

At low Reynolds numbers, any flow disturbances are damped out by viscosity; the more viscous the fluid, the more difficult for disturbances to grow. In contrast, if the inertial force is the strongest, disturbances can grow unchecked and the flow ceases to be smooth and enters a regime of chaotic motion, hence turbulent flow.

For smooth channel flows generally a Reynolds number significantly above 4000 is likely to be turbulent, while a Reynolds number below 2000 is classified as being under laminar flow conditions. The range between laminar and turbulent flow is termed the transitional region. The actual value of a critical Reynolds number that separates laminar and turbulent flow can vary widely depending on the nature of the surfaces bounding the flow and the magnitude of perturbations in the flow, further discussion on the transition from laminar to turbulent flow can be found in the work of Hinze[11] or Versteeg and Malalasekera[86] amongst others. Small disturbances associated with distortions in a laminar fluid flow will inevitably lead to turbulent conditions; these disturbances may originate from wall roughness for example.

Most flows of engineering interest are classified as turbulent. Examples include the flow of water in a stream or river becoming turbulent in regions where rocks and other obstructions are encountered, often forming "white water" rapids. Likewise, the water in the wake of a

speedboat and the air in the wakes left by airplanes and other moving vehicles also represent turbulent flow.

The current investigation concentrates on the flow over electronic components which can be classified as being in a state of transition between laminar and fully turbulent flow conditions due to the low velocities, small length scales and flow obstructions encountered. Commercially accessible general purpose CFD procedures often neglect transitional flow entirely and classify flows as either laminar or fully turbulent. Clearly the drawback of such an assumption means that modelling errors are likely to occur.

4.1.1 Turbulence Closure Problem

The origin of turbulence modelling is the Reynolds decomposition where it is assumed that all the quantities can be decomposed into a mean and a fluctuating part. Then, equations for the time-averaged part of these quantities are derived by substituting the decomposed form into the continuity and Navier-Stokes equations. As a consequence of averaging, six new unknown quantities (time-averaged products of fluctuating velocities known as Reynolds stresses) are introduced without adding any extra equations to balance the system. In order to close the equation set, a method for approximating these quantities is needed before any solution can be obtained. This problem is known as the turbulence closure problem.

To achieve closure, additional algebraic or differential relations are required. The type (algebraic or differential) and the number of auxiliary equations define the closure level. The set of mathematical equations which provide unknown quantities is called a turbulence closure model. The task of the turbulence model is to attempt to capture the effects of the Reynolds stresses on the flow behaviour.

Engineering calculation of turbulent flow involves the solution of a time-averaged system of equations that represent mean flow quantities; these equations use turbulence models. The RANS models investigated in this work include the effects of the Reynolds stresses through a turbulent viscosity which therefore treats the turbulence as isotropic. In summary these RANS models calculate a turbulent viscosity which couples with the momentum equations through the diffusion term. For example in the general transport equation for momentum the diffusion coefficient is given by:

$$\Gamma = \rho\left(v_l + v_t\right) \qquad\qquad (4.2)$$

Where v_l and v_t are the kinematic laminar and turbulent viscosities. The challenge is the calculation of the kinematic turbulent viscosity.

4.1.2 Turbulent Boundary Layer Flows

One can think of a boundary layer in terms of an airplane moving through air were the physical body of the plane is covered with a film of air which is continuously dragged along as the plane is in flight. A submarine also experiences a similar blanket, only thicker because of the submarine's lower speed in a fluid more viscous than air. The blanket region is where the shear stresses exist; outside this layer the shear stresses are negligible. For electronic applications it is important to understand the boundary layer concept as its presence greatly affects the flow around an obstacle and the majority of the heat transfer from a component to the air occurs within the boundary layers formed on its surfaces.

The boundary layer concept was proposed in 1904 by Prandtl. He hypothesized that the effects of fluid friction at high Reynolds numbers are limited to a narrow region near the boundary of a body. Thus, close to a body in the boundary layer is where the shear stresses exert an increasingly larger effect on the fluid as the solid boundary is approached due to the increasing velocity gradient $\partial u/\partial y$ as $y \rightarrow 0$. But outside the boundary layer where the effect of the shear stresses on the flow is small compared to values inside the boundary layer (since the velocity gradient $\partial u/\partial y$ is negligible), the fluid particles experience no vorticity, and the flow is similar to potential flow.

The development of the velocity boundary layer on a flat plate is shown in Figure 4.1. The thickness of the boundary layer, δ, is arbitrarily taken as the distance away from the surface where the velocity reaches 99% of the free stream velocity. The boundary layer thickness increases with distance from the leading edge of the body, the flat plate in this case, until its maximum is reached in fully developed flow.

Graph of velocity u against distance y from
the surface at point X (gradient $\partial u / \partial y$)
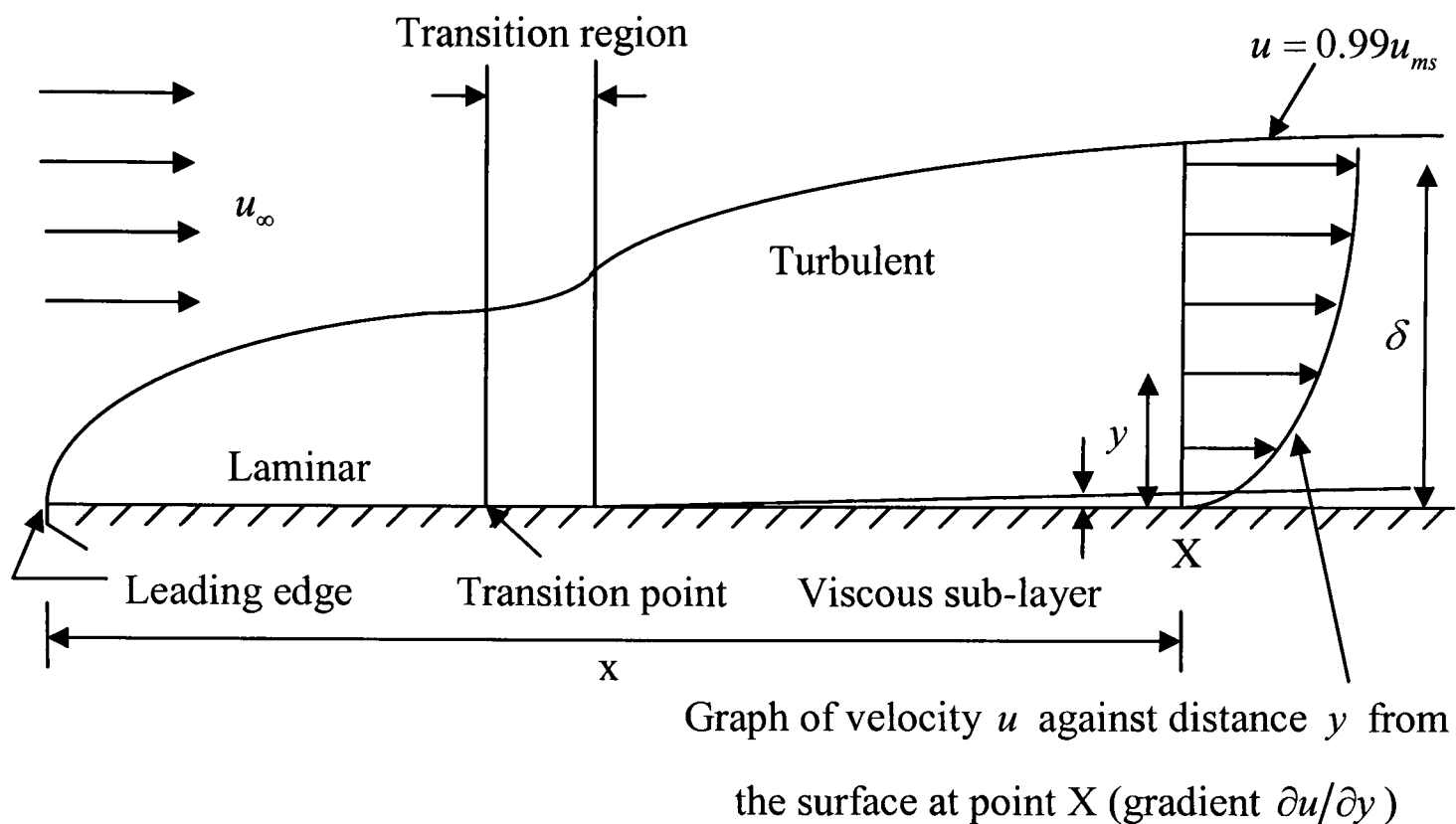
Figure 4.1 Boundary layer development

Within the laminar region the viscous shear stresses hold the fluid particles in steady layers. The viscous stress becomes small as the boundary layer increases in thickness and the velocity gradient gets smaller. Eventually they are no longer able to hold the flow in layers and the fluid starts to experience instabilities, this is the onset of the transition region. The instabilities cause the fluid to rotate and soon after fully turbulent motion is detected.

Fluid from the fast-moving free stream moves the slower fluid in the boundary layer transferring momentum and thus maintaining the fluid at the boundary in motion. Conversely, the slow moving boundary layer fluid tends towards the faster free stream fluid which has the effect of slowing down the overall flow in the domain. The net effect is an increase in momentum in the boundary layer.

At points very close to the boundary the velocity gradients become very large with the viscous shear forces again becoming large enough to maintain the fluid in a laminar flow status. This region is identified as the viscous sub-layer and occurs within the turbulent region. The layer is very thin – a few hundredths of a mm.

For a more detailed account of boundary layer flow phenomena the reader is referred to the works of Schlichting[91] and Hinze.[11]

4.2 Brief History of Turbulence Modelling

The derivation of the time-averaged Navier-Stokes equations dates back to the late 19th century when Reynolds[92] published conclusions from his research on turbulence. However the earliest attempt that was made at developing a mathematical description of the turbulent stresses, which is the core of the closure problem, was performed by Boussinesq[93] with the introduction of the eddy viscosity concept.

Much of the physics of viscous flows was a mystery in the 19th century, and further progress waited Prandtl's discovery of the boundary layer in 1904. Focusing upon turbulent flows, Prandtl[94] introduced the concept of the mixing-length model, referred to as an algebraic model, which prescribes an algebraic relation for the turbulent stresses. The mixing-length hypothesis, closely related to the eddy-viscosity concept, formed the basis of virtually all turbulence modelling research for the next twenty years.

To develop a more realistic mathematical model of the turbulent stresses Prandtl[95] later introduced the first one-equation model by proposing that the eddy viscosity depends on the turbulent kinetic energy. This one-equation model improved the turbulence predictions by taking into account the effects of flow history; however the problem of specifying a turbulent length scale still remained. Turbulence models that do not include a length scale are mathematically considered to be incomplete.

The length scale, which can be thought of as a characteristic scale of the turbulent eddies, changes for different flows, and thus is required for a complete description of turbulence. A more complete model would be one that can be applied to a given turbulent flow by prescribing boundary and/or initial conditions. Kolmogorov[96] introduced the first complete turbulence model, by modelling the turbulence kinetic energy, k, and introducing a second parameter w that he referred to as the rate of dissipation of energy per unit volume and per unit time. Due to the complexity of the mathematics involved, which required the solution of non-linear differential equations, the model remained virtually unused for many years.

Rotta[97] pioneered the use of the Boussinesq approximation in turbulence models to solve for the Reynolds stresses. This approach is termed a second-order or second-moment closure. Such models naturally incorporate non-local and history effects, such as streamline curvature

and body forces. For a three-dimensional flow, these second-order closure models introduce seven equations, one for a turbulence length scale, and six for the Reynolds stresses.

By the early 1950's four main categories of turbulence models had been developed:

- Zero-Equation (Algebraic) Models
- One-Equation Models
- Two-Equation Models
- Second-Order Closure Models

With the increase of computer capabilities since the early 1960's and measurement techniques, further development of all four of these classes of turbulence models has occurred, while algebraic and two-equation models have received the most attention and met with the most success in practical applications.

4.3 Classification of Turbulence Models

The intention of any eddy-viscosity model is to portray the association between the eddy viscosity and physically tangible flow quantities. The RANS-based models can be categorised depending on the level of complexity of the model:

- Zero-equation model:

  Algebraic equations are used to describe the relationship between the eddy viscosity and the flow quantities. Only the Navier-Stokes equations and no extra turbulence differential equations are used.

- One-equation model:

  An extra partial differential transport equation is solved which models the turbulent kinetic energy.

- Two-equation model:

  Two extra PDEs, one differential equation modelling the turbulence velocity scale and a second modelling the turbulence length scale are solved.

- Stress equation models:

  Models involving differential equations for all components of the Reynolds stress tensor and a length scale are solved.

By definition, an n-equation model signifies a model that requires solution of n additional differential transport equations in addition to those expressing conservation of mass, momentum and energy for the mean flow.

In addition to the RANS models discussed, alternative methods of turbulence modelling can be used but at the expense of substantially increasing both the computational solution time and the data storage requirement. These are:

- Large Eddy Simulation (LES):

  Originally implemented in the 1970's by atmospheric scientists to study the weather. This technique directly computes the large, energy-containing eddies, while the remaining smaller eddies are modelled, using a subgrid-scale (SGS) model. Filtering of the Navier-Stokes equations to separate those scales which will be modelled from those which will be solved directly is required.

- Direct Numerical Simulation (DNS):

  Method attempts to solve all time and spatial scales. As a result the solution obtained is of high numerical accuracy. The computational mesh density would need to be extremely fine, resulting in an extraordinarily long time to solve with today's technology.

Figure 4.2 illustrates the computational expense associated with the turbulence modelling techniques mentioned.
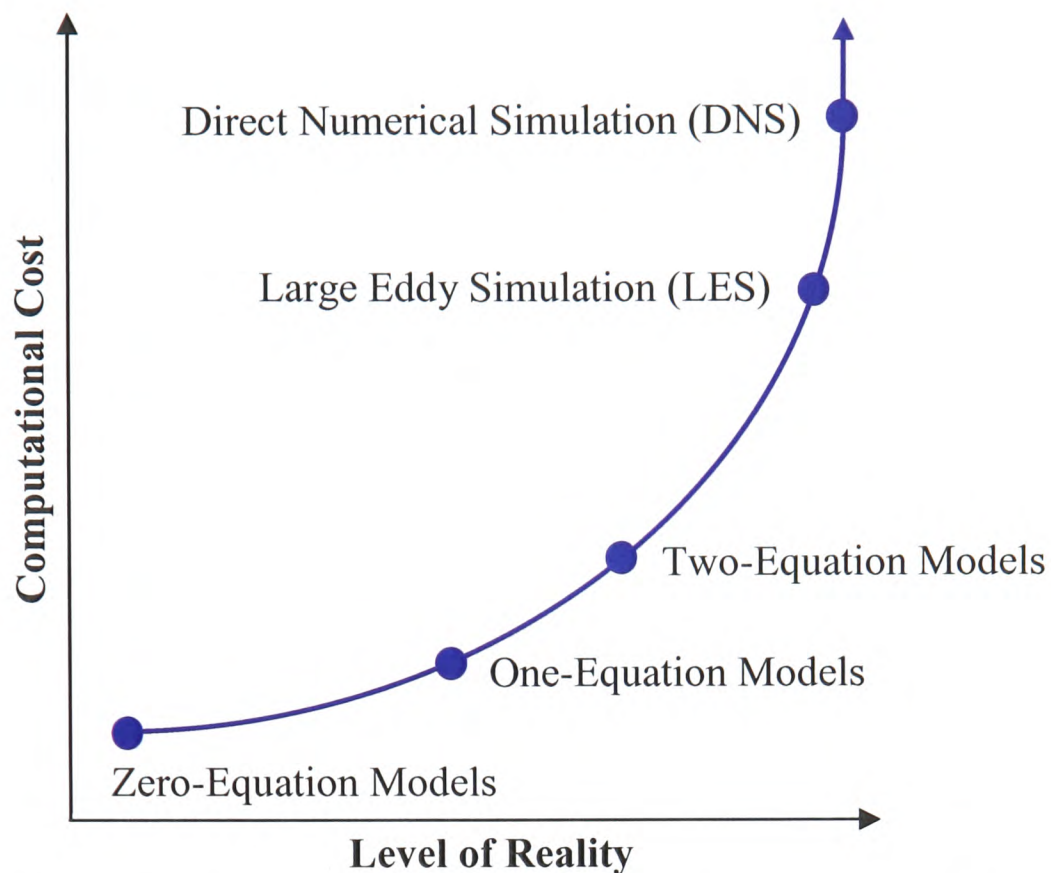
Figure 4.2 Illustration of increasing computational cost dependent on turbulence model technique employed

Traditionally CFD simulations would employ RANS models to predict the turbulent phenomena taking place within the solution domain. RANS-based turbulence models have always been extremely popular within commercial CFD codes for their cost-effectiveness and reasonable accuracy for a wide class of flows. Under certain conditions this method can be very accurate; however it is not suitable for transient flows, because the averaging process eliminates most of the important characteristics of a time-dependent solution. Commercial CFD code vendors are now seeking alternative means of modelling turbulent phenomena but not at the expense of significantly increasing the computational time and storage capacity as electronic thermal design engineers still require the tool to be usable within an industrial environment where product lead times are continuingly being reduced.

Zonal models are fast becoming an attractive alternative to the inaccuracies of a single RANS model and the computational expense of LES and DNS techniques. The sophistication of zonal models is that, without user interaction, an appropriate turbulence model is selected depending on the phenomena taken place within the system environment. Hence near a wall boundary a turbulence model would be employed which is known to predict well for wall bounded flows and as the bulk flow is approached a second model would be activated. Both purely RANS-based and RANS/LES, termed Detached Eddy Simulation (DES), zonal models are currently available. The area of zonal turbulence modelling will be discussed in Chapter 8.

Discussion will now be turned to particular RANS-based turbulence models. It is noted that this text is by no means a complete catalogue of all currently available turbulence models. Full detail on each turbulence model has only been provided for those models which have been selected for further analysis within the structure of this work. The reader is directed to the references provided for all other models mentioned.

4.4 Zero-Equation Models

Zero-equation turbulence models are the least computationally demanding and can be appropriate for situations which deal with fairly simple geometry and flow characteristics. Unfortunately this class of model does not give accurate results if there is considerable flow separation or recirculation. Nevertheless the mixing-length model has been extensively applied throughout turbulence theory and has been very successful in describing the turbulent transport features in homogeneous, incompressible flows.

Examples of zero-equation models include the LVEL[98] model derived from Prandtl's mixing-length hypothesis. This model has long been considered as a candidate model for the fast-paced electronics industry as wall effects dominate the turbulence in these cluttered geometries. The mixing-length can be specified by simple empirical formulae. The key advantage of this model is its economy in terms of computing resources.

Further examples include Van Driest[99] who derived a viscous damping correction for the mixing-length model. Cebeci and Smith[100] refined the eddy viscosity/mixing-length concept for better use with attached boundary layers. Baldwin and Lomax[101] proposed an alternative algebraic model to eliminate some of the difficulty in defining a turbulence length scale from the shear-layer thickness. The Cebeci and Smith and the Baldwin and Lomax models are frequently used for aerodynamics and computing the flow around airfoils, aeroplanes etc. as these models often produce good results. However when dealing with complex three-dimensional flows including separation these models are probably not that suitable.

Three zero-equation turbulence models have been implemented within the structure of this work: LVEL, LVEL_CAP and the newly formulated AUTO_CAP. Each of these models will

be discussed in greater detail below. All of these models were implemented within the University of Greenwich code PHYSICA V2.12.[3]

4.4.1 LVEL Turbulence Model

The term LVEL originates from this particular model only requiring the distance from the nearest wall (L), the local velocity (VEL) and the laminar viscosity to calculate the effective viscosity.

The model computes a length scale, varying from point to point, based on distance from objects in the computational domain. This scale, together with the locally computed velocity is used to calculate the turbulent viscosity.

The implementation of the LVEL model within PHYSICA V2.12 is identical to the so-called Automatic Algebraic turbulence model available within FLOTHERM V3.2.

Firstly an approximate wall distance field must be computed. This is achieved by the solution of Poisson's equation given by equation (4.3) with $\phi = 0$ at solid-fluid boundaries.

$$\nabla^2 \phi = -1 \qquad (4.3)$$

A maximum local length scale, D, is calculated which is used to compute the local distance to the nearest wall, L.

$$D = \sqrt{\left|\nabla\phi\right|^2 + 2\phi} \qquad (4.4)$$

$$L = D - \left|\nabla\phi\right| \qquad (4.5)$$

Hence in the limit as the wall is approached L tends to the exact distance.

Once the laminar dynamic viscosity is obtained a field of local Reynolds numbers are calculated using L and the local velocity V.

$$\text{Re} = \frac{\rho V L}{\mu_l} \qquad (4.6)$$

Using the relationship $\text{Re} = u^+ y^+$ together with the following representation of the universal law of the wall $u^+ = \min\left(y^+, \frac{1}{\kappa}\ln\left(Ey^+\right)\right)$ a y^+ field is calculated using an iteration process which is detailed later.

$$\begin{array}{cc} \textit{Lam.} & \textit{Turb.} \end{array}$$
$$u^+ = \min\left(\frac{\tanh\left(\alpha y^+\right)}{\alpha}, \frac{1}{\kappa}\ln\left(Ey^+\right)\right) \qquad (4.7)$$

If the first argument in equation (4.7) is selected for u^+ then

$$u^+ = \frac{\tanh\left(\alpha y^+\right)}{\alpha}$$
$$\frac{dy^+}{du^+} = (\cosh[\alpha y^+])^2 \qquad (4.8)$$

Else the second argument must be selected for u^+

$$u^+ = \frac{1}{\kappa}\ln\left(Ey^+\right) \rightarrow u^+ = \frac{1}{\kappa}\left(\ln\left(E\right) + \ln\left(y^+\right)\right)$$
$$\frac{du^+}{dy^+} = \frac{1}{\kappa}\left(0.0 + \frac{1}{y^+}\right)$$
$$\frac{du^+}{dy^+} = \frac{1}{\kappa y^+} \qquad (4.9)$$
$$\frac{dy^+}{du^+} = \kappa y^+$$

The dimensionless effective viscosity ν^+ can now be found to determine if the flow is in the laminar or turbulent regime

$$y^+ \leq 23.9522 \quad \text{then} \quad v^+ = (\cosh[\alpha y^+])^2$$
$$y^+ > 23.9522 \quad \text{then} \quad v^+ = \kappa y^+ \qquad\qquad (4.10)$$
$$\alpha = 0.0769251$$

Finally the turbulent dynamic viscosity is calculated as stated in equation (4.11)

$$\mu_t = \mu_l \left(v^+ - 1.0 \right) \qquad\qquad (4.11)$$

The iteration process used to determine y^+ is discussed in more detail, where the initial guess for y^+ is taken to be the $\sqrt{\text{Re}}$.

DO (N = 1, 20)

    IF ($y^+ < 23.9522$)

$$u_{new}^+ = \frac{\tanh[\alpha y^+]}{\alpha}$$

    ELSE

$$u_{new}^+ = \frac{\ln[Ey^+]}{\kappa}$$

    END IF

$$y_{previous}^+ = y^+$$

$$y_{new}^+ = \frac{\text{Re}}{u_{new}^+}$$

$$y^+ = \frac{(y_{new}^+ + y_{previous}^+)}{2}$$

END DO

It is noted that the von-Karman constant, κ, is set to 0.435, E is an integration constant that depends on the roughness of the wall. For smooth walls with constant shear stress E has the value 9.0. The remaining model constants used above are those used in FLOTHERM V3.2.

Further model details can be found in Dyson.[102, 103]

4.4.2 LVEL_CAP Turbulence Model

The LVEL_CAP turbulence model calculates a single value for the turbulent viscosity based on a user-specified velocity and length scale, but allows the value to vary according to the log-law of the wall for any cells close to solid surfaces.

Model derivation is identical to the LVEL model previously discussed, but in this case an upper bound constrains the turbulent viscosity. This upper bound is:

$$\mu_{t-\max} = 0.01 \rho L V \qquad (4.12)$$

The model constant used in equation (4.12) was determined to produce the correct pressure drop down a channel.

The recommendations[7] for setting the above constants L and V for channel flow cases are:

$$L = \frac{1}{6} \text{ of channel width}$$

$$V = \text{ average inlet velocity}$$

4.4.3 Automatic Cap – Dimensionless Length Technique

The current drawback of the implemented LVEL_CAP, termed Revised Algebraic in the commercial CFD software Flotherm V3.2/4.1[1] is that the user is required to define the local length and velocity scales, therefore introducing questionable parameters into the CFD predictions. The dimensionless length technique has been proposed by the author to solve such a problem.

Using the maximum local length scale, D, and local distance to the nearest wall, L, which was computed from the original LVEL model a field of the dimensionless wall distance is calculated using (4.13).

$$L^+ = \frac{L}{D} \qquad (4.13)$$

A form of volume averaging, $\bar{V}$, is performed to determine an appropriate value for the velocity scale based on equation (4.14).

$$\left|\bar{V}\right| = \frac{\sum\limits_{i=1}^{n} Vol \cdot \left|V\right|}{\sum\limits_{i=1}^{n} Vol} \qquad (4.14)$$

Due to the recommendations stated for channel flow configurations a value for the length scale is obtained from equation (4.15).

$$L_{val} = \frac{\max(L)}{3.0} \qquad (4.15)$$

Finally the maximum limit, or cap for the model can be calculated as stated in equation (4.16).

$$\mu_{t\_\max} = 0.01\rho L_{val}\left|\bar{V}\right| \qquad (4.16)$$

The cap is only applied if $L^+ > L_{crit}^+$. The critical length, L_{crit}^+, will require an investigation process to determine which value is best suited to electronic applications. This is discussed in Chapter 6.

4.4.4 Performance of Zero-Equation Models

All the models discussed here are based on the mixing-length hypothesis which works well for comparatively simple flows such as thin shear-layer flows, wall boundary-layer flows, jets and wake flows, because the mixing-length can be specified by simple empirical formulas in such situations. However the models do not account for the transport and history effects of turbulence. In particular, these models are not suitable when processes of convection or diffusive transport of turbulence are significant – such as in rapidly developing flows. More generally, these models are often difficult to apply in complex flows because of the difficulties in specifying the mixing-length in these circumstances.

Advantages:

- Prandtl's mixing-length hypothesis is well established.

- Simple to implement as no additional differential equations must be solved.

- Computationally inexpensive and easily applied to three-dimensional problems, it has therefore been recommended for electronics cooling applications.

- Particularly suitable for flows with many obstacles, where mesh density is insufficient to resolve velocity profiles accurately for gradient-based models.

- Resulting from the large number of objects which may be present in the solution domain, this means that it is often necessary to represent the gaps between the objects with very few mesh intervals. In these circumstances the employment of methods which require the accurate computation of the velocity gradients for instance cannot be justified.

- Good quality predictions obtained for thin shear layers, boundary layer flows, jets and wake flows. This is due to the small variation of the mixing-length across the layer width so that the velocity profiles can be moderately well predicted.

- Although mixing-length models are not of great use close to a wall, unless modified in the manner suggested by Van Driest,[99] the processes occurring there can often be handled adequately by use of an empirically-based wall function.

Disadvantages:

- Prandtl's mixing-length model implies that the local level of turbulence depends only upon the local generation and dissipation rates, but in reality turbulence may be carried or diffused to locations where no turbulence is actually being generated at all. The model can not represent this.

- Completely incapable of estimating the distribution of the mixing-length magnitudes with acceptable accuracy for flows which deal with separation and recirculation.

- Distance from the nearest solid wall is to be evaluated for every point in the calculation field.

- The mixing-length models lack generality as they are difficult to apply to complex flows.

4.5 One-Equation Models

One-equation models employ a much simpler modelling approach than two-equation or second-order closure models, however they have been to some extent unpopular and have not showed a great deal of success, except for specific applications such as aerofoil cases.

One conceptual advance made by moving from a purely algebraic mixing-length model to a one-equation model is that the latter permits one model parameter to vary throughout the flow (usually the kinetic energy of turbulence, k), being governed by a PDE of its own. In most one-equation models, a length parameter still appears but is generally evaluated by an algebraic expression dependent upon only local flow parameters.

The one-equation models of Baldwin-Barth[104] and Spalart-Allmaras[53] have provided greater agreement with experimental data for some separated flows than has generally been possible with algebraic models. The Baldwin-Barth model includes seven closure coefficients and three empirical damping functions. The Spalart-Allmaras model includes eight closure coefficients and three empirical damping functions. The large number of empirical constants limits the generality of these models.

On the whole, however, the performance of the majority of one-equation models (for both incompressible and compressible flows) has been disappointing, in that relatively few cases have been observed in which these models offer an improvement over the predictions of the algebraic models.

Generally speaking, one-equation turbulence models have not been used to any great extent as stand alone models for electronics applications as these would not be expected to work well for the highly recirculating flows usually encountered in electronic systems. One-equation models have been more frequently seen as a branch of zonal model formulations such as Rodi's $k - \varepsilon / k - l$ model[68] and the Chen and Patel turbulence model.[105]

Model equations will be provided for the one-equation turbulence models of Wolfshtein[106] and Norris and Reynolds.[107] These models have been incorporated within zonal models in the past and have therefore been selected for implementation into PHYSICA.

4.5.1 Wolfshtein Turbulence Model

Wolfshtein reports that the influence of turbulence on the flow at near-wall regions within a one-dimensional framework, when the fluid's condition at any point can be expressed as a function related to the distance from the wall only, is an important stage in the development of solution procedures for two-dimensional turbulent flows. This importance stems from two key features associated with the mathematically simpler one-dimensional structure. Firstly it is considered easier to formulate turbulent viscosity hypotheses and compare their implications with experimental data. Secondly because substantial computing time can be saved in the computation of two-dimensional flows if one-dimensional solutions are employed for near wall cells where, due to the existence of a boundary-layer, a large number of mesh points would otherwise be necessary.

The structure of the model comprises of a single transport equation for the turbulent kinetic energy and then applies empirical functions to describe the turbulent mixing and dissipation lengths. A number of modifications have been suggested for the empirical functions used, which are discussed later.

$$\frac{\partial \rho k}{\partial t} + div(\rho \underline{u} k) = div\left(\left(\mu_l + \frac{\rho v_t}{\sigma_k}\right) grad\ k\right) + \rho v_t G - \rho \varepsilon \qquad (4.17)$$

$$\varepsilon = \frac{C_\mu^{3/4} k^{3/2}}{l_\varepsilon} \qquad (4.18)$$

$$v_t = C_\mu^{1/4} k^{1/2} l_\mu \tag{4.19}$$

The turbulent mixing-length, l_μ, and the dissipation length, l_ε, are specified algebraically as stated in equations (4.20) and (4.21) respectively.

$$l_\mu = \kappa L \left(1 - \exp^{-0.016 y^*}\right) \tag{4.20}$$

$$l_\varepsilon = \kappa L \left(1 - \exp^{-0.263 y^*}\right) \tag{4.21}$$

4.5.2 Norris and Reynolds Turbulence Model

The one-equation Norris and Reynolds[107] turbulence model formulated in 1975 is one such modification to the empirical functions used in the Wolfshtein model discussed above.

Here the algebraic expressions used to represent the turbulent mixing and dissipation lengths are altered to the equations specified below.

$$l_\mu = \kappa L \left(1 - \exp^{-0.0198 y^*}\right) \tag{4.22}$$

$$l_\varepsilon = \kappa L \frac{y^*}{y^* + 2\kappa / C_\mu^{3/4}} \tag{4.23}$$

After the development of the model in the early 1970's it remained predominately redundant until Rodi[68] made use of the empirical functions as part of a two-layer zonal model approach in 1991.

4.5.3 Performance of One-Equation Models

In general, one-equation models do have a reduced need for model adjustment from case to case compared to mixing-length models. However the improvement in prediction accuracy would not be considered significant.

There has been some renewed interest in one-equation models over the past several years due to the ease with which they can be solved numerically, relative to more complex two-equation or second-order closure models.

Advantages:

- Compared to the zero-equation turbulence model category the one-equation models are more realistic as one model parameter can vary throughout the flow.

- Greater agreement with experimental data is noted with one-equation models for some separated flows than has generally been possible with the algebraic models.

- For Wolfshtein's low Reynolds number model the number of closure coefficients is actually fewer than the zero-equation Baldwin-Lomax model. Hence Wolfshtein's model can be considered to be simpler than the zero-equation Baldwin-Lomax model.

- Spalart-Allmaras model is highlighted in the literature[60] as offering improved results compared to zero-equation models. However model disadvantages exist, as discussed below.

- Spalart-Allmaras predictions are satisfactory for many engineering applications. It is especially attractive for airfoil and wing applications, for which it has been originally designed.

Disadvantages:

- One-equation models are considered to be incomplete as the turbulent length scale is still an algebraic quantity. There is no transport of length scales in a flow.

- Most one-equation models require recalibration of the length scale for each new application.

- The majority of one-equation models don't offer much improvement over algebraic models.

- They are computationally more expensive than zero-equation models.

- One-equation models are often criticised for their inability to rapidly accommodate changes in the length scale, as might be necessary when the flow changes abruptly from a wall-bounded to a free shear flow.

- The Spalart-Allmaras model requires a user-defined trip point. This has already been discussed in Chapter 2.

- The Spalart-Allmaras model is inappropriate for applications involving jet-like free shear regions.

- The Baldwin-Barth model is extremely sensitive to free stream conditions. The model developers themselves warn of possible numerical difficulties.

4.6 Two-Equation Models

This category of models has experienced the most popularity for a wide range of engineering analysis and research. Within the structure of these models independent transport equations for both the turbulent length scale, or some equivalent parameter, and the turbulent kinetic energy are provided. With the specification of these two variables, two-equation models are complete; hence no additional information regarding the turbulence is necessary in order to use the model for a given flow scenario.

While considered complete in that no new information is required, the two-equation model is to some degree limited to flows in which its fundamental assumptions are not grossly violated. For example, most two-equation models make the same fundamental assumption of local equilibrium, where turbulent production and dissipation balance. This assumption further implies that the scales of turbulence are locally proportional to the scales of the mean flow; therefore, most two-equation models will be in error when applied to non-equilibrium flows. Though somewhat constrained, two-equation models are still extremely popular and can be used to give results well within engineering accuracy when applied to appropriate cases.

While Kolmogorov's[96] $k - w$ model was the first two-equation model, the development of the model is rather brief and doesn't even establish values for all the closure coefficients. The most extensive two-equation work has been performed by Launder and Spalding,[64, 108] their eddy viscosity $k - \varepsilon$ turbulence model is by far the most widely-used model to date. Another popular two-equation model is Wilcox's $k - \omega$[59] which has shown greater agreement with experimental data but with significant computational overheads. Both of these models will be discussed in greater detail later.

Other two-equation models include those of Jones and Launder[109, 110] who extended the original $k - \varepsilon$ model to a low Reynolds number form which allows for calculations right down to the wall. Lam and Bremhorst[111] also developed a new form of the high Reynolds number $k - \varepsilon$ model. Unlike many previously proposed forms of the $k - \varepsilon$ model, their model does not have to be applied in conjunction with empirical wall function formulas. Lam and Bremhorst conducted a study where the predictions from their newly formulated model were compared with measurements for fully developed pipe flow. The conclusion drawn from this study was that satisfactory predictions were obtained by the new model and the agreement with the available experimental data was found to be good. However since the low Reynolds number extension does not employ wall functions, a fine computational mesh is required to resolve the flow field into the laminar sub-layer and down to the wall, the computer storage and run-time requirements for this approach are much greater than those using wall functions.

The brief history of two-equation turbulence models presented here is by no means a complete description of all available two-equation turbulence models. Many other variants of the $k - \varepsilon$ and $k - \omega$ models have been formulated. Examples include models of Launder and Sharma,[112] Daly and Harlow,[113] Chen and Kim's[114] modified $k - \varepsilon$ model. Saffman[115] and later Spalding[116] formulated an improved $k - w$ model in comparison to the original Kolmogorov $k - w$ model.

Studies dedicated to analysing the predictive accuracy of turbulence models for classic test case configurations exist. Two such studies recommended are those of Heyerichs and Pollard[58] and Patel et al.[117] where a significant number of turbulence models are reviewed.

The standard two-equation turbulence models which have been applied to test case configurations within the framework of this research are the high Reynolds number $k - \varepsilon$ model developed by Launder and Spalding[64] and the low Reynolds number $k - \omega$ model of Wilcox.[59] These two models are standard components of PHYSICA Version 2.12.

4.6.1 Standard High Reynolds Number k-ε Model

Launder and Spalding's $k - \varepsilon$ model is one of the most prominent turbulence models, having been implemented in all general purpose CFD codes, and is considered the industrial standard turbulence model. It has proven to be stable and numerically robust and has a well established regime of predictive capability. It has achieved notable success in calculating a wide variety of thin shear layer and recirculating flows and confined flows without the need for case-by-case adjustment of the model constants. For general purpose simulations, the $k - \varepsilon$ model offers a good compromise in terms of accuracy and robustness.

The structure of the model constitutes transport equations for both the velocity and length scales which are used to form the eddy viscosity. As in one-equation models, the turbulent kinetic energy is almost universally used to obtain the velocity scale. The most popular approach for the length scale is to develop a transport equation for the dissipation rate of turbulence, ε, because ε appears explicitly in the k-equation. These two transport equations have been stated in equations (4.24) and (4.25) respectively.

$$\frac{\partial \rho k}{\partial t} + div\left(\rho \underline{u} k\right) = div\left(\left[\mu_l + \frac{\rho v_t}{\sigma_k}\right] grad\ k\right) + \rho v_t G - \rho \varepsilon \qquad (4.24)$$

$$\frac{\partial \rho \varepsilon}{\partial t} + div\left(\rho \underline{u} \varepsilon\right) = div\left(\left[\mu_l + \frac{\rho v_t}{\sigma_\varepsilon}\right] grad\ \varepsilon\right) + C_{1\varepsilon}\rho v_t G\frac{\varepsilon}{k} - C_{2\varepsilon}\rho\frac{\varepsilon^2}{k} \qquad (4.25)$$

where the turbulent viscosity is identified in equation (4.26).

$$v_t = C_\mu \frac{k^2}{\varepsilon} \qquad (4.26)$$

The above equations accommodate five empirical constants: $\sigma_k, \sigma_\varepsilon, C_\mu, C_{1\varepsilon}$ and $C_{2\varepsilon}$. The standard Launder and Spalding version model employs values for these constants arrived at by comprehensive data fitting for a generous array of turbulent flows, given in equation (4.27)

$$\sigma_k = 1.00, \quad \sigma_\varepsilon = 1.30$$
$$C_\mu = 0.09, \quad C_{1\varepsilon} = 1.44, \quad C_{2\varepsilon} = 1.92 \tag{4.27}$$

The turbulent generation rate, G, present in both the production terms of equations (4.24) and (4.25) can be expressed using equation (4.28).

$$G = 2\left(\left[\frac{\partial u}{\partial x}\right]^2 + \left[\frac{\partial v}{\partial y}\right]^2 + \left[\frac{\partial w}{\partial z}\right]^2\right) + \left(\frac{\partial u}{\partial y} + \frac{\partial v}{\partial x}\right)^2 + \left(\frac{\partial u}{\partial z} + \frac{\partial w}{\partial x}\right)^2 + \left(\frac{\partial w}{\partial y} + \frac{\partial v}{\partial z}\right)^2 \tag{4.28}$$

The production and destruction of turbulent kinetic energy are closely linked. The dissipation rate ε is large where production of k is large. The model equation (4.25) for ε assumes that its production and destruction terms are proportional to the production and destruction terms of the k-equation (4.24). Implementation of such forms ensures that ε increases rapidly if k increases rapidly and that it decreases sufficiently fast to avoid negative values of turbulent kinetic energy if k decreases. The factor ε/k in the production and destruction terms enables these terms to be dimensionally correct in the ε-equation. See Versteeg and Malalasekera.[86]

4.6.1.1 Performance of k-ε Model

The $k-\varepsilon$ two-equation model transports two turbulent properties (turbulent energy, k, and dissipation, ε). This makes it possible for $k-\varepsilon$ models and other two-equation models to account for history effects in a way which zero-equation models such as Baldwin-Lomax can not. Hence, $k-\varepsilon$ is a more advanced model with the potential of predicting more complex phenomena.

In spite of the numerous successes the standard $k-\varepsilon$ model has enjoyed only moderate agreement when dealing with unconfined flows. The model is reported not to perform well in weak shear layers and the spreading rate of axisymmetric jets in stagnant surroundings is severely over predicted. The model also has problems in swirling flows and flows with large,

rapid, extra strains (e.g. highly curved boundary layers and diverging passages) since it does not contain a description of the subtle effects of streamline curvature on turbulence. The latter effects are due to turbulence anisotropy, which only higher order closure models can accommodate.

Advantages:

- Well established, the most widely validated two-equation turbulence model.

- Simplest turbulence model for which only boundary conditions are required.

- No requirement for a fine computational mesh near to walls provided suitable wall functions are used.

- Excellent performance for many industrially-significant flows.

- Performs especially well in confined flows. This includes a broad range of flows with industrial engineering applications, which explains the model's popularity.

Disadvantages:

- More expensive in terms of implementation and CPU time than both zero- and one-equation models as additional PDE's need to be solved.

- The predominant drawback of the $k - \varepsilon$ turbulence model, for electronics applications, is that the model was originally designed for high Reynolds number flows; consequently poor model accuracy is anticipated when dealing with fluid flow over populated PCBs which is usually classified as being low Reynolds number flow due to the small velocities and length scales encountered.

- Not appropriate for use in the viscous sub-layer, unless in low Reynolds number form.

- Model assumes isotropy, i.e. that the eddy viscosity is indistinguishable for all the Reynolds stresses. Measurements however indicate that this is not the case even in simplistic turbulent flows.

- It has been shown that for channel flow test cases the model overestimates v_t in the central region of the channel.

- Poor performance in an assortment of important cases such as:
  - Some unconfined flows
  - Flows containing large extra strains. For example curved boundary layers, swirling flows.
  - Rotating flows
  - Separated flows
  - Fully developed flows in non-circular ducts

4.6.2 Low Reynolds Number k-ω Model

The Wilcox $k - \omega$ model is gaining in popularity. In this model the standard k-equation is solved, but as a length determining equation ω is used which represents the frequency of the vorticity fluctuations. The modelled k and ω equations are:

$$\frac{\partial \rho k}{\partial t} + div\left(\rho \underline{u} k\right) = div\left(\left[\mu_l + \frac{\rho v_t}{\sigma_k}\right] grad\ k\right) + \rho v_t G - \beta^* \rho \omega k \qquad (4.29)$$

$$\frac{\partial \rho \omega}{\partial t} + div\left(\rho \underline{u} \omega\right) = div\left(\left[\mu_l + \frac{\rho v_t}{\sigma_\omega}\right] grad\ \omega\right) + \rho \alpha \frac{\omega}{k} G - \beta \rho \omega^2 \qquad (4.30)$$

where the turbulent viscosity is defined in equation (4.31).

$$v_t = \frac{\alpha^* k}{\omega} \qquad (4.31)$$

Table 4.1 details the wall boundary conditions, constants and damping functions.

Low Reynolds number Wilcox $k-\omega$ model[59]			
Nomenclature	Expression	Nomenclature	Expression
$k_w - B.C$	0.0	$\omega_w - B.C$	$6\nu_l / \beta y^2$
σ_k	2.0	σ_ω	2.0
α_0	1/10	α_0^*	$\beta/3$
R_β	8.0	R_k	6.0
R_t^*	$k/\omega\nu_l$	R_w	2.7
α	$\dfrac{5}{9}\dfrac{\alpha_0 + R_t^*/R_w}{1 + R_t^*/R_w}\left(\alpha^*\right)^{-1}$	α^*	$\dfrac{\alpha_0^* + R_t^*/R_k}{1 + R_t^*/R_k}$
β	3/40	β^*	$\dfrac{9}{100}\dfrac{5/18 + \left(R_t^*/R_\beta\right)^4}{1 + \left(R_t^*/R_\beta\right)^4}$

Table 4.1 Specification of boundary conditions, constants and damping functions for Wilcox $k-\omega$ model

The ω-equation has considerable advantages in close proximity to solid surfaces and accurately predicts the turbulent length scale in difficult to solve pressure gradient flows, leading to enhanced wall shear stress and heat transfer predictions. Furthermore, the model has a straightforward low Reynolds number formulation which does not require extra non-linear wall damping functions.

The main difference between the $k-\varepsilon$ and $k-\omega$ approaches is the modelling of turbulence near a wall. For the $k-\varepsilon$ model the dimensionless wall distance lies within the approximate range $30 \le y^+ \le 150$ whereas for the $k-\omega$ model a sufficiently fine computational mesh close to a wall is required to allow the turbulent quantities to be resolved accurately. Further analysis of wall function techniques will be discussed later.

4.6.2.1 Performance of $k-\omega$ Model

The $k-\omega$ model, although not as popular as the $k-\varepsilon$ model, has several advantages. Most importantly, the model is significantly more accurate for two-dimensional boundary layers with both adverse and favourable pressure gradient. However this greater model accuracy comes at the cost of increases in computational time and data storage capacity due to the fine

mesh requirement at the wall. Menter et al.[75] argue that the core deficiency of the $k - \omega$ model is the sensitivity of the solution to free stream values of ω external to the boundary layer. A possible solution to this problem is the combination of the $k - \omega$ model near the wall and the $k - \varepsilon$ model in the bulk flow, which lead to the SST zonal model.

Advantages:

- Relatively easy turbulence model to implement as the calculation of the wall shear stress, distance from the wall and additional terms is not required. This simplifies the programming required to handle cases that are three dimensional, involve complex geometry or blockages.

- Reasonable sub-layer behaviour is achieved through a simple Dirichlet boundary condition for the ω-equation.

- High prediction accuracy for many cases.

- Compared to the $k - \varepsilon$ model, the low Reynolds number $k - \omega$ model is more accurate for two-dimensional boundary layers with both adverse and favourable pressure gradient.

- Reported to perform better than the $k - \varepsilon$ model for transitional flows.

- Evidence suggests that the Wilcox $k - \omega$ model performs better than the standard $k - \varepsilon$ model for flows involving deceleration and/or separation resulting from adverse pressure gradients.

- This low Reynolds number version is more economical and elegant than the majority of low Reynolds number $k - \varepsilon$ models, in that it does not require the calculation of wall distances, additional source terms and/or damping functions based on the friction velocity.

Disadvantages:

- Significantly large computational mesh requirement as wall function approach is not used. For best results the first grid point away from the wall should be in the vicinity of $y^+ \leq 1$.

- Greater data storage capacity and CPU time requirements in comparison to zero- and one-equation models together with the standard $k - \varepsilon$ model.

- Sensitive to the free-stream boundary condition for ω when dealing with free-shear flows.

4.6.3 Performance of Two-Equation Models

Two-equation models are widely used, as they offer a good compromise between the numerical effort and computational accuracy and have proven that they perform well for a wide range of flows of engineering interest. However their application is limited to flows that closely follow the implicit assumptions upon which most two-equation models are based:

- Flow does not deviate significantly from local equilibrium.

- Reynolds number is high enough that the local isotropy is approximately satisfied.

Generally the $k - \omega$ model is considered to be superior to the standard $k - \varepsilon$ model for flows with adverse pressure gradient, although it should be noted that many variants of the $k - \varepsilon$ model with correction for factors such as streamline curvature, buoyancy, swirl, etc. for such cases exist.

Neither model is capable of producing quantitatively good predictions for more complicated flows dealing with curved surfaces, secondary motions, and separation. Although two-equation models may be able to give qualitative results for such flows, generally a further level of complexity is required in the model to obtain close agreement with experimental data. This is when higher order models are called upon such as LES or DNS, but these have the disadvantage of the huge increase in run time. Another approach that could be more accurate is the zonal approach which keeps the advantage of using RANS models.

4.7 Near-Wall Treatment

When dealing with turbulent flow RANS simulations there are two main approaches which can be adopted for the treatment of the near-wall region: low Reynolds number turbulence modelling and the wall function approach.

The low Reynolds number approach requires an extremely fine mesh density at near-wall regions so the sharp gradients experienced can be accurately resolved. This calculation method is time consuming, expensive with regards to data storage, and may be impractical for industrial applications where often complex three-dimensional geometries are investigated. To reduce this computational burden, high Reynolds number turbulence models have been developed that do not resolve the viscous sub-layer but instead incorporate standard wall function techniques that aim to replace the differential equations solved on a very fine mesh across the sub-layer by low-cost algebraic formulae. As only a fraction of the computational effort is required for this technique it is strongly favoured for industrial applications. Figure 4.3 further illustrates the different approaches for handling wall bounded flows.

Low Reynolds number

approach

No assumptions regarding the near-wall variations of the velocity, temperature and turbulent flow parameters

u^+

$$u^+ = \frac{1}{\kappa}\ln\left(Ey^+\right)$$

$u^+ = y^+$

30

20

10

0

Predictions

10   100

$\ln y^+$

Wall function

approach

Involves assumptions regarding the near-wall variations of the velocity, temperature and turbulent flow parameters

u^+

$$u^+ = \frac{1}{\kappa}\ln\left(Ey^+\right)$$

$u^+ = y^+$

30

20

10

0

Predictions

Boundary layer flow assumed

10   100

$\ln y^+$

Figure 4.3 Strategies for dealing with wall bounded flows

A variety of wall function methods are available. Differences between wall functions arise from the assumptions made about the near-wall behaviour and the calculation technique used for the wall shear stress, wall temperature and cell-averaged turbulent parameters.

4.7.1 Standard Log-Law Wall Functions

"Universal" log-laws connect the wall conditions, for example the wall shear stress, to the dependent variables at the near-wall cell which is presumed to lie outside the viscous sub-layer in fully turbulent flow. This technique is widely used and preferred for many practical purposes. Therefore the majority of commercially available CFD codes incorporate such a technique as standard practice.

Standard wall functions are based on empirical near-wall logarithmic profiles of velocity and temperature, also various other assumptions related to the behaviour of turbulence parameters, such as a constant or linearly varying shear stress which yield average values for source and sink terms across the near-wall cells. For channel and pipe flows for example these assumptions are often adequate and wall functions can significantly improve computing times, however when dealing with complex non-equilibrium flows, often found in industrial applications, these assumptions are inadequate. However given the affordable number of cells for a given computational study, it is often preferable to use the wall function approach which allows for the use of a fine computational mesh in other important regions where the gradients of the solved variables are also large.

The standard wall functions which are available within PHYSICA V2.12 have been detailed below. The contribution of the wall function is incorporated into the transport equations via the source term. For momentum transport the source term takes the form stated in equation (4.32). U denotes the in-cell velocity.

$$S_{mom} = \lambda \left(U_w - U \right)$$
$$\lambda = \max \left(\rho s \left| U_r \right| A \, ; \rho v_l A / y \right)$$

(4.32)

The laminar and turbulent components of the momentum wall function, $u^+ = y^+$ and $u^+ = 1/\kappa \ln \left(E y^+ \right)$ respectively, can be recast to obtain expressions in terms of the skin friction factor s as defined in equation (4.33).

$$u^+ = y^+ \rightarrow s = \frac{1}{\text{Re}}$$

$$u^+ = \frac{1}{\kappa}\ln\left(Ey^+\right) \rightarrow \sqrt{s} = \frac{\kappa}{\ln\left(E\,\text{Re}\,\sqrt{s}\right)}$$

(4.33)

Therefore, the turbulent component of the wall function requires an iterative method to obtain the skin friction factor.

When turbulence quantities are also being solved, the source terms for k, ε and ω take the forms stated in equation (4.34).

$$S_k = 10^{10} Vol\left(k_w - k\right)$$

$$S_\varepsilon = 10^{10} Vol\left(\varepsilon_w - \varepsilon\right)$$

$$S_\omega = 10^{10} Vol\left(\omega_w - \omega\right)$$

(4.34)

where k, ε and ω denotes the in-cell values of the solved variables and the wall values are defined in equation (4.35).

$$k_w = \frac{sV^2}{\sqrt{C_\mu}}, \quad \varepsilon_w = \frac{C_d k^{1.5}}{\kappa y}, \quad \omega_w = \frac{80\nu_l}{y^2}$$

(4.35)

When the $k - \omega$ model is activated the value of k in the near-wall cell is set to zero.

The large source coefficient value '10^{10}' has the effect of 'fixing' the in-cell quantity to that of the wall.

For temperature transport at external walls there is a simple effective diffusion link between the wall and in-cell temperature values. It is noted that no turbulent logarithmic wall function for temperature exists within the current structure of the code for internal solid-fluid interfaces. This deficiency has been addressed in Chapter 5.

To summarise, wall functions are empirical laws which attempt to reproduce measured near-wall experimental data for boundary layers. With these laws it is possible to express the mean

velocity and temperature parallel to the wall and turbulence quantities outside the viscous sub-layer in terms of the distance to the wall and subsequently the wall heat transfer. Therefore wall functions can be used to provide valuable near-wall boundary conditions for the momentum, temperature and turbulence transport equations rather than conditions at the wall itself. This in turn means that the viscous sub-layer does not require resolution and the need for a very fine mesh is avoided.

4.8 Turbulence Model Range

A summary of the turbulence models used within the structure of this work has been provided in Table 4.2. Three CFD codes have been considered: FLOTHERM, PHOENICS and PHYSICA. The models implemented by the author within PHYSICA are in italic font.

Model class	Turbulence model		
	FLOTHERM V3.2/4.1	PHOENICS V3.4	PHYSICA V2.12
Zero-equation	LVEL, LVEL_CAP	LVEL	*LVEL, LVEL_CAP, AUTO_CAP*
One-equation	N/A	KLMODL	*Wolfshtein, Norris & Reynolds*
Two-equation	Standard $k-\varepsilon$	Standard $k-\varepsilon$, Wilcox $k-\omega$	Standard $k-\varepsilon$, Wilcox $k-\omega$
Zonal	$k\varepsilon - LVEL$	N/A	$k\varepsilon - LVEL$, $k\varepsilon / kl$, *SST*

Table 4.2 Range of turbulence models

VERIFICATION OF EXISTING TURBULENCE MODELS

The objective of this chapter is to highlight that the standard turbulence models ($k - \varepsilon$ and $k - \omega$) currently available within the PHYSICA framework produce comparable results to the commercially available CFD codes FLOTHERM and PHOENICS. This validation was undertaken to ensure that all three codes gave consistent results. It should be noted that PHYSICA is unstructured and FLOTHERM and PHOENICS are structured, but consistent results between the three codes was taken to justify future implementation and testing within the PHYSICA code.

5.1 Parallel Plates

This case was originally aimed at a target audience of FLOTHERM users interested in flow validation cases where FLOTHERM predictions are compared with analytical or empirical data.[7]

The case considers flow between two smooth parallel plates (i.e. Poiseuille flow) over a range of Reynolds numbers covering both laminar and turbulent flow conditions. A uniform velocity field has been assumed across the entrance of the channel with a variety of inlet velocity values corresponding to a Reynolds number range of 100 (laminar) to 10^4 (turbulent).
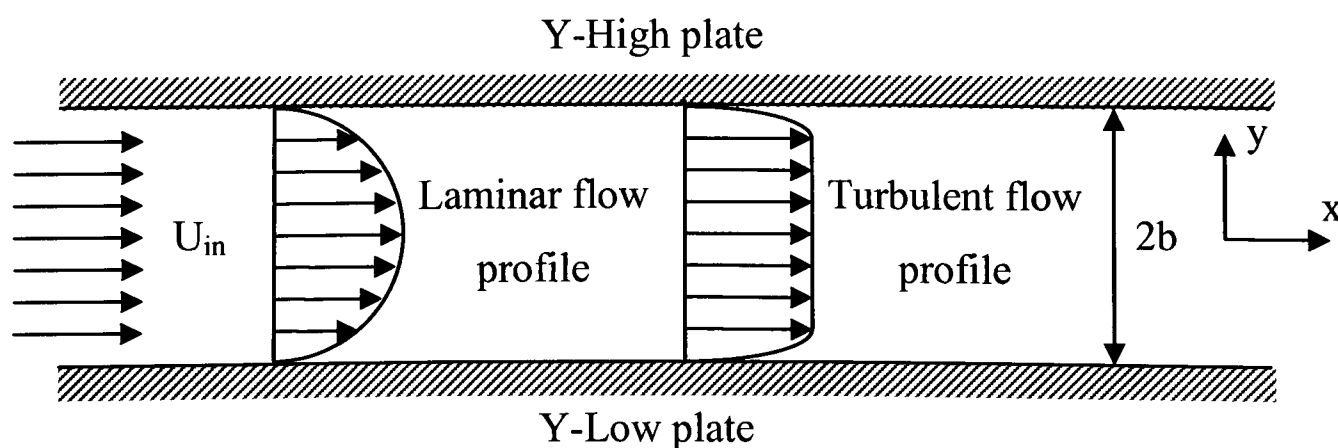
Figure 5.1 Schematic representation of the parallel plates test geometry

The computational domain length in the flow direction was made long enough to ensure that the flow field was fully developed.[118] The flow is driven by a pressure gradient acting in the direction of flow, and is retarded by viscous drag along both plate surfaces, such that these forces are in balance. The Upwind differencing scheme has been used and the gravitational effects have been neglected for all simulation work conducted.

This case study is relevant for many electronic flow applications:

- Flow within passages which may or may not experience temperature variations

- Flow between the fins of a heat sink

- Flow in a printed-circuit board passage, in which the flow over the upper surfaces of components share some of the characteristics of the simpler case considered here

- Any flow over or between surfaces particularly when pressure drop, surface heat transfer or surface temperature are of importance.

It is worth noting that this case is purely forced convection. However, it is also relevant to sub-systems within natural-convection systems where local 'forced-convection' conditions arise as a result of heating elsewhere in the system.

The flow field has been investigated under both laminar and turbulent flow conditions using the standard high Reynolds number $k - \varepsilon$ and the Wilcox $k - \omega$ turbulence models where appropriate.

5.1.1 Laminar Flow Conditions

The Reynolds number, based on the hydraulic diameter of the channel, has been calculated as 100. The dimensions of the solution domain are presented in Figure 5.2.
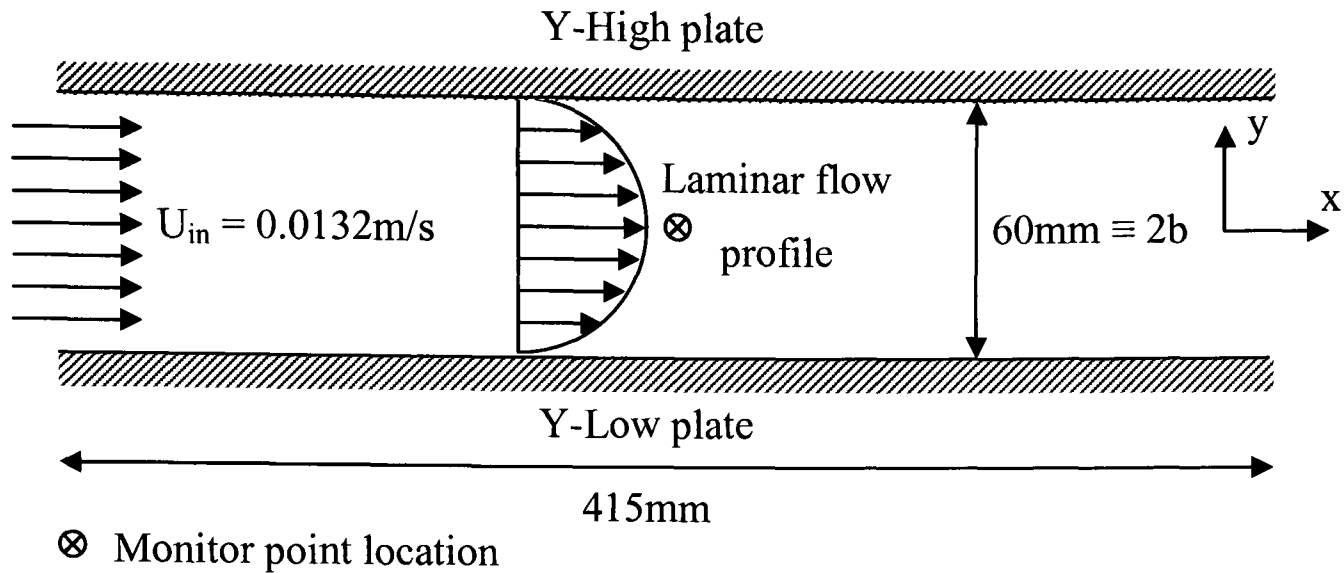
Figure 5.2 Parallel plates test case laminar solution domain

The fluid material properties have been set to air at 30°C therefore giving a fluid density of $1.1614 kg/m^3$ and a kinematic viscosity of $1.5842 \times 10^{-5} m^2/s$. A uniform mesh density of (40 x 20) mesh elements have been set in the x- and y-directions respectively.

To assess the accuracy of the computational predictions presented in this section comparisons are made against the fully developed laminar analytical solution stated in equation (5.1), the derivation of which can be found in Appendix B1.

$$\frac{U}{U_{in}} = \frac{3}{2}\left[1-\left(\frac{y}{b}\right)^2\right]$$

(5.1)

To ensure that the flow field under investigation remains smooth, and in a state of streamlined flow, a low uniform velocity is specified at the inlet and the boundary plates are modelled as being smooth. The resulting Reynolds number based on the hydraulic diameter of the channel is calculated to be 100.

PHYSICA results are presented to demonstrate the development of the velocity profile and the creation of the boundary layer in Figure 5.3 and Figure 5.4 respectively.
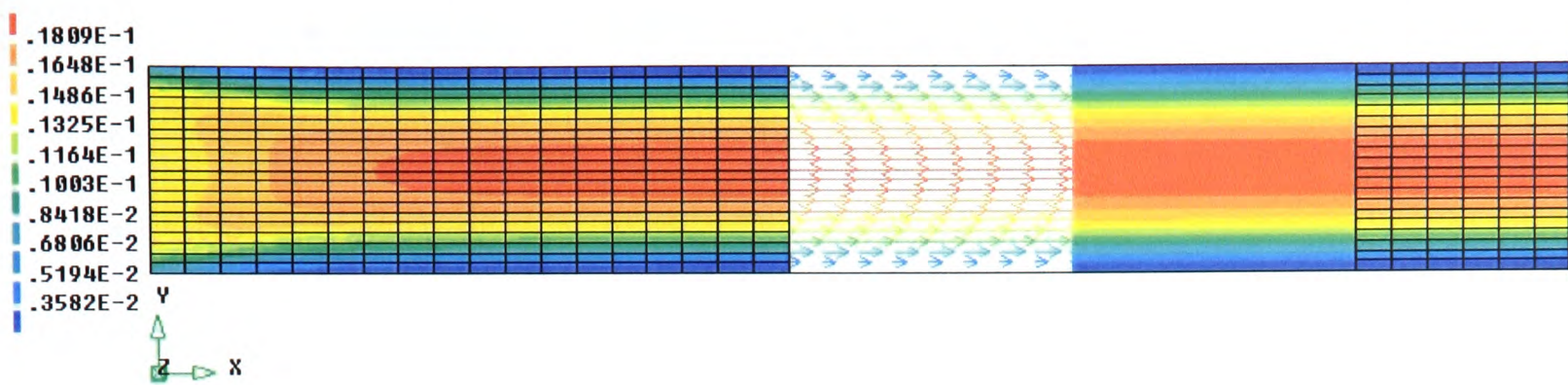
Figure 5.3 Developing laminar velocity profile with view of mesh distribution
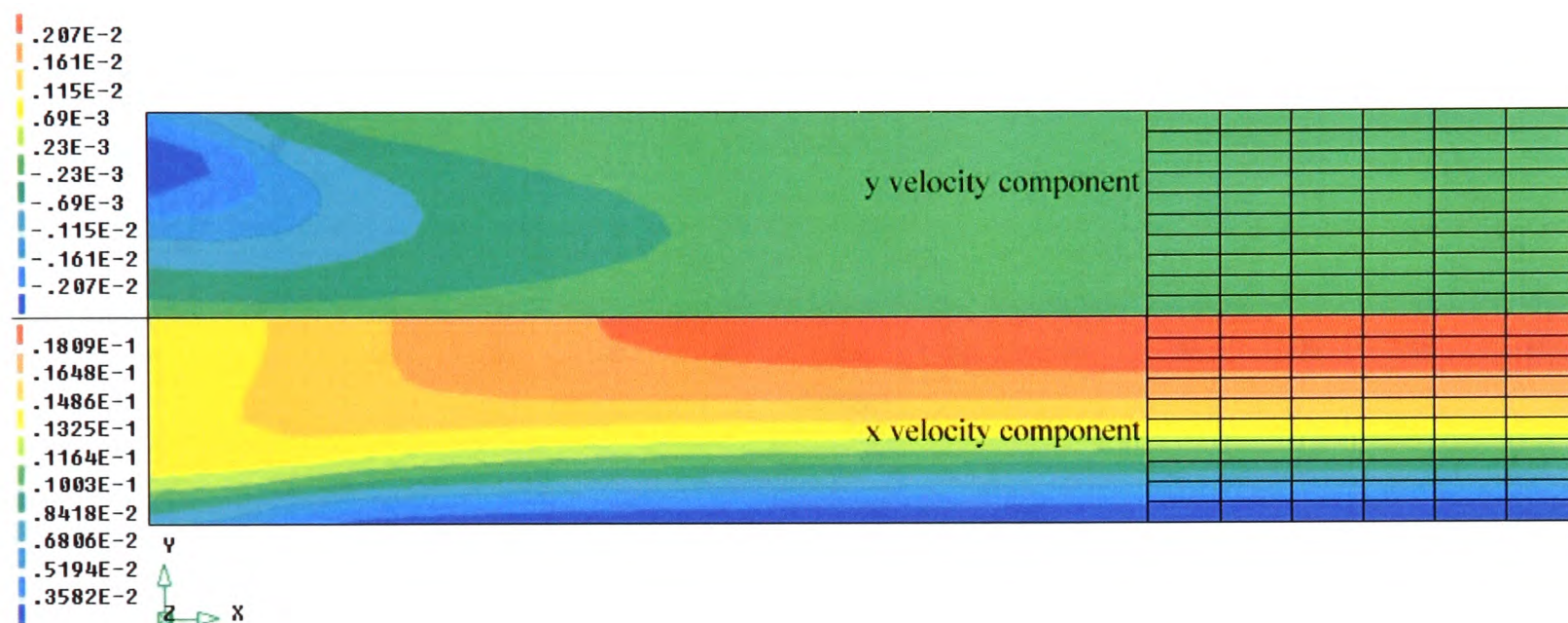
Figure 5.4 Velocity components located at channel entrance and view of developing boundary layer

The y-velocity component shows the displacement of the fluid to the centre of the channel as the boundary layer begins to develop. Since the mass flow rate is constant, the flow accelerates in the centre of the channel to compensate for the velocity loss close to the walls. The result is a parabolic velocity profile when the flow fully develops, as shown in Figure 5.5 taken at a x-position of 316mm downstream of the inlet.
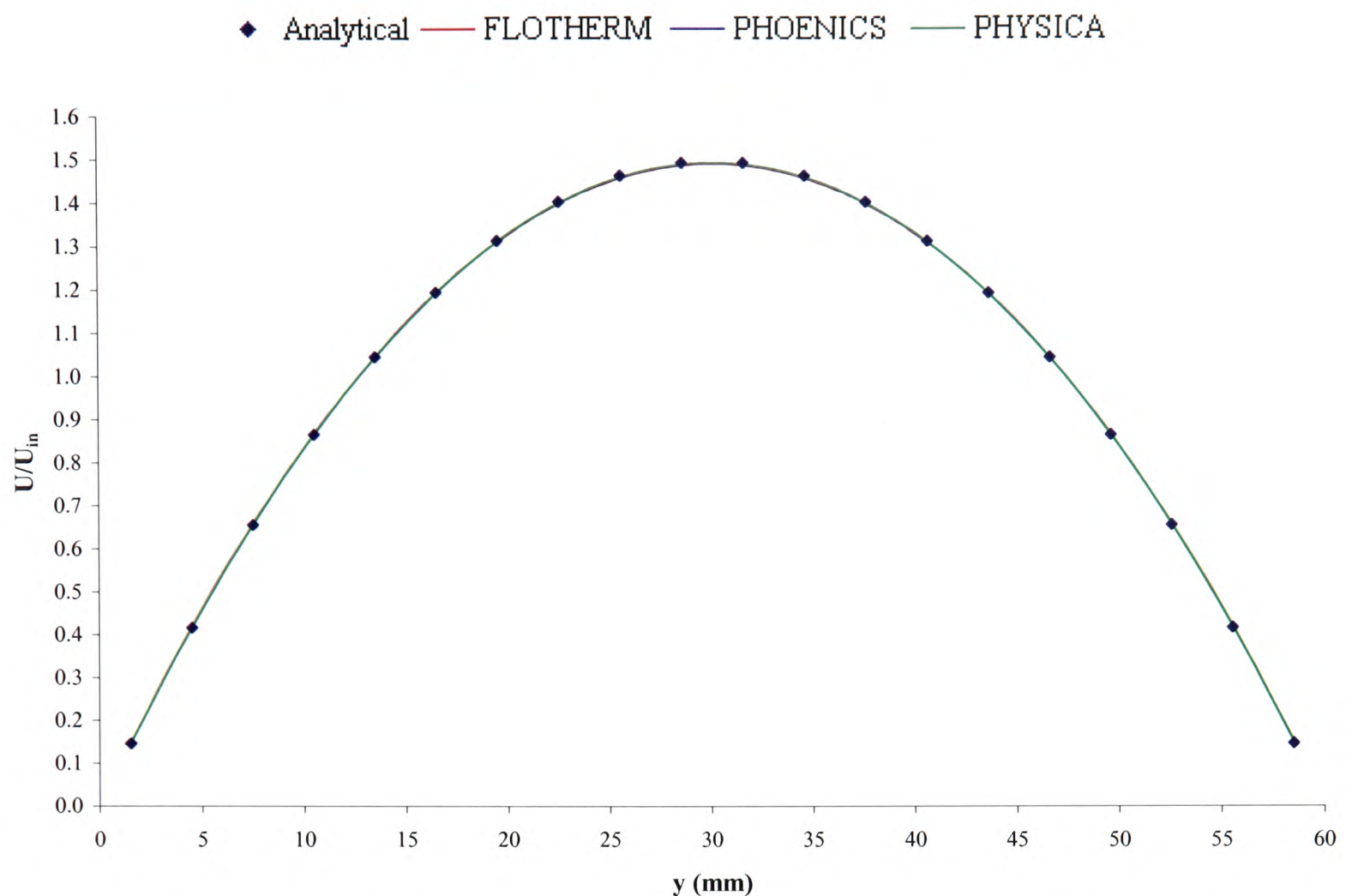
Figure 5.5 Laminar velocity profile

From the fully developed velocity profile presented in Figure 5.5 it can be concluded that all three codes produce identical velocity profiles, furthermore the velocity profile is parabolic as expected by theory. This supports the argument that all three codes produce the same results for the laminar flow example.

5.1.2 Turbulent Flow Conditions

The Reynolds numbers for this case is set to 10,000 based on the hydraulic diameter of the channel. The fluid material properties have been set to air at 30°C therefore resulting in a fluid density of 1.1614kg/m^3 and a kinematic viscosity of $1.5842 \times 10^{-5}\, \text{m}^2/\text{s}$. The construction of the geometry under investigation is shown in Figure 5.6. For further case specifications the reader is referred to Appendix A1.2.

Y-High plate

$U_{in} = 1.3202 m/s$

$k_{in} = 0.1743 m^2/s^2$

$\varepsilon_{in} = 0.4881 m^2/s^3$

$\omega_{in} = 31.1142 s^{-1}$

Turbulent flow profile

$60mm \equiv 2b$

Y-Low plate

10m

⊗ Monitor point location
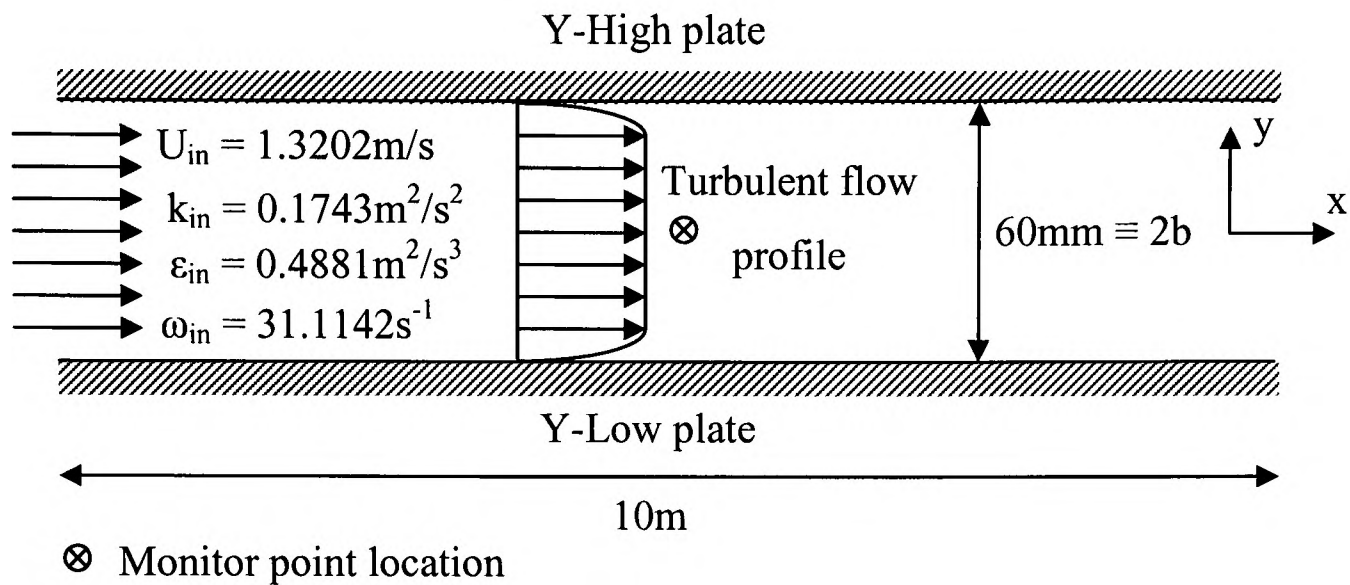
Figure 5.6 Parallel plates test case turbulent solution domain

The mesh density used for the majority of the turbulence models considered is (640 x 48) in the x- and y-directions respectively. However due to the fine mesh constraint imposed by the $k-\omega$ and SST models these simulation cases use a mesh density of (1600 x 120) in the x- and y-directions respectively and also use the mesh grading technique located at the plate surfaces to ensure that the mesh is finest near the wall, where the velocity gradient is highest. Figure 5.7 presents the generated fine mesh density employed for the simulations undertaken using the $k-\omega$ and SST turbulence models.
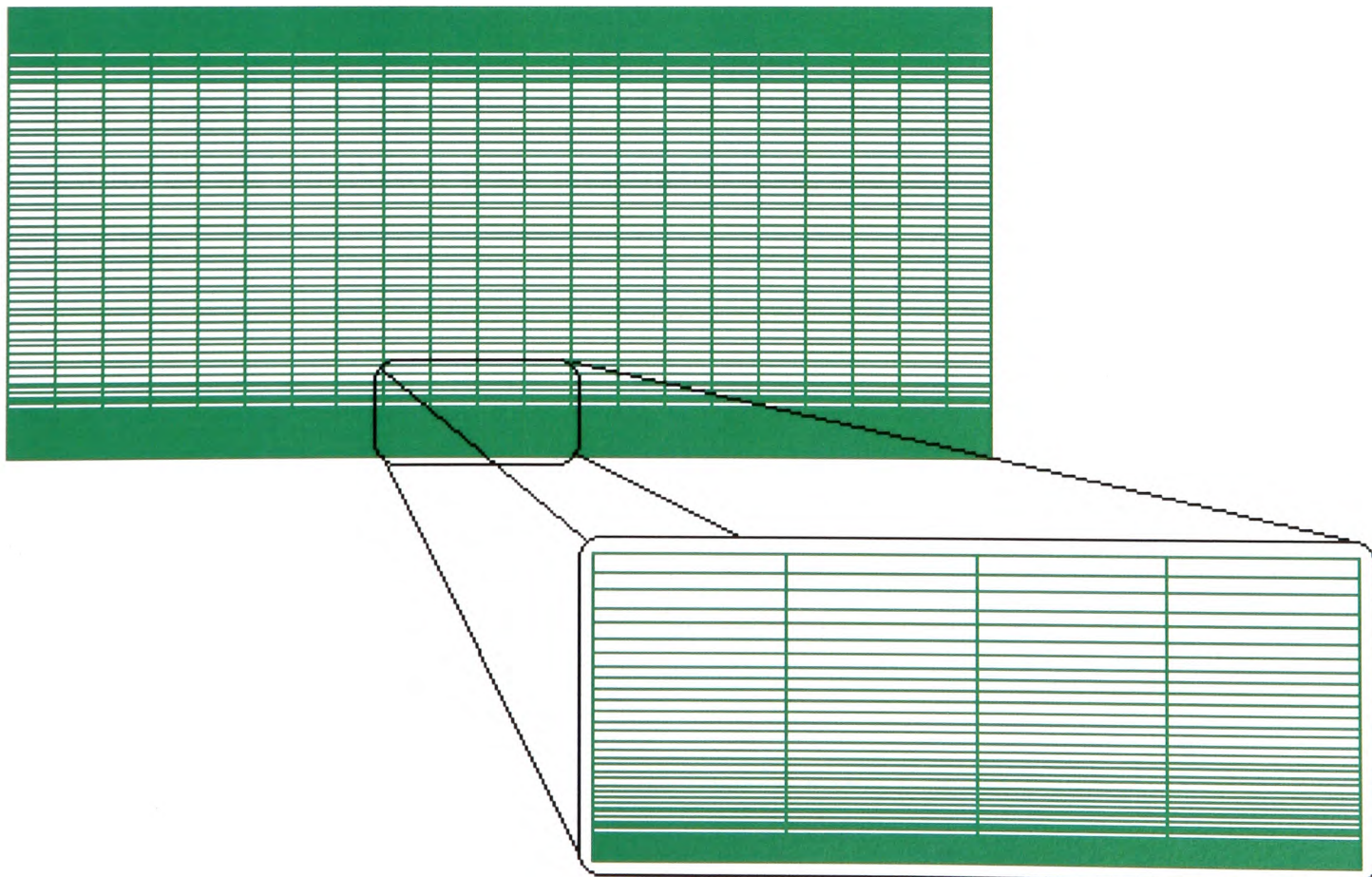
Figure 5.7 Parallel plates mesh density employed for the k - ω and SST turbulence models

The two turbulence models to be considered in this section are the standard high Reynolds number $k - \varepsilon$ and the low Reynolds number Wilcox $k - \omega$ models both classified as two-equation turbulence models.

Model accuracy will be assessed by comparison of the computational predictions against the fully developed turbulent analytical solution stated in equation (5.2), the derivation of which can be found in Appendix B2. All numerical predictions have been extracted at a x-position of 9.8m downstream of the inlet.

$$\frac{U}{U_{in}} = 1 + \left[\left(\frac{f}{2} \right)^{0.5} \Big/ \kappa \right] \left[\frac{5}{6} + \ln\left(1 - \left(\frac{y}{b} \right)^{0.5} \right) + \left(\frac{y}{b} \right)^{0.5} \right] \qquad (5.2)$$

Firstly considering the $k - \varepsilon$ model results it can be concluded from the velocity profiles presented in Figure 5.8 and the turbulent dynamic viscosity profiles shown in Figure 5.9 that all three codes produce similar velocity results and that the differences in the turbulent viscosity field do not significantly influence the velocity field for this case. It is clear from the profiles that the near-wall treatment used in FLOTHERM differs from that used in the remaining CFD codes.

The results suggest that the activation of the turbulence module has been successfully completed for all the simulation work undertaken here, and that the three codes have a similar implementation.
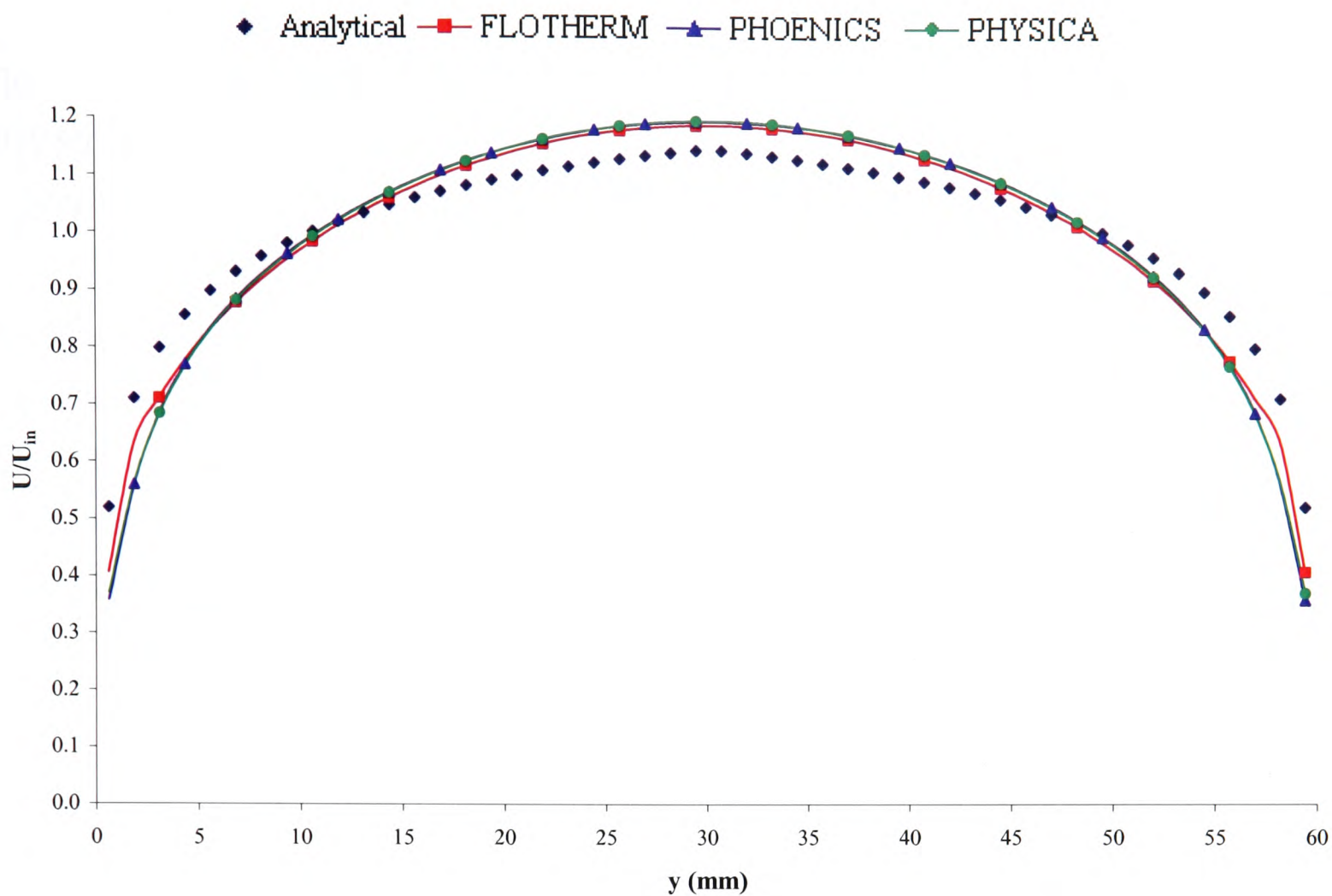
Figure 5.8 Standard k - ε velocity profile
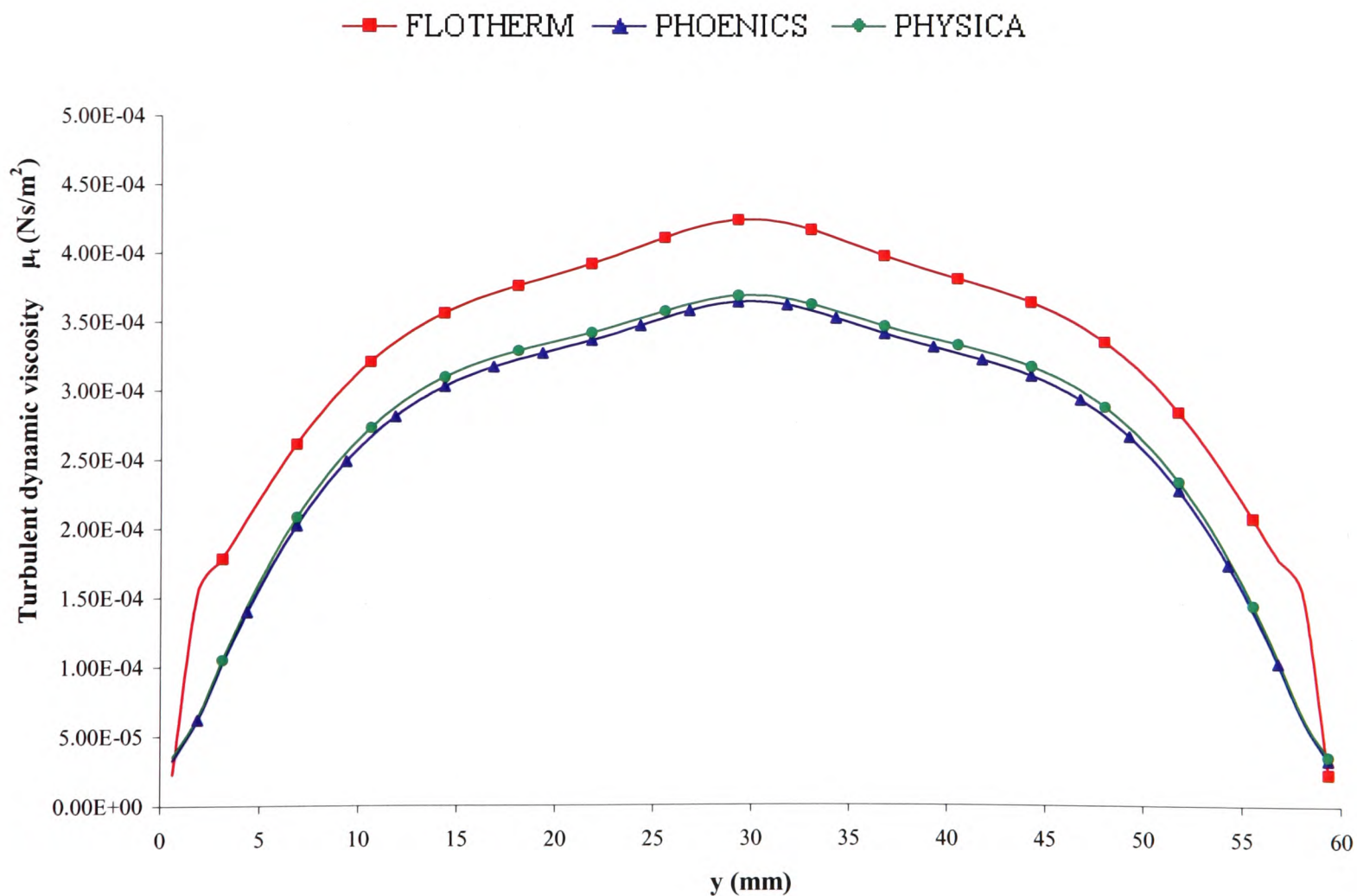
Figure 5.9 Standard k - ε turbulent dynamic viscosity

The $k-\omega$ model result comparisons can only be performed between PHOENICS and PHYSICA as this low Reynolds number turbulence model is not currently available in FLOTHERM Versions 3.2 to 5.1.

Studying the velocity profile presented in Figure 5.10 it can be concluded that the two codes produce similar results. Both PHOENICS and PHYSICA use a graded mesh to concentrate the mesh density close to the walls. It is noted that the density of the mesh at these wall boundaries differs slightly which may have attributed to the 12% difference at the centreline of the channel seen in the turbulent dynamic viscosity field.
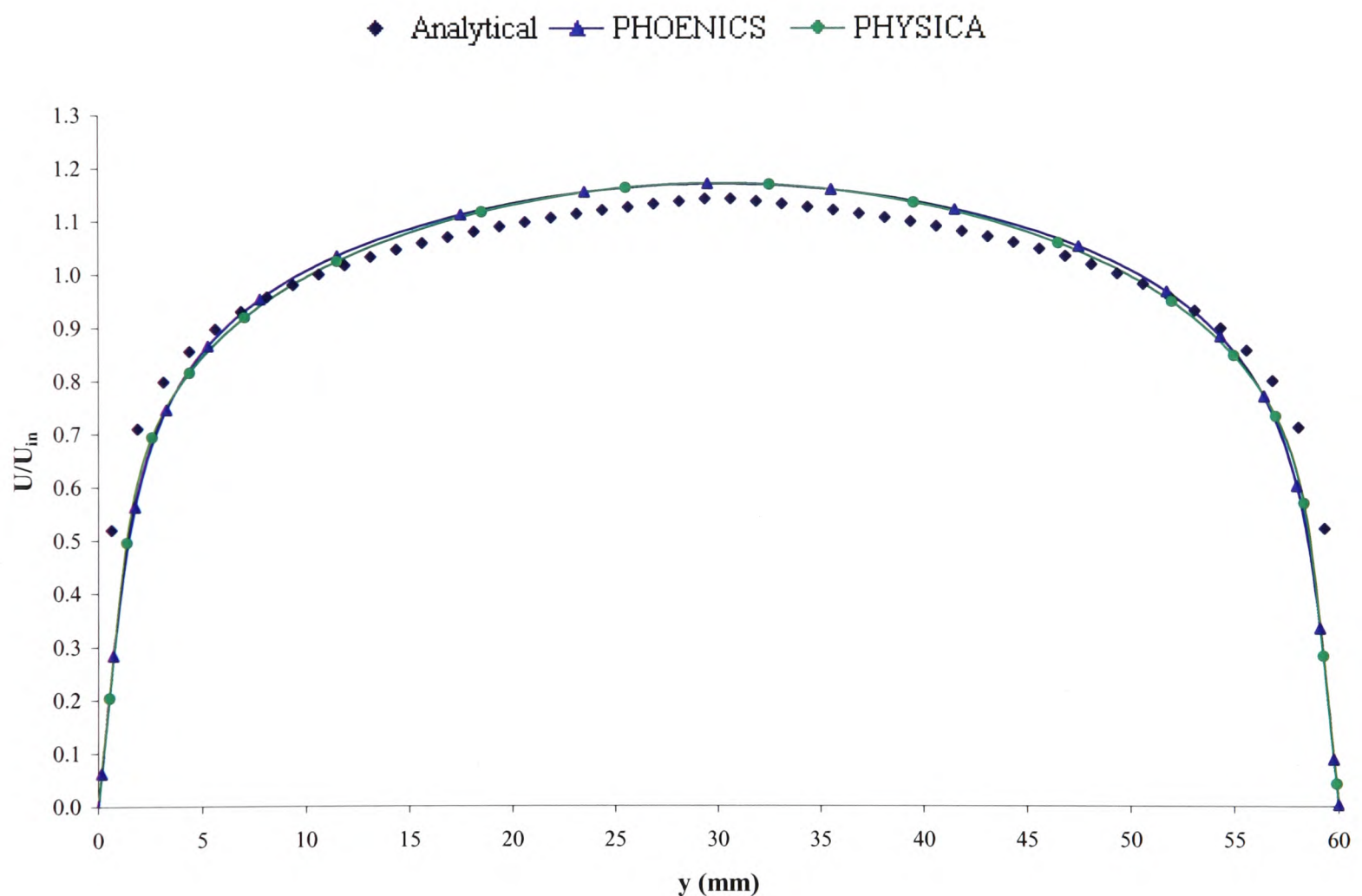
Figure 5.10 Velocity profile distribution obtained by the k - ω turbulence model

Figure 5.11 Turbulent dynamic viscosity profile distribution obtained by the $k - \omega$ turbulence model

It is observed that the fully developed turbulent velocity profile is much flatter towards the centre of the channel in comparison to the laminar profile. The rather flat profile indicates a much more rigorous exchange of momentum between successive fluid layers, due to turbulence. This flatter profile can be approximated relatively well with a power law, referred to as the one-seventh power law that is dependent on the friction factor. This power law gives a good general description of the shape of the turbulent core velocity profile, even though it fails in regions close to the boundary plate. The one-seventh power law will be discussed later.

In conclusion both laminar and turbulent flow conditions have been investigated for a simple channel flow configuration. The standard turbulence models which are commonly available within the CFD codes examined are shown to be in agreement with one another at least in predicting the correct mean velocity. The prediction of more complex flow which includes recirculation regions can now be investigated having established that the underlining foundations of the three CFD codes considered are, broadly speaking, very similar.

5.2 Two-Dimensional Inlet/Outlet

The case considers flow within a rectangular enclosure, with the inlet and outlet locations offset to create an s-type flow pathway. The Reynolds number for the case is set to 10,422 based on the inlet height. A schematic of the solution domain together with the dimensions used for this case have been detailed in Figure 5.12.
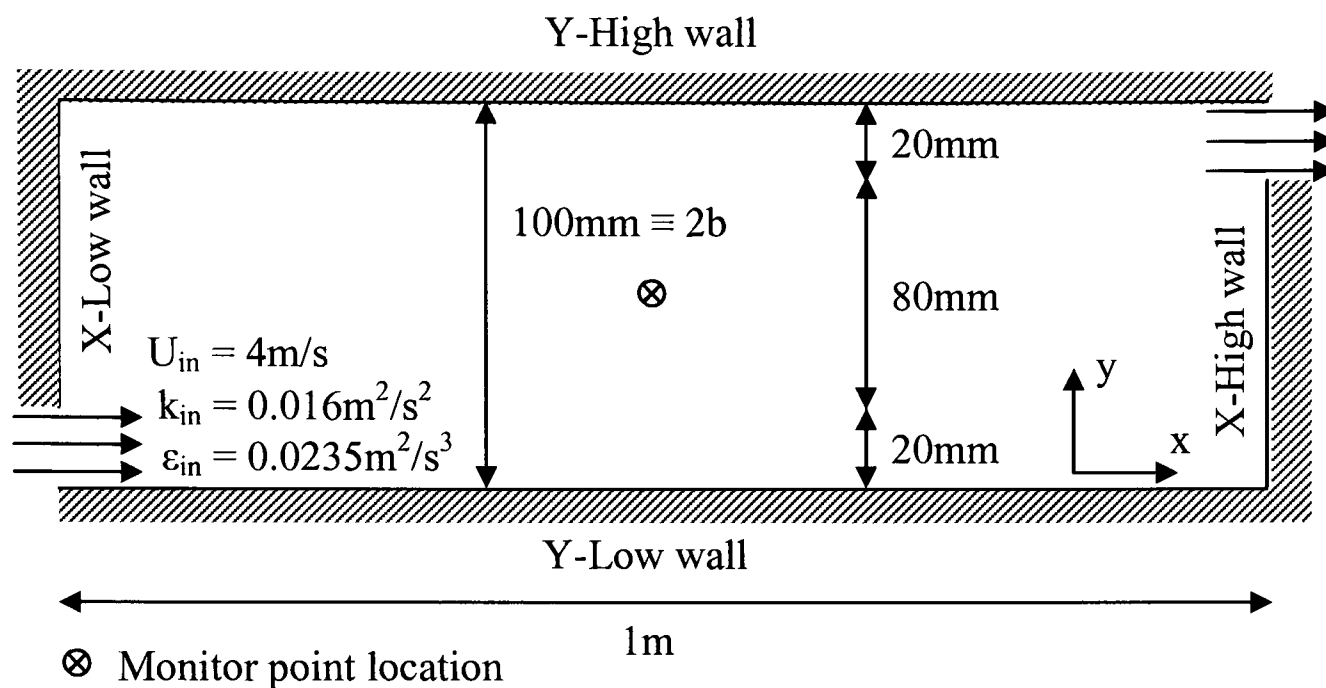
Figure 5.12 Inlet/Outlet test case solution domain

The uniform mesh density which has been employed for this test case is (500 x 50) mesh elements in the x- and y-directions respectively, which was found to ensure a mesh independent solution. The fluid material properties have been set to air at 20°C therefore resulting in a fluid density of 1.188kg/m^3 and a kinematic viscosity of $1.5353 \times 10^{-5} \text{m}^2/\text{s}$. The differencing scheme employed for all the simulation work conducted is the first order accurate Upwind differencing scheme.

The reader is referred to Appendix A2 for any further description of the test case geometry and boundary conditions. This test case is intended as a step forward from the parallel plates case discussed earlier as now flow recirculation regions are affecting the phenomena taking place within the solution domain.

Fully developed velocity profiles have been extracted as the flow progresses downstream normal to the Y-Low wall boundary. Code comparisons between FLOTHERM and

PHYSICA have been presented in Figure 5.13 for the standard $k - \varepsilon$ turbulence model at increments of 200mm from the inlet.
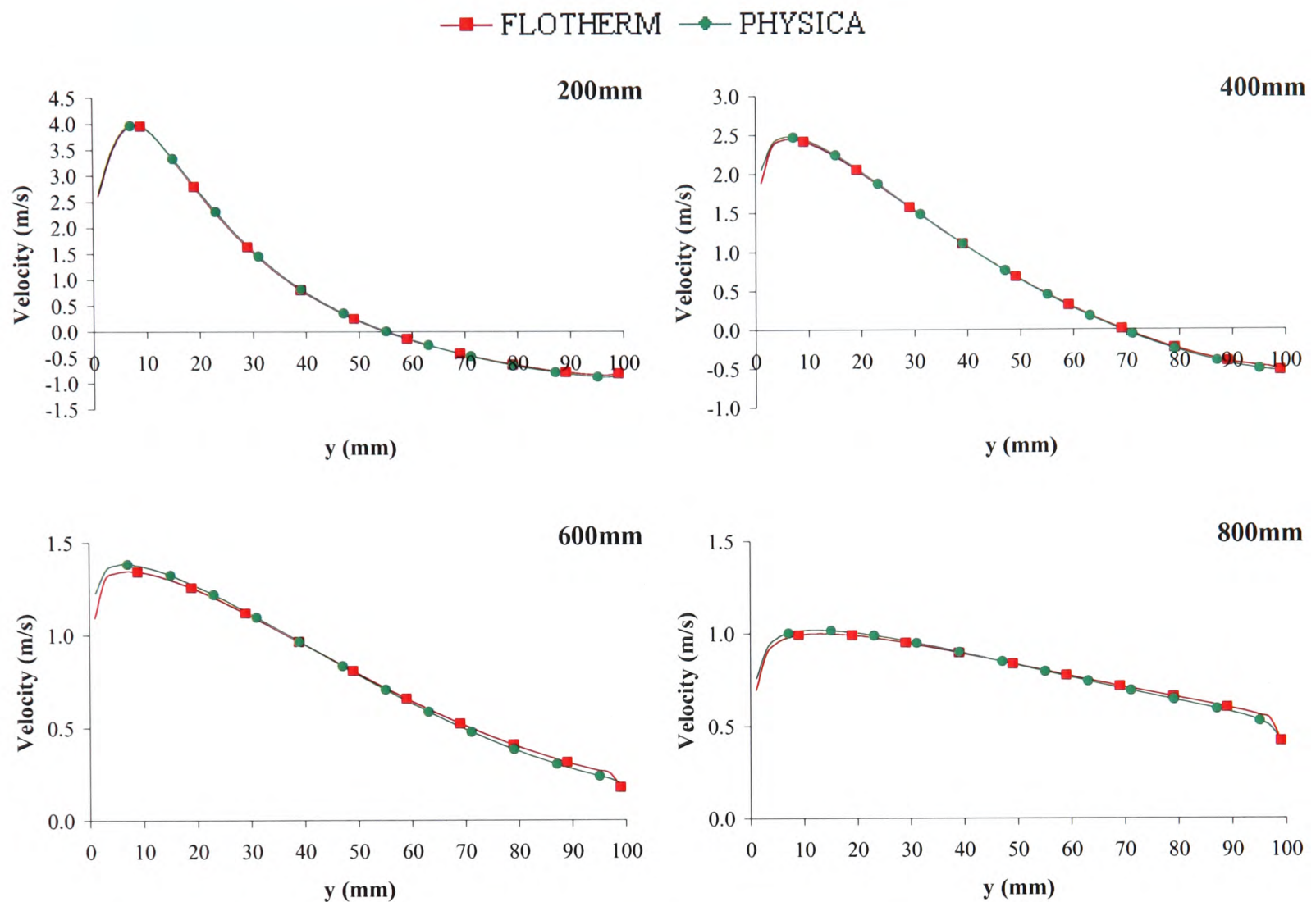
Figure 5.13 Velocity profile comparisons 200mm increments from inlet

Comparisons between FLOTHERM and PHYSICA are in good agreement initially and deteriorate slightly as profiles further down the solution domain are considered. This deterioration in the results is most likely due to small differences between the wall functions implemented in the two codes as the near-wall cells show the greatest discrepancy.

In order to achieve a meaningful comparison, the two codes used the same numerical discretisation scheme (Upwind in this case). This means numerical diffusion affects the results to the same extent in each code.

5.3 Backward Facing Step

Turbulent flow over a backward facing step is a frequently used benchmark problem to evaluate the performance of turbulence models in the prediction of separated flows. Although

the backward facing step is the simplest reattaching flow, the flow field is still complex. Figure 5.14 illustrates some of the complexities observed.

I	Corner eddy	IV	Reattachment zone
II	Backflow zone	V	Redeveloping near-wall flow
III	Separated shear layer	VI	Relaxing outer shear layer
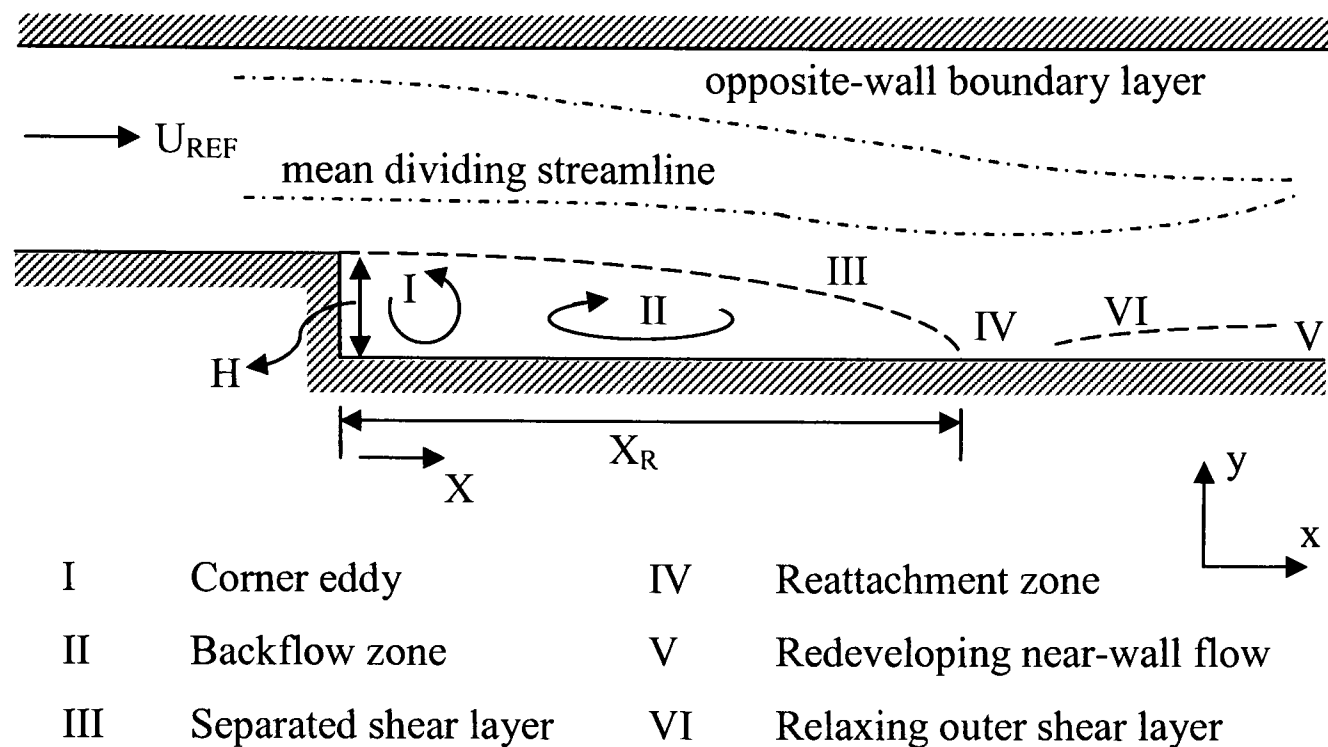
Figure 5.14 Schematic of the single-sided backward-facing step

The geometry of the backward facing step fixes some of the parameters, such as the separation point, but still produces all the flow regions of interest. Upstream of the separation point, an ordinary turbulent boundary layer develops in a long, flat section. This boundary layer then separates at the sharp corner and forms a free shear layer which is almost unaffected by the presence of the upper and lower walls. This shear layer grows by entrainment from both the free stream and the recirculation region beneath it. Due to the pressure gradient and its own expansion, this shear layer turns and reattaches at the lower wall.

The reattachment length, X_R, is a universally used parameter to determine the capability of a turbulence model to accurately simulate the backward facing step. It is defined as the distance from the backward facing step to the point, on the lower channel wall, where the axial velocity changes from a negative to a positive value. As stated earlier the reattachment point for the turbulent regime is dependent on Reynolds number, but usually taken to be in the range 7.0 ± 1.0 times the step height. However the simulation work of Nallasamy and Chen[17] shows that the reattachment point predicted by the standard high Reynolds number $k - \varepsilon$ turbulence model lies in the range of $5.8 - 6.1$ step heights.

Two backward facing step configurations have been considered for investigation, both of which use the Hybrid differencing scheme. The first looks at the single-sided backward-facing step test case which originates from the work of Vogel and Eaton.[13] The primary goal of their work was to investigate the causes of the high heat transfer rate in the reattachment region. The second configuration originates from the AFOSR-HTTM-Sanford Conference on Complex Turbulent Flows,[18] the reason for considering two configurations will be discussed later.

5.3.1 Reynolds Number 28,000

Vogel and Eaton have noted that the majority of the work undertaken in the area of reattaching shear layers has been emphasised on the fluid dynamics of the flow, mainly due to the advances in instrumentation. The heat transfer processes and their interaction with the fluid dynamics of the flow are much more poorly understood.

Due to the relevance of reattaching shear layers in practical heat transfer situations, such as within electronic circuitry; this area is attracting great attention by thermal engineers because reattaching flows can cause large variations of the local heat transfer coefficient as well as substantial overall heat transfer augmentation. However for the purpose of this investigation, which concentrates on the validation of turbulence models for predicting the flow reattaching point, the heat transfer affects will be ignored. The computational results have only been compared against the skin friction experimental data available. Hence the lower wall downstream of the step, which had a constant heat flux of 130W/m^2, has been modelled as an adiabatic wall.

In order to concentrate specifically on the reattachment process and the corresponding action of the surrounding fluid, the experimental facility used for this work was a two-dimensional, sudden-expansion wind tunnel. It consists of a blower and a turbulence management section, a boundary layer development section, and a sudden expansion test section.

Air is filtered upstream of the blower and meets the turbulence management section which consists of a honeycomb, four small mesh screens, and a 4:1 two-dimensional contraction. The test boundary layer develops on the bottom surface of the (150 x 510)mm development section, which is 2.5m long. The side wall boundary layers are removed by scoops upstream

of the test section to reduce the strength of any secondary flows. The scoops narrow the test section to a width of 450mm. After the scoops there is a flat section before the boundary layer flows over the 37.9mm high backward facing step (expansion ratio 1.25). A free stream velocity of 11m/s is stated corresponding to a Reynolds number, based on the step height, of 28,000 and a boundary layer thickness which is 1.1 times the step height.

The experimental apparatus is constructed as an open circuit wind tunnel. A schematic of the wind tunnel facility is shown in Figure 5.15, for further explanation on the experimental configuration see Vogel and Eaton.[13, 119]
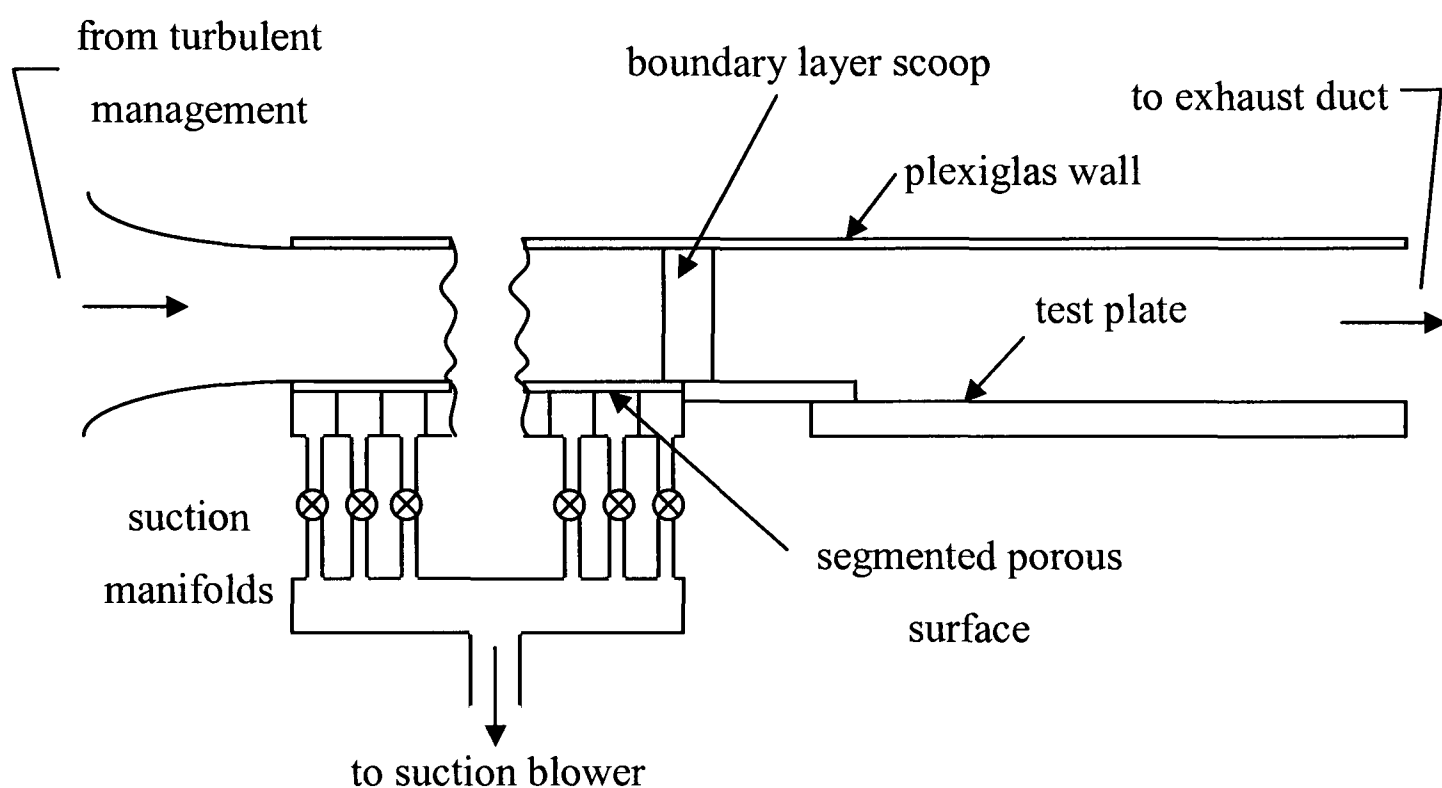
Figure 5.15 Schematic of the wind tunnel facility used for the reattaching flow heat transfer research

The computational solution domain structure simulated for this test case is presented in Figure 5.16. The mesh density used is presented in Figure 5.17, it is noted that mesh grading has been used to ensure that a fine mesh concentration is located close to the wall boundaries of the domain. (333 x 160) cells upstream of the step and (333 x 220) cells downstream of the step have been distributed in the x- and y-directions respectively.
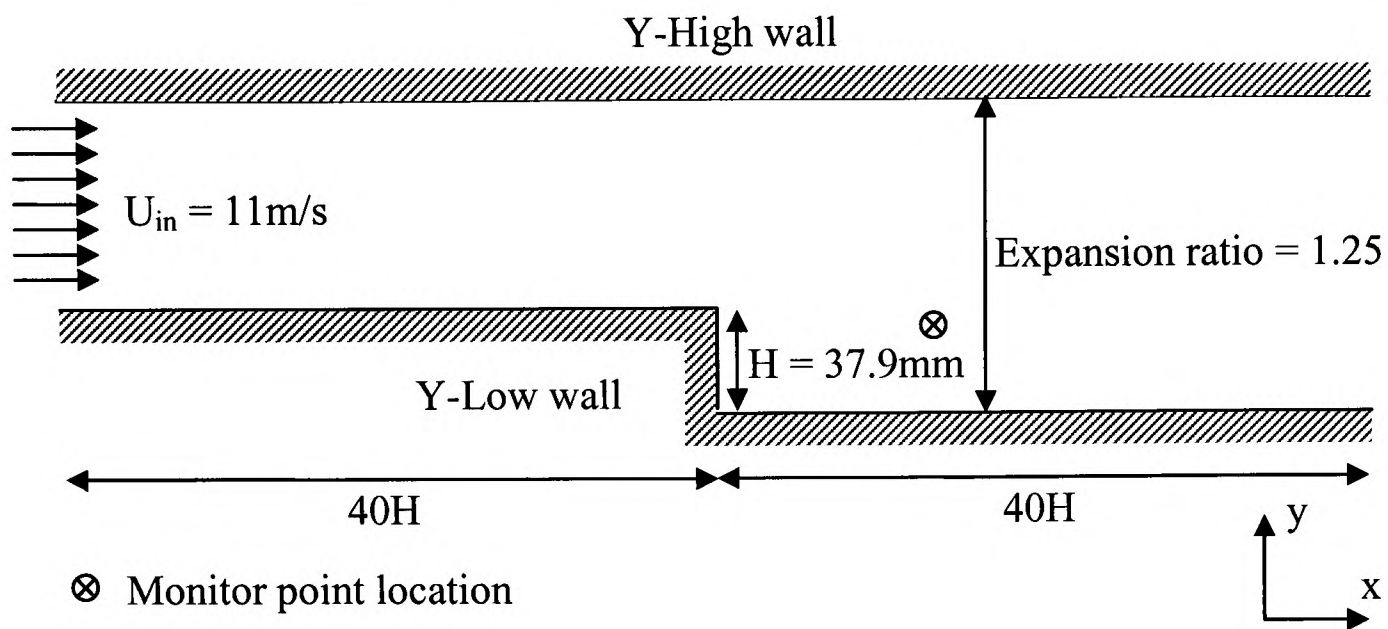
Figure 5.16 Backward facing step solution domain Re = 28,000
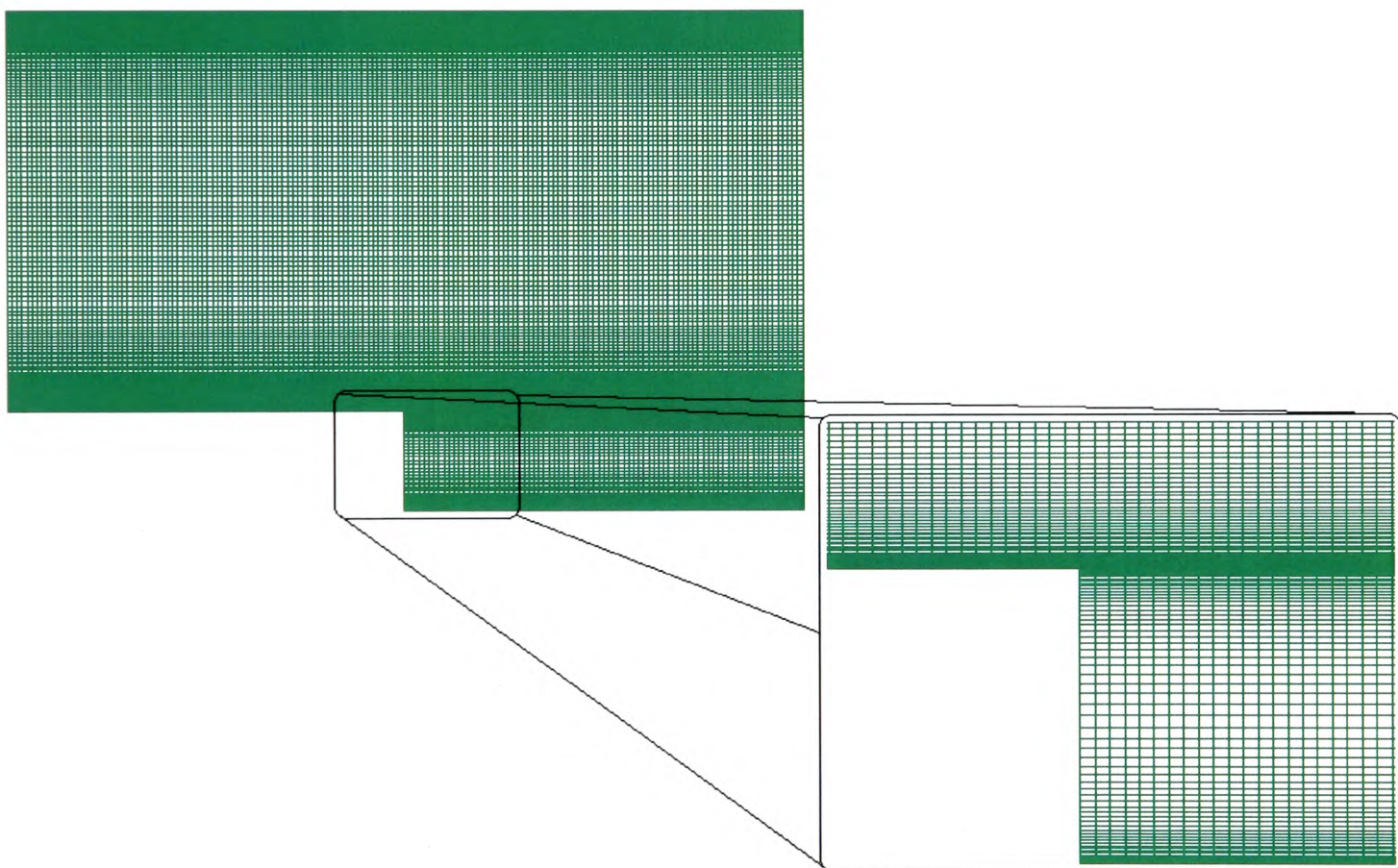
Figure 5.17 Mesh density employed for the backward facing step case Re = 28,000

The experimental data available indicates that the flow is laminar at the centreline of the channel; therefore both the turbulent parameters at the inlet have been set to 1.0×10^{-10}. The fluid material properties specified for this case use a density of 1.2kg/m^3 and a kinematic viscosity of $1.4889 \times 10^{-5} \text{m}^2/\text{s}$. The configuration simulated specified a uniform inlet velocity and allowed the variable profiles to develop along a significantly long channel upstream of the step. A complete description of the configuration, mesh density and boundary conditions employed are provided in Appendix A3.1.

The CFD predictions presented in this section have been compared against the experimental data of Vogel and Eaton.[13] As discussed in Appendix A3.1, inadequate information regarding the inlet boundary condition, which featured a boundary layer suction device, has made this test case extremely difficult to simulate accurately.

Nevertheless the simulations attempted for this case are worth reporting upon. The initial attempt made on this case was to allow the velocity and turbulence to naturally develop without any influence from the suction device. Due to the ambiguous nature of the inlet boundary condition it was necessary that the initial simulation work was performed with a turbulence model which had some kind of consensus related to the model's performance regarding the reattachment length predicted. Hence the $k - \omega$ turbulence model has been selected due to the fact that the large majority of researchers[58, 61, 62, 120, 121] which have undertaken work on backward facing step configurations agree that the reattachment length lies in the range of 7.0 ± 1.0 step heights.

As experimental data could be extracted for the velocity and turbulent kinetic energy from the report produced by Vogel and Eaton[13] it was considered logical to assess how the predicted profiles compared with the experimental data for this configuration. Figure 5.18 and Figure 5.19 represent the u-component velocity profile and turbulent kinetic energy profile at an upstream measurement location (75mm upstream of the step) predicted by the $k - \omega$ turbulence model respectively.

Figure 5.18 shows that the total flow at the measurement location is too high, presumably due to this being reduced by the suction device present in the experimental set up, but not modelled due to inadequate information.
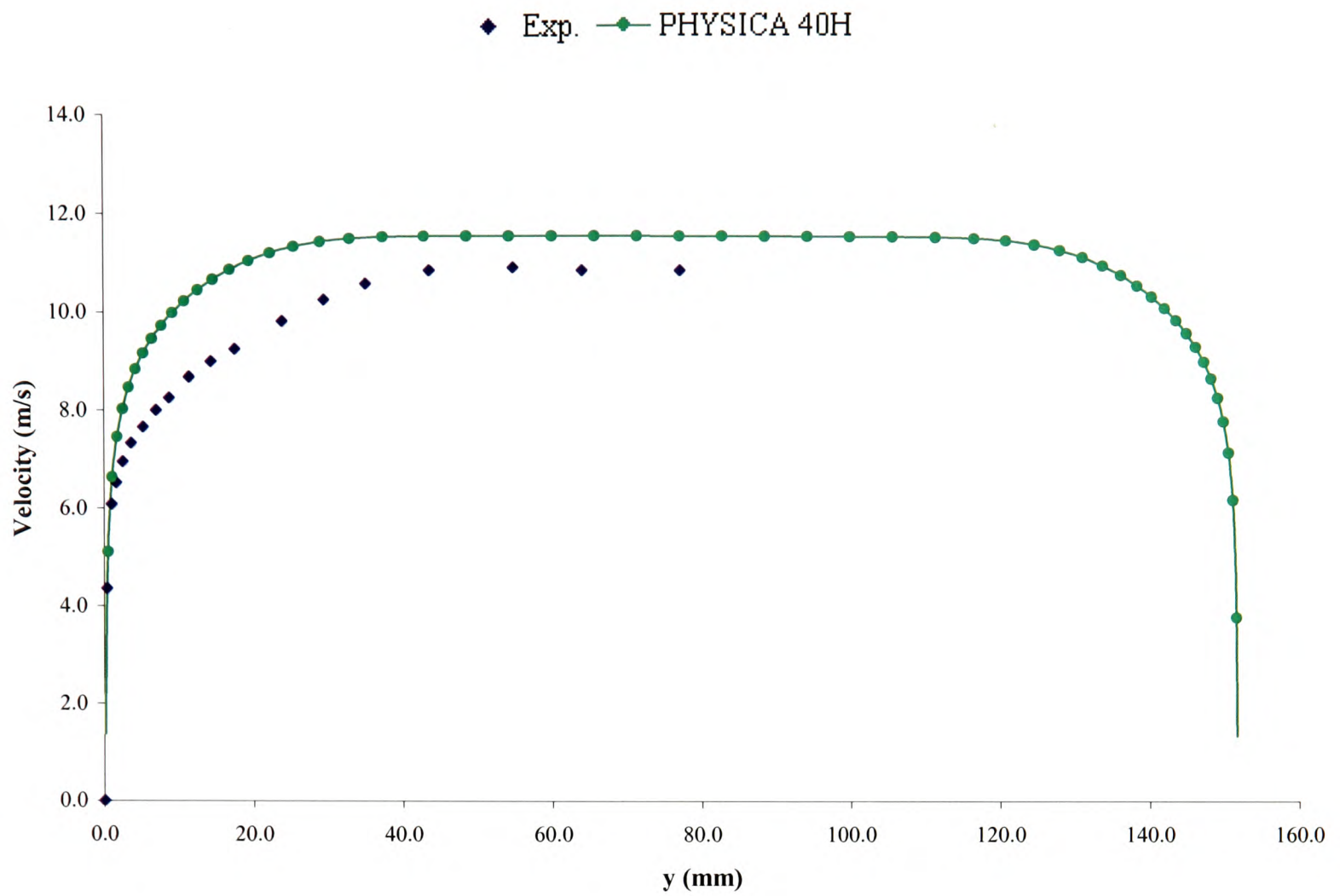
Figure 5.18 u-component velocity profile upstream of step (40H channel)
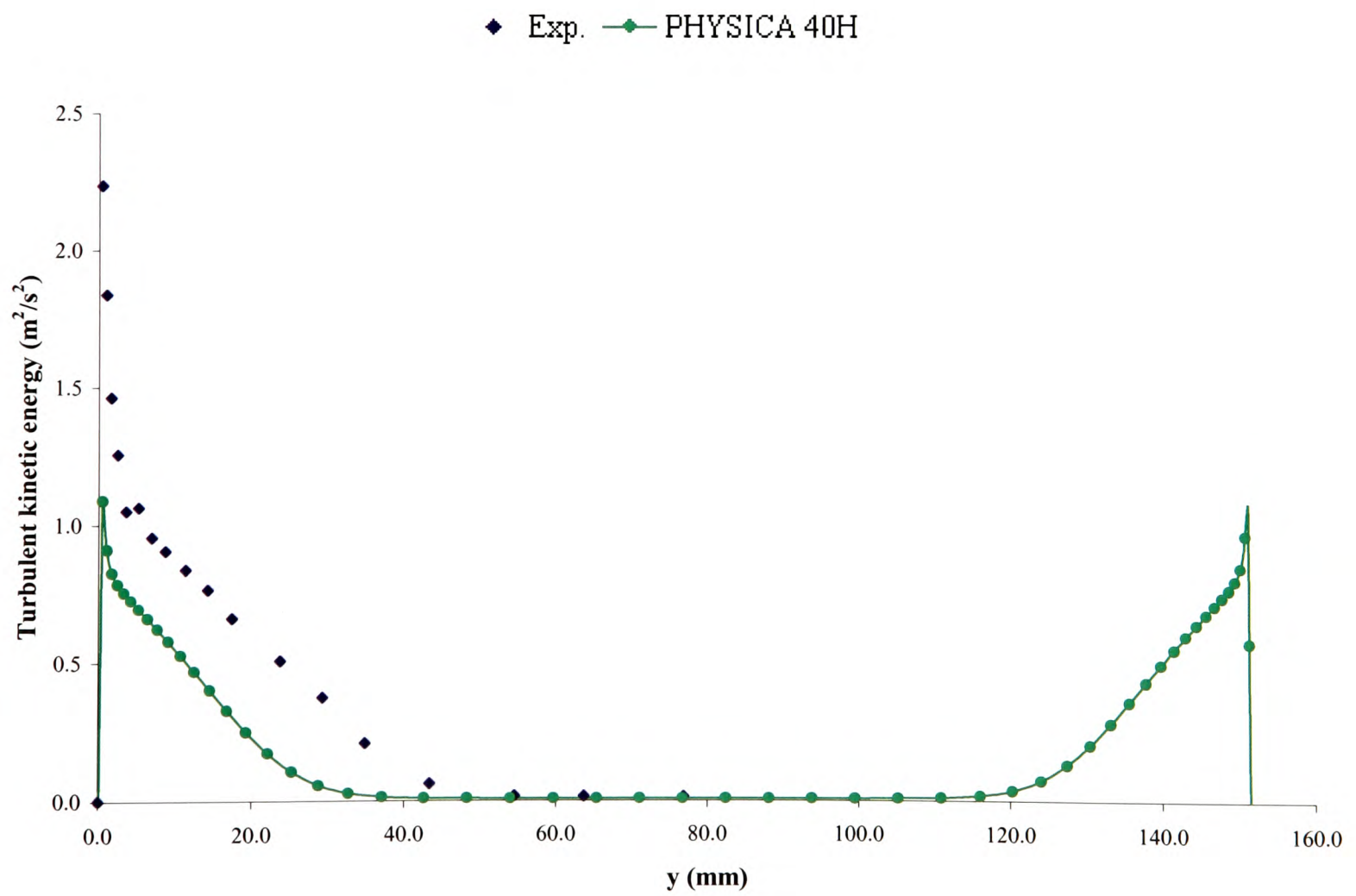
Figure 5.19 Turbulent kinetic energy profile upstream of step (40H channel)

Using this extended channel upstream of the step it can be determined from Figure 5.18 and Figure 5.19 that the experimental flow distribution at the measurement location is markedly different from a fully developed flow as the suction device acts to remove the boundary layer, this is also noted by Vieser et al.[121] At this point it is clear that this $40H$ test case configuration, which produced a fully developed flow profile by approximately $30H$, will not produce adequate predictions of the complete skin friction distribution along the Y-Low wall downstream of the step.

From the predicted skin friction coefficient the reattachment length can be determined. Figure 5.20 defines a reattachment length of 7.2 step heights which lies in good agreement with the acceptable range of 7.0 ± 1.0 step heights. It can also be determined from this figure that a slightly faster velocity recirculation region is predicted in comparison to the experimental data. This may be due to the total flow being too high as the effect of the suction device was not included in the simulation.
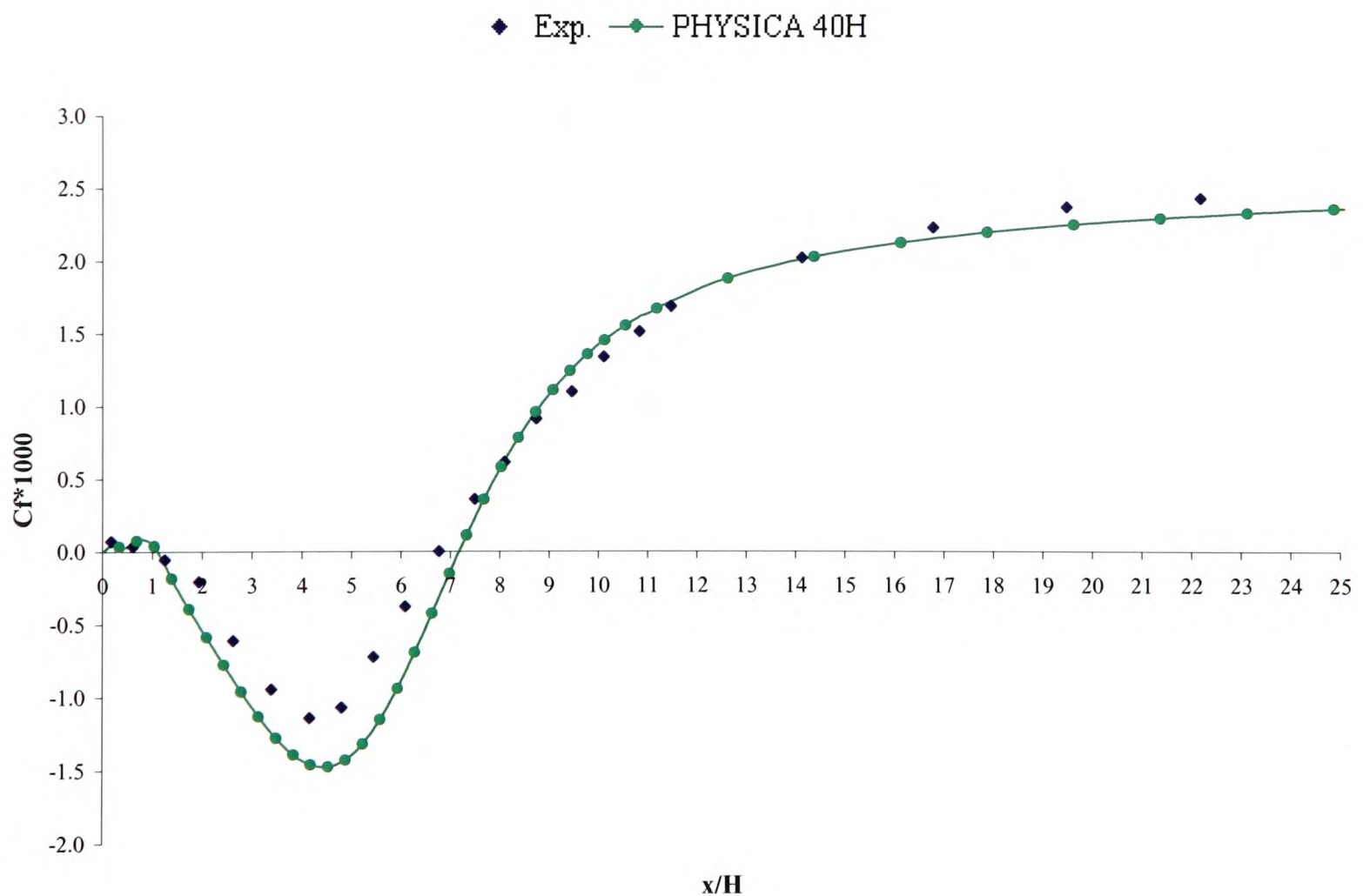
Figure 5.20 Skin friction coefficient on the lower wall boundary downstream of the step
(k - ω model 40H channel)

Regarding the accuracy of the predicted skin friction profile with respect to the experimental data it can be concluded that simulating this extended development section before the step and ignoring the suction device has nevertheless resulted in a reasonable profile comparison.

In order to improve on the initial PHYSICA results obtained three avenues were pursued. Firstly the work of Vieser et al.[121] was considered. Vieser et al. had used the Vogel and Eaton experimental data in 2002 to validate the performance of the SST turbulence model, the computational domain considered for this work is detailed in Appendix A3.1.

Simulations have been conducted using the geometry, boundary conditions and mesh density employed by Vieser et al. (PHYSICA 3.8H) with little improvement noted in the skin friction results as can be seen in Figure 5.21.
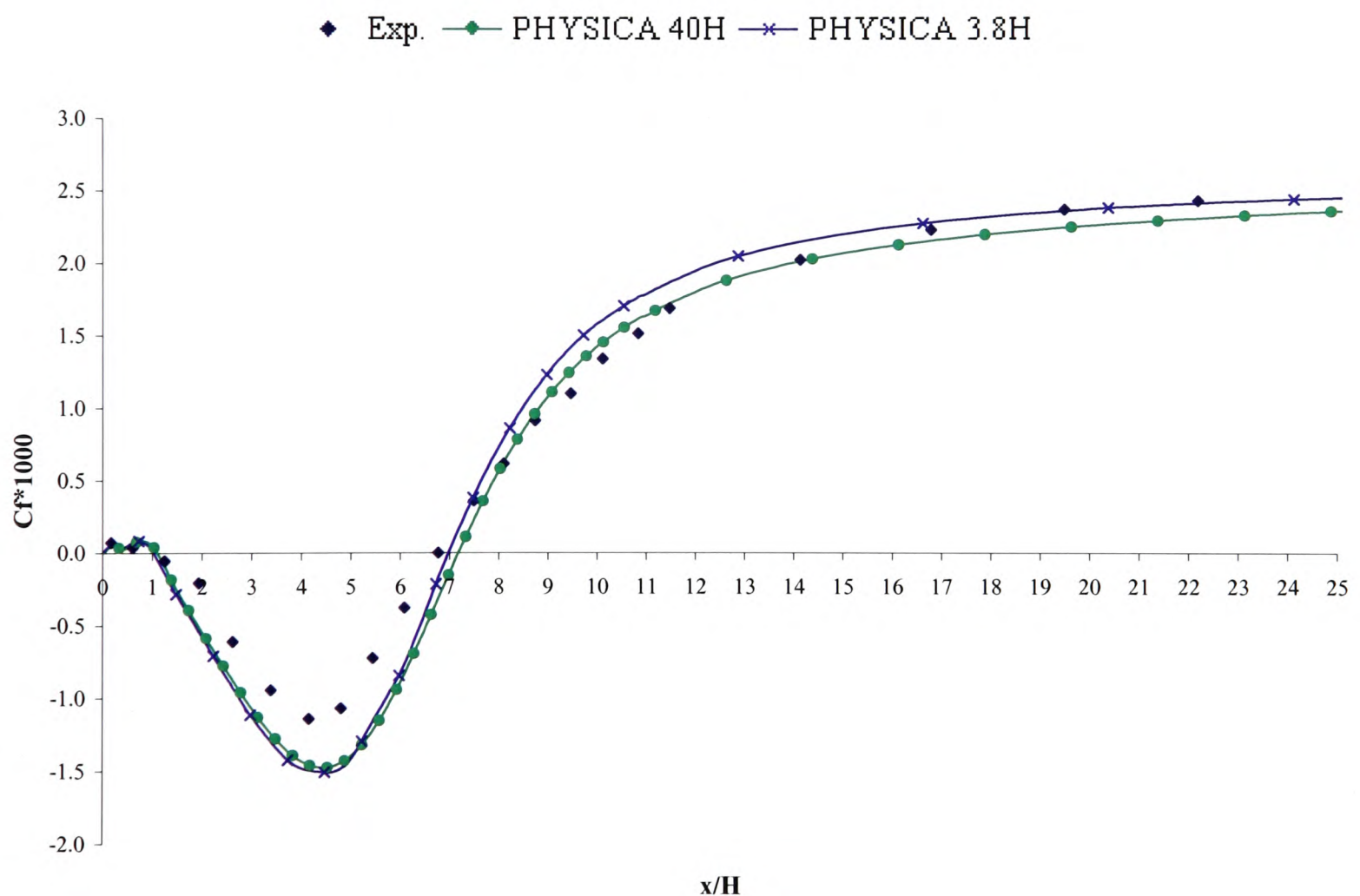
Figure 5.21 Prediction of reattachment length (3.8H channel)

The following quotation has been taken from Vieser et al.[121] regarding Vogel and Eaton's specification of the inlet boundary for the backward facing step.

"The upstream flow was not a fully developed turbulent boundary layer. In the experiment the boundary-layer evolved in a rectangular duct. The thickness of the boundary-layer was controlled by a suction facility. From the references it was not clear, in which way the experiment was influenced by the suction. Only the integral quantities of the boundary-layer at a certain position upstream of the step are known. In order to model the inflow conditions under these circumstances, separate simulations were done until the parameters of the experimental inlet profile were achieved."

The difficulty of specifying appropriate inlet boundary conditions for this backward facing step case have been highlighted by Vieser et al. In the current work attempts to replicate the experimental inlet profile were not successful.

The second attempt made to improve the prediction of the reattachment length a variation of linear, polynomial, logarithmic and power equations were fitted to the experimental data and manually prescribed as symmetric inlet boundary conditions located at the upstream measurement station. Figure 5.22 and Figure 5.23 give an example of one of the combinations of fitted equations used for the velocity and turbulent kinetic energy respectively.

The equations shown in the figure are:

$y = -1737.4x^2 + 168.83x + 6.8155$

$y = -0.5247x + 10.916$

$y = -1069.9x^2 + 135.99x + 7.2048$

$y = 17.565x^{0.158}$

$y = -59308x^2 + 716.75x + 5.5387$

$y = 1.4706 \ln(x) + 16.125$

$y = 12449x$
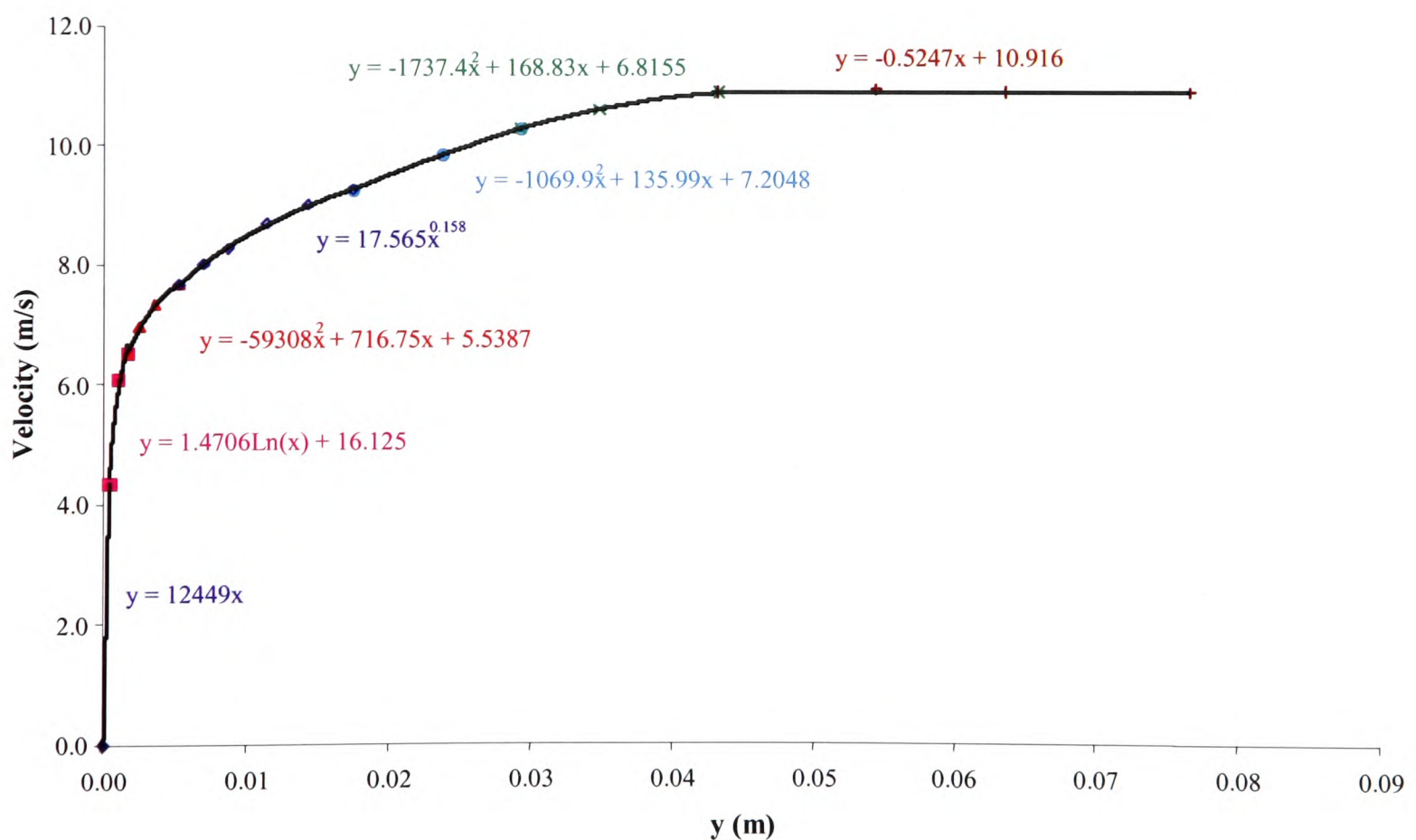
Figure 5.22 Fitted equations to the upstream u-component velocity profile
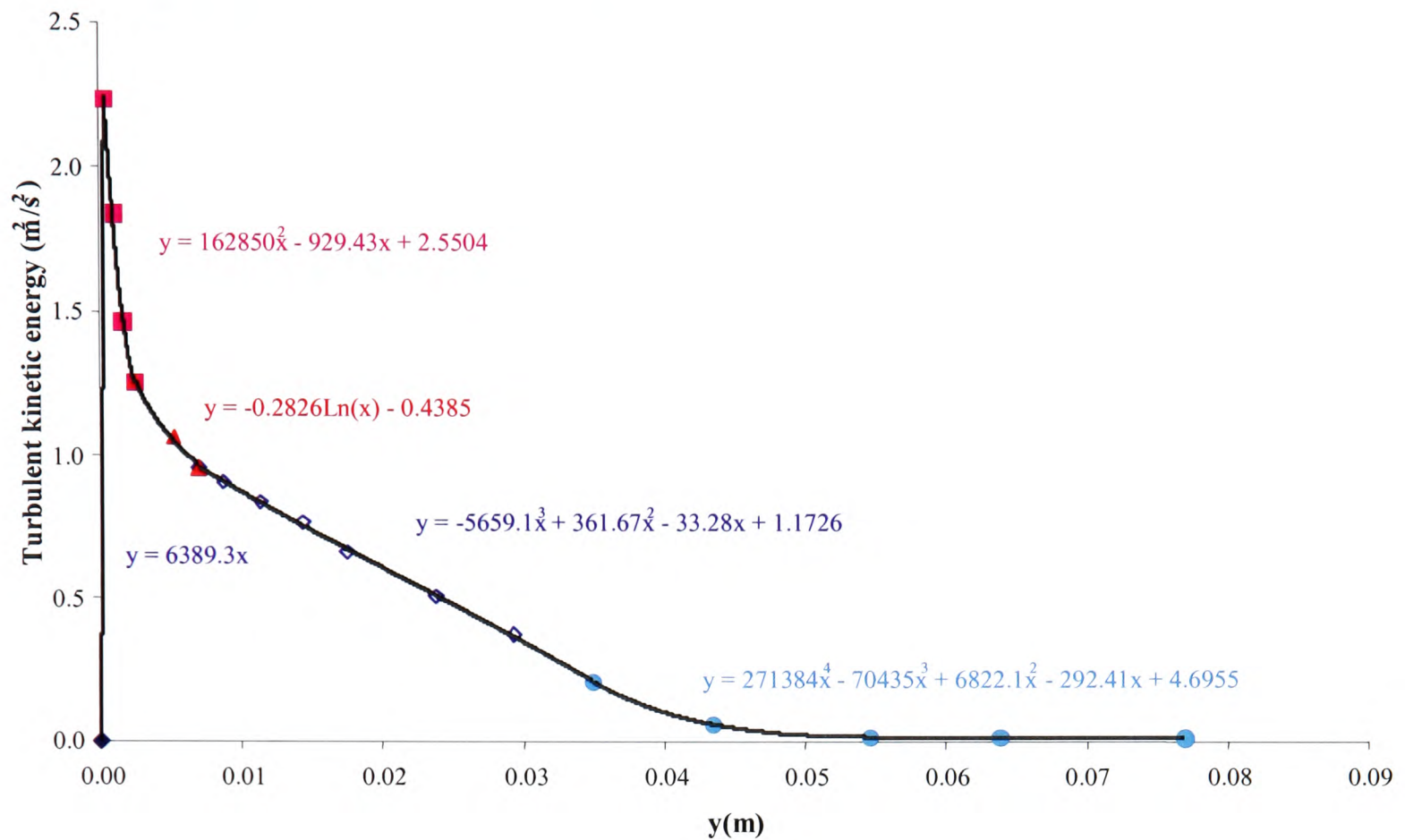
Figure 5.23 Fitted equations to the upstream turbulent kinetic energy profile

The clear disadvantage of this method is that it is now assumed that the velocity and turbulent kinetic energy profiles are symmetric, hence the suction device exists on both upper and lower y-directional boundary walls.

Figure 5.24 (Prescribed Profiles) shows the reattachment length predicted when profiles of the axial velocity and turbulence kinetic energy have been prescribed at the upstream measurement location.
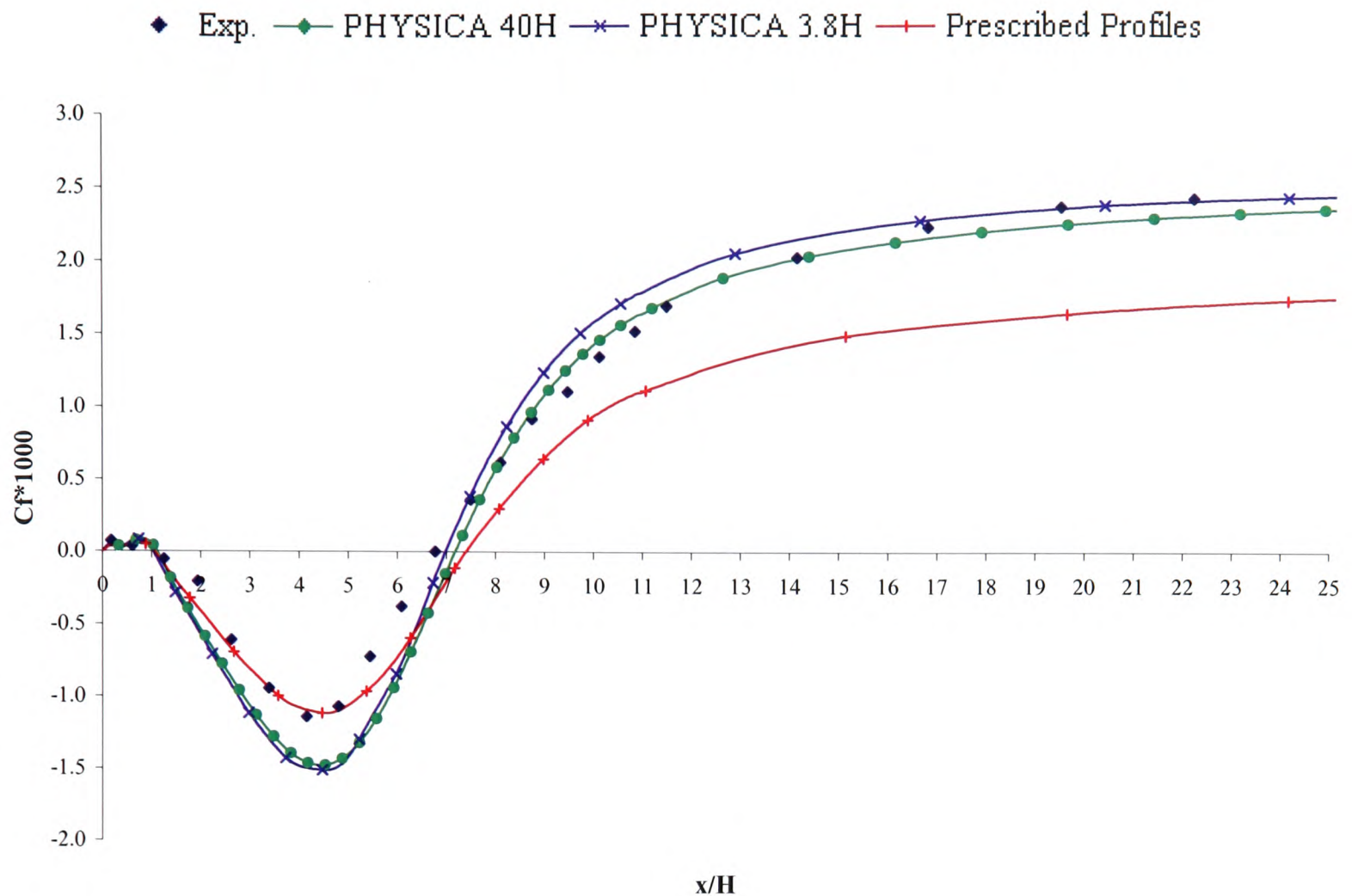
Figure 5.24 Prediction of reattachment length using prescribed profiles at measurement location

It is concluded that although in this case the recirculation region is well predicted, the boundary layer beyond reattachment develops at a slower pace compared to the experiments. The results obtained here are consistent with the $k - \omega$ findings presented by Heyerichs and Pollard.[58]

In a final attempt to improve the reattachment length predictions the well known one-seventh power law has been used, which was implemented in PHYSICA as part of this research. Details of the boundary condition specifications have been provided in Figure 5.25. This method was utilized by Heyerichs and Pollard[58] when they were assessing the performance of a range of turbulence models and wall function implementations against the Vogel and Eaton experimental data.
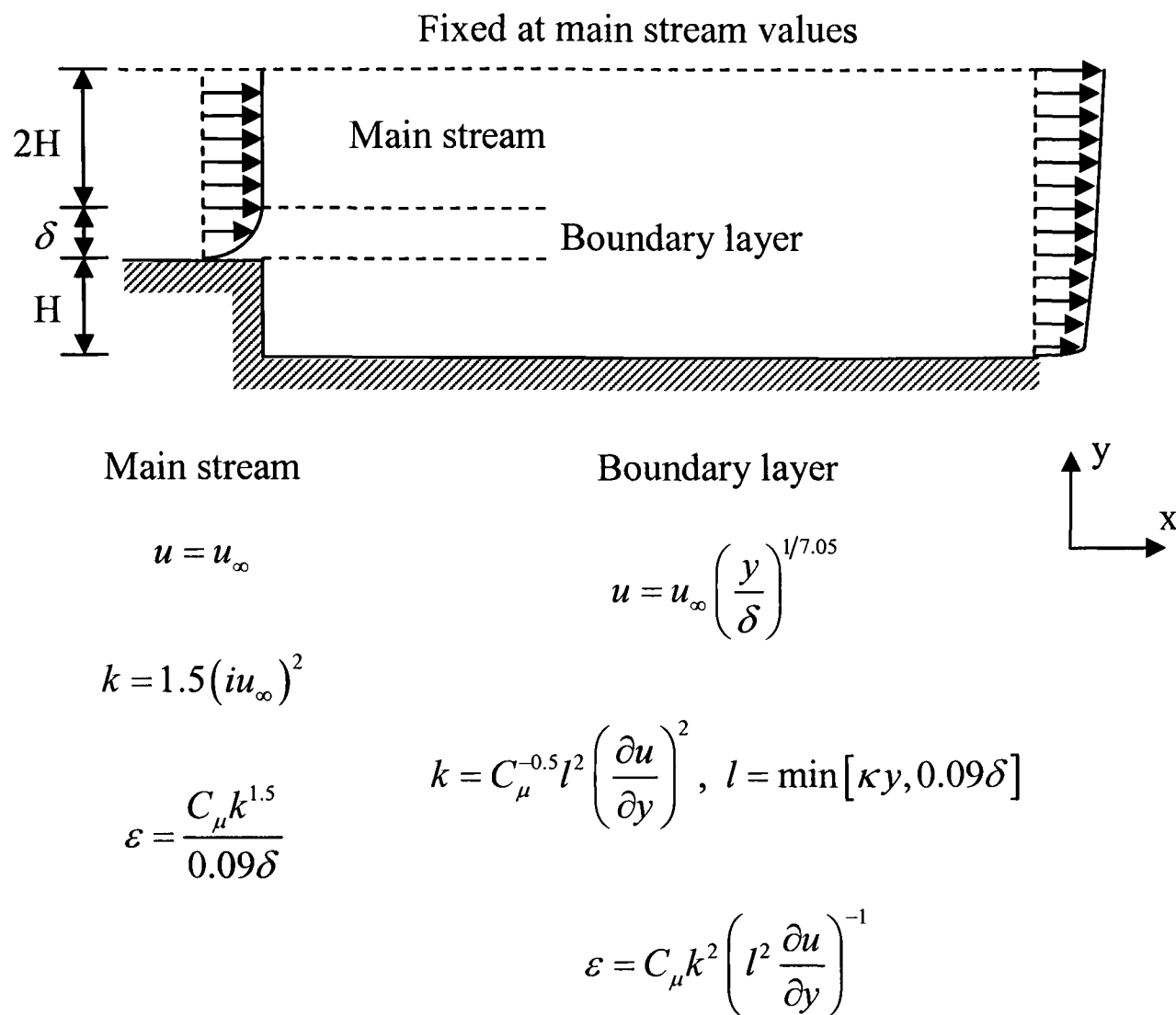
Figure 5.25 Specifications of one-seventh power law

Simulation work was undertaken using the one-seventh power law $(\delta = 1.1H)$ on both the $40H$ and $3.8H$ backward facing step geometry configurations together with a combination of equations to approximate turbulent kinetic energy and dissipation rate values at the inlet. Unfortunately no clear improvements in the results were noted.

Due to the uncertainties this case was eventually abandoned.

5.3.2 Reynolds Number 88,000

The computational domain uses a channel height which is three times the height of the step with the inlet boundary condition specified four step heights upstream of the step itself. The inlet velocity is calculated to result in a Reynolds number, based on the step height, of 88,000. The outlet boundary is positioned twenty step heights downstream of the step, ensuring that the outlet boundary condition would not influence the recirculation region behind the step. The fluid material properties specified for this case use a density of 1.161kg/m^3 and a kinematic viscosity of $1.5586 \times 10^{-5}\,\text{m}^2/\text{s}$.

The dimensions employed for this case have been presented in Figure 5.26. Turbulence models not requiring a fine near-wall mesh were run on a uniform mesh of (8 x 10) upstream and (40 x 30) downstream of the step in the x- and y-directions respectively. Figure 5.27 shows the mesh density used for any model, such as the $k-\omega$ model, which requires a fine near-wall mesh. The generation of this mesh exploits a grading technique to ensure a fine mesh concentration near to wall surfaces. (40 x 40) cells are used upstream of the step and (200 x 70) downstream of the step in the x- and y-directions respectively.
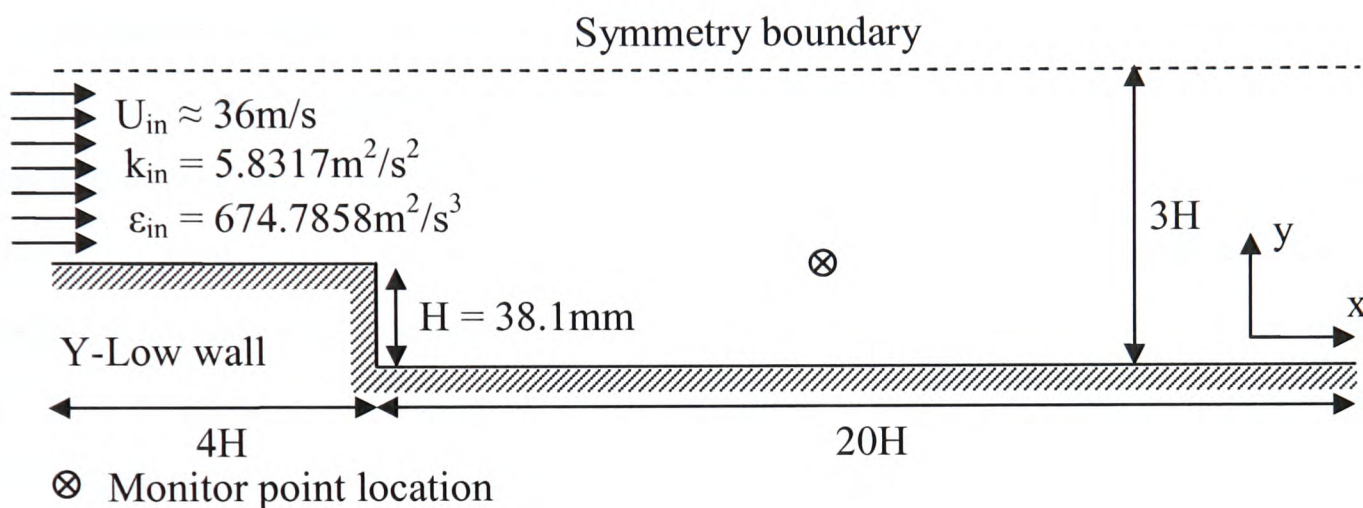
Figure 5.26 Backward facing step solution domain Re = 88,000
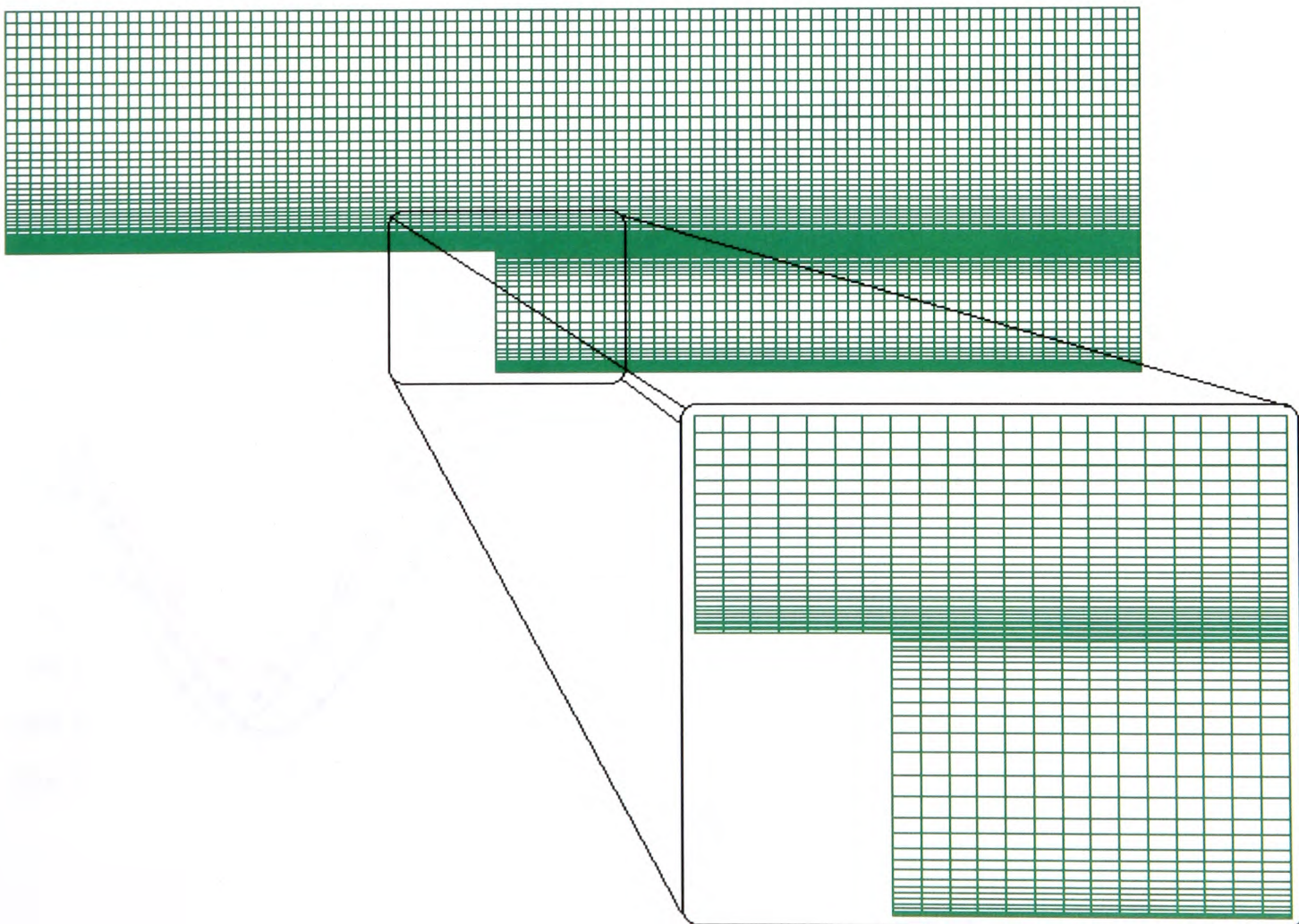
Figure 5.27 Mesh density employed for the backward facing step case Re = 88,000

The simulated CFD results obtained have been compared against the numerical work presented in the Ph.D. investigation undertaken by Croft.[122] The mesh density employed is similar to the mesh used by Croft. Instead of the skin friction results the x-velocity component has been presented, which is the main flow direction along the channel for the row of cells immediately adjacent to the lower boundary wall downstream of the step in order to determine the point of flow reattachment.

Figure 5.28 presents the reattachment length predicted by the standard high Reynolds number $k - \varepsilon$ turbulence model. The FLOTHERM predictions compare exceptionally well, especially after the flow has reattached, with the numerical work produced by Croft predicting a reattachment length of $6.0H$. The other commercially available CFD code PHOENICS, manages to predict a reattachment length of $7.1H$ which is in excellent agreement with experimental data that suggest a reattachment range of 7.0 ± 1.0 step heights. Finally PHYSICA predicts a reattachment length of $5.8H$ which would be considered as the norm for this particular turbulence model.
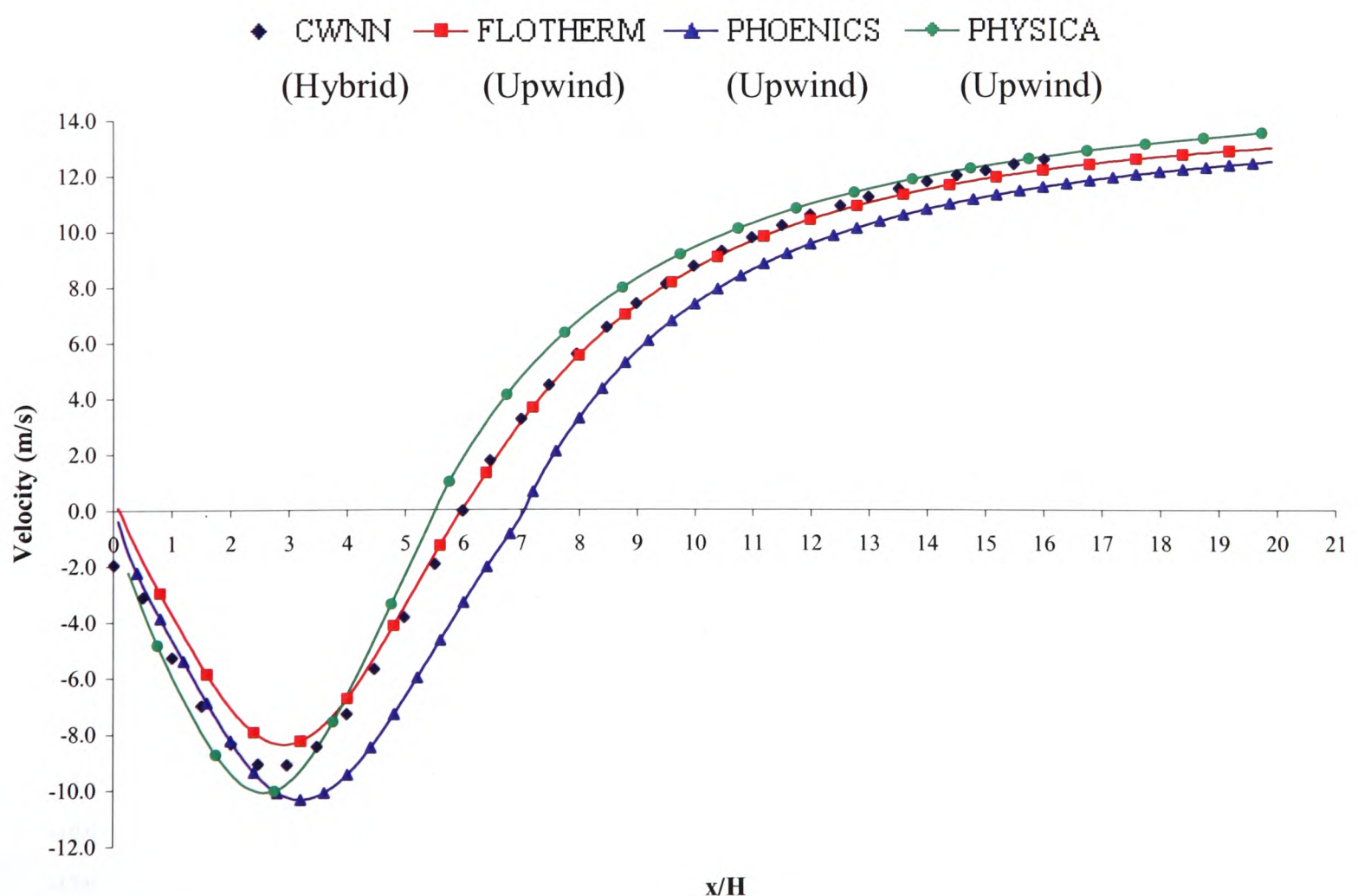
Figure 5.28 Standard k - ε model reattachment length

The FLOTHERM and PHYSICA results comfortably rest within the range of reattachment length values $5.8 - 6.1$ step heights stated by Nallasamy and Chen[17] for the standard high Reynolds number $k - \varepsilon$ turbulence model. It is not clear why PHOENICS gives a different answer.

The CFD code employed by Croft in 1998 was known as Code_With_No_Name (CWNN) which later was renamed PHYSICA. The reason for highlighting this fact is that it is felt by the author that the current PHYSICA results should be identical to the results obtained by Croft some years earlier. Therefore one would be able to conclude that after many years of software development the basic structure of PHYSICA remains in a state of stability.

Re-simulation work has been undertaken to determine the cause of the slight discrepancy between the results obtained by CWNN and PHYSICA. One reason for the discrepancy could be due to the differencing scheme adopted. Since Croft used the Hybrid scheme in his work, the calculations were repeated, switching from Upwind to Hybrid. It can be concluded from Figure 5.29 that if the differencing scheme is changed from Upwind to Hybrid the comparison between CWNN and PHYSICA is identical.
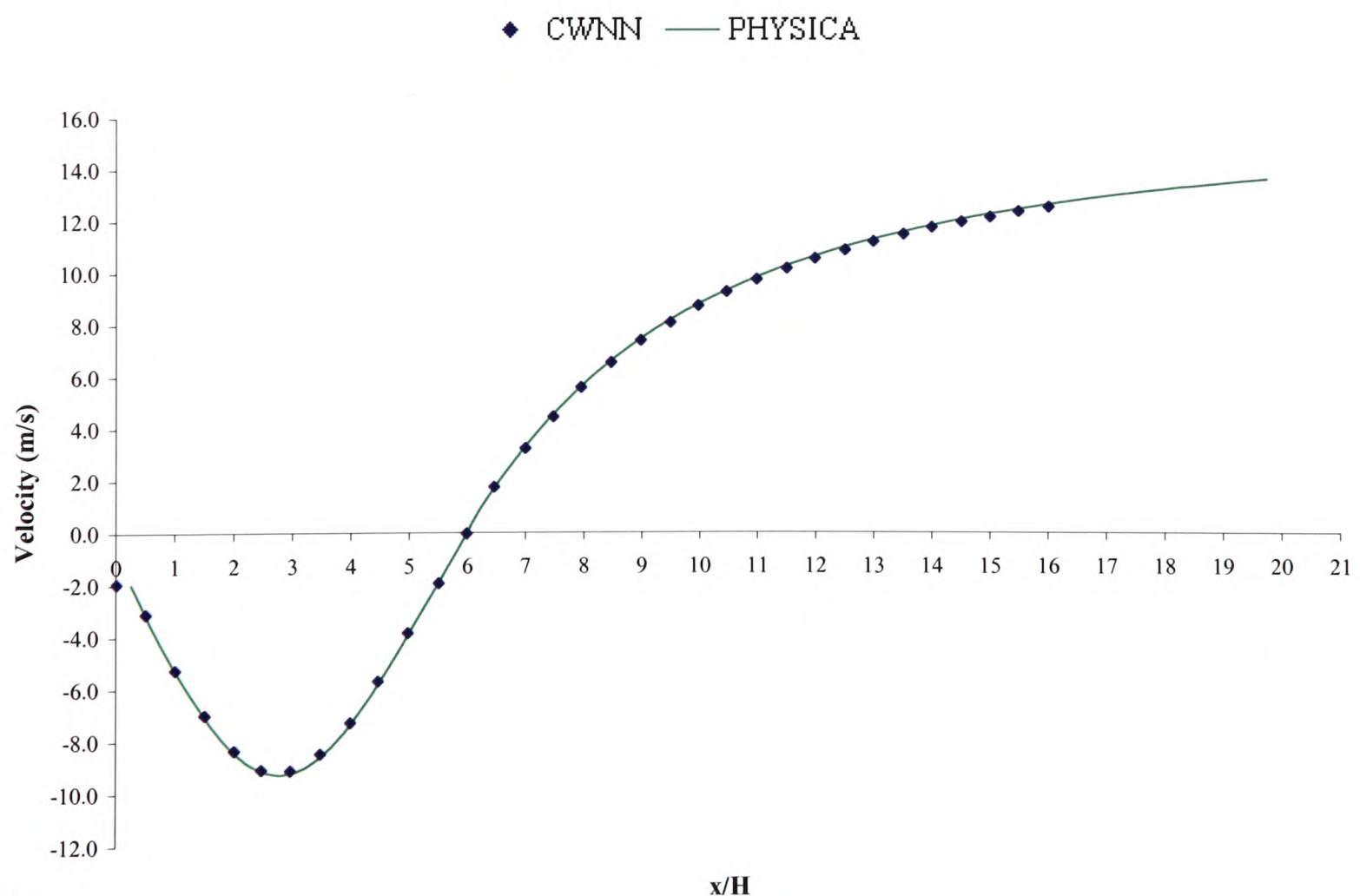
Figure 5.29 Standard $k - \varepsilon$ model reattachment length Hybrid differencing scheme

This does not suggest that the results obtained by the Upwind scheme are incorrect; it simply suggests that the differencing scheme has an influence on the results.

At this point it would be reasonable to further examine the impact of the differencing scheme on the reattachment length results obtained. This has been achieved by conducting a mesh refinement study. Numerical result comparisons, for the original mesh density, are shown in Figure 5.30 for the first order schemes against the SMART[89] higher order differencing scheme.

It is noted that SMART required heavier relaxation parameters to obtain a converged solution.
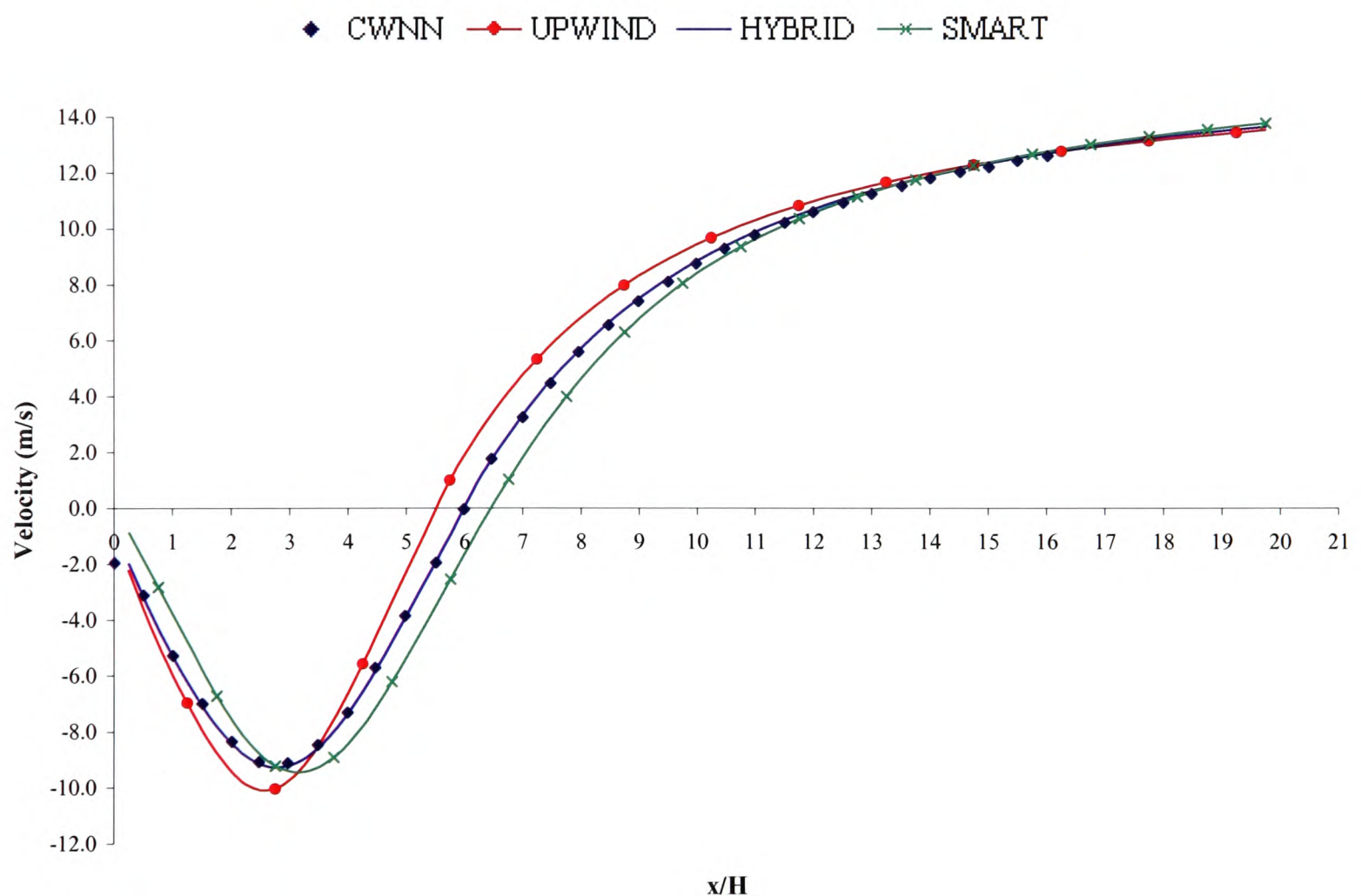
Figure 5.30 Standard k - ε model reattachment length affect of differencing scheme

From the mesh refinement study it was found that the Hybrid scheme originally predicted a reattachment length of $6.0H$, this increased to $6.5H$ as the mesh density was doubled in all directions and remained at this value after subsequent mesh refinements. With SMART the original mesh density predicted a reattachment length of $6.5H$, as the mesh was doubled this

increased to $6.9H$ and then reduced down to $6.6H$ where is stayed for successive mesh refinements.

SMART has shown a slight increase in accuracy with regards to the prediction of the reattachment length, however this scheme was harder to converge and revealed higher CPU timings in comparison to the first order schemes, approximately a 30% increase was found. Therefore it can be concluded that for the type of geometry configurations considered throughout this work no significant advantages are gained if the move towards a higher order differencing scheme, such as SMART, is made, provided a reasonably fine mesh is used. This study was also repeated in PHOENICS where similar results were obtained.

The Wilcox $k - \omega$ turbulence model was not available as a standard model in 1998 when Croft was undertaking his research therefore no data comparison can be made. However a reattachment length of 7.0 ± 1.0 times the step height is considered adequate validation of turbulence model accuracy. Figure 5.31 illustrates that the reattachment length predicted by PHOENICS and PHYSICA for the $k - \omega$ model is 6.9 step heights, this agrees well with the range of acceptance stated above.
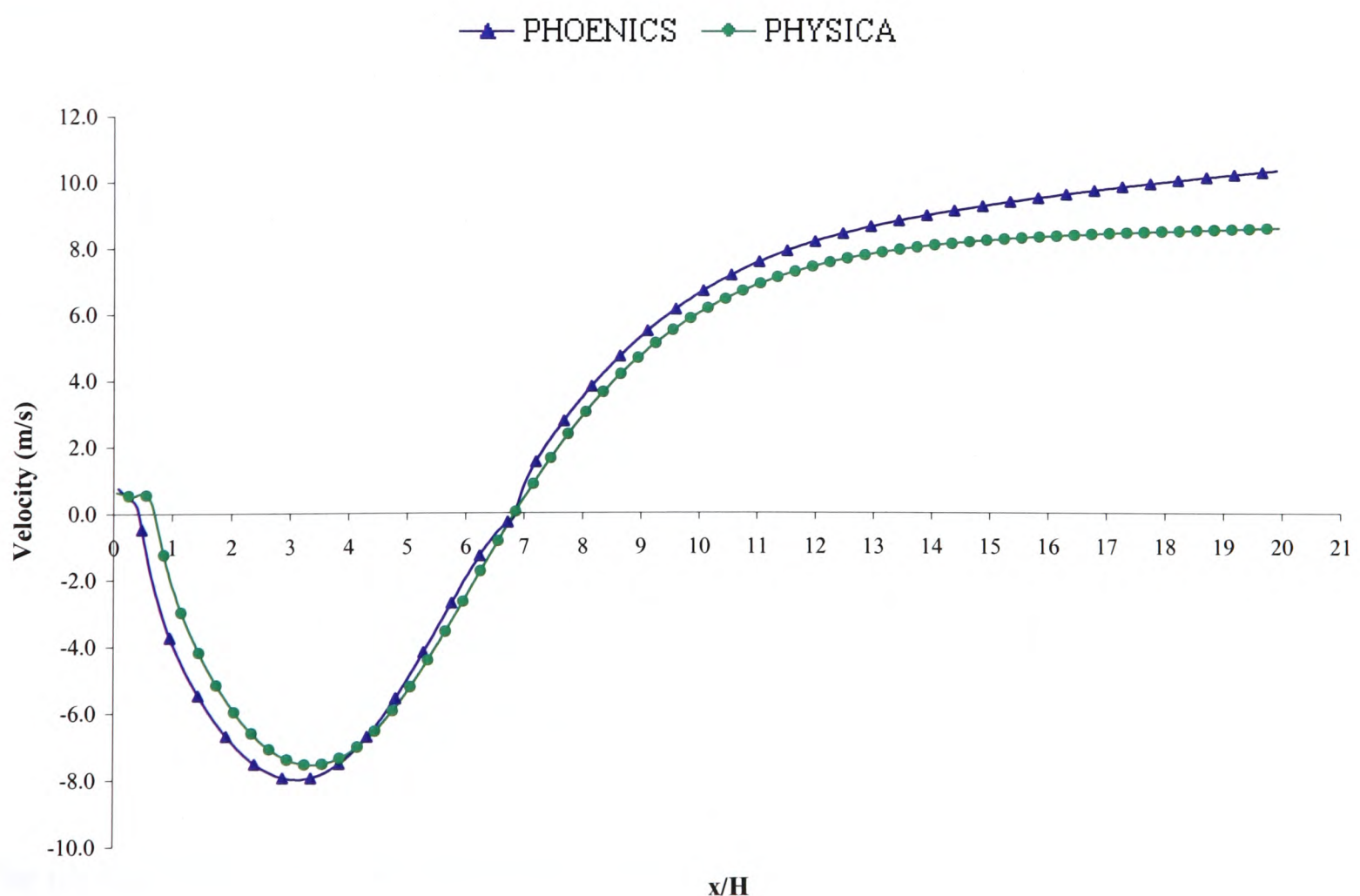
Figure 5.31 Wilcox k - ω model reattachment length

The conclusion which can be drawn from the predictions of the Wilcox $k - \omega$ turbulence model is that the model has been successfully implemented within PHYSICA's unstructured multi-physics framework.

Up to this point flow CFD code comparisons have been undertaken with a high degree of success which should therefore make the reader feel comfortable with the further development and testing of new turbulence models to be solely undertaken within PHYSICA. The next stage for the validation process would be to investigate the performance of the three codes with regards to heat transfer phenomena.

5.4 Flow over a Heated Rib

This section investigates the thermal log-law wall functions currently implemented within the three CFD codes under investigation. The standard high Reynolds number $k - \varepsilon$ turbulence model has been selected for this case.

The test geometry has been detailed in Figure 5.32. The inlet air temperature for the solution domain is set to 20°C. All the material properties are detailed in Appendix A4.
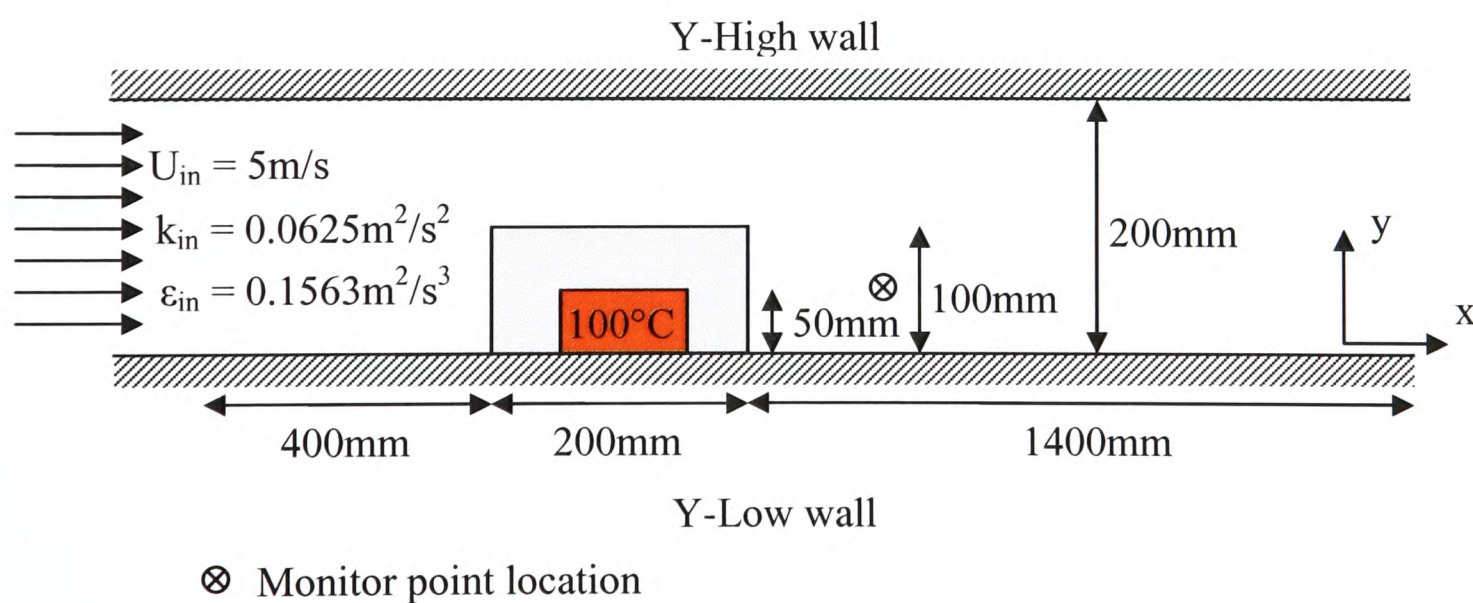
Figure 5.32 Two-dimensional flow over a heated rib test geometry

The rib is constructed of two materials. The core of the rib measuring (100 x 50)mm in the x-and y-directions respectively is kept at a constant temperature of 100°C and is made from the

high conducting material copper. This copper is then encapsulated by an epoxy resin material of 50mm in thickness for all of the copper surfaces which are exposed to the fluid.

A uniformly distributed mesh density has been employed for this test case of (300 x 30) mesh elements in the x- and y-directions respectively. The mesh concentration in and around the rib has been presented in Figure 5.33. The reader is referred to Appendix A4 for a full description of the configuration under investigation.
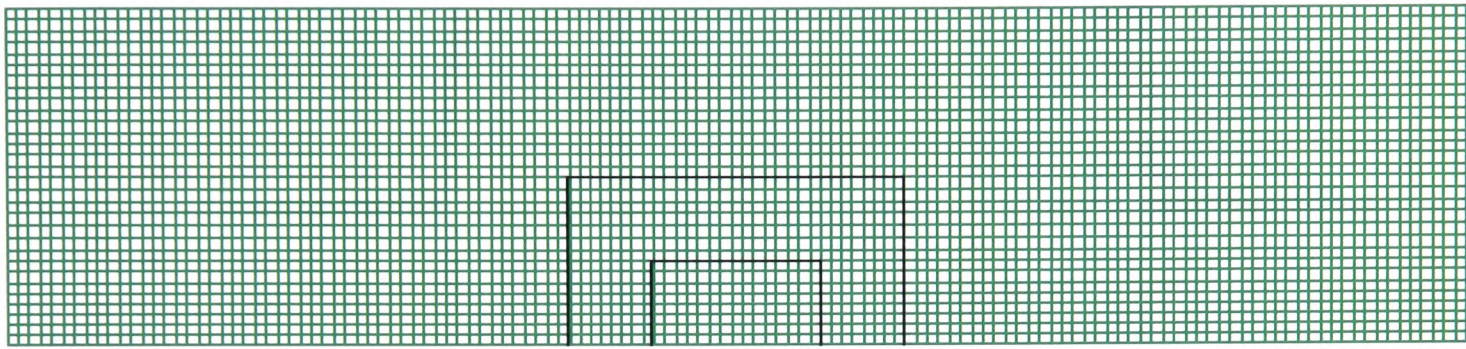
Figure 5.33 Mesh density located around the rib region

In order to measure the performance of the three codes a single temperature profile has been presented which runs through both the fluid and solid materials within the solution domain at a y-location of 25mm from the Y-Low wall.

Figure 5.34 presents the initial results obtained. It can be concluded from the results that PHYSICA is experiencing a problem with regards to the dissipation of heat from the rib. This is an important conclusion to emerge from this investigation which must be corrected before further heat transfer investigations are undertaken.
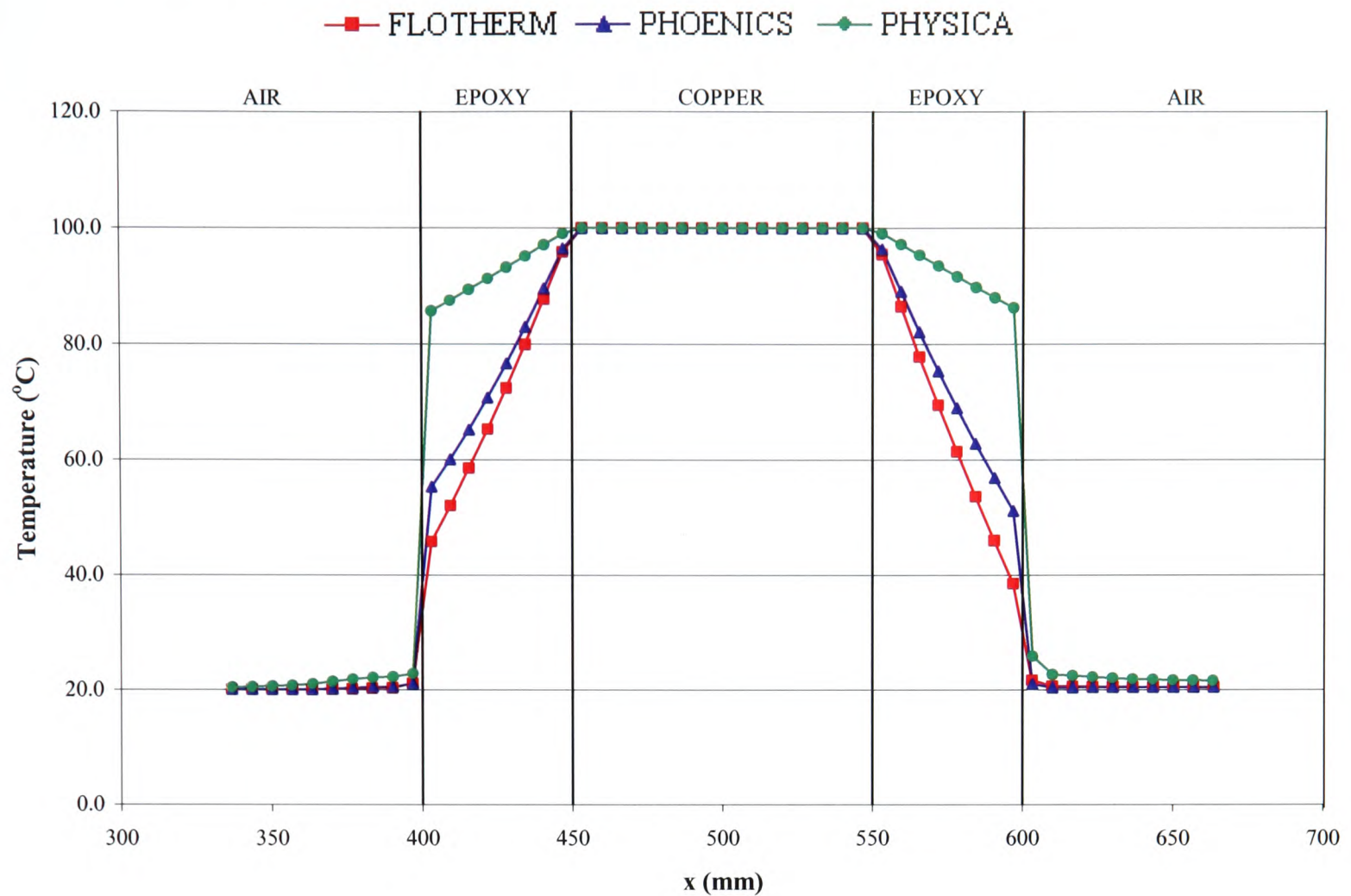
Figure 5.34 Temperature profile through Air/Epoxy/Copper/Epoxy/Air materials pre turbulent heat transfer boundary condition implementation

In order to rectify the problem identified in Chapter 4 (page 72) i.e. that PHYSICA V2.12 currently only has available a laminar heat transfer wall function link for internal wall boundaries, the implementation of the equilibrium log-law wall functions was undertaken by the author. The reference source for this implementation originates from the PHOENICS literature,[123] the reader is also referred to Appendix C for a full description of the equations implemented. The results obtained after boundary condition implementation are presented in Figure 5.35.
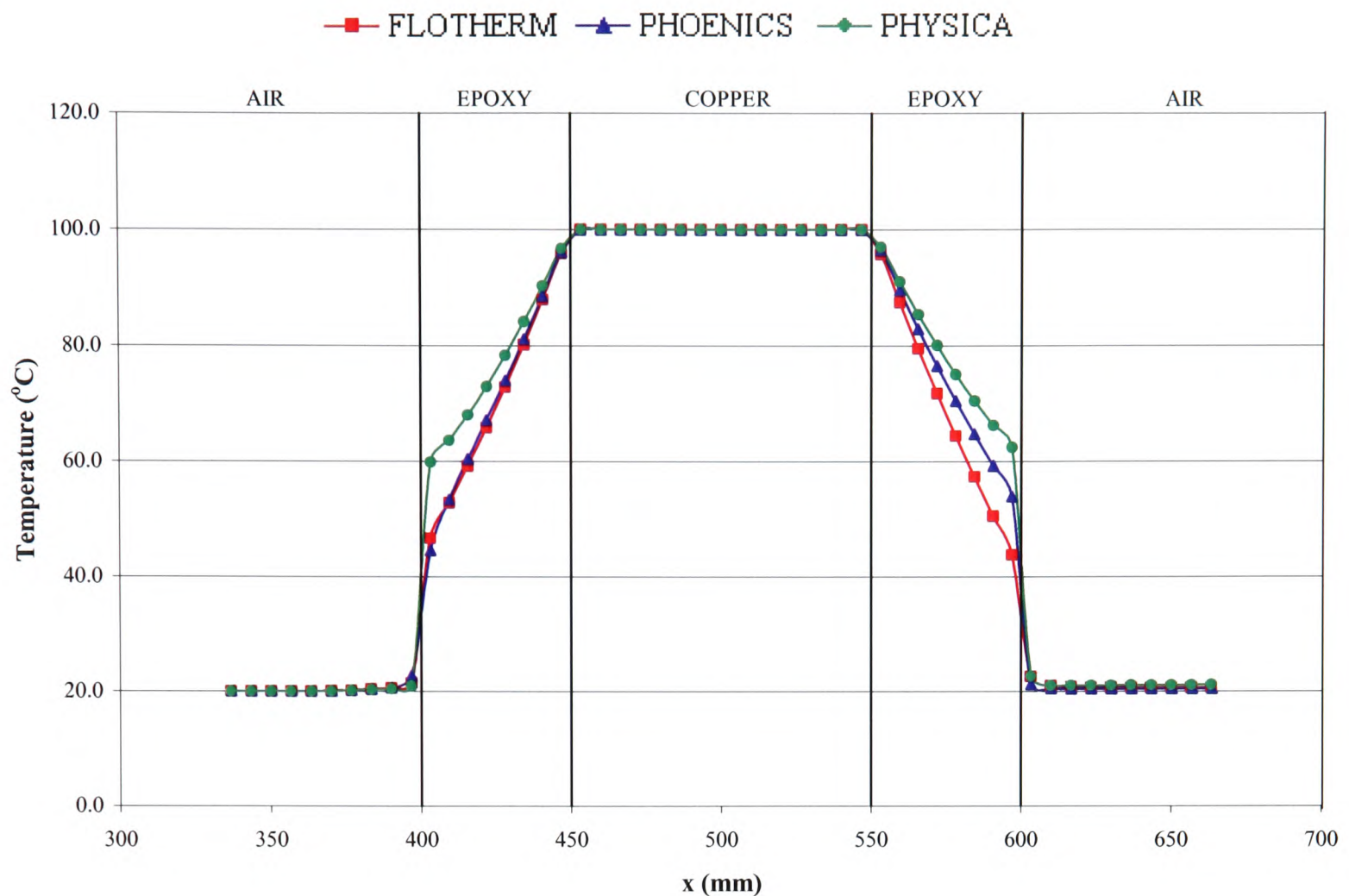
Figure 5.35 Temperature profile through Air/Epoxy/Copper/Epoxy/Air materials post turbulent heat transfer boundary condition implementation (Upwind)

It is noted that all three CFD codes have been set to use the Upwind differencing scheme to allow for code comparisons. However as most CFD codes would use the Hybrid differencing scheme as the default setting it was considered sensible to also present results using this differencing scheme to determine which of the two schemes would be employed for the remainder of the simulation work undertaken.

The temperature profile predicted by PHOENICS and PHYSICA using the Hybrid differencing scheme is presented in Figure 5.36. The conclusion which can be drawn from this figure is that the prediction of the temperature profile is in slightly better agreement between the two CFD codes when this differencing scheme is employed compared with Upwind. Therefore the remainder of simulation work undertaken in this thesis will be conducted using the Hybrid differencing scheme. It is also noted that the difference in temperature is more significant in the downstream side of the heated rib, i.e. coinciding with the recirculation region.
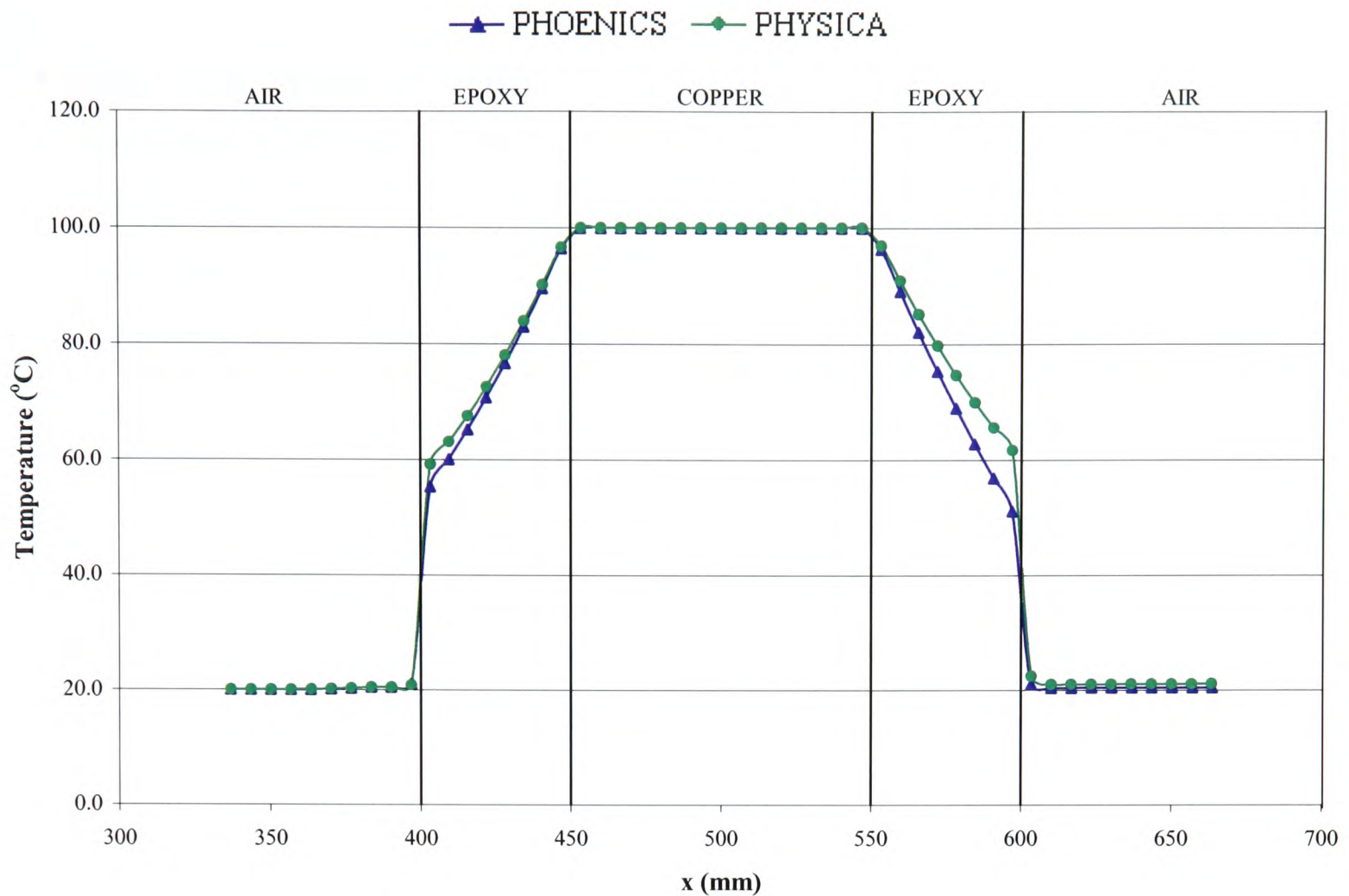
Figure 5.36 Temperature profile through Air/Epoxy/Copper/Epoxy/Air materials post turbulent heat transfer boundary condition implementation (Hybrid)

The key conclusion drawn from this investigation is that the implementation of the turbulent heat transfer boundary condition within PHYSICA has been successfully completed by the author within a reasonable degree of accuracy in comparison to other commercially available CFD codes currently on the market.

5.5 Concluding Remarks

The main conclusions which can be drawn from this chapter are highlighted below:

- The codes produce identical results in the laminar flow case.

- The standard turbulence models which are available in the three CFD codes examined are in good agreement with one another for all other test cases considered.

- Slight differences exist between the CFD codes with regards to the wall functions employed.

- Due to the limited information provided regarding the inlet boundary condition and the affect of the suction device employed in the experimental work conducted by Vogel and Eaton this test case was not completed successfully. However it can be concluded from the second backward facing step test case investigated that the implementation of the standard turbulence models currently available in PHYSICA are correct.

- A mesh refinement study has been conducted for the second backward facing step test case in order to examine the impact of the applied differencing scheme on the reattachment length predictions. It can be concluded that there is no significant advantage moving to a higher order differencing scheme, such as SMART, for the type of cases that will be considered later in this work.

- The Hybrid differencing scheme will be employed for the remaining simulation work to be undertaken.

- The equilibrium log-law wall functions with regards to turbulent heat transfer have been successfully implemented and validated within PHYSICA by the author.

Sufficient validation of PHYSICA has been provided, allowing further turbulence model development and validation to be exclusively performed within the structure of the CFD code PHYSICA.

IMPLEMENTATION & TESTING OF ZERO & ONE EQUATION TURBULENCE MODELS

Following on from the base-case comparisons given in the previous chapter, the objective of this chapter is to validate a range of new turbulence models which have been implemented within the PHYSICA framework as part of this research. The five turbulence models which have been integrated within PHYSICA and described in detail in Chapter 4 are:

- Zero-equation:
    - LVEL
    - LVEL_CAP
    - AUTO_CAP (which is a new model developed by the author)
- One-equation:
    - Wolfshtein[106]
    - Norris & Reynolds[107]

Model validation is achieved through comparisons against the fully developed turbulent analytical solution stated in equation (6.1) for the parallel plates test case. Another test case used for validation is the backward facing step where the reattachment length is compared. Where appropriate the commercially available CFD software tools FLOTHERM and PHOENICS will be made use of.

$$\frac{U}{U_{in}} = 1 + \left[\left(\frac{f}{2}\right)^{0.5} \bigg/ \kappa\right]\left[\frac{5}{6} + \ln\left(1 - \left(\frac{y}{b}\right)^{0.5}\right) + \left(\frac{y}{b}\right)^{0.5}\right]$$ (6.1)

6.1 Parallel Plates

The reader is referred to the parallel plates turbulent flow conditions test case detailed in Appendix A1.2 for the full model specification. It is noted that all the numerical results presented in this section are taken at a x-position of 9.8m downstream of the inlet.

The first algebraic model to be validated is the LVEL model where comparisons can be undertaken using all three CFD codes; FLOTHERM, PHOENICS and PHYSICA. The fully developed velocity profile predicted using the LVEL model is presented in Figure 6.1.
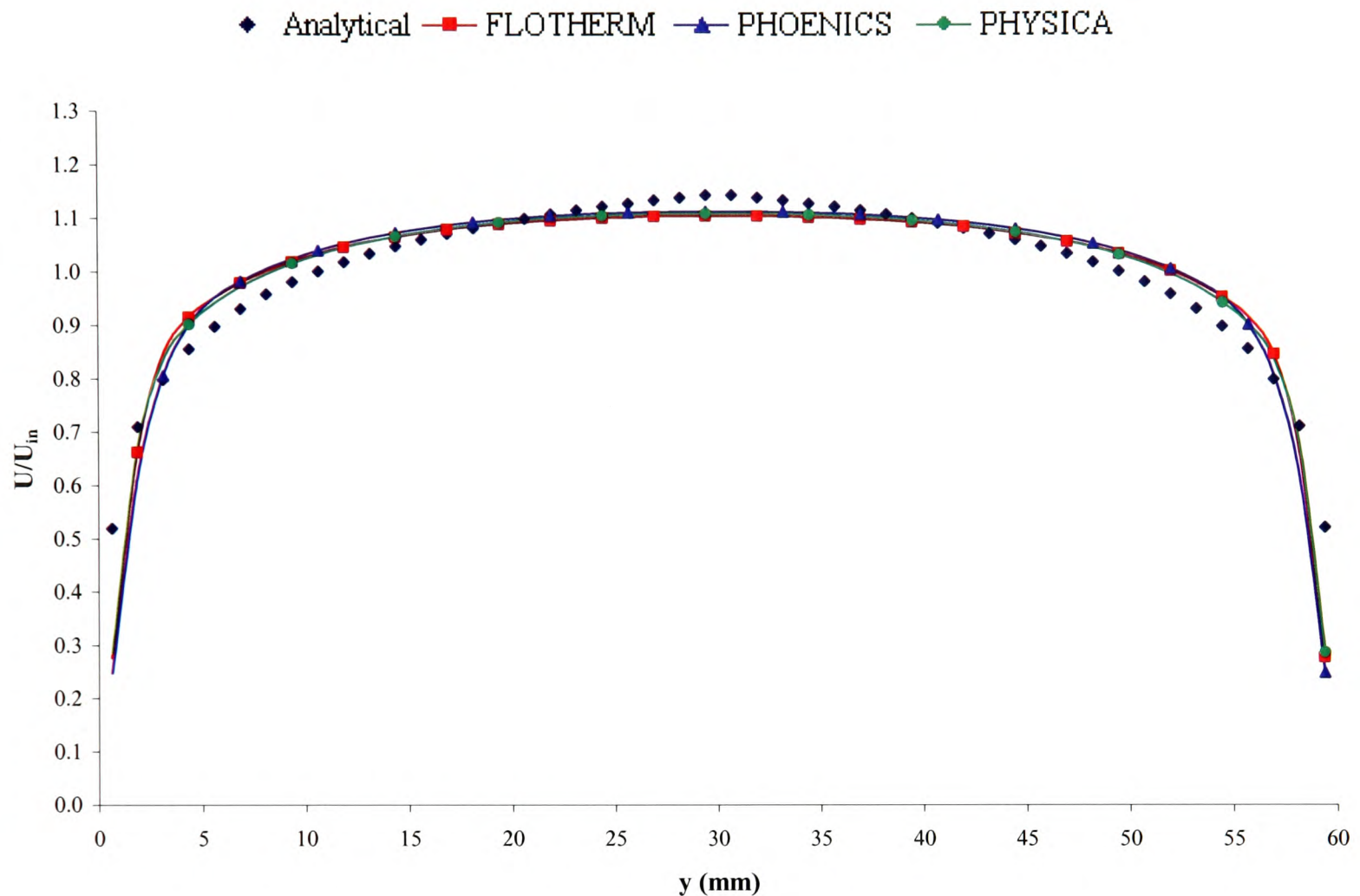
Figure 6.1 Parallel plates velocity profile LVEL turbulence model

From the velocity field it can be concluded that all three codes are in excellent agreement with one another. Collectively the codes predict a flatter velocity profile at the centre of the channel in comparison to the analytical solution.

To ensure that the PHYSICA implementation is correct the turbulent dynamic viscosity profile between the three codes has been presented in Figure 6.2.
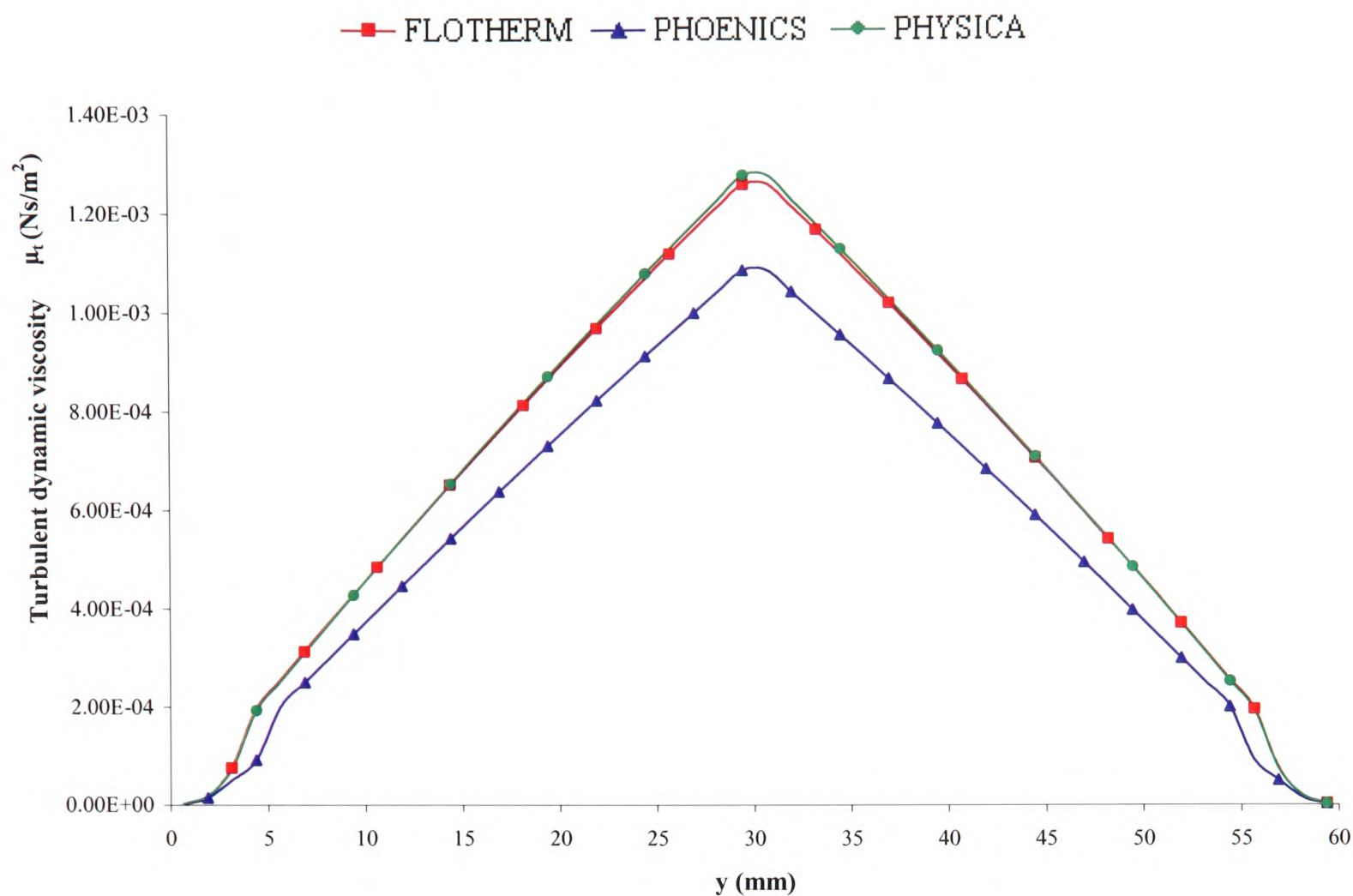
Figure 6.2 Parallel plates turbulent dynamic viscosity profile LVEL model

FLOTHERM and PHYSICA are in close agreement with one another. This supports the conclusion that the PHYSICA LVEL model, which is based on the FLOTHERM method, has been correctly implemented.

The PHOENICS turbulent dynamic viscosity predictions are approximately 20% lower than both FLOTHERM and PHYSICA at the centreline of the channel, but it should be noted that the implementation of the model is somewhat different within PHOENICS which used the Taylor series expansion.[124]

Finally it can be concluded that for this case, the influence of the turbulent viscosity field on the developed axial velocity profile is relatively weak since a 20% difference in the turbulent viscosity field between PHOENICS and the other two codes does not result in a significant difference in the velocity profiles.

The second algebraic model to be evaluated is a variant of the LVEL model. As LVEL predicts a turbulent viscosity field that increases continuously away from a wall, a form of

capping is applied in order to achieve more realistic turbulent dynamic viscosity values in the bulk flow.

As PHOENICS does not have a capped version of the LVEL model currently implemented within the structure of the code, comparisons will be made against FLOTHERM only. Considering the velocity profile presented in Figure 6.3 it is clear that both codes show very good agreement with one another.
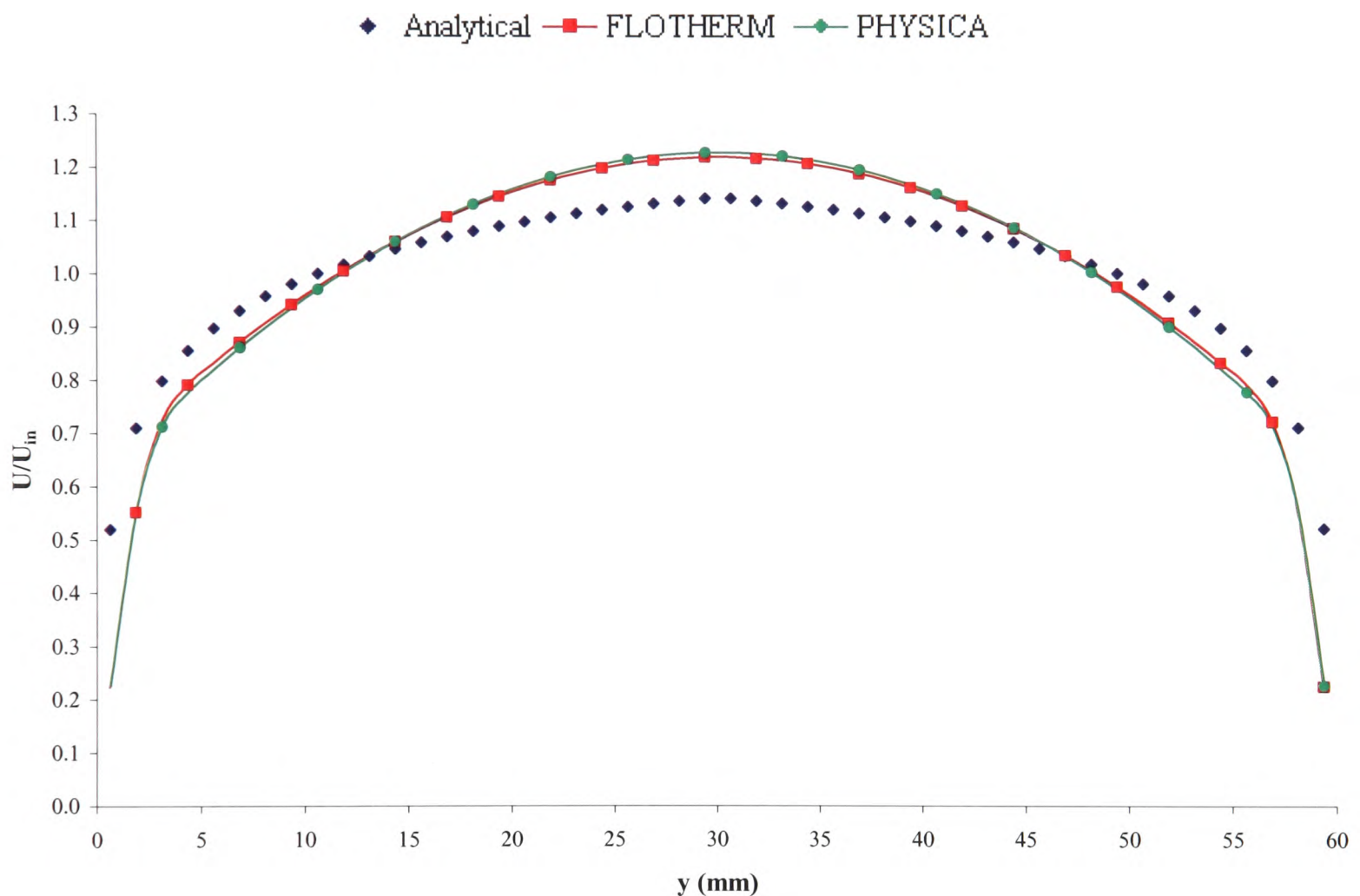
Figure 6.3 Parallel plates velocity profile LVEL_CAP model

Figure 6.4 presents the fully developed turbulent dynamic viscosity field between the two codes. Also presented on this figure is the PHYSICA LVEL prediction, this is to illustrate where the cap is being physically applied in the domain. The results suggest that the implementation of the LVEL_CAP turbulence model, as coded in FLOTHERM, has been successfully implemented within PHYSICA.
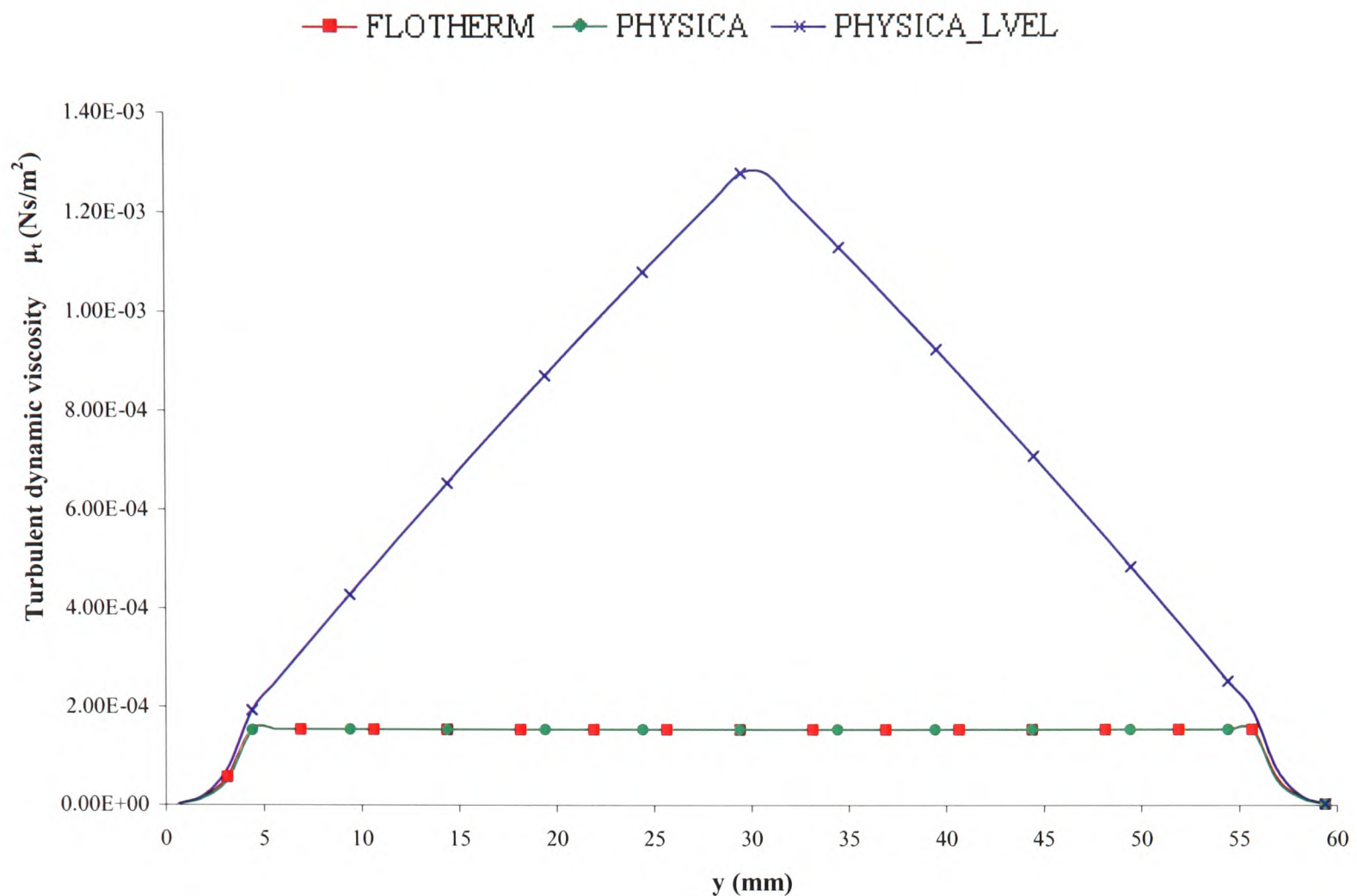
Figure 6.4 Parallel plates turbulent dynamic viscosity profile LVEL_CAP model

The last algebraic model to be considered is the newly formulated AUTO_CAP turbulence model. It was noted in Chapter 4 that the overwhelming drawback of the LVEL_CAP turbulence model is that the CFD code user is required to specify a characteristic velocity and length scale. (LVEL_CAP: $L = 10\text{mm}, V = 1.3202\text{m/s}$)

During the development of this project, evolution rather than replacement of the current turbulence models available within FLOTHERM was considered desirable. Therefore developing an automatic technique, termed the AUTO_CAP turbulence model, to cap the turbulent viscosity field predicted by the LVEL model without the need for any user interaction became the preferred avenue to pursue.

Before the performance of the AUTO_CAP model can be assessed an investigation into the value of the model constant, L_{crit}^{+}, needs to be undertaken with electronic systems considered to be the specific application field.

Ideally the results obtained by the AUTO_CAP model should be identical to the LVEL_CAP model. Therefore velocity and turbulent viscosity comparisons have been performed against the PHYSICA LVEL_CAP model as this is the model the AUTO_CAP is attempting to replace.

As the PHYSICA turbulent viscosity profile predicted by the LVEL_CAP model was in excellent agreement with FLOTHERM (see Figure 6.4) the AUTO_CAP model constant will attempt to mimic this variable as closely as possible.

After a lengthy trial and error study to determine a suitable value for the AUTO_CAP model constant it was found that the most appropriate value selected for L_{crit}^+ to three decimal places was 0.125.

The final results obtained by the AUTO_CAP model in comparison to the LVEL_CAP model for the predicted velocity profile is presented in Figure 6.5 with the turbulent dynamic viscosity profiles shown in Figure 6.6 for the parallel plates test configuration.
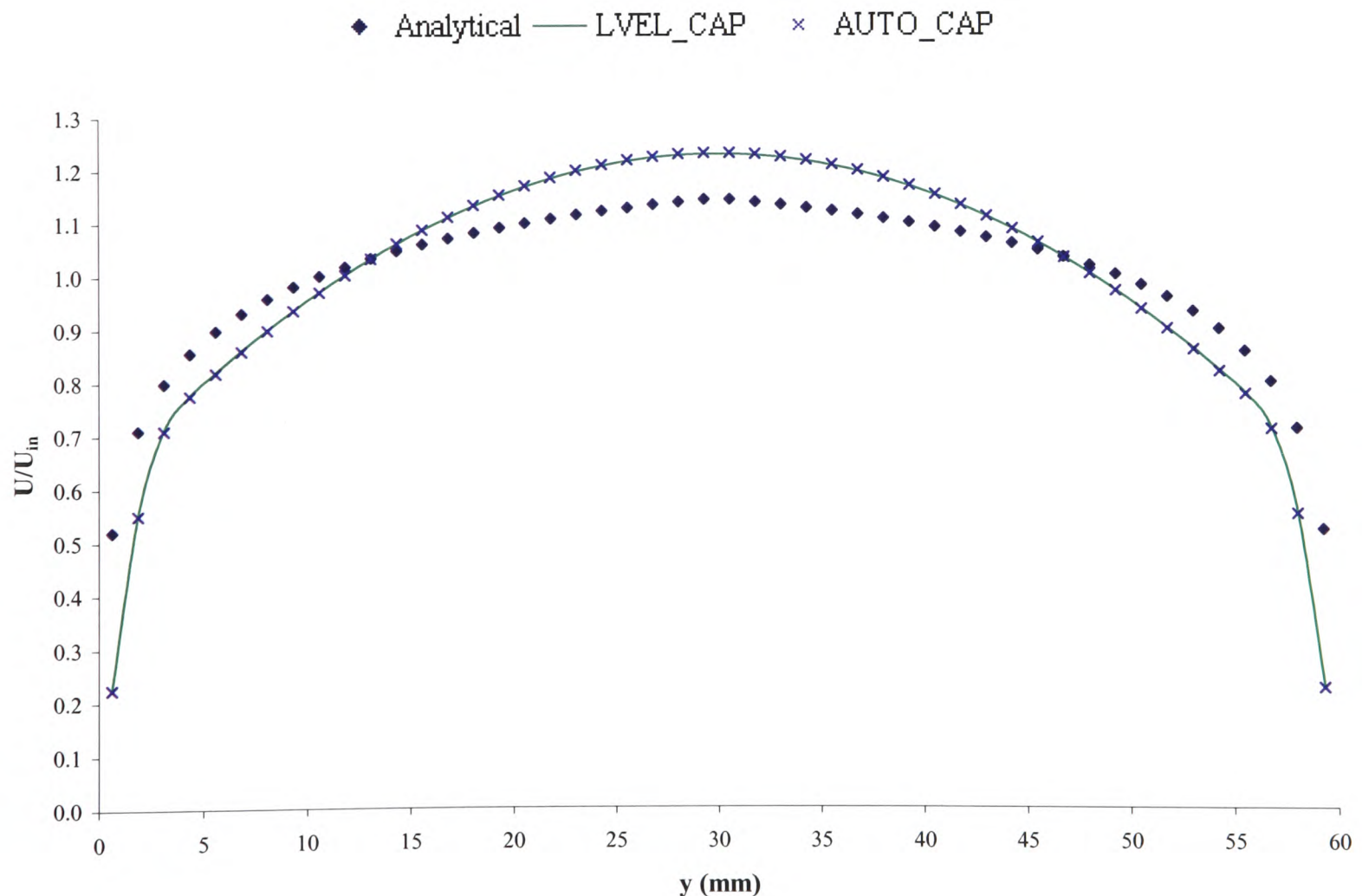
Figure 6.5 Parallel plates velocity profile AUTO_CAP model
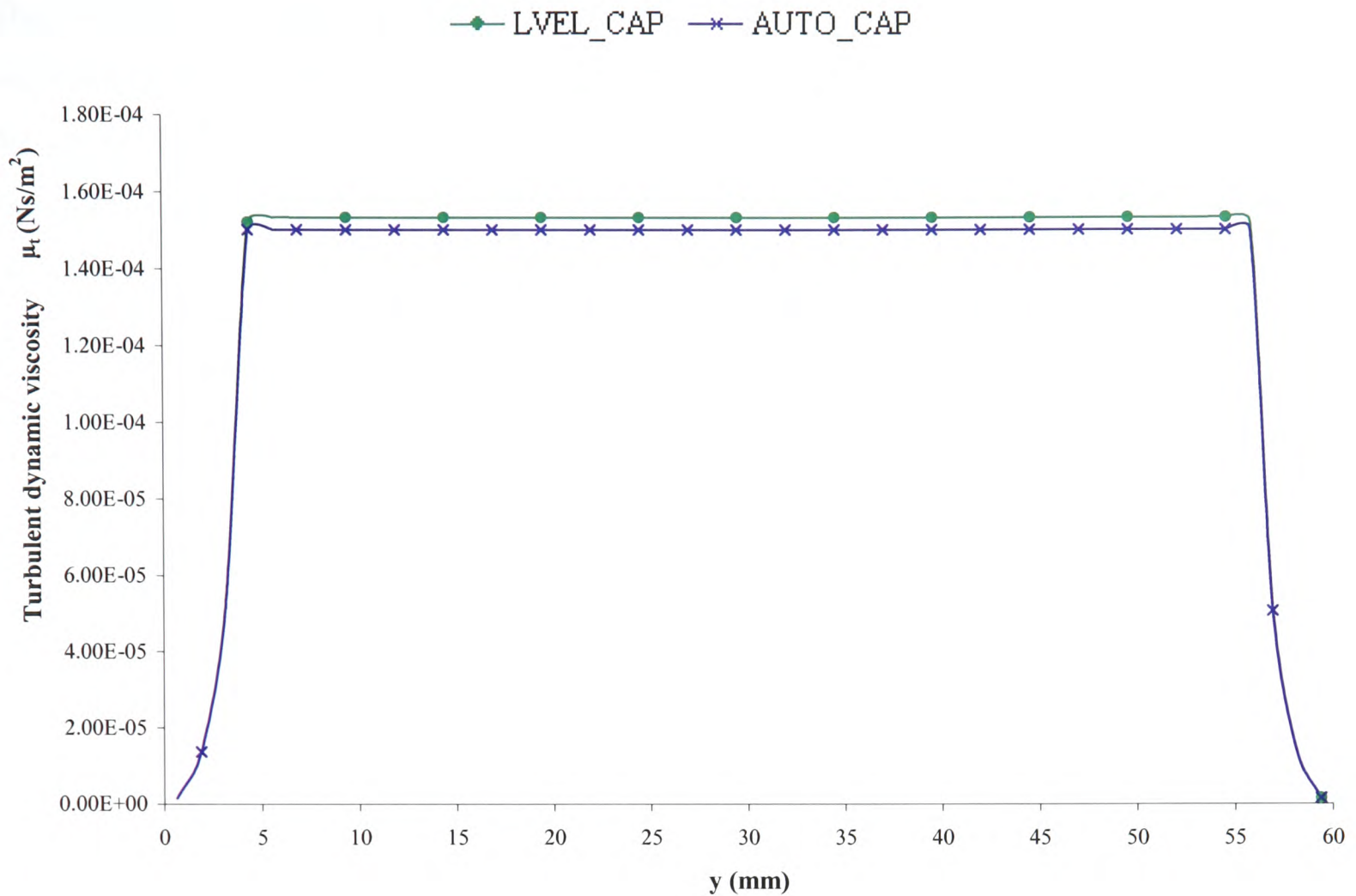
Figure 6.6 Parallel plates turbulent dynamic viscosity profile AUTO_CAP model

It can be concluded from the velocity profile that LVEL_CAP and AUTO_CAP are in excellent agreement with one another which suggests that the automatic capping technique is working correctly.

It has already been determined that the turbulent viscosity field only weakly influences the velocity profile in the simple duct case. Whereas the impact of the 2% difference noted in the turbulent viscosity profiles between the LVEL_CAP and AUTO_CAP models on the predicted flow field is negligible, it may be more significant for other cases. This will be discussed later for the backward facing step configuration.

Unfortunately the two one-equation turbulence models which have been implemented into the PHYSICA framework by the author can not be compared against the commercial CFD codes FLOTHERM and PHOENICS as these turbulence models are not currently available within the standard structure of the two codes. Therefore comparisons have been made against the analytical fully developed velocity profile solution.

The validation of both the one-equation Wolfshtein and Norris & Reynolds turbulence models will be performed together as the two models only slightly differ in the constants used within the empirical functions to describe the turbulent mixing and dissipation lengths and should therefore produce similar results. Comparing the two models simultaneously will also strengthen the argument of correct model implementation. Comparisons of the fully developed velocity profile have been made in Figure 6.7.
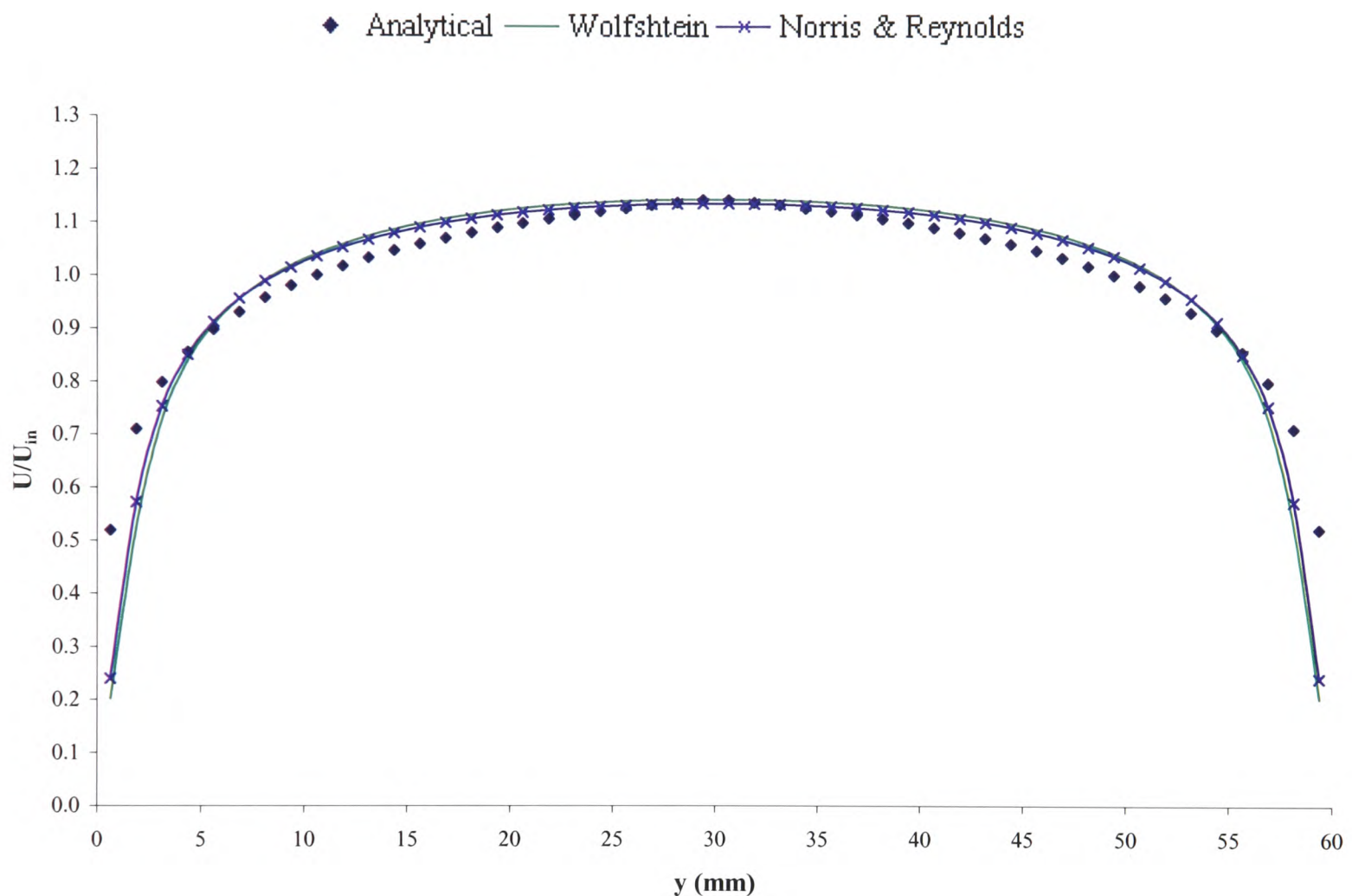
Figure 6.7 Parallel plates velocity profile Wolfshtein and Norris & Reynolds models

The conclusion which can be drawn from Figure 6.7 is that both the turbulence models agree well with the analytical velocity solution which suggests that both models have been correctly implemented into PHYSICA.

The turbulent dynamic viscosity profiles presented in Figure 6.8 show a difference between the two turbulence model predictions of approximately 17% at the centre of the channel. This can be considered as reasonable agreement as the purpose of this comparison is to determine

that the models produce similar results, identical predictions are not expected as the model constants differ.
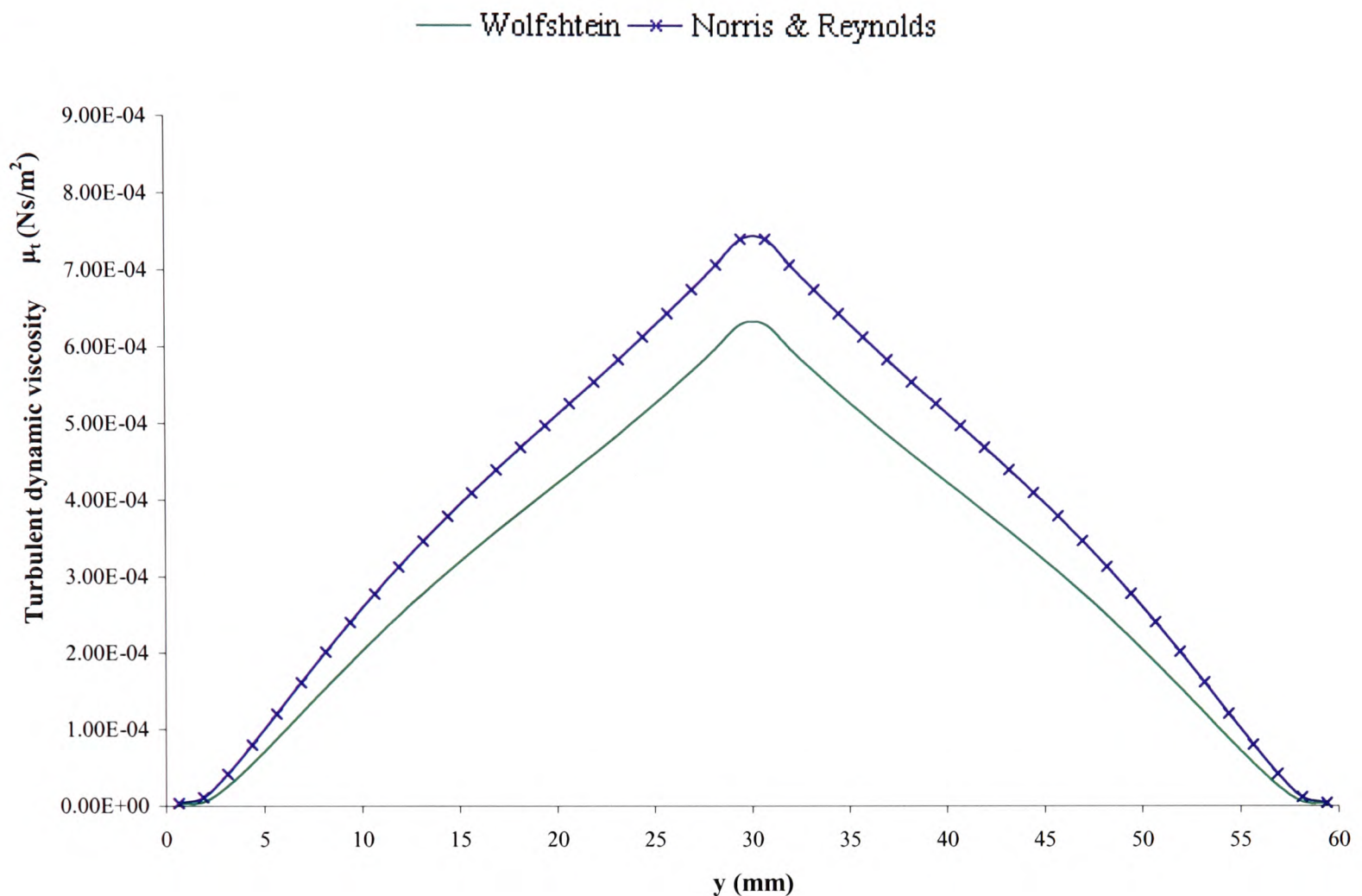
Figure 6.8 Parallel plates turbulent dynamic viscosity profile Wolfshtein and Norris & Reynolds models

The conclusions which can be drawn at the end of this section is that for this particular test case the predicted results suggest that all zero- and one-equation turbulence models have been correctly implemented within PHYSICA. However further investigation is required for the velocity predictions made by the zero-equation models.

6.2 Backward Facing Step

To further validate the zero-equation turbulence models the classic backward facing step configuration has been simulated. The reader is referred to Appendix A3.2 for a full description of this test case.

To ensure that this distance field has been correctly calculated profiles have been extracted normal to the Y-Low boundary wall for x-locations of 1H through to 8H, a schematic of

which is shown in Figure 6.9. The distance profile comparing FLOTHERM and PHYSICA at 4H has been presented in Figure 6.10 for a uniformly distributed mesh density of (40 x 20) upstream and (200 x 30) downstream of the step in the x- and y-directions respectively. Excellent agreement was noted for all other x-location distance profile comparisons between FLOTHERM and PHYSICA. The contour plot presented in Figure 6.11 shows the operation of the distance function obtained from PHYSICA.
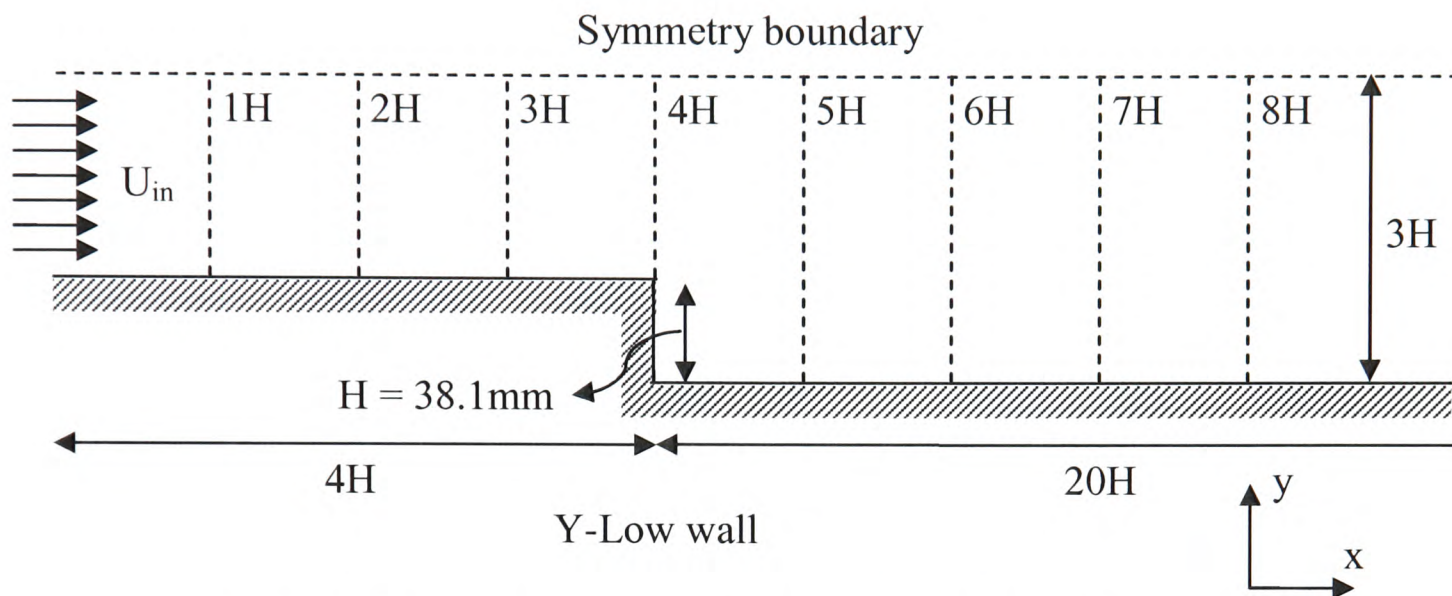
Figure 6.9 Schematic representation of the examined profile locations
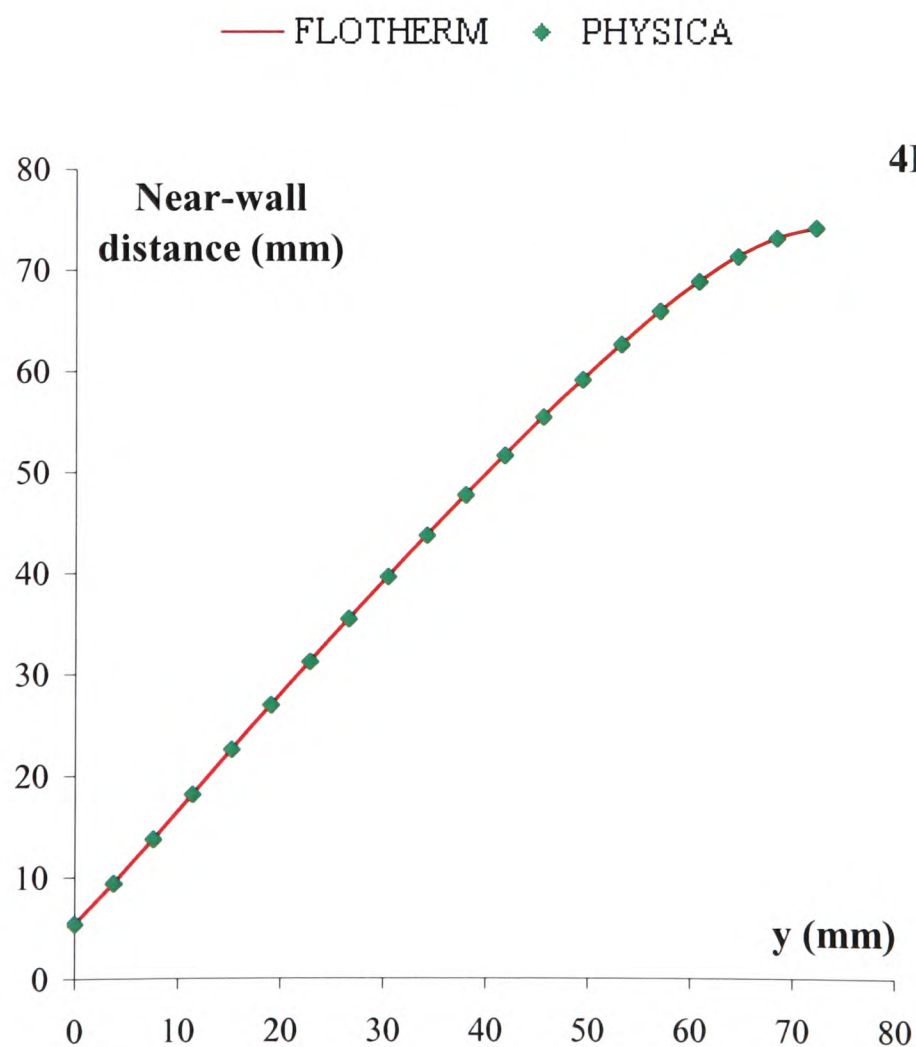
Figure 6.10 Distance to the nearest wall boundary x = 4H

Wall distance (m)

.1023
.9223E-1
.8214E-1
.7205E-1
.6196E-1
.5187E-1
.4178E-1
.317E-1
.2161E-1
.1152E-1
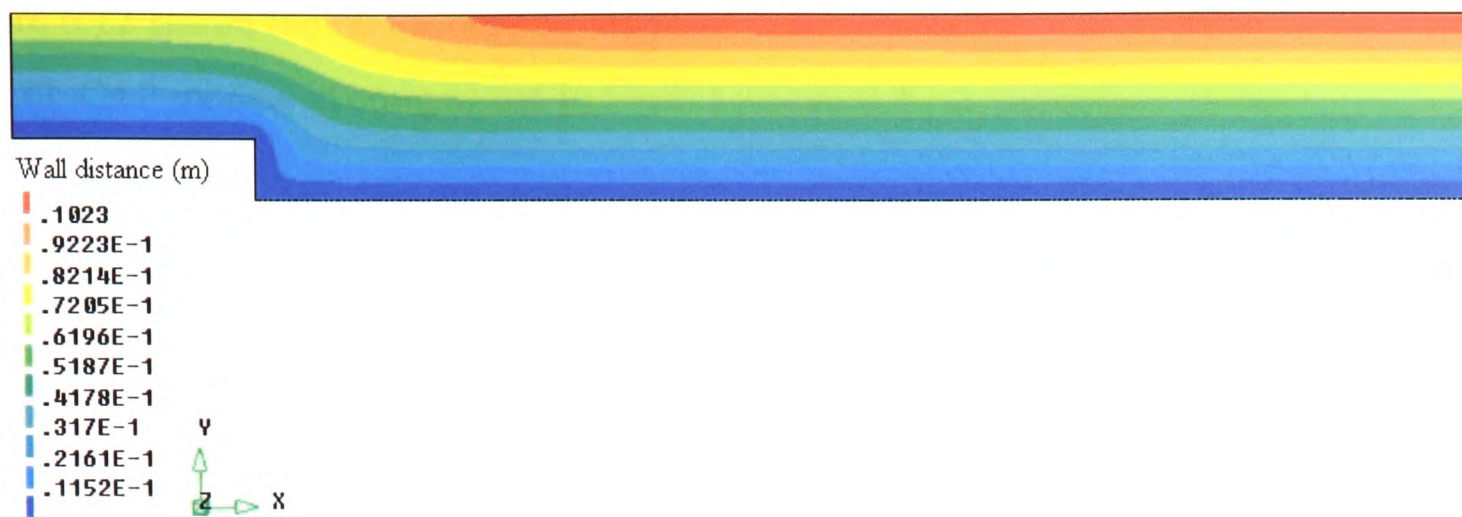
Figure 6.11 Operation of distance function

It can be concluded that the calculation of the distance to the nearest wall within PHYSICA's LVEL turbulence model has been successfully completed. Therefore correct model implementation is noted up to this point in the algorithm which corresponds to equation (4.5) stated in Chapter 4.

The next and final stage of the LVEL algorithm is the calculation of the dimensionless effective viscosity. Again excellent agreement between FLOTHERM and PHYSICA was noted for all x-location distance profile comparisons.

The two remaining zero-equations turbulence models, LVEL_CAP and AUTO_CAP, are both variations of the LVEL model. Fortunately the additional implementation required for the LVEL_CAP model is minimal. The algorithm is detailed in Chapter 4. Only one extra equation, which places an upper limit on the turbulent viscosity variable, is required to complete the LVEL_CAP model.

It has already been determined that the LVEL_CAP model predicts the turbulent viscosity profile for the parallel plates test case well, and in agreement between FLOTHERM and PHYSICA. Therefore backward facing step comparisons can be performed solely within PHYSICA to assess the behaviour of the LVEL_CAP and AUTO_CAP models. The mesh density employed is (64 x 32) upstream and (320 x 48) downstream of the step in the x- and y- directions respectively.

Figure 6.12 shows the reattachment length predicted by both the PHYSICA LVEL_CAP and AUTO_CAP models in comparison to Croft's standard $k - \varepsilon$ numerical work.
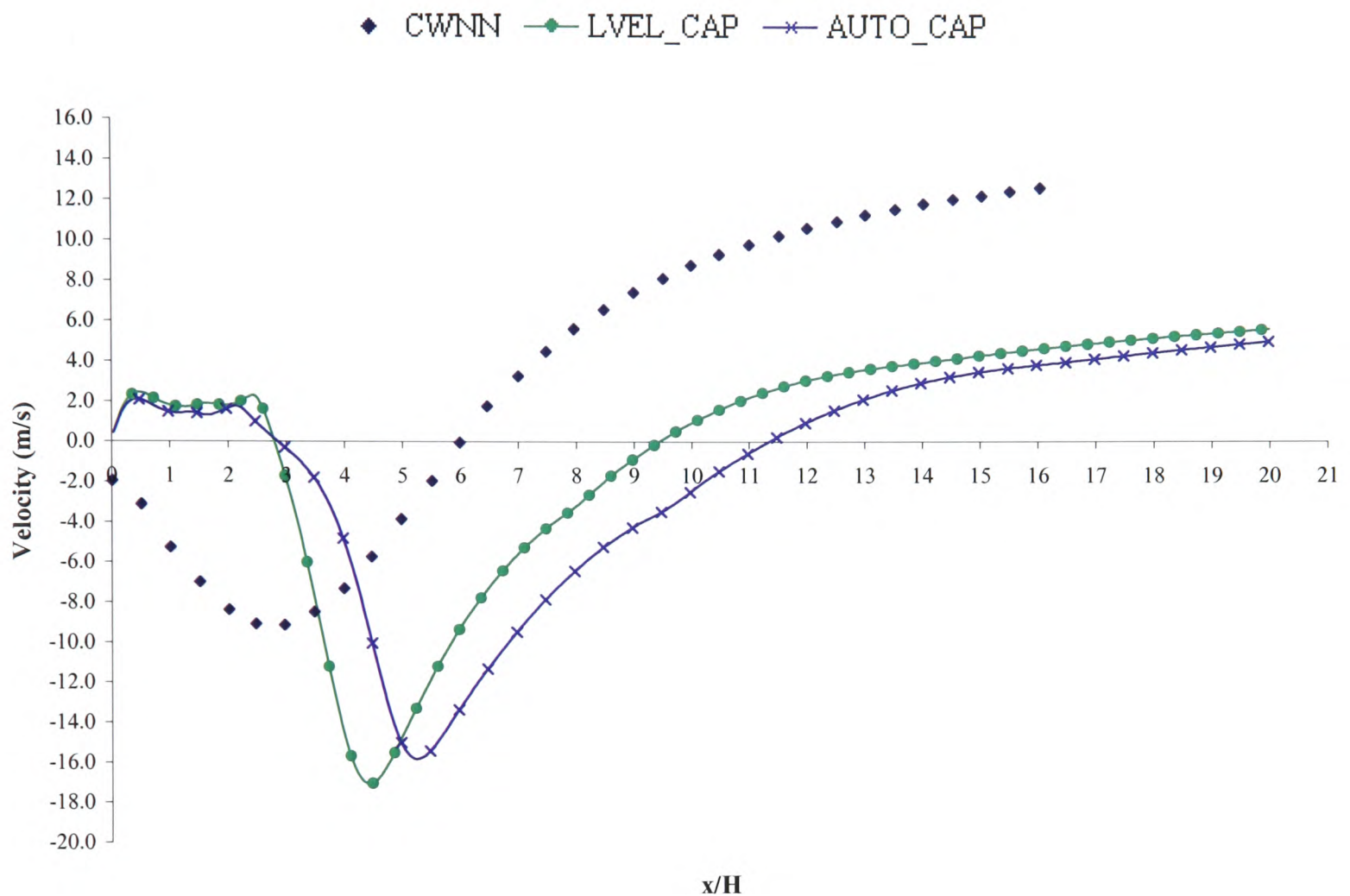
Figure 6.12 Reattachment length predictions LVEL_CAP and AUTO_CAP

The reattachment lengths predicted by the capped models are too large for a turbulent flow, being more characteristic of laminar flows, where the reattachment length has been observed to exceed $8H$ for Reynolds numbers greater than 200.[16]

The conclusions which can be drawn from Figure 6.12 are that both the cap models predict an unrealistically large recirculation region behind the step and the results suggest that further revisions of the AUTO_CAP model are required.

To remove the doubt of incorrect turbulence model implementation the characteristic length and velocity scales calculated by the AUTO_CAP model (38.1mm and 26.2m/s respectively) have been substituted into the LVEL_CAP model. The reattachment length predicted when this model manipulation is performed is shown in Figure 6.13.
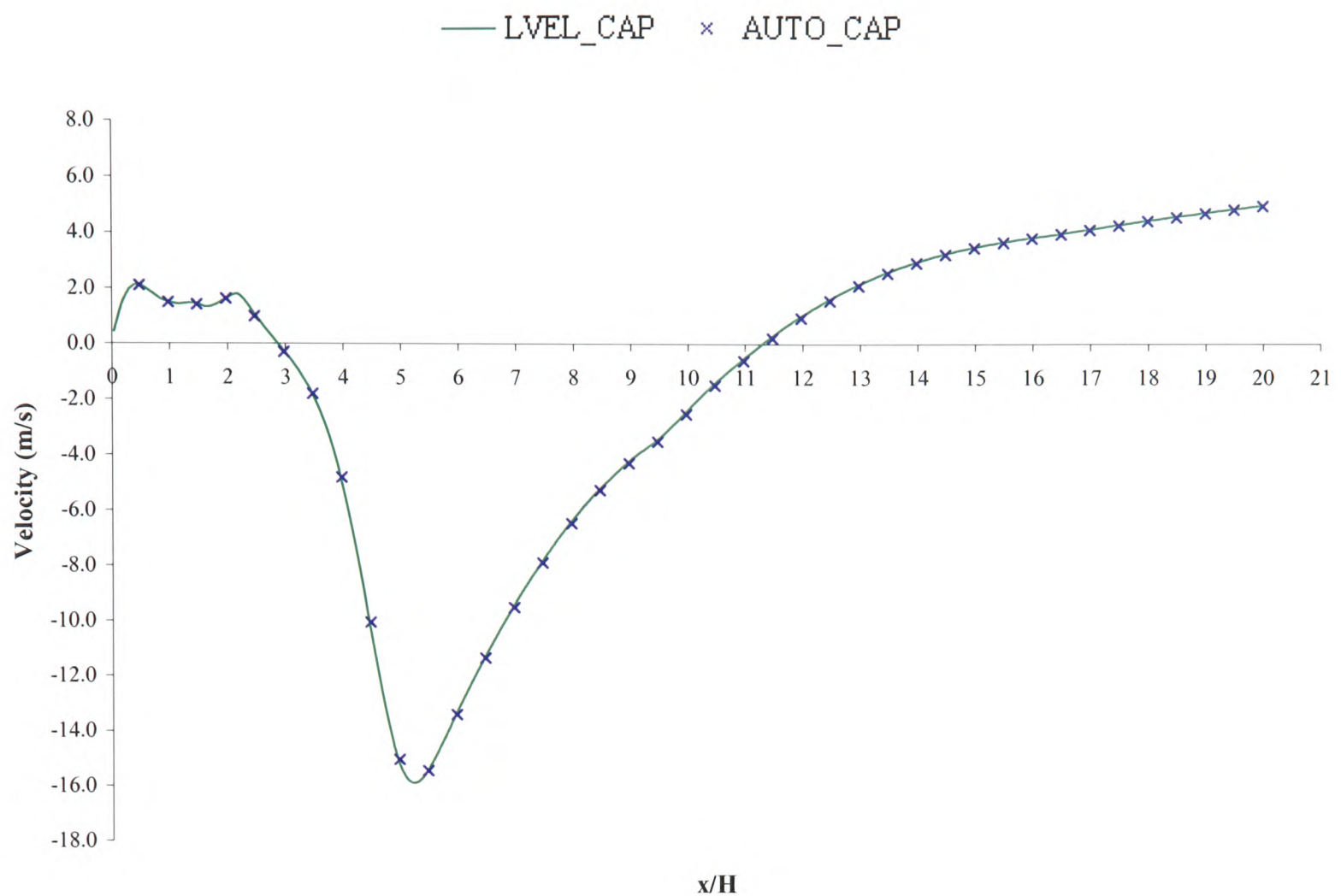
Figure 6.13 Reattachment length predictions LVEL_CAP (characteristic scales manipulated)
and AUTO_CAP

Figure 6.13 suggests that the influencing factor in the AUTO_CAP model is the calculation of the characteristic velocity scale. This can be determined as the characteristic length and velocity scales set for the LVEL_CAP model were the step height (38.1mm) and the inlet velocity (36.0m/s) respectively. Therefore the velocity scale must be the major influencing factor for the difference in the results obtained between LVEL_CAP and AUTO_CAP rather than the AUTO_CAP model constant requiring adjustment.

The accuracy of the one-equation turbulence models can only be evaluated within PHYSICA as neither of the other CFD codes considered currently have the Wolfshtein or Norris & Reynolds turbulence models available in the standard versions of the code.

Firstly a mesh independence study has been undertaken for both the one-equation models to ensure that an adequate mesh density is being employed. Figure 6.14 presents the uniform mesh density comparisons for the Wolfshtein turbulence model, similar results were obtained by the Norris & Reynolds model. It can be concluded that continuing to use a mesh density of

(384 x 48) seems reasonable. The mesh is distributed as (64 x 32) upstream and (320 x 48) downstream of the step in the x- and y- directions respectively.
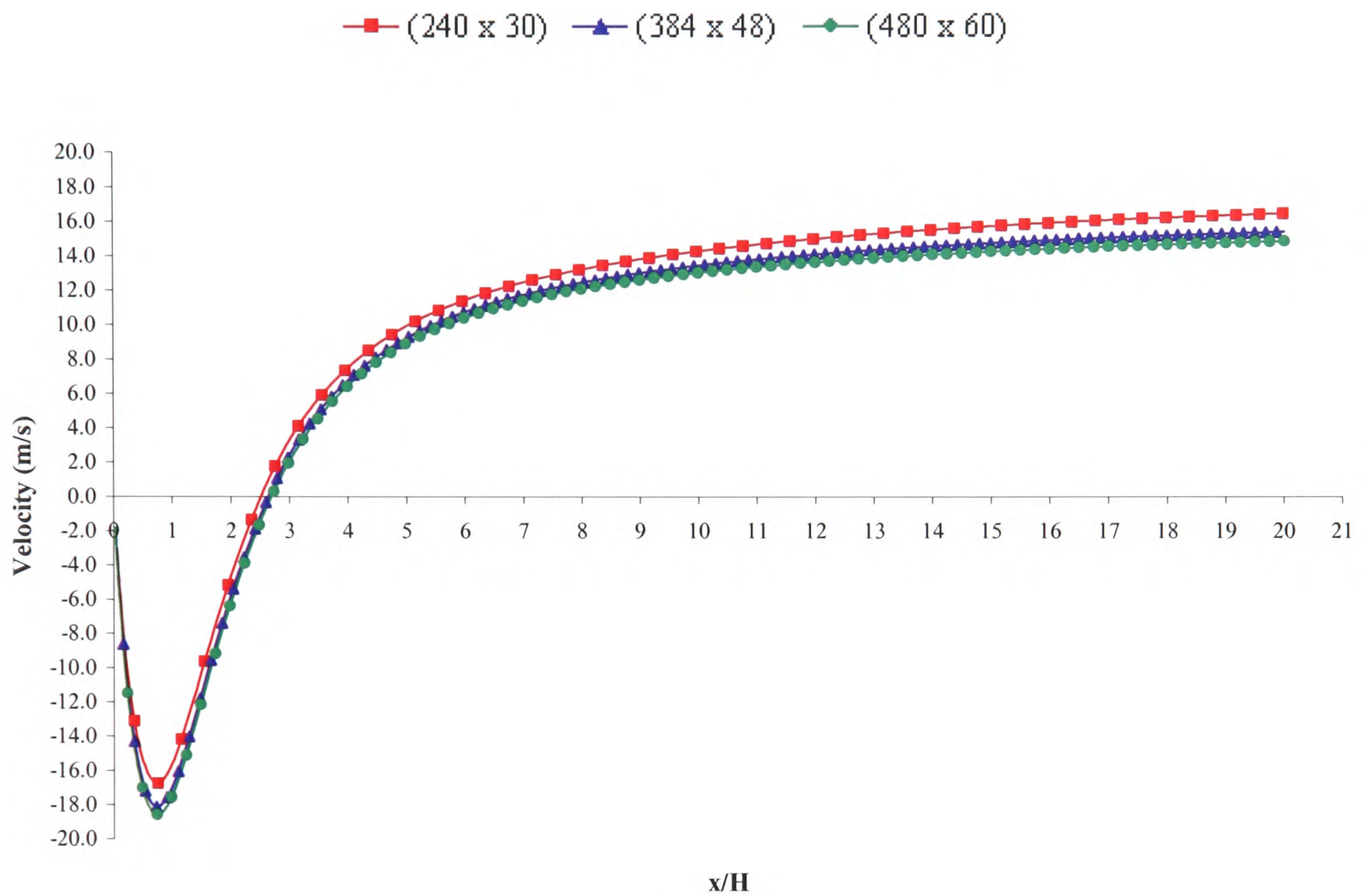
Figure 6.14 Wolfshtein model mesh independence study for the backward facing step

Figure 6.15 displays the reattachment lengths predicted by both the Wolfshtein and Norris & Reynolds turbulence models.
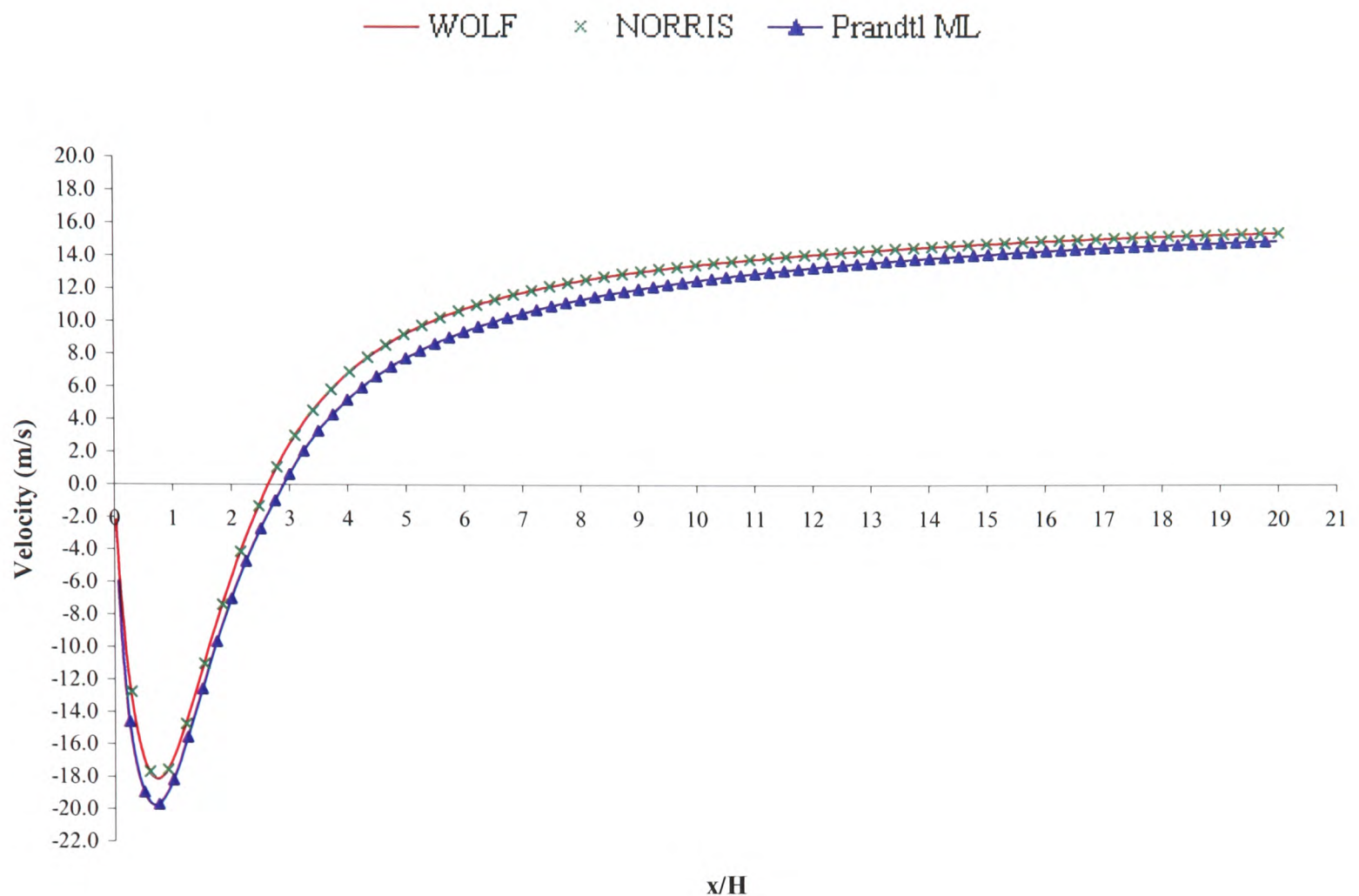
Figure 6.15 Reattachment length predictions one-equation turbulence models

The predicted reattachment lengths of approximately 2.7 step heights for both the one-equation models suggest that a single small recirculation bubble exists which is clearly not in the reattachment range noted in the experimental work of Vogel and Eaton.[13] Therefore to further validate the implementation of the PHYSICA models and to determine if this under prediction in the reattachment length is a trend of one-equation models this test case has been repeated with the available one-equation model in PHOENICS, referred to as the KLMODL, which is the Prandtl mixing length model with a prescribed length scale.[124]

Also shown in Figure 6.15 is the reattachment length predicted by the PHOENICS one-equation model in comparison to the one-equation models implemented in PHYSICA.

The reattachment length predicted by the KLMODL model is 2.9 which suggests that the one-equation models investigated here show a trend of under prediction with regards to the reattachment length independent of the CFD code employed. Therefore it can be further concluded that the one-equation models of Wolfshtein and Norris & Reynolds which have been implemented within PHYSICA by the author are correct.

6.3 Concluding Remarks

The key conclusions to be drawn from this chapter are highlighted below:

- The LVEL turbulence model, based on the FLOTHERM method, has been correctly implemented within PHYSICA.

- The LVEL_CAP model, based on the FLOTHERM method, has been correctly implemented within PHYSICA.

- The newly developed AUTO_CAP model has been correctly implemented within PHYSICA.

- The AUTO_CAP model seems to be an interesting model to pursue since, if both factors (L and V) can be automated this is a significant improvement on the current LVEL_CAP model, as it removes the need for user interaction. However further investigation with regards to the calculated velocity scale is required.

- Other one-equation models: Prandtl's mixing length with a prescribed length scale; Wolfshtein, Norris and Reynolds grossly under predict the backward facing step reattachment length which is reported to be in the range 7.0 ± 1.0 step heights by Vogel and Eaton.[13]

- Both one-equation models are shown to be correctly implemented by comparison with each other and the Prandtl mixing length model with a prescribed length scale in PHOENICS.

MARTINUZZI HIGH REYNOLDS NUMBER SINGLE CUBE

The standard $k - \varepsilon$ and LVEL turbulence models discussed in the previous chapters have been further tested on a three-dimensional test configuration as components of these models are used later in the formulation of a novel zonal turbulence model. It is noted that all the simulation work undertaken for this case study use the Upwind differencing scheme as the Hybrid differencing scheme is not available in FLOTHERM.

In 1995 this case study served as a reference case for the Workshop on Large Eddy Simulation of Flows Past Bluff Bodies held in Germany.[66] Later the case served as a reference dataset for the validation of numerical simulations at an ERCOFTAC workshop held at Delft University of Technology.[41]

The flow over prismatic obstacles in fully developed channel flow is representative of a large number of practical flow situations in industrial processes and of complex turbulent flows in general. Bluff body flows are of fundamental interest due to the complex nature of the interaction between turbulence and the generally periodic, coherent structures in the wake of an obstacle. The understanding gained from these studies finds application in predicting dispersion around buildings (e.g. pollutant transport) and heat transfer (e.g. cooling of electronic components and heat exchangers).

The experiments were conducted in a (3900 x 600 x 50)mm (l x w x h) wind tunnel at a Reynolds number of 80,000 based on the channel height. The boundary layer was tripped at the inlet in order to obtain fully-developed conditions at least 5h upstream of the cubes leading edge. The cube of half channel height, $H = h/2$, was mounted at the centreline with the leading edge located 52h downstream of the trip wires. The channel extended approximately 16h downstream of the cubes trailing edge so that the outlet conditions are not expected to affect the wake flow.[21, 22]

The computational domain modelled is presented in Figure 7.1. Due to the symmetry of the geometry only half of the flow domain has been modelled.
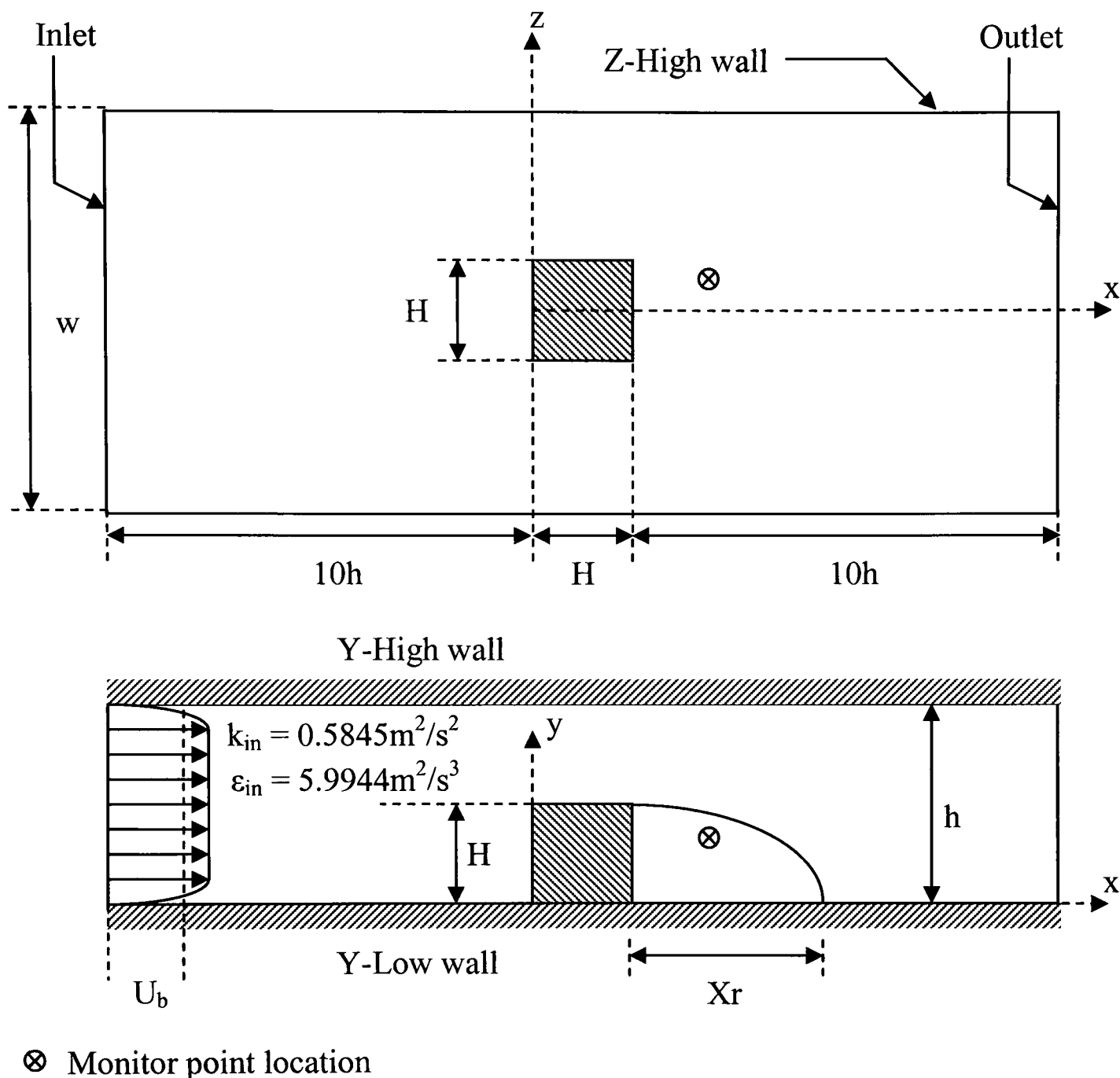
Figure 7.1 Martinuzzi single cube configuration

The x- and y-axes are taken in the streamwise and wall-normal directions respectively. The coordinate system originates at the centre of the cubes leading face from the base to the top surface of the channel, Y-Low and Y-High walls respectively as detailed in Figure 7.1.

Using material property values associated with air at 20°C and the Reynolds number relationship an inlet velocity value of 24.176m/s has been calculated.

All computations have been performed using the Upwind differencing scheme and employ a stretched Cartesian mesh with (222 x 51 x 68) mesh cells in the x-, y- and z-directions

respectively. On the surface of the cube 26 cells have been applied uniformly in the x- and y-directions with 13 cells distributed in the z-direction. The computational mesh employed can be viewed in Figure 7.2.
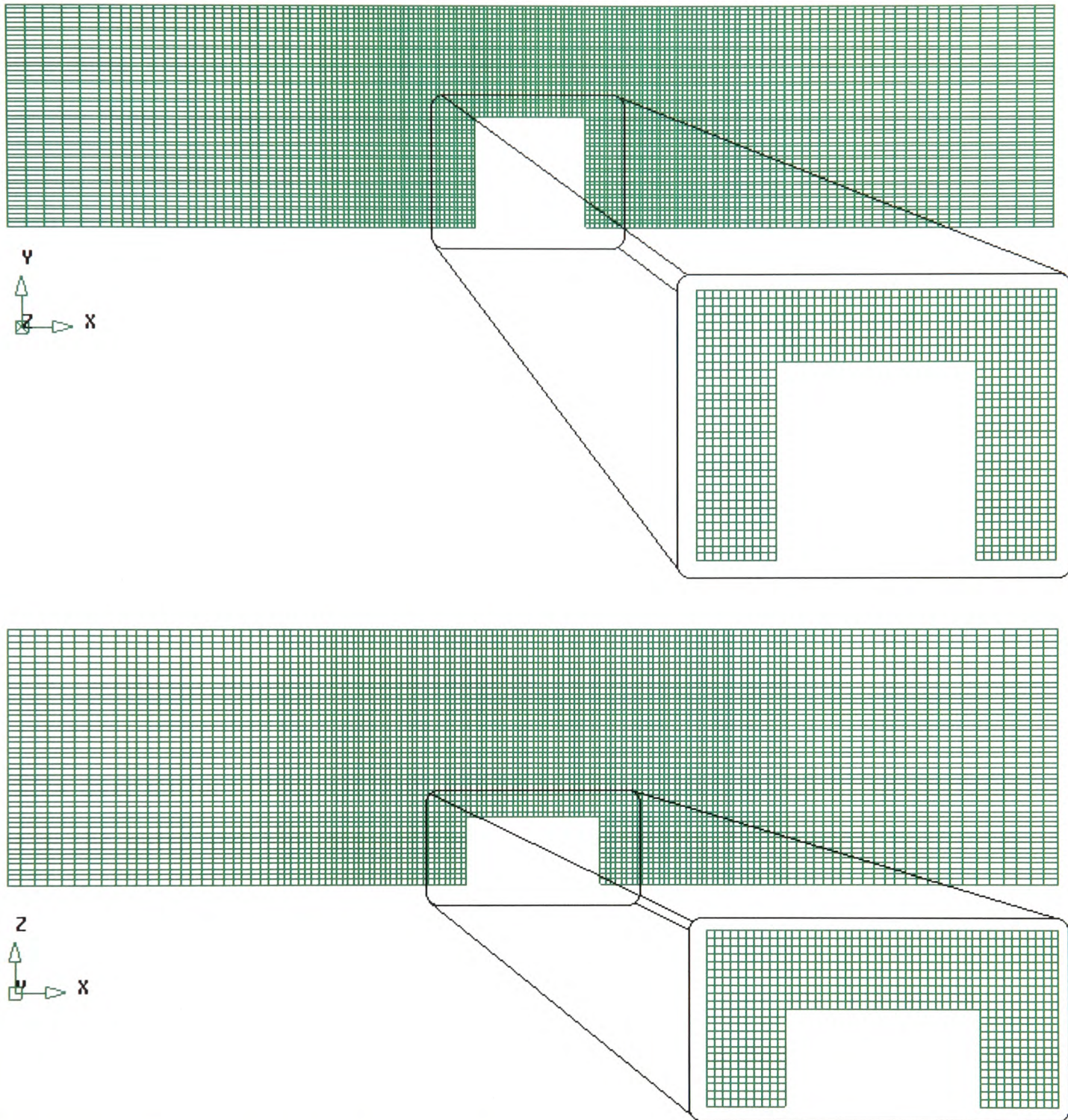
Figure 7.2 Mesh density employed for Martinuzzi single cube case study

The mesh density employed for this case is similar to those considered by the participants of the 6th ERCOFTAC workshop where it is noted that the corresponding range of y^+ is 1-5.[125] Full model specifications have been provided in Appendix A5.

The flow around surface-mounted, three-dimensional obstacles is characterised by streamwise vortices generated within the shear layer. These vortices drastically affect the flow in the

obstacle's vicinity and influence the downstream recovery region. As a result, the flow field for three-dimensional obstacle flows is intrinsically more complex than for two-dimensional cases.

Investigations performed by Fackrell and Pearce[126] and later by Logan and Lin[127] show that the separation length, Xr, and the recovery region downstream of the obstacle are much shorter for three-dimensional cases than for two-dimensional ones. This can be proven by comparing the reattachment length predicted for this case study with that of the universally accepted reattachment length of 7.0 ± 1.0 step heights for the two-dimensional backward facing step configuration discussed in earlier chapters. This shorter reattachment length for three-dimensional configurations is probably due to the fact that the flow is mostly around, as opposed to over the obstacle.

This three-dimensional high Reynolds number case study considers flow around a surface-mounted cube within a rectangular blower-type air channel. The Reynolds number based on the channel height, Re_h, is 80,000. Geometrically the flow configuration is rather simple, however, physically the flow is quite complex with multiple separation regions and vortices.

The flow over surface-mounted bluff bodies is often associated with the separation of shear layers at the sides and top faces of the body in question. These shear layers may reattach either on the channel wall or between neighbouring obstacles when considering a matrix array of obstacles.

It has been identified in previous work[21, 23, 37] conducted in this area that when experiments of this type of phenomena are being undertaken four main flow features are observed. With reference given to Figure 7.3, the most pronounced flow feature that emerges is the structure of the horseshoe vortex which originates upstream of the windward face and extends around both lateral sides of the cube whilst weakening in the streamwise direction. The flow in proximity to the horseshoe vortex is characterised as being in an unsteady turbulent state while the core flow in the corridor above the cube remains almost undisturbed.

The separation of the top shear layer results in a bound recirculation vortex located at the leading top edge of the cube and is most prominent on the first cube when considering a

matrix of cubes. Experimentally the footprint left by the vortex is identified as being two counter rotating circles.[27]
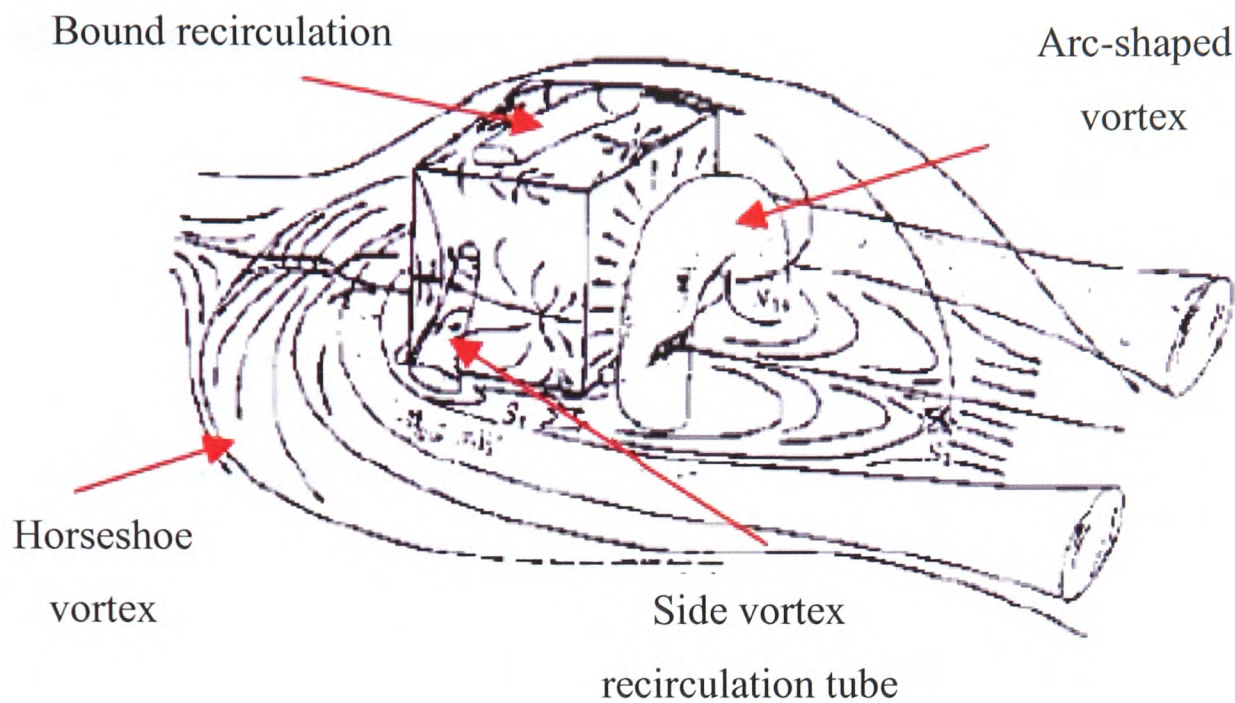
Figure 7.3 Schematic representation of the macroscopic structures characterising the mean flow around a surface-mounted cube (Martinuzzi and Tropea[21])

The separated side shear layers are the result of high vorticity recirculations close to the leading edge. Their origins are located at the base of the channel with the vortex tubes covering a significantly large surface area of both the side faces. The vortex tubes are observed to be confined by the main flow and the presence of the cube. Finally an arc-shaped vortex confined to the depth and height of the cube dominates the wake flow. This vortex is caused by a strong up wash close to the leeward face. A counter rotating footprint, similar to that found on the top surface of the cube is also observed.

The reader is referred to the references provided for further details on the flow structures observed when dealing with fully developed flow over bluff bodies.

An extensive amount of experimental data is available for this configuration. In addition to the direct measurements of the three mean velocity components and the five elements of the Reynolds stress tensor $\left(\rho\overline{u^2}, \rho\overline{v^2}, \rho\overline{w^2}, \rho\overline{uv}, \rho\overline{uw} \right)$, seven third-order correlations $\left(\overline{u^3}, \overline{v^3}, \overline{w^3}, \overline{u^2v}, \overline{uv^2}, \overline{u^2w}, \overline{uw^2} \right)$ and nine fourth-order correlations

$\left(\overline{u^4}, \overline{v^4}, \overline{w^4}, \overline{u^3 v}, \overline{u^2 v^2}, \overline{uv^3}, \overline{u^3 w}, \overline{u^2 w^2}, \overline{uw^3}\right)$ are also available. Information on the three velocity components and their correlations were obtained using single and two-component LDA techniques. Due to the vast experimental data available the reconstruction of the turbulent kinetic energy variable has been undertaken by the author using equation (7.1).

$$k = \frac{1}{2}\left(\overline{u'^2} + \overline{v'^2} + \overline{w'^2}\right) \qquad (7.1)$$

The experimental data locations available for comparison are illustrated in Figure 7.4. The locations chosen for comparison here are those presented at the 6th ERCOFTAC workshop. Twelve locations have been examined moving in the streamwise direction through the channel configuration highlighted by the square symbols in Figure 7.4.
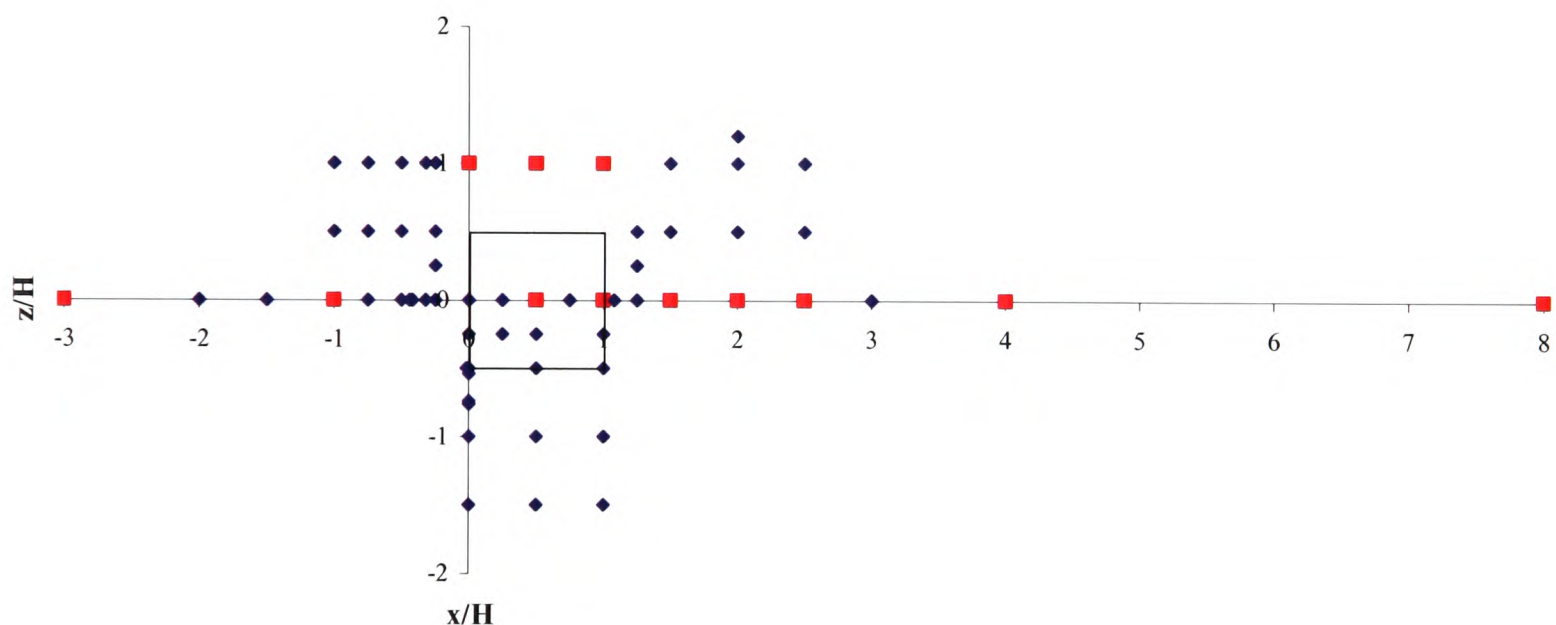
Figure 7.4 Experimental data measurement locations (ERCOFTAC database)

The reconstruction of the turbulent kinetic energy has only been preformed for the twelve measurement allocations selected for comparison. CFD predictions have been undertaken using the commercial software FLOTHERM V3.2 and the University of Greenwich code PHYSICA V2.12.

7.1 Results and Discussion

The participants of the 6th ERCOFTAC workshop were split into five groups depending on the turbulence model used for the numerical work undertaken. The division of the groups has been detailed in Table 7.1.

Group	Turbulence Model
A	Large Eddy Simulations
B	Second moment closures with wall functions
C	Low Reynolds number $k - \varepsilon$ models
D	Alternative low Reynolds number models
E	Standard $k - \varepsilon$ based models with wall functions

Table 7.1 Group division for the 6th ERCOFTAC workshop

Reference will be made to the workshop results via the group identifier throughout this chapter in order to gage the performance of the turbulence models investigated by the author.

The two turbulence model classes utilised for this case study are the zero-equation LVEL and two-equation standard $k - \varepsilon$ models. Where possible the three velocity components and the turbulent kinetic energy will be compared against experimental data. However in some instants the experimental data for the $\overline{w'^2}$ fluctuating velocity component has not been made available and therefore only two of the three velocity components have been analysed.

Before discussion of the comparison of numerical predictions against the experimental measurement locations is undertaken streamlines of the mean flow will be analysed. Three-dimensional streamlines starting on a line in the symmetry plane through the centre of the cube are presented in Figure 7.5. What is seen in the figures represents a projection of the streamlines in the chosen plane. Figure 7.6 shows three-dimensional streamlines released along a horizontal line adjacent to the floor of the wind tunnel. Far from the symmetry plane these streamlines stay close to the floor and pass around the side of the cube. Those released closer to the symmetry plane interact with the horseshoe vortex. As viewed from above, these lines appear to cross one another in the projected image as the fluid is moving in different directions at different vertical locations. As such these can not be compared directly with the oil-film visualisation results, which show the near-wall flow behaviour.

a. Experimental measurements[128]
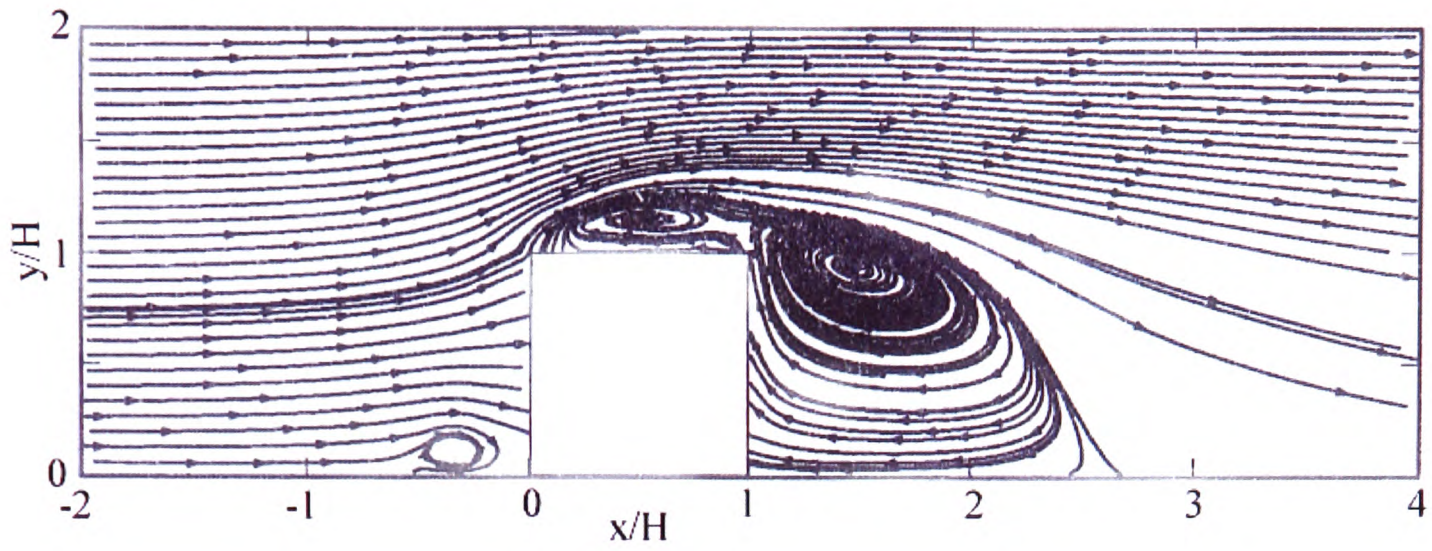
b. LVEL turbulence model predictions
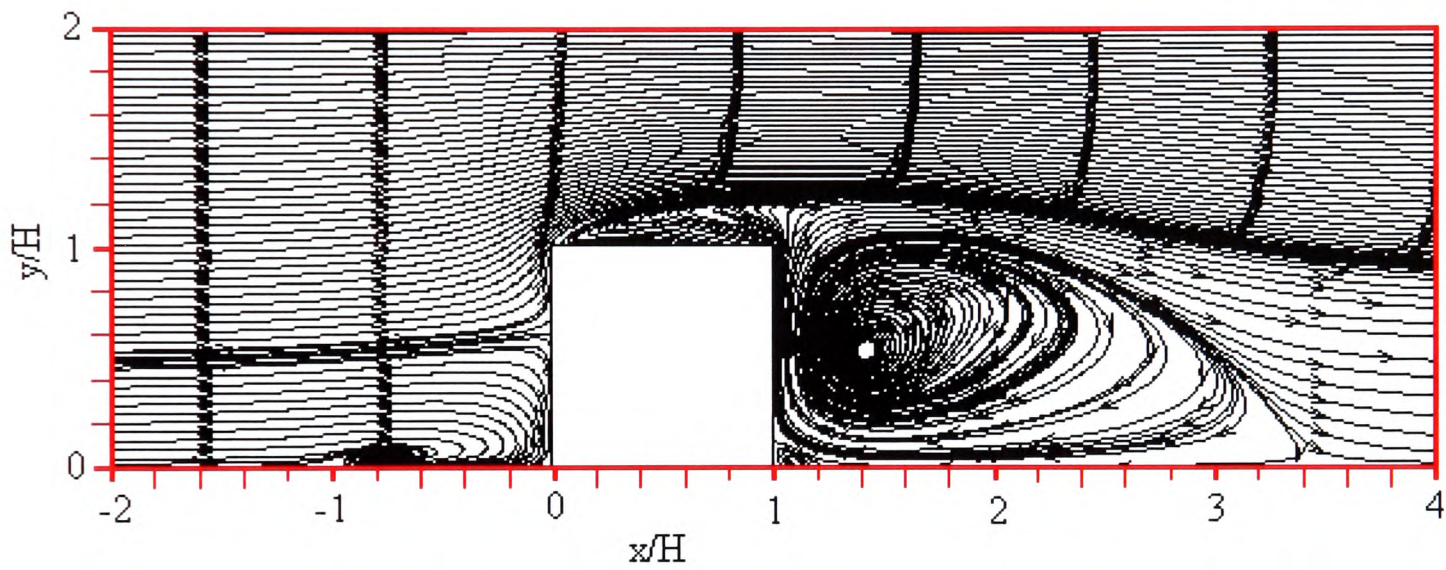
c. Standard $k - \varepsilon$ turbulence model predictions
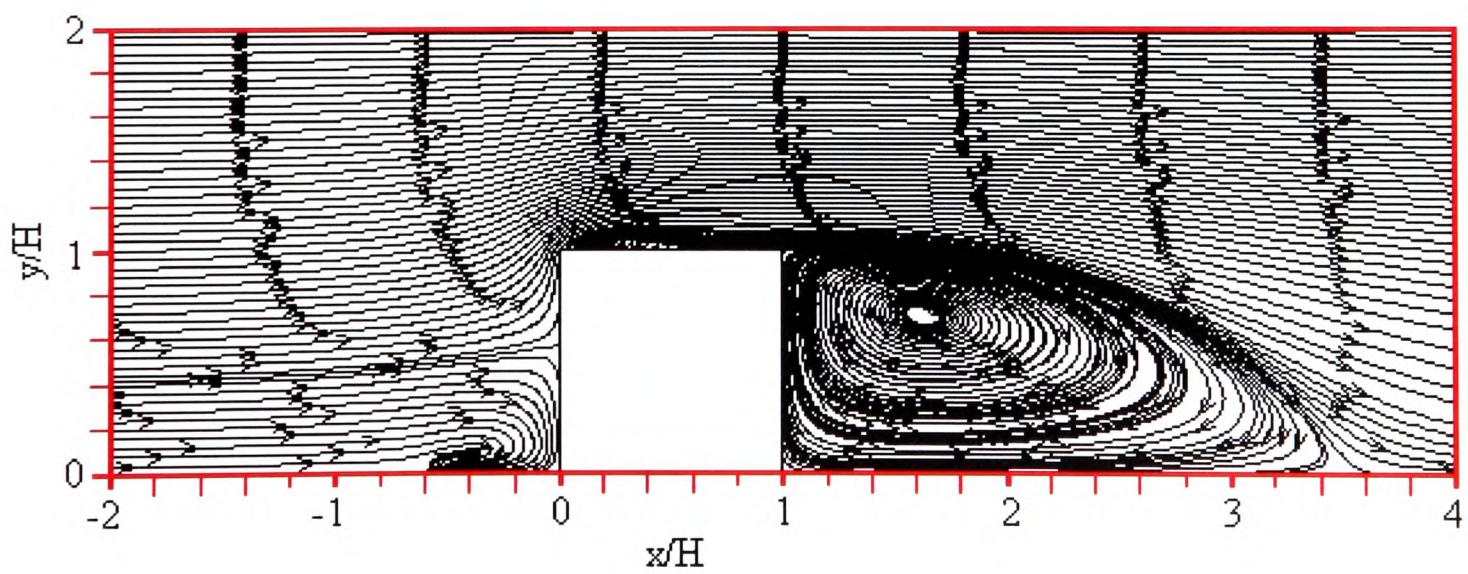
Figure 7.5 Streamlines of the mean flow on the symmetry plane through the high Reynolds number single cube (xy-plane)

a. LVEL turbulence model predictions
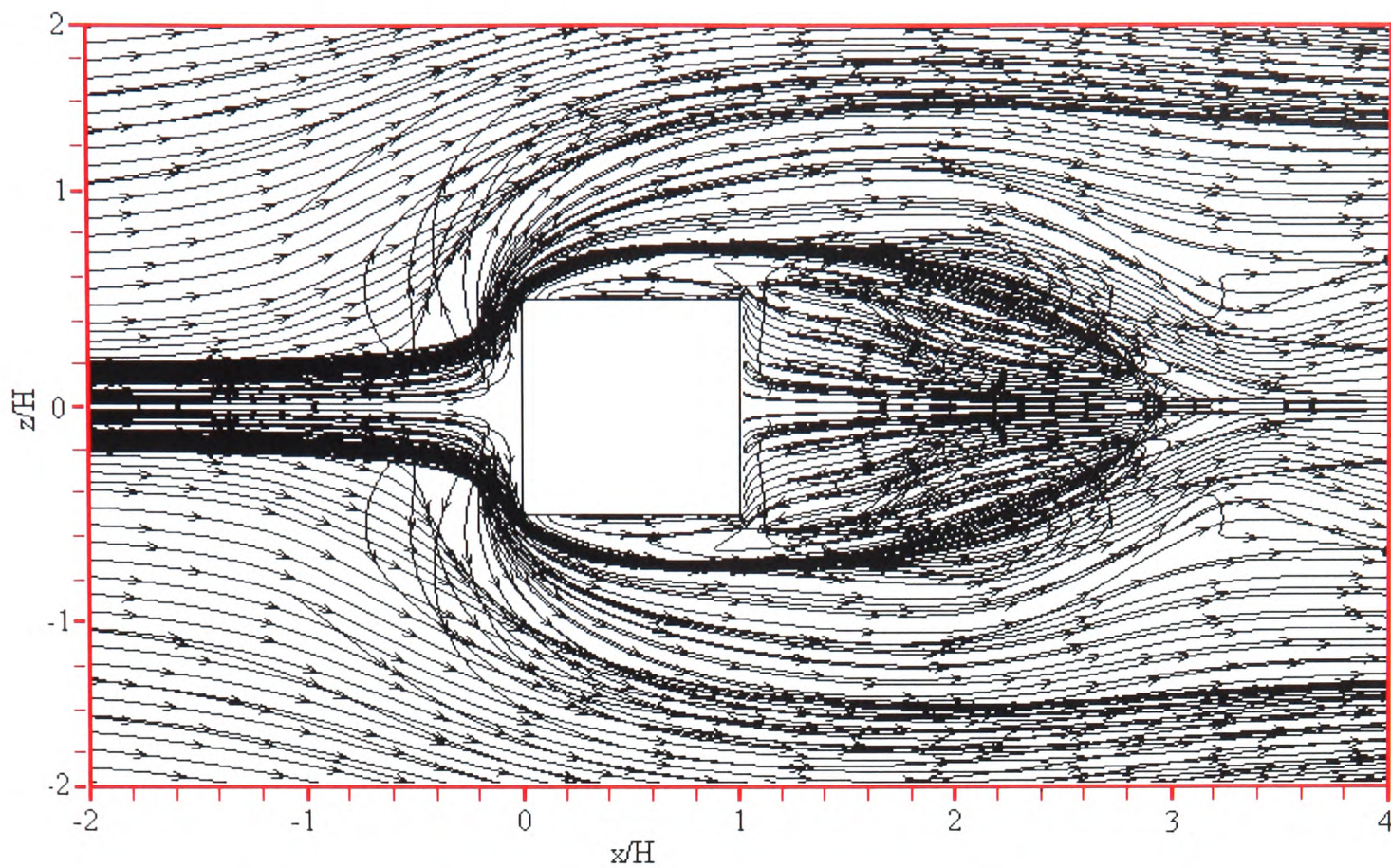
b. Standard $k - \varepsilon$ turbulence model predictions
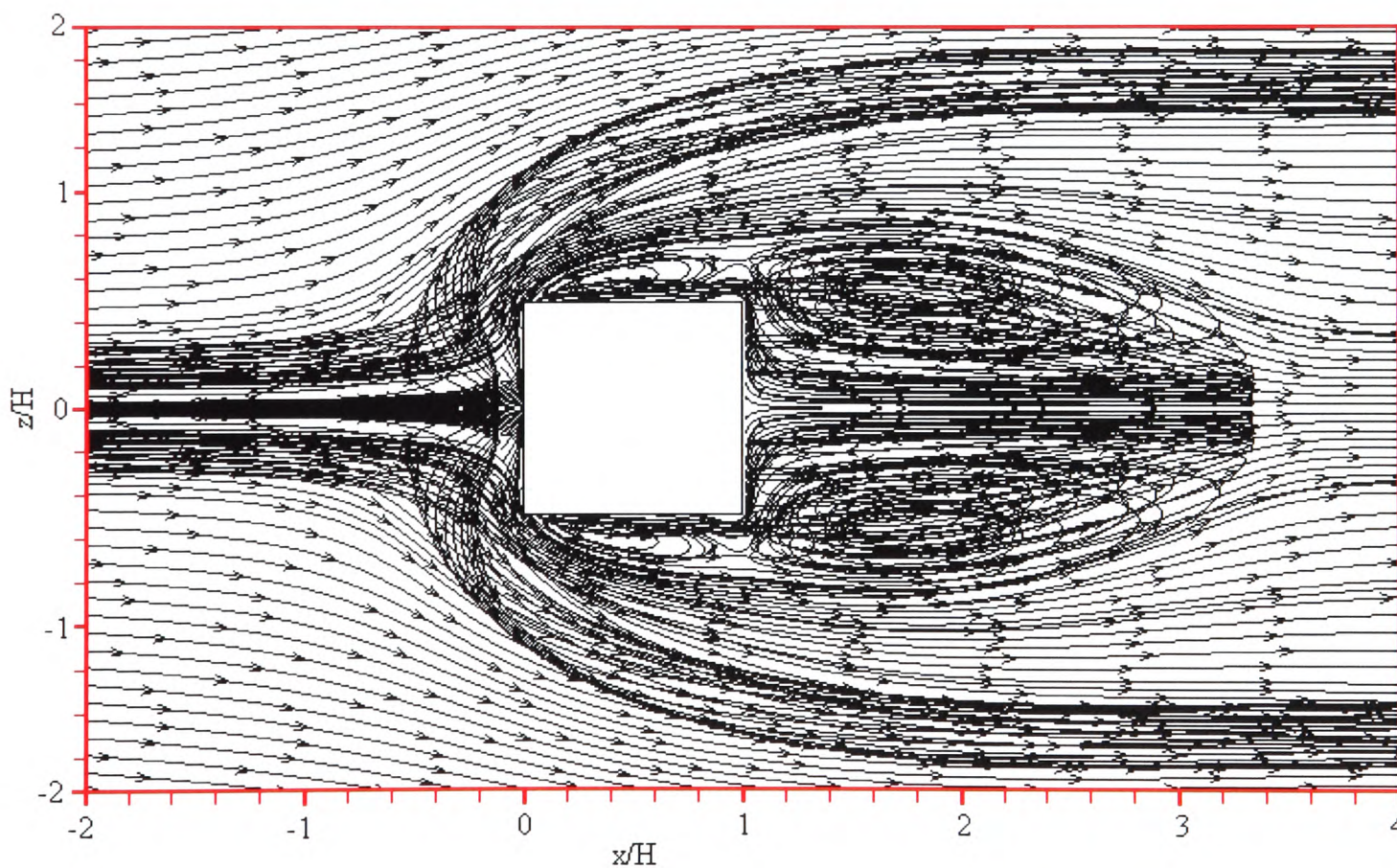
Figure 7.6 Streamlines of the mean flow on the base of the high Reynolds number channel (xz-plane)

The classic flow recirculation features (see Figure 7.3) can all be identified in Figure 7.5 and Figure 7.6 i.e. horseshoe, bound, side and wake vortices. The bound separation bubble is better predicted by LVEL than the standard $k - \varepsilon$ model, whereas the location of the

horseshoe and the centre of the wake vortices are well captured by $k - \varepsilon$. Overall the two-equation model would be regarded to be in greater agreement with the experimental observations.

The experimental streamline measurements presented in Figure 7.5a can be directly compared against the numerical CFD predictions presented in Figure 7.5b and c. The horseshoe vortex which is deflected downstream of the cube is experimentally determined to originate at $x/H \approx -0.4$. This vortex origin is predicted reasonably well by the $k - \varepsilon$ model but is over predicted by the LVEL model to $x/H \approx -1.0$.

The bound vortex located on the top face of the cube is shown to extend across the entire top surface. The LVEL model manages to identify this vortex well, the $k - \varepsilon$ model on the other hand demonstrates a weak recirculation vortex which closes on the top surface of the cube contrary on the experimental results.

The experimental reattachment length $Xr/H \approx 1.5$ is also over-predicted by both the RANS turbulence models at $Xr/H \approx 2.4$. However this over prediction in the reattachment length was also noted by Group E, which is the group most closely related to the models currently under investigation by the author, therefore illustrating that the turbulence models under investigation are performing consistently with other RANS-based models. One zonal Group E classified model (algebraic expression for the mixing length for near-wall flow and $k - \varepsilon$ for the bulk) predicted a reattachment length of $Xr/H \approx 4.0$, so the results presented here are by no means unusual.

The numerical predictions presented in Figure 7.6 can not be directly compared against experimental measurement. However the side vortices, which are known to cover a significantly large portion of these surfaces, are identifiable for both turbulence models investigated. Similar features were noted at the ERCOFTAC workshop.

As noted in Figure 7.4 nine of the twelve measurement locations rest on the centreline of the geometry. These profiles will be examined first, followed by the remaining three off-centre profiles.
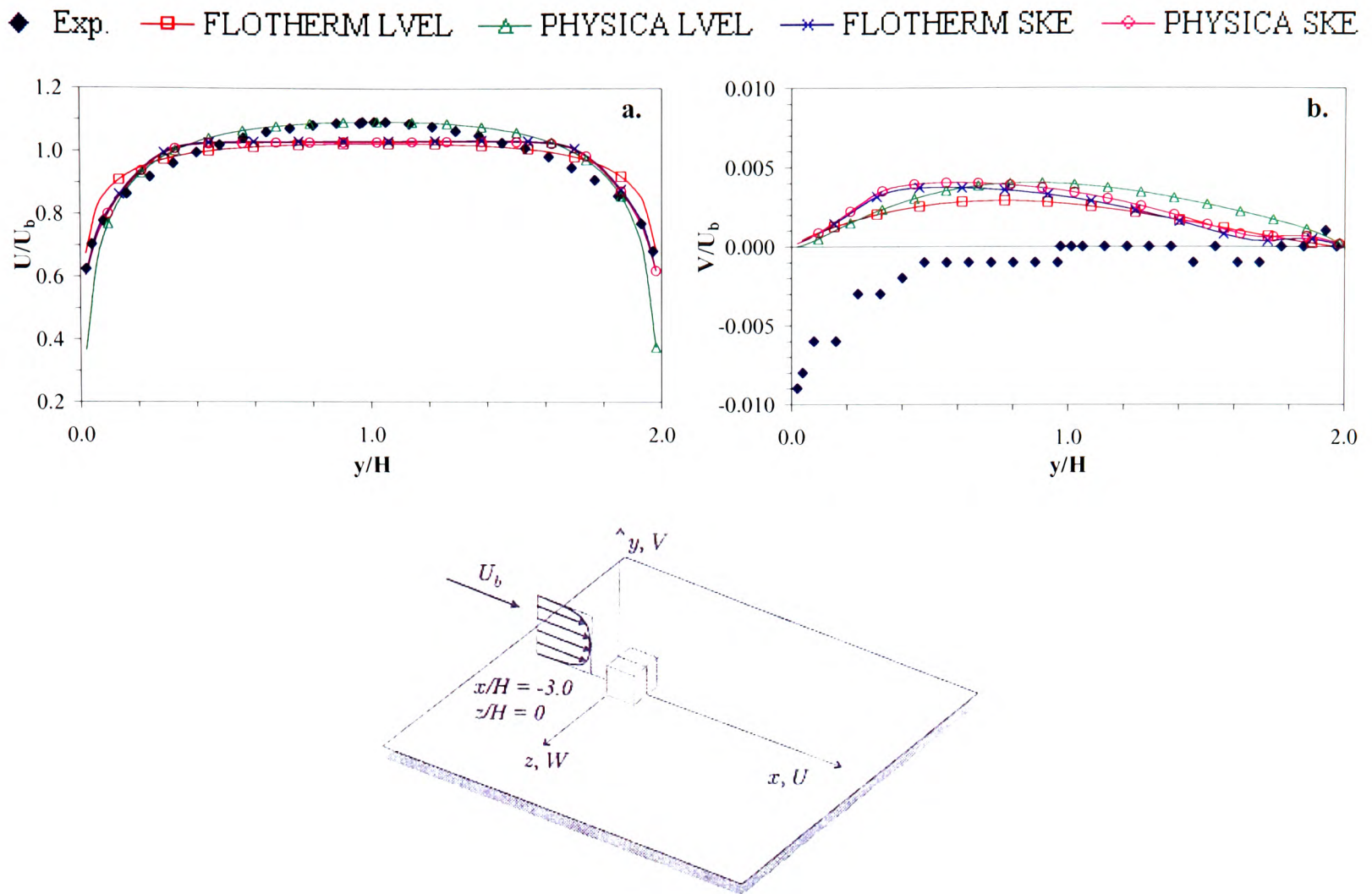
Figure 7.7 Mean velocity components for measurement location x/H = -3.0, z/H = 0
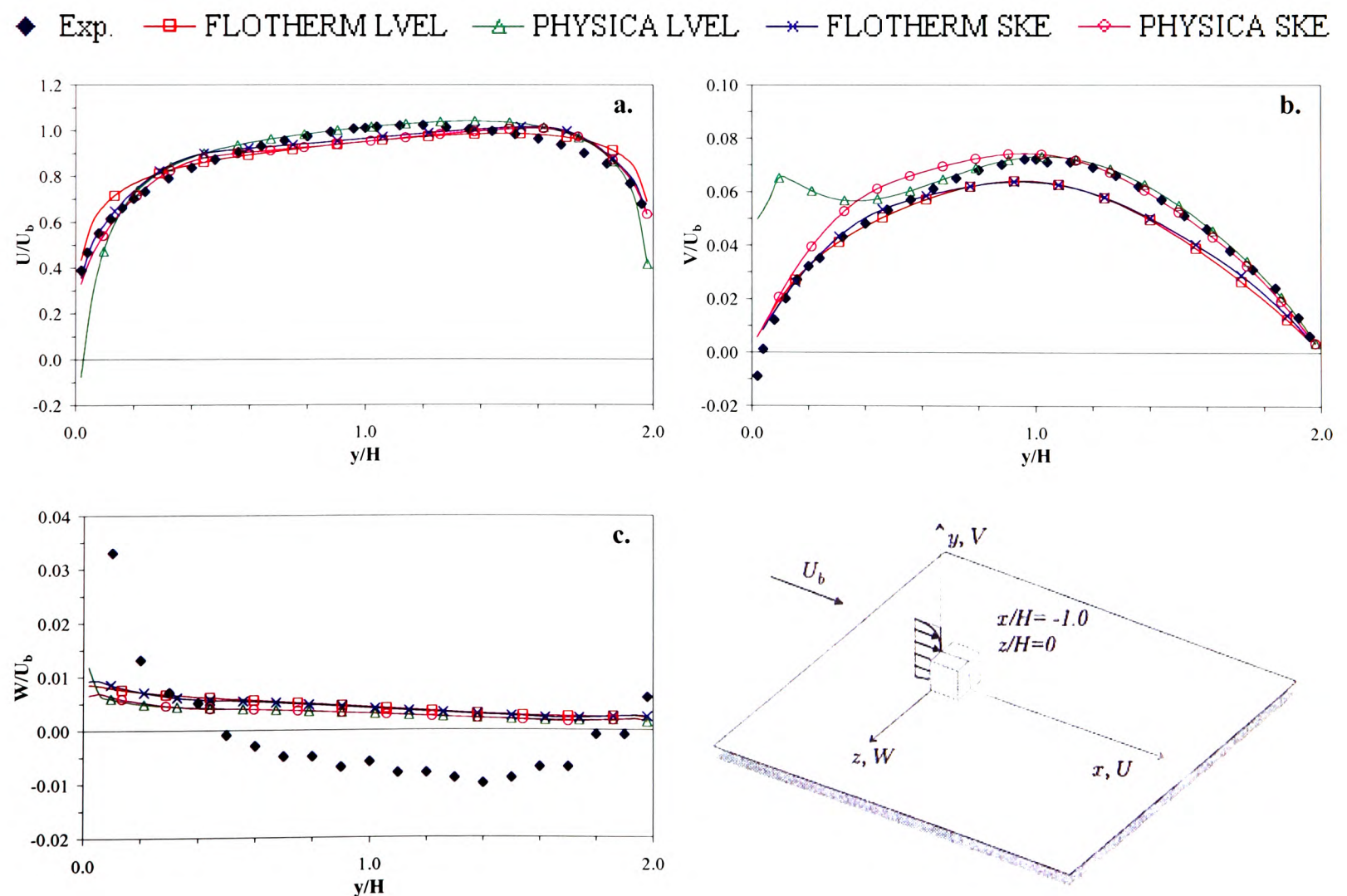
Figure 7.8 Mean velocity components for measurement location x/H = -1.0, z/H = 0
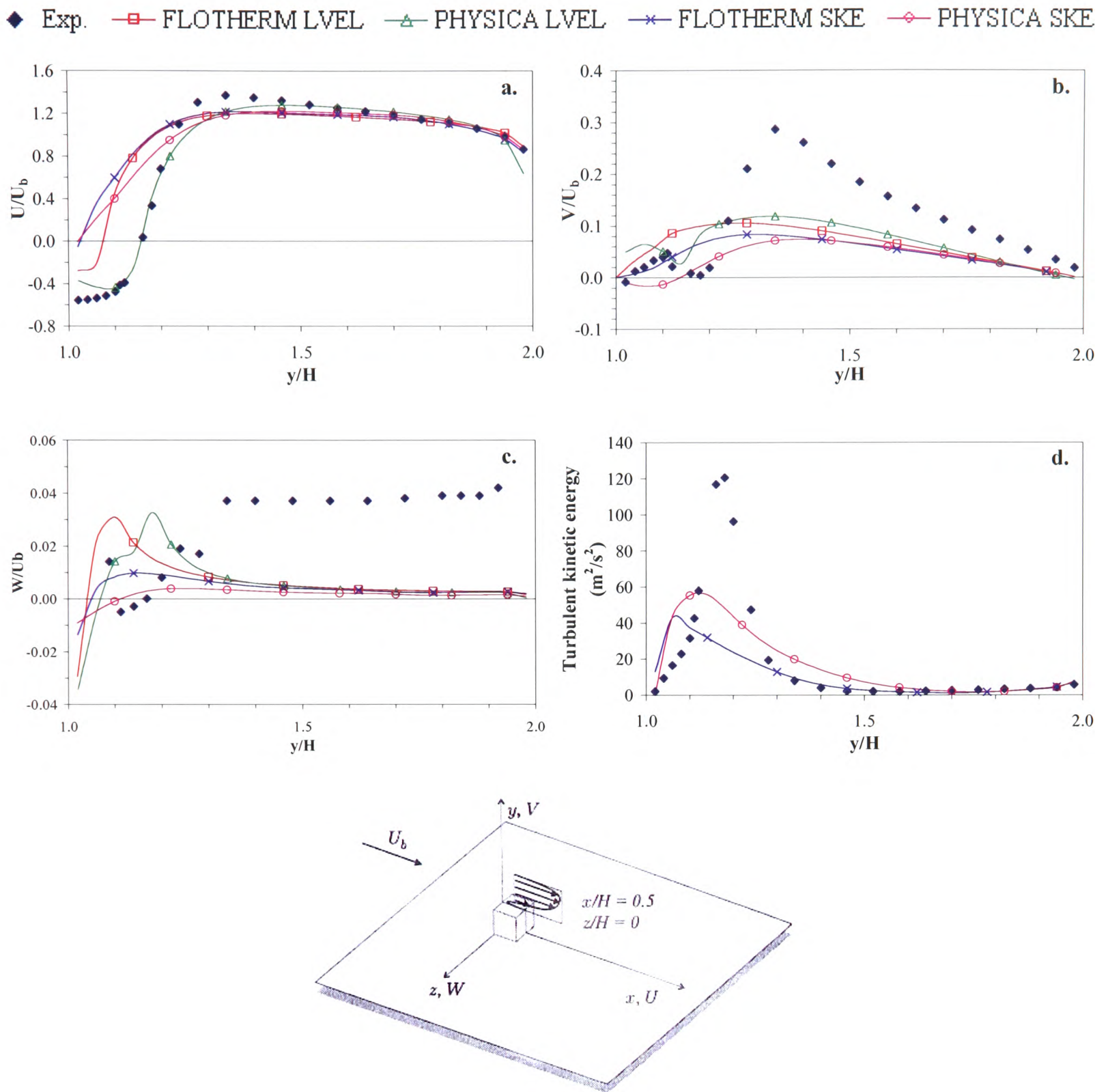
Figure 7.9 Mean velocity components and turbulent kinetic energy for measurement location x/H = 0.5, z/H = 0
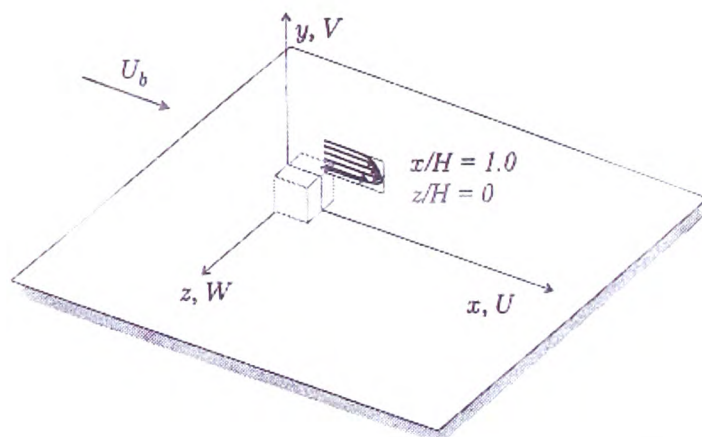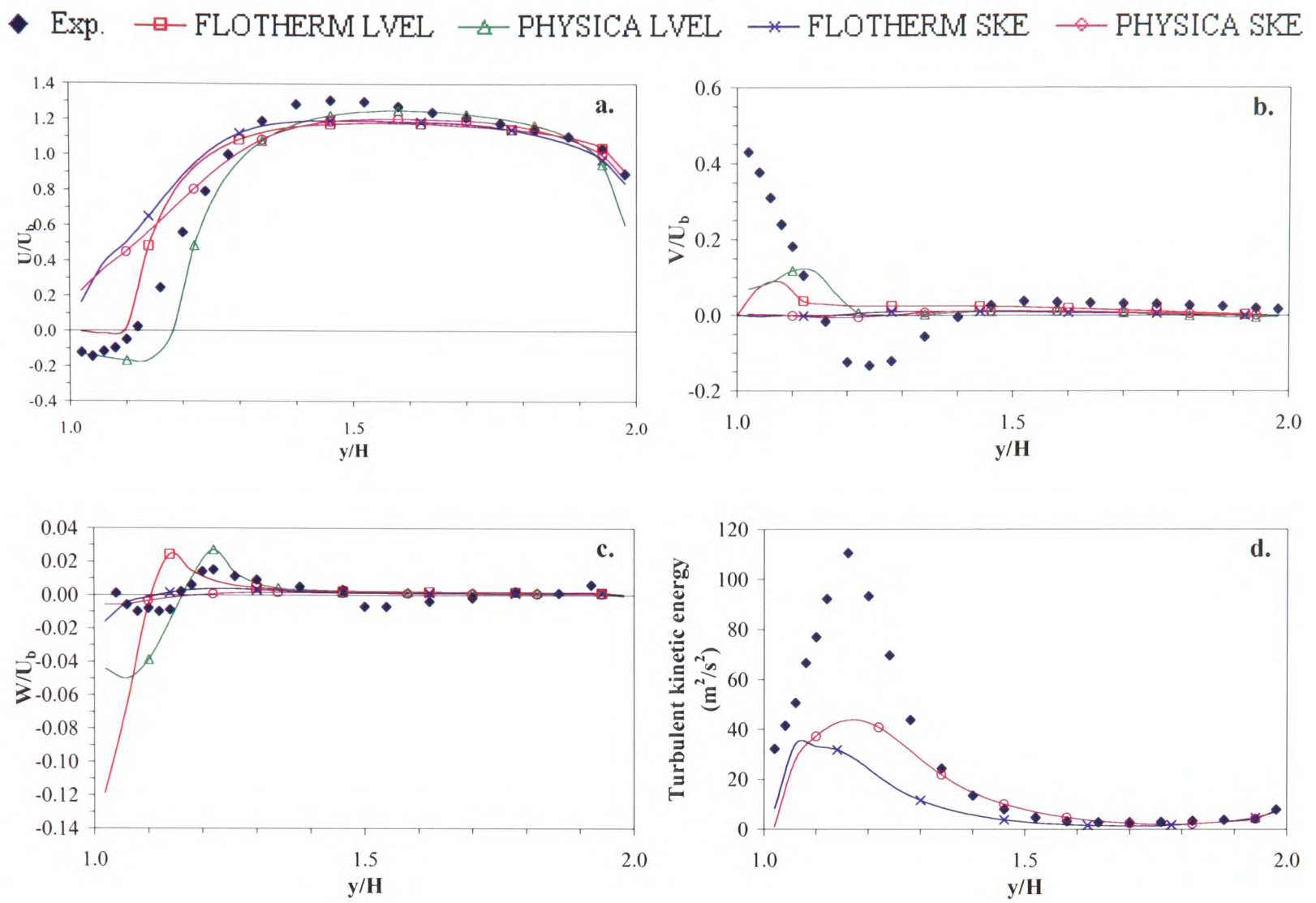
Figure 7.10 Mean velocity components and turbulent kinetic energy for measurement location x/H = 1.0, z/H = 0
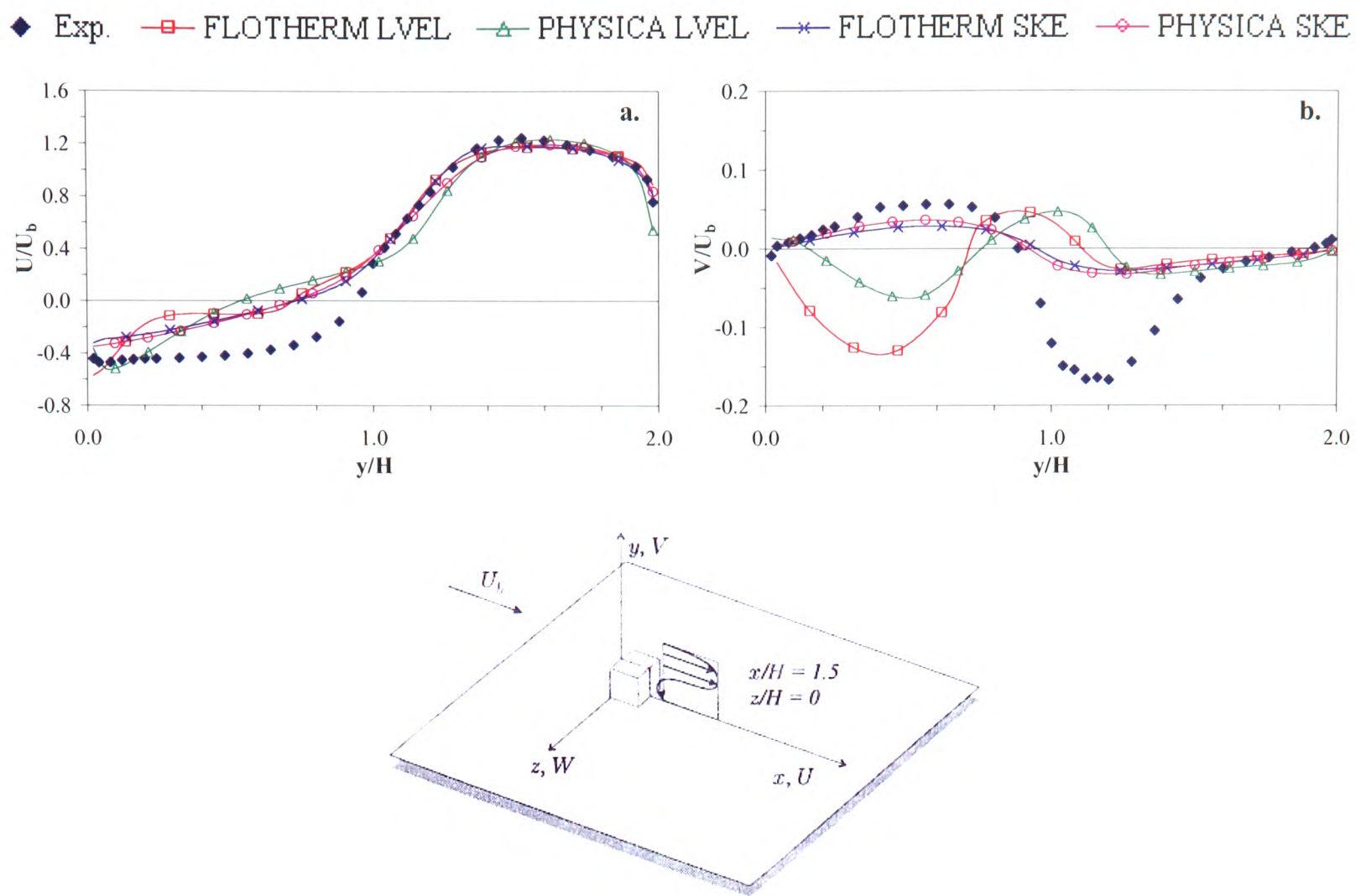
Figure 7.11 Mean velocity components for measurement location x/H = 1.5, z/H = 0
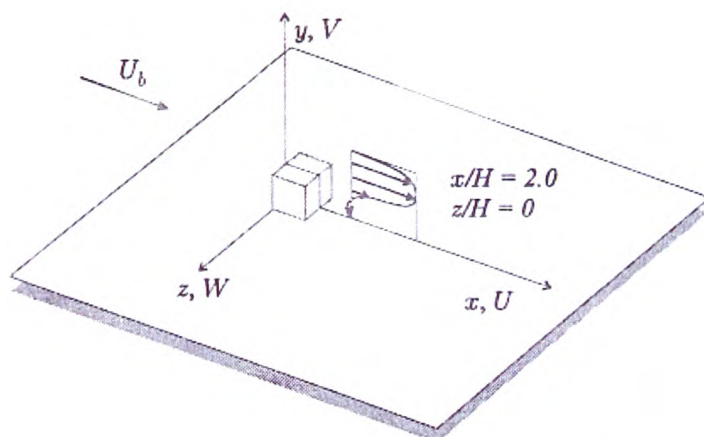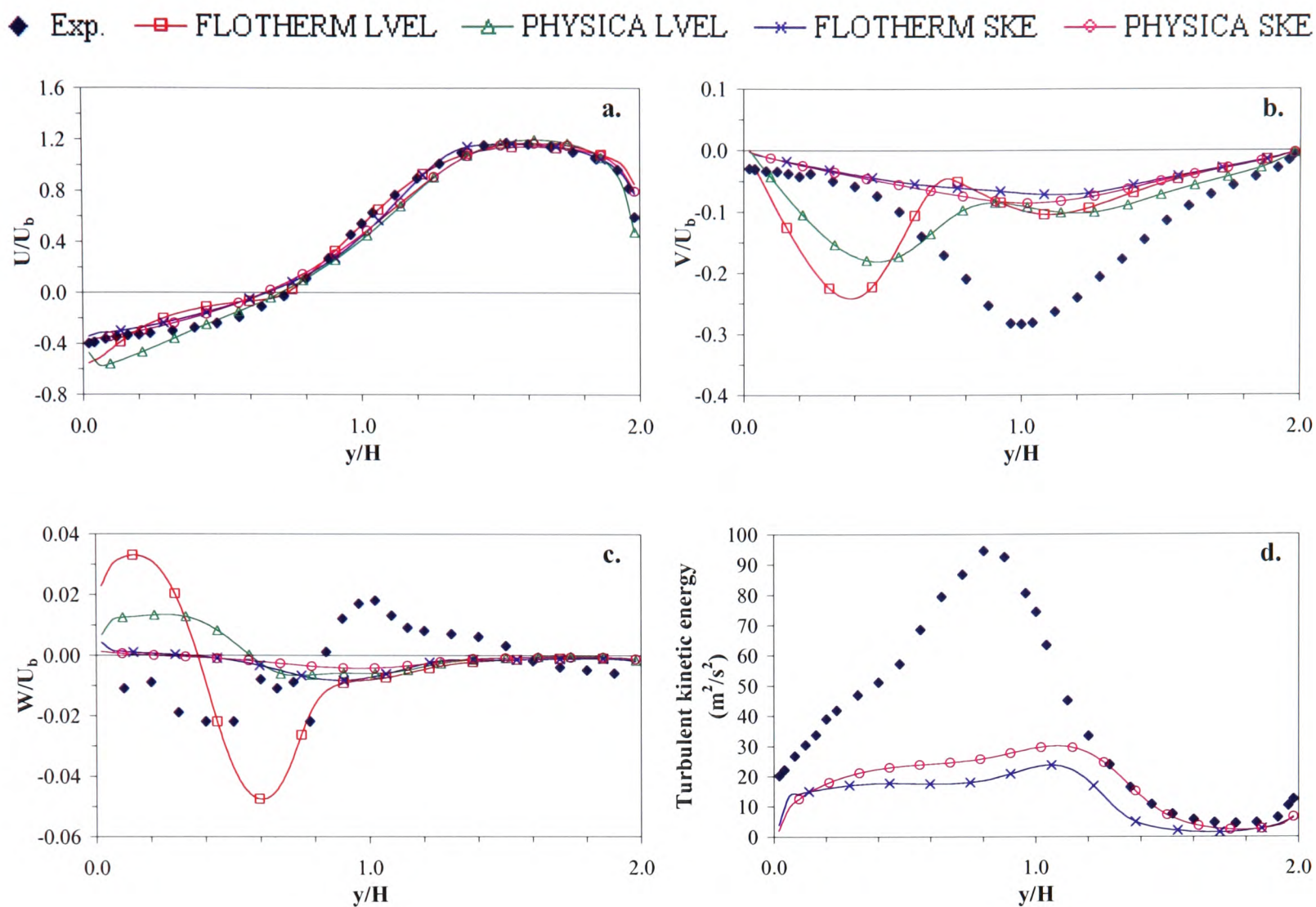
Figure 7.12 Mean velocity components and turbulent kinetic energy for measurement location x/H = 2.0, z/H = 0
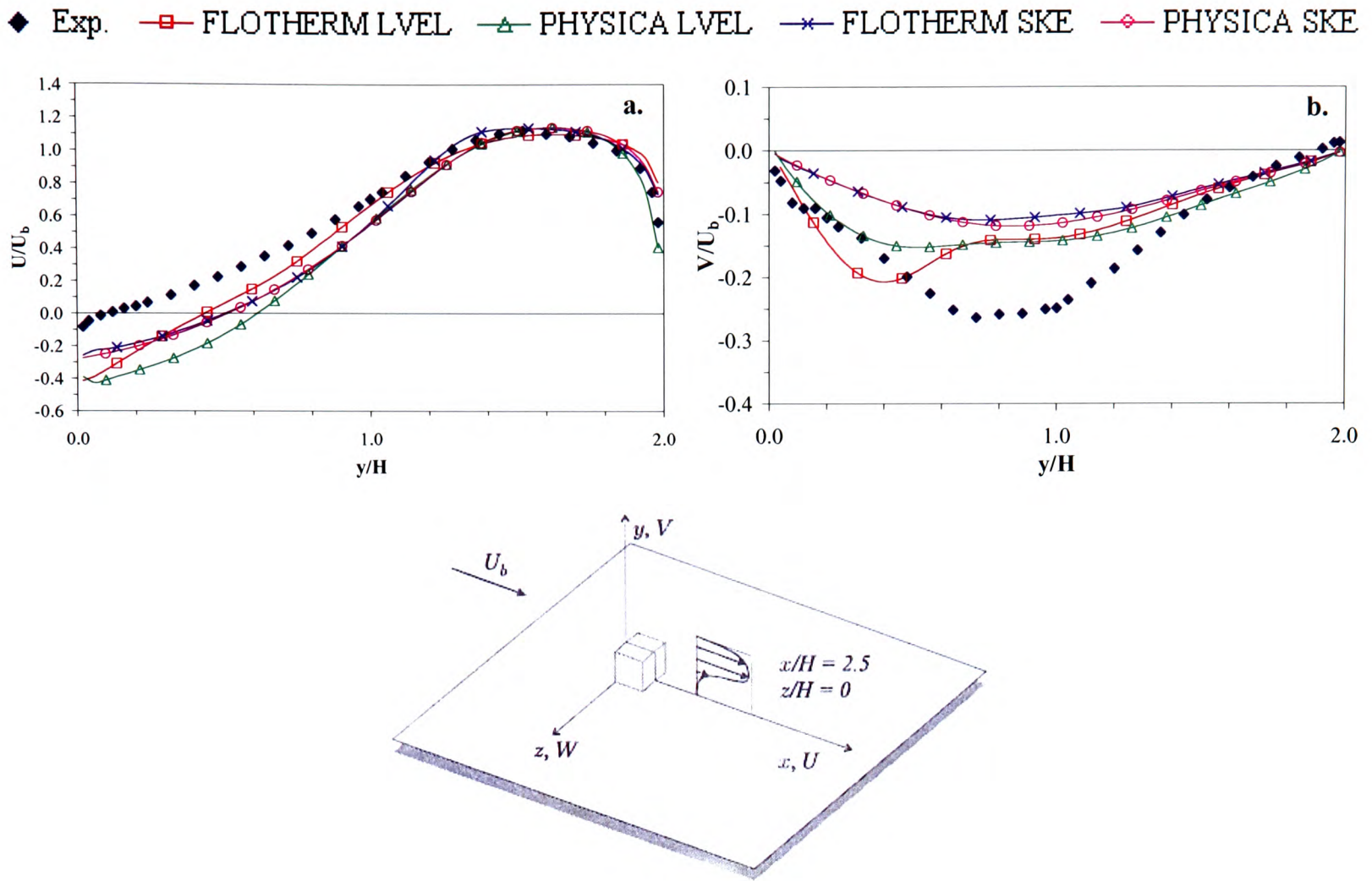
Figure 7.13 Mean velocity components for measurement location x/H = 2.5, z/H = 0
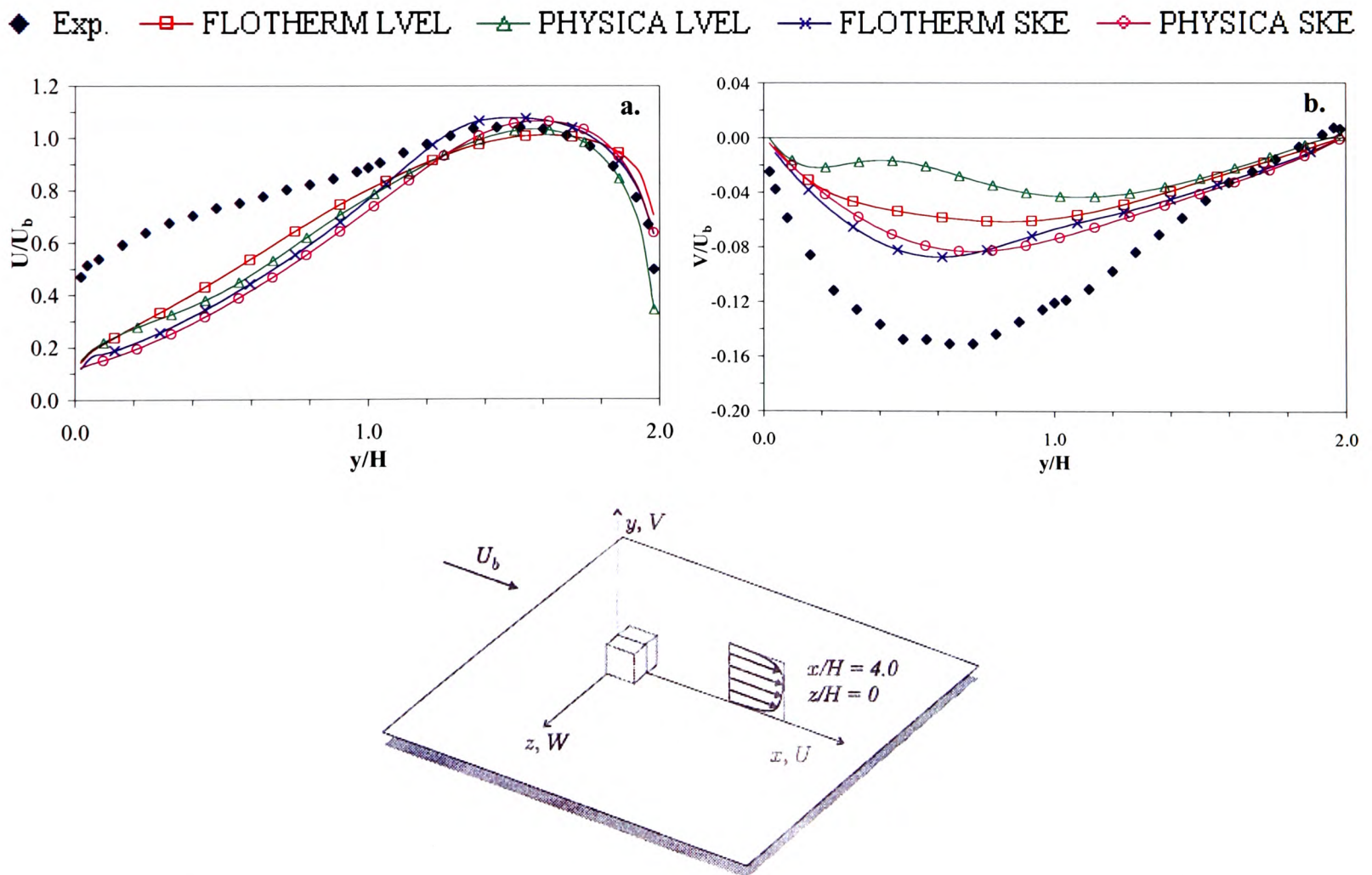
Figure 7.14 Mean velocity components for measurement location x/H = 4.0, z/H = 0
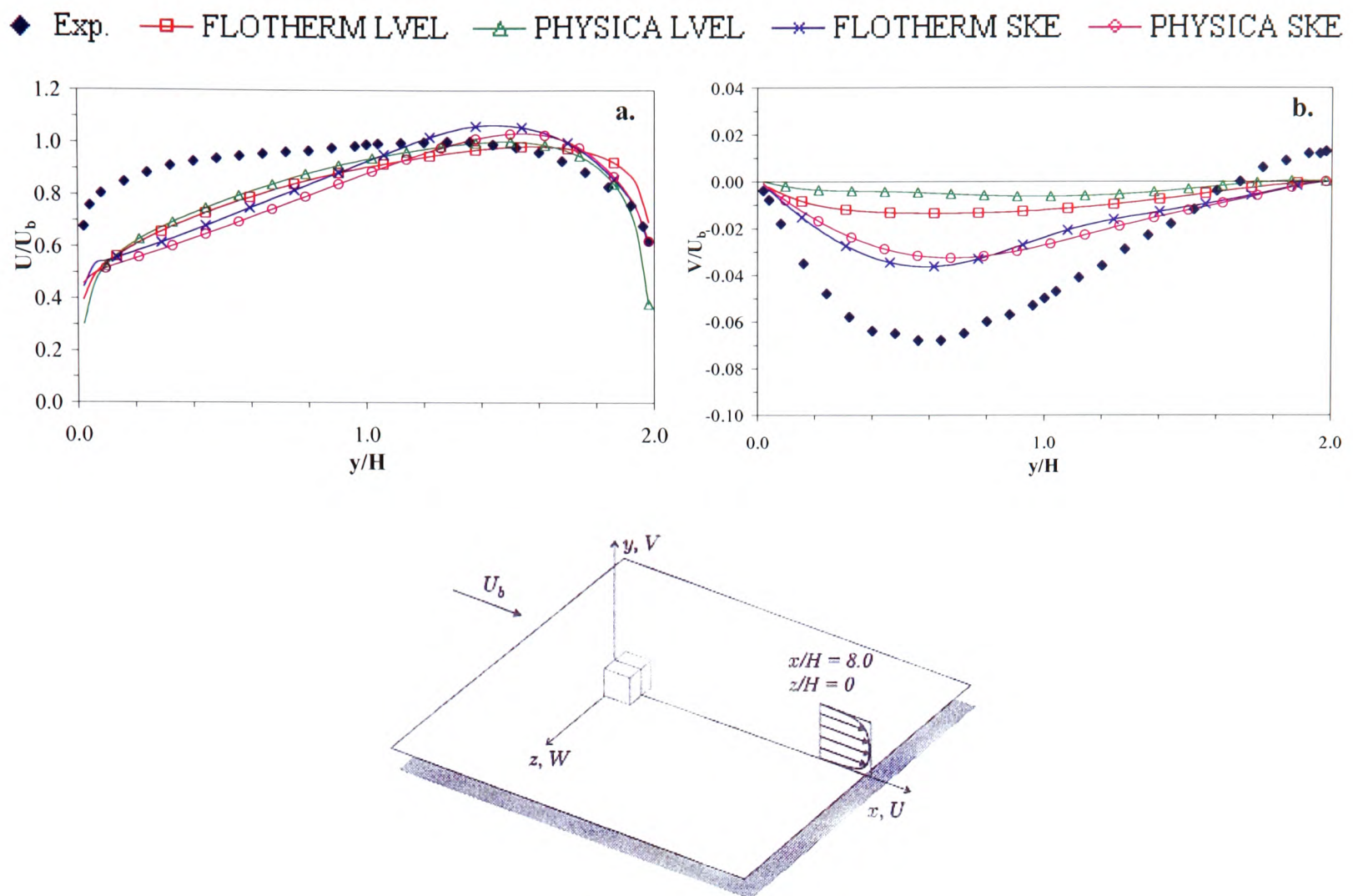
Figure 7.15 Mean velocity components for measurement location x/H = 8.0, z/H = 0

The centreline measurement locations have been presented in Figure 7.7 through to Figure 7.15. A brief discussion of some important conclusions which can be drawn from these figures will now be undertaken before moving on to the off-centre measurements.

Referring to Figure 7.7a it can be concluded that all turbulence models investigated reproduce the experimental channel flow profile. Both codes give very similar results for the standard $k - \varepsilon$ models, reinforcing the argument that the core underlying foundations of the two codes are indeed similar.

The turbulence model which shows the closest agreement with the experimental data is the PHYSICA LVEL model. The accurate prediction of LVEL over the $k - \varepsilon$ model is not a coincidence. The LVEL model was originally designed for boundary layer flows, which is the class of flow under investigation at this point in the solution domain, as no disturbances will affect the flow field until the presence of the cube has been detected.

Both the normalised velocity components presented in Figure 7.7 are in good agreement with the numerical work presented at the workshop for all groups. Considering Group E in greater detail it can be determined that the $k-\varepsilon$ models used here together with the FLOTHERM LVEL model produce flatter profiles towards the centre of the channel.

An interesting feature of the PHYSICA LVEL model is noted in Figure 7.8a. Although this model agrees most accurately with the overall experimental data profile this model is also the only tested model which manages to predict a slight onset of the recirculation vortex located at the base of the channel. In line with the experimental data at this measurement location all other models investigated do not identify this flow feature. This also stands true for the models used at the workshop. This suggests that the PHYSICA LVEL model is predicting a larger vortex length in front of the cube. The remaining turbulence models in both CFD codes predict this recirculation vortex closer to the cube's front face, as can be seen from the flow streamlines presented in Figure 7.5 and Figure 7.6.

Considering Figure 7.8b it is noted that the PHYSICA LVEL model is the only model which experiences a sharp increase in the v-velocity close to the base of the channel which must be associated with the recirculation vortex identified by this model. The only model to experience a similar trend in results with regards to this peak in the v-velocity component investigated at the workshop was the SST[54, 62] two-layer model which is classed as a Group D model.

Of the two codes tested overall the PHYSICA models are in closest agreement with the experimental data especially for $y/H > 1.0$ at this particular measurement location.

The general trend in the accurate performance of the PHYSICA LVEL model continues when considering Figure 7.9a. Both LVEL models predict to some extend the top recirculation vortex. However the FLOTHERM LVEL model fails to predict the full vortex height of $0.16H$ instead a prediction of $0.08H$ is made. PHYSICA LVEL on the other hand predicts both the height and the speed of the bound vortex exceptionally well. This model agrees most accurately with the complete experimental data profile.

Both the standard $k-\varepsilon$ models fail to capture the full magnitude of the bound vortex only predicting a weak separation on the top face of the cube. The same trend is noted for four of

the five turbulence models presented at the workshop for Group E. The only Group E model that predicts, rather accurately, the recirculation vortex is a $k - \varepsilon$ based two-layer model which uses the approach of Chen and Patel.[105]

None of the investigated models predict the peak in the v-velocity, see Figure 7.9b, which is consistent with most of the $k - \varepsilon$ results predicted by Group E. However the PHYSICA LVEL model is following the trend of the experimental data the closest.

Assessment of Figure 7.9c, which presents the w-velocity component, shows the initial inaccuracies developing in the LVEL models. It was only a matter of time before these inaccuracies were highlighted as the model is a boundary layer model and is known not to cope well with separated flow phenomena. Unfortunately the consequences of these inaccuracies will lead to poor numerical predictions due to the eventual propagation of errors further downstream the channel.

The extent to which the LVEL model, in either code, recovers is of interest. Imagine a matrix array configuration similar to that discussed in Chapter 9. If the LVEL model experiences a poor recovery rate then the errors generated at the first electronic component will simply propagate downstream and magnify as the flow proceeds. These inaccurate predictions of the flow field will consequently lead to inaccurate predictions of the heat transfer from the components within the system.

Figure 7.9d demonstrates that the levels of turbulent kinetic energy are clearly under predicted by the $k - \varepsilon$ investigated turbulence models. The FLOTHERM $k - \varepsilon$ model agrees most accurately with the majority of the experimental data at this location but the PHYSICA $k - \varepsilon$ model predicts a greater peak in results. Similar trends are noted in Figure 7.10 as have been discussed for Figure 7.9.

The first assessment of the wake vortex is undertaken at the measurement location $x / H = 1.5$, $z / H = 0$ which corresponds to Figure 7.11. From Figure 7.11a it can be concluded that the vertical height of the wake vortex is poorly predicted by all turbulence models tested for this case study. The LVEL models, which predicted rather well the profiles discussed previously, now, as expected, show poor numerical behaviour in comparison to the experimental data, which records a vertical reattachment height of approximately $1.0H$. Both

$k - \varepsilon$ models also fail to accurately predict this reattachment point but show much greater agreement to the overall trend of the experimental data especially once the vertical height of the cube is surpassed.

The deficiency of the LVEL models with regards to separated flow phenomena is again highlighted in Figure 7.11b where both CFD codes are experiencing difficulties accurately predicting the v-velocity component in this wake vortex region. The $k - \varepsilon$ models fail to predict the full extend of the vortex but follow the experimental trend. Similar numerical results were obtained by Group E at the ERCOFTAC workshop for the $k - \varepsilon$ models investigated.

Figure 7.12 shows similar tendencies to those noted in Figure 7.11. The height of the wake vortex, determined experimentally as approximately $0.7H$ from Figure 7.12a, at this measurement location has been predicted relatively well by all turbulence models, however the $k - \varepsilon$ models still show better overall agreement with the experimental data than the LVEL models. The smoothness in the u-velocity profiles experienced by the $k - \varepsilon$ models is still lacking in the LVEL models. Nevertheless at least some form of recovery for the LVEL models can be identified.

The workshop Group E numerical results are similar to those presented here for the remaining velocity components displayed in Figure 7.12.

Figure 7.13a is an interesting measurement location to discuss as the experimental data shows that the majority of the wake recirculation vortex is now closed whereas the numerical work conducted at the workshop for Groups B, C, D and E together with the results presented here show that the predicted length of this wake vortex is larger than that recorded in the experiments.

When considering the main flow direction it can be concluded that the LVEL models have generally recovered by the measurement location $x/H = 2.5$, $z/H = 0$ which may be thought of as a too slow recovery rate considering the target application is extremely densely packed electronics systems.

The remaining centreline measurement locations presented in Figure 7.14 and Figure 7.15 show the flow profiles gradually redeveloping after the disturbance of the cube. The rate at which the redevelopment is taking place is not as fast as that noted by the experimental data but this is attributed to the deficiencies of the RANS turbulence models used as this consistent trend was also seen in the workshop numerical results obtained for all Groups excluding Group A (LES).

Attention will now be turned to the off-centre measurement locations $x/H = 0$, $z/H = 1.0$, $x/H = 0.5$, $z/H = 1.0$ and $x/H = 1.0$, $z/H = 1.0$ respectively.
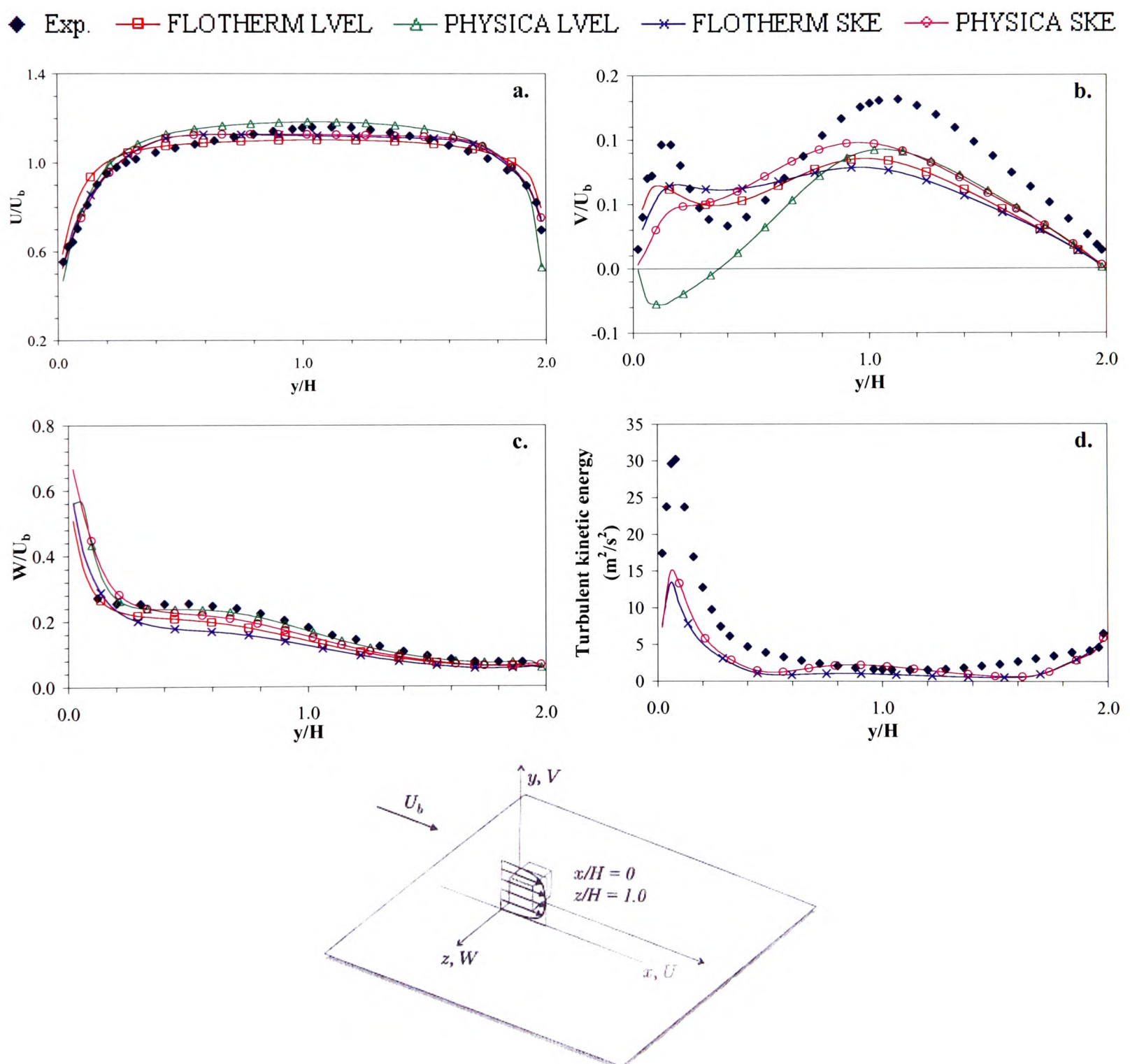
Figure 7.16 Mean velocity components and turbulent kinetic energy for measurement location x/H = 0, z/H = 1.0
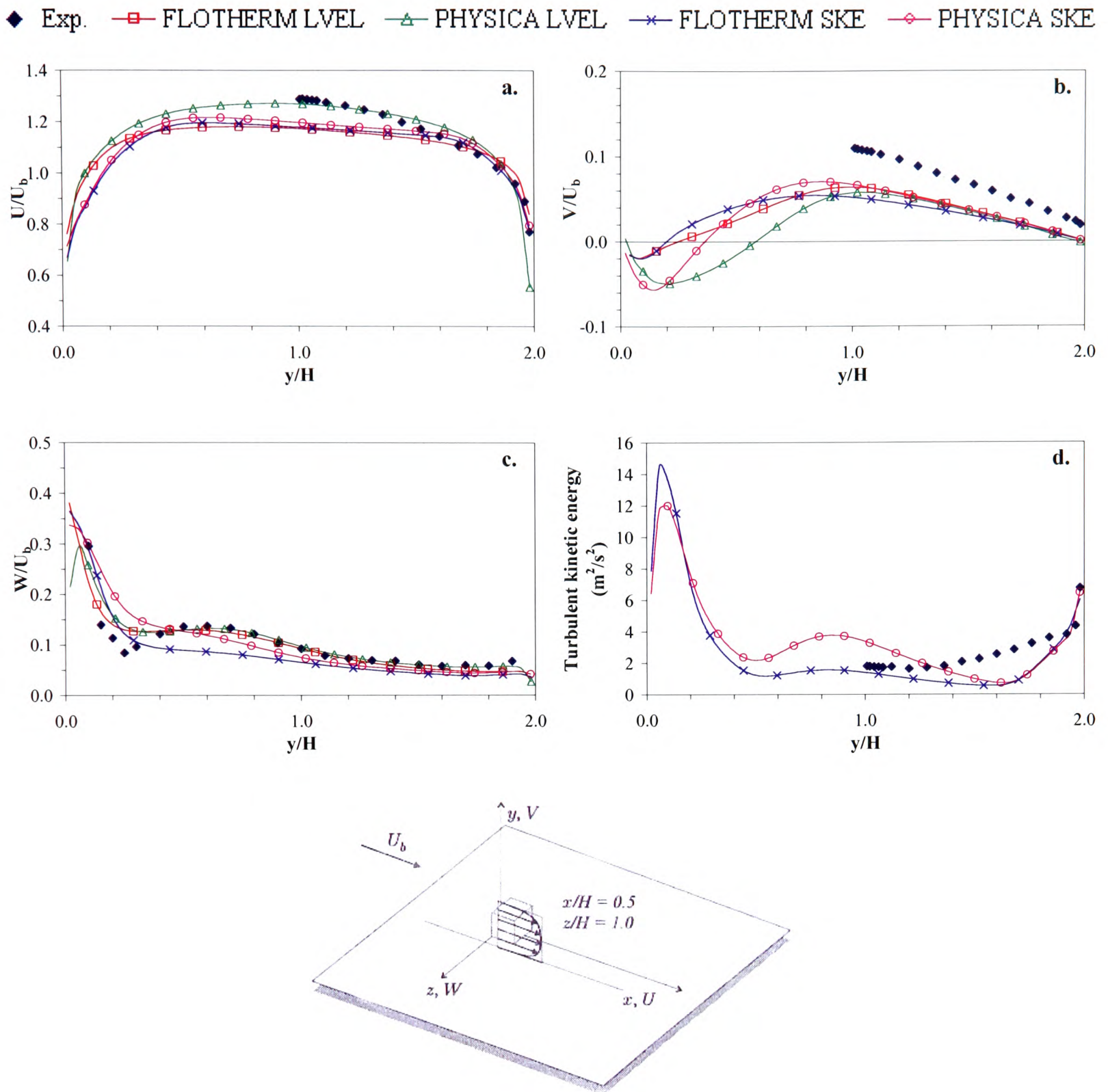
Figure 7.17 Mean velocity components and turbulent kinetic energy for measurement location x/H = 0.5, z/H = 1.0
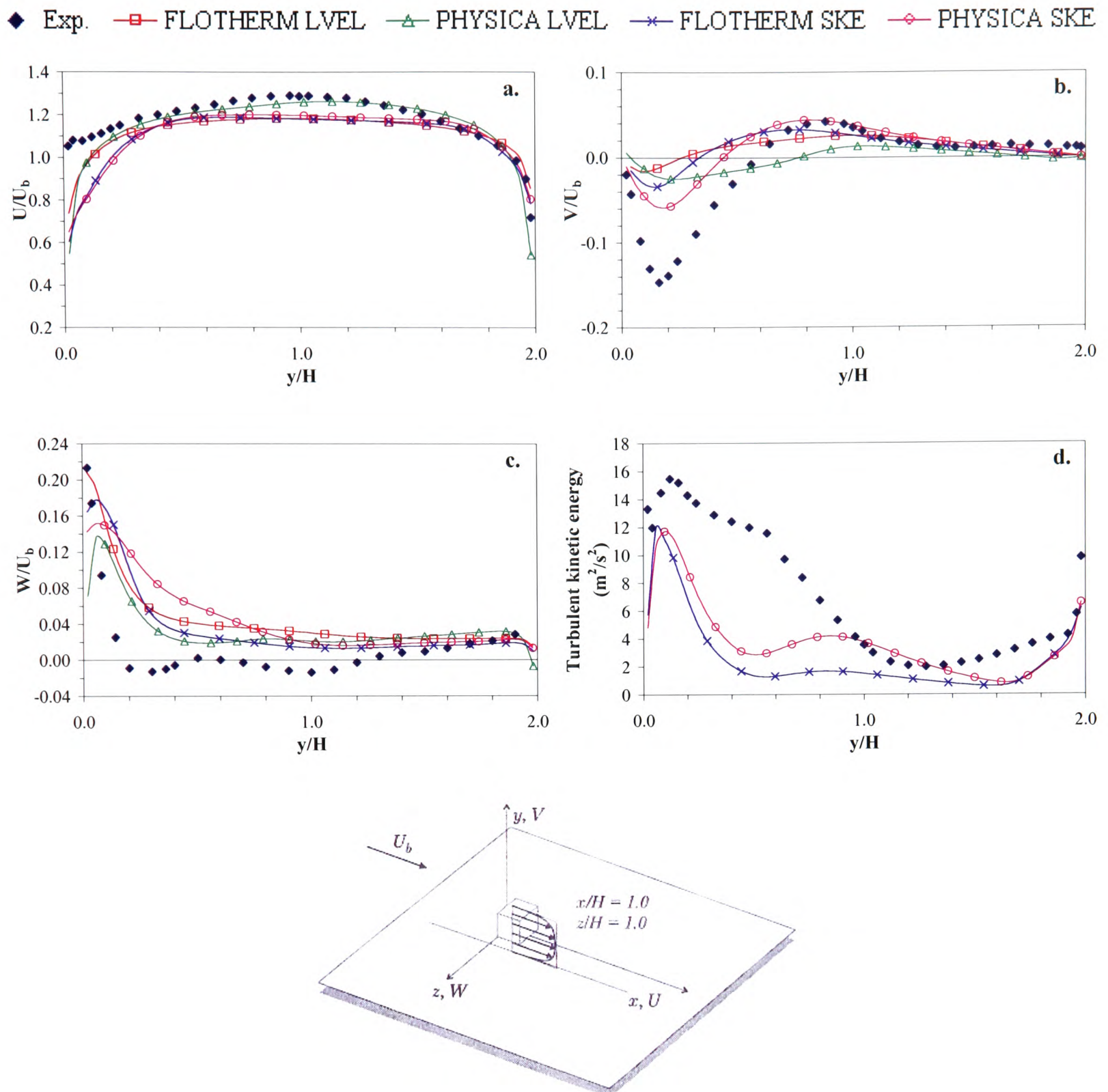
Figure 7.18 Mean velocity components and turbulent kinetic energy for measurement location x/H = 1.0, z/H = 1.0

The numerical predictions presented in Figure 7.16a and c show good agreement produced by all turbulence models considered for the u- and w-velocity components which agrees well with all the workshop groups. The largest discrepancies that were seen at the workshop for these two velocity components originated from Group B.

The results presented in Figure 7.16b are comparable to the Group E workshop results. Ignoring the PHYSICA LVEL model the remaining turbulence models all follow the trend of the experimental data to some degree therefore making it difficult to highlight one particular

model which could be considered as superior to the other models investigated. This seems to be a trend throughout this case study.

Figure 7.16d illustrates the turbulent kinetic energy predicted by both $k-\varepsilon$ model CFD codes. Both codes fail to capture the peak feature in the experimental data close to the base of the channel. However the remaining experimental data is predicted fairly well.

For the measurement location $x/H = 0.5$, $z/H = 1.0$ which corresponds to Figure 7.17 only the upper portion $\left(y/H > 1.0\right)$ of the experimental data was available for the u- and v-velocity components. Therefore the numerical work conducted by the author for these profiles will be compared against the results obtained by Group E as a measure of their accuracy.

Figure 7.17a compares well with both the experimental data and the Group E numerical results. The PHYSICA LVEL model seems to cope well with the flow moving around the cube and is the most accurate at this measurement location. Figure 7.17b is also comparable to the Group E results. Clearly some form of recirculation is being identified at this location however the reattachment point and the vortex speed is very difficult to determine from Figure 7.17b and the Group E workshop results due to the large spread in the various turbulence model predictions. Therefore the numerical predictions of Group A have been called upon as representing the most superior results predicted of all Groups.

By assessing the Group A results it can be determined that the reattachment point is located at approximately $0.5H$ and the vortex speed is $V/U_b = -0.1$. Reassessment of Figure 7.17b concludes that all turbulence models investigated fail to accurately identify the reattachment point and the speed of the vortex which suggests that a smaller recirculating vortex is predicted by the RANS turbulence models compared to that recorded by Group A.

Figure 7.18 shows a similar trend in the numerical predictions obtained as has been seen for Figure 7.17. The recirculation vortex identified in Figure 7.18b is clearly under predicted which is consistent with the workshop predictions for the majority of the groups. The extent of the recirculation vortex, with regards to the speed, strangely enough was under predicted by Group A rather dramatically in comparison to the predictions made by the remaining

groups. The only turbulence model throughout all the groups which accurately predicted this vortex was a $k - \varepsilon$ based two-layer Group E model.

7.2 Concluding Remarks

Several conclusions can be drawn from the assessment undertaken of the single cube high Reynolds number configuration. This task assesses the performance of two CFD codes; one structured (FLOTHERM) one unstructured (PHYSICA) for one zero-equation model (LVEL) and the standard $k - \varepsilon$ model.

- The numerical work conducted by the author, generally speaking, is in good agreement with the Group E (standard $k - \varepsilon$ based models with wall functions) results presented at the 6th ERCOFTAC workshop.

- The numerical results presented by Group A (LES) at the 6th ERCOFTAC workshop are far superior to the other turbulence models considered at the workshop and by the author here. However, the difference in computing cost was alarming. The proceedings of the workshop state:

  "On a SNI S660/20 vector computer RANS computations with wall functions took only 15 minutes of CPU time, the two-layer models took 6 hours, whereas the LES required 160 hours!"

  Clearly these relatively common CPU time comparisons are not encouraging CFD vendors to move towards LES based modelling techniques for this application field.

- PHYSICA turbulence models overall seem to perform better than the FLOTHERM models but only by a small margin.

- The LVEL model, and noticeably the PHYSICA LVEL model, shows good agreement with the experimental data especially upstream of the cube. This is expected as the model was originally designed for boundary layer flows rather than a separated flow phenomenon which is the class of flow under investigation before the disturbances of the cube are detected by the flow field at which point the $k - \varepsilon$ models prevail.

- The LVEL models perform better as the boundary layer is developing before the cube and the $k - \varepsilon$ models work better when considering separated flow phenomena. This is not a surprising conclusion to arrive at, however this does not help the author to conclude which overall superior turbulence model should be suggested for such configurations.

- Even though the recovery rate for the LVEL models was not too bad: $2.5H$ in the mean flow direction. In reality electronic components are generally very tightly clustered and would therefore not allow this model sufficient time to recover.

- The reattachment length behind the cube has been experimentally determined to have a value of $Xr / H \approx 1.5$. Standard $k - \varepsilon$ models usually yield too small recirculation in front of the cube and a too large separation region behind it.[41] The solutions presented here indicate that the RANS turbulence models predict a reattachment length of $Xr / H \approx 2.4$. This is consistent with the 6th workshop results for Group E.

- The $k - \varepsilon$ models in both CFD codes have only predicted a very weak separation on the top of the cube which also reattaches on this surface contrary to experimental data. The LVEL models predict a much more prominent separation which does not close on the top surface of the cube, in line with the experimental and Group A computations.

- A conclusion drawn at the 6th ERCOFTAC workshop was that all models (including LES) failed to reproduce satisfactorily the kinetic energy at most measurement locations. A trend also seen in the present study.

- As comparisons of the turbulent kinetic energy numerical profiles were not conducted at the 6th ERCOFTAC workshop it can only be assumed that the turbulent kinetic energy profiles presented in this chapter would be representative of the turbulent profiles that would have been obtained by Group E as the velocity components assessed have demonstrated good agreement with Group E. However it is noted that for all measurement locations assessed the turbulent kinetic energy was under predicted by the $k - \varepsilon$ models considered here.

- No clear winning RANS turbulence model for this case study can be identified from the models tested here or the 6th ERCOFTAC workshop results. The Group A (LES) predictions on the whole show good agreement with the experimental data. However this case is dealing with a much idealised view of an electronic system environment, therefore the reader is encouraged to use the turbulence models which have been highlighted in Chapter 9 as the Matrix of Cubes configuration is much more realistic of the phenomena taking place within an electronic environment.

Traditionally CFD simulations have employed RANS models to predict the turbulent phenomena taking place within the solution domain. RANS-based turbulence models have always been extremely popular within commercial CFD codes for their cost-effectiveness and reasonable accuracy for a wide class of flows. At the other end of the spectrum are methods such as LES, DES and DNS. Even though the simulation time taken by all three of these methods would be considered very substantial in comparison to the RANS models the predictions obtained are of high numerical accuracy.

In between RANS-based models and more sophisticated turbulence modelling techniques such as the approaches used by LES, DES or DNS are zonal turbulence models. Zonal models are fast becoming an attractive alternative to the time consuming and large data storage capacity required by LES, DES and DNS techniques.

The attractiveness of zonal models is that, without user interaction, an appropriate turbulence model is selected depending on the phenomena taking place within the solution domain. Hence close to a wall boundary a turbulence model would be employed which is known to predict well for wall-bounded flows, within the bulk flow a second model would be activated.

Numerous zonal models exist which are generally based on some form of calculation to the nearest wall boundary. Combinations of purely RANS-based zonal models and zonal LES or DES approaches are also becoming available, but the time dependent zonal approaches will still suffer from increases in computational expense in comparison to the RANS approach.

Examples of zonal RANS-based models include Rodi's $k - \varepsilon / k - l$ model[68] which combines the standard $k - \varepsilon$ model with a one-equation model near the wall. Chen and Patel[105] also consider coupling a simple, but more reliable, turbulence model for the flow close to the wall with a more general model for the flow in the main stream, another $k - \varepsilon / k - l$ model. Menter's SST model[54] also fits into this category, as the model combines the $k - \varepsilon$ and $k - \omega$ models. This model will be discussed in some detail later.

Zonal LES models include Camelli and Löhner's model[129] which combines the Baldwin-Lomax and Smagorinsky subgrid-scale models. For further examples of zonal LES or DES approaches the reader is referred to the extensive work performed by Tucker and colleagues.[71, 72, 74, 130, 131, 132] Also the work of Menter[75] covers the zonal Shear-Stress Transport Detached Eddy Simulation (SST-DES) model among others.

The three zonal models discussed in this chapter are the SST model and two variations of the standard high Reynolds number $k - \varepsilon$ model, namely the $k\varepsilon - LVEL$ and the newly formulated two-layer hybrid $k\varepsilon / kl$ model.

All the models discussed in this chapter have been implemented and tested within PHYSICA's framework as part of this study.

8.1 Shear-Stress Transport (SST)

The SST model was originally designed for aeronautics applications, but has since made its way into most commercial, and many research-based CFD codes. This hybrid model is based on blending functions, which ensure a suitable selection of the $k - \varepsilon$ and $k - \omega$ models without the need for user intervention. The additional complexity of the model compared to standard models lies in calculating the distance to the nearest wall, which requires a search process, used in the calculation of the blending functions. This distance is calculated in a similar fashion to the method used in the LVEL model discussed in Chapter 4.

Two versions of the SST model have been coded within the PHYSICA framework. The first of which has been recommended for implementation through correspondence with the original developer of the model, Dr F. Menter (October 2003) will be referred to as SST.[75] This version is very similar to that available in the commercial CFD code CFX V5.7.[133] The second version has been taken from the manual of the CFD code FLUENT V6.1,[134] this older version of the model has also been implemented. This second model is referred to as SST_V.

The model formulation of the two-equation hybrid SST turbulence model recommended for use by Menter is stated below.

$$\frac{\partial \rho k}{\partial t} + div\left(\rho \underline{u} k\right) = div\left(\left[\mu_l + \sigma_k \rho \nu_t\right] grad\, k\right) + \widetilde{P}_k - \beta^* \rho k \omega \qquad (8.1)$$

$$\frac{\partial \rho \omega}{\partial t} + div\left(\rho \underline{u} \omega\right) = div\left(\left[\mu_l + \sigma_\omega \rho \nu_t\right] grad\, \omega\right) + \alpha \alpha^* \rho S^2 - \beta \rho \omega^2 +$$
$$2\left(1 - F_1\right)\rho \sigma_{\omega 2} \frac{1}{\omega} grad\, k \cdot grad\, \omega \qquad (8.2)$$

The blending function, F_1 used to merge the turbulence models, is defined in equation (8.3).

$$F_1 = \tanh\left\{\left\{\min\left[\max\left(\frac{\sqrt{k}}{\beta^* \omega y}, \frac{500\nu_l}{y^2 \omega}\right), \frac{4\rho \sigma_{\omega 2} k}{CD_{k\omega} y^2}\right]\right\}^4\right\} \qquad (8.3)$$

F_1 is equal to zero away from the wall $(k - \varepsilon)$ and switches over to one inside the boundary layer $(k - \omega)$.

To blend the two components of the SST model together, the standard high Reynolds number $k - \varepsilon$ model has been transformed into equations based on k and ω. This leads to the introduction of the cross diffusion term as stated in equation (8.4).

$$CD_{k\omega} = \max\left(2\rho \sigma_{\omega 2} \frac{1}{\omega} grad\, k \cdot grad\, \omega, 10^{-10}\right) \qquad (8.4)$$

The turbulent eddy viscosity is calculated using equation (8.5)

$$\nu_t = \frac{a_1 k}{\max\left(\left(a_1 \omega\right)/\alpha^*, SF_2\right)} \qquad (8.5)$$

where S is the modulus of the mean rate-of-strain tensor. In terms of the implementation of the model the G term, defined in Chapter 4 for the two-equation models, is equal to S^2.

The second blending function F_2 appearing in equation (8.5) has been defined in equation (8.6).

$$F_2 = \tanh\left[\left[\max\left(\frac{2\sqrt{k}}{\beta^* \omega y}, \frac{500\nu_l}{y^2 \omega}\right)\right]^2\right] \qquad (8.6)$$

To prevent the build-up of turbulence in the stagnation regions the production limiter, defined in equation (8.7), is used within the k-transport equation.

$$P_k = \mu_t \frac{\partial U_i}{\partial x_j}\left(\frac{\partial U_i}{\partial x_j} + \frac{\partial U_j}{\partial x_i}\right) \rightarrow \widetilde{P_k} = \min\left(P_k, 10 \cdot \beta^* \rho k \omega\right) \qquad (8.7)$$

The model "constants" are calculated using the F_1 blending function

$$\phi = F_1 \phi_1 + (1 - F_1)\phi_2 \qquad (8.8)$$

$$a_1 = 0.31 \qquad R_k = 6.0 \qquad R_t^* = \frac{k}{\omega \nu_l}$$

$$\alpha_1 = 5/9 \qquad \alpha_2 = 0.44 \qquad \alpha^* = \frac{\alpha_0^* + R_t^*/R_k}{1 + R_t^*/R_k} \qquad \alpha_0^* = \frac{1}{40}$$

$$\beta_1 = 3/40 \qquad \beta_2 = 0.0828 \qquad \beta^* = 0.09$$

$$\sigma_{k1} = 0.85 \qquad \sigma_{k2} = 1.0$$

$$\sigma_{\omega 1} = 0.5 \qquad \sigma_{\omega 2} = 0.856$$

The differences between the two implemented versions of the SST model are that the SST model uses strain rate, whereas the SST_V version uses vorticity, and so removes the need for the production limiter within the model. Also within the cross diffusion term of the SST model a factor of 10 is used instead of 20 as proposed in the SST_V model.[54, 62] The later version uses the strain rate because it is invariant with system rotation. For standard aerodynamics applications this has no relevance. The factor within the cross diffusion term has been reduced to improve model robustness during the convergence process. The FLUENT version, SST_V, of the SST model is documented in Appendix D.

The disadvantage of the SST model is highlighted when considering recirculating flows, separation and reattachment as it has been noted that poor flow recovery after an obstacle has

been encountered. This has promoted the formulation of the zonal SST-DES model also formulated by Menter et al.[75]

8.1.1 Validation of Shear-Stress Transport (SST)

For the parallel plates test case, the SST model switches to $k - \omega$ over the large majority of the channel, replicating the $k - \omega$ results; the model behaviour is therefore as expected. Validation of SST has been performed on the backward facing step configuration where the switch between models is highlighted. The reader is referred to Appendix A3.2 for the full specification of the case. It is noted that the generation of this mesh exploits a grading technique to ensure a fine mesh concentration near to wall surfaces. The mesh density employed is (40 x 40) upstream and (200 x 70) downstream of the step in the x- and y-directions respectively.

To ensure that the two implemented versions of the SST model produce similar results, comparisons of the reattachment length have been undertaken and the results are presented in Figure 8.1 for the SST and the SST_V models.
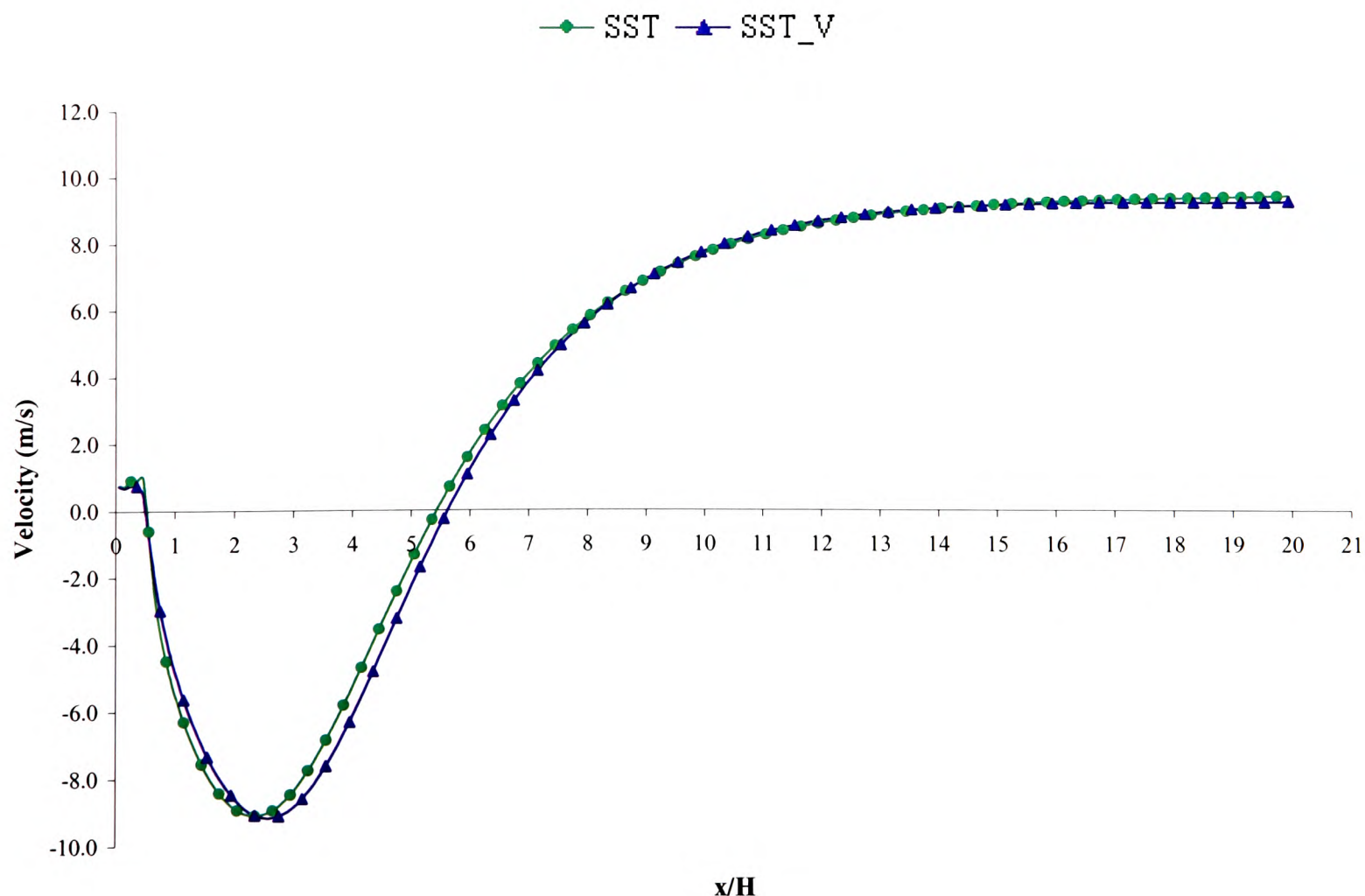
Figure 8.1 Reattachment length prediction SST and SST_V model

It can be concluded from Figure 8.1 that the modifications which have been made to the older SST_V model in comparison to the SST model only have a minor influence for this case. Also, as good agreement is noted between the SST and SST_V models this suggests that the implementation of both models is correct.

It can be determined that the reattachment length predicted by the SST models is approximately 5.4 step heights (x/H) for this particular test case. This reattachment length is closer to the range predicted by the standard high Reynolds number $k - \varepsilon$ model of $5.8 - 6.1$ step heights rather than the universally accepted range of 7.0 ± 1.0 step heights. Therefore further investigation is necessary.

The SST_V model will not be discussed further as it is expected to produce similar results to the SST model. Also the SST model was recommended for implementation in preference to the SST_V model by the developer of the models. Therefore all further work will be carried out solely using the newer SST model.

As stated by Menter et al.[75] the F_1 blending function is the driving force with regards to correct turbulence model selection. If F_1 is equal to zero the $k - \varepsilon$ model is employed as F_1 switches over to one inside the boundary layer the $k - \omega$ model is activated.

Given that the reattachment length predicted by the SST model is approximately 5.4 step heights the work of Nallasamy[120] is used to aid in the explanation as to why an under prediction is noted in the results. Nallasamy's work reviewed the reattachment lengths predicted by a range of turbulence models including the standard high Reynolds number $k - \varepsilon$ model and many of its variations, a modified $k - \omega$ model, algebraic stress and Reynolds stress models.

The conclusion drawn by Nallasamy to explain the reason for an under prediction of the reattachment length noted in all turbulence models considered has been stated:

"All the methods overpredict the shear stress in the separated shear layer. This implies that in this region, the computed turbulent viscosity will be higher than that existing in an actual

flow. This is one of the main reasons for the under prediction of the reattachment in all the predictions."

As the standard high Reynolds number $k-\varepsilon$ model is known to under predict the reattachment length, if the $k-\varepsilon$ model is selected for use in the separated shear layer by the SST model then an under prediction would be seen in the predicted reattachment length. To determine if this is the case it has been assumed that when the SST model is in use the selection of the $k-\varepsilon$ model takes place if the calculated value of the F_1 blending function is less than 0.5 and the $k-\omega$ model is selected for values greater than 0.5.

Figure 8.2 presents a contour plot of the F_1 blending function with the step change between models taken at 0.5.
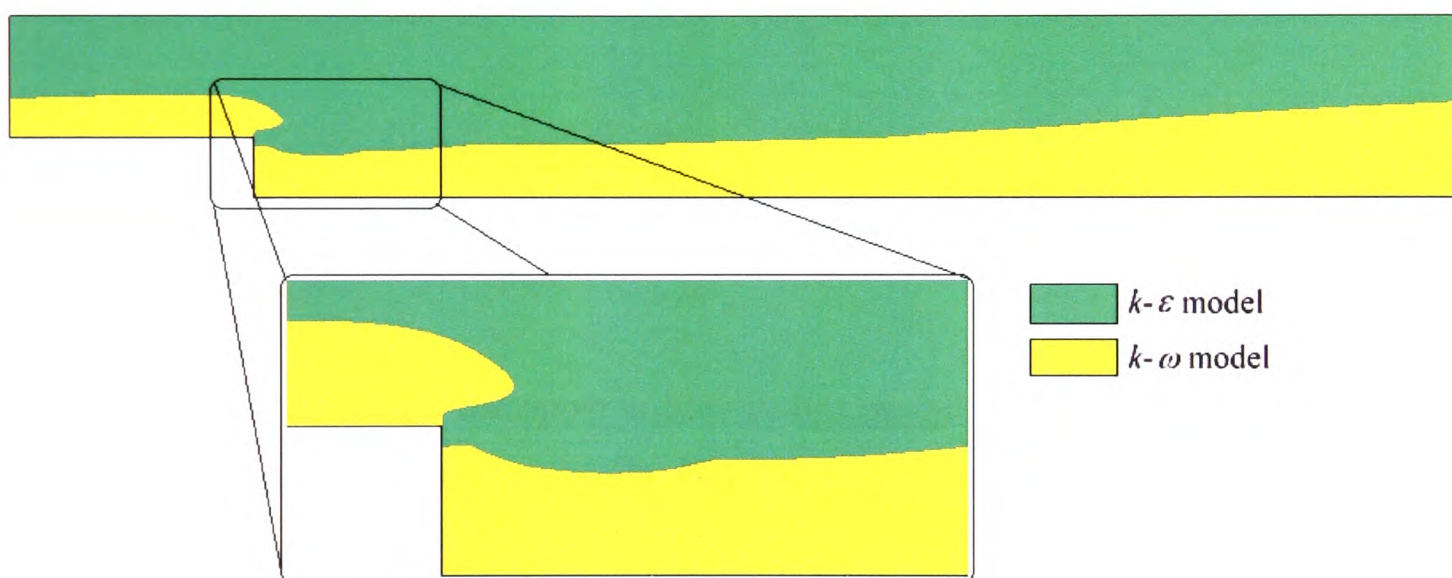
Figure 8.2 F_1 blending function contours model selection determined at 0.5

It can be concluded that the high Reynolds number $k-\varepsilon$ model is indeed selected as the appropriate turbulence model for the separated shear layer by the SST model. Therefore it is not surprising that an under prediction for the reattachment length is noted as this agrees with Nallasamy's conclusion.

To further ensure that the implementation of the SST model is correct an alternative method based on the statement made by Menter with regards to turbulence model selection is utilised. The blending function F_1 in the SST model is forced to the values of 0.0 and 1.0 in an attempt to obtain the model predictions of the $k-\varepsilon$ and $k-\omega$ models respectively.

In order to convert the SST model to the $k - \omega$ model the following changes need to be made to the model once the F_1 blending function has been set to the constant 1.0:

- Diffusion term of the k-transport equation: the model constant σ_k needs to be set to 0.5 rather than the SST calculated value of 0.85.

- Source term of the k-transport equation: rather than using the production limiter function employed in the SST model $\widetilde{P_k}$ will simply be set to P_k.

- Source term of the k-transport equation: the model constant β^* is required to be set to the formula specified in equation (8.9) rather than the calculated value of 0.09 in the SST model.

$$\beta^* = \frac{9}{100} \frac{5/18 + \left(R_t^*/R_\beta\right)^4}{1 + \left(R_t^*/R_\beta\right)^4}, \quad R_t^* = \frac{k}{\omega v_l}, \quad R_\beta = 8.0 \qquad (8.9)$$

- Source term of the ω-transport equation: the model constant α must be constrained to the formulae stated in equation (8.10) rather than the SST calculated constant of $5/9$.

$$\alpha = \frac{5}{9} \frac{\alpha_0 + R_t^*/R_w}{1 + R_t^*/R_w} \left(\alpha^*\right)^{-1}$$

$$\alpha_0 = \frac{1}{10}, \quad R_w = 2.7, \quad \alpha^* = \frac{\alpha_0^* + R_t^*/R_k}{1 + R_t^*/R_k}, \quad \alpha_0^* = \frac{1}{40}, \quad R_k = 6.0 \qquad (8.10)$$

- Turbulent viscosity equation: to ensure that the equations to calculate the turbulent viscosity variable are consistent between the two models the blending function F_2 must be constrained to the constant value of 0.0 in the SST model.

Figure 8.3 presents the reattachment length predicted by the SST model when the model has been forced to replicate the $k-\omega$ model. To determine if the SST model converts back to the $k-\omega$ model when the F_1 blending function is set to 1.0 model comparisons have been made against the standard SST and $k-\omega$ models.
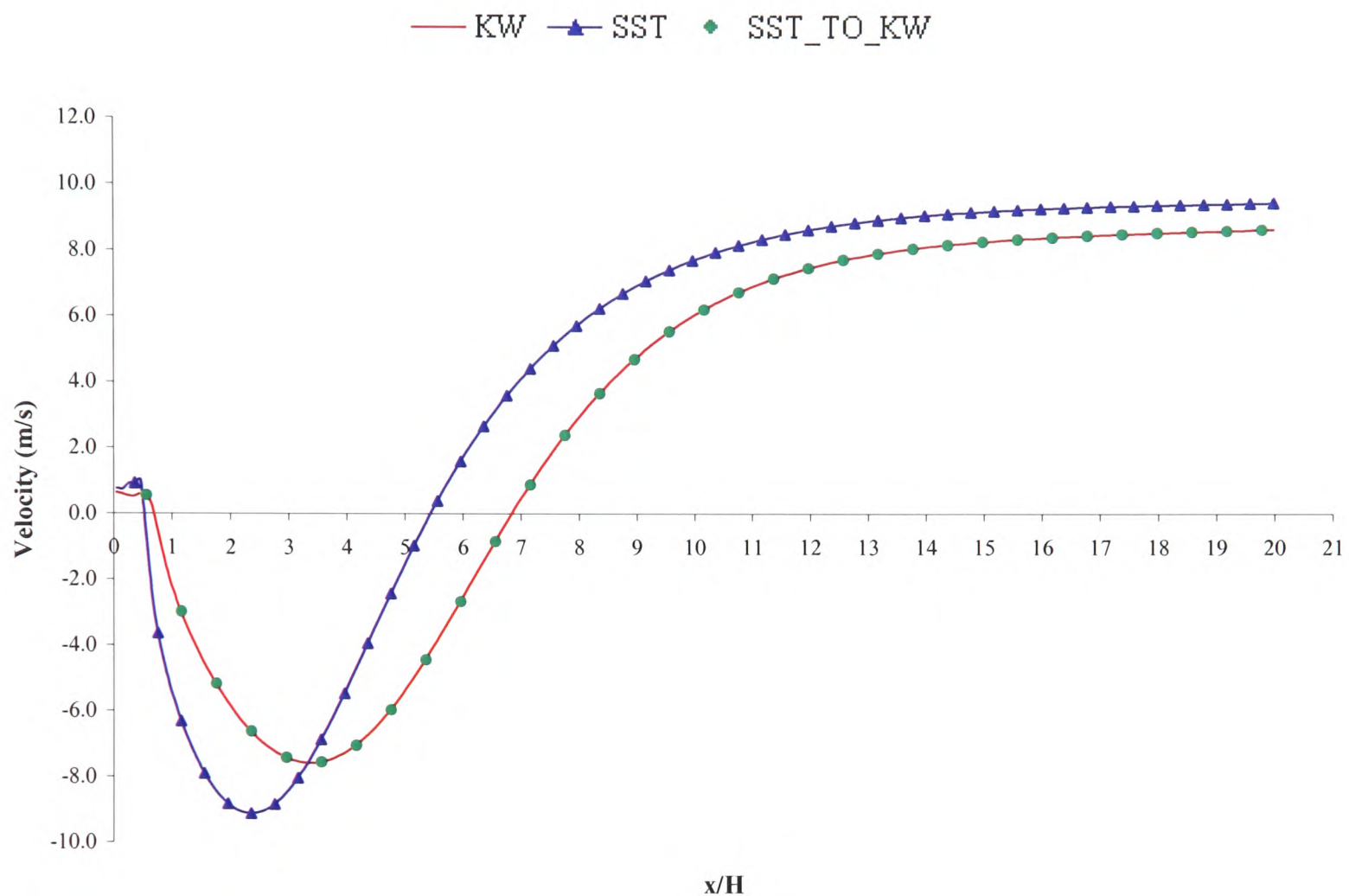
Figure 8.3 Reattachment length predictions SST converted to k - ω

As the $k-\omega$ and the converted SST model (SST_TO_KW) results lie directly on top of one another the conclusion drawn from Figure 8.3 is that the SST model has successfully been transformed to the $k-\omega$ model, strengthening the argument that the SST model has been correctly implemented within PHYSICA. It can also be concluded that the difference in the reattachment length is therefore consistent with the different behaviour of the $k-\varepsilon$ and $k-\omega$ models. In addition to converting F_1 for the numerical work undertaken here a mathematical derivation has also been provided in Appendix E.

The second component of the SST model, which is used in the bulk flow, is the standard high Reynolds number $k-\varepsilon$ model. Converting the SST model to $k-\varepsilon$ is a more complicated task as the ω-transport equation must be transformed to an ε-transport equation. It is stated

by Menter et al.[75] that F_1 is equal to zero away from the surface ($k - \varepsilon$ model), and switches over to one inside the boundary layer ($k - \omega$ model). After private communication with Dr F. Menter (December 2004) it was determined that in order to force the SST model to replicate the standard high Reynolds number $k - \varepsilon$ model additional blending functions would need to be devised but nevertheless the sub-layer would still be treated with the $k - \omega$ model. This indicates that the SST model never truly transforms back to the standard high Reynolds number $k - \varepsilon$ turbulence model.

Therefore the method used to attempt to convert the SST model to the closest form of the standard high Reynolds number $k - \varepsilon$ model is very basic. Within the SST model the distance to the nearest wall variable field has been set to the constant value of 500m which in theory should "trick" the model into applying the $k - \varepsilon$ model throughout the solution domain. The predicted reattachment length when the SST model has been manipulated in this way is shown in Figure 8.4. Comparisons have been made against the standard SST and the $k - \varepsilon$ models.
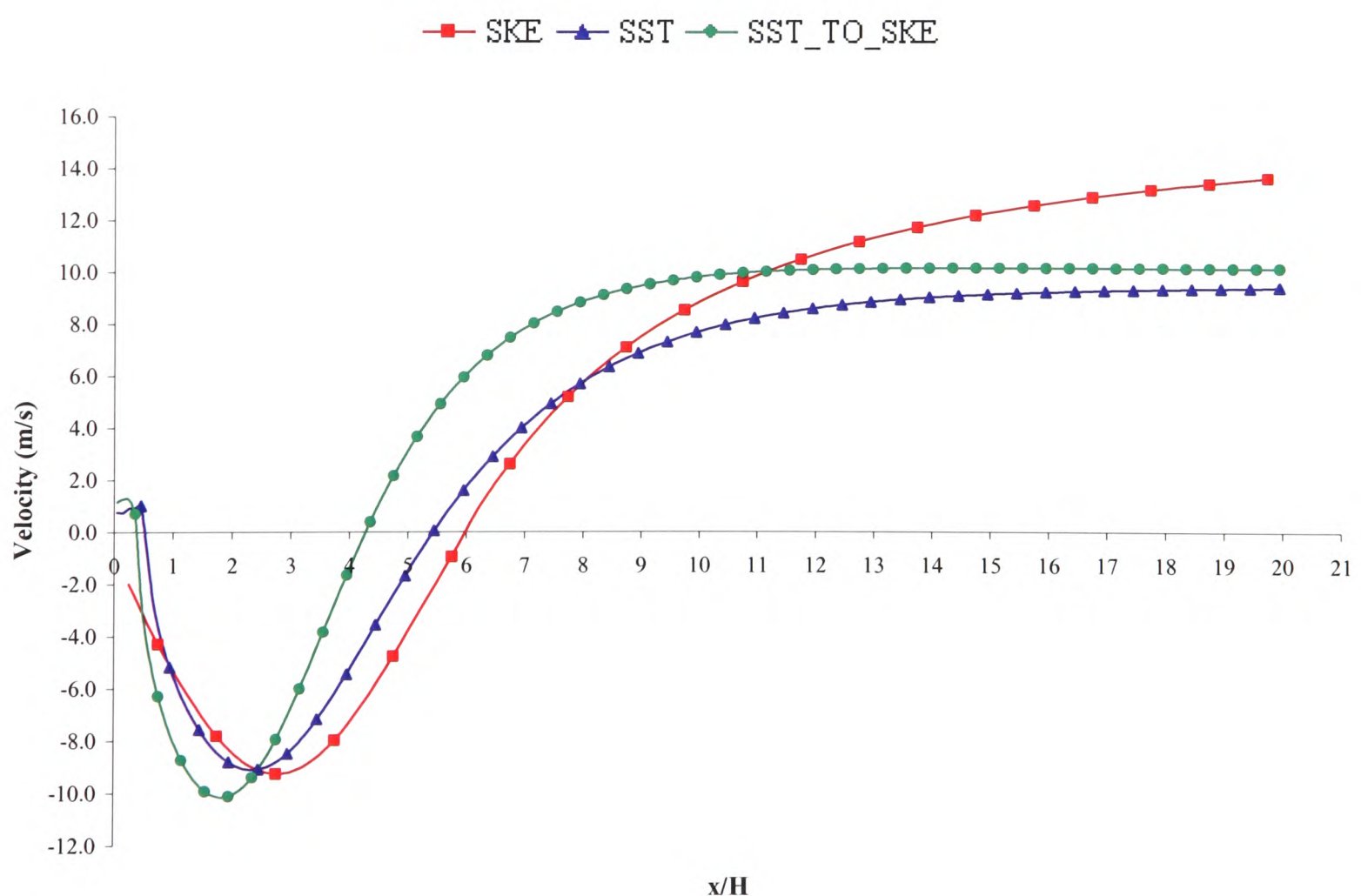
Figure 8.4 Reattachment length predictions SST converted to $k - \varepsilon$

The conclusion which can be drawn from Figure 8.4 is that the SST model clearly does not fully convert to the $k-\varepsilon$ model. Many attributes may have contributed to the reasons as to why the reattachment length predicted by the $k-\varepsilon$ model is not successfully recovered when the SST model manipulation is undertaken. One obvious reason would be that the SST model constants would never truly transform to the $k-\varepsilon$ model constants.

A simpler test case has been considered to further understand the numerical prediction obtained by the SST model. A summary of this is provided below and the reader is referred to Appendix A6 for the full specification of the case.

The case considers a two-dimensional flow channel with an associated fluid temperature of 30°C, therefore resulting in a fluid density of 1.1614kg/m^3 and a kinematic viscosity of $1.5842 \times 10^{-5} \text{m}^2/\text{s}$. The inlet velocity is calculated to ensure that a Reynolds number of 10,000 is obtained.

The mesh employed has been distributed uniformly which ensures that each mesh element is (1 x 1)m in the x and y-directions respectively. The dimensions of the test geometry have been detailed in Figure 8.5.
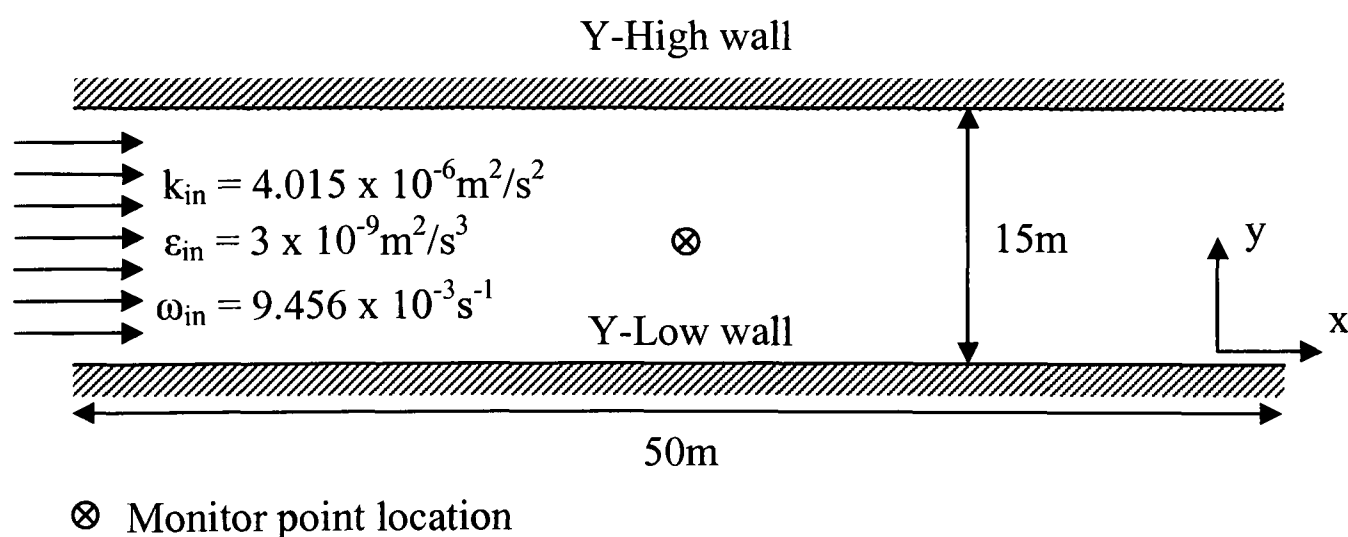
Figure 8.5 Channel flow test case geometry

It is assumed that as the hybrid SST model combines the $k-\varepsilon$ and $k-\omega$ turbulence models and it has been determined that the SST model can not truly be converted to replicate the $k-\varepsilon$ model results. If it can be determined that when SST is manipulated to attempt to duplicate some form of the $k-\varepsilon$ model results then the numerical predictions obtained

should lie somewhere between the predictions of the $k - \varepsilon$ and $k - \omega$ models. If so, the SST model validation will be considered complete.
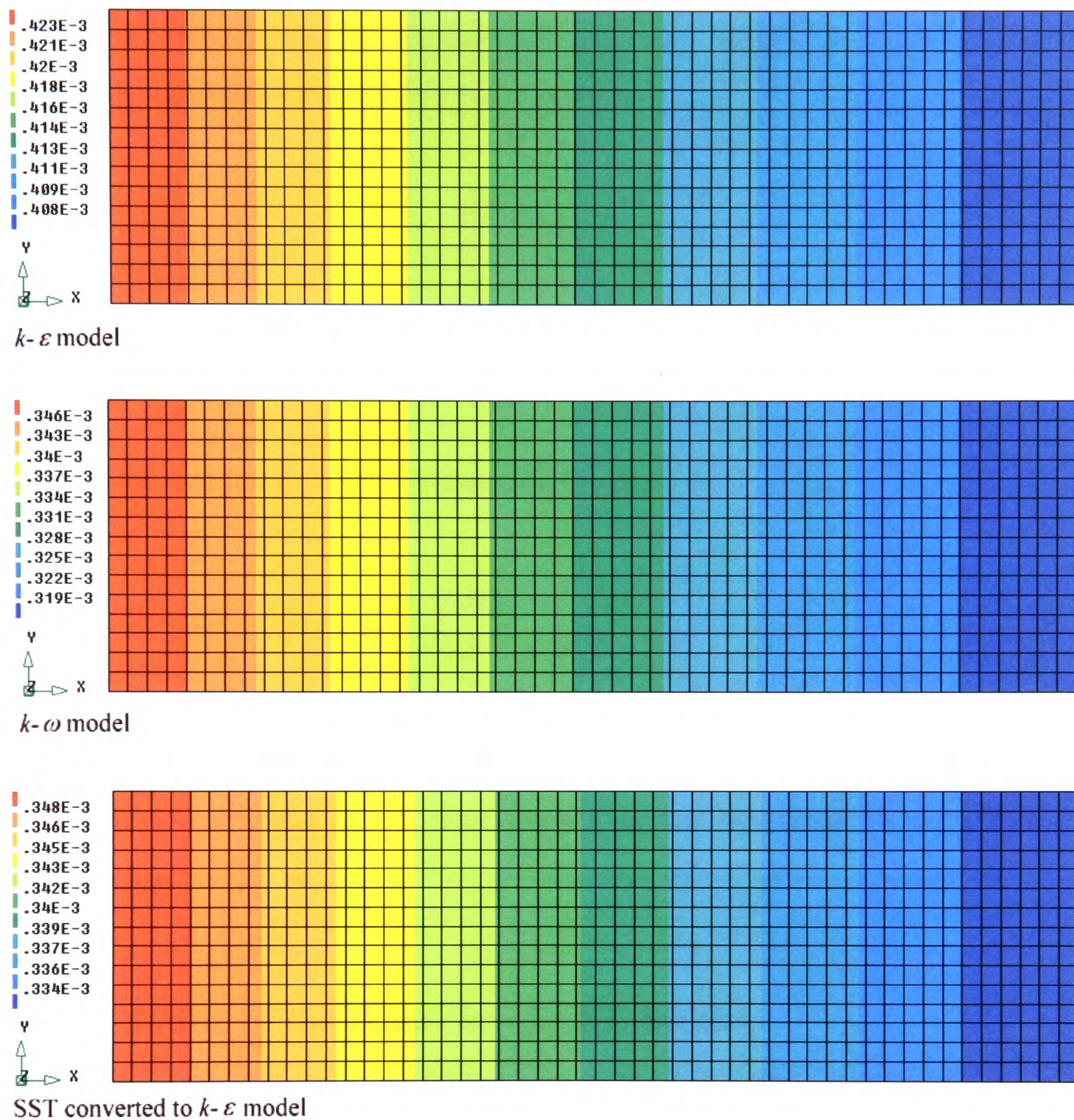
Figure 8.6 Channel flow turbulent kinematic viscosity contours

Figure 8.6 shows that when the SST model manipulation is undertaken the numerical turbulent kinematic viscosity results obtained lie between the range predicted by the $k - \varepsilon$ and $k - \omega$ turbulence models. Therefore it can be concluded that the standard SST model has been correctly implemented within PHYSICA.

8.2 Zonal *kε-LVEL* Model

This hybrid turbulence model originates from the FLOTHERM V4.1 documentation.[103]

The $k\varepsilon - LVEL$ model uses the standard high Reynolds number $k - \varepsilon$ model but applies damping to the near-wall turbulent dynamic viscosity.

$$\mu_t \times f_\mu \qquad (8.11)$$

$$f_\mu = \left(1 - \exp^{\left(-\beta y^+\right)}\right) \qquad (8.12)$$

Where β is the step function stated in equation (8.13).

$$\begin{aligned}
\beta &= 0.005 \quad y^+ < 5 \\
\beta &= 0.2 \quad y^+ > 10 \\
\beta &= 0.039 y^+ - 0.19 \quad 5 \le y^+ \le 10
\end{aligned} \qquad (8.13)$$

The y^+ field is calculated in the same manner as that described for the LVEL model discussed earlier.

8.2.1 Validation of the Zonal *kε-LVEL* Model

The validation of this turbulence model has been performed on the parallel plates test case the reader is referred to Appendix A1.2 for a full description of the case.

The determining factor for the switch between the models is the f_μ function. As f_μ tends towards 1.0 the high Reynolds number $k - \varepsilon$ model is recovered. Therefore assessment of this function is first undertaken by means of a variable contour plot presented in Figure 8.7.
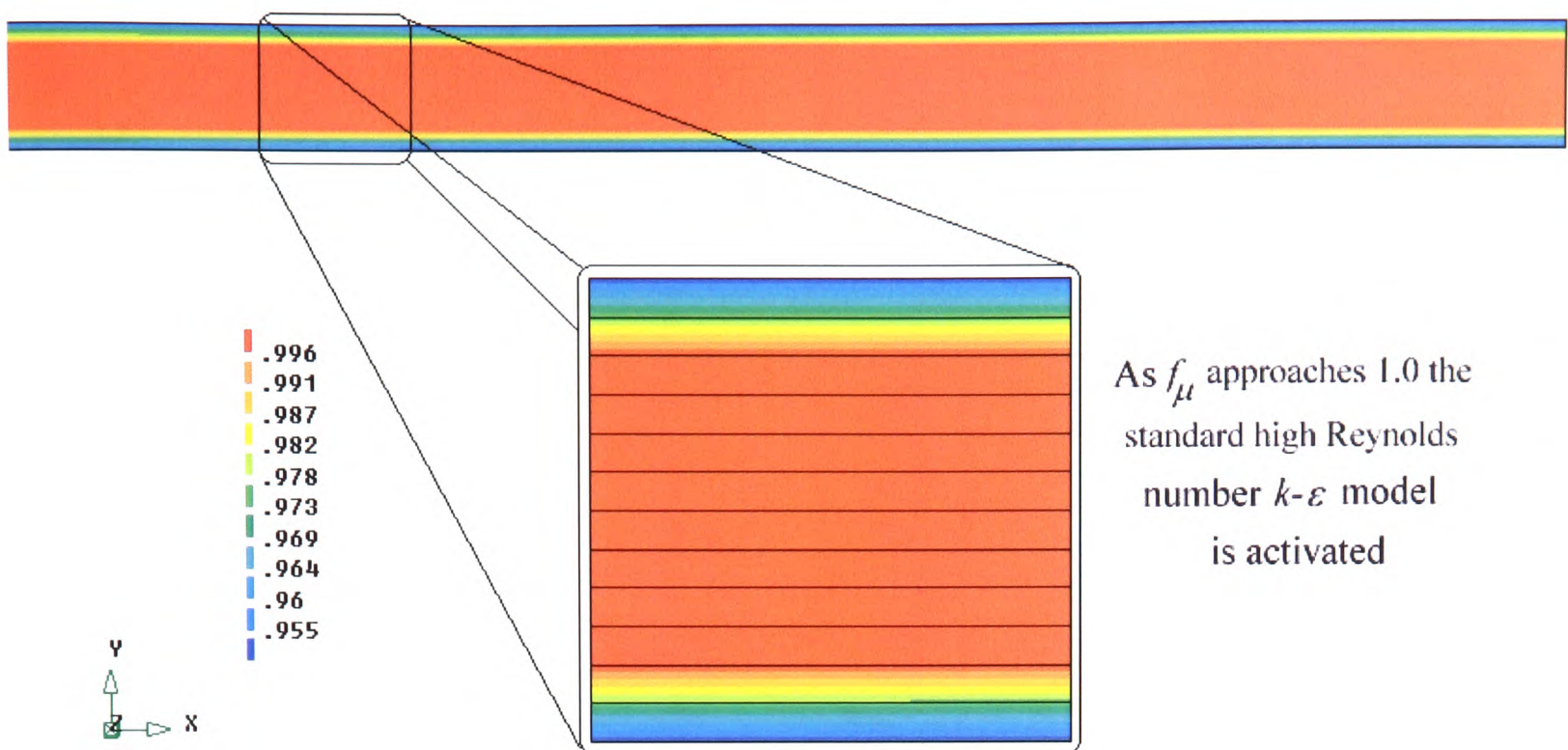
Figure 8.7 Portion of f_μ function for the $k\varepsilon$ - $LVEL$ model

Figure 8.7 suggests that the switch between the two turbulence models is occurring close to the wall boundary. Therefore the majority of the solution domain is using the standard high Reynolds number $k - \varepsilon$ model. One shortcoming of the $k\varepsilon - LVEL$ model is that the f_μ function tends to a value of 1.0 almost immediately. This will be discussed in greater detail later.

The predicted velocity profile obtained by the $k\varepsilon - LVEL$ model has been compared against the analytical solution for a fully developed turbulent velocity profile when considering flow between two parallel plates and with the predictions of the $k - \varepsilon$ model in Figure 8.8. The turbulent dynamic viscosity comparison against the $k - \varepsilon$ model is presented in Figure 8.9. The numerical results are extracted at a x-position of 9.8m downstream of the inlet.
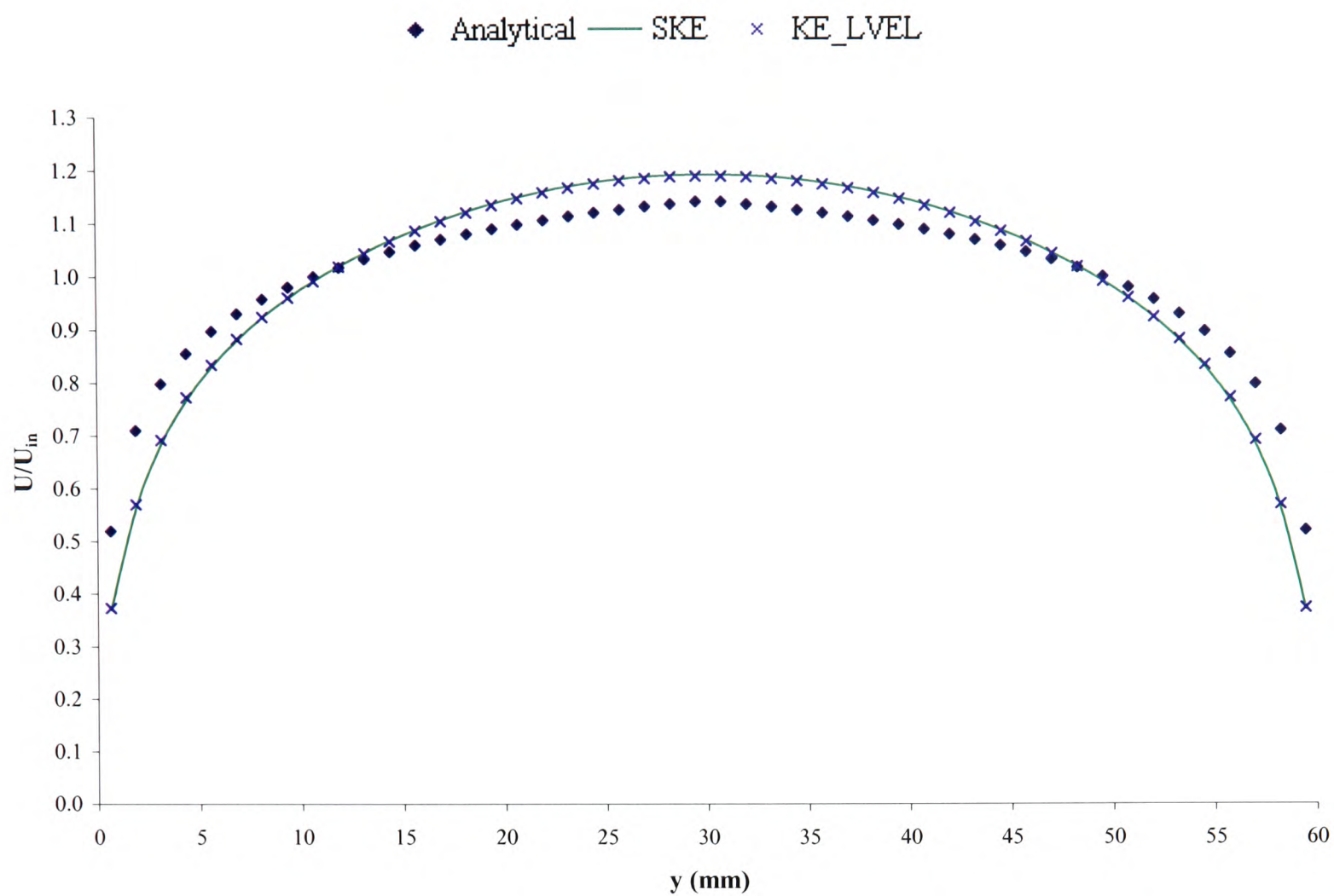
Figure 8.8 Parallel plates velocity profile $k\varepsilon$ **-** $LVEL$ **model**
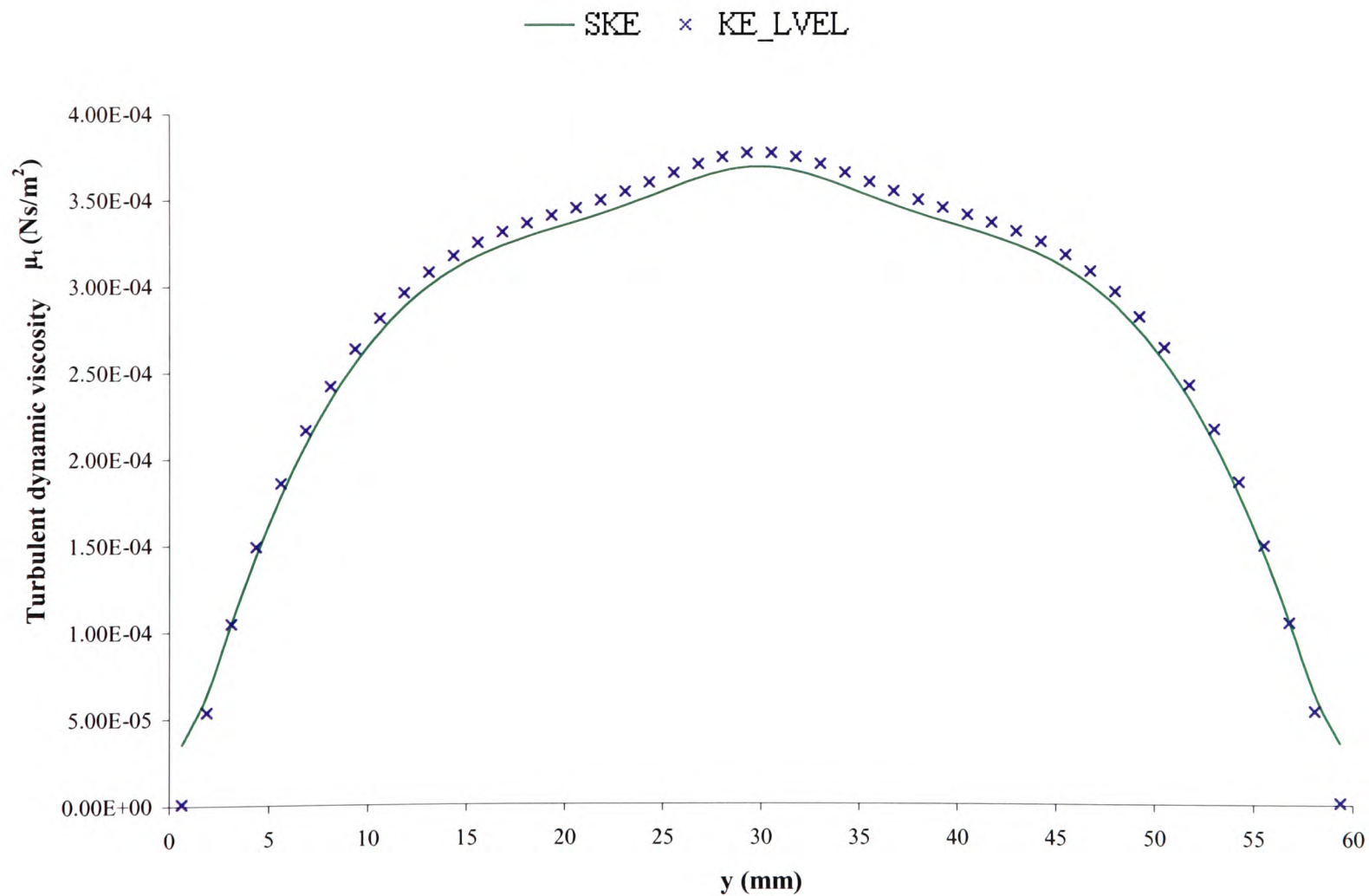
Figure 8.9 Parallel plates turbulent dynamic viscosity profile $k\varepsilon$ **-** $LVEL$ **model**

The conclusion that can be drawn from Figure 8.8 is that the predicted velocity profiles obtained by the $k\varepsilon - LVEL$ and $k - \varepsilon$ models are identical between the two models. Figure 8.9 clearly shows that the affect of the $LVEL$ model within $k\varepsilon - LVEL$ is minimal for this simple case.

Assessment of the employed f_μ function and suggestions on how this model can be improved upon will be discussed later.

8.3 Two-Layer Hybrid $k\varepsilon/kl$ Turbulence Model

This section outlines the newly formulated two-layer hybrid $k\varepsilon/kl$ turbulence model as implemented in PHYSICA. This hybrid turbulence model can be classified as a two-equation model solving the standard high Reynolds number $k - \varepsilon$ model in the bulk flow and a single equation $k - l$ model at near-wall regions.

To assist in the explanation of the idea behind this hybrid turbulence model reference has been given to the idealised situation represented in Figure 8.10.

$k\text{-}\varepsilon$ model (Region A) $k\text{-}l$ model (Region B)
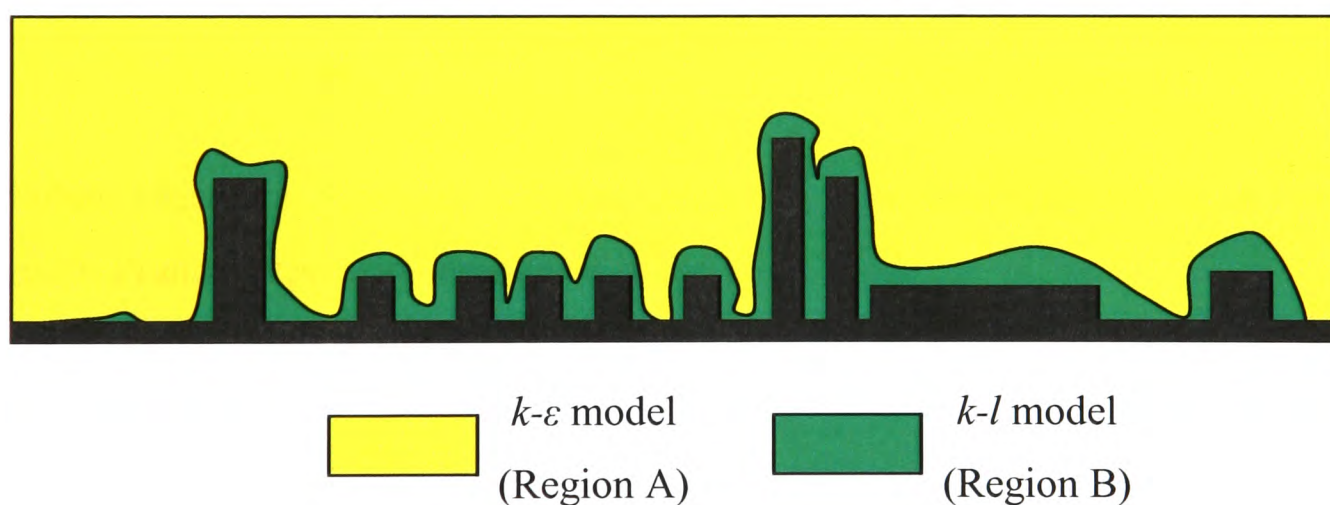
Figure 8.10 Schematic representation of the region definition used for the hybrid turbulence model

This hybrid turbulence model exploits the advantages of the standard $k - \varepsilon$ model by using the original model equations at a sufficient distance away from the enclosure walls and any electronic packages and then drops down to the single equation model similar to that of Norris and Reynolds in the vicinity of solid devices.

The model divides the test geometry into two regions; as depicted in Figure 8.10; the allocation of the division is determined by using a critical Reynolds number. Region A solves the standard $k-\varepsilon$ model equations; Region B on the other hand switches to the $k-l$ model and solves an appropriate set of equations which represent the turbulent dissipation rate. The $k-l$ model also employs the use of wall functions and damping functions to make this model economical in terms of run-time. To bridge the gap between the two turbulence models a novel matching technique has been used.

Firstly taking into consideration Region A. The transport equations implemented calculate the turbulent viscosity for the fluid cells not immediately adjacent to solid surfaces as a function of two field variables the kinetic energy of turbulence and its rate of dissipation. These two field variables are determined by the solution of the $k-\varepsilon$ equations expressed in equations (8.14)-(8.15).

$$\frac{\partial \rho k}{\partial t} + div(\rho \underline{u} k) = div\left(\left[\mu_l + \frac{\rho v_t}{\sigma_k}\right] grad\, k\right) + \rho v_t G - \rho \varepsilon_A \qquad (8.14)$$

$$\frac{\partial \rho \varepsilon_A}{\partial t} + div(\rho \underline{u} \varepsilon_A) = div\left(\left[\mu_l + \frac{\rho v_t}{\sigma_\varepsilon}\right] grad\, \varepsilon_A\right) + C_{1\varepsilon}\rho v_t G \frac{\varepsilon_A}{k} - C_{2\varepsilon}\rho \frac{\varepsilon_A^2}{k} \qquad (8.15)$$

The turbulent kinematic viscosity is calculated using equation (8.16) which is the standard Kolmogorov-Prandtl expression employed in the $k-\varepsilon$ model.

$$v_{t\_A} = C_\mu C_d \frac{k^2}{\varepsilon_A} \qquad (8.16)$$

Once Region B has been identified the transport equation for k is solved:

$$\frac{\partial \rho k}{\partial t} + div(\rho \underline{u} k) = div\left(\left[\mu_l + \frac{\rho v_t}{\sigma_k}\right] grad\, k\right) + \rho v_t G - \rho \varepsilon_B \qquad (8.17)$$

with the dissipation rate determined using equation (8.18).

$$\varepsilon_B = C_d \cdot f_2 \cdot \frac{k^{3/2}}{L_m} \tag{8.18}$$

The equation employed to calculate the turbulent viscosity is stated in equation (8.19)

$$v_{t\_B} = C_\mu \cdot f_1 \cdot k^{1/2} \cdot L_m \tag{8.19}$$

The functions f_1 and f_2 relate to the damping and smoothing functions respectively and are defined as follows

$$f_1 = 1 - \exp\left(-\beta \cdot \mathrm{Re}_{k-l}\right) \tag{8.20}$$

$$f_2 = 1 + \frac{\alpha}{\mathrm{Re}_{k-l}} \tag{8.21}$$

Where Re_{k-l} is the turbulent fluctuation Reynolds number, defined as follows:

$$\mathrm{Re}_{k-l} = \frac{k^{1/2} L}{v_l} \tag{8.22}$$

The main advantage of such a hybrid model is that it is computationally cheap in terms of the mesh requirement and therefore makes it fast and economical to run. Also the $k - \varepsilon$ model advantages will filter through to the $k\varepsilon / kl$ model; these advantages include reliable performance for many industrially significant flows such as confined flow phenomena. The model should also overcome the disadvantage of using a one-equation $k - l$ model alone.

8.3.1 Determination of Critical Reynolds Number

At the critical Reynolds number it is assumed that there is no discontinuity between the viscosity, turbulent kinetic energy and the turbulent dissipation rate moving from one region into the other. Matching the length scale between the $k - \varepsilon$ and $k - l$ models guarantees good numerical behaviour and increased accuracy as the eddy length scale for example does not

experience a sharp jump moving from one model to the next rather a smooth transition between the models is noted due to the blending function used.

Assuming equations (8.16) and (8.19) are equivalent at the boundary between the two turbulence models the following expression for ε_A can be derived.

$$\varepsilon_A = \frac{C_d \cdot k^{3/2}}{f_1 \cdot L_m}$$

(8.23)

Assuming equation (8.18) and the newly formulated equation (8.23) are equivalent at the boundary interface an expression for the relationship between the damping and smoothing functions f_1 and f_2 respectively can by derived and is stated in equation (8.24).

$$\frac{1}{f_1} = f_2$$

(8.24)

Figure 8.11 represents the relationship stated in equation (8.24). The intersection between the two curves will determine the value of the critical Reynolds number.
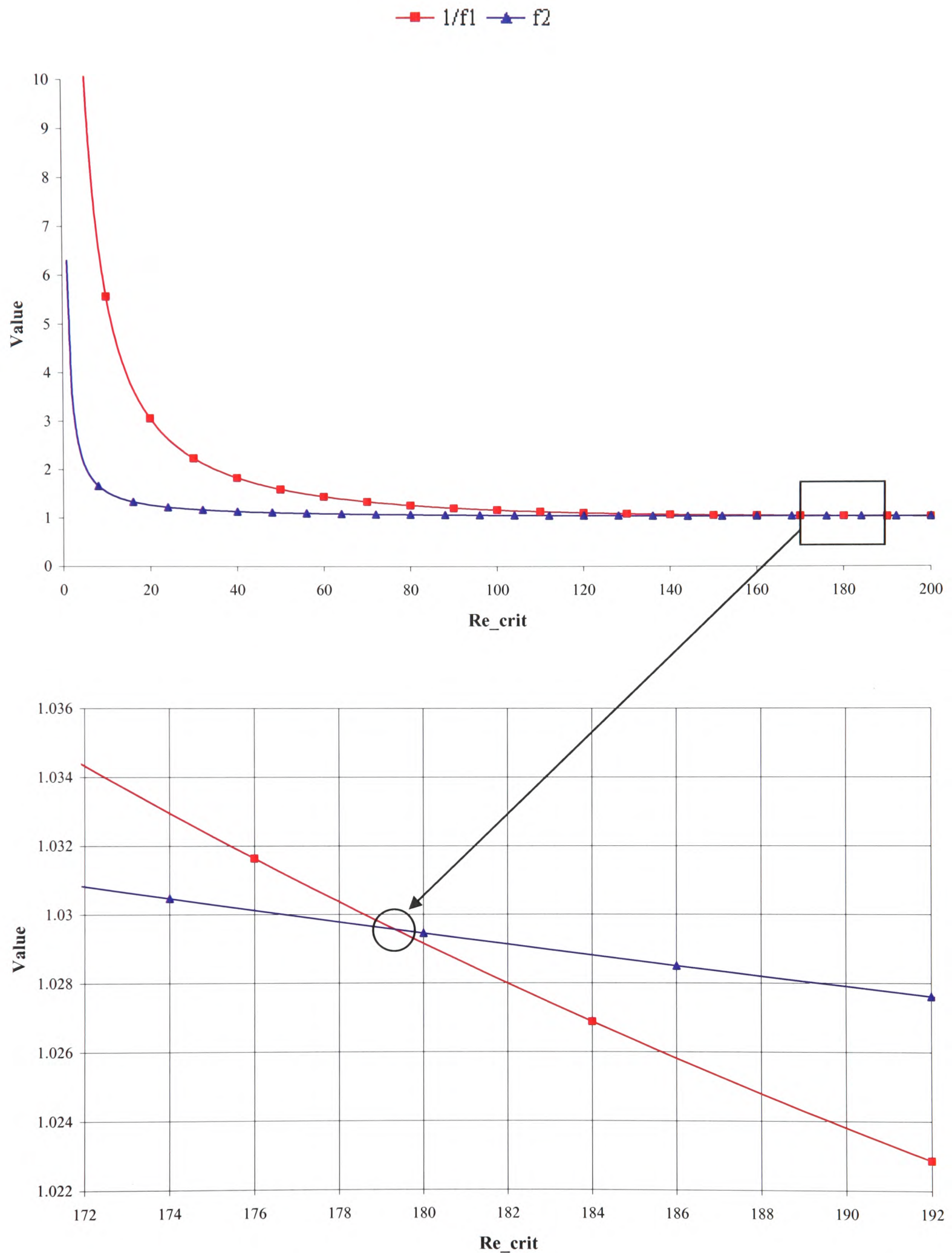
Figure 8.11 Function relationship *kε/kl* **model**

Figure 8.11 suggests that an appropriate critical Reynolds number to employ within the two-layer hybrid $k\varepsilon / kl$ turbulence model would be a value of 180.

To the author's knowledge the development of this method in the current work, which ensures k, ε and v_t transition smoothly between the two regions, is unique. The advantage of this physically realistic behaviour is its numerical stability.

A number of techniques have been used to merge turbulence models, Launder and Patel and their colleagues match two models at preselected grid lines running along the wall. Other methods developed require a y^+ value to be stated for the cross-over between the two models. Iacovides and Launder[135] report that matching would take place in a y^+ range of 80 to 120, whereas Rodi[68] performs the switch between models in a y^+ range of 80 to 90. Chen and Patel[105, 136] match along a grid line where the minimum of Re_y is of the order of 250, which corresponds to a y^+ value of approximately 135, they found that the results are not sensitive to the matching criterion as long as the minimum value of Re_y was greater than 200.

Clearly the variety of matching techniques available and the corresponding range of y^+ values suggest that no one method is considered to be best practice. The behaviour of the overall turbulence model will determine the best approach to employ to match a particular combination of turbulence models.

Alternative methods of matching turbulence models within the $k\varepsilon/kl$ model have been investigated in the earlier work of Dhinsa et al.,[137, 138, 139] however the technique used here of ensuring variable continuity shows greater numerical stability and will therefore be used for the remainder of the simulation work.

8.3.2 Validation of Hybrid Turbulence Model

The validation of the two-layer hybrid $k\varepsilon/kl$ turbulence model has been performed on both the parallel plates test case, which will be discussed first, followed by the backward facing step. The reader is referred to Appendices A1.2 and A3.2 respectively for the test case specifications.

To fully understand the results obtained by the $k\varepsilon/kl$ model the location of the turbulence model region division has been presented by means of contours in Figure 8.12.
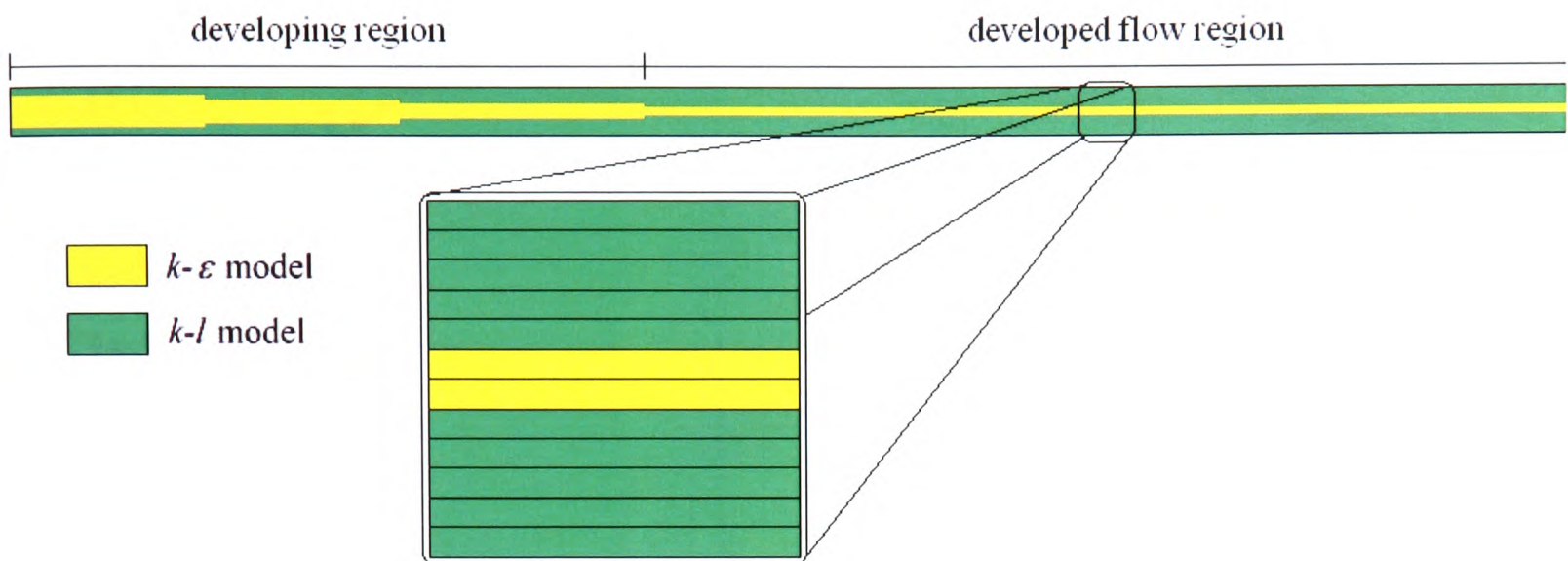
Figure 8.12 $k\varepsilon/kl$ **region division parallel plates test case**

Figure 8.12 clearly identifies that after the development region the majority of the solution domain is using the $k-l$ model. There are a few cells in the centre of the flow channel which employ the $k-\varepsilon$ model. The $k-l$ model is used mainly in the developing boundary layer region nearest to the wall as expected, whilst the $k-\varepsilon$ model is used in the core of the duct.

Figure 8.13 shows the predicted velocity profile obtained with the $k\varepsilon/kl$ model at the downstream position $x = 9.8\text{m}$. Comparisons have been made against the fully developed turbulent analytical solution stated in equation (8.25) for the flow between parallel plates and the predicted velocity profiles obtained by the standard versions of the Norris & Reynolds $k-l$ model and the $k-\varepsilon$ model.

$$\frac{U}{U_{in}} = 1 + \left[\left(\frac{f}{2} \right)^{0.5} \Big/ \kappa \right] \left[\frac{5}{6} + \ln\left(1 - \left(\frac{y}{b} \right)^{0.5} \right) + \left(\frac{y}{b} \right)^{0.5} \right] \qquad (8.25)$$
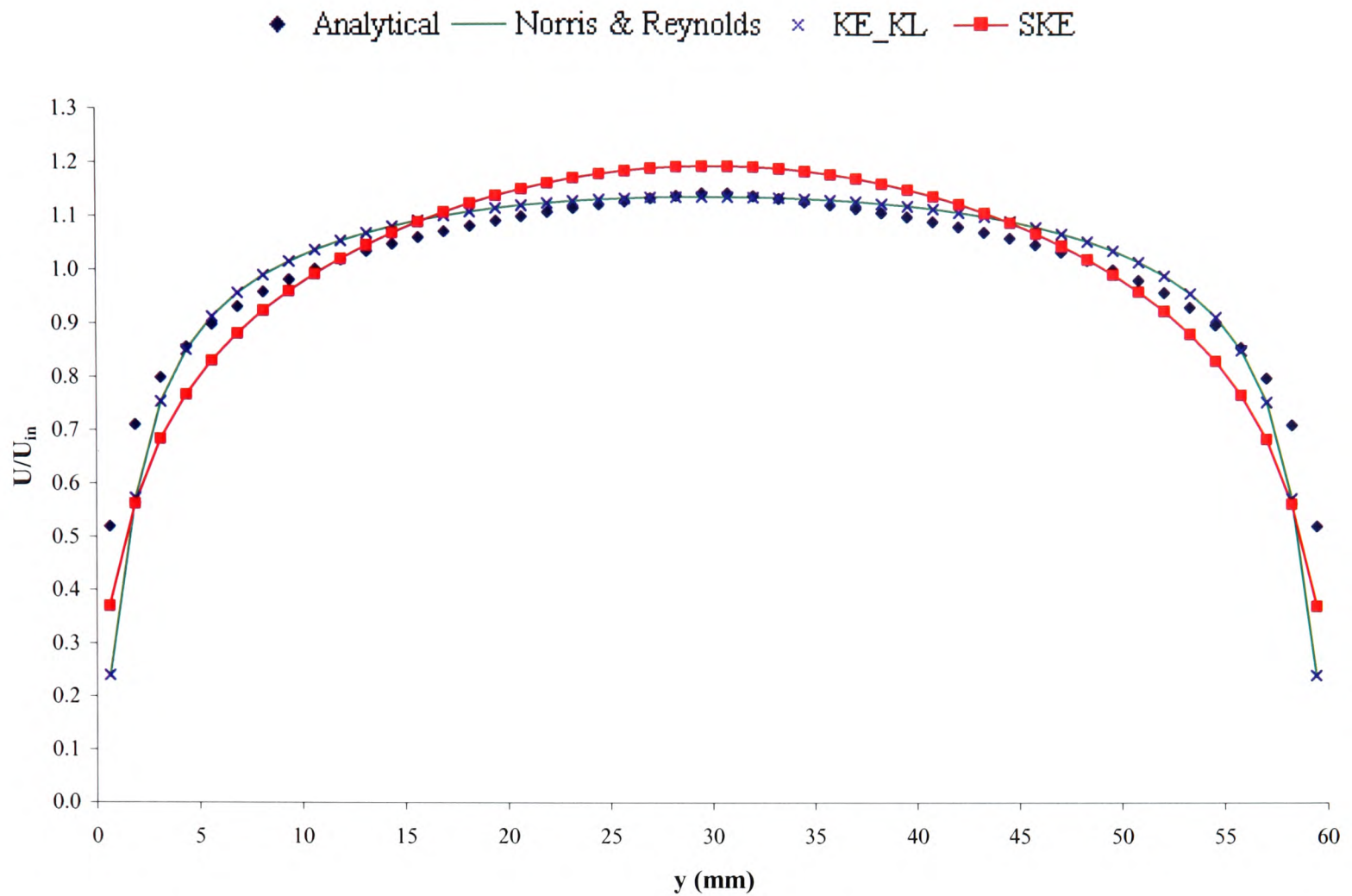
Figure 8.13 Parallel plates velocity profile $k\varepsilon/kl$ **model**

From Figure 8.13 it can be concluded that the $k\varepsilon/kl$ predicted velocity profile is in good agreement with the analytical solution. The profile is slightly flatter towards the centre of the channel in comparison to the profile predicted by the standard high Reynolds number $k - \varepsilon$ model. However the $k\varepsilon/kl$ predictions are more likely to be closer to the standard version of the Norris and Reynolds model as the majority of the $k\varepsilon/kl$ flow channel is identified as being Region B.

Presented in Figure 8.14 is the $k\varepsilon/kl$ predicted turbulent dynamic viscosity profile in comparison to the standard Norris and Reynolds turbulence model.
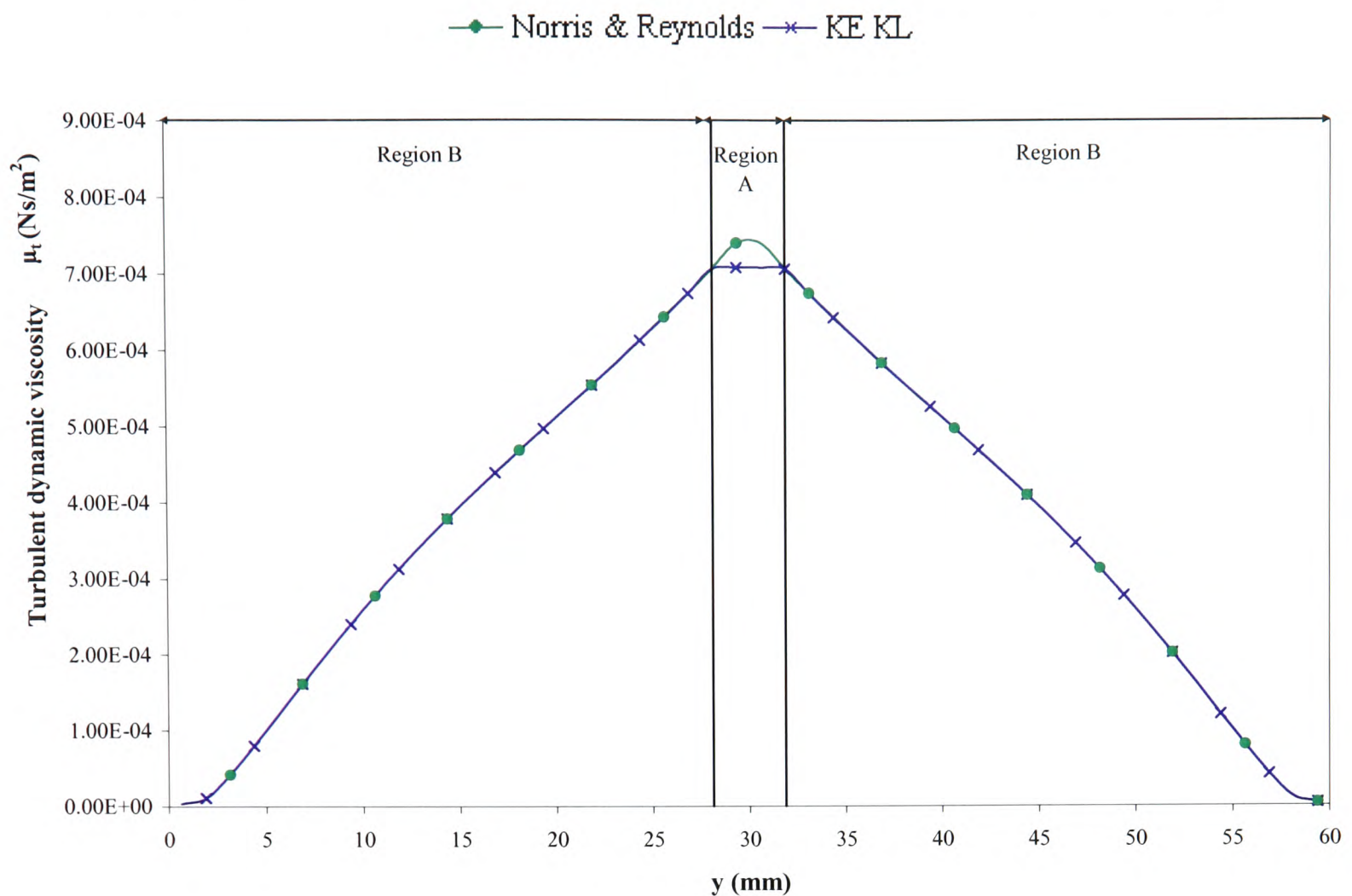
Figure 8.14 Parallel plates turbulent dynamic viscosity profile *kε/kl* **model**

Figure 8.14 clearly shows where the switch between the two turbulence models is occurring at $y = 28$mm and $y = 31$mm. Also the conclusion determined in Chapter 5 with regards to the bulk turbulent viscosity not significantly influencing the predicted velocity profile for this case is reiterated here.

Now the examination of the parallel plates test case has been completed for the two-layer hybrid $k\varepsilon/kl$ turbulence model it can be concluded that the velocity prediction obtained for this test case is in good agreement with the analytical solution and the model is identifying the division between regions as expected. The results suggest that the new matching technique employed is indeed ensuring a smooth transition between turbulence models and correct model implementation has been achieved within PHYSICA; however further validation of model implementation will also be undertaken on the backward facing step configuration, where flow separation and recirculation are important factors. The mesh density adopted for the numerical work undertaken is (8 x 10) upstream and (40 x 30) downstream of the step in the x- and y- directions respectively.

Assessment of the reattachment length for this case has been examined for the backward facing step test case to validate the $k\varepsilon/kl$ turbulence model. The reader is reminded that the universally accepted reattachment length for turbulent flow is stated to be in the range 7.0 ± 1.0 step height.

As with the parallel plates test case for the SST model the $k\varepsilon/kl$ model is employing the $k-\varepsilon$ model for the large majority of the solution domain due to the large Reynolds number stated for this case. Therefore correct model implementation can not be determined without altering the test case specifications slightly.

In order for the $k-l$ model to be selected over more of the domain the Reynolds number must be reduced. The laminar kinematic viscosity for the simulation has been multiplied by a factor of 20 to $3.1172\text{E}-04\text{m}^2/\text{s}$. Figure 8.15 presents the new region division contours for the $k\varepsilon/kl$ model with a $k-l$ region clearly identifiable.

k-ε model k-l model
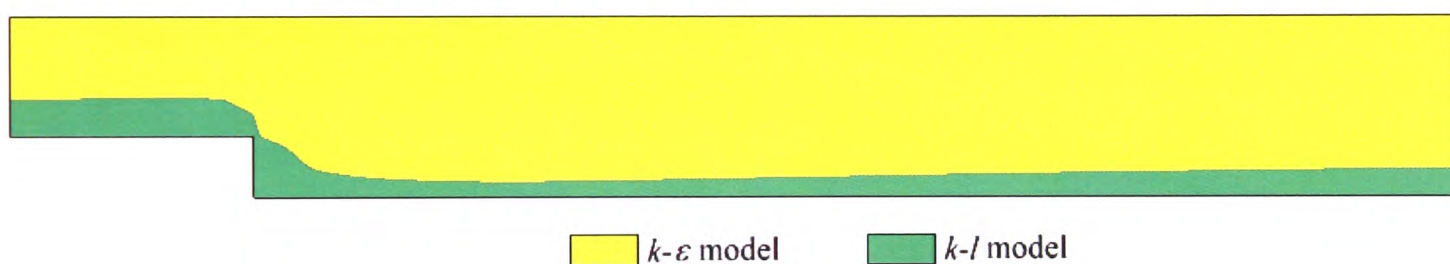
Figure 8.15 $k\varepsilon/kl$ region division backward facing step test case laminar kinematic viscosity increased to $3.1172\text{E}-04\text{m}^2/\text{s}$

The reattachment length predicted by the $k\varepsilon/kl$ model when the laminar kinematic viscosity has been manipulated to identify both the standard high Reynolds number $k-\varepsilon$ and the one-equation Norris and Reynolds $k-l$ model regions is presented in Figure 8.16.
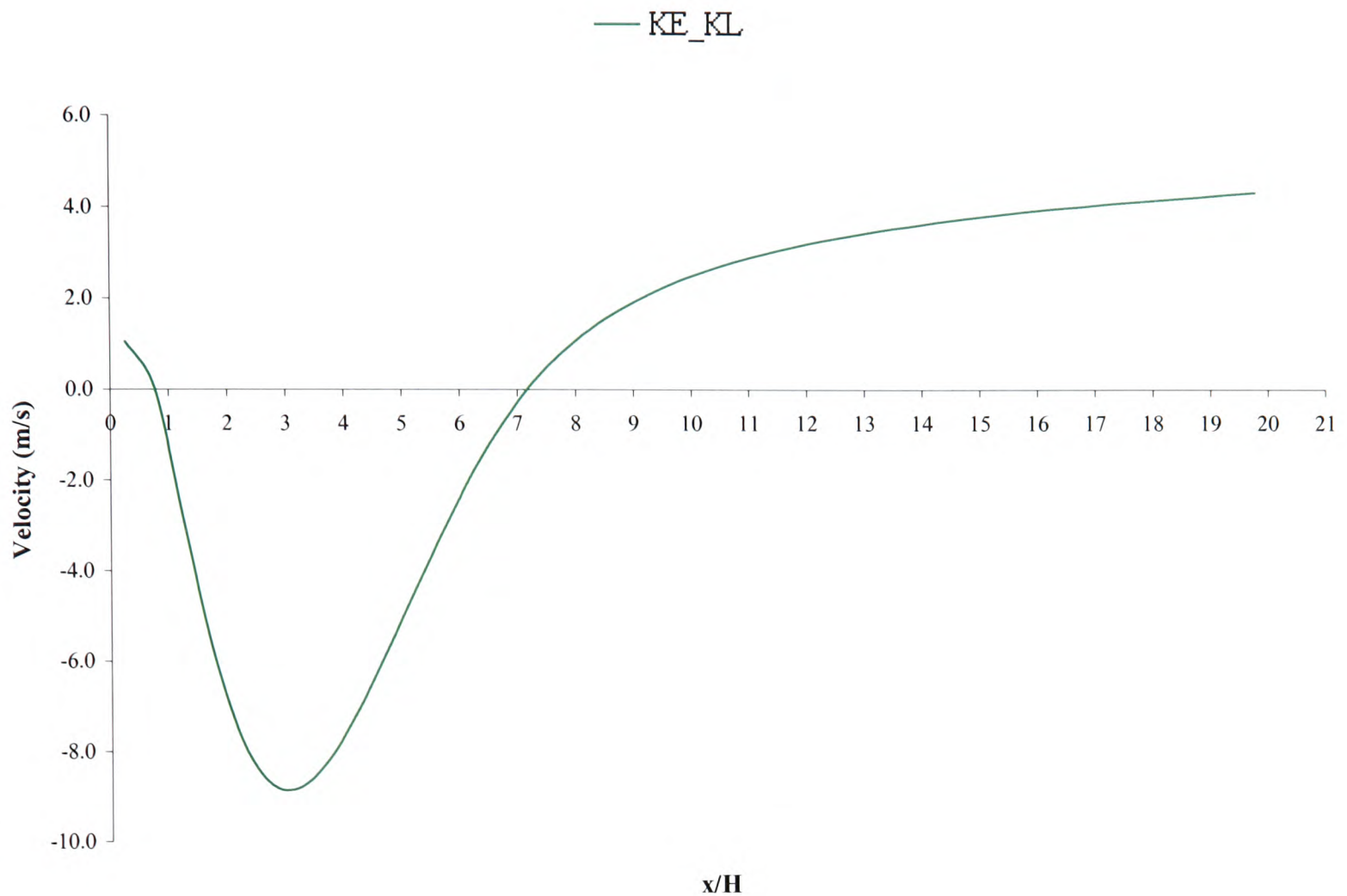
Figure 8.16 Reattachment length predictions $k\varepsilon/kl$ **model laminar kinematic viscosity**
increased to $3.1172E - 04m^2/s$

Figure 8.16 clearly identifies the small corner eddy located close to the step face and predicts a reattachment length of 7.2 step heights which agrees well with the experimental data of Vogel and Eaton[13] which was conducted at a Reynolds number of 28,000.

The conclusion which can be drawn after the examination of the classic backward facing step case is that the newly formulated two-layer hybrid $k\varepsilon/kl$ turbulence model has been correctly implemented within PHYSICA and predicts the correct flow behaviour.

8.3.3 Why Use the Hybrid Turbulence Model

The two-layer hybrid $k\varepsilon/kl$ turbulence model carries with it all the advantages of both the standard high Reynolds number $k - \varepsilon$ model and the one-equation Norris and Reynolds model.

Advantages:

- Simple turbulence model for which only initial and/or boundary conditions are required.

- Promises reliable performance for many industrially significant flows.

- The standard $k - \varepsilon$ model is well established and this filters through into the hybrid model.

- Performs particularly well in confined flows where the Reynolds shear stresses are of utmost importance.

- Low computational mesh requirement as wall functions are used and consequently fast/economical to run.

- The overriding drawback of the standard $k - \varepsilon$ turbulence model is that it is designed to be correct for high Reynolds number flows, therefore resulting in inaccuracies in slow flow regions near walls and in recirculating zones. The two-layer $k\varepsilon / kl$ model rectifies this problem.

Disadvantages

It should be noted that the following disadvantages apply to Launder and Spalding's standard $k - \varepsilon$ turbulence model.

- Assumed that the eddy viscosity is indistinguishable for all the Reynolds stresses. Measurements however advocate that this is not the case even for simple turbulent flows.

- Poor performance in an assortment of important cases such as:
  - Some unconfined flows.
  - Flows containing large extra strains (e.g. curved boundary layers, swirling flow).
  - Rotating flows.

- Fully-developed flows in non-circular ducts – electronic applications.

- More expensive to implement than the mixing-length model as there are two additional PDE's to accommodate.

The two-layer hybrid $k\varepsilon/kl$ turbulence model addresses the main disadvantage of the $k-\varepsilon$ model – designed to be a high Reynolds number model – by introducing a $k-l$ model in the low Reynolds number regions (i.e. near-wall and recirculating zones).

8.4 The Function f_μ

The distribution of the f_μ functions of the $k\varepsilon-LVEL$ and two-layer hybrid $k\varepsilon/kl$ turbulence models have been discussed with reference to the study conducted by Patel et al.[117] in which a number of turbulence models for near-wall and low Reynolds number flows were considered.

Among the models examined by Patel et al.[117] were those of Chien (CH),[140] Dutoya and Michard (DM),[141] Hassid and Poreh (HP),[142] Hoffmann (HO),[143] Lam and Bremhorst (LB),[111] Launder and Sharma (LS),[112] and Reynolds (RE)[144] all of which are variations of the standard high Reynolds number $k-\varepsilon$ model. Note that only RE and LB employed a transport equation for the rate of turbulent dissipation, while the remaining models solve for some alternative quantity.

Various proposals of the function f_μ, which multiplies the eddy viscosity relation and is introduced to mimic the direct effect of molecular viscosity on the shear stress, were specified in the turbulence model range considered. The proposed f_μ functions were examined according to a range of criteria:

- Comparison against empirical distribution

- Their influence in the logarithmic region

- The implied near-wall distribution of $-\overline{uv}$

The last specified criterion examined was considered to be of least importance by Patel et al.[117] as the turbulent stress was small compared to the viscous stress in the immediate vicinity of the wall and will therefore not be discussed any further.

The variation of the f_μ function with respect to the distance to the wall is presented in Figure 8.17 for the turbulence model range considered by Patel et al.[117] Also the distributions obtained from the f_μ functions of the $k\varepsilon - LVEL$ and $k\varepsilon / kl$ $\left(f_1 \equiv f_\mu \right)$ models are presented.
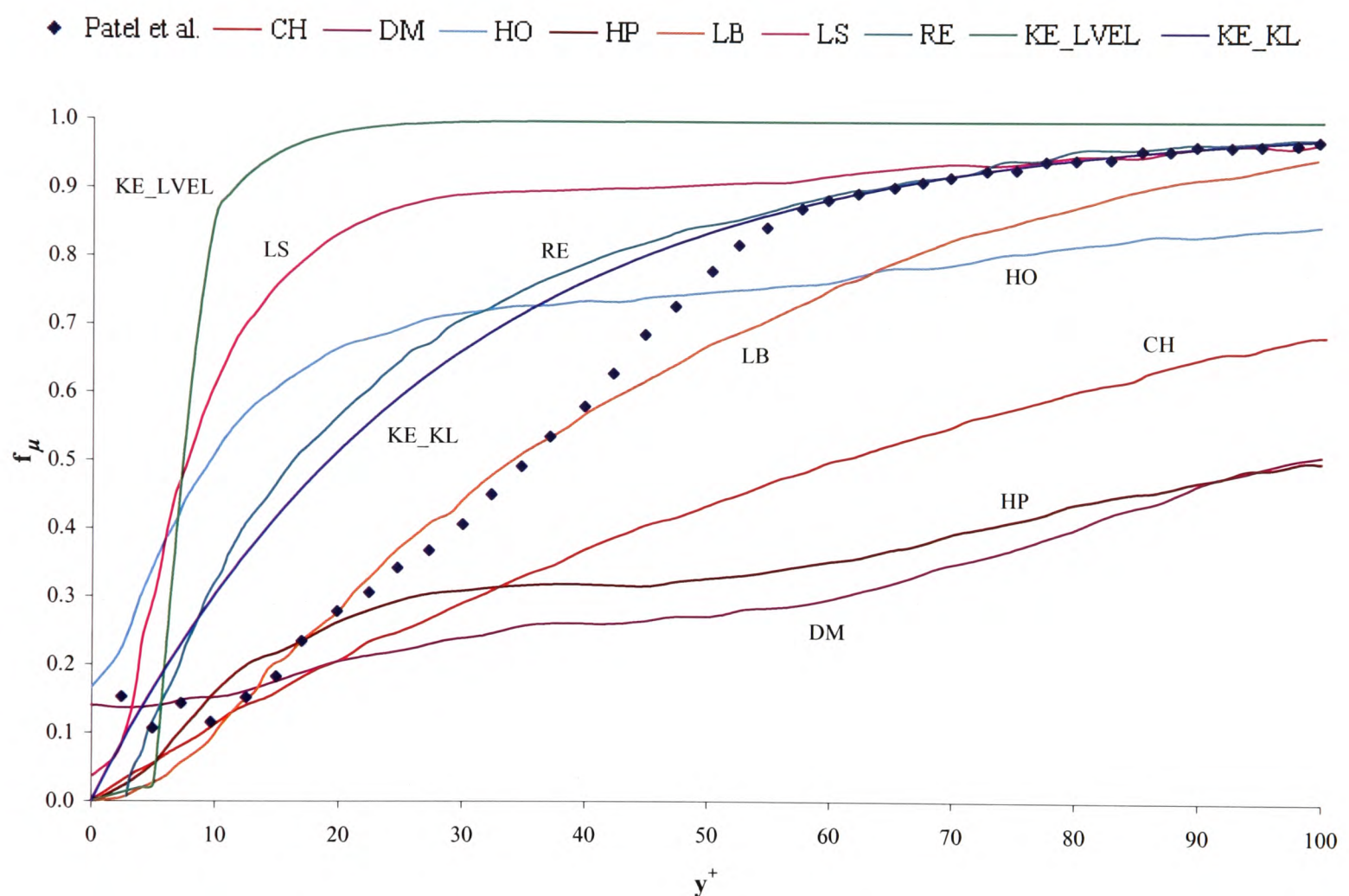
Figure 8.17 Variation of the function f_μ with wall distance

An almost constant value for the empirical distribution is seen for $y^+ < 15$ followed by an approximately linear increase up to $y^+ = 60$, then moving more gradually towards unity. Assessment of Figure 8.17 shows that none of the model functions considered follows the distribution suggested by the data over the whole range of y^+. The function suggested by LB

is in greatest agreement with the distribution in the viscous zone $\left(y^{+} < 40\right)$ with the function used in the $k\varepsilon / kl$ model agreeing best in the fully turbulent regime $\left(y^{+} > 40\right)$.

The formulae employed by LS and the $k\varepsilon - LVEL$ model yield relatively high values in the viscous zone however LS does show better agreement in the fully turbulent regime. The problem associated with the $k\varepsilon - LVEL$ model discussed earlier is reiterated here as the f_{μ} function tends towards unity much sooner than any other model. This suggests that the high Reynolds number $k - \varepsilon$ model is being selected almost immediately, which defeats the purpose of the zonal approach.

The functions of CH, DM and HP, and to some extend HO, increase too slowly with wall distance, suggesting that some form of revision is required.

Assessing the performance of f_{μ} in the fully turbulent logarithmic layer where f_{μ} must tend towards unity if the high Reynolds number $k - \varepsilon$ model is to be recovered allows for conclusions to be drawn with regards to the most appropriate function employed within a turbulence model.

The empirical data suggests that the viscous effects become negligible for $y^{+} > 60$, whereas Figure 8.17 shows that the majority of the functions reach an asymptotic value of one well beyond $y^{+} = 60$. The $k\varepsilon - LVEL$ model reaching a value of approximately one too quickly (at around $y^{+} = 28$), this is the only model which exhibits such behaviour.

The values of y^{+} at $f_{\mu} = 0.95$ are shown in Table 8.1 for all the turbulence models considered.

Model	$y^+ \left(f_\mu = 0.95 \right)$
Hassid & Poreh (HP)	438.0
Hoffman (HO)	363.5
Chien (CH)	260.5
Dutoya & Michard (DM)	222.1
Lam & Bremhorst (LB)	102.4
Reynolds (RE)	82.9
$k\varepsilon / kl$	82.6
Launder & Sharma (LS)	78.4
$k\varepsilon - LVEL$	14.9

Table 8.1 Limiting values for the function f_μ

It is clear that within the models of HP, HO, CH, and DM the wall damping effect extends out to unrealistically large wall distances. It is noted that the wall functions used in connection with the standard high Reynolds number $k - \varepsilon$ model are usually applied in the region $30 < y^+ < 200$.

The conclusions drawn by Patel et al.[117] after a number of test cases were examined suggested that the models of Launder and Sharma,[112] and to some extend, Lam and Bremhorst[111] yield comparable results and performed considerably better than the other models. However, even these models need further refinement if they are to be used with confidence to calculate near-wall and low Reynolds number flows.

The conclusion drawn by Patel et al.[117] implies that the $k\varepsilon - LVEL$ model requires further revision, this conclusion is somewhat expected. The $k\varepsilon / kl$ model is in good agreement with the most favoured model of Launder and Sharma[112] suggesting that the zonal $k\varepsilon / kl$ turbulence model is a good model to pursue.

8.5 Modifications of $k\varepsilon$-$LVEL$ Model

In the previous section it was concluded that the f_μ function employed within the two-layer hybrid $k\varepsilon / kl$ turbulence model seemed to agree well with the work conducted by Patel et al.[117] Therefore the first suggested modification to the $k\varepsilon - LVEL$ model will attempt to mimic the f_μ distribution obtained by the $k\varepsilon / kl$ model.

The f_μ function stated in equation (8.12) is replaced by equation (8.26).

$$f_\mu = \left(1 - \exp^{\left(-\beta_1 y^+ - \beta_2 \left(y^+ - 5\right)\right)}\right) \tag{8.26}$$

The β step function which replaces equation (8.13) is stated in equation (8.27).

$$
\begin{aligned}
\beta_1 &= 0.035 \\
\beta_2 &= 0.0 \quad y^+ < 5 \\
\beta_2 &= 0.001 \quad y^+ \geq 5
\end{aligned}
\tag{8.27}
$$

The f_μ distribution obtained for this first proposal is presented in Figure 8.18. Comparisons have been made against the original $k\varepsilon - LVEL$ distribution and the predicted zonal $k\varepsilon / kl$ model distribution.
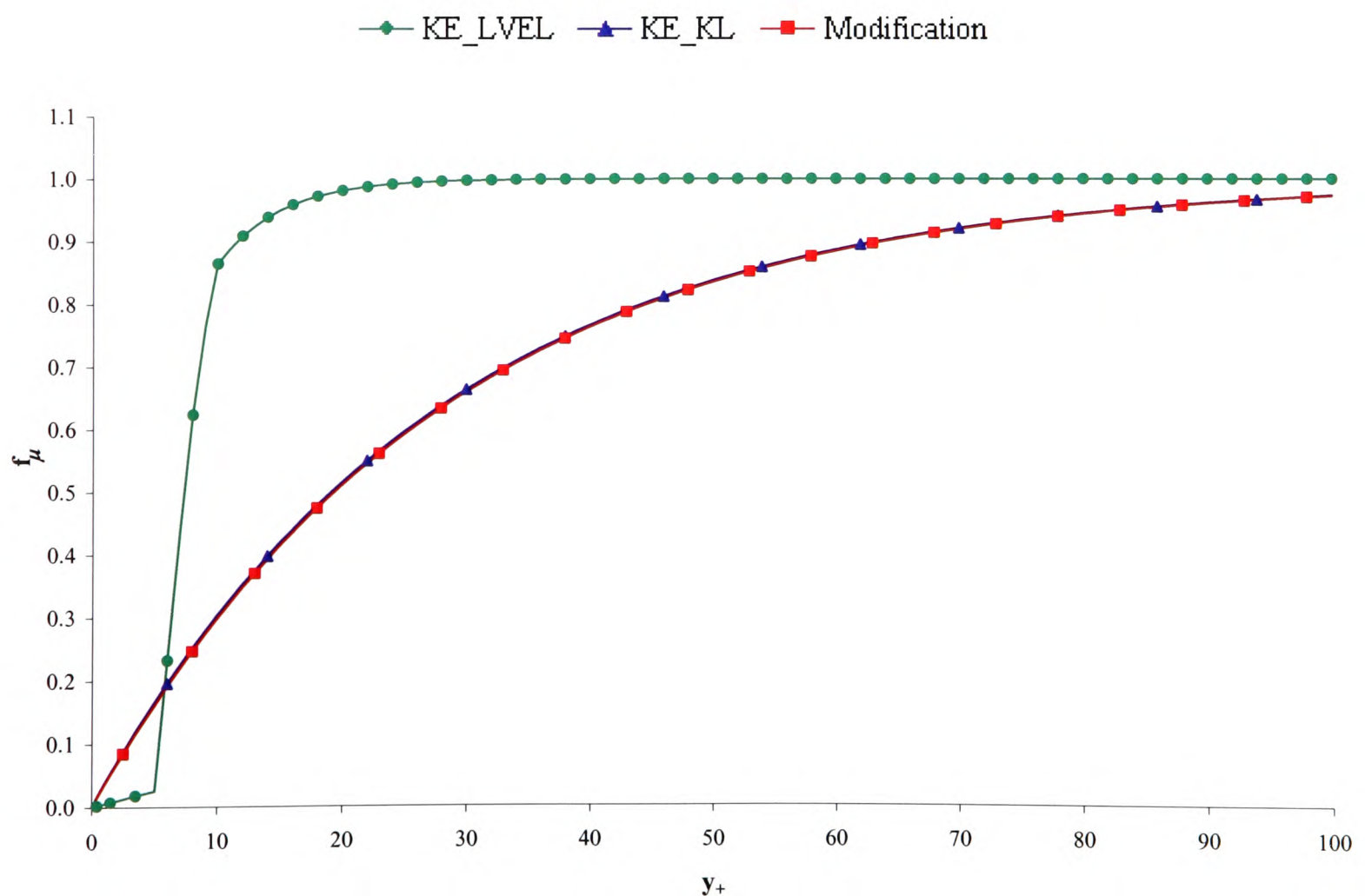
Figure 8.18 Variation of f_μ function with respect to wall distance $k\varepsilon$ - $LVEL$ model first modification

The distribution obtained by the suggested modifications to the $k\varepsilon - LVEL$ model follow the $k\varepsilon / kl$ predicted f_μ distribution exceptionally well which was the objective of this task.

The same f_μ function is used as that stated in equation (8.26) but the step function employed for β is altered to the function stated in equation (8.28).

$$\beta_1 = 0.005$$
$$\beta_2 = 0.0 \quad y^+ < 5 \qquad (8.28)$$
$$\beta_2 = 0.05 \quad y^+ \geq 5$$

The f_μ distribution obtained by this second suggested modification is presented in Figure 8.19. Comparisons have been made against the distributions predicted by the original version of the $k\varepsilon - LVEL$ and $k\varepsilon / kl$ models.
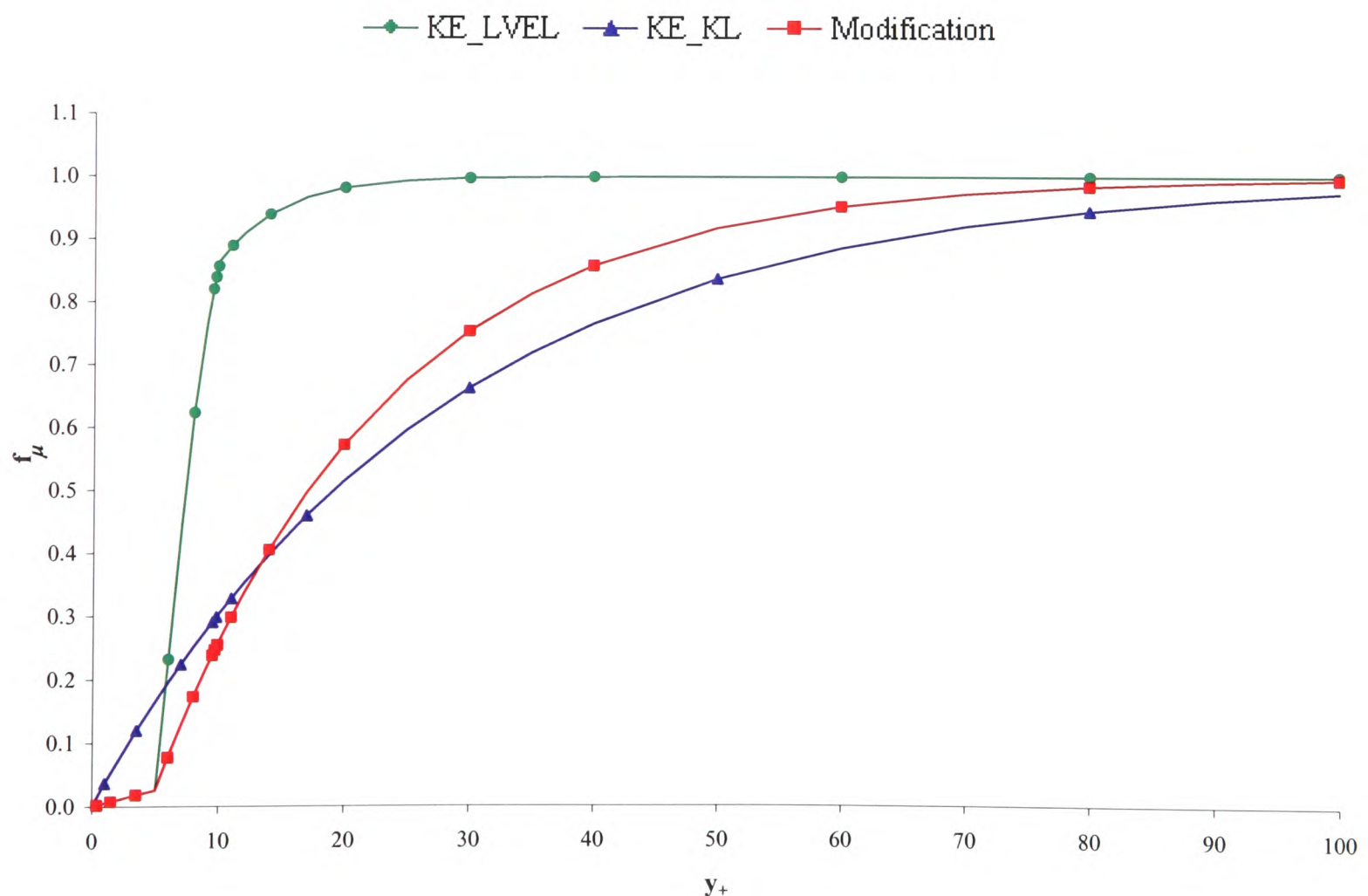
Figure 8.19 Variation of f_μ function with respect to wall distance $k\varepsilon$ - $LVEL$ model second modification

It can be concluded from Figure 8.19 that this second modification mimics the distribution predicted by the original $k\varepsilon - LVEL$ model for $y^+ < 5$ and then attempts to smoothly develop to an asymptotic value of one.

This second modification is physically more realistic as $y^+ < 5$ would be considered to be within the laminar sub-layer and therefore no turbulence damping would be required. This argument is strengthened by the distribution of the empirical data presented in Figure 8.17 where an almost constant value for f_μ is seen for $y^+ < 15$.

In conclusion the second suggested modification would be initially recommended for implementation as this would introduce limited change to the original $k\varepsilon - LVEL$ model. However the first suggested modifications have not been made redundant as it can be determined from Figure 8.17 that a number of turbulent model developers adopt an approach of fitting a smooth curve within the laminar regime and therefore assessment of the first stated modifications should also be undertaken.

8.6 Concluding Remarks

The conclusions which have been highlighted in this chapter are stated below:

- The SST model can successfully revert to the $k - \omega$ model.

- It has been demonstrated that the opposite is not possible i.e. the SST model can not mathematically revert to the standard high Reynolds number $k - \varepsilon$ model predictions without the specification of new blending functions introduced within the structure of the model.

- The SST model has been correctly implemented within PHYSICA, but it is found to have limitations in separated flows – the transition point from $k - \varepsilon$ to $k - \omega$ is important.

- Modifications have been suggested for the standard version of $k\varepsilon - LVEL$ to prevent the f_μ function reaching a value of one so swiftly.

- A novel matching technique has been derived and used to determine the critical Reynolds number within the hybrid $k\varepsilon/kl$ model.

- A critical Reynolds number of 180 has been determined for use within the structure of the hybrid $k\varepsilon/kl$ turbulence model. This value lies comfortably within the range considered by other zonal model developers.

- The reattachment length predicted by the hybrid $k\varepsilon/kl$ model agrees exceptionally well with experimental data and also identifies a small corner eddy close to the step face, in line with the experimental observations of Vogel and Eaton.[13]

- The two-layer hybrid $k\varepsilon/kl$ model has been correctly implemented within PHYSICA ensuring variable continuity as the switch between turbulence models occurs.

- The f_{μ} function used within the $k\varepsilon/kl$ model agrees well with the work conducted by Patel et al.[117]

- One of the main objectives of this research was to develop a low Reynolds number transitional turbulence model for electronic applications. This model is required to be fast and have acceptable accuracy. The hybrid $k\varepsilon/kl$ model fulfills these requirements and therefore stands as a competitor within the area of turbulence models designed for electronic applications.

- The two-layer hybrid $k\varepsilon/kl$ turbulence model seems to be a promising model to pursue. Therefore the performance of this model will be assessed when dealing with more realistic geometries with regards to electronics.

MEINDERS LOW REYNOLDS NUMBER CONFIGURATIONS

The configurations discussed in this chapter originate from a Ph.D. research project which was financially supported by Philips Electronics conducted at the Heat Transfer section of the faculty of Applied Physics, Delft University of Technology. The project entitled "Experimental Study of Heat Transfer in Turbulent Flows over Wall-Mounted Cubes"[145] was performed by E. R. Meinders under the supervision of Professor K. Hanjalić in 1998.

Four test configurations were investigated in this experimental study: Single Cube, Array of Nine Cubes, Tandem of Two Cubes and Matrix of Cubes. The two cases selected for the current work are the Single Cube and Matrix of Cubes configurations due to their relevance to electronic applications.

A range of RANS-based turbulence models have been applied to both of the chosen case studies. From the basic zero-equation LVEL to the more complex two-equation hybrid SST turbulence model. All simulation work has been conducted using the finite volume CFD code PHYSICA V2.12.

9.1 Single Cube

Fluid flow and heat transfer CFD predictions are compared against Meinders experimental data for low Reynolds number flow around a single wall-mounted cube. The case specification is detailed in Figure 9.1.

Figure 9.1 Meinders single cube test geometry

The test channel has dimensions (1215 x 61 x 600)mm and uses an inlet velocity of 4.47m/s, with the inlet air temperature kept at 20°C, resulting in a Reynolds number based on the cube height, $Re_H = 4440$. The cube of size H = 15mm is mounted x/H = 50 downstream of the inlet boundary on the centreline allowing the use of a symmetry boundary condition in the z-direction.

The test channel base plate is constructed from phenol-formaldehyde which is 10mm in thickness and has a thermal conductivity of 0.33W/mK. The cube is constructed from two materials; the core of the cube measuring 12mm is constructed from copper which is kept at a constant temperature of 75°C. An epoxy resin encapsulates the copper and has a uniform thickness of 1.5mm.

The numerical predictions for this case employed a stretched Cartesian mesh. Three mesh densities were investigated in order to ensure mesh independence. The results presented here are for the finest mesh, having 122 x 90 x 63 mesh elements in the x-, y- and z-directions respectively, with 44 x 44 x 22 mesh elements in the cube. This gave a dimensionless wall distance, y^+ of 2.2 at the top centre of the cube. The computational mesh and can be viewed in Figure 9.2.
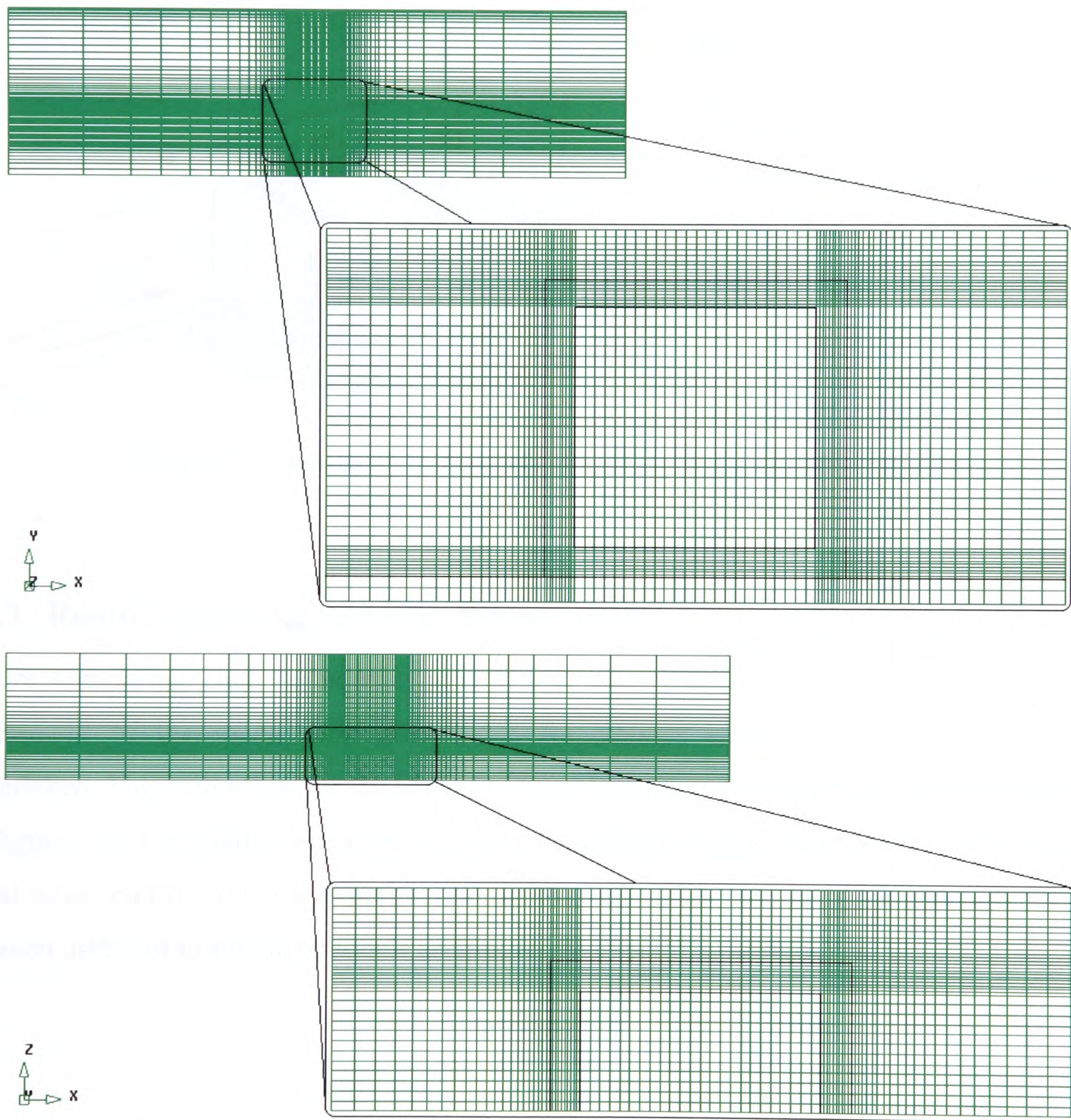
Figure 9.2 Computational mesh density employed for the single cube configuration

For a full description of the specifications of this case study the reader is referred to Appendix A7.1.

The flow structures observed for this case study are similar to those discussed when considering the experimental work conducted by Martinuzzi in Chapter 7 and will therefore not be repeated here. Instead a brief summary of the flow field has been illustrated in Figure 9.3.
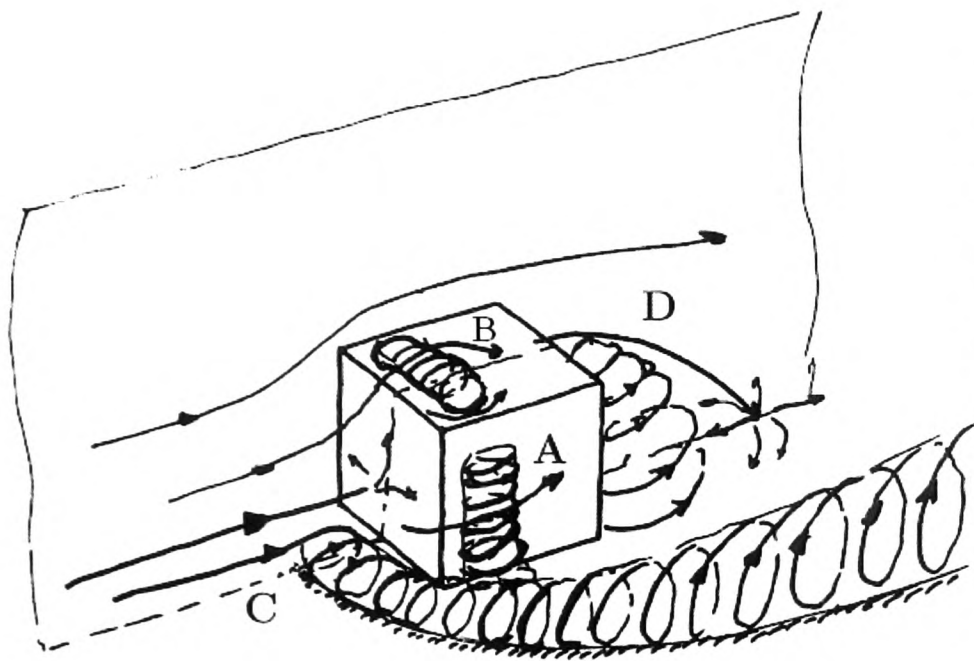
A: Side vortex caused by separated side shear layer

B: Bound vortex caused by separation of top shear layer

C: Horseshoe vortex originates at the base of the windward stagnation region

D: Arc-shaped vortex confined by the cube height and fluid flow

Figure 9.3 Schematic of the flow field around the single cube (Meinders[146])

9.1.1 Results and Discussion: Streamlines

Before comparing each turbulence model with experimental data at particular locations, assessment of the mean flow streamlines for various two-dimensional planes will be undertaken. This will allow for the identification of the four dominant flow features illustrated in Figure 9.3. The predictive accuracy of the turbulence models will be discussed in greater detail when considering the experimental data as streamline comparisons can only be made between different turbulence models as apposed to experimental data.
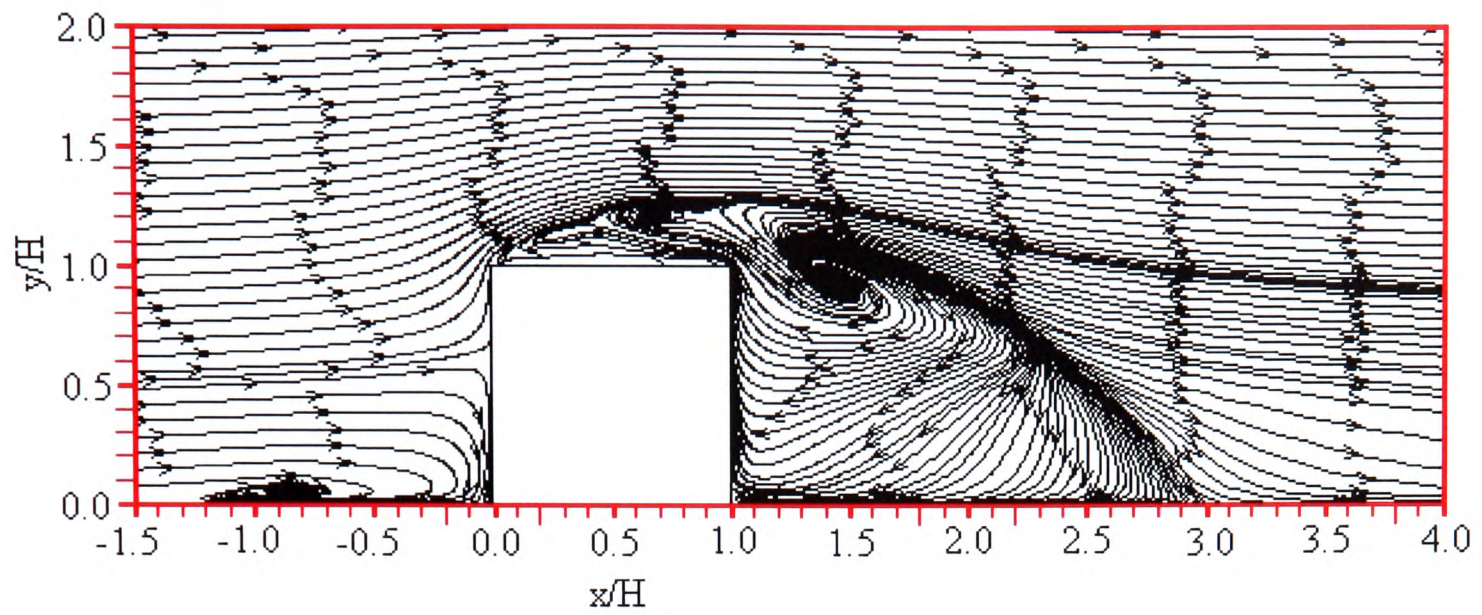
a. LVEL turbulence model predictions

b. LVEL_CAP turbulence model predictions
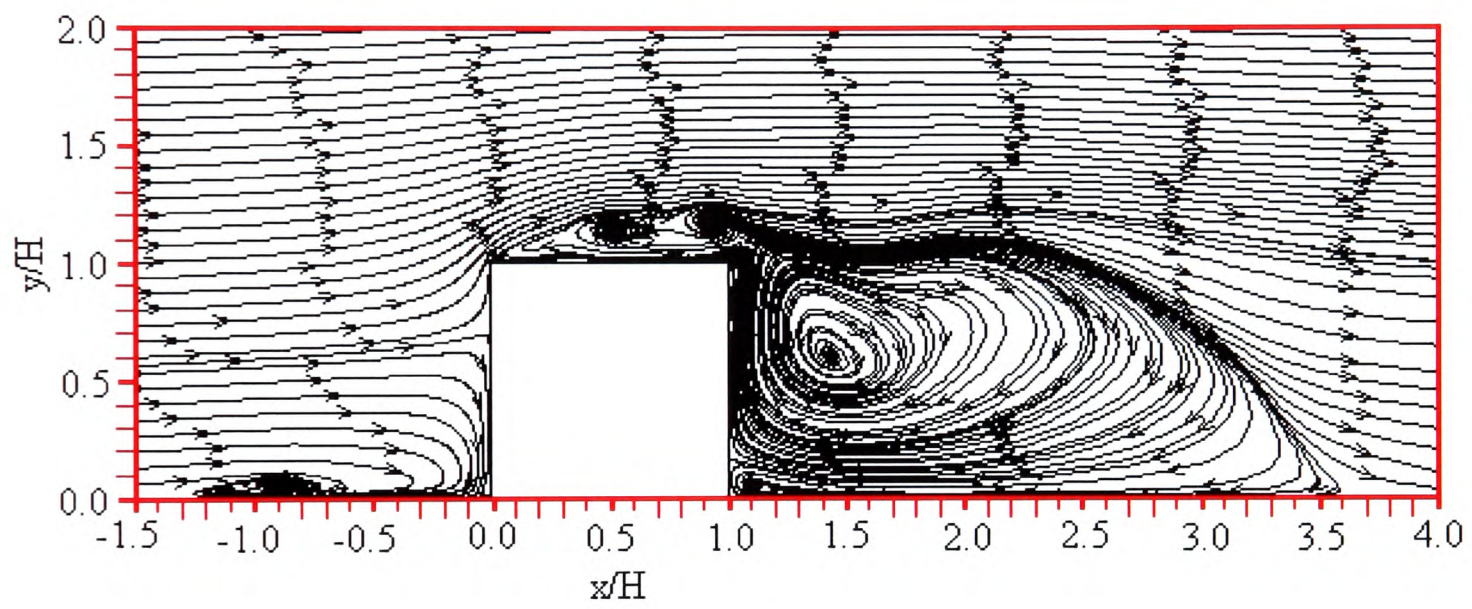
c. Standard $k - \varepsilon$ turbulence model predictions
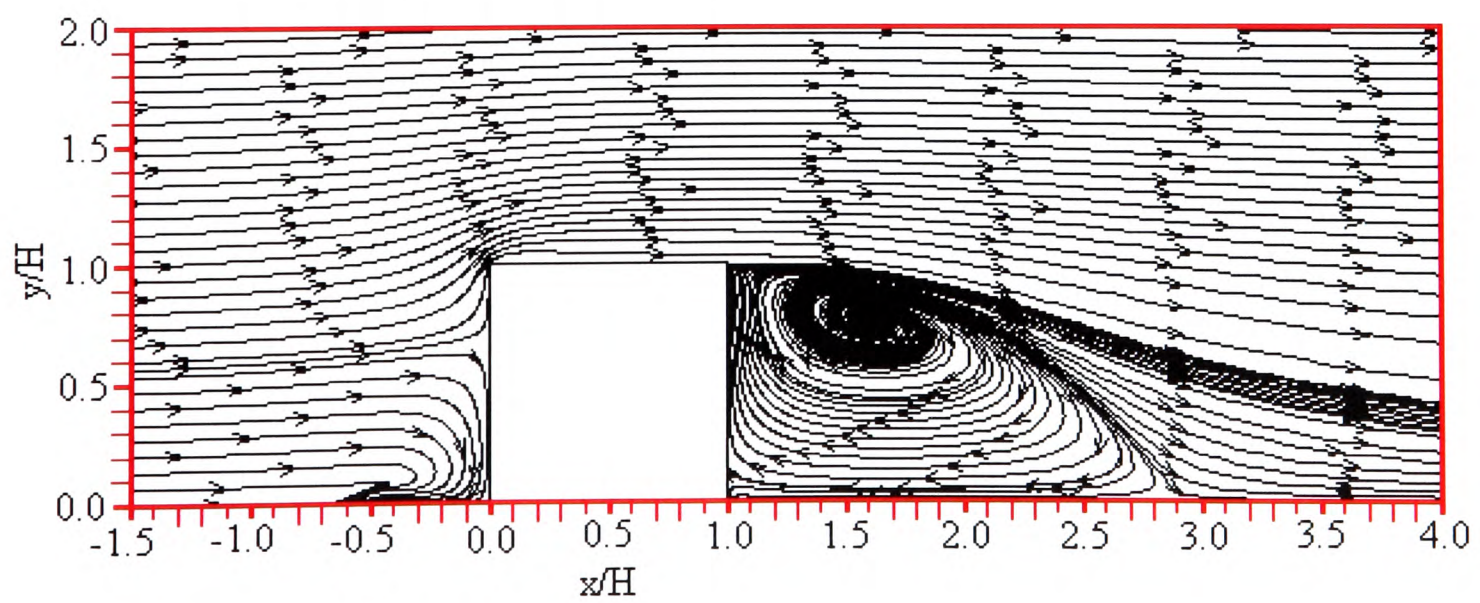
d. Two-layer $k\varepsilon / kl$ turbulence model predictions
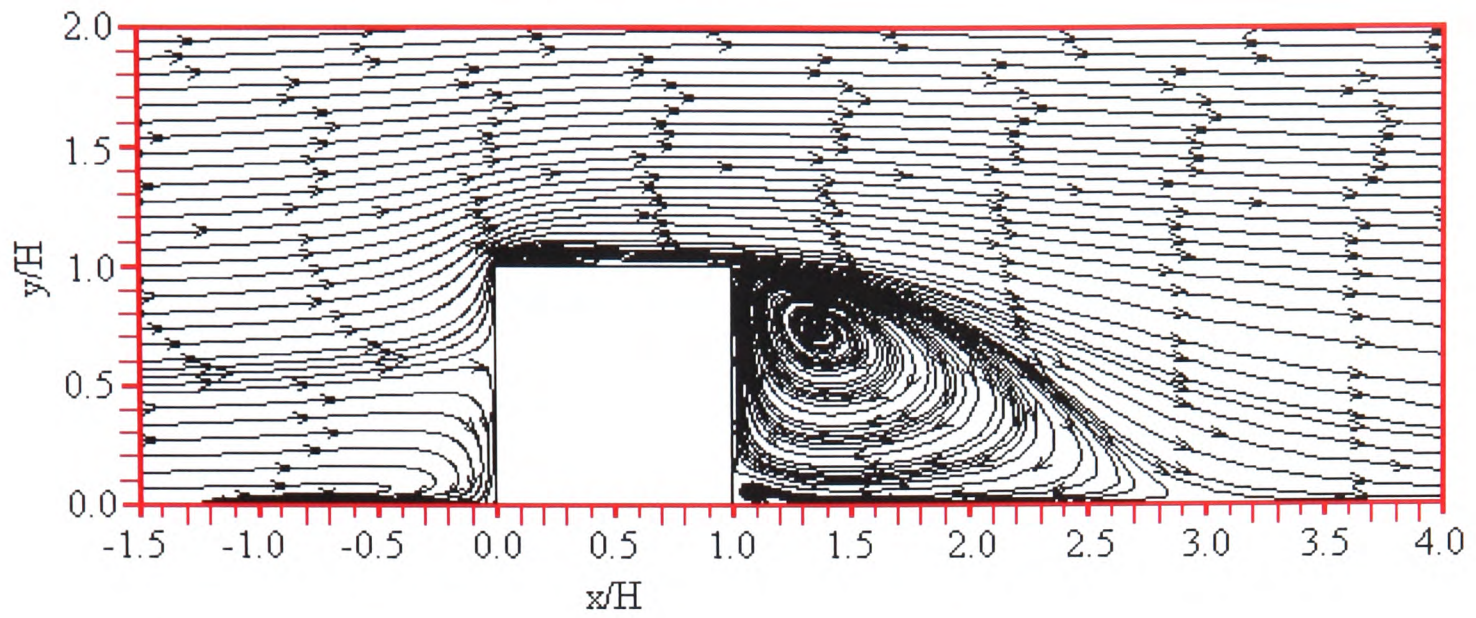
e. Low Reynolds number $k - \omega$ turbulence model predictions
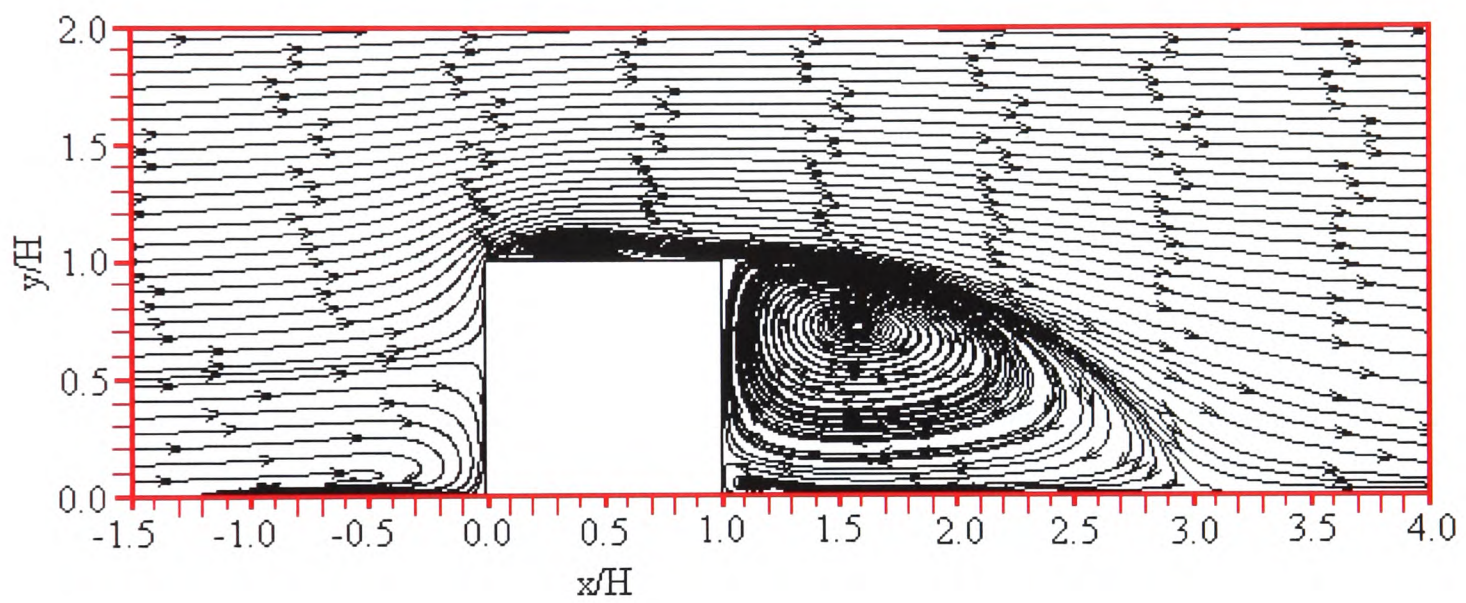
f. Two-layer SST turbulence model predictions
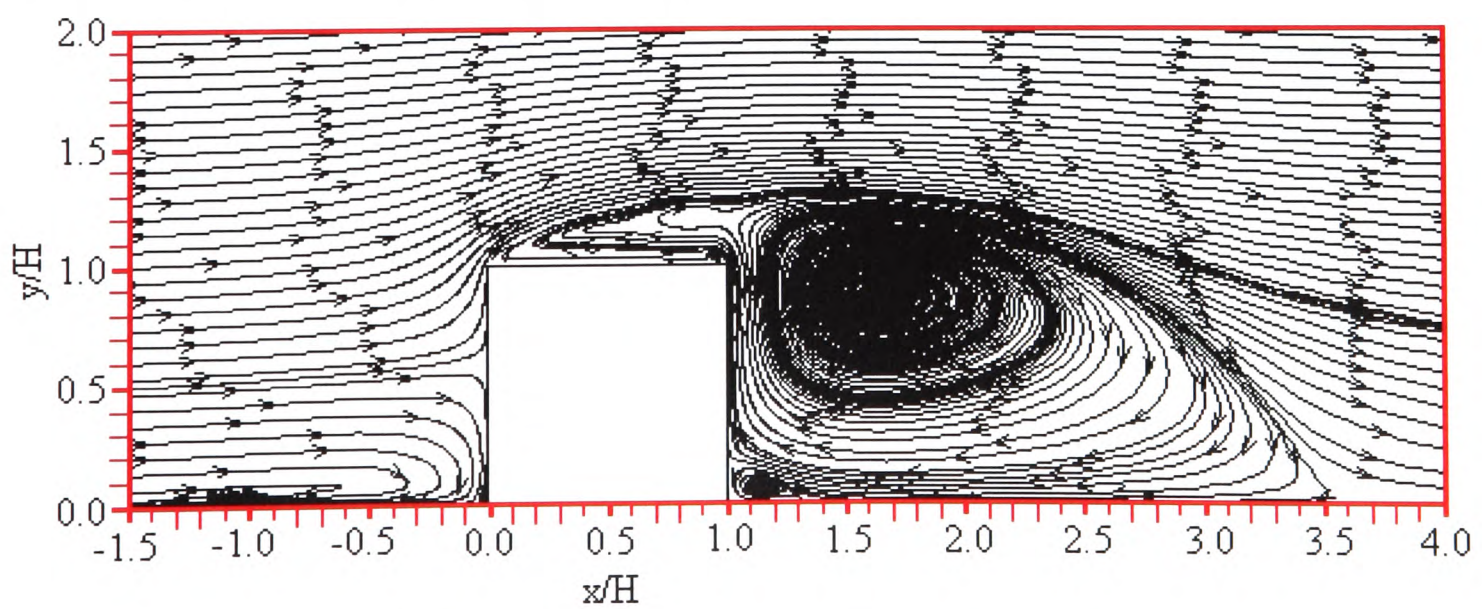
Figure 9.4 Streamlines of the mean flow on symmetry plane through the single cube (xy-plane)
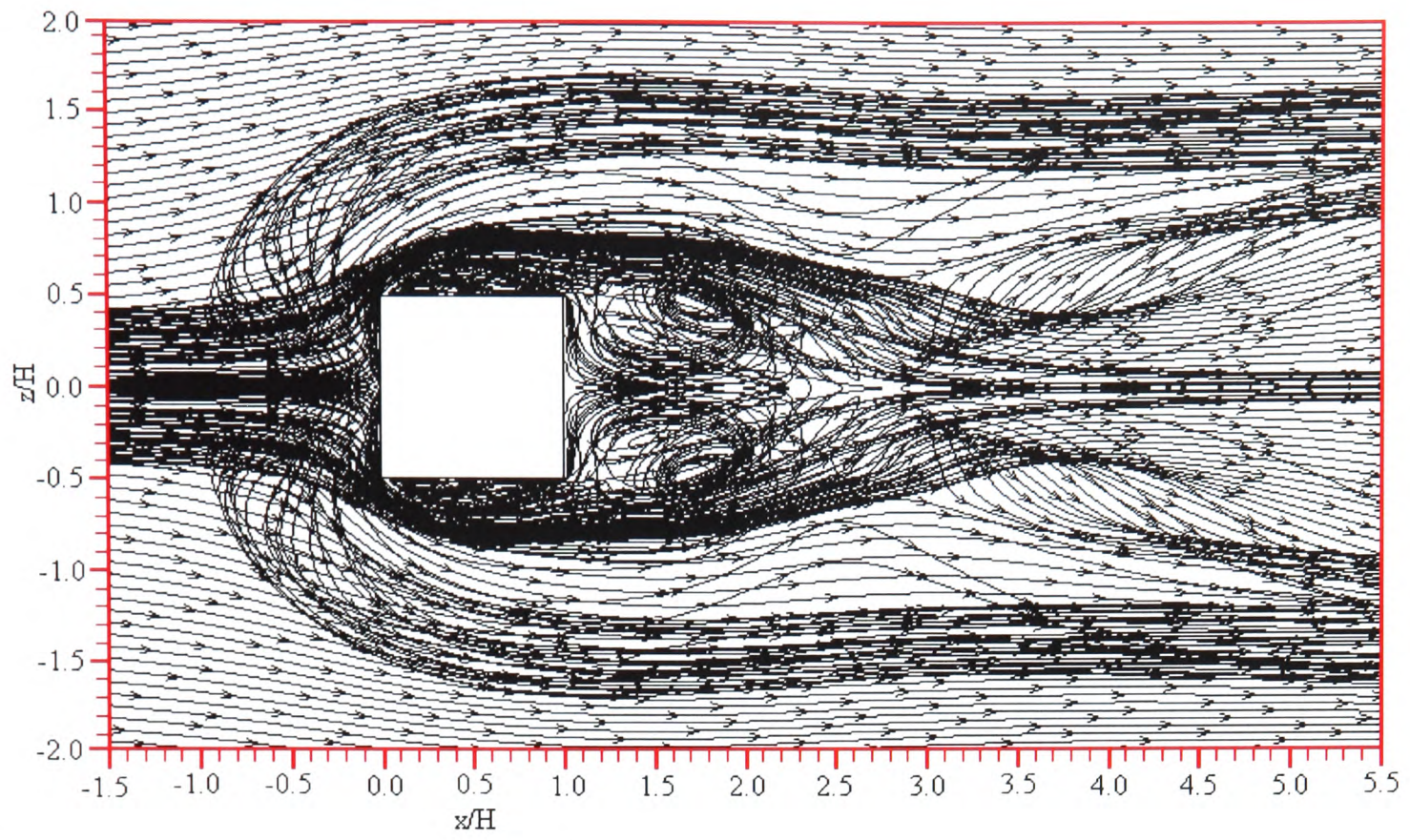
a. LVEL turbulence model predictions

b. LVEL_CAP turbulence model predictions
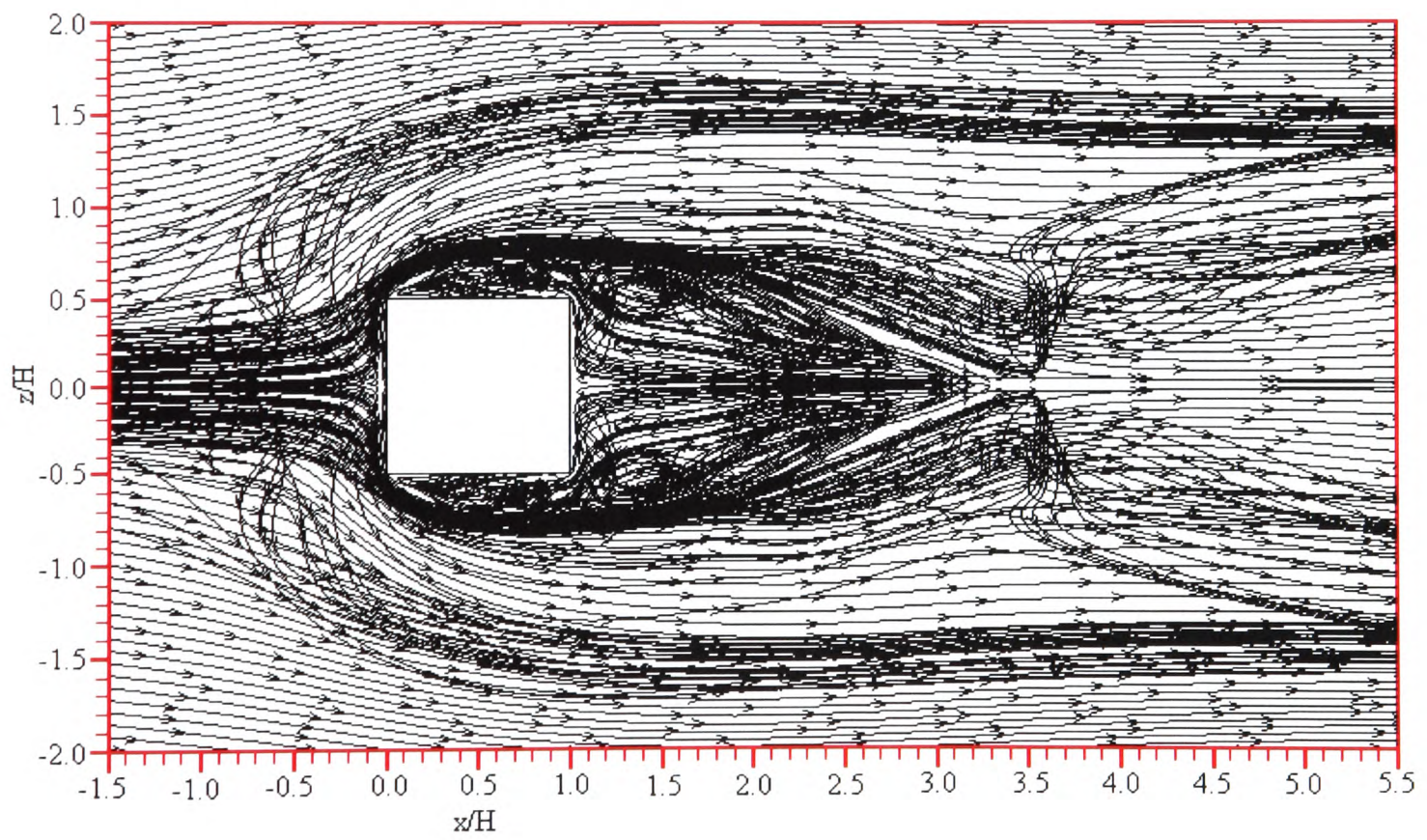
c. Standard $k - \varepsilon$ turbulence model predictions
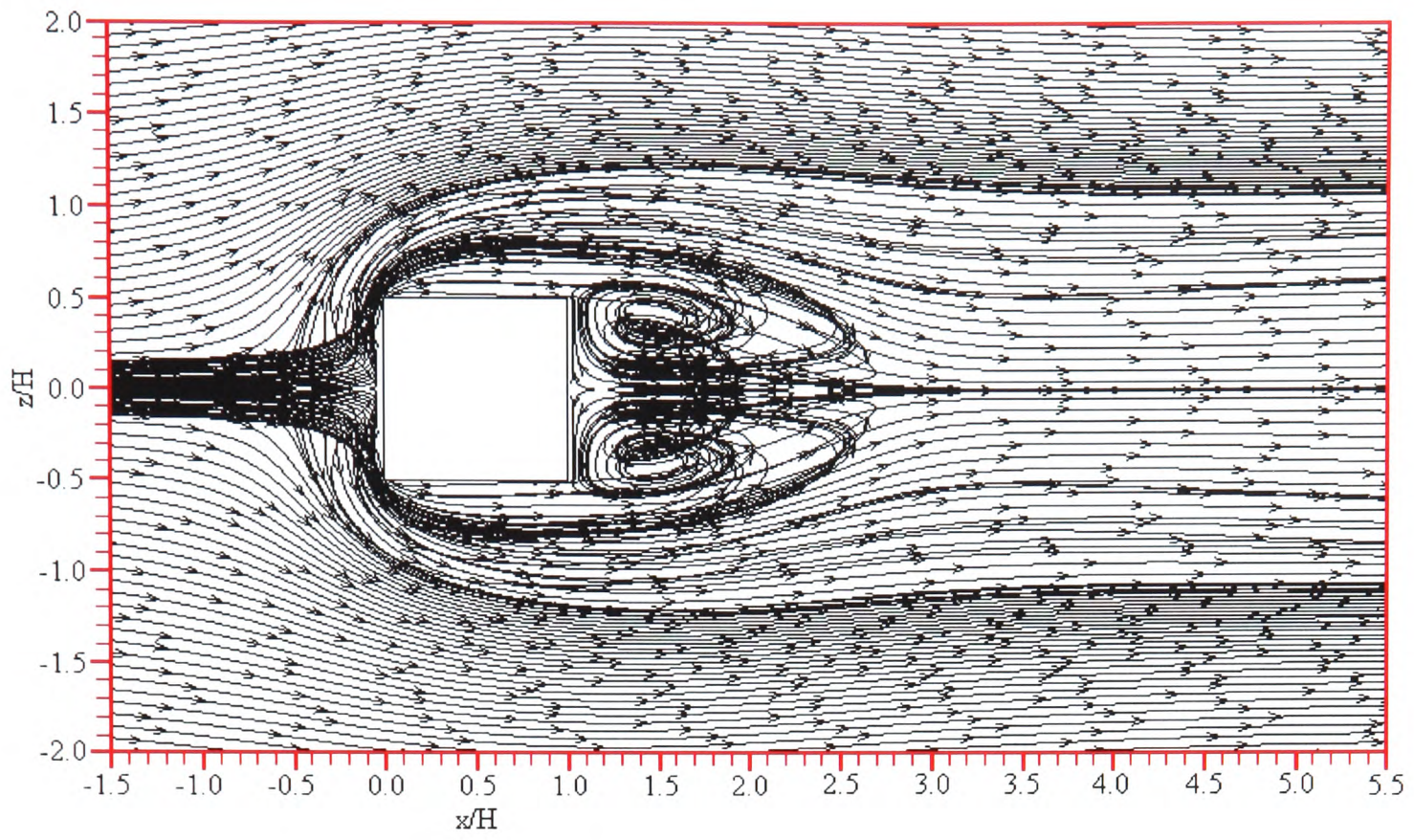
d. Two-layer $k\varepsilon / kl$ turbulence model predictions
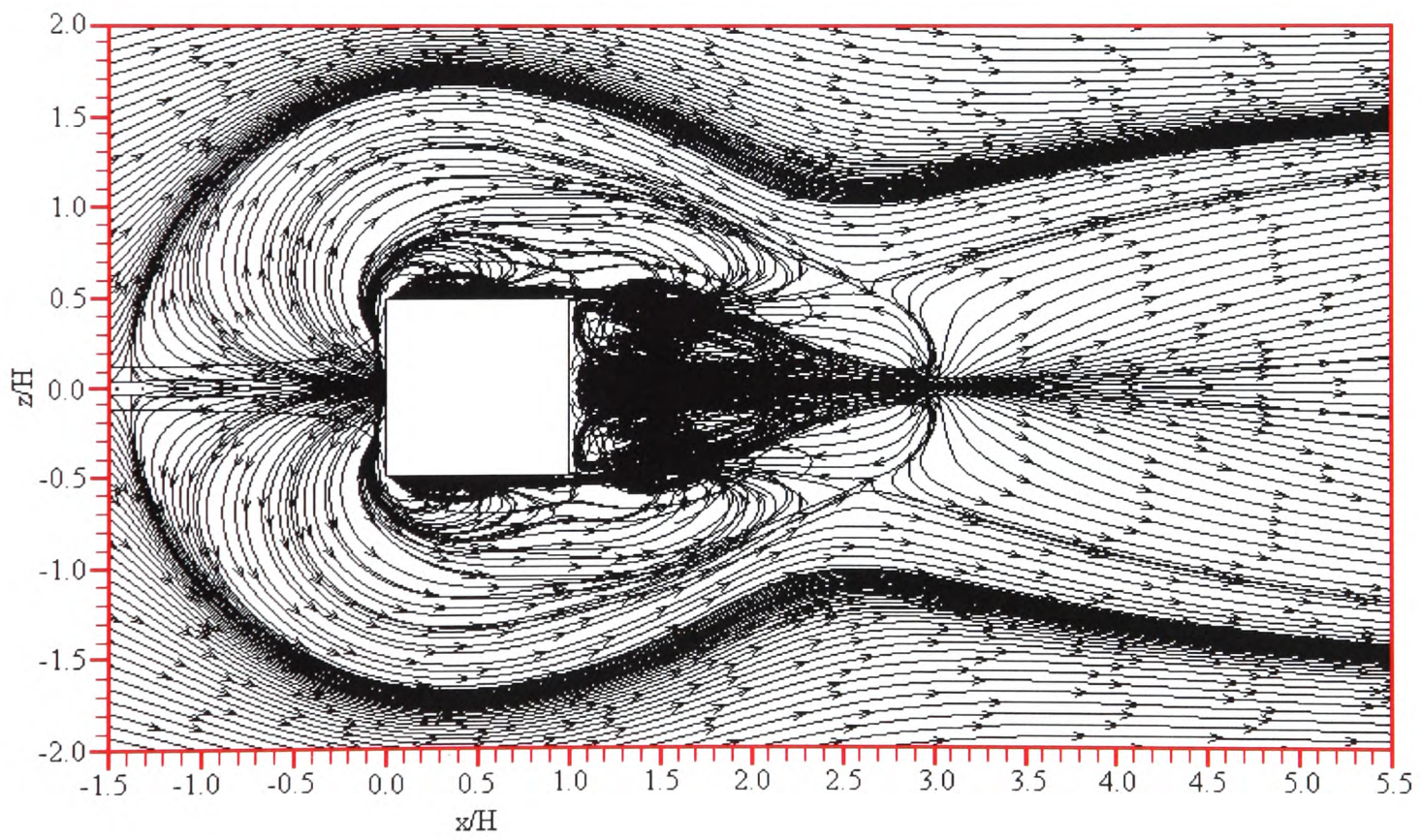
e. Low Reynolds number $k - \omega$ turbulence model predictions
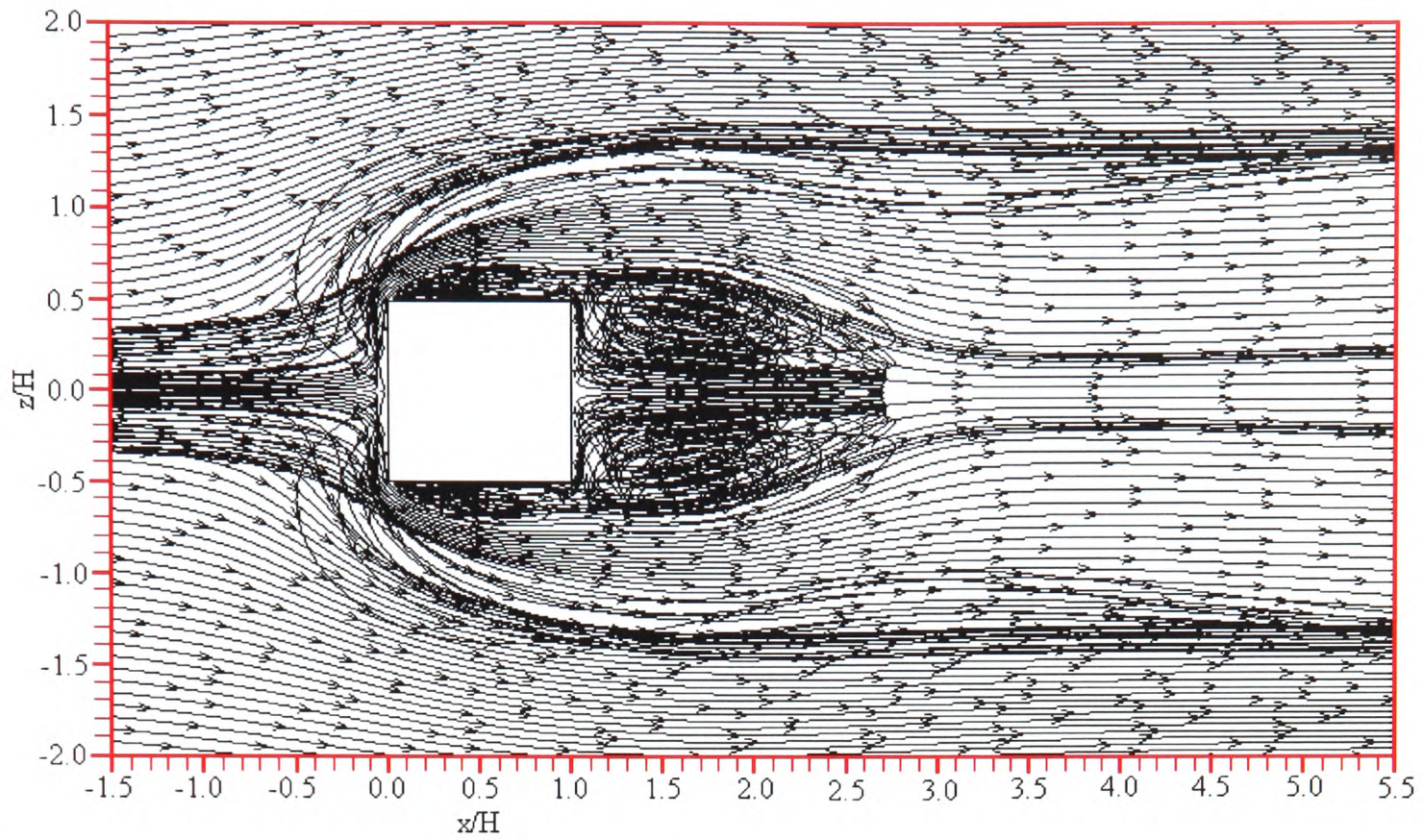
f. Two-layer SST turbulence model predictions
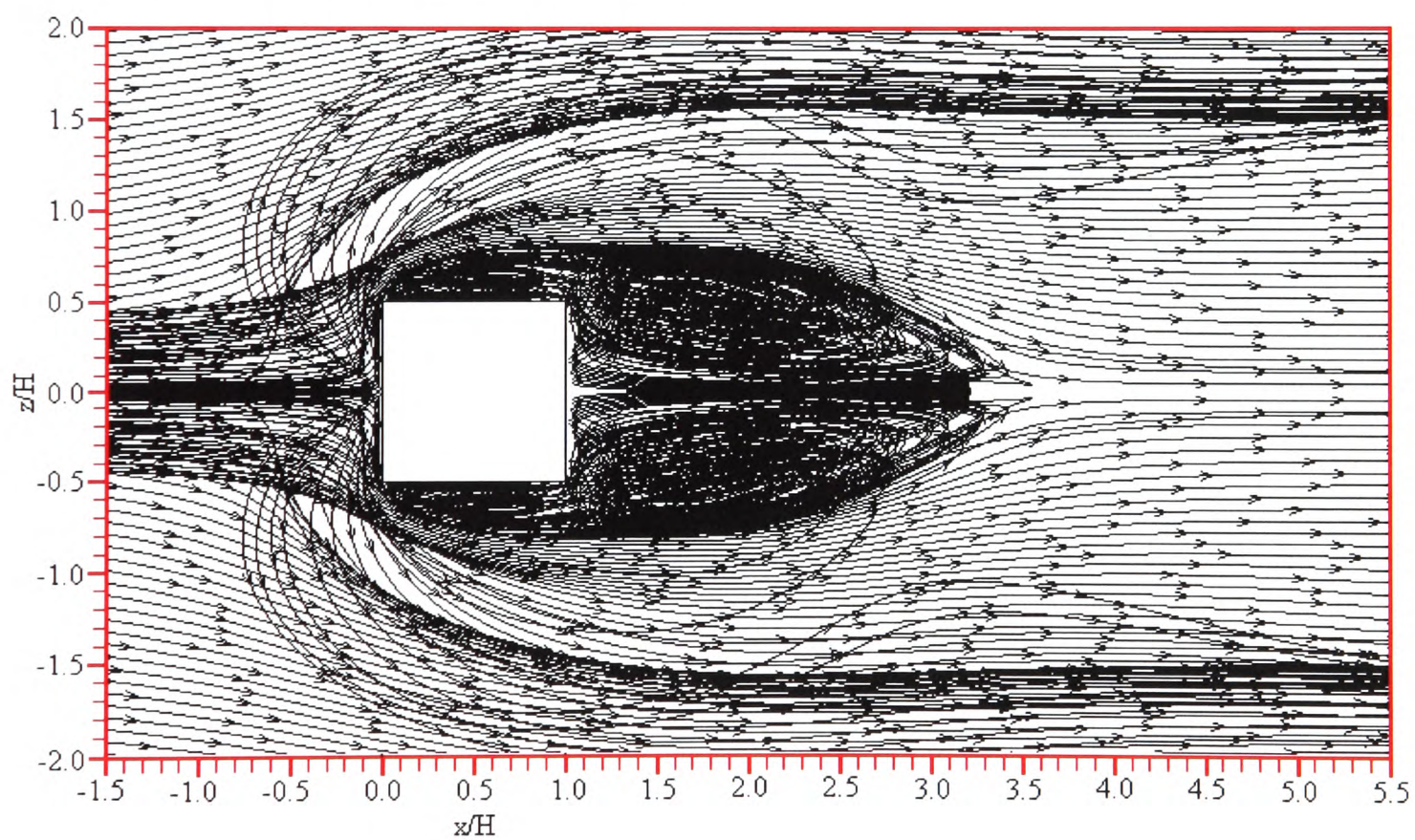
Figure 9.5 Streamlines of the mean flow on the base plate of the single cube channel (xz-plane)
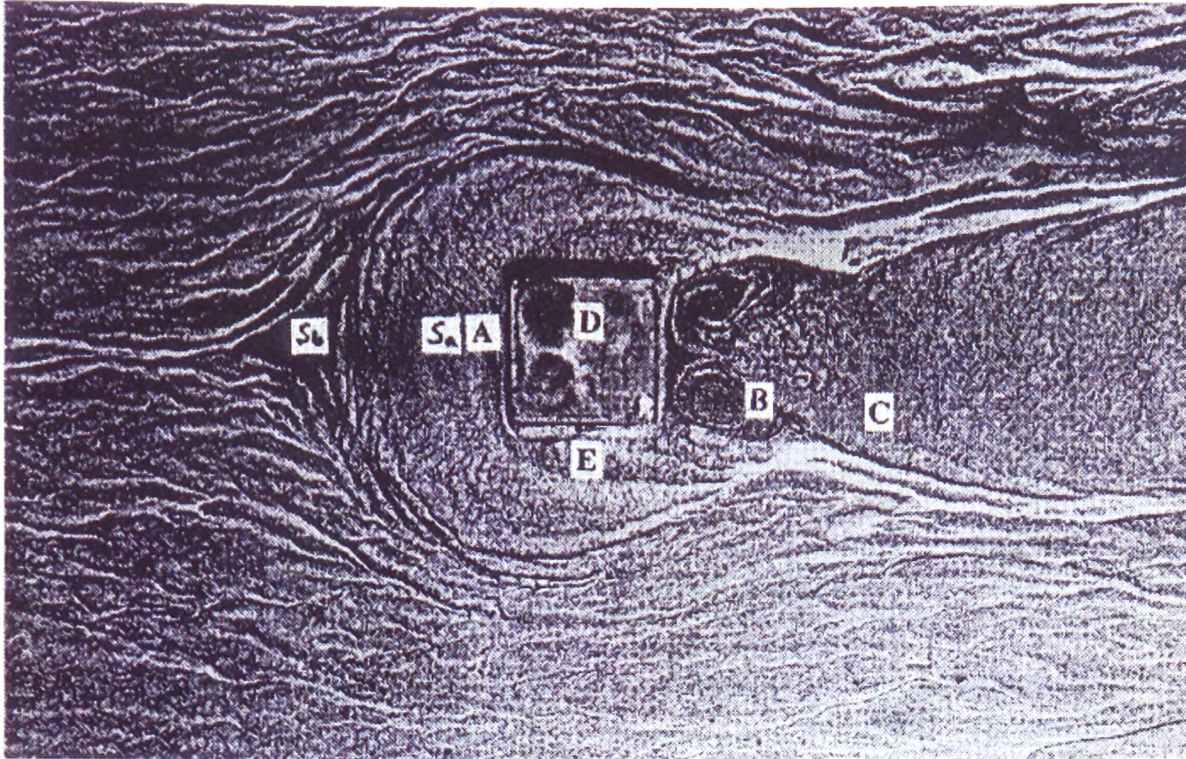
Figure 9.6 Oil-film visualisation of the surface flow pattern for the single cube in the turbulent flow channel $\left(\text{Re}_H = 8000\right)$ (Meinders[147])

To allow for some form of assessment of the streamline plots presented in Figure 9.4 (xy-plane) and Figure 9.5 (xz-plane) reference will be made to the oil-film visualisation plane provided in Figure 9.6. This oil-film visualisation was obtained for $\text{Re}_H = 8000$, however it has been noted by Meinders that for experiments at both lower and higher Reynolds numbers similar oil pattern observations were revealed.

Meinders concluded from the oil-film visualisation results presented in Figure 9.6 that the primary horseshoe vortex can be identified from the pigment pattern labelled **A**. The flow separation caused at this point resulted in the saddle point, labelled $\mathbf{S_a}$. A system of induced vortices is located upstream of the primary horseshoe vortex which extends up to the saddle point $\mathbf{S_b}$ that is located approximately $1.4H$ upstream of the windward face of the cube. The flow separation line originates at this saddle point and is delimited by the pigment line which is extended laterally and then further downstream of this point.

If analysis of Figure 9.4 and Figure 9.5 is undertaken firstly it can be concluded that all four flow features discussed earlier are reproduced, to some extent, by all six turbulent models investigated. The saddle point $\mathbf{S_b}$ located approximately $1.4H$ upstream of the windward

face of the cube can be assessed for the six investigated turbulence models. The numerical results for this saddle point have been detailed in Table 9.1.

Turbulence model	Approximate S_b
Oil film experiment	1.4H
LVEL	1.0H
LVEL_CAP	1.0H
Standard $k - \varepsilon$	0.6H
Two-layer $k\varepsilon/kl$	**1.4H**
Low Reynolds number $k - \omega$	0.7H
Two-layer SST	0.8H

Table 9.1 Turbulence model predictions for the saddle point S_b

Clearly the most accurate turbulence model for the prediction of the saddle point S_b is the two-layer hybrid $k\varepsilon/kl$ model. This is likely to be attributed to the one-equation turbulence model integrated within this model as the one-equation model is activated for the near-wall boundary layer flow within the hybrid model structure.

The two zero-equation models predict the saddle point to be located at $1.0H$ which is not a bad approximation. These two models are expected to predict the boundary layer features rather well as these models were originally designed for this class of flow. The standard $k - \varepsilon$ model is noted to perform most poorly, predicting a saddle point location of $0.6H$. To some extent this is not a surprising result as this model is known not to be well suited to such flow conditions that involve flow impingement, flow separation and vortex shedding.

The two vorticity concentration nodes labelled **B** shown in Figure 9.6 are the counter rotating footprints of the wake vortex. The shear layer separates at the top leading edge and reattaches approximately $1.5H$ downstream of the leeward face at $x/H = 2.5$ along the reattachment line labelled **C**. The counter rotating wake vortex is identified for all turbulence models. In order to assess model accuracy attention must be turned to the prediction of the reattachment point which has been summarised in Table 9.2.

Turbulence model	Reattachment point
Oil film experiment	2.5H
LVEL	3.0H
LVEL_CAP	3.6H
Standard $k - \varepsilon$	2.9H
Two-layer $k\varepsilon/kl$	**2.8H**
Low Reynolds number $k - \omega$	3.0H
Two-layer SST	3.5H

Table 9.2 Turbulence model predictions of the wake reattachment point

Again the turbulence model which produces the most accurate prediction is the two-layer hybrid $k\varepsilon/kl$ model. Closely followed by the standard $k - \varepsilon$ model. It is not surprising that the LVEL_CAP model produces the poorest predictions as mixing length models are not well suited to separated flow conditions.

The oil-film visualisation presented in Figure 9.6 also shows two vorticity concentration nodes labelled **D**, which are attributed to the footprints of the bound vortex. As can be seen from Figure 9.4 all the investigated turbulence models identify some form of recirculation vortex located on the top surface of the cube. The standard $k - \varepsilon$ model results shown in Figure 9.4c experience a very weak bound vortex on the top face which is not clearly displayed by the streamlines presented here. $k\varepsilon/kl$ and $k - \omega$ give realistic looking streamline plots. LVEL, LVEL_CAP and SST show too much separation, consistent with the wake reattachment over prediction.

The side vortex tubes labelled **E** in Figure 9.6 have origins at the node close to the leading edge corner on the base of the channel. Again all the turbulence models tested identified these side vortices. However, as with the bound vortex located on the top of the cube, the standard $k - \varepsilon$ model displays the least prominent vortex recirculation region on the side surfaces of the cube.

Overall it can be concluded from the streamline figures presented here that the two-layer hybrid $k\varepsilon/kl$ turbulence model most accurately predicts the flow features experimentally observed around this three-dimensional obstacle in a turbulent flow channel.

9.1.2 Results and Discussion: Velocity & Turbulence

A number of comparisons have been made against experimental data at particular measurement locations. All the experimental data have been extracted from Meinders' Ph.D. thesis manuscript using the data digitalisation program WinDIG[148] Version 2.5. This is a rather crude method of data extraction and therefore slight inaccuracies may exist.

The experimental measurement locations extracted represent profiles downstream of the cube and traversing around the cube itself. At certain measurement locations it has been possible to reconstruct the turbulent kinetic energy. Horizontal and vertical surface temperature paths have also been extracted around the cube for comparison.

It is noted that the profiles for the turbulent kinetic energy presented here have been reconstructed using the experimental data provided for the normal Reynolds stresses. Since the component $\overline{v'^2}$ was not measured for all configurations and measurement locations, this component was estimated using equation (9.1).

$$\overline{v'^2} = 0.5\left(\overline{u'^2} + \overline{w'^2}\right) \tag{9.1}$$

Substitution of equation (9.1) into the standard kinetic energy (per unit mass) associated with the turbulence stated in equation (9.2)

$$k = 0.5\left(\overline{u'^2} + \overline{v'^2} + \overline{w'^2}\right) \tag{9.2}$$

leads to the expression defined in equation (9.3).

$$k = 0.75\left(\overline{u'^2} + \overline{w'^2}\right) \tag{9.3}$$

Meinders concludes that although the Reynolds normal stresses are anisotropic this approach leads to reasonably accurate values for k.

Results at downstream measurement locations will be assessed first, before discussing comparisons around the cube. Turbulence model comparisons for the downstream measurement location at $x/H = 6.7$, $z/H = 0$ are presented in Figure 9.7.
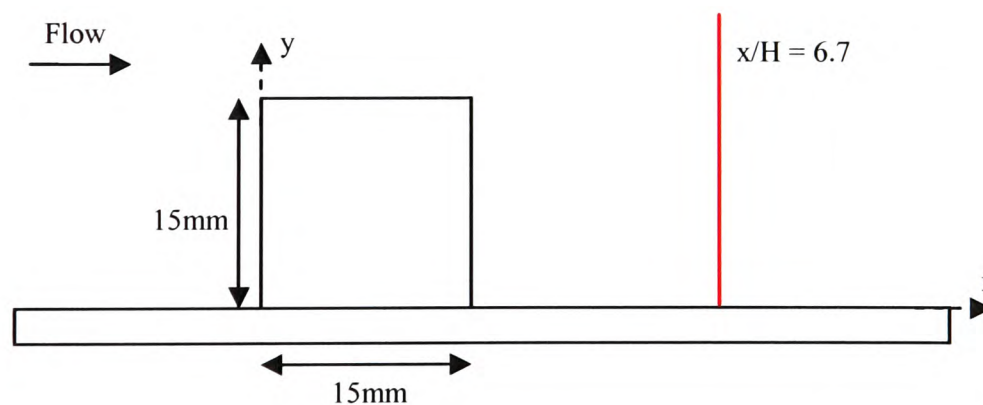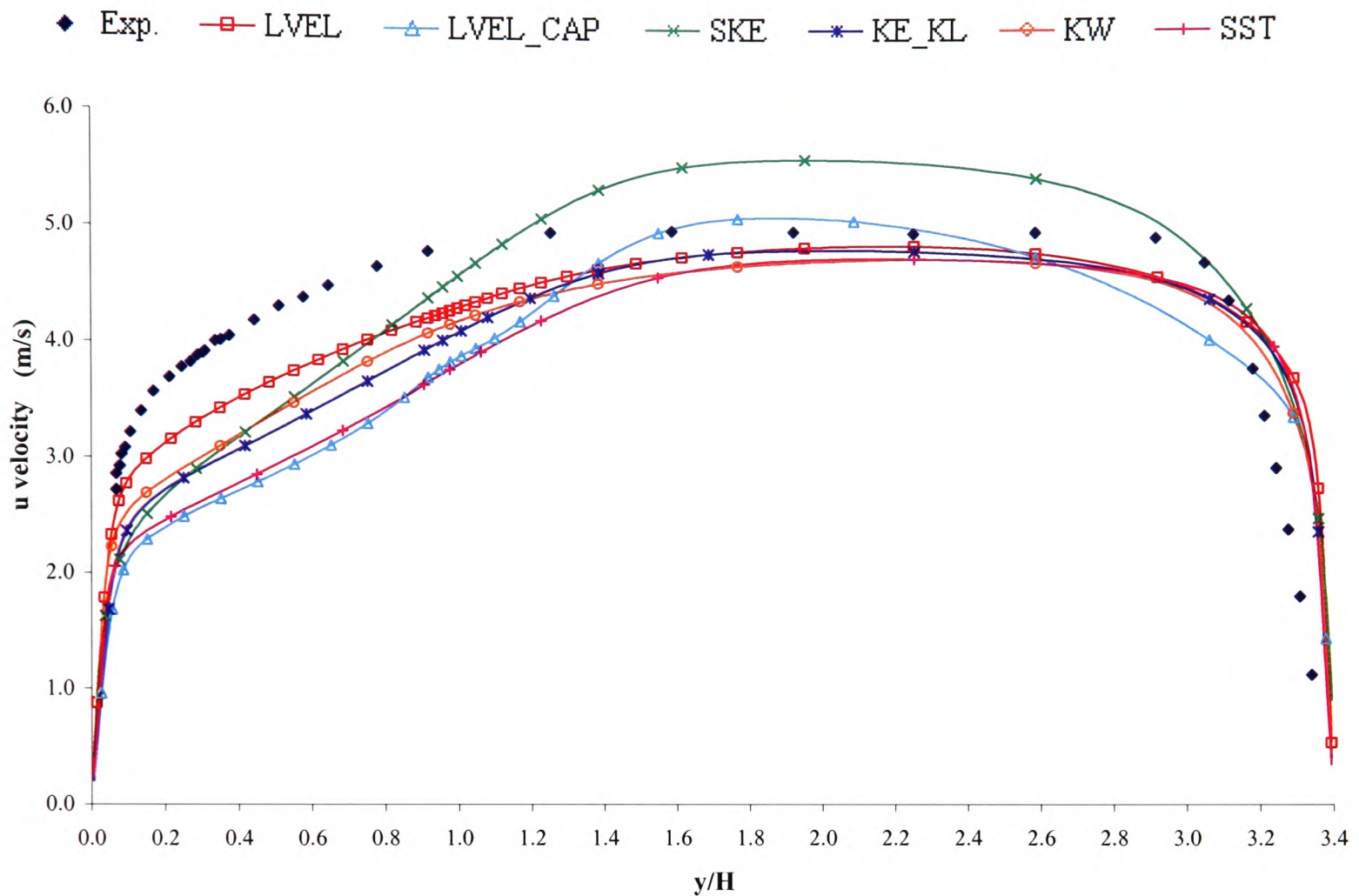
Figure 9.7 Turbulence model comparisons of the streamwise velocity profile located at
x/H = 6.7, z/H = 0

Due to the gradual redevelopment of the boundary layer in the downstream direction, the velocity deficit in the boundary layer resulted in an acceleration of the displaced flow in the core region (due to the incompressibility of the flow). The standard high Reynolds number $k-\varepsilon$ turbulence model clearly over predicts this flow acceleration affect contrary to the experimental data and all other models investigated. However all models fail to capture the

full redevelopment of the boundary layer at this location which is attributed, to some degree, to the over prediction of the reattachment point.

The model which may be considered to predict the profile most accurately with respect to the experimental data would be the zero-equation LVEL model, despite over-predicting the reattachment length.

Discussions will now be turned to the profiles traversing around the cube. These measurement locations would be considered to be of more interest to the electronics design community as flow inaccuracies in the vicinity of a heat dissipating component will directly affect the predictions of the rate of heat transfer from the component itself.

The streamwise velocity predictions for the five measurement locations at different heights at the front centreline of the cube are presented in Figure 9.8 with the reconstructed turbulent kinetic energy distributions shown in Figure 9.9.
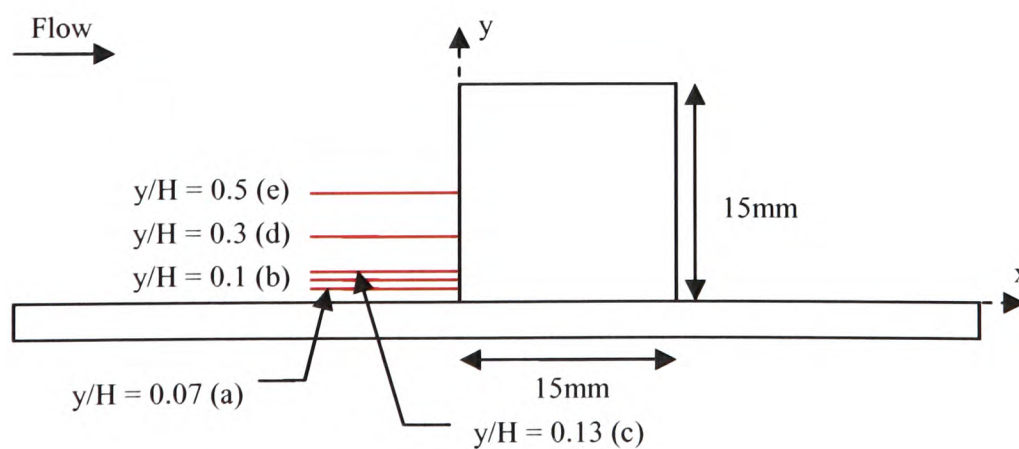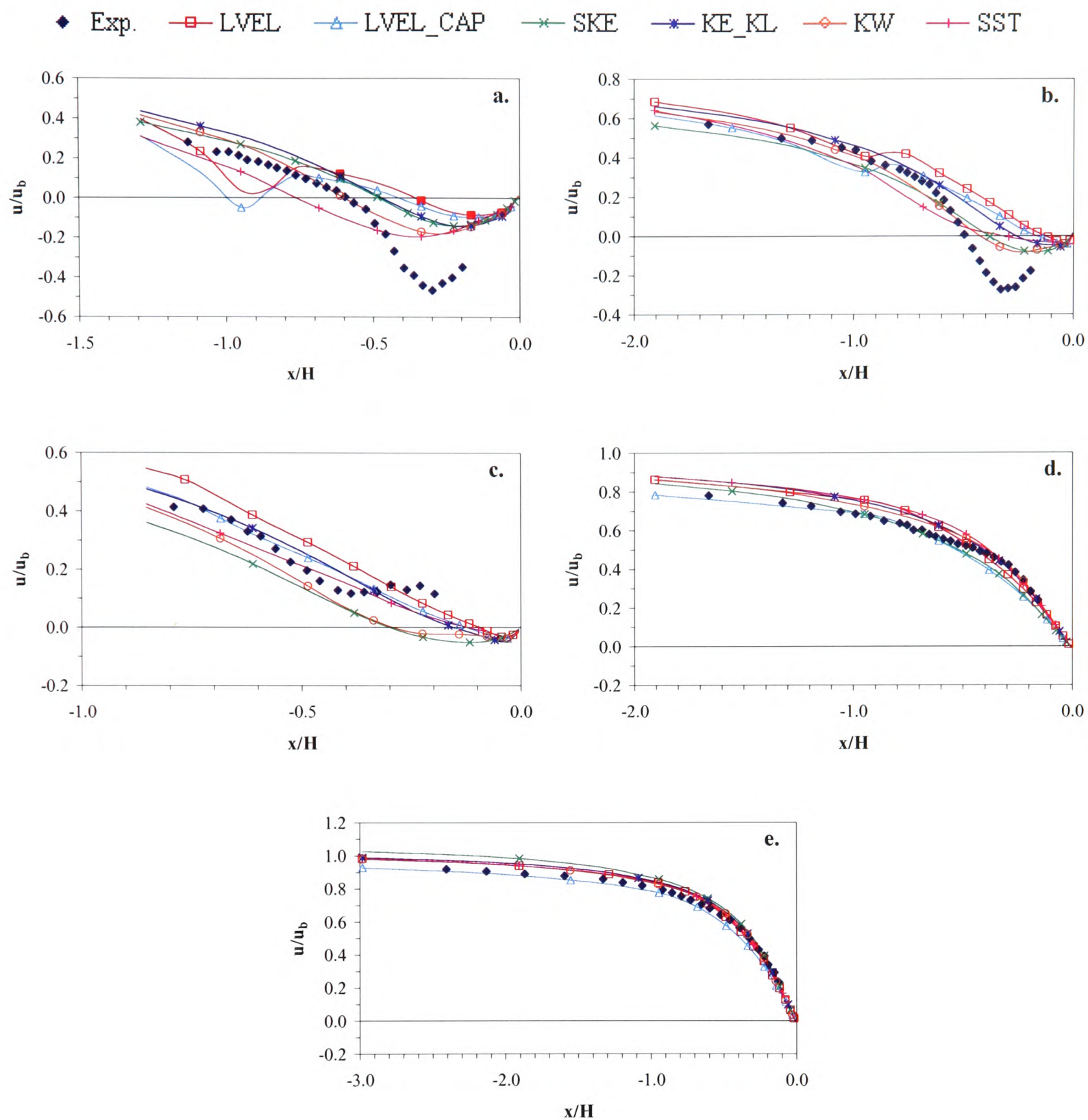
Figure 9.8 Turbulence model comparisons of the streamwise velocity profiles located upstream of the cube along the symmetry plane z/H = 0

Figure 9.9 Turbulence model comparisons of the turbulent kinetic energy profiles located upstream of the cube along the symmetry plane z/H = 0

Experimentally the location of the horseshoe vortex can be identified as the region of negative streamwise velocities, this suggests that the vortex extends upstream of the cube to approximately $0.5H$. Vertically the detection of the horseshoe vortex is non-existence by the third measurement location of $y/H = 0.13$, $z/H = 0$.

Numerically the speed of the recirculation vortex is not captured well by any of the turbulence models. The reattachment point is most accurately predicted by the low Reynolds number $k - \omega$ model. This is likely to be due to the concentration of computational mesh in the near-

wall region and the overall structure of the model. Using the same reasoning one would therefore expect that the SST model would also predict the upstream reattachment point just as well as the $k - \omega$ model due to the two-layer structure of the model. However referring to Figure 9.8a it can be seen that this is clearly not the case. The over prediction of the SST model therefore must be attributed to the blending techniques used within this model for this particular configuration.

Once the vertical height has exceeded the horseshoe vortex all turbulence models predict the overall trends in the experimental data rather well. However Figure 9.8c shows that all the investigated turbulence models at this location still predict a slight recirculation vortex which is contrary to the experimental data. Figure 9.8d and e suggest that the LVEL_CAP turbulence model is producing the most accurate predictions at these locations upstream of the cube. This is a reasonable conclusion to draw as the boundary layer was probably accurately predicted by this LVEL-based model.

The reconstruction of the turbulent kinetic energy based on equation (9.3) has only been undertaken for three of the five measurement locations. As the required experimental velocity fluctuations $\left(\overline{u'^2}, \overline{w'^2} \right)$ were not available at all measurement locations.

The peak in the experimental turbulent kinetic energy data seen in Figure 9.9b is identified to be in the proximity of the horseshoe vortex and is due to the large velocity gradients present in this region. The peak in the experimental data is under predicted by all turbulence models. For the remaining measurement locations presented in Figure 9.9 the zonal models $k\varepsilon / kl$ and SST are noted to perform well.

The streamwise velocity and the turbulent kinetic energy profiles at five y / H locations downstream of the cube along the symmetry plane are given in Figure 9.10 and Figure 9.11 respectively.
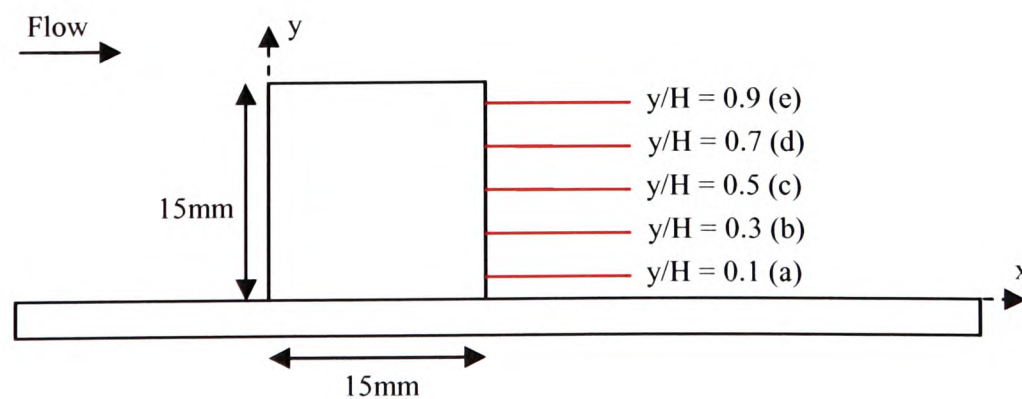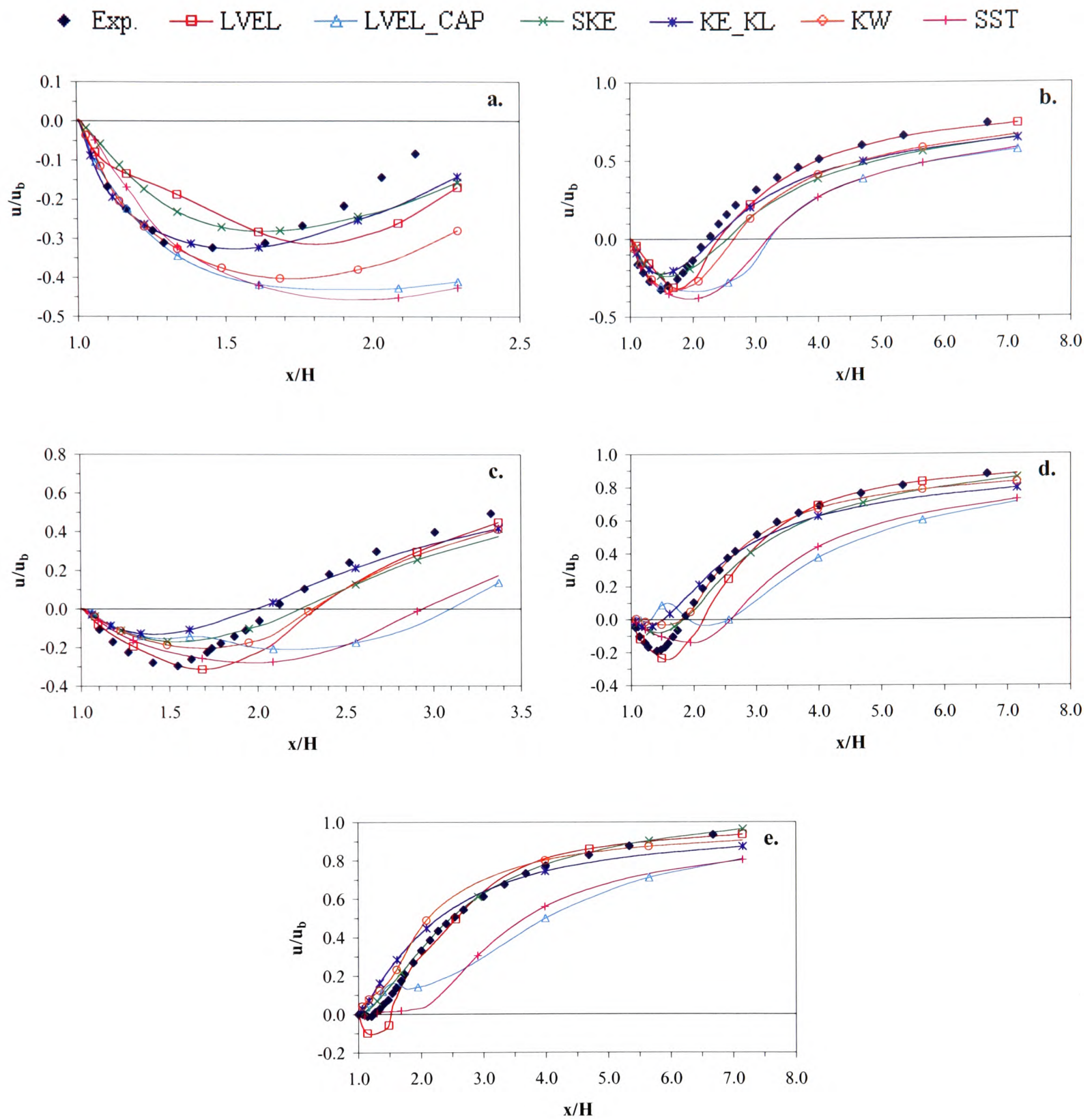
Figure 9.10 Turbulence model comparisons of the streamwise velocity profiles located downstream of the cube along the symmetry plane z/H = 0
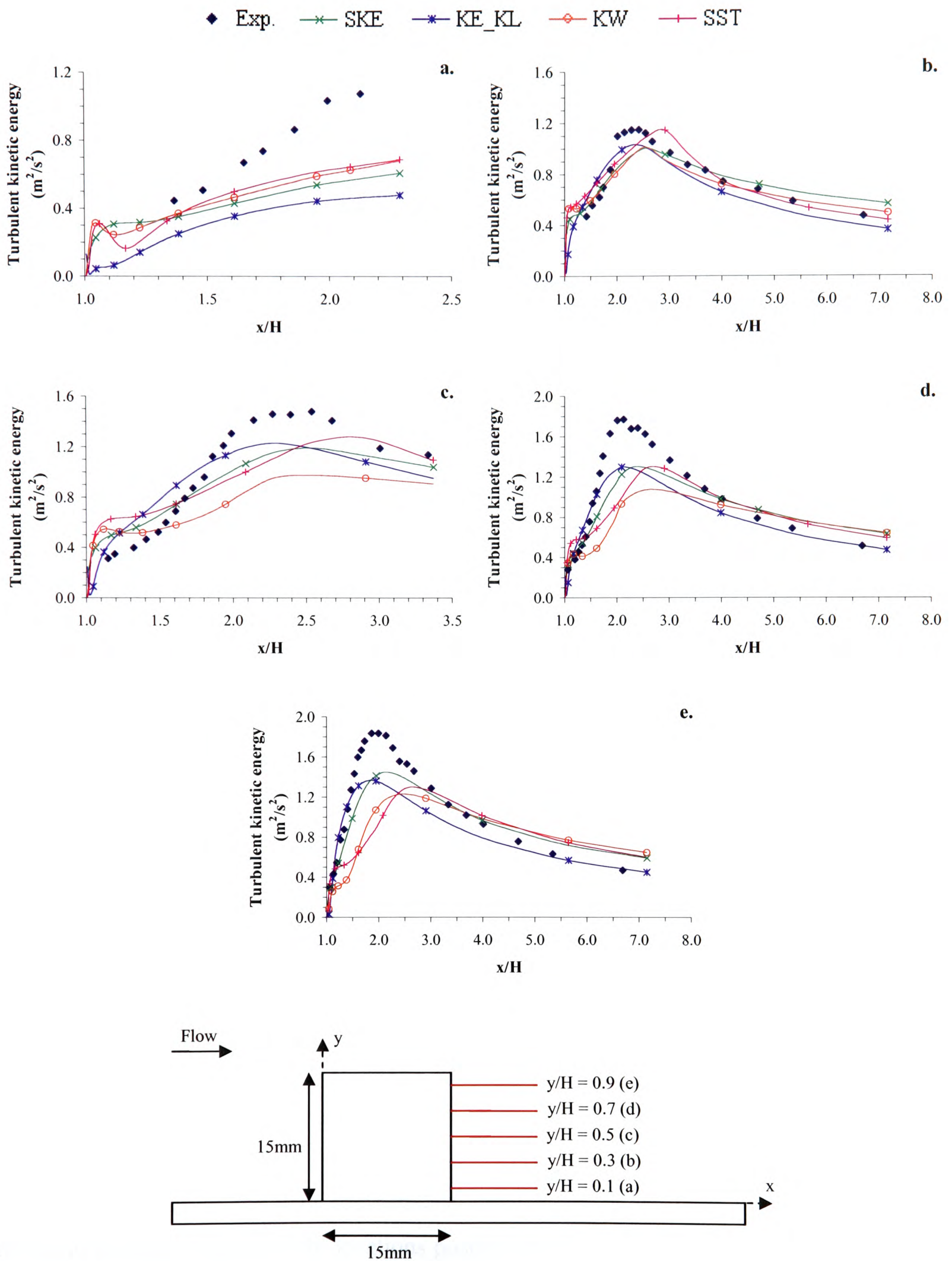
Figure 9.11 Turbulence model comparisons of the turbulent kinetic energy profiles located downstream of the cube along the symmetry plane z/H = 0

Experimentally the arch-shaped vortex is identifiable from the negative velocities displayed in Figure 9.10. The line where the velocities change sign is referred to as the separation line.

Meinders derived the reattachment point at the channel floor from an extrapolation of the separation line and determined that the reattachment point occurred at $x/H = 2.4 - 2.5$, which is in good agreement with the oil-film visualisation presented in Figure 9.6.

Figure 9.10a shows that the two-layer $k\varepsilon/kl$ predicts the experimental points most accurately, which echoes the conclusions drawn from the streamline planes discussed earlier. Figure 9.10b clearly shows the over prediction in the horizontal size of the arch vortex determined by the LVEL_CAP and SST models. It can also be concluded that the LVEL model is recovering well after the interaction with the cube; this also stands true for the velocity profile locations presented in Figure 9.10c and d.

The final velocity profile (Figure 9.10e) at $y/H = 0.9$, $z/H = 0$ is located in the shear layer. The LVEL model is still experiencing the recirculation of the arch vortex contrary to the experimental data and all other turbulence models investigated. The predictions of the LVEL_CAP and the SST models reiterate that these models experience a larger recirculation vortex and therefore predict slower velocity values at this location. The standard $k - \varepsilon$ model predictions at this location would be considered the most accurate agreeing well with the experimental data.

All turbulence models replicate the overall trend of the experimental data for the measurement locations presented in Figure 9.11 to some extent. As would be expected it can be determined from Figure 9.11d and e that higher levels of turbulent kinetic energy are seen in the shear layer profiles $y/H = 0.7$ and 0.9. The stronger velocity gradients cause high shearing and thus an increase in the level of turbulent production. It can be determined from the results presented that the two-layer $k\varepsilon/kl$ model seems to agree most strongly with the experimental turbulent kinetic energy data profiles displayed here.

Still concentrating on the data comparisons downstream of the cube our attention is now turned to the three measurement locations positioned at a constant height of $y/H = 0.5$ with distance increments taken in the z-direction. The experimental data available at these three measurement locations only allowed for the reconstruction of the turbulent kinetic energy.
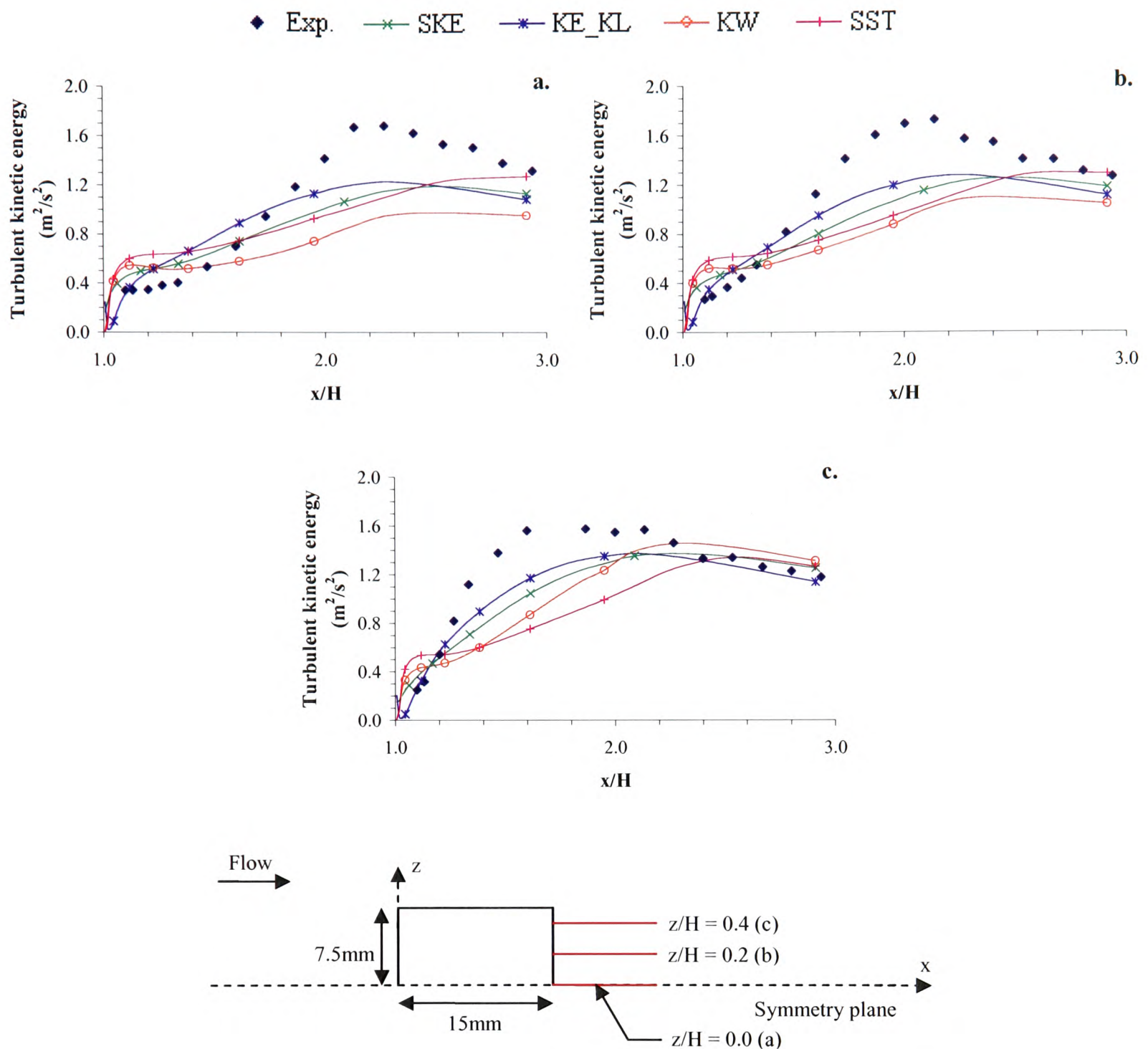
Figure 9.12 Turbulence model comparisons of the turbulent kinetic energy profiles located in the wake of the cube at y/H = 0.5

Although all the models considered predict the trends in the experimental data it can still be concluded that the two-layer $k\varepsilon / kl$ turbulence model is in greatest agreement with the data presented at these measurement locations.

Traverses of the streamwise velocity and the turbulent kinetic energy at the top centreline of the cube at different values of x / H are plotted in Figure 9.13 and Figure 9.14 respectively.
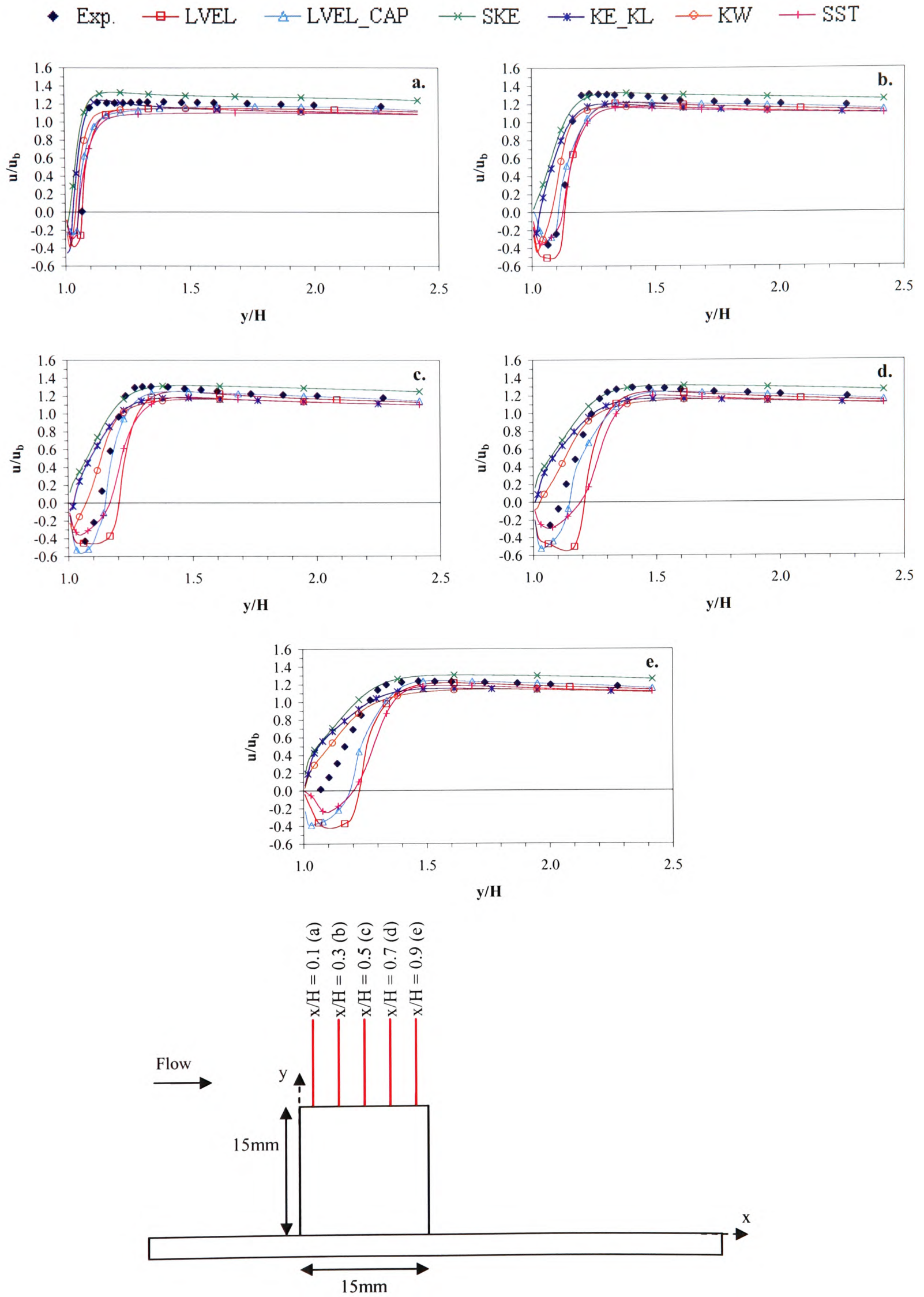
Figure 9.13 Turbulence model comparisons of the streamwise velocity profiles located at the top of the cube along the plane z/H = 0

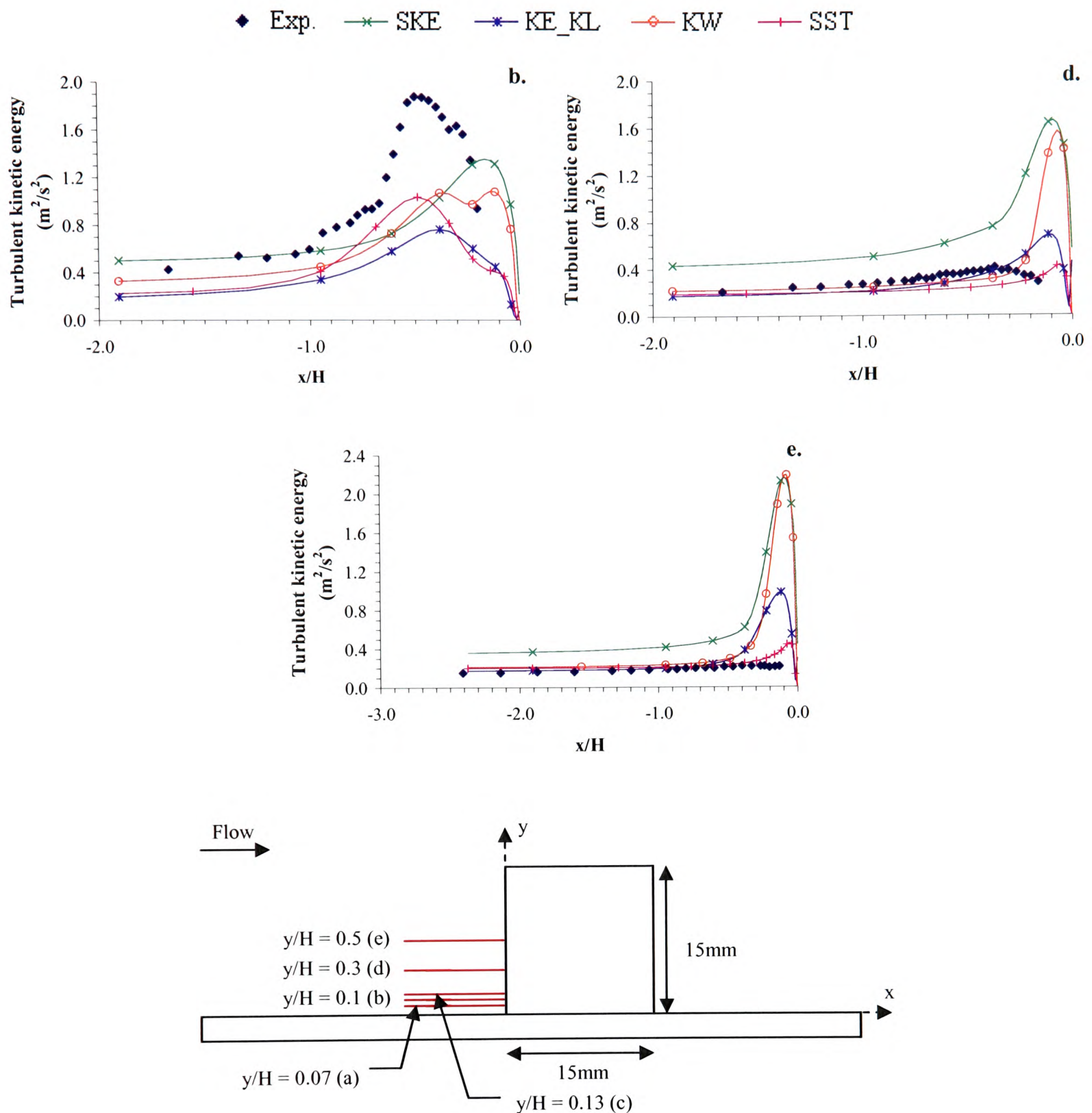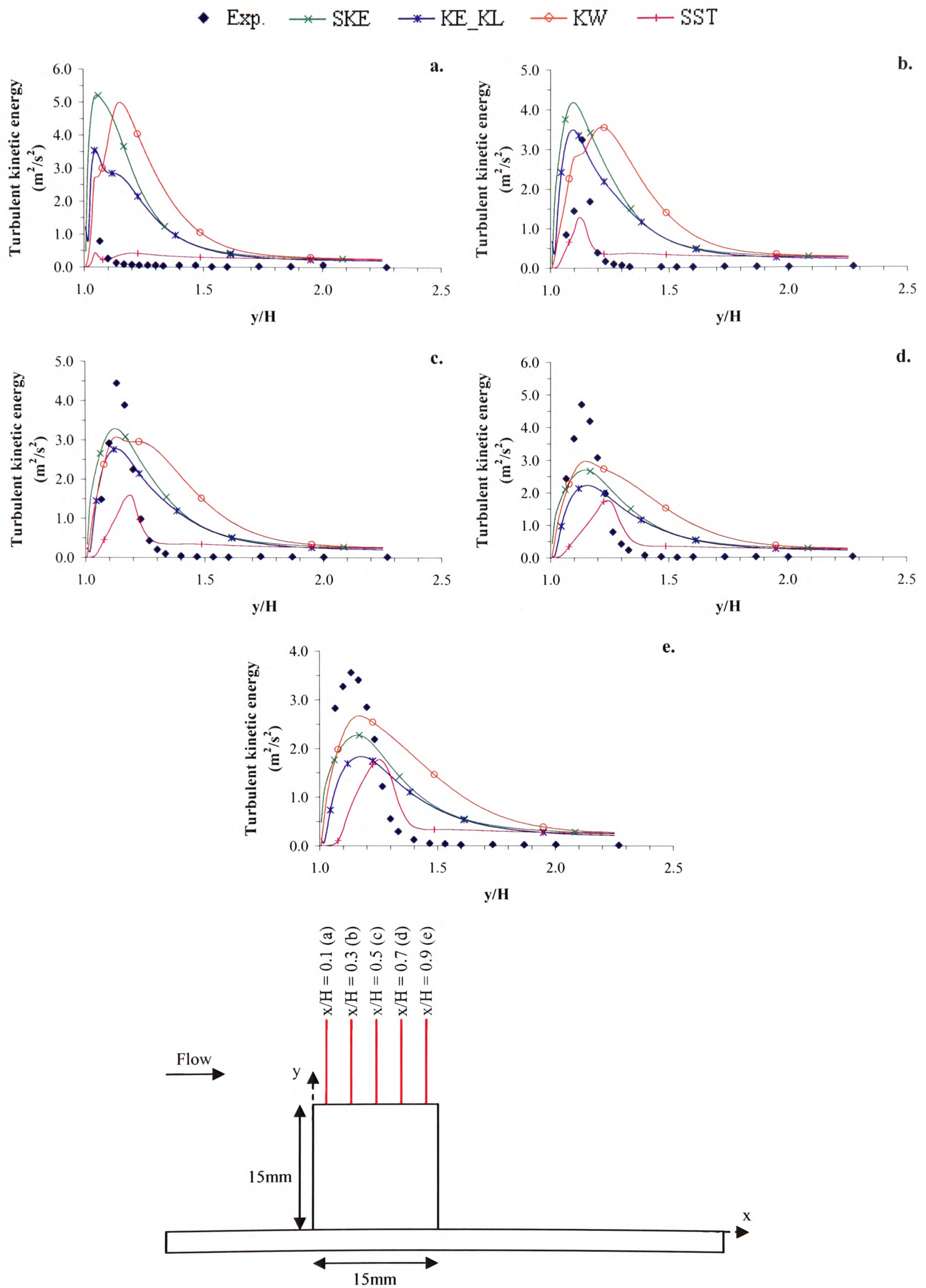**Figure 9.14 Turbulence model comparisons of the turbulent kinetic energy profiles located at the top of the cube along the plane z/H = 0**

Experimentally it can be determined that a strong recirculation bubble progresses in the downstream direction where the largest negative velocities are observed for the measurement location $x/H = 0.5$. Figure 9.13a shows the model predictions as the flow initially encounters the leading top edge of the cube. All turbulence models at this location are in fairly good agreement with the experimental data with the LVEL model predicting the top reattachment point most accurately.

The two-layer $k\varepsilon/kl$ model is the only model which manages to accurately predict the speed of the flow immediately above the bound vortex. Consistent with the conclusion that was drawn from the streamline analysis conducted earlier that the standard $k - \varepsilon$ model predicts a weak recirculation vortex on this face is reiterated here. The knock-on effect of this weak prediction of the bound vortex by the $k - \varepsilon$ model is the consistent over prediction of the axial velocity over the top of the cube for all measurement locations considered on this face.

Figure 9.13e clearly shows that three of the six tested models: LVEL, LVEL_CAP and SST predict a bound vortex which is too high in comparison to the experimental data which has reattached by this location as u/u_b is positive, for all y/H.

The profiles of the turbulent kinetic energy presented in Figure 9.14 show maxima at approximately $0.13H$ above the top wall of the cube. All turbulence models predict an increase in the turbulent levels around the stated maxima but none of the models fully capture the phenomena noted.

The final velocity and turbulent kinetic energy comparisons are located on the side of the cube at a vertical height of $y/H = 0.5$.
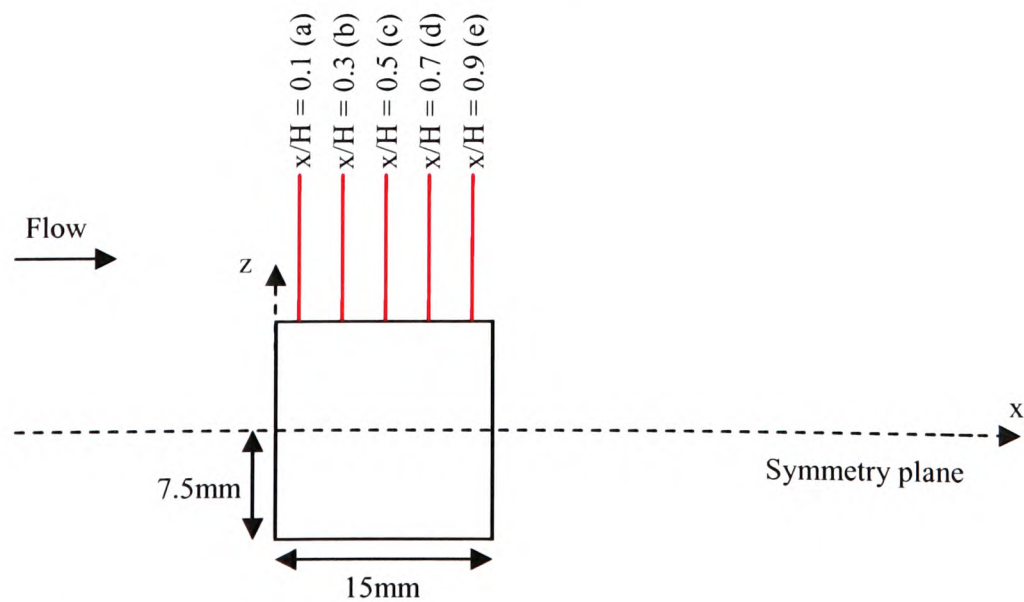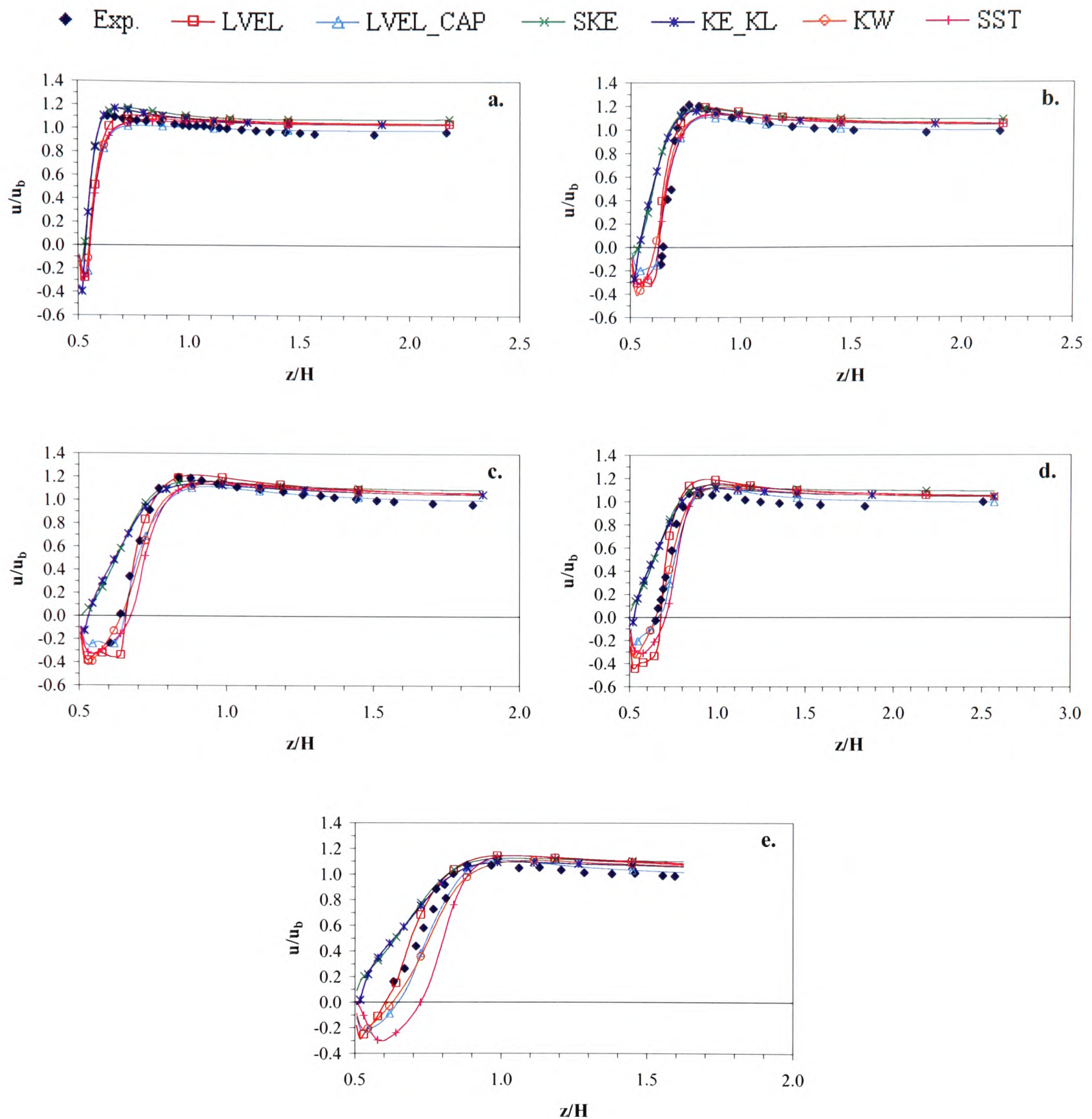
Figure 9.15 Turbulence model comparisons of the profile locations traversing in the spanwise direction at the lateral face of the cube at y/H = 0.5 u-velocity
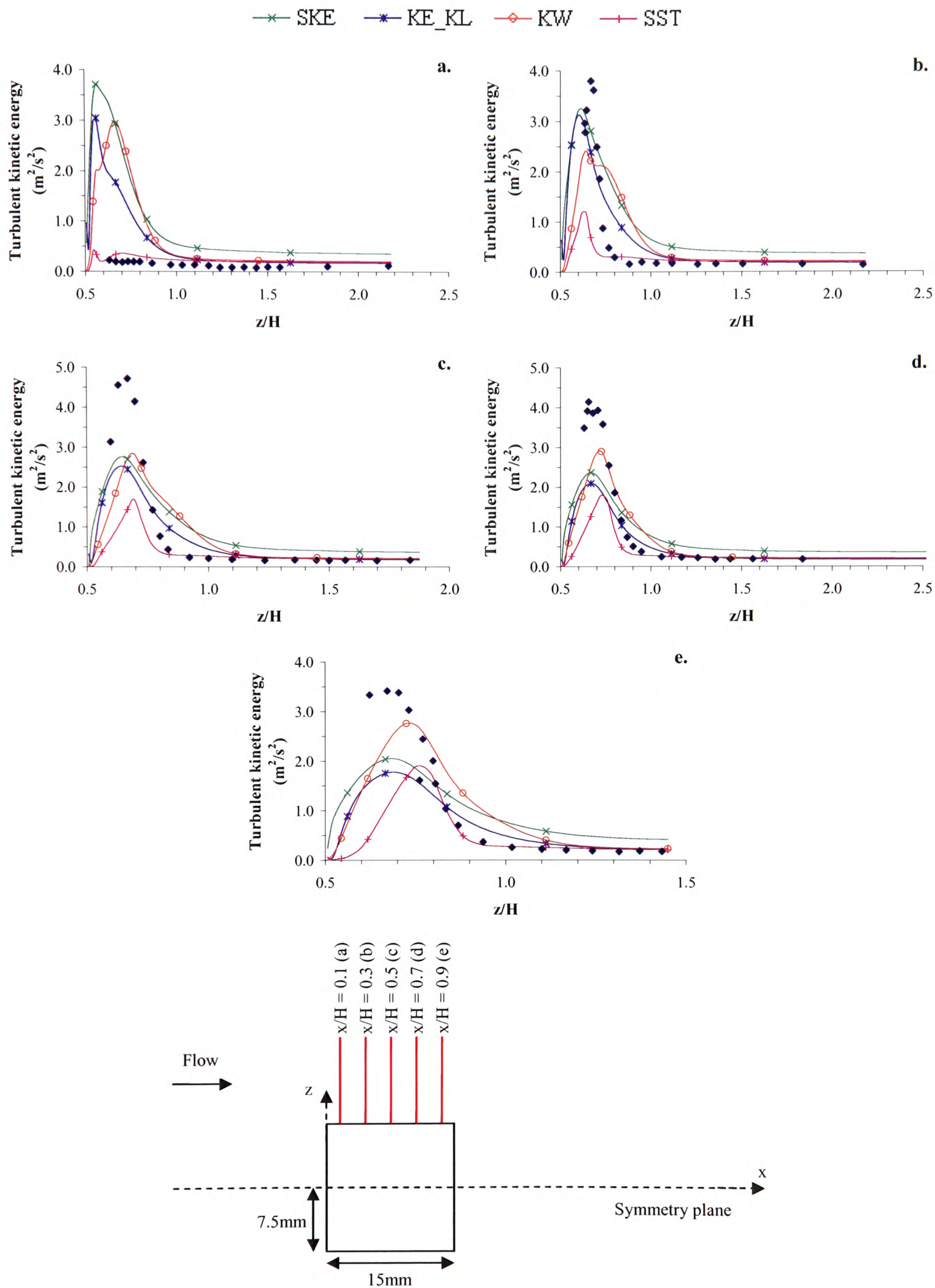
Figure 9.16 Turbulence model comparisons of the profile locations traversing in the spanwise direction at the lateral face of the cube at y/H = 0.5 turbulent kinetic energy

Experimentally it was noted that negative velocities extend to approximately $x/H = 0.75$. Assessing Figure 9.15d, which is the closest experimental profile available to $x/H = 0.75$, it can be concluded that the standard $k - \varepsilon$ model fails to predict any recirculation effect at all for this face. The two-layer $k\varepsilon/kl$ model is noted to predict a small side vortex at this location but the remaining turbulence models considered produce results which are of greater accuracy in comparison to the experimental data but nevertheless fail to close the side recirculation vortex across the entire face. The low Reynolds number $k - \omega$ model manages to predict the reattachment point well, but over predicts the peak axial velocity towards the core of the channel. Overall the LVEL_CAP model would be considered the most accurate model at this one location predicting the reattachment point and the core channel flow region rather well.

However when analysis of Figure 9.15e is undertaken it is clear that the side vortex has managed to reattach itself, but the majority of the turbulence models tested predict a side vortex which covers the entire face contrary to the experimental observations. Only the standard $k - \varepsilon$ and the two-layer $k\varepsilon/kl$ models show that the side vortex has reattached. Due to the fact that the $k - \varepsilon$ model has been noted to reattach too quickly this leads to the conclusion that **the $k\varepsilon/kl$ turbulence model would be considered favourite at the measurement location.**

The levels of turbulent kinetic energy have been presented in Figure 9.16. As expected the higher turbulent kinetic energy values are noted close to the side face of the cube and are due to the presence of the shear layer. All models fail to capture the experimental peaks displayed. Moving towards the core of the channel the SST model is noted to produce the most accurate results for all five measurement locations, but most severely fails to capture the experimental peak in the data in comparison to the other models tested.

9.1.3 Results and Discussion: Temperature

As mentioned earlier on in this chapter turbulence model comparisons have been undertaken for the horizontal and vertical surface temperature paths around the cube. Discussion will now be turned to these predictions. Figure 9.17 corresponds to the cross-section ABCDA which denotes a plane parallel to the mounting base at $y/H = 0.5$. Figure 9.18 corresponds to the

cross-section ABCD denoting a plane perpendicular to the mounting base at the symmetry plane $z / H = 0$.

As analysis is undertaken of the horizontal and vertical temperature profiles shown in Figure 9.17 and Figure 9.18 respectively it is worth noting that if inaccuracies exist in the flow domain these will also filter through to the temperature domain, suggesting that an initial temperature result forecast can already be made for the LVEL-based and standard $k - \varepsilon$ models. It has been shown these models poorly predict the actual flow phenomena taking place within the system, suggesting that these models are likely to demonstrate poor temperature predictions.
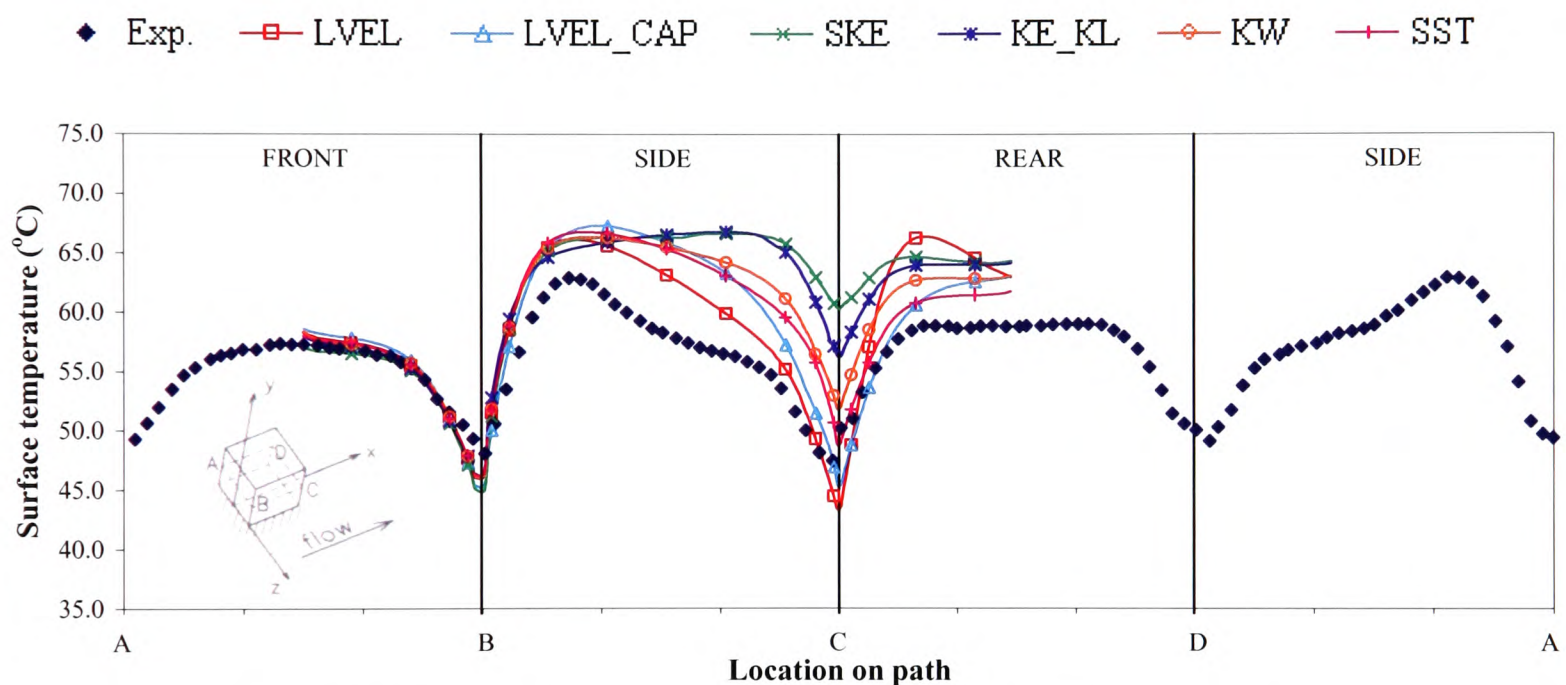
Figure 9.17 Horizontal surface temperature profile along the path ABCDA
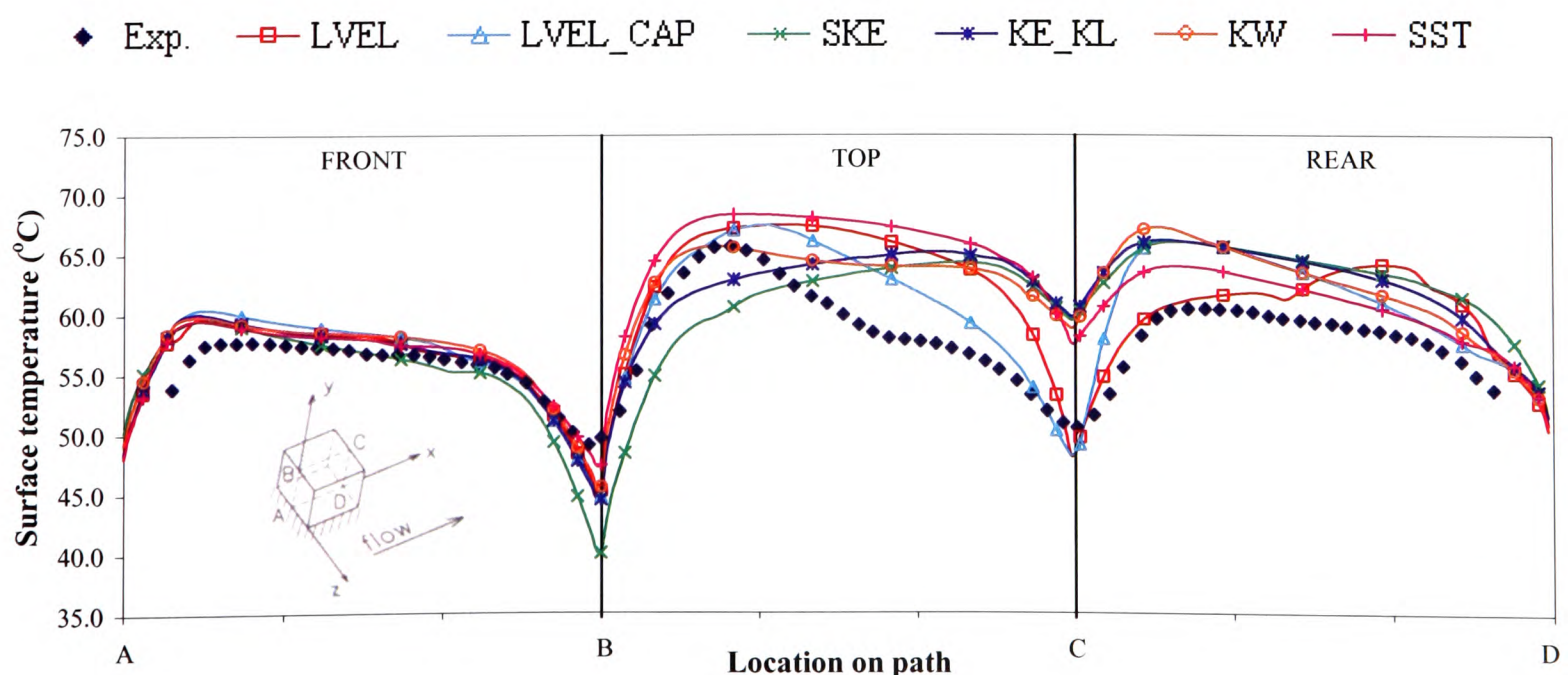
Figure 9.18 Vertical surface temperature profile along the path ABCD

A short note is made here with regards to the vertical experimental data profile presented in Figure 9.18. Meinders[149] states in his Ph.D. thesis that:

"It was impossible to measure accurately the temperature distribution with sufficient spatial resolution for the interface between the base plate and the cube. One can think of thermocouple measurements, but the resolution can never compete with that obtained from the thermography measurements. Therefore, the epoxy layer between the base plate and the copper core was imaginary removed from the computational domain. The temperature distribution of this imaginary plane was composed of the copper temperature for the mid-plane (the square mid-section of size 12 × 12 mm) and a linear interpolation between the surface temperature of the outer wall and the copper temperature. The remaining numerical domain consisted of the copper core inclusive the epoxy layer covering the top and the four side faces. The dimensions of the computational domain were then 15 × 13.5 × 15 mm."

Therefore the experimental measurements were not available for the complete height of the cube, stopping 1.5mm short of the base plane. However the CFD predictions have been presented for the complete cube height of 15mm. This explains the slight shift in the path locations detailed in Figure 9.18.

As assessment of temperature results is being embarked upon one would expect the predictions obtained at the front face of the cube to be in greatest agreement with the experimental data as this is the first face to come in contact with the flow field. As the flow continues downstream one would expect the numerical discrepancies to increase as the flow field becomes less stable and errors accumulate. This behaviour can be clearly identified for both the horizontal and the vertical paths presented here.

At the front face of the cube on the vertical path (see Figure 9.18) a very slight dip in the experimental data is seen approximately half way up this face which corresponds to the stagnation point on this face (see Figure 9.4) where cold turbulent flow impinges onto the surface. The resulting high heat transfer coefficient and cold fluid lowers the surface temperature. All the turbulence models under investigation fail to capture this slight reduction in the temperature values and instead predict the reverse effect of higher temperature values.

The shear stress analogy wall functions implemented within PHYSICA and other codes are only appropriate for boundary layer flows. Therefore as the shear stress at the reattachment point is low, a low heat transfer coefficient is calculated which means higher temperature values are predicted. Generalised wall functions.[64, 78, 79, 80, 81, 82, 83, 84] would be required within PHYSICA to better capture the heat transfer around reattachment points. However it is noted that the impact of this on the predicted results is small relative to the models abilities to predict the overall trends in the surface temperature.

The side face in Figure 9.17 and the top face in Figure 9.18 show evidence of the presence of the vortices adjacent to these faces. The side face initially experiences high temperature values due to the trapped hot fluid in the side recirculation region. The reattachment point at this face has been experimental determined to be located approximately at $x/H = 0.75$. The standard $k - \varepsilon$ and two-layer $k\varepsilon/kl$ show temperature increasing across the central region of the face, consistent with little or no separation having occurred. All other turbulence models predicted that the recirculation vortex extends along the entire side face resulting in temperature profiles that are more consistent with the experimental results.

Experimentally it has been determined that the top face of the cube shown in Figure 9.18 experienced a large bound recirculation bubble which trapped hot fluid, resulting in higher temperature values over this part of the face. The reattachment point for this surface occurred at some point after $x/H = 0.7$. The LVEL and LVEL_CAP models predict a bound vortex which extends over the entire top surface of the cube. Figure 9.4a and b show that in both cases the vortex appears to have become detached from the surface. The closer agreement seen for the LVEL_CAP model is noted, but not due to good flow prediction. The only turbulence model to show a slight inflection in the temperature profile for this face is the low Reynolds number $k - \omega$ model. This inflection is seen to correspond to the bound vortex reattachment point predicted by this model, as shown in Figure 9.4e.

By the time the flow field has reached the rear face of the cube highly irregular motion is expected which therefore suggests that the surface temperature predictions made by any of the RANS-based turbulence models investigated here is likely to be poor. From the horizontal and vertical temperature profile predictions it is indeed true that poor results are noted, but the overall trend in the experimental data can be identified.

A short comment is provided regarding the numerical predictions of the surface temperature at the edges of the cube; this will be expanded upon later in the Matrix of Cubes section where other numerical work can be assessed.

Meinders used Infrared Thermography (IR) to measure the steady-state surface temperature distribution of the cube. He notes that care must be taken when using this technique for surface temperature measurements near to the extremities of small heated three-dimensional obstacles as unacceptable errors may occur. Consequently the experimental uncertainties are greater at the edges of the cube.

9.1.4 Single Cube Concluding Remarks

The key conclusions drawn from this low Reynolds number single cube configuration are stated below.

- The streamline predictions of the saddle point S_b and the wake reattachment point is most accurately predicted by the two-layer hybrid $k\varepsilon/kl$ turbulence model.

- From the range of turbulence models investigated, it can be concluded from the streamline figures that the two-layer hybrid $k\varepsilon/kl$ turbulence model most accurately captures the flow features observed around this three-dimensional obstacle in a turbulent flow channel.

- The upstream reattachment point is most accurately predicted by the low Reynolds number $k-\omega$ model (see Figure 9.8) but, at the expense of higher computational costs.

- The standard high Reynolds number $k-\varepsilon$ model predicts extremely weak bound and side recirculation vortices.

- Generally flow velocity predictions are closer to experiments than temperature predictions.

- There are uncertainties as to the accuracy of experimental temperature measurements near the edges of the cube, where large discrepancies exist.

- Identifying one superior turbulence model for this test configuration is a difficult task as each tested model has its own advantages and disadvantages. An ideal turbulence model would be one that predicts reasonable results for the whole solution domain rather than a model which is only accurate within a small sub-section of the domain. Also taken into consideration are the computational expenses and data storage capacity required by the model, which is a key parameter for this particular application field as users of commercial CFD software within the electronics industry don't have the time to spend on highly accurate but computationally expensive simulations. Consequently on balance the two-layer hybrid $k\varepsilon/kl$ turbulence model was selected as the most accurate model amongst the turbulence models tested. The results from a more realistic case study are required to substantiate the conclusions drawn here. For this reason the matrix of cubes was the next test case investigated.

9.2 Matrix of Cubes

This case study served as a reference dataset for the validation of numerical simulations on three occasions at ERCOFTAC workshops held at Delft University of Technology,[41] the University of Manchester[42] and Helsinki University of Technology.[43]

The experimental domain consists of a single heated cube in an equidistantly-spaced matrix array of wall-mounted cubes placed on the base plate of a rectangular wind tunnel. The tunnel dimensions are specified as having a channel height of 51mm and a width of 600mm. The base plate and the structure of the cubes take the same form as that specified for the single cube case discussed in the previous section. The Reynolds number based on the bulk velocity and the cube height is $\mathrm{Re}_H = 3854$. The complete matrix consists of 25 x 10 cubes in the streamwise and spanwise directions respectively which caused periodic turbulent flow far downstream in the matrix. A schematic sub-section of the array is shown in Figure 9.19.

A summary of the case is provided below. A full specification is given in Appendix A7.2.

x, y, z: Co-ordinate axis

H: Dimensions of cubes = 15mm

h: Channel height = $3.4H$

S: Pitch of cubes = $4H$

U_b: Bulk velocity = 3.86m/s
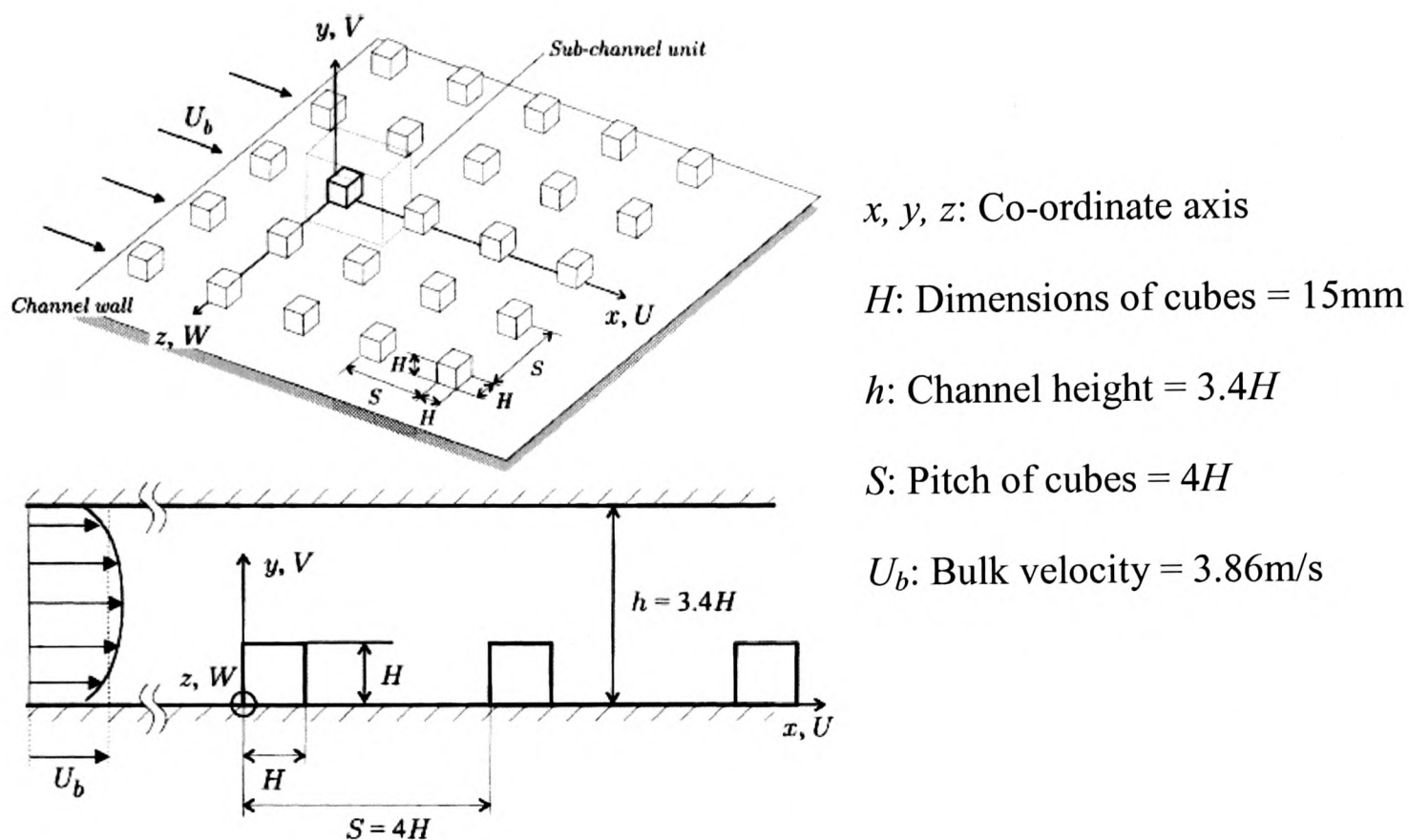
Figure 9.19 Three-dimensional representation of the matrix array of cubes on the channel base plate (upper plot) and the side view of the configuration (lower plot). (Meinders[150])

Note that the sub-channel unit shown in Figure 9.19 is merely an example for the choice of computational domain and the x- and y-axis have been taken in the streamwise and wall-normal directions respectively with the z-axis denoting the spanwise direction.

Fluid flow and heat transfer measurements have been taken around the 18th row from the inlet, at mid-height of the channel. For this location, the flow was observed to be fully developed in the streamwise direction and symmetric in the spanwise direction which facilitates the use of periodic boundary conditions for the computational work undertaken at the two workshops.

For the simulations work undertaken here both the inlet and outlet domain boundaries did not use periodic conditions due to the addition of heat from the cube to the air stream which would have resulted in a non-periodic thermal field. As an alternative, five upstream cubes and two downstream cubes either side of the heated cube have been modelled with the use of symmetry boundary conditions on the two spanwise sides of the domain. In the work conducted by Bornoff and Parry[151] this configuration was found to be sufficient to ensure that the flow experienced fully developed conditions at the measurement section.

The computational framework employed for this test case is presented in Figure 9.20.

Figure 9.20 Modelled flow domain for the matrix of cubes test case

All the cubes for this test case have an identical structure to the cube detailed in the single cube test case. However cubes 1-5 and 7-8 are dummy cubes which are only present as periodic boundary conditions are not employed in the streamwise direction. Only the copper core of cube six is kept at a constant temperature of 75°C. The phenol-formaldehyde base plate is treated as adiabatic. The material properties used in this case test are identical to those in the single cube case discussed earlier with the addition of a dummy material for cubes 1-5 and 7-8.

All computations have been performed on a stretched Cartesian mesh with 211 x 80 x 43 mesh elements in the x-, y- and z-directions respectively. On the surface of the cube 34

elements in total have been applied in the x- and y-directions with 17 elements distributed in the z-direction. The computational mesh employed can be viewed in Figure 9.21.
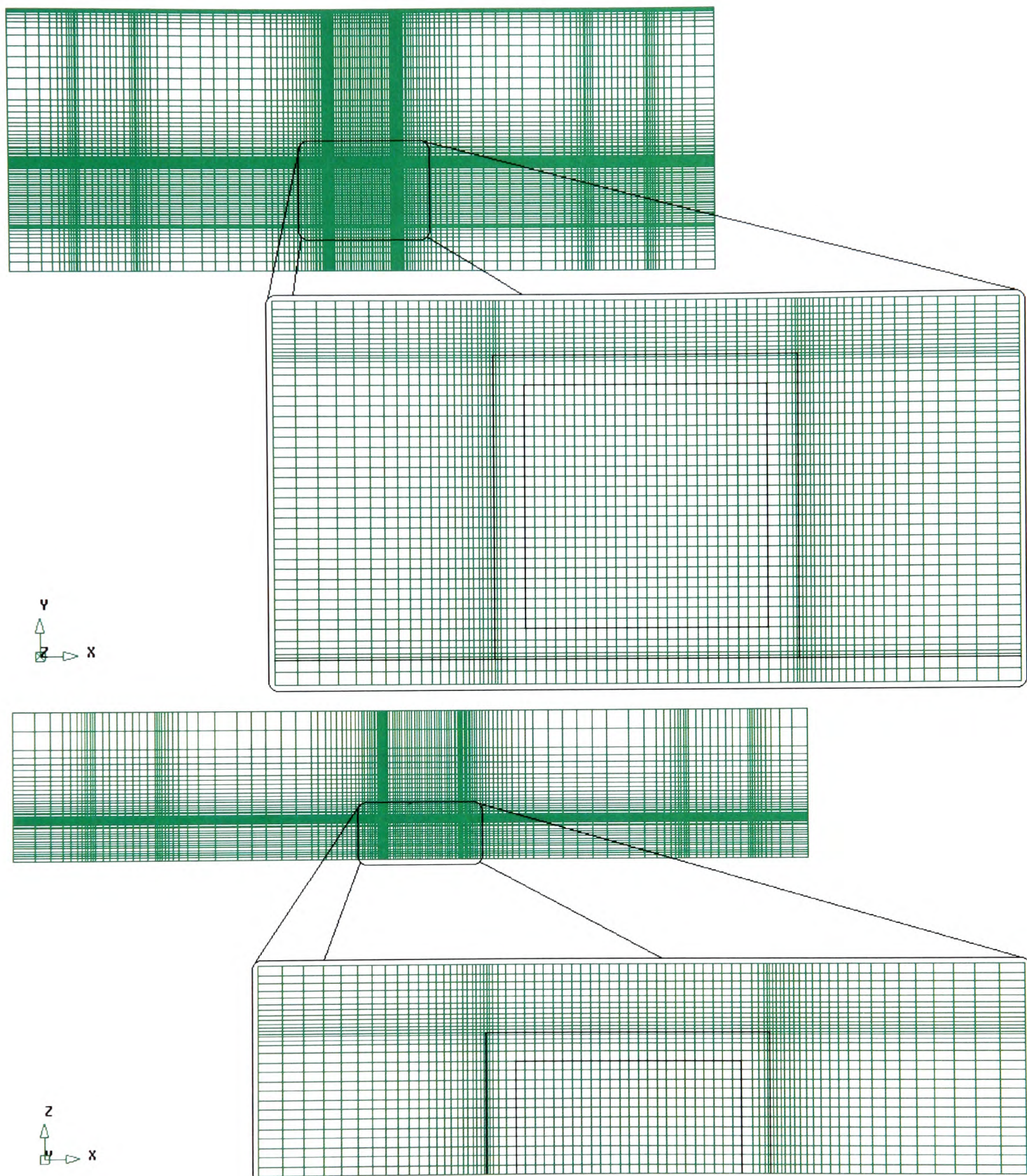
Figure 9.21 Computational mesh density employed for the matrix configuration

The mesh density employed for this case is comparable to that used for the single cube configuration, therefore producing similar y^+ values as those reported in the previous section and hence ensuring mesh independent solutions.

The employed mesh density is finer than those run by any of the participants of the 6th ERCOFTAC workshop. Jansson,[152] one of the participants of the workshop who used the standard $k - \varepsilon$ model for the bulk flow and a one-equation model near to the wall, notes that for the mesh located at the near-wall boundaries the approximate y^+ values were within the range 2-5. Similar y^+ values were used by Mathey et al.[153] at the 8th workshop for LES calculations. Furthermore Zhong and Tucker[71, 72] apply comparable y^+ values for their work on this case using a zonal LES/RANS model. Therefore the y^+ values employed in the current study agree well with the mesh densities used by the participants of both ERCOFTAC workshops and others cited in the literature.

This experimental configuration simulates a simplified air-cooled electronic circuit board, resembling the phenomena taking place within an electronic cabinet. The incentive behind the selection of this case study is that it most closely approximates the cluttered geometry found in electronics systems, in which downstream components are cooled by fluid which has been preheated by upstream components.

9.2.1 Results and Discussion: Streamlines

The flow structures that one would expect to find when considering such a matrix of cubes are similar to the single cube features discussed in the previous section. A three-dimensional impression of the flow field is presented in Figure 9.22.
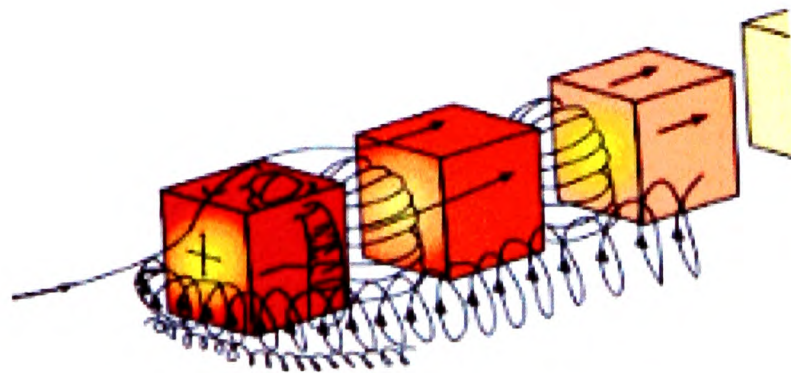
Figure 9.22 Schematic representation of the flow field around a matrix of cubes (Meinders and Hanjalić[30])

Distinct vortex structures are observed in the immediate proximity of the cubes, while the core flow in the region above the cubes remained undisturbed. Two-dimensional mean flow streamline planes have been provided in Figure 9.23 for the xy-plane and Figure 9.24 for the

xz-plane to allow for further analysis of the flow structures predicted by the various turbulence models investigated. Cube 6 (heated cube) is shown in Figure 9.23, the region depicted in Figure 9.24 lies between cubes 6 and 7.

a. LVEL turbulence model predictions
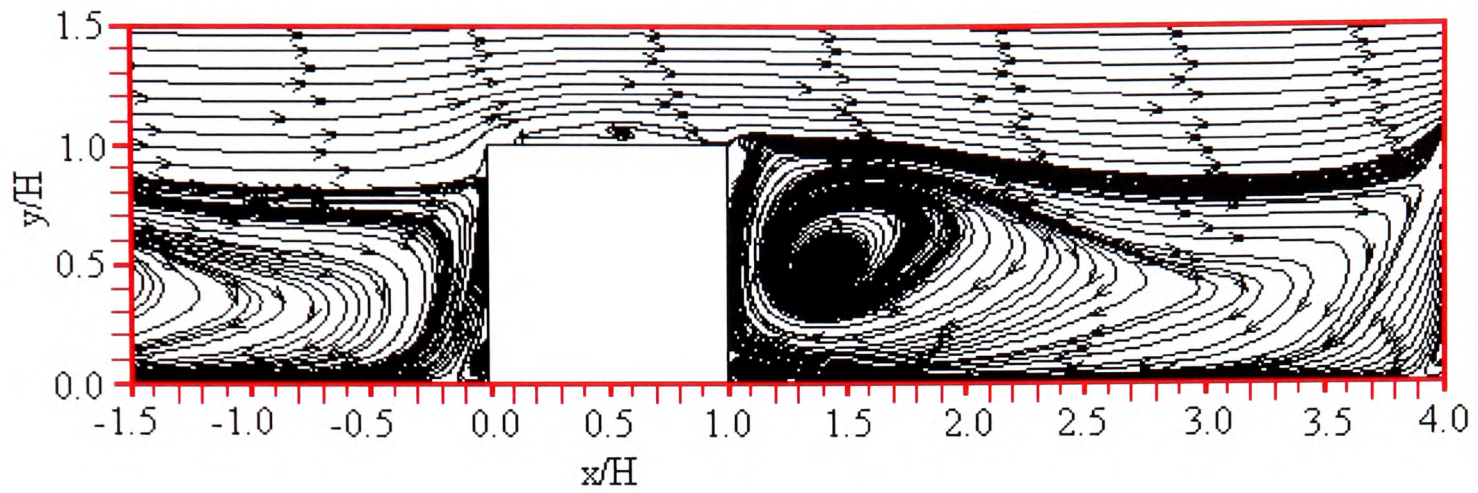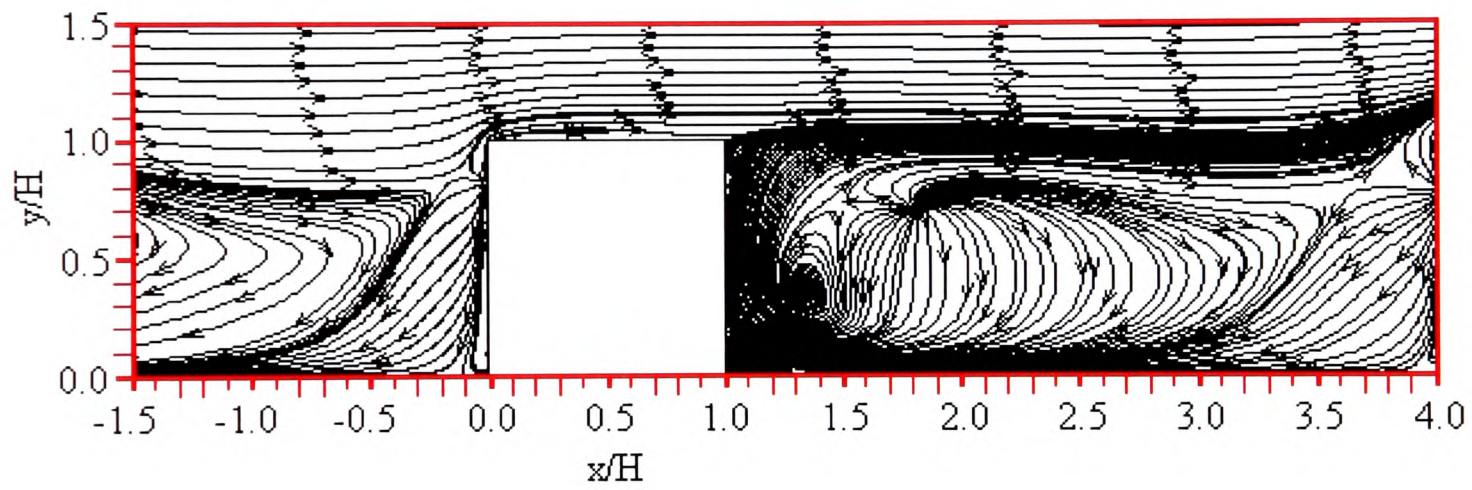
b. LVEL_CAP turbulence model predictions

c. Standard $k - \varepsilon$ turbulence model predictions
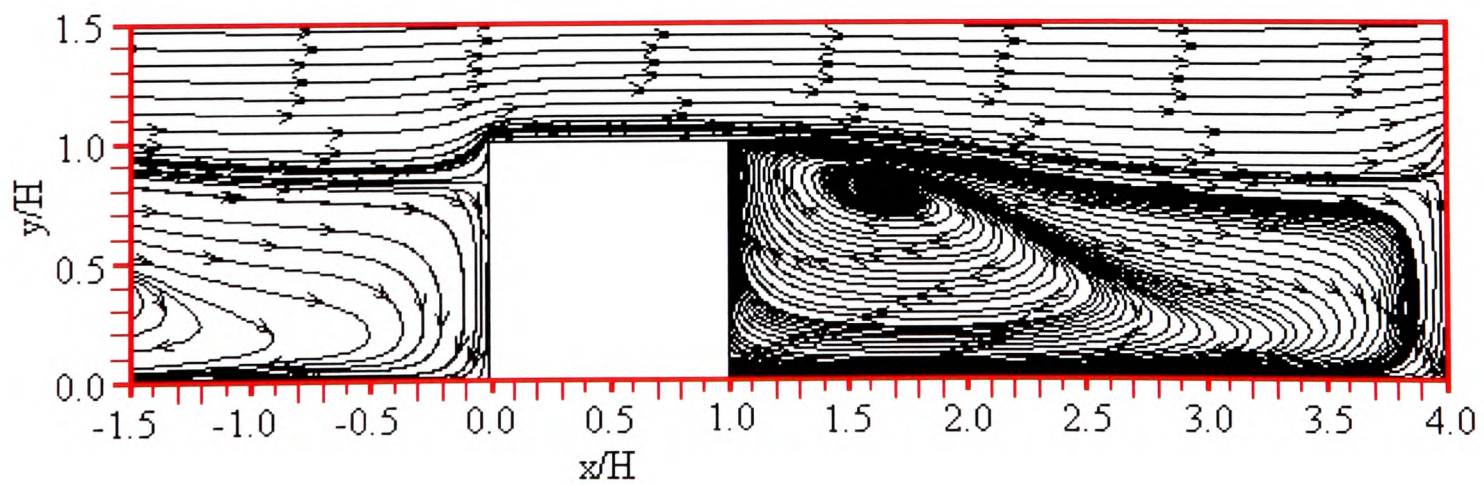
d. Two-layer $k\varepsilon/kl$ turbulence model predictions
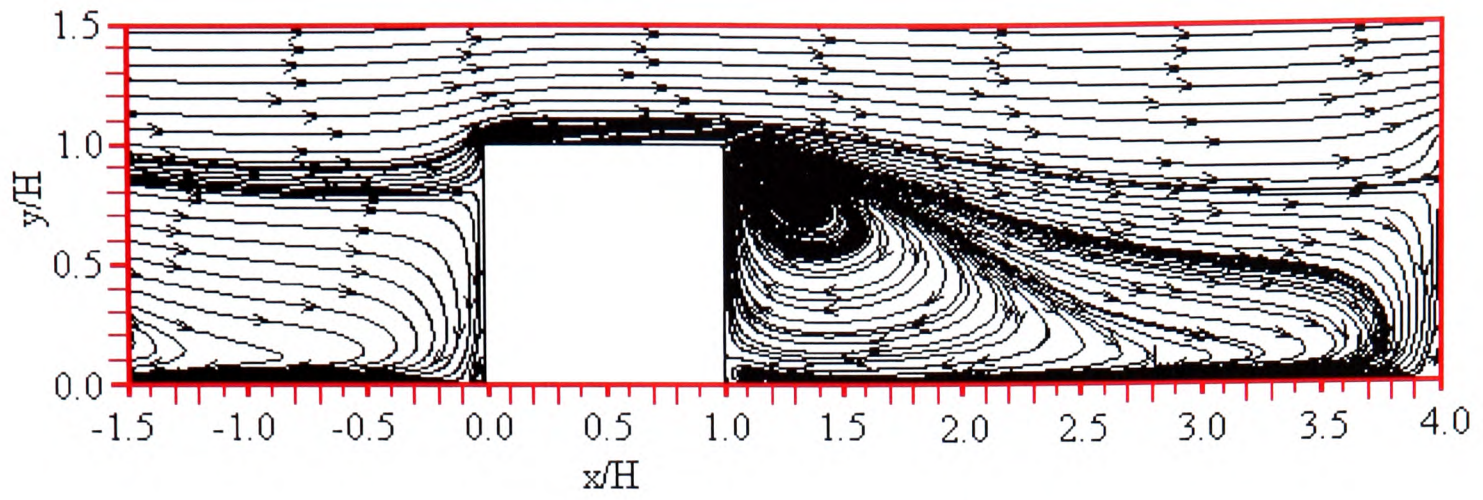
e. Low Reynolds number $k-\omega$ turbulence model predictions
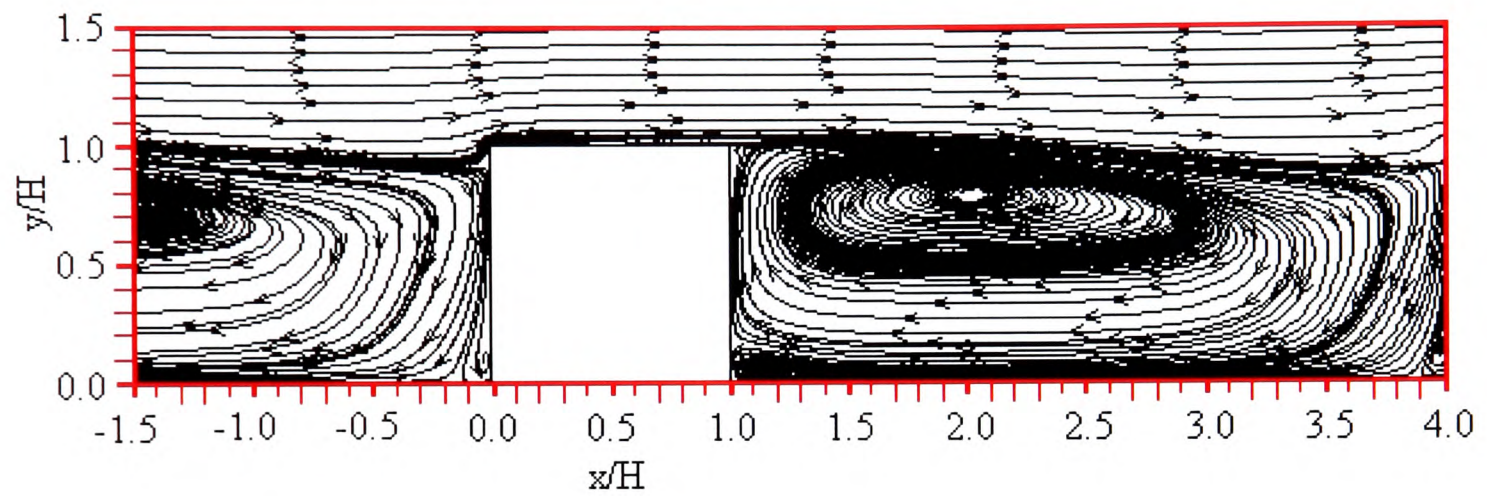
f. Two-layer SST turbulence model predictions
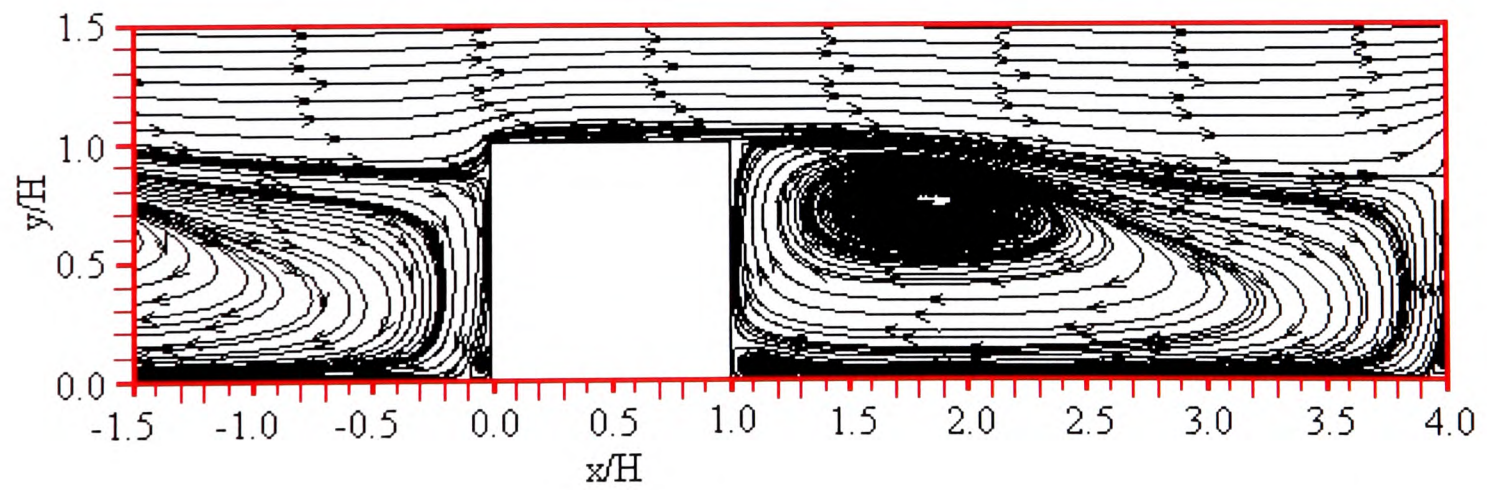
Figure 9.23 Streamlines of the mean flow on the symmetry plane through the matrix of cubes (xy-plane)

a. LVEL turbulence model predictions
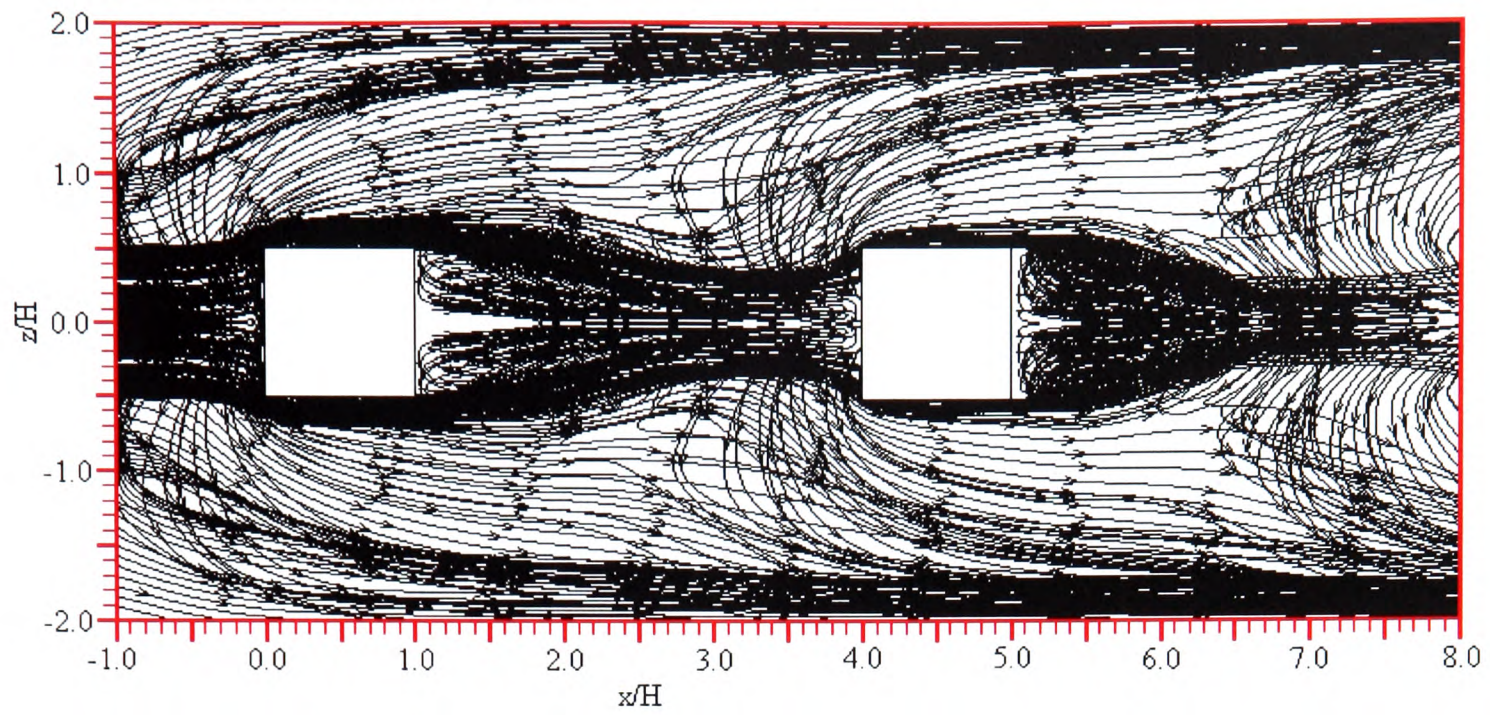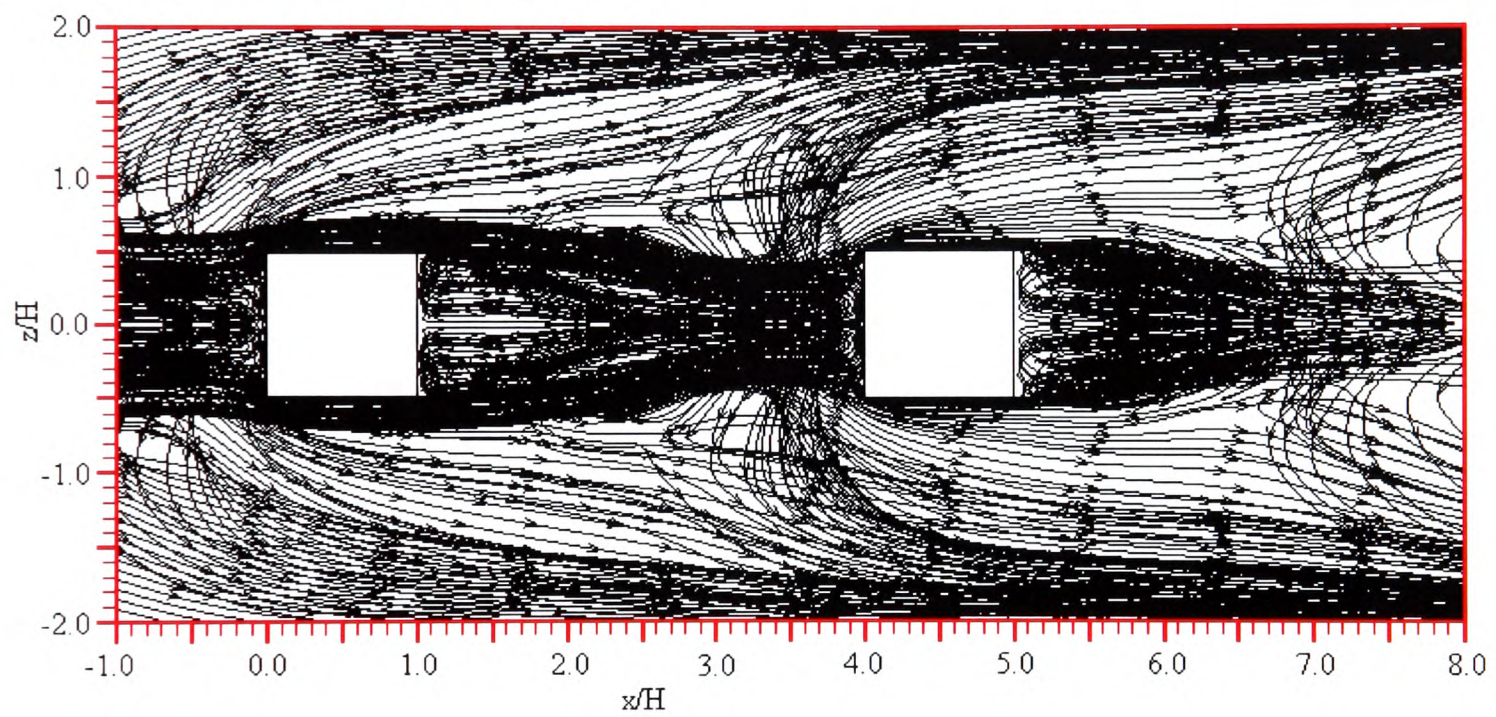
b. LVEL_CAP turbulence model predictions

c. Standard $k - \varepsilon$ turbulence model predictions
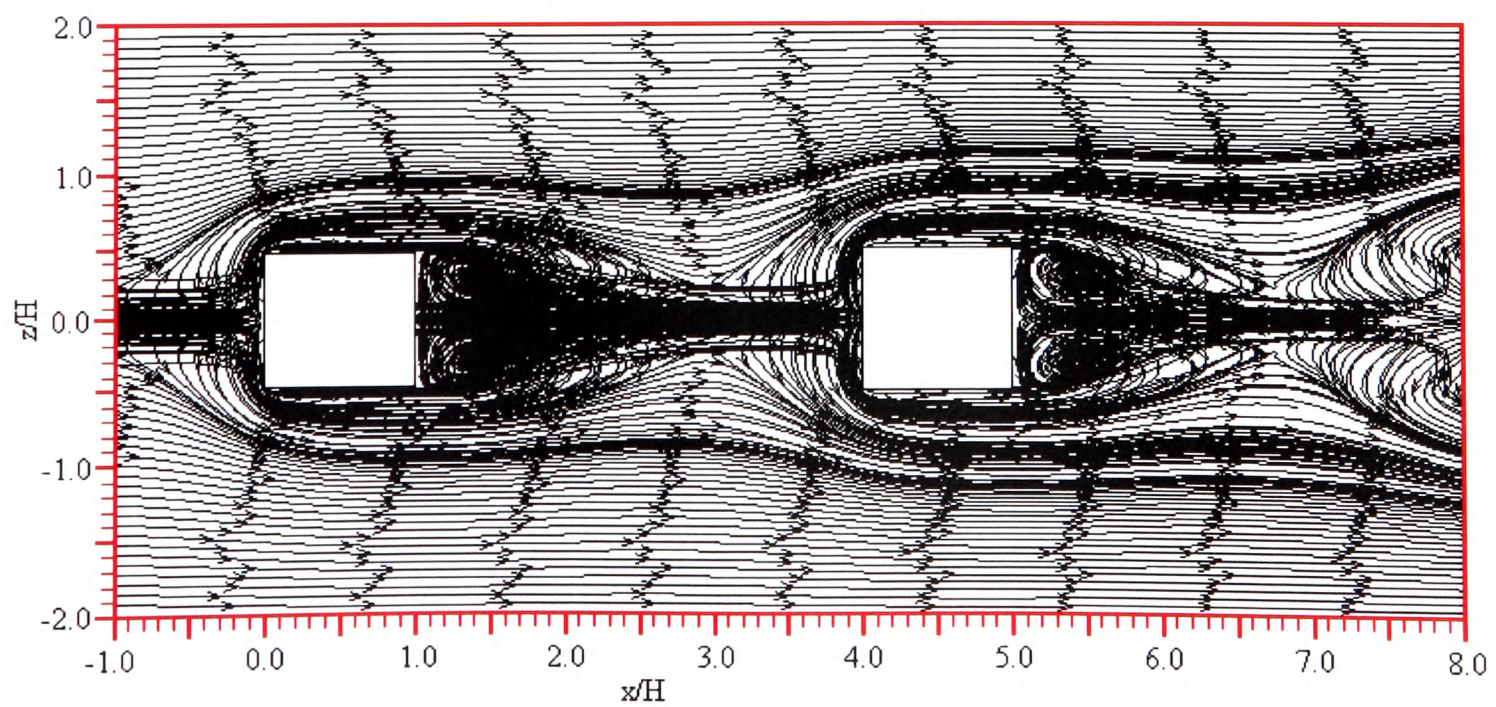
d. Two-layer $k\varepsilon / kl$ turbulence model predictions
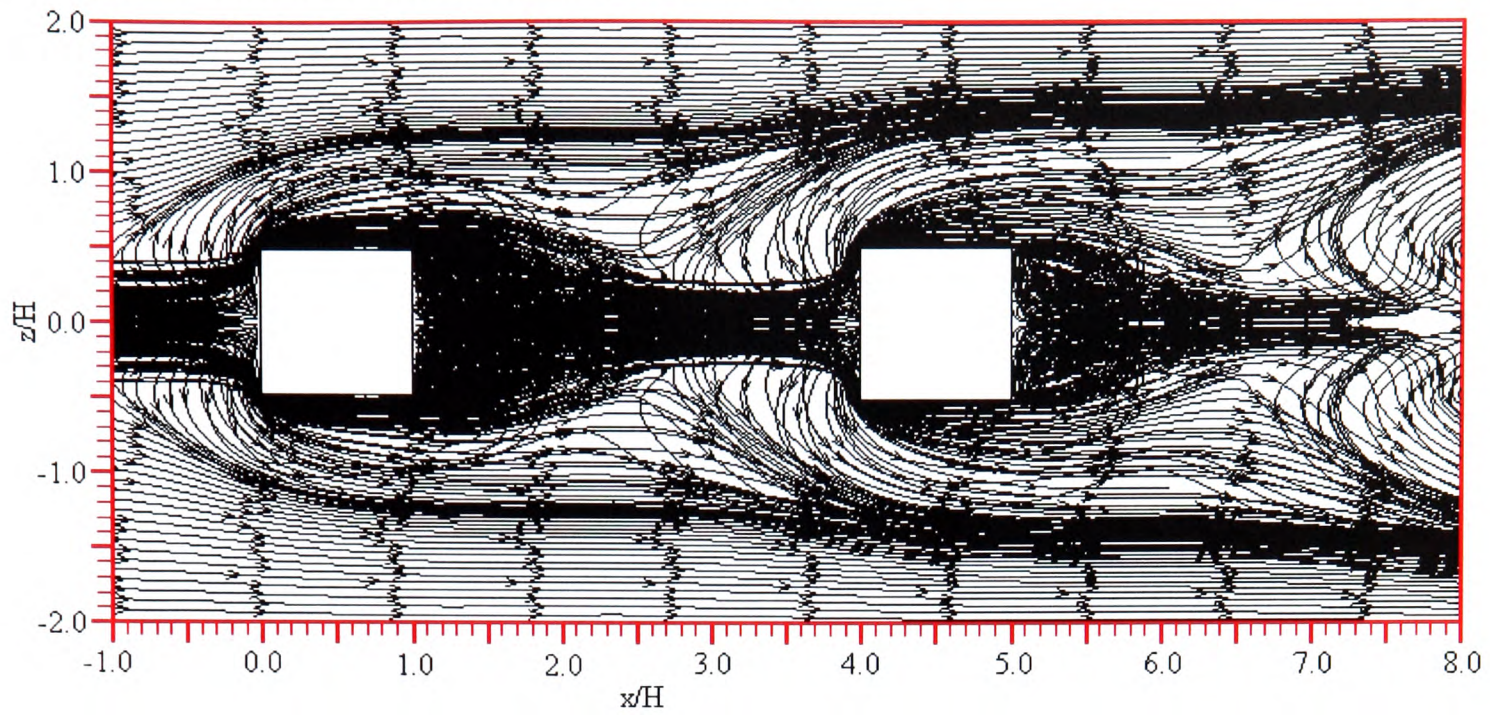
e. Low Reynolds number $k - \omega$ turbulence model predictions
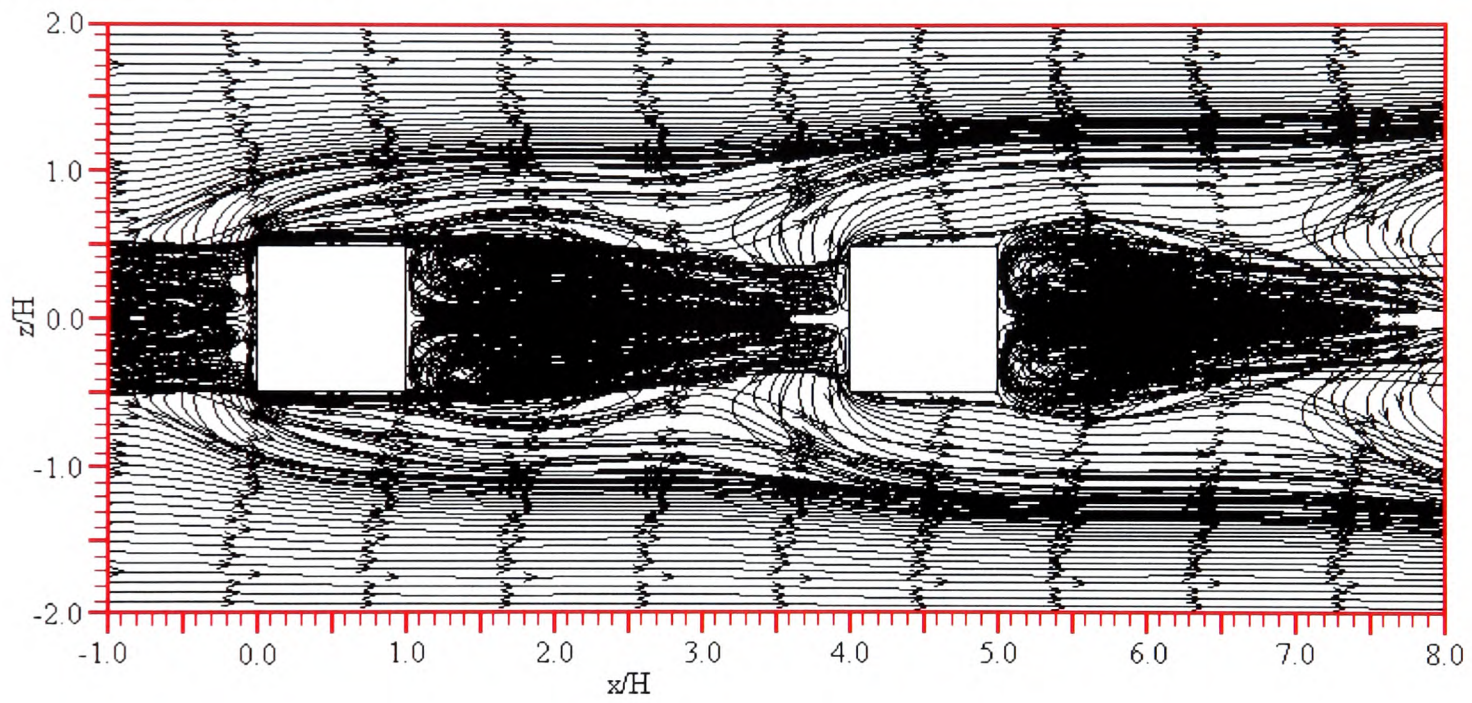
f. Two-layer SST turbulence model predictions
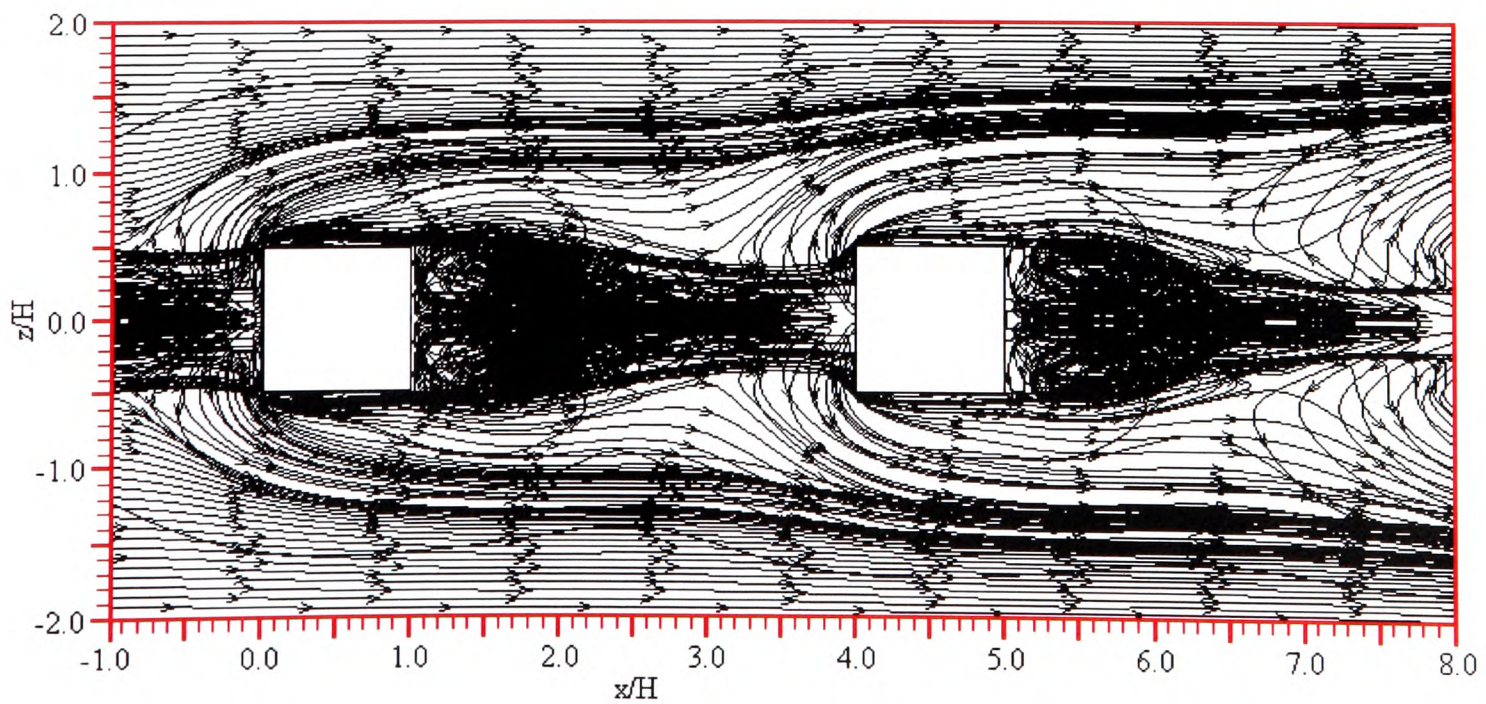
Figure 9.24 Streamlines of the mean flow on the base plate of the matrix of cubes channel (xz-plane)

227

Again to allow for the assessment of the streamline plots presented in Figure 9.23 (xy-plane) and Figure 9.24 (xz-plane) reference will be made to the oil-film visualisation plane provided in Figure 9.25.
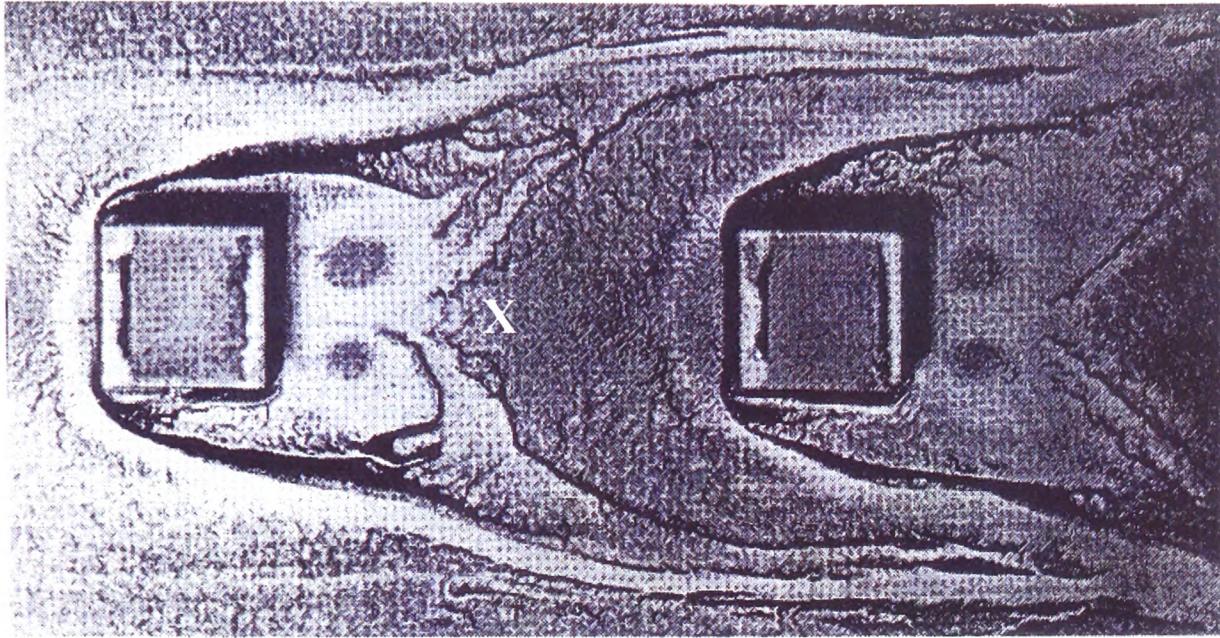
Figure 9.25 Oil-film visualisation of the surface streak lines for the matrix of cubes (Meinders[154])

Meinders notes that the flow in the inter-obstacle space is characterised by a two-cell structure arising from the intermittent reattachment of the shear layer separated at the leading top edge of the upstream cube. The flow reattachment occurred at a distance of approximately $1.5H \ (x/H = 2.5)$ from the leeward face, marked with an X in Figure 9.25. This shear layer bounds the arch-shaped vortex in the wake of the upstream cube.

From the streamline xy-plane presented in Figure 9.23 it can be concluded that all the turbulence models experienced a much larger wake recirculation vortex than that observed in the experimental work. All the tested turbulence models predict a wake vortex which occupies the entire inter-obstacle space. The LVEL_CAP model seems to produce a recirculation vortex which seems physically unrealistic.

From the oil-film visualisation plane, Figure 9.25, a horseshoe vortex can be identified at the windward face of the cube and is seen to deflect downstream along both sides of the cube, weakening further downstream through the interaction with the counter-rotating vortex along the neighbouring cubes. It can be concluded from the streamline xz-plane presented in Figure

9.24 that all the turbulence models predict, to some extent, this development of the horseshoe vortex.

From the oil-film visualisation plane it can be determined that the horseshoe vortices interact with one another at approximately $x/H = 0.5$ at a spanwise distance of $z/H = 1.5$ but do not fully merge. Both the LVEL-based turbulence models predict the interaction between the horseshoe vortices to take place slightly further downstream and at a larger spanwise distance. The high Reynolds number standard $k - \varepsilon$ and low Reynolds number $k - \omega$ models predict the interactions of the vortices at the correct streamwise location but under predict the spanwise distance. The $k - \varepsilon$ model suffers most severely by the under prediction of the spanwise distance. **Both the two-layer $k\varepsilon/kl$ and SST models agree most accurately with the streamwise and spanwise locations stated for the interaction between the horseshoe vortices.** It can also be concluded that overall the predictions made by these two turbulence models replicate the flow field with the greatest degree of accuracy in comparison to the oil-film visualisation plane presented in Figure 9.25.

At the leading top edge of the cube the flow separates and causes a recirculation bubble to exist in this vicinity. This flow reversal is apparent from the surface streak lines of the oil-film visualisation given in Figure 9.25. The top face shows pigment removal close to the leading edge which originated from the recirculating bound vortex. Experimentally the flow reattached at $x/H \approx 0.27$ (equivalent to 4mm) downstream of the leading edge. The reattachment of this bound recirculation vortex is difficult to identify from the streamline xy-planes presented in Figure 9.23, therefore streamlines have been provided in Figure 9.26 which specifically focus on the top face of the cube.

a. LVEL turbulent model predictions
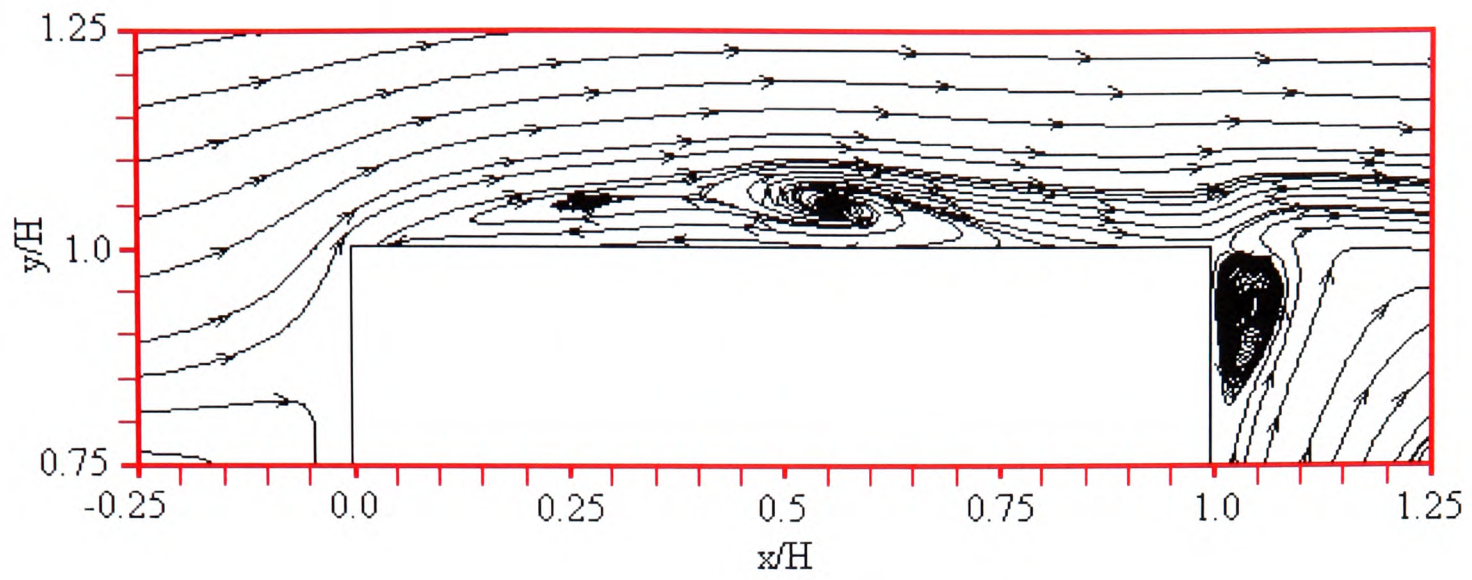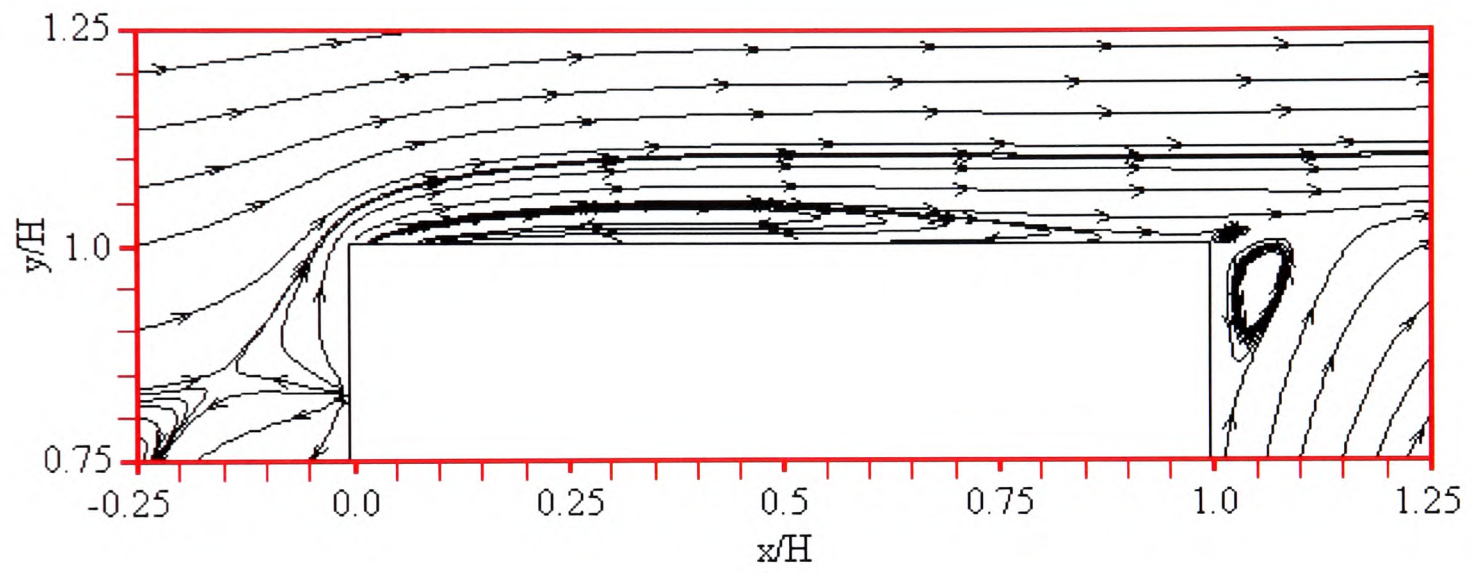
b. LVEL_CAP turbulence model predictions

c. Standard $k - \varepsilon$ turbulence model predictions
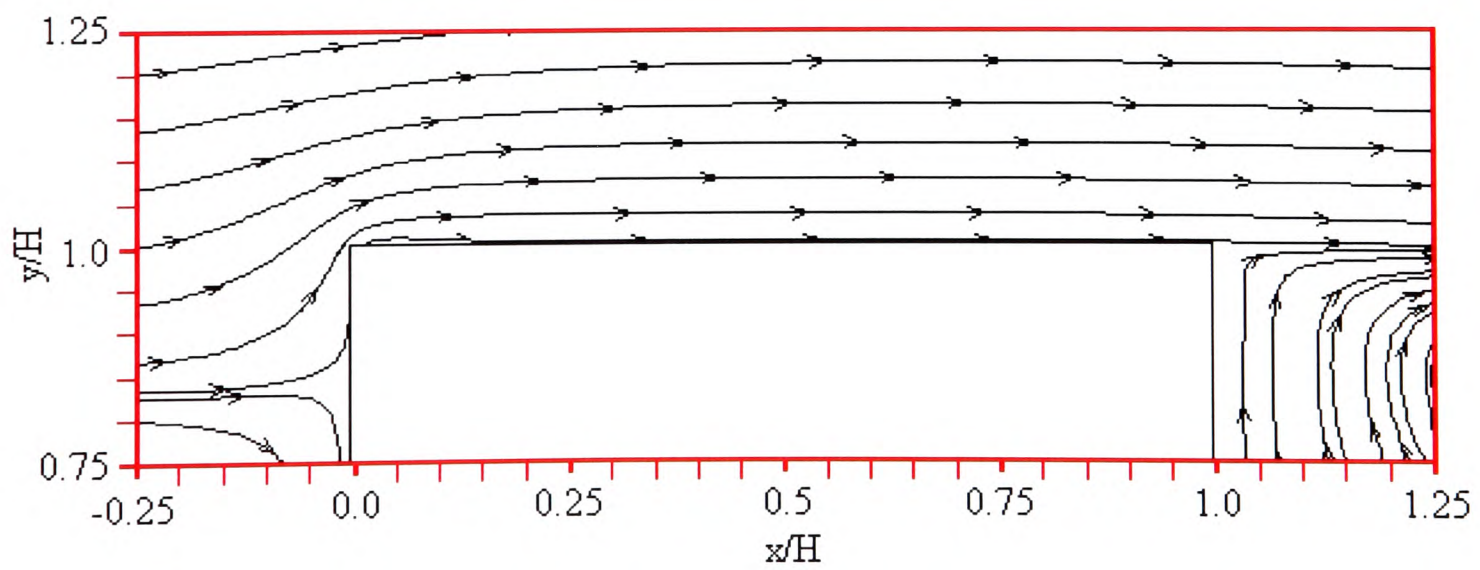
d. Two-layer $k\varepsilon\,/\,kl$ turbulence model predictions
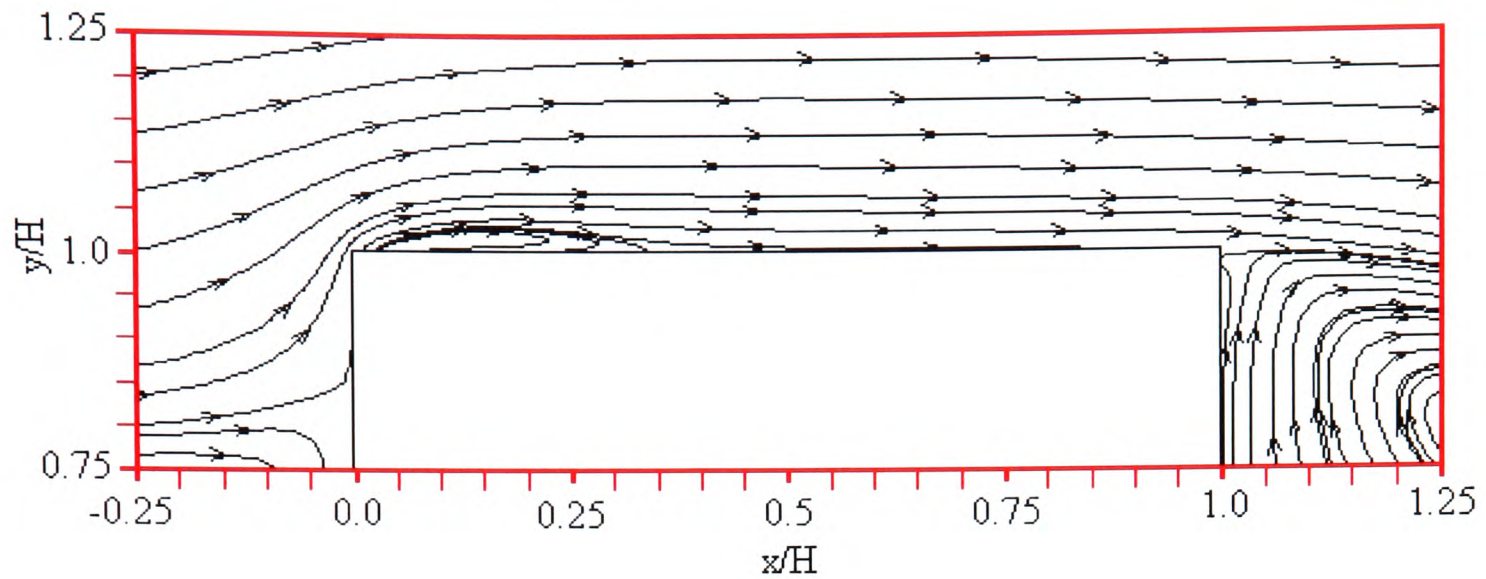
e. Low Reynolds number $k-\omega$ turbulence model predictions
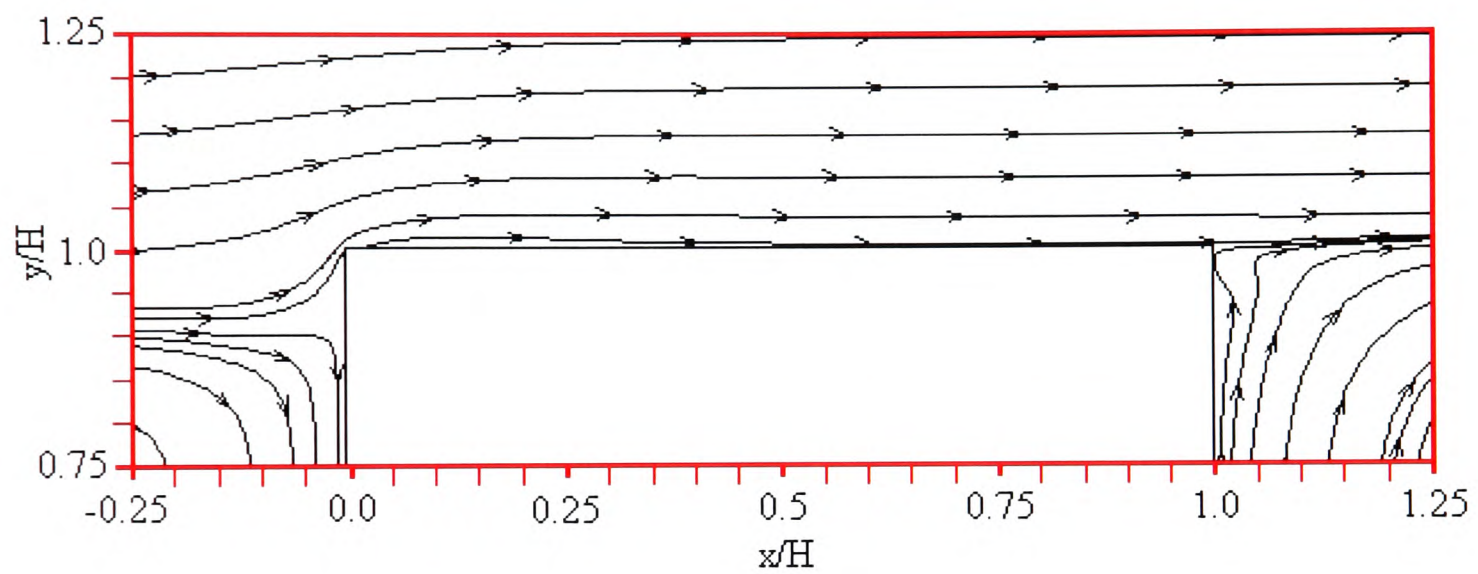
f. Two-layer SST turbulence model predictions
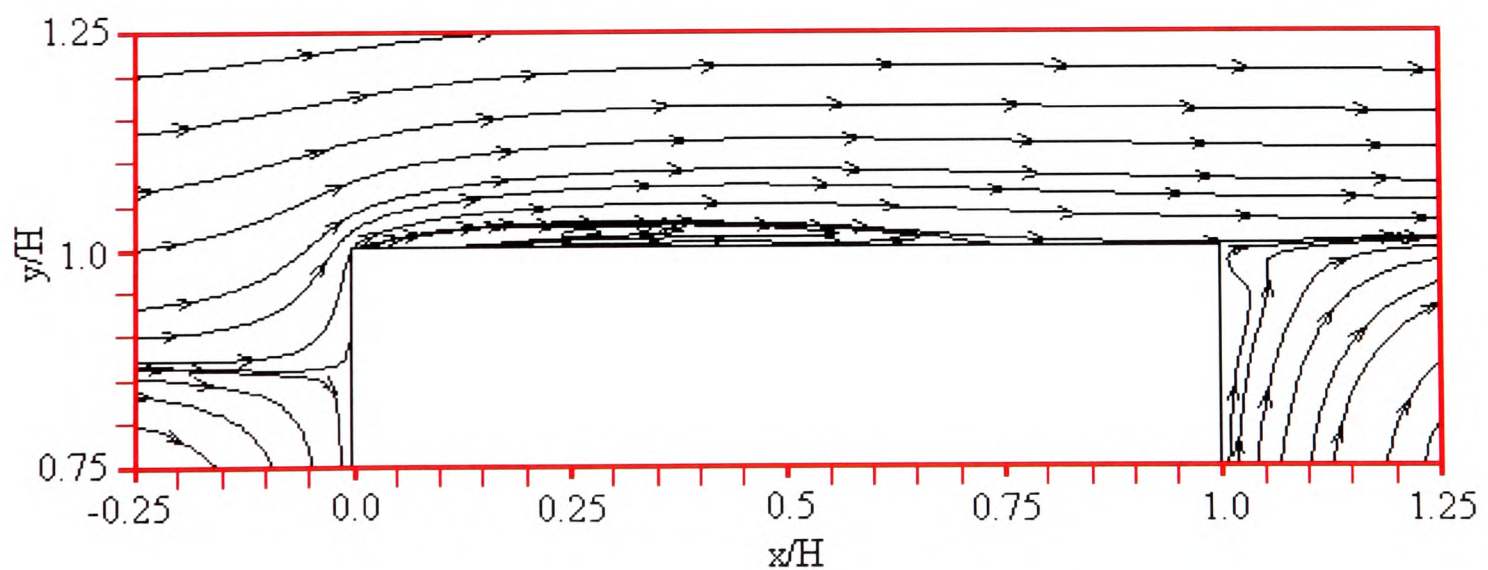
Figure 9.26 Streamlines of the mean flow on symmetry plane through the matrix of cubes highlighting the top bound vortex (xy-plane)

Both LVEL-based turbulence models and the SST model clearly over predict the reattachment point of the bound vortex. The $k-\varepsilon$ and $k-\omega$ models fail to identify the recirculation at all.

The two-layer hybrid *kε/kl* model predicts the location of the reattachment point at *x/H* ≈ 0.3 which is in good agreement with the experimentally observed value.

Finally the leading side edge of the cube also experienced a separation. As a consequence, the shear layer reattaches at $x/H = 1/3$ (equivalent to 5mm) downstream from the side edge. The turbulence model predictions of the side reattachment point at $y/H = 0.5$ have been summarised in Table 9.3.

Turbulence model	Reattachment point x/H
Oil film experiment	1/3
LVEL	0.95
LVEL_CAP	0.83
Standard $k - \varepsilon$	0.05
Two-layer *kε/kl*	**0.46**
Low Reynolds number $k - \omega$	0.2
Two-layer SST	0.83 (2dp)

Table 9.3 Turbulence model predictions of the side reattachment point

From the results presented in Table 9.3 it can be concluded that, as with the bound vortex, both the LVEL-based turbulence models and the SST model over predict the reattachment point of the side vortex. The $k - \varepsilon$ model significantly under predicts the location of the reattachment point predicting a very weak side vortex. The two-layer $k\varepsilon/kl$ model and the $k - \omega$ low Reynolds number model respectively over and under predict the reattachment length by approximately 50% so are judged to predict this vortex with equal accuracy.

In conclusion as in the case of the single cube, it can be determined that overall the turbulence model which replicates most accurately the flow structures observed in the experimental work is the two-layer hybrid $k\varepsilon/kl$ turbulence model. Therefore one would anticipate that the predictions of this turbulence model with regards to heat dissipation from the surface of the cube would be of greatest numerical accuracy among the models investigated. The validity of this assumption will be assessed later in this chapter.

9.2.2 Results and Discussion: Velocity & Turbulence

A range of experimental data profiles are available for comparison. The locations chosen for assessment are those presented at the 6th and 8th ERCOFTAC workshops. Both vertical and horizontal planes have been examined for the five locations detailed in Figure 9.27. Several horizontal and vertical temperature paths have also been assessed.
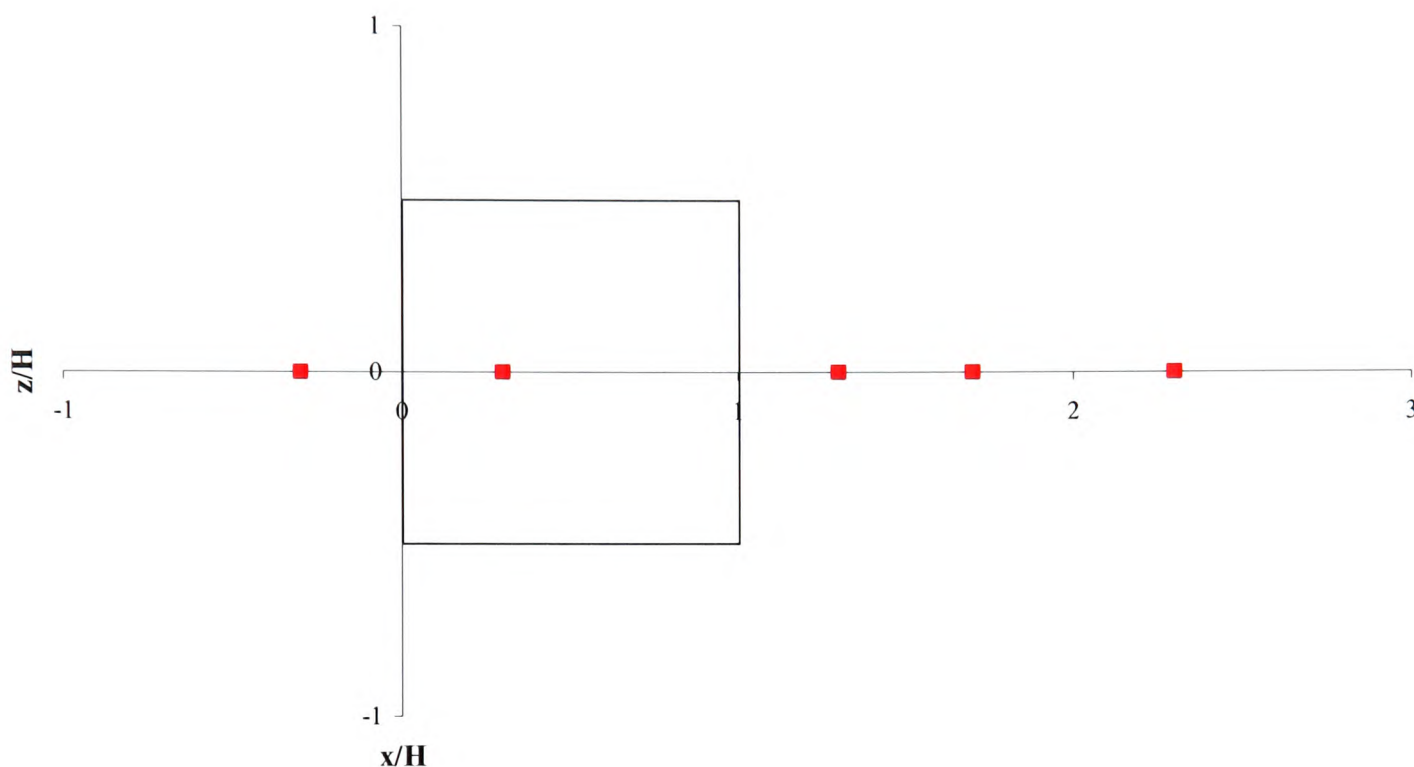
Figure 9.27 Matrix array experimental data measurement locations

It is noted that the turbulent kinetic energy profiles have been reconstructed by the author using equation (9.3) as recommended by Meinders. Since equation (9.3) implicitly assumes isotropy $(u' = v' = w')$ to derive the unknown v' component, inaccuracies will be evident especially in regions of high shear.

Throughout the assessment of the various experimental data locations reference will be made to the turbulence model predictions presented at the 8th ERCOFTAC workshop. The participants of the workshop were divided into two main groups. Group A consisted of the simulations which were based on RANS calculations. Two of the participants of Group A used the standard $k - \varepsilon$ and SST models therefore allowing for direct turbulence model comparisons with those investigated in the current study. Group B represented the LES and DNS simulation work.

Assessment of the velocity and turbulent kinetic energy profiles located at the symmetry plane will be undertaken first followed by the surface temperature.
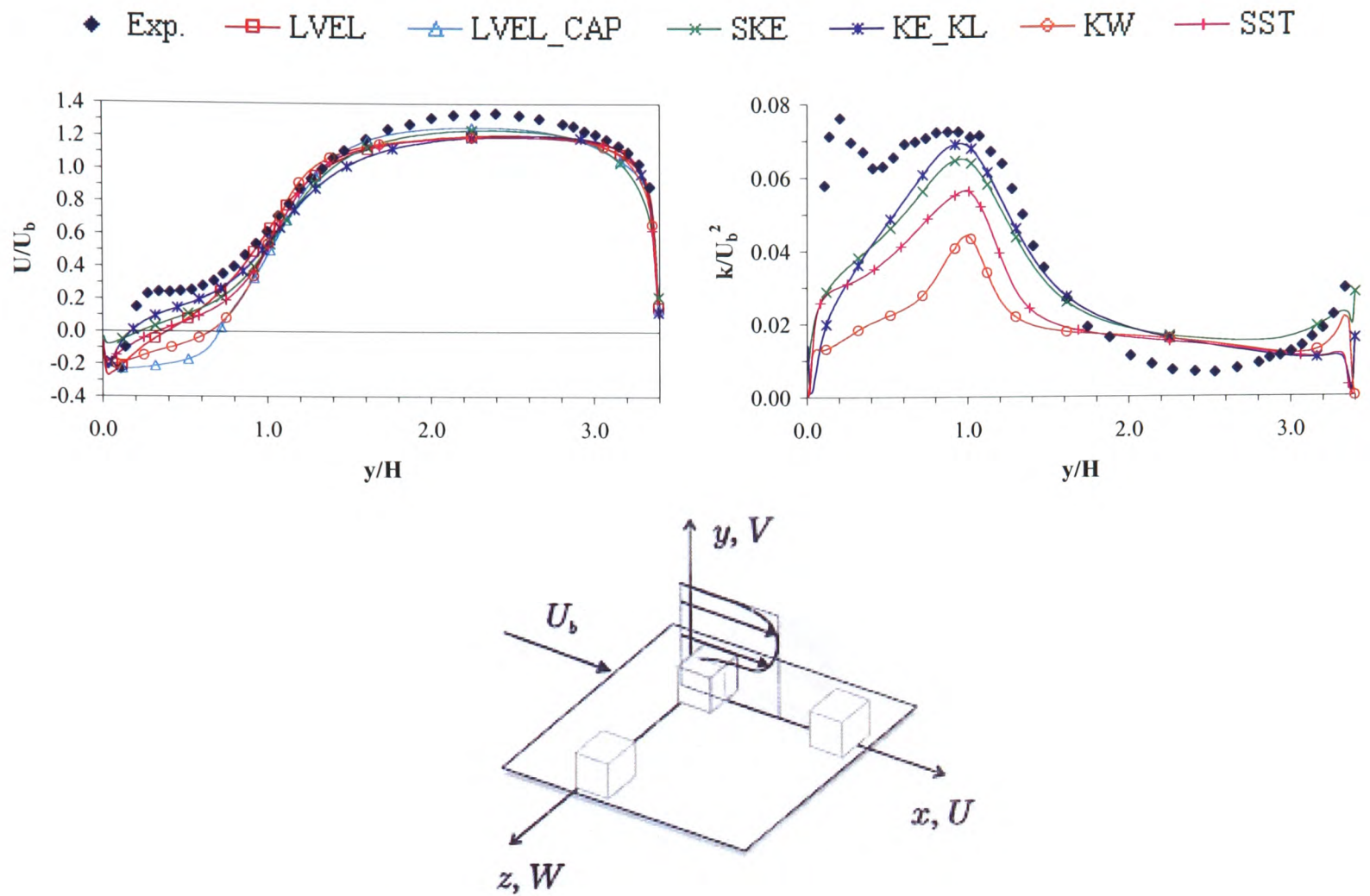
Figure 9.28 Turbulence model comparisons of the profile located at x/H = -0.3
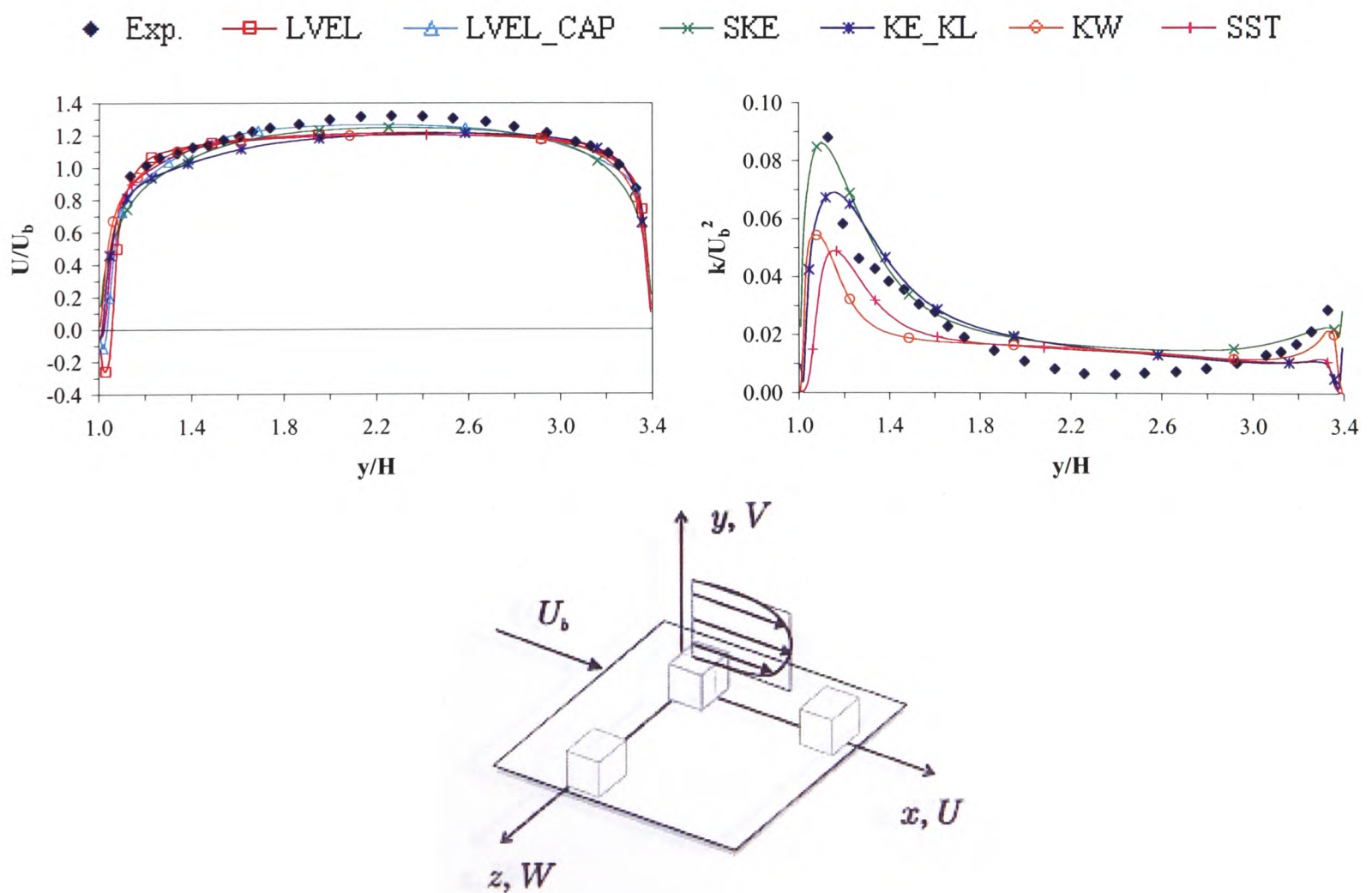
Figure 9.29 Turbulence model comparisons of the profile located at x/H = 0.3
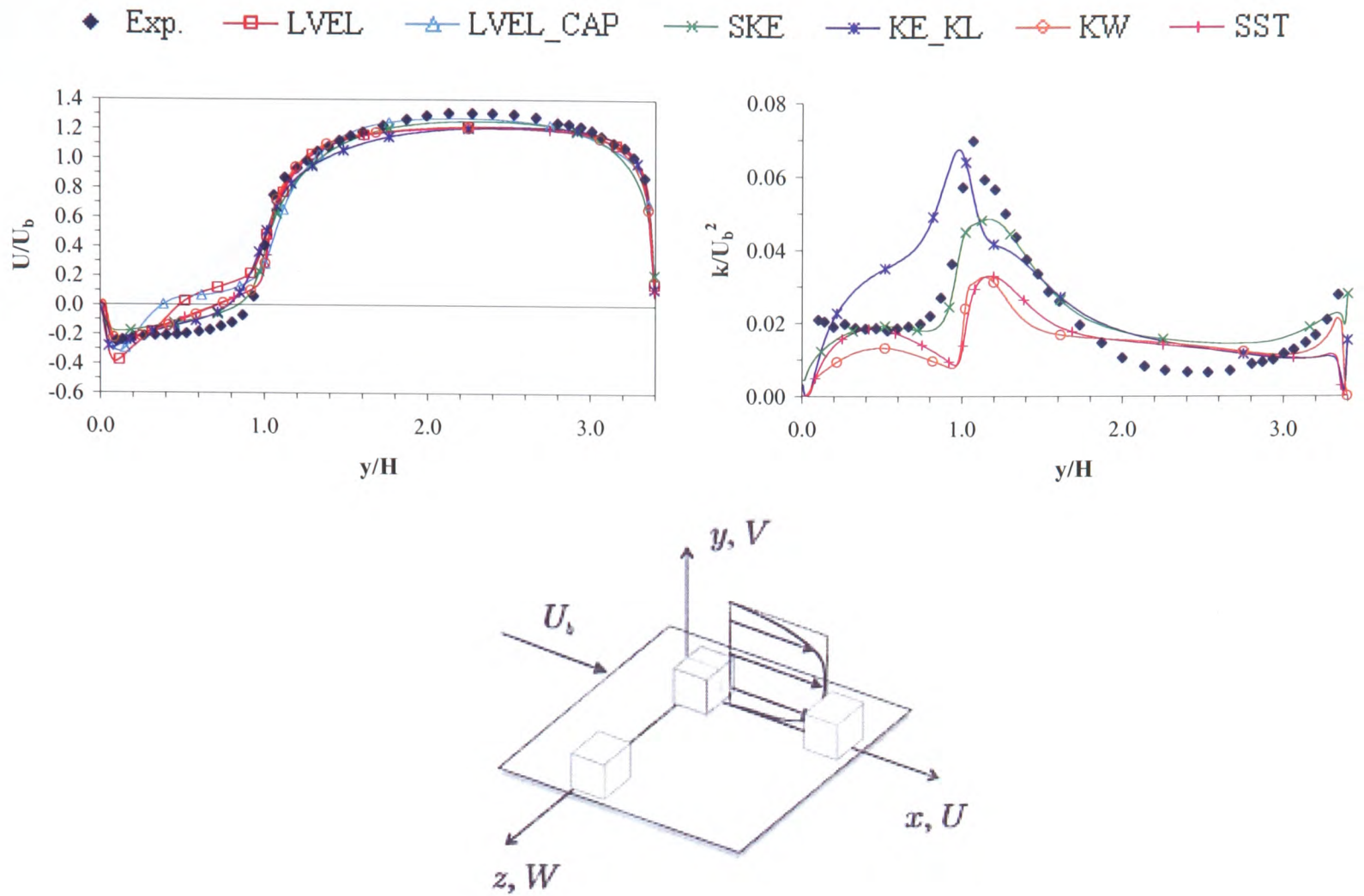
Figure 9.30 Turbulence model comparisons of the profile located at x/H = 1.3
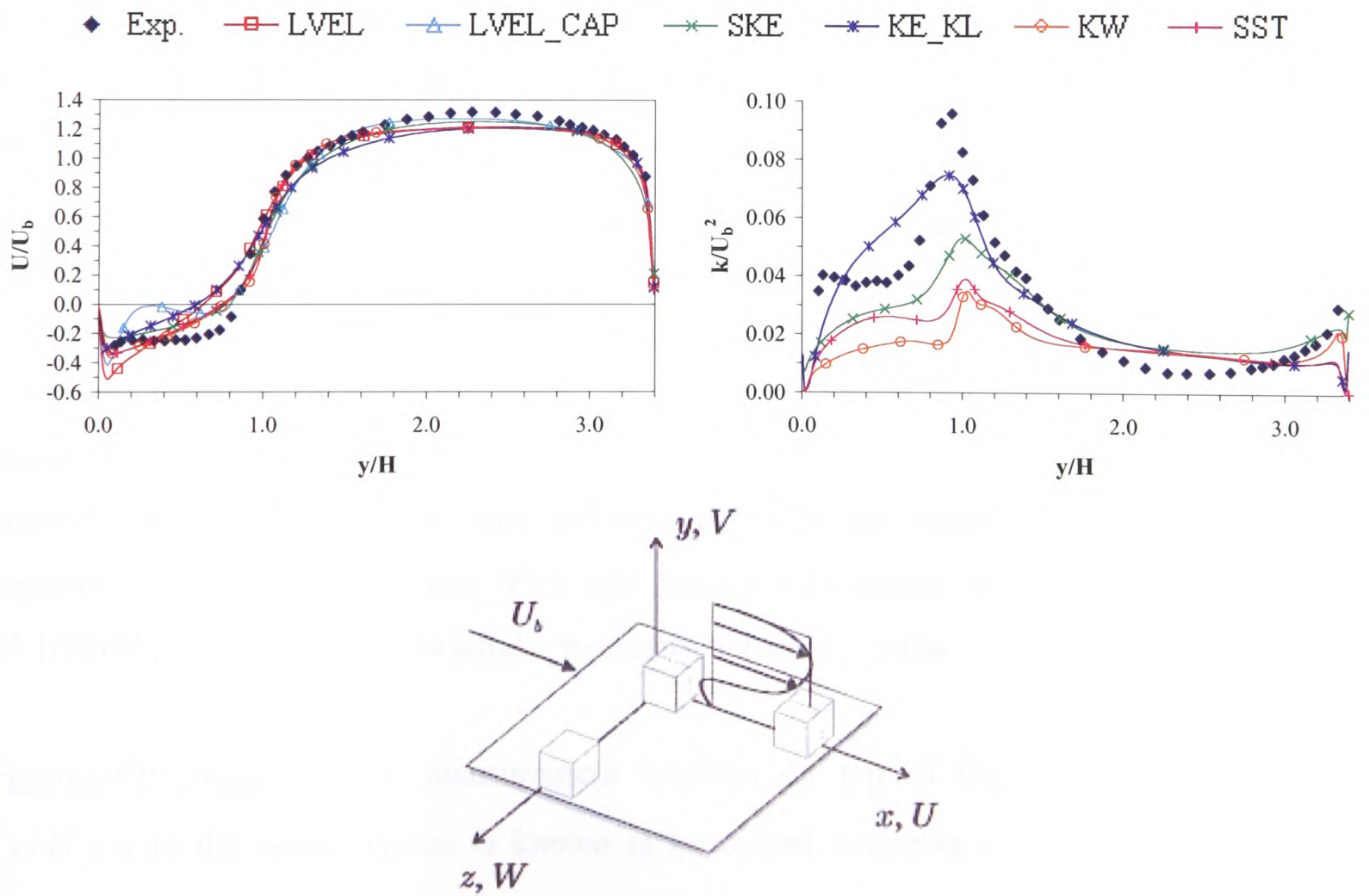
Figure 9.31 Turbulence model comparisons of the profile located at x/H = 1.7
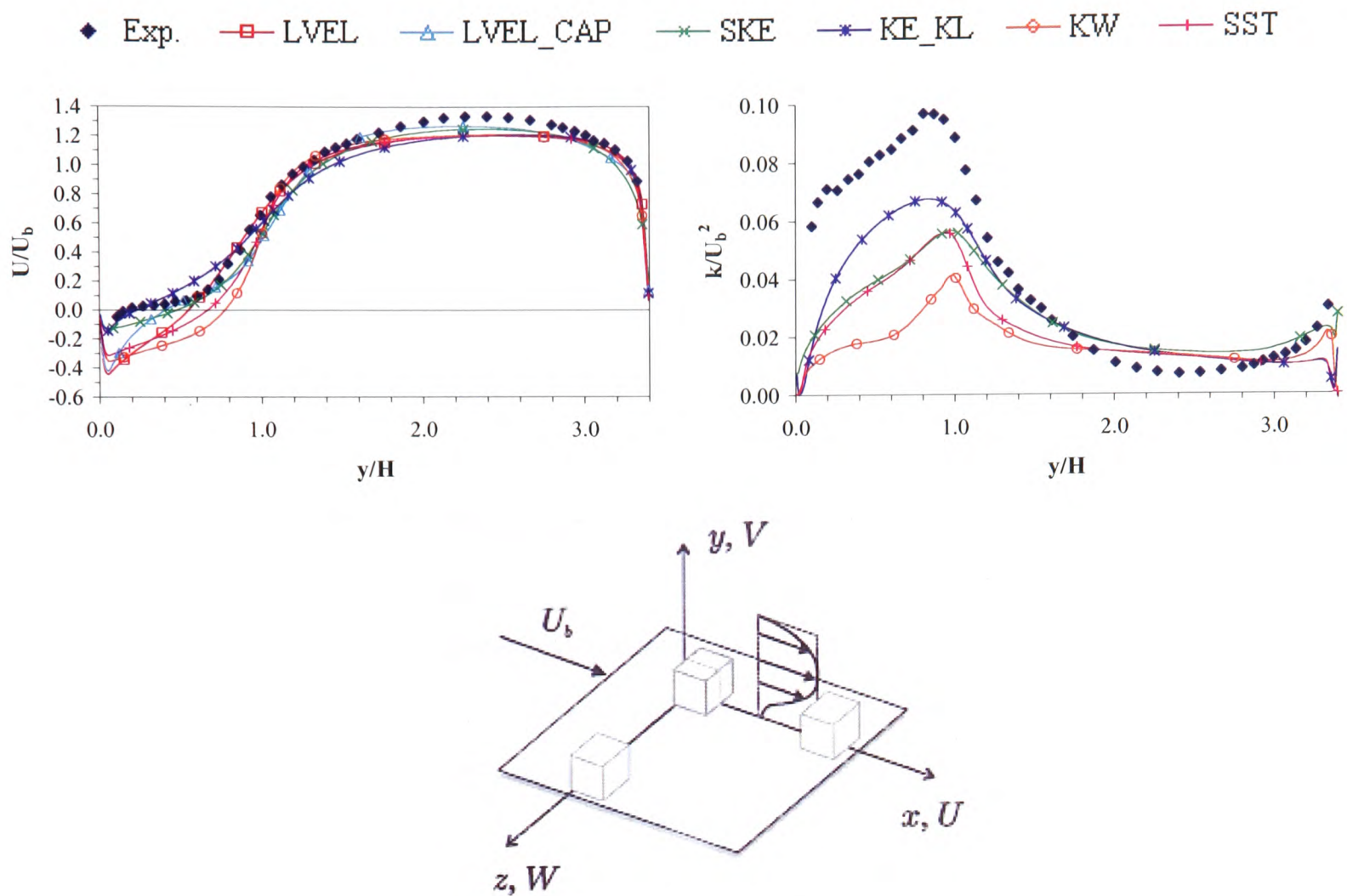
Figure 9.32 Turbulence model comparisons of the profile located at x/H = 2.3

The velocity profile comparisons presented in Figure 9.28 through to Figure 9.32 generally are in good agreement with the majority of the experimental data and the 8th ERCOFTAC workshop simulation work carried out.

From Figure 9.28, which corresponds to the measurement location just upstream of the cube, the front recirculation vortex can be identified. The reattachment point of this vortex is most accurately predicted by the two-layer $k\varepsilon / kl$ turbulence model. Both the LVEL_CAP and low Reynolds number $k - \omega$ models predict that the reattachment point is much higher than that observed in the experiments. This is consistent with the assessment of the mean flow streamlines presented in Figure 9.23 and Figure 9.24 where it was concluded that the LVEL_CAP model seems to produce physically unrealistic behaviour.

Figure 9.29 relates to the measurement location on top of the cube. At this location $(x / H = 0.3)$ the bound vortex is known to be closed, however only the $k - \varepsilon$ and $k - \omega$ turbulence models show this to be the case. This does not suggest that these two models are the most accurate - quite the opposite, these models failed to identify a bound vortex at all. All

other tested models still show the affects of the bound vortex at this location, with the LVEL model predicting the largest vortex bubble. Both the two-layer models would probably be considered that most accurate showing the smallest recirculation affects.

The measurement location considered after the cube in the wake region is presented in Figure 9.30. Both the LVEL-based turbulence models produce poor numerical predictions at this location; expected due to the poor prediction at upstream locations. This is also noted for the measurement locations further downstream.

As the flow develops in the downstream direction, see Figure 9.31, it can be determined that all the turbulence models, consistent with the experimental data, still predict the presence of the wake vortex. By the measurement location $x/H = 2.3$ it can be concluded that most of the turbulence models predict a large recirculation vortex contrary to the experimental data. Only the two-layer $k\varepsilon/kl$ model predicts a reattachment point which is relatively close to the experimental data observations.

With regards to the prediction of the turbulent kinetic energy all the turbulence models tested follow the trends in the experimental data. All models seem to under predict the experimental peaks observed in the turbulent kinetic energy. Similar trends were noted at the 8th ERCOFTAC workshop for both Group A and B. However the two-layer hybrid $k\varepsilon/kl$ turbulence model consistently shows a greater degree of accuracy than the other turbulence models under investigation.

The turbulence model which overall appears to be the most accurate for the five centreline measurement locations discussed above would be the two-layer hybrid $k\varepsilon/kl$ model.

Experimental data comparisons have also been undertaken at the mid-height of the cubes $(y/H = 0.5)$ at the same x/H measurement locations as those shown in Figure 9.27.
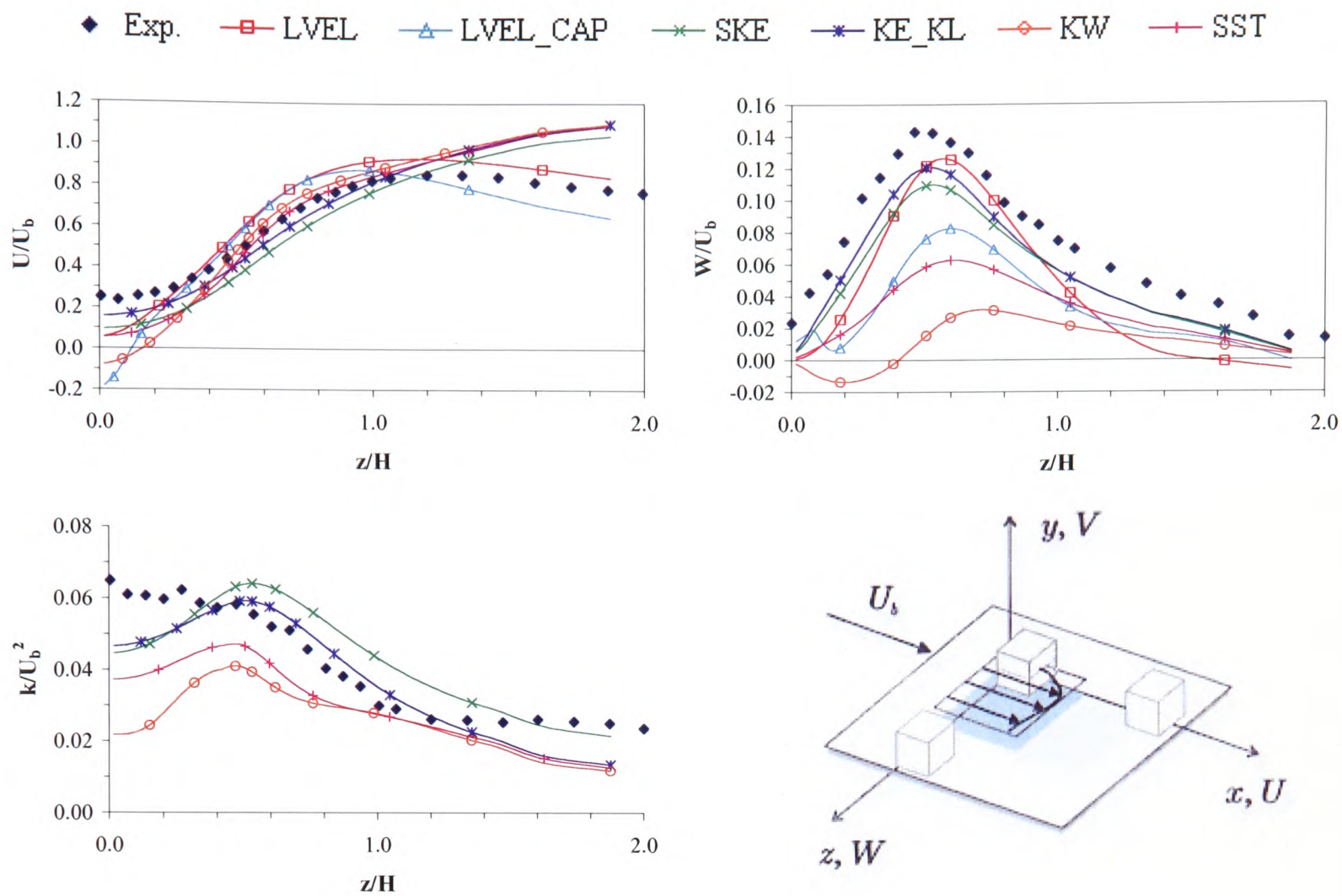
Figure 9.33 Turbulence model comparisons of the profile located at x/H = -0.3, y/H = 0.5
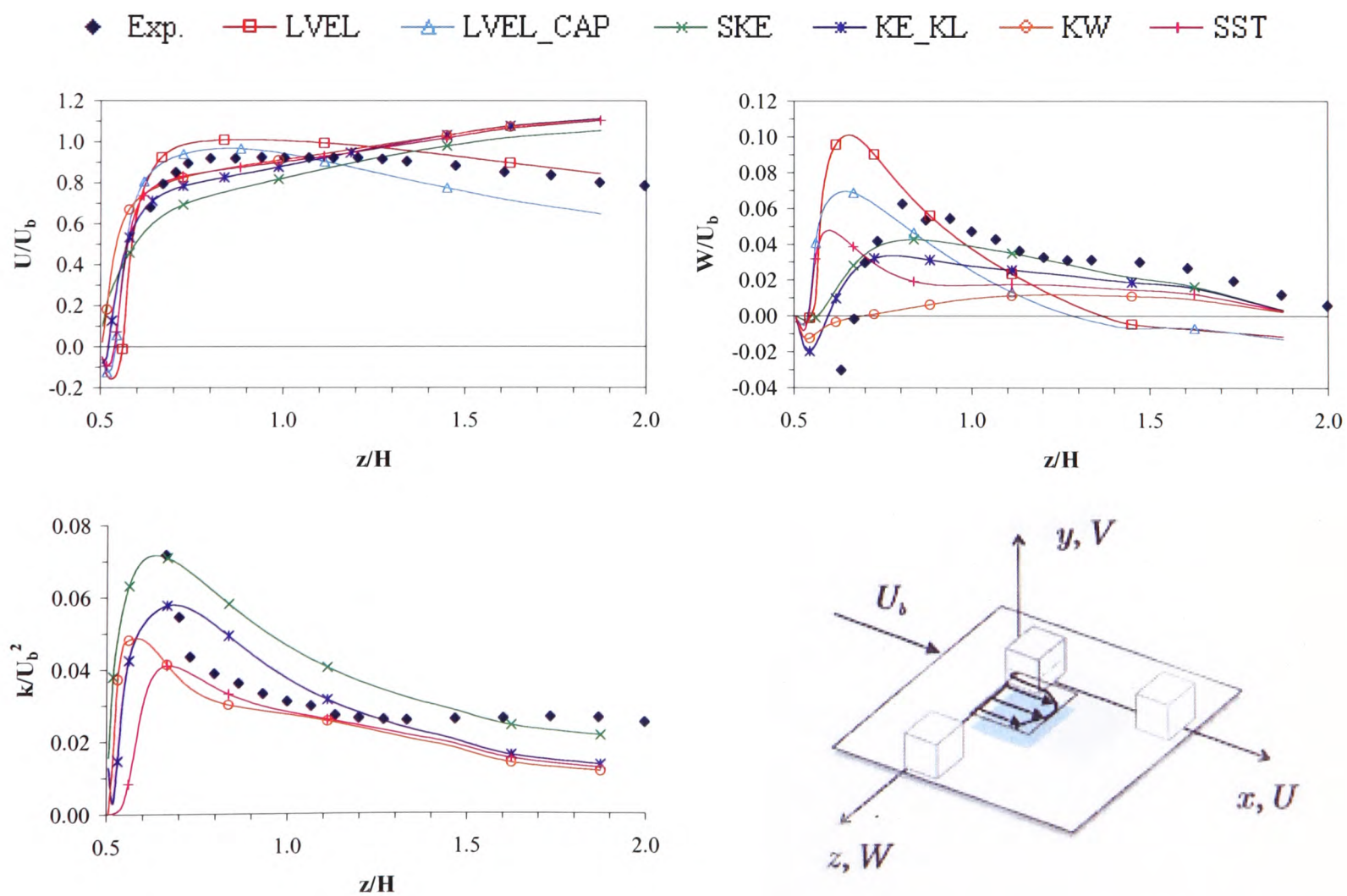
Figure 9.34 Turbulence model comparisons of the profile located at x/H = 0.3, y/H = 0.5
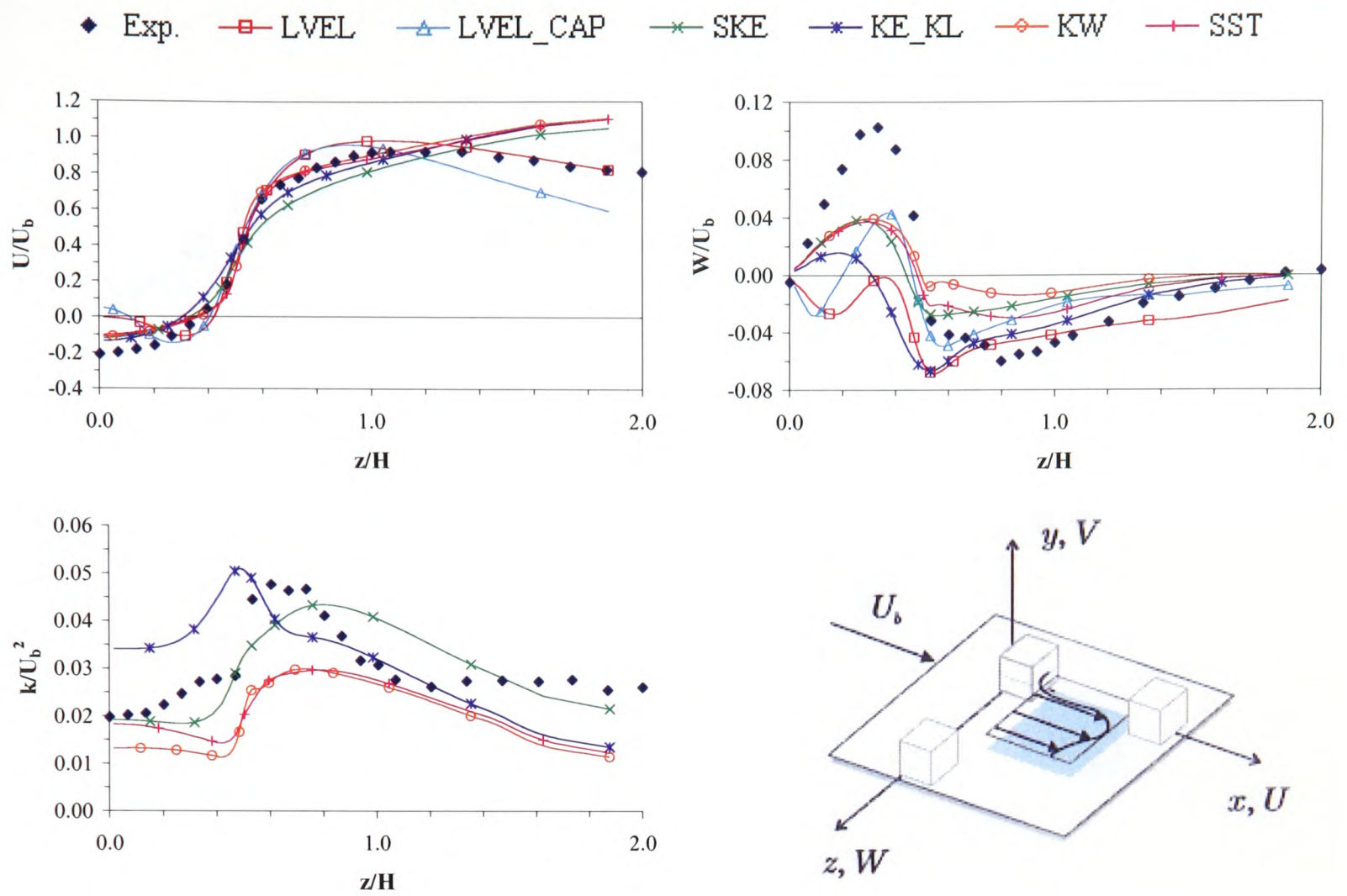
Figure 9.35 Turbulence model comparisons of the profile located at x/H = 1.3, y/H = 0.5
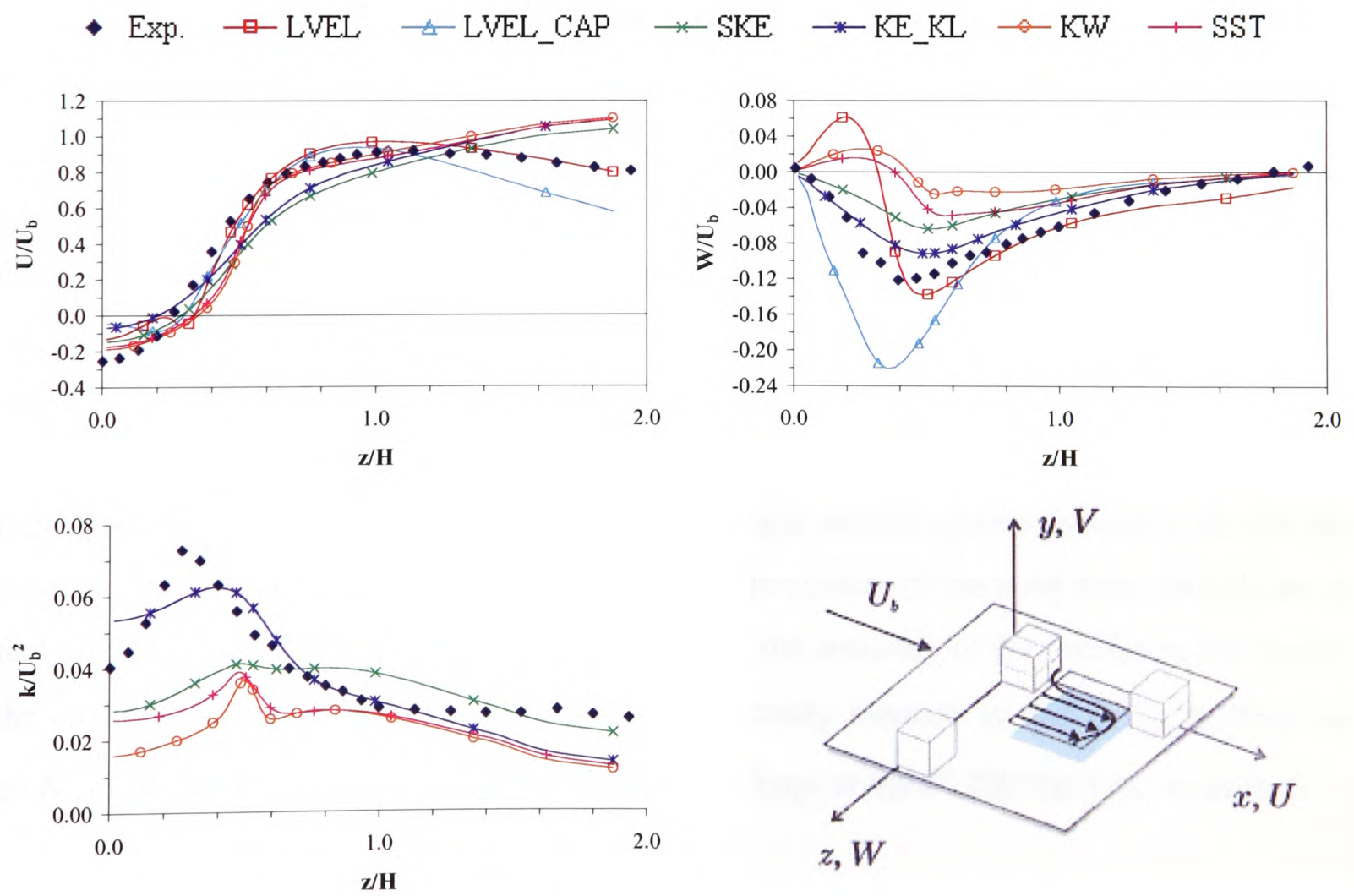
Figure 9.36 Turbulence model comparisons of the profile located at x/H = 1.7, y/H = 0.5
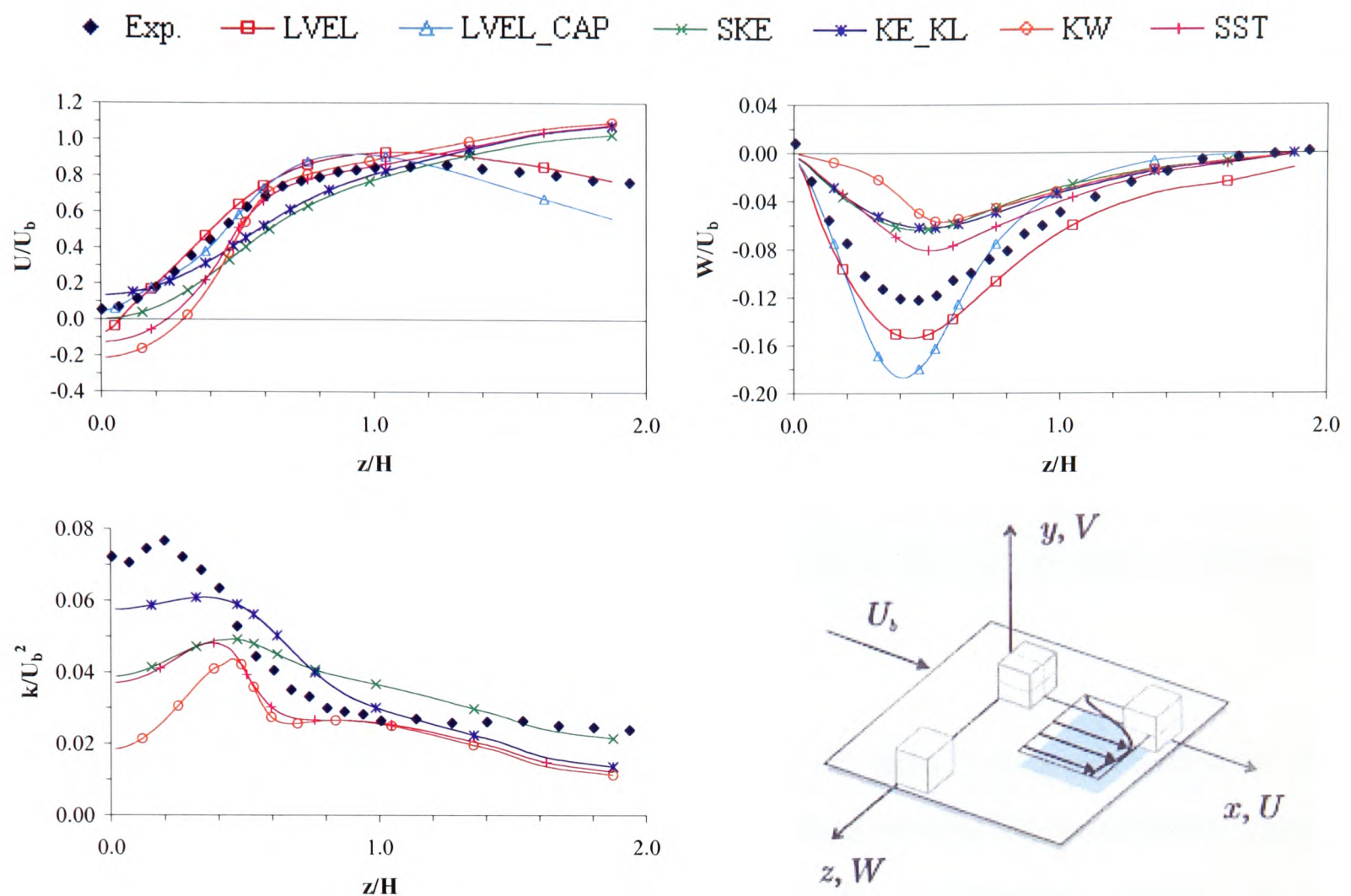
Figure 9.37 Turbulence model comparisons of the profile located at x/H = 2.3, y/H = 0.5

Consistently it can be concluded from the U/U_b graphs presented in Figure 9.33 through to Figure 9.37 that the gradual decay of the experimental velocity is due to the influence of the spanwise neighbouring cube. The mixing-length models, noticeably the LVEL model, produce much better agreement with the experimental data for $z/H > 1.0$ than the other turbulence models investigated. This is probably attributed to the gaps in the spanwise direction not being greatly influenced by the presence of the rows of cubes. Therefore a more boundary layer type flow development occurs.

It can also be concluded that although the mixing-length models agree relatively well with the experimental profiles for $z/H > 1.0$ in the immediate vicinity of the cube these models are in fact predicting the worst results. This far out weighs the accuracy of the models in the core of the channel. All other turbulence models show a steady increase in the U/U_b profiles for $z/H > 1.0$ which is consistent with the Group A findings at the 8th ERCOFTAC workshop.

From the U/U_b upstream measurement location presented in Figure 9.33 it can be determined that the two-layer $k\varepsilon / kl$ model is in greatest agreement with the experimental data. Contrary

to the experimental data the LVEL_CAP and $k-\omega$ models both predict negative velocities corresponding to the recirculation at the front face of the cube. The W/U_b profile is also captured most accurately by the two-layer $k\varepsilon/kl$ model.

The majority of the turbulence models presented in the U/U_b and W/U_b graphs shown in Figure 9.34 identify the side recirculation vortex at this measurement location $x/H = 0.3$. Although the reattachment point is most accurately predicted by the $k-\omega$ model for the W/U_b experimental data, the overall velocity development is poorly predicted by this model. The two-layer $k\varepsilon/kl$ model would be considered to produce the most accurate predictions at this measurement location for W/U_b and k/U_b^2 .

The measurement locations downstream of the cube all show consistent behaviour with regards to the U/U_b experimental data. All the turbulence models fail to accurately capture the complete experimental data profile but follow the experimental trends. By the measurement location $x/H = 2.3$ the experimental data no longer shows signs of the wake recirculation vortex. However the LVEL, $k-\omega$ and SST models still predict recirculation features. The LVEL_CAP model prediction is in close agreement with the experimental data for $z/H < 1.0$. Further assessment of the three downstream measurement locations reveals that overall, the standard $k-\varepsilon$ and two-layer $k\varepsilon/kl$ model predictions would be considered to be in closest agreement with the trends in the experimental data.

The W/U_b experimental data for the three downstream measurement locations show experimental peaks which are under predicted by all turbulence models. The LVEL and LVEL_CAP models clearly struggle at these locations predicting unrealistic behaviour. Both the two-layer models are in greatest agreement with the experimental data downstream of the cube.

With regards to the turbulent kinetic energy predictions it can be concluded that to some extent all the turbulence models tested follow the trends exhibited by the experimental data. Overall the two-layer hybrid $k\varepsilon/kl$ turbulence model tends to agree most closely with experimental data than the other models tested. **This strengthens the conclusion drawn earlier that from the turbulence models investigated the two-layer $k\varepsilon/kl$ model would be considered most accurate for these types of configurations.**

9.2.3 Results and Discussion: Temperature

As mentioned earlier, turbulence model comparisons have been undertaken for several horizontal and vertical surface temperature paths around the cube. Attention will now be turned to these predictions. Figure 9.38 corresponds to the cross-section ABCDA which denotes a plane parallel to the mounting base at $y/H = 0.5$. Figure 9.39 corresponds to the cross-section ABCD denoting a plane perpendicular to the mounting base at the symmetry plane $z/H = 0$. The additional six surface temperature profiles presented in Figure 9.40 represent horizontal and vertical paths at different y/H and z/H locations.
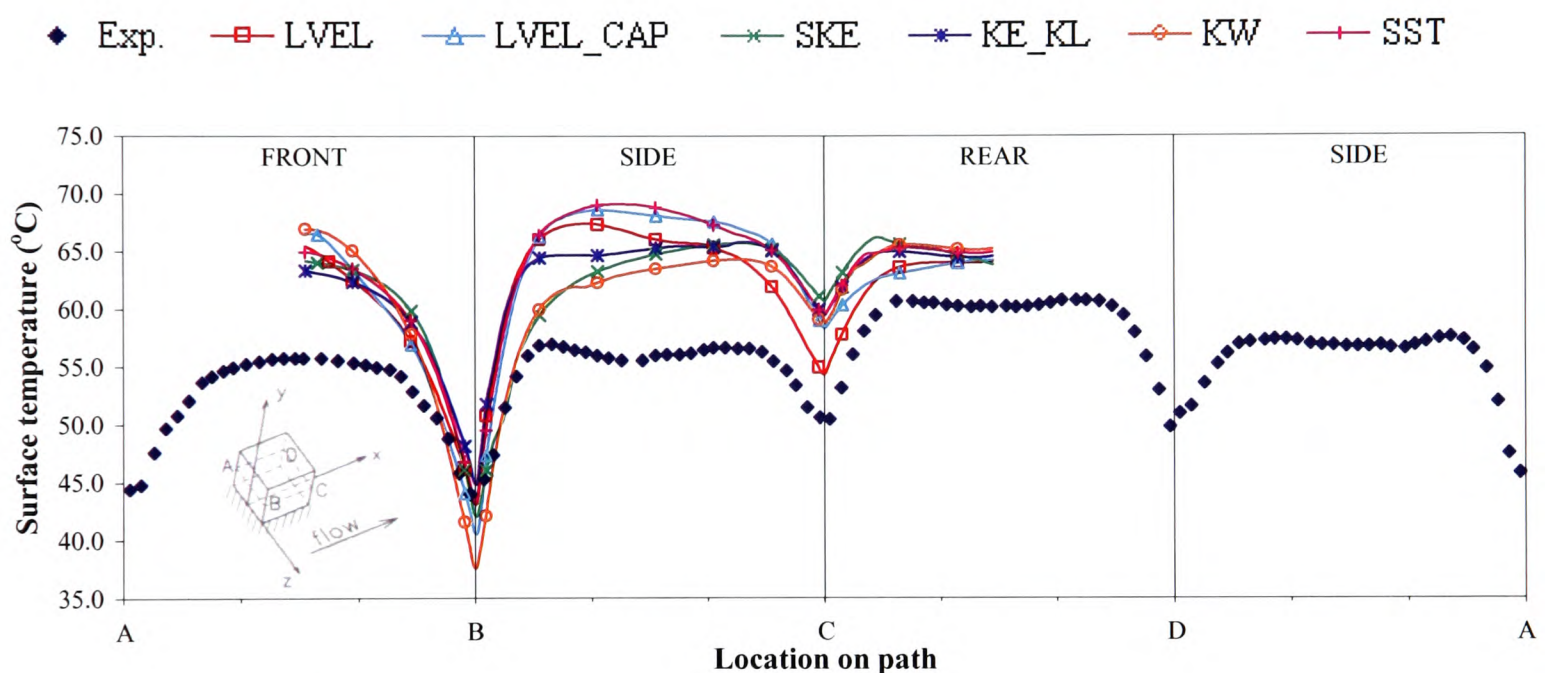
Figure 9.38 Horizontal surface temperature profile along the path ABCDA
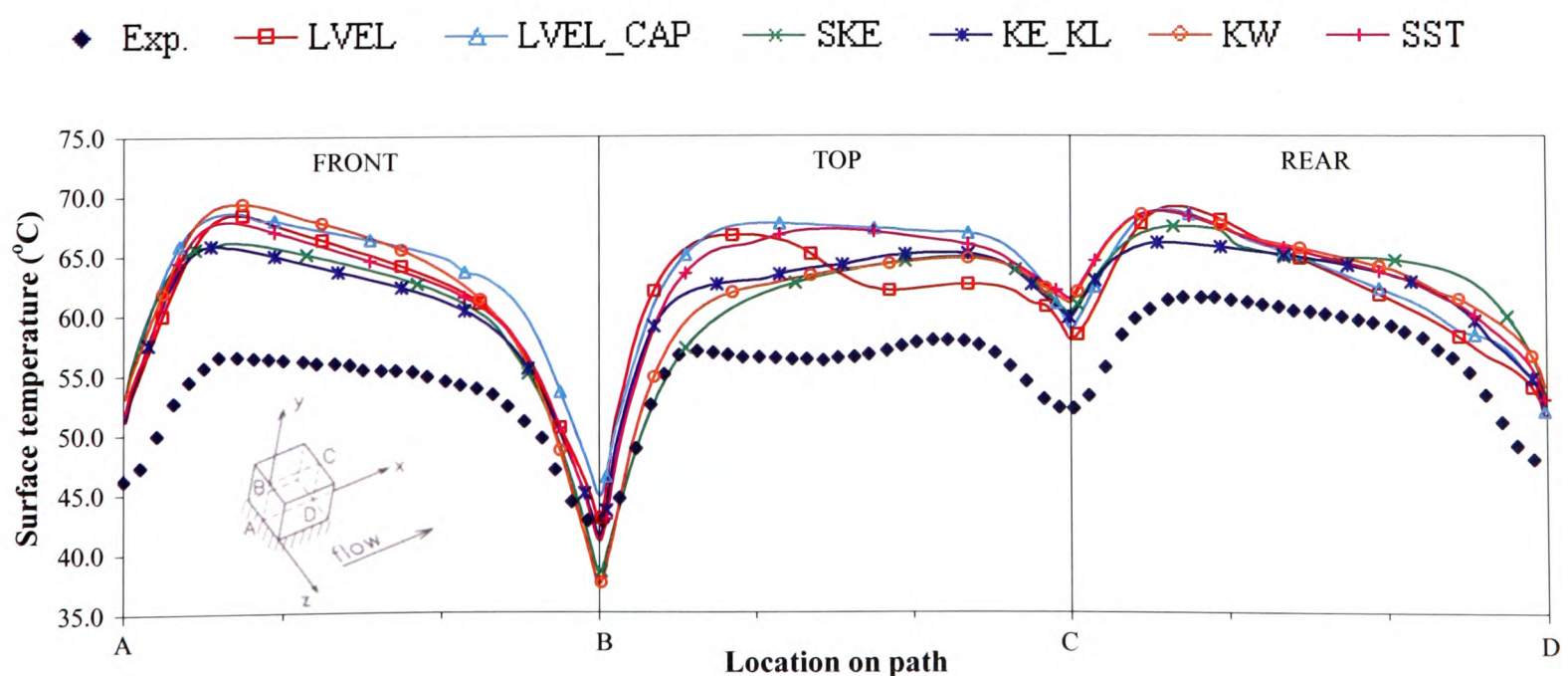
Figure 9.39 Vertical surface temperature profile along the path ABCD
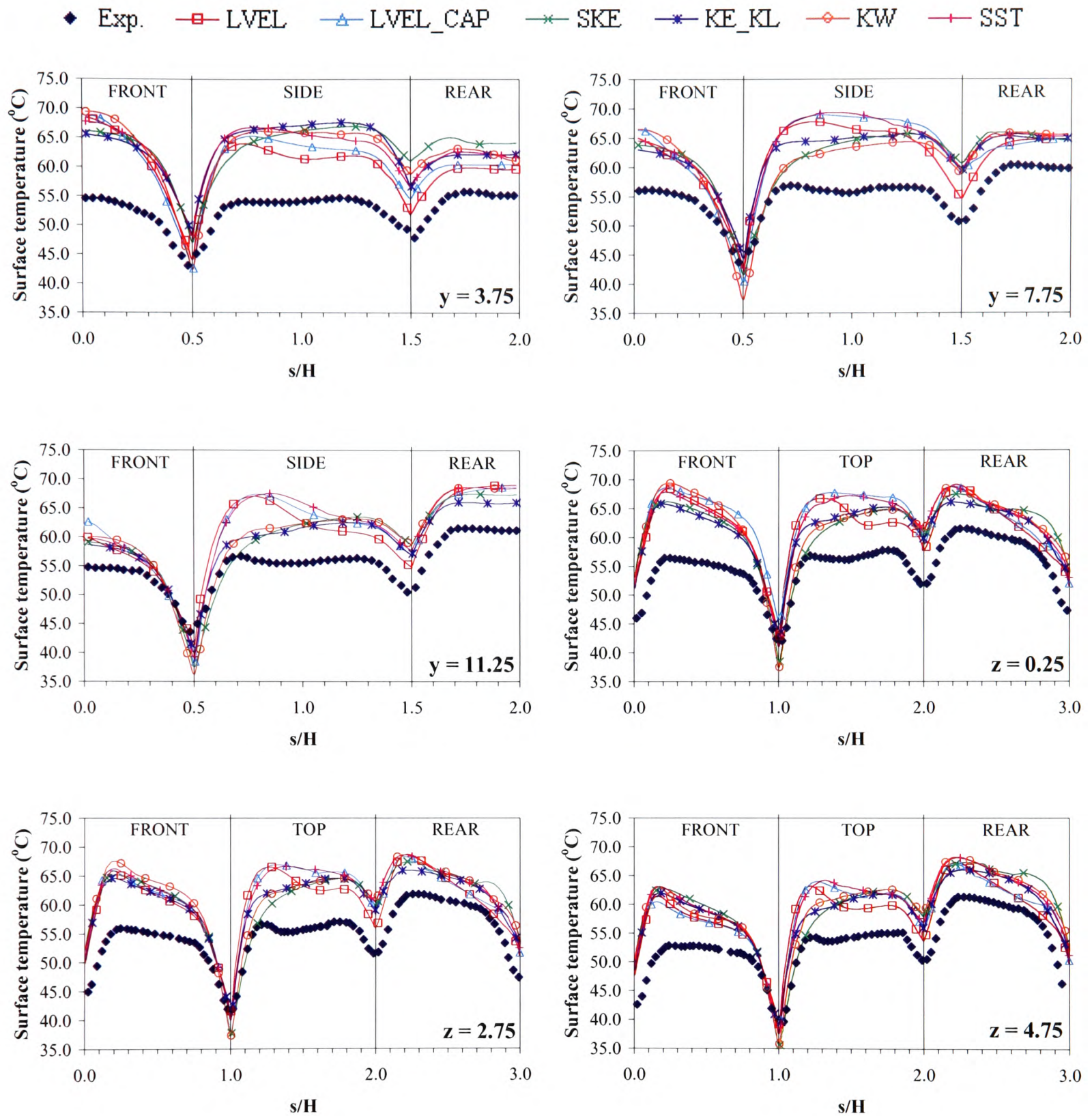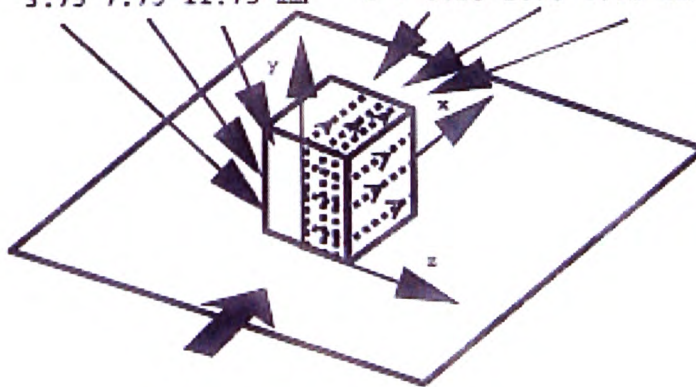
Figure 9.40 Horizontal and vertical surface temperature comparisons

Direct comparison of the surface temperature predictions can not be made with the simulation work conducted at the 8th ERCOFTAC workshop as results are only available for one Group A (RANS) model and by the participants of Group B (LES and DNS) which suggests that less accurate results were predicted by the members of Group A.

The horizontal and vertical surface temperature profile presented in Figure 9.39 shows a small decrease in the temperature on the front face of the cube. This is consistent with the experimental observation that the flow reattached in the inter-obstacle space, as the flow after the reattachment point impinges on the front of the cube causing a high heat transfer coefficient due to the colder, turbulent fluid being transported to this surface, decreasing the surface temperature.

Numerically none of the investigated turbulence models experience such a flow phenomena, this is due to all the models to some degree predicting a large wake recirculation vortex which does not reattach in the inter-obstacle space but instead occupies the entire space. This can be clearly seen from the xy-plane streamlines presented in Figure 9.23. This enlarged wake vortex acts as a large pocket of hot trapped fluid and consequently increases the temperature predictions at the front face of the cube.

The experimental temperature profiles between the single cube and matrix of cubes configurations clearly differ, most noticeably on the side and top faces of the cube. This suggests that vortex shedding experienced by the matrix of cubes is not as severe as that observed for the single cube case study discussed earlier.

From the numerical temperature predictions made at the side face of the cube, see Figure 9.38, it can be concluded that the $k\varepsilon/kl$ model best captures the relatively uniform surface temperature profile across the inner part of this face. The remaining turbulence models show either increasing temperature ($k-\varepsilon$ and $k-\omega$) or decreasing temperature (LVEL, LVEL_CAP and SST). The performance of the $k\varepsilon/kl$ model is therefore judged to be superior at this location.

The surface temperature measurements at the edges of the cube have already been highlighted as a possible area of experimental uncertainty. The numerical predictions presented here show consistent discrepancies in comparison to the experimental data. This trend was also noted at

the 8th ERCOFTAC workshop[43] for the numerical predictions obtained using RANS, LES and DNS techniques. Also the zonal LES/RANS model investigated by Zhong and Tucker[71] shows a similar trend.

As the reattachment of the wake recirculation vortex is not accurately captured by any of the tested turbulence models one would not expect the temperature predictions to be accurate either. The most that can be said about temperature predictions at the rear face of the cube is that the numerical work conducted follows the trends experienced by the experimental data.

All six of the measurement locations presented in Figure 9.40 show similar trends in the temperature predictions for the various faces of the cube as those for the two mid-plane horizontal and vertical profiles already discussed. Therefore further explanation will not be provided for these surface temperature profiles.

In conclusion it can be determined that the surface temperature results are not well predicted by any of the models tested. However it is noted that the $k\varepsilon/kl$ turbulence model most accurately captures the extent of the bound vortex on top of the cube and the temperature predictions for this model are arguably most consistent with the trend in the experimental data, being relatively flat, particularly for the side face.

9.2.4 Matrix of Cubes Concluding Remarks

The key conclusions which can be drawn from this low Reynolds number configuration of the matrix of cubes have been stated below.

- It was noted at the 6th ERCOFTAC workshop that such a configuration which emulates an idealised electronics circuit-board with neighbouring cubes tends to stabilise vortex shedding making the flow more steady than in the case of the single cube configuration discussed earlier. This is clearly convenient for steady RANS computations.

- The two-layer models, $k\varepsilon/kl$ and SST, show the most accurate agreement at the streamwise and spanwise locations stated for the interaction between the horseshoe vortices. These two turbulence models replicate the xz-plane flow field with the

greatest degree of accuracy in comparison to the oil-film visualisation plane presented in Figure 9.25.

- The two-layer hybrid $k\varepsilon/kl$ model predicts the location of the bound reattachment point as $x/H \approx 0.3$ which is in good agreement with the experimentally observed value of $x/H \approx 0.27$.

- The two-layer $k\varepsilon/kl$ turbulence model produces the most accurate prediction of the side reattachment point at $x/H = 0.46$. The experimentally observed value is stated as $x/H = 0.33$.

- The turbulence model that overall replicates most accurately the flow structures which were observed in the experimental work is the two-layer hybrid $k\varepsilon/kl$ model.

- The numerical work undertaken here is of similar quality to the simulation work presented at the 8th ERCOFTAC workshop.

- Poor numerical behaviour is consistently noted by the zero-equation LVEL-based turbulence models. Due to the fact that these mixing-length models were originally designed for the accurate prediction of boundary layer development this conclusion is not surprising.

- From the six turbulence models investigated consistently the two-layer hybrid $k\varepsilon/kl$ turbulence model produces the most accurate results for the turbulent kinetic energy. It should be noted that doubts exist as to the construction of k from measured fluctuations, which assumes isotropy.

- Generally the temperature predictions are inferior to velocity predictions, irrespective of turbulence model used. Further study is needed to establish the role of wall functions for heat transfer in this respect.

- Consistently the SST model produces comparable results to the simulation work presented at the 8th ERCOFTAC workshop. This reiterates the correct implementation by the author of the SST turbulence model within PHYSICA V2.12.

- Further investigation into the use of wall function techniques is required in order to fully understand the predictive accuracy of the investigated turbulence models.

- **Within the constraints faced by commercial CFD software developers the turbulence model which would be recommended for such a configuration as that discussed in this section would be the two-layer hybrid *kε/kl* model due to its consistent, generally accurate, behaviour noted.**

CONCLUSIONS & FUTURE WORK

This chapter has been divided into three sections. Firstly a summary from relevant chapters is provided, detailing some of the key findings arising from those chapters. This is then followed by a conclusions section. Lastly areas of further investigation have been identified.

10.1 Chapter Summaries

The following brief summaries highlight the conclusions drawn from relevant chapters that detail the CFD modelling work and validation. This is to present an overall picture of the conclusions drawn from this research.

Chapter 5: Verification of Existing Turbulence Models

This validation chapter compared the standard turbulence models available in PHYSICA Version 2.12[3] $(k - \varepsilon$ and $k - \omega)$ against the commercial CFD codes FLOTHERM Version 3.2[1] and PHOENICS Version 3.4.[2]

The conclusions drawn from this chapter are that these three CFD codes are in good agreement with each other for the test cases considered. Differences are noted with regards to the wall functions applied as the near-wall cell comparisons differ slightly. It has also been determined that moving from a first order to a higher order differencing scheme, SMART,[89] for the class of configurations investigated throughout this thesis did not offer any significant prediction improvements provided a reasonably fine mesh in used.

The author identified and corrected how the PHYSICA code handles the heat transfer calculation at internal walls. This correction resulted in good agreement with other commercial CFD codes. The validation performed in this chapter provided confidence to proceed and use the PHYSICA code as a framework to implement and investigate other turbulence models.

Chapter 6: Implementation & Testing of Zero & One Equation Turbulence Models

This chapter discussed the validation of five zero- and one-equation turbulence models implemented within the PHYSICA code by the author. Also detailed is the performance of the newly developed zero-equation turbulence model, termed AUTO_CAP.

The chapter concludes that all five turbulence models have been correctly implemented. It also suggests further investigation regarding the automatic calculation of the velocity scale within the AUTO_CAP model is required to ensure the correct recovery of the LVEL_CAP results.

Chapter 7: Martinuzzi High Reynolds Number Single Cube

The high Reynolds number experimental configuration discussed in this chapter comprises a single cube mounted on the base of a wind tunnel. The purpose of this three-dimensional test case was to further examine the predictive capability of the zero-equation LVEL and the standard high Reynolds number $k - \varepsilon$ models which are used as components of the novel two-layer $k\varepsilon / kl$ model discussed in Chapter 8. This chapter also provided additional comparison between FLOTHERM and PHYSICA.

PHYSICA performed slightly better than FLOTHERM when comparing the predicted velocity and turbulent kinetic energy profiles with experimental data. The results also showed good agreement with other numerical work presented at the 6th ERCOFTAC workshop on Refined Flow Modelling.[41]

The LVEL models performed well upstream of the cube whereas the $k - \varepsilon$ models showed better agreement with experimental data in the separated flow regions. This made it difficult to conclude which is the better turbulence model. From these results it is clear that some form of hybrid approach is required which allows use of the best model for particular regions of the flow. This generated the interest in zonal turbulence modelling which is investigated in Chapter 8.

The two-layer zonal model $k\varepsilon / kl$ was also used to simulate this high Reynolds number test case. But it was found that due to the high Reynolds number only a small $k - l$ region could be identified and hence this model converted back to the standard $k - \varepsilon$ model. This

confirmed that the $k\varepsilon/kl$ model is only applicable to low Reynolds number turbulent and transitional flows.

Chapter 8: Zonal Models

This chapter discusses existing zonal turbulence models and a new implementation of the $k\varepsilon - LVEL$ model. Both $k\varepsilon - LVEL$ and the SST models were implemented into the PHYSICA code. The SST model recently being highlighted as a possible candidate for turbulence modelling of airflow in electronics cooling applications.

The zonal turbulence model developed in this chapter is termed the two-layer hybrid $k\varepsilon/kl$ model. This model incorporates a novel matching (or blending) technique which gives a smooth transition between the two models, ensuring numerical stability.

This chapter identified the deficiency of the f_μ function incorporated within the $k\varepsilon - LVEL$ model and suggests further investigation into improvements for this model. Regarding the hybrid $k\varepsilon/kl$ model, a suitable Reynolds number to use when performing the switch between models was considered to be 180, as this agreed well with the investigation of Patel et al.[117]

Chapter 9: Meinders Low Reynolds Number Configurations

This chapter compares a range of turbulence models against the low Reynolds number experimental data generated by Meinders. These configurations are considered to be representative of electronic cooling applications and were therefore considered to be the ultimate test for the turbulence models selected for further investigation.

As highlighted within this chapter it is considered paramount that experimentally observed flow features are recovered by the turbulence models in order to enhance the predictive capability of the calculated heat transfer from the electronic components and those downstream.

The only turbulence model to exhibit all of the observed flow features was the new zonal turbulence model $k\varepsilon/kl$, although no clear winner could be identified when considering the predictions of the component surface temperature.

10.2 Conclusions

Airflow around electronic devices has a crucial role in controlling package temperature. Thermal design engineers are increasingly using CFD tools to predict airflow and temperature in electronic systems. This is helping to identify optimal thermal management strategies and so design reliable electronic devices much more quickly than could be achieved through physical prototyping alone.

The primary goal of this research has been the development of a low Reynolds number turbulence model which combines accuracy and efficiency for airflows found in an electronics cooling environment. The research has lead to the development of a two-layer hybrid $k\varepsilon/kl$ model. This hybrid model uses a novel technique to merge the two turbulence models ($k-\varepsilon$ and $k-l$) together. The hybrid model combines the favourable characteristics of the standard $k-\varepsilon$ model in the high Reynolds number region with a single transport equation $k-l$ model in the low Reynolds number region.

The developed hybrid model approach ensures that whilst the turbulent kinetic energy is solved continuously throughout the solution domain, the dissipation length scale that is most affected by viscous damping is represented by the local mixing-length L_m $\left(\varepsilon_B = C_d \cdot f_2 \cdot k^{3/2}/L_m\right)$ in the low Reynolds number region. Novel variable matching has been performed for the turbulent dissipation rate and the turbulent viscosity. Ensuring this variable matching has resulted in a continuous smooth blending between the models. A step change was found to cause numerical instability leading to poor convergence and consequently needed heavier relaxation. The mixing-length is computed automatically following the approach of Agonafer et al.[98] A critical Reynolds number of 180 was found to agree well with the experiments of Patel et al.[117]

Comparisons against a number of turbulence models appearing in the electronics cooling literature have been undertaken. These ranged from the mixing-length model LVEL, to the low Reynolds number model $k-\omega$ and also the standard $k-\varepsilon$ model. In addition to these models the SST model, which also uses the two-layer philosophy, has been considered.

When comparing the various models considered for the Meinders low Reynolds number configurations it was found that the $k\varepsilon/kl$ model performed rather well, especially when

predicting the flow profile in the wake of an obstacle and when predicting the reattachment point of the flow. The $k - \varepsilon$ model was found to perform very poorly. This is not surprising since the standard form was designed to work for high Reynolds number regions. In contrast to previously published results, conducted on flat-pack type geometries producing small recirculation regions in the flow, the SST model was found to have serious shortcomings especially in the wake region where flow recovery was poor. This was also noted by Menter et al.[75] who has since proposed an improved DES version as an alternative. This model has not been tested in this research.

Electronic systems have high aspect ratio obstacles placed in the path of the airflow. This will result in significant airflow recirculation throughout the system which requires a suitable turbulence model. For this reason, models that have been developed to represent flow over streamline bodies (such as the Spalart-Allmaras model[53]) are likely to be less successful for airflow with large amounts of recirculation. The standard SST model was also developed for flow over streamline bodies and hence will also have similar deficiencies.

Considering the prediction of turbulent quantities, such as k, it has been shown that the $k\varepsilon / kl$ model again performs as well as, or better than, the other RANS models tested. Uncertainties in deriving k from experiments explains some of the discrepancies. Further research is needed in this area.

Temperature predictions are not as successful as velocity predictions, irrespective of the turbulence model used. This is due to the wall function employed in the PHYSICA code which is based on the wall shear stress. The more sophisticated wall treatment recommended by Craft et al.[78] has been reported to improve model accuracy and is therefore suggested for implementation within PHYSICA.

Overall for the range of test cases considered consistently the two-layer $k\varepsilon / kl$ model can be regarded as the best turbulence model with respect to the flow field. Temperature predictions are not so good.

The study is by no means conclusive. More numerical and indeed experimental wind tunnel work is required in order to ascertain the most appropriate values for the parameters in the $k\varepsilon / kl$ model, however so far it appears to be a promising one to pursue.

LES and some zonal LES/RANS based turbulence models are clearly a way forward for the accurate prediction of turbulence flow. However their very significant computational cost relative to any RANS alternative makes it questionable whether any electronics designer would have the luxury of the time needed to run such models. The answer to this question is likely to remain "no" for the foreseeable future.

10.3 Further Investigation

Areas remain where further work is required to improve the turbulence model predictions presented in this thesis.

10.3.1 Subgrid Wall Functions

Throughout this thesis the universal log-law wall function has been employed. Future work should investigate the use of the so-called "generalised" wall functions which relate heat transfer to k at the wall. Advanced wall treatment is an area widely discussed by Craft et al.[78]

As discussed in the literature review improved turbulence model predictions have been noted when advanced treatment is applied to the wall boundary and therefore it stands to reason that this would be echoed for the turbulence models discussed in the current work.

10.3.2 Velocity Scale for AUTO_CAP

The validation work performed during the course of this thesis has identified that the novel zero-equation AUTO_CAP model requires some alternative calculation of the velocity scale to improve the model's ability to replicate the LVEL_CAP model predictions.

However, the poor performance of the LVEL model, particularly the non-physical flows predicted for the Meinders configurations suggests the model's use should be discontinued, rather than the model improved for this type of application.

10.3.3 Modifications for $k\varepsilon$ - $LVEL$

Two novel modifications have been discussed in Chapter 8 for the current implementation of the zonal $k\varepsilon - LVEL$ turbulence model. Both new treatments show good comparison with the work of Patel et al.[117]

The first proposal applies a smooth variation of the damping function f_μ through both the laminar and turbulent regions of the computational domain. The second proposal suggests that within the laminar sub-layer the distribution of f_μ should be constant.

Both recommendations should be implemented and tested to further understand the benefits of one particular approach over another.

10.3.4 Modifications for $k\varepsilon/kl$

The two-layer hybrid $k\varepsilon/kl$ model is considered to be complete.

A logical extention would be to look at the effect of varying the critical Reynolds number used to make the switch between the near-wall and bulk turbulence models on the predictive behaviour of the overall model by changing the constant β in the damping function f_1 (equation (8.20) page 169). A wider range of experimental test cases characteristic of electronics cooling applications would be needed for the results of such an exercise to be considered conclusive. Unfortunately more extensive experimental data is not known to exist.

ACME
Association for Computational Mechanics in Engineering.

Aspect Ratio
The ratio of two sides of a grid cell.

Assembly
A collecton of items of geometry.

AUTO_CAP
Automatic capping of LVEL model.

B.C
Boundary Condition.

BFS
Acronym for Backward Facing Step.

BGA
Acronym for Ball Grid Array. A BGA is a type of surface-mount packaging used for integrated circuits.

Bluff Bodies
A body is defined as "bluff" when the flow streamlines do not follow the surface of the body, but detach from it leaving regions of separated flow and a wide trailing wake. Computational complexities related to flows around bluff bodies include difficulties related to flow impingement, flow separation and vortex shedding.

Boundary Layer
In fluid flow, a narrow region next to a fixed boundary or surface where the fluid velocity rapidly changes from zero to some finite value.

Buoyancy Force
The force resulting from temperature differences within a fluid.

Cells
The domain of integration is sub-divided into a regular array of non-overlapping, contiguous, cuboidal volumes known individually as cells and collectively as the grid. This sub-division is done for the purpose of discretizing the flow-governing differential equations.

CFD
Acronym for Computational Fluid Dynamics.

Characteristic Length
The typical length scale for the flow under investigation.

Characteristic Velocity
The typical velocity scale for the flow under investigation.

Command Center Scenarios
A quick method of observing the effects of varying the project parameters.

Contour Plot
2D plot of a given variable joining points of equal value.

Control Volume
The area that is being modelled, the computational domain, is divided into parts (Control Volumes) to allow for the transport equation that is in the form of a PDE can be solved.

CPU
Acronym for Computer Processing Unit.

CTE
Coefficient of Thermal Expansion.

CWNN
Code With No Name.

Dependent Variables
The field which satisfy the flow-governing PDEs. The three velocity components, the temperature and the pressure fields are all dependent variables in this sense.

DES
Detached Eddy Simulation.

DNS
Direct Numerical Simulation.

DoE
Design of Experiments.

EMAP
International Symposium on Electronics Materials and Packaging.

EPSRC
Acronym for Engineering and Physical Sciences Research Council.

EPTC
Electronics Packaging Technology Conference.

ERCOFTAC
Acronym for European Research Community on Flow, Turbulence and Combustion.

EuroSimE
Conference on Thermal & Mechanical Simulation and Experiments in Micro-Electronics and Micro-Systems.

EUROTHERM
European Committee for the Advancement of Thermal Sciences and Heat Transfer.

Field
A quantity for which storage is provided for the value of it in every cell of the integration domain.

Fluid
The type of coolant flowing through the model; air is the default.

Grid Point
The points formed by the corners of the control volumes.

Heat Flux
The outward flow of heat from a heat source. Heat flow per unit area.

ICHMT
International Symposium on Turbulence, Heat & Mass Transfer.

IEEE
Institute of Electrical and Electronics Engineers.

Initial Conditions
The solution of the equations for the field variables starts from a set of initial values of the fields. In steady-state operation, the initial conditions constitute guesses for the solution (and the better the guess the less work the solver will have to do). In transient operation the initial conditions form a part of the problem specification.

IR
Infrared Thermography.

Isotroptic
Values are the same in all coordinate directions.

ITHERM
Intersociety Conference on Thermal, Mechanics and Thermomechanical Phenomena in Electronic Systems.

KLMODL
PHOENICS one-equation model.

Laminar
The flow in which fluid layers are moving steadily without interference.

Laminar Viscosity
The molecular viscosity (or friction) between the fluid elements themselves and between the fluid and solid surfaces with which the fluid is in contact.

LDA
Laser Doppler Anemometry.

LES
Large Eddy Simulation.

LHS
Left Hand Side.

Linear Relaxation
A simple form of damping the solution.

LSI
Large Scale Integration (of electronic circuitry).

LVEL
Length-velocity turbulence model, developed by Dereje Agonafer, Liao Gan-Li and Brian Spalding. This turbulence model was developed for applications that involve many solids of differing shapes and sizes where only a small number of fluid grid cells between solid surfaces can be realised.

LVEL_CAP
Capped version of LVEL model.

Monitor Point
Solver grid cells in which the values of the variables are recorded at each outer-iteration or time-step.

MUSCL
Acronym for Monotonic Upwind Scheme for Conservation Laws.

Node Point
The corners of the control volume.

PCB
Acronym for Printed Circuit Board.

PDA
Acronym for Personal Digital Assistant.

PDE
Acronym for Partial Differential Equation.

Pitch
The nominal centerline-to-centerline dimension between adjacent conductors.

PQFP
Acronym for Plastic Quad Flat Pack.

PREP
Postgraduate Research Conference in Electronics, Photonics, Communications & Software.

QUICK
Acronym for Quadratic Upwind Interpolation for Convective Kinetics.

RANS
Reynolds Averaged Navier-Stokes.

RHS
Right Hand Side.

RNG
ReNormalisation Group.

RSM
Reynolds Stress Model.

SEMI-THERM
Semiconductor Thermal Measurement and Management Symposium.

SET
Science, Engineering and Technology.

SGS
Subgrid-Scale.

Shear Layer
A shear layer in a fluid is a region where the velocity of a layer of fluid is different from the velocity of an adjacent layer of fluid.

SMART
Acronym for Sharp and Monotonic Algorithm for Realistic Transport.

SMC
Second-Moment Closure.

Solution Domain
Defines the extent of the geometry model included in the calculations.

SSI
Small Scale Integration (of electronic circuitry).

SST
Shear-Stress Transport.

SST-DES
Shear-Stress Transport Detached Eddy Simulation.

SST_V
Shear-Stress Transport model based on vorticity.

Stagger
The displacement of locations of the values of the velocity components from those of the pressure.

Symmetry Boundary
A frictionless, impermeable and adiabatic planar surface.

Transitional Flow
The transition between laminar and turbulent flow.

Turbulent Flow
The motion of the fluid layers are affected by irregular, fluctuating and chaotic eddy currents.

Turbulent Viscosity

Turbulent flows are modelled by solving the time-averaged equations representing the mean behaviour of the flow. The time-averaged momentum equations contain terms involving the cross-correlation of fluctuating quantities, the so-called Reynolds stresses, conventionally denoted by $\rho(u'v')$. These stresses are represented by the Boussinesq approximation in which $\rho(u'v')$ is taken to be proportional to the gradient of the mean velocities u and v, the constant of proportionality is known as the turbulent viscosity.

$$\rho(u'v') = -\mu_t\left(\frac{\partial u}{\partial y} + \frac{\partial v}{\partial x}\right)$$

ULSI

Ultra Large Scale Integration (of electronic circuitry).

Variables

Variables are field quantities, i.e. they have a distinct value for each cell.

Vector Plot

A plot of vectors representing the fluid velocity at the centre of each computational grid cell.

VLSI

Very Large Scale Integration (of electronic circuitry).

WSI

Wafer Scale Integration (of electronic circuitry).

A Case Descriptions

This appendix details the test cases considered throughout this thesis. Details of the solution domain, boundary conditions, mesh density and material properties are given to allow the recreation of any case. A monitor point has been located in a region of the flow where the stability of the solved variables would be considered to be difficult to achieve, yet indicative of the solution being fully converged, e.g. partly within a recirculation behind an obstacle.

The two differencing schemes used are the first order accurate Upwind and Hybrid schemes. In the majority of instances the Upwind differencing scheme has been employed so comparisons with FLOTHERM can been undertaken, as the Upwind scheme is the only option available within the structure of this code.

The modelling assumptions for all test cases are that flow is considered to be at a steady state and all wall boundaries are treated as smooth. When a turbulent state is identified standard log-law wall functions are applied except for those turbulence models which require resolution of the near-wall flow.

For all simulation work undertaken the results obtained have been considered to be fully converged if the normalised residual values for all solved variables have reduced by at least four orders of magnitude and the values of the solved variables at the monitor point have stopped changing with iteration. For cases where the residuals have been unable to reduce by a minimum of four orders of magnitude, due to the fact that the initial guess for the system domain variables is relatively accurate, convergence has been determined by examining the monitor point to ensure that all variables have flat-lined. All test cases considered in this thesis have fully converged to the required tolerance.

Note that all numerical work presented in this thesis is mesh independent. Specifications of the mesh density used for a particular case have been stated.

A1 Parallel Plates

This case was originally aimed at a target audience of FLOTHERM users interested in flow validation cases where FLOTHERM predictions are compared with analytical or empirical data.[7]

The case considers flow between two smooth parallel plates (i.e. Poiseuille flow) over a range of Reynolds numbers covering both laminar and turbulent flow conditions. A uniform velocity field has been assumed across the entrance of the channel with a variety of inlet velocity values corresponding to a Reynolds number range of 100 (laminar) to 10^4 (turbulent).
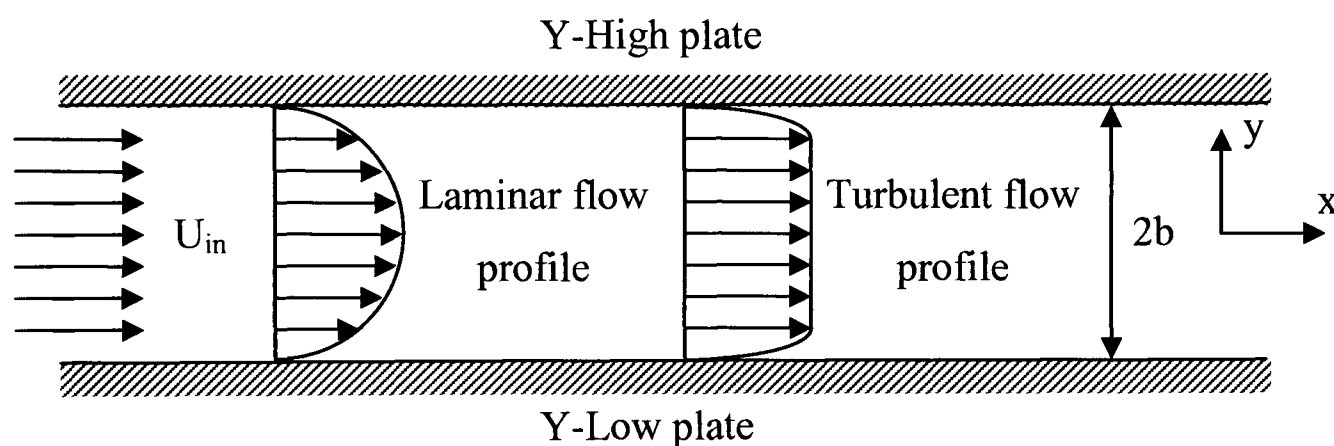
Figure A.1 Schematic representation of the parallel plates test geometry

The computational domain length in the flow direction was made long enough to ensure that the flow field was fully developed.[118] The flow is driven by a pressure gradient acting in the direction of flow, and is retarded by viscous drag along both plate surfaces, such that these forces are in balance. The Upwind differencing scheme has been used and the gravitational effects have been neglected for all simulation work conducted.

The majority of the default settings for all codes considered have been preserved; details have been provided where default changes have been made.

A1.1 Laminar Flow Conditions

The Reynolds number, based on the hydraulic diameter of the channel, has been calculated as 100. The dimensions of the solution domain are presented in Figure A.2.
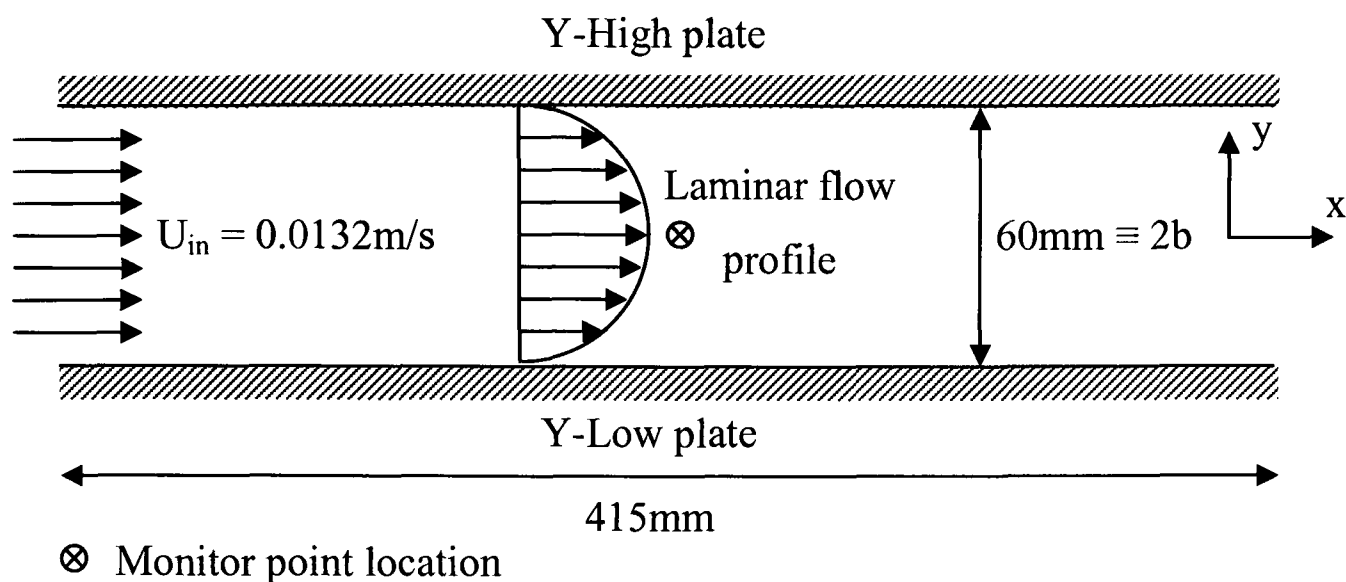
Figure A.2 Parallel plates test case laminar solution domain

The fluid material properties have been set to air at 30°C therefore giving a fluid density of 1.1614kg/m^3 and a kinematic viscosity of 1.5842×10^{-5} m^2/s. A uniform mesh density of (40 x 20) mesh elements have been set in the x- and y-directions respectively.

The simulated results are compared with analytical data for the fully developed velocity profile. For laminar flow conditions the fully developed velocity profile is the well known parabolic profile and can be derived analytically. For the derivation see Appendix B1.

$$\frac{U}{U_{in}} = \frac{3}{2}\left[1 - \left(\frac{y}{b}\right)^2\right] \tag{A.1}$$

A1.2 Turbulent Flow Conditions

The Reynolds numbers for this case is set to 10,000 based on the hydraulic diameter of the channel. The construction of the geometry under investigation is shown in Figure A.3.
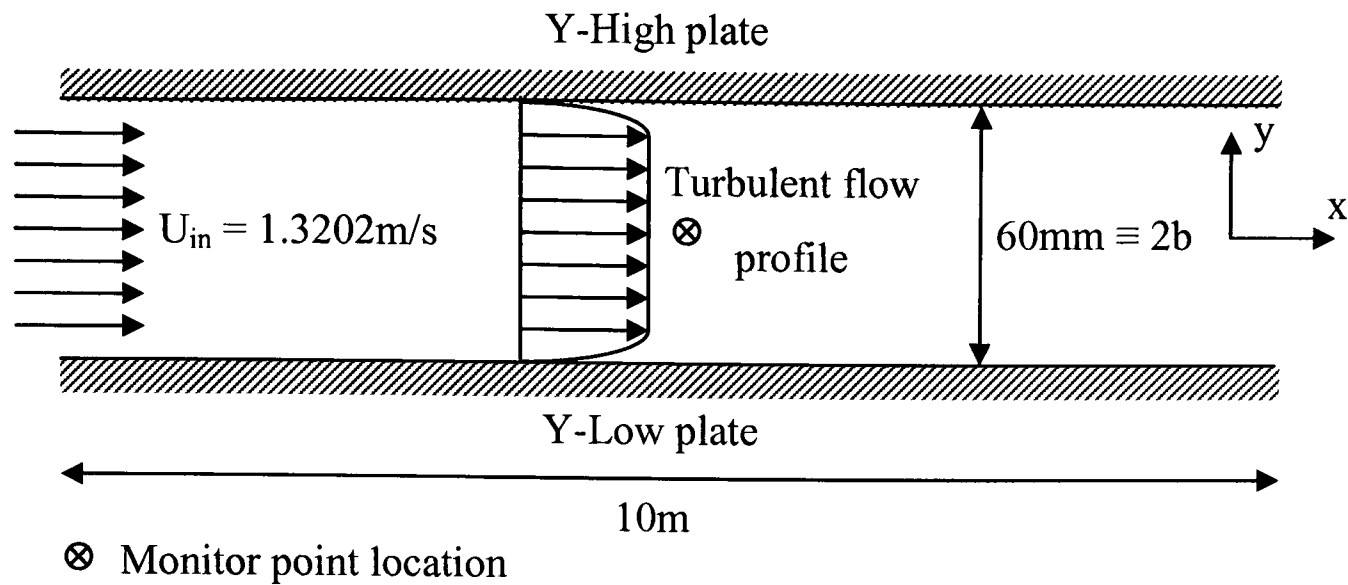
Figure A.3 Parallel plates test case turbulent solution domain

At the inlet boundary the turbulent quantities are estimated using equations (A.2)-(A.4) depending on the turbulence model being employed.

$$k_{in} = 10^{-1} \times (U_{in})^2 \tag{A.2}$$

$$\varepsilon_{in} = \frac{0.1643 \times (k_{in})^{1.5}}{l_i} \tag{A.3}$$

where $l_i = 0.1 \times (\text{norminal inlet area})^{0.5}$

$$\omega_{in} = \frac{\varepsilon_{in}}{0.09 \times k_{in}} \tag{A.4}$$

The fluid material properties have been set to air at 30°C therefore resulting in a fluid density of 1.1614kg/m^3 and a kinematic viscosity of $1.5842 \times 10^{-5} \text{m}^2/\text{s}$.

The mesh density used for the majority of the turbulence models considered is (640 x 48) in the x- and y-directions respectively. However due to the fine mesh constraint imposed by the $k - \omega$ and SST models these simulation cases use a mesh density of (1600 x 120) in the x- and y-directions respectively and also use the mesh grading technique located at the plate surfaces to ensure that the mesh is finest near the wall, where the velocity gradient is highest. Figure A.4 presents the generated fine mesh density employed for the simulations undertaken using the $k - \omega$ and SST turbulence models.
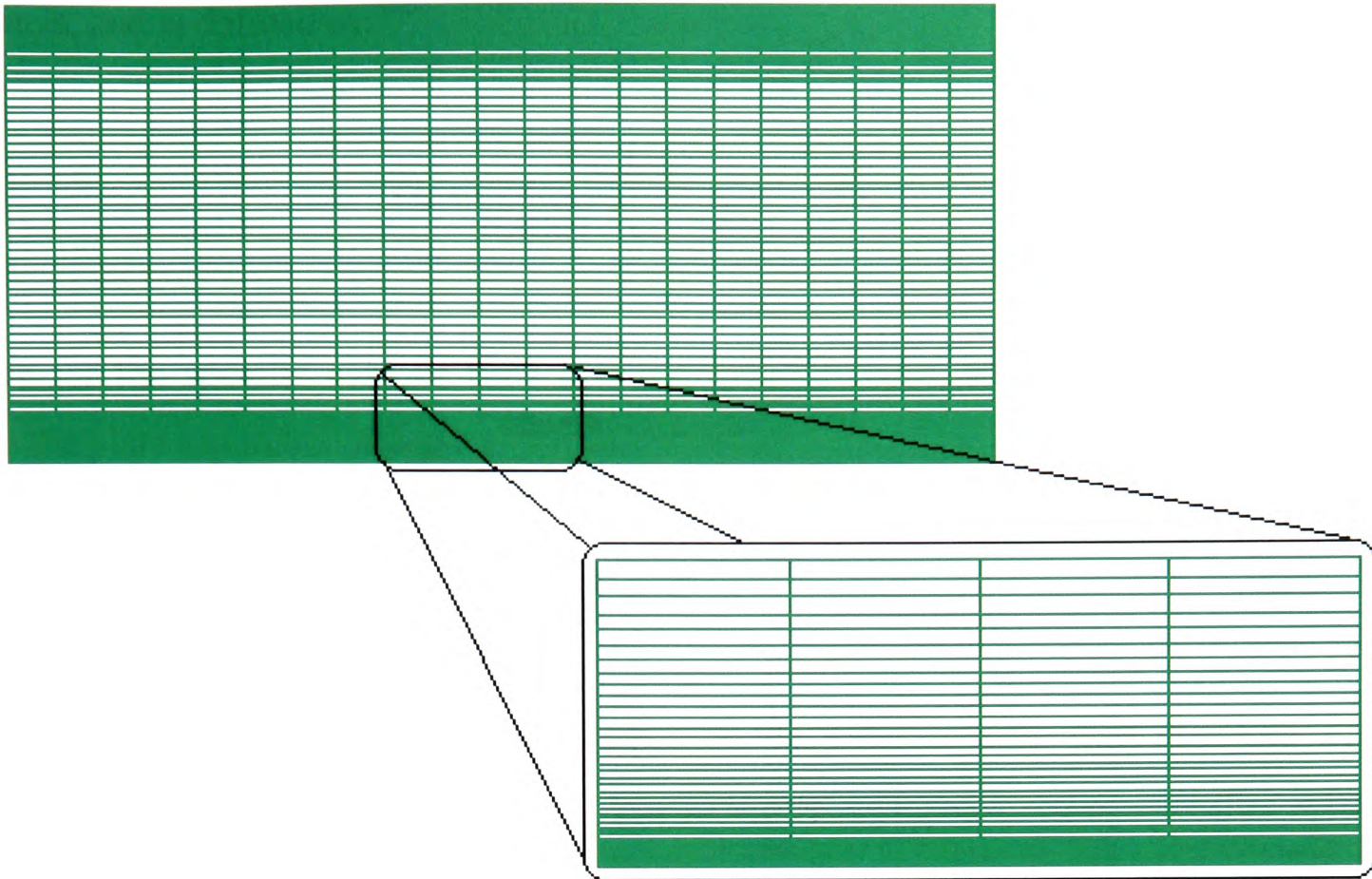
Figure A.4 Parallel plates mesh density employed for the k - ω and SST turbulence models

The turbulent flow profile is much 'flatter' towards the centre of the channel compared to the laminar velocity profile discussed earlier, an expression for the fully developed velocity profile can be written in the form stated in equation (A.5). For the derivation of this profile refer to Appendix B2.

$$\frac{U}{U_{in}} = 1 + \left[\left(\frac{f}{2} \right)^{0.5} \Big/ \kappa \right] \left[\frac{5}{6} + \ln \left(1 - \left(\frac{y}{b} \right)^{0.5} \right) + \left(\frac{y}{b} \right)^{0.5} \right] \qquad (A.5)$$

The Fanning friction factor, f, is a non-dimensional measure of the friction effect of the boundary plate and the consequent pressure drop. It expresses the linear relationship between the velocity and the pressure gradient.

$$f = - \left(\frac{D_h \dfrac{dp}{dx}}{2\rho U_{in}^2} \right) \qquad (A.6)$$

The hydraulic diameter, D_h, is a commonly used term when dealing with flow in non-circular channels, and is defined as:[155]

$$D_h = \frac{4 \times Area}{Wetted\ Perimeter} = \frac{4A}{P}$$ (A.7)

Hence for the specific case of flow between parallel plates the hydraulic diameter equals twice the plate separation distance.[156, 157]

$$D_h = 4b$$ (A.8)

The Fanning friction factor varies with respect to the distance in the flow direction x. As x increases and the flow fully develops f approaches an asymptotic value, hereafter referred to as f_{fd}.

For laminar flow conditions f_{fd} is given by the analytical expression stated in Kakac et al.[156]

$$f_{fd} = \frac{24}{Re}$$ (A.9)

For turbulent flow conditions empirical correlations are available for various ranges of Reynolds numbers. Kakac et al.[156] suggest the following empirical values

$$f_{fd} = \frac{0.1268}{Re^{0.3}} \text{ for } 5000 < Re < 3 \times 10^4$$ (A.10)

$$f_{fd} = \frac{0.0868}{Re^{0.25}} \text{ for } 1.2 \times 10^4 < Re < 1.2 \times 10^6$$

To determine the flow regime under consideration and to select the appropriate f_{fd} expression the definition of the Reynolds number is stated.

$$Re = \frac{\left(D_h \rho U_{in}\right)}{\mu}$$ (A.11)

A2 Inlet/Outlet

This case was designed for the purpose of comparing the two CFD codes FLOTHERM and PHYSICA when flow recirculation plays a key role in the phenomena taking place within the solution domain.

The case considers flow within an enclosure which has an inlet height specified to be 20% of the overall domain height in the flow normal direction measured from the Y-Low wall. The outlet also has a height of 20% of the complete solution domain in the flow normal direction, but is located at the Y-High wall of the enclosure thus creating an s-type flow pathway. The Reynolds number for the case is set to 10,422 based on the inlet height. A schematic of the solution domain together with the dimensions used for this case have been detailed in Figure A.5.
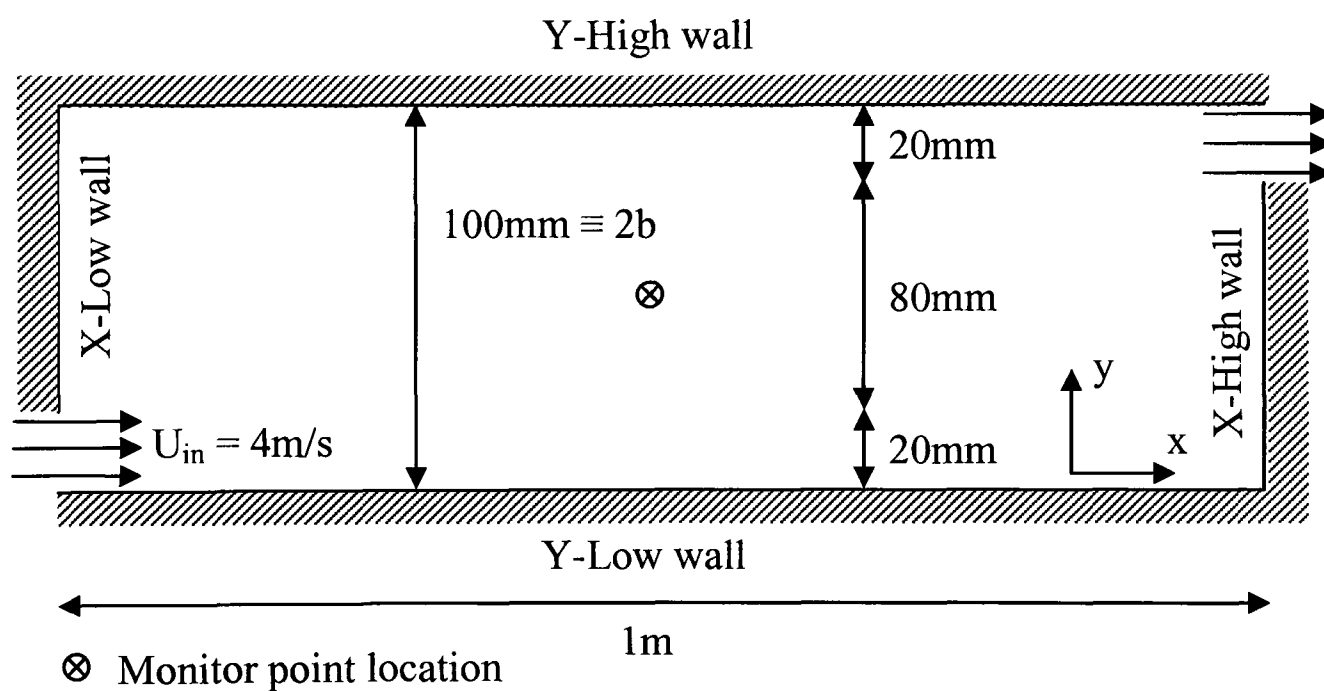
Figure A.5 Inlet/Outlet test case solution domain

The turbulent quantities entering the solution domain have been estimated using the equations stated below

$$k_{in} = 10^{-3} \times \left(U_{in} \right)^2 \qquad \text{(A.12)}$$

$$\varepsilon_{in} = \frac{0.1643 \times \left(k_{in} \right)^{1.5}}{l_i} \qquad \text{(A.13)}$$

$$l_i = 0.1 \times \left(\text{norminal inlet area} \right)^{0.5}$$

The uniform mesh density which has been employed for this test case is (500 x 50) mesh elements in the x- and y-directions respectively, which was found to ensure a mesh independent solution. The fluid material properties have been set to air at 20°C therefore resulting in a fluid density of 1.188kg/m^3 and a kinematic viscosity of $1.5353 \times 10^{-5} \text{m}^2/\text{s}$. The differencing scheme employed for all the simulation work conducted is the first order accurate Upwind differencing scheme.

A3 Backward Facing Step

Two backward facing step configurations have been considered for investigation, both of which use the Hybrid differencing scheme. The first looks at the single-sided backward-facing step test case which originates from the work of Vogel and Eaton.[13] The primary goal of their work was to investigate the causes of the high heat transfer rate in the reattachment region. The second configuration originates from the AFOSR-HTTM-Sanford Conference on Complex Turbulent Flows,[18] the reason for considering two configurations will be discussed later.

A3.1 Backward Facing Step Re = 28,000

The computational solution domain structure simulated for this test case is presented in Figure A.6. The mesh density used is presented in Figure A.7, it is noted that mesh grading has been used to ensure that a fine mesh concentration is located close to the wall boundaries of the domain. (333 x 160) cells upstream of the step and (333 x 220) cells downstream of the step have been distributed in the x- and y-directions respectively.

Figure A.6 Backward facing step solution domain Re = 28,000
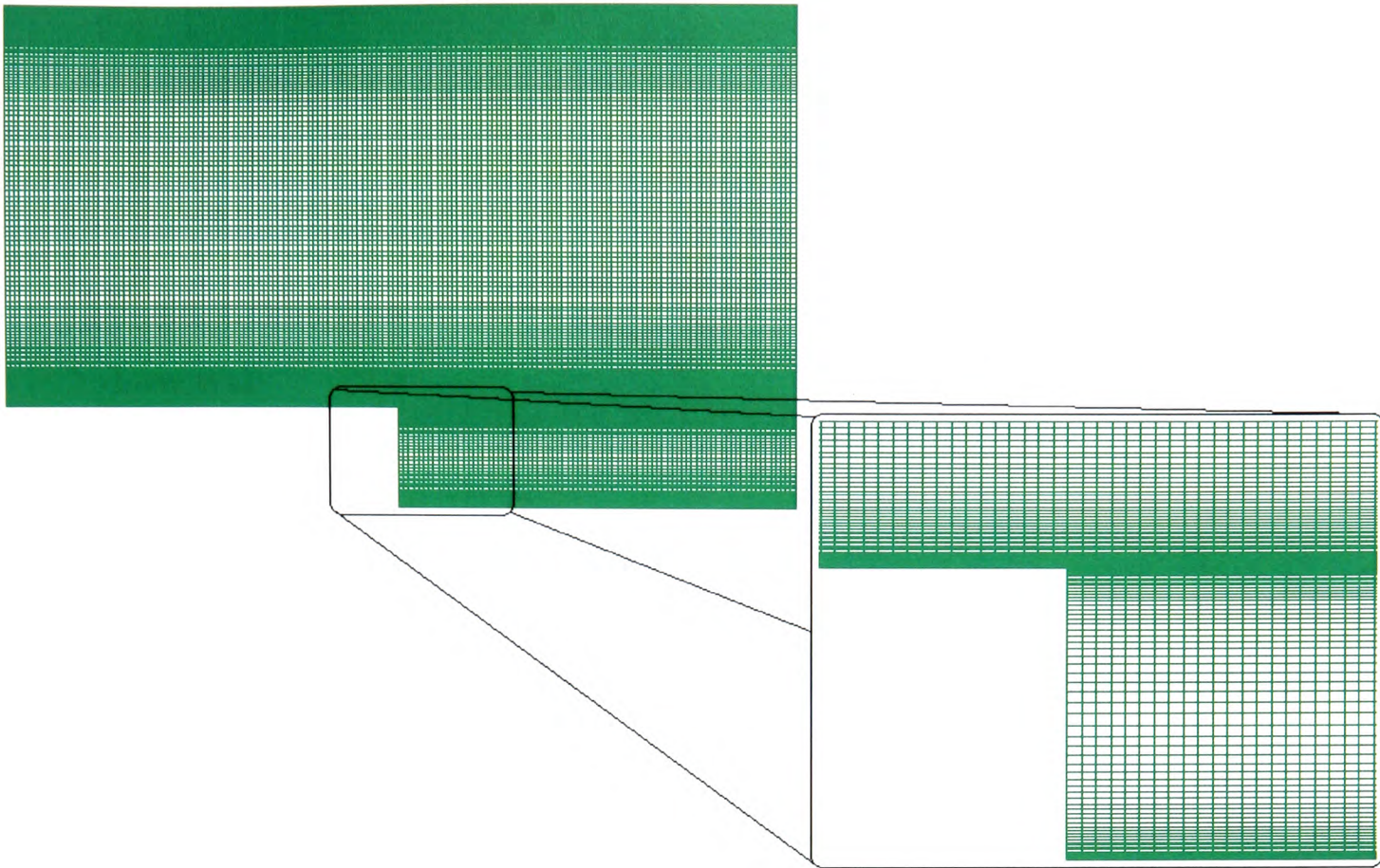
Figure A.7 Mesh density employed for the backward facing step case Re = 28,000

The experimental data available indicates that the flow is laminar at the centreline of the channel; therefore both the turbulent parameters at the inlet have been set to 1.0×10^{-10}. The fluid material properties specified for this case use a density of 1.2kg/m^3 and a kinematic viscosity of $1.4889 \times 10^{-5} \text{m}^2/\text{s}$.

This test case was also investigated by Menter's colleagues Vieser et al.[121] as a validation case for the SST turbulence model. The geometry configuration used is presented in Figure A.8. The turbulent inlet values used by Vieser et al. are stated in equations (A.14) and (A.15)

$$k_{in} = 0.18 \text{m}^2/\text{s}^2 \tag{A.14}$$

$$\varepsilon_{in} = 0.078 \text{m}^2/\text{s}^3 \tag{A.15}$$
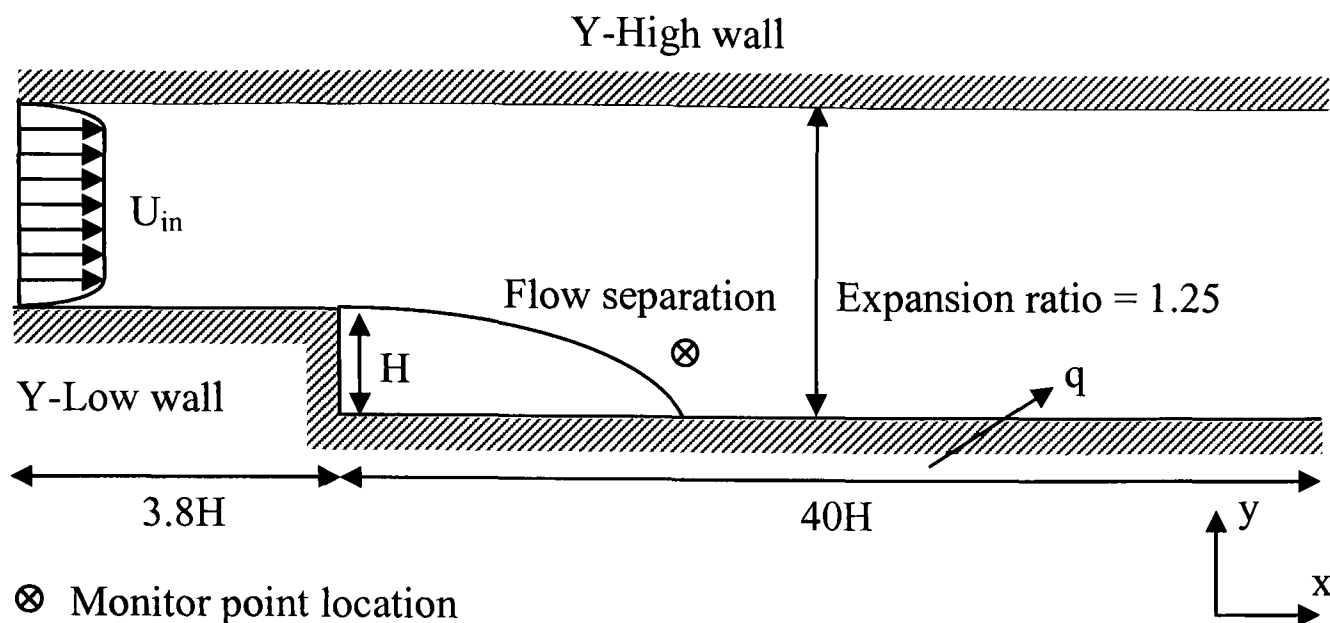
Figure A.8 Computational domain for the turbulent flow over a backward facing step (CFX)

This test configuration, which uses a distance of 3.8H upstream of the step, was also simulated using the inlet boundary condition specified in Heyerichs and Pollard[58] for the Vogel and Eaton dataset, this paper exploits the one-seventh power law in the boundary layer and relevant conditions in the main stream just upstream of the step.

The available experimental data extracted from the Vogel and Eaton reference was a velocity and turbulent kinetic energy profile, calculated using a relationship based on the U_{rms} data. The data extended from the top surface of the step to the channel centreline. The location of this measurement data is defined as being 75mm upstream of the step, but details of the geometry configuration upstream of this location are unclear.

The suction device applied to the lower wall upstream of the step is expected to strongly affect the near-wall velocity profile and hence the turbulence quantities. Therefore it is not valid to simply reverse the profile for the top half of the channel, which has no suction device attached. On this surface a normal turbulent boundary layer will develop, but will be affected by the suction on the opposite wall. The experimental results show that a uniform velocity from approximately a quarter of the channel height above the step to the centreline, where the turbulence kinetic energy shows the flow to be laminar.

It can therefore be concluded that adequate information regarding the affects of the suction device on the inlet boundary condition have not been clearly specified. As such, no firm

conclusions could be made regarding the performance of the turbulence models investigated from the results they produced for this case.

As the case appeared to be supported by high quality experimental data, Dr Parry (October 2004) felt it worthwhile to attempt to predict the velocity and turbulence profiles at the measured location by modelling the development section upstream of the measured location.

Dr Parry used FLOTHERM's Command Center optimiser to control changes in the unknown input parameters – the flow rate into the development section (assumed uniform), the suction flow rate (assumed uniform), the size and location of the suction region within the 2.5m long development section.

The objective function minimised was:

$$\sum_1^M \left(\left| u_{calculated} - u_{measured} \right| \right) \tag{A.16}$$

Where M is the number of measurement points.

Ranges of the input parameters chosen were refined as the optimiser approached the optimum by defining a new Design of Experiments (DoE) around the best design.

As work on this case progressed it was deemed necessary to model the rounded inlet, guessing the extent and curvature. Furthermore, to most closely match the velocity profile it was found necessary to model the surface of the suction region as rough, thereby adding the roughness of the suction section as another unknown input variable.

Given the large number of unknown input parameters, the response surface generated by the optimiser will have many local minima. The risk of predicting a variable profile close to the measured experimental profiles with the wrong values for the input parameters is high. This was confirmed by the poor fit for the turbulence kinetic energy profile observed in the optimum design predicted by fitting the velocity profile.

Dr Parry concluded that the experimental set up is inadequately defined for the case to be used as a benchmark.

Several combinations of inlet boundary conditions and geometry configurations were simulated to seek improvements to the initial results obtained. However due to the ambiguous nature of the inlet boundary condition it was felt necessary that a second backward facing step configuration should to be pursued to reinforce the turbulence model validation.

A3.2 Backward Facing Step Re = 88,000

The technical source for this case description originates from a Ph.D. investigation undertaken by Croft.[122] The computational domain uses a channel height which is three times the height of the step with the inlet boundary condition specified four step heights upstream of the step itself. The inlet velocity is calculated to result in a Reynolds number, based on the step height, of 88,000. The outlet boundary is positioned twenty step heights downstream of the step; this ensured that the outlet boundary condition would not influence the recirculation region behind the step.

The x- and y-directions mesh densities upstream and downstream of step employed for this case were as follows:

Chapter 5; standard $k - \varepsilon$ model; (8 x 10) upstream & (40 x 30) downstream

Chapter 5; Wilcox $k - \omega$ model; (40 x 40) upstream & (200 x 70) downstream

Chapter 6; LVEL model; (40 x 20) upstream & (200 x 30) downstream

Chapter 6; LVEL_CAP, AUTO_CAP, Wolfshtein and Norris & Reynolds models; (64 x 32) upstream & (320 x 48) downstream

Chapter 8; SST model; (40 x 40) upstream & (200 x 70) downstream

Chapter 8; two-layer hybrid $k\varepsilon / kl$ model; (8 x 10) upstream & (40 x 30) downstream

The dimensions employed for this case have been presented in Figure A.9. Presented in Figure A.10 is the mesh density used for any model, such as the $k - \omega$ model, which requires a fine mesh located at the wall boundaries. The generation of this mesh exploits a grading technique to ensure a fine mesh concentration near to wall surfaces. (40 x 40) cells are used upstream of the step and (200 x 70) downstream.

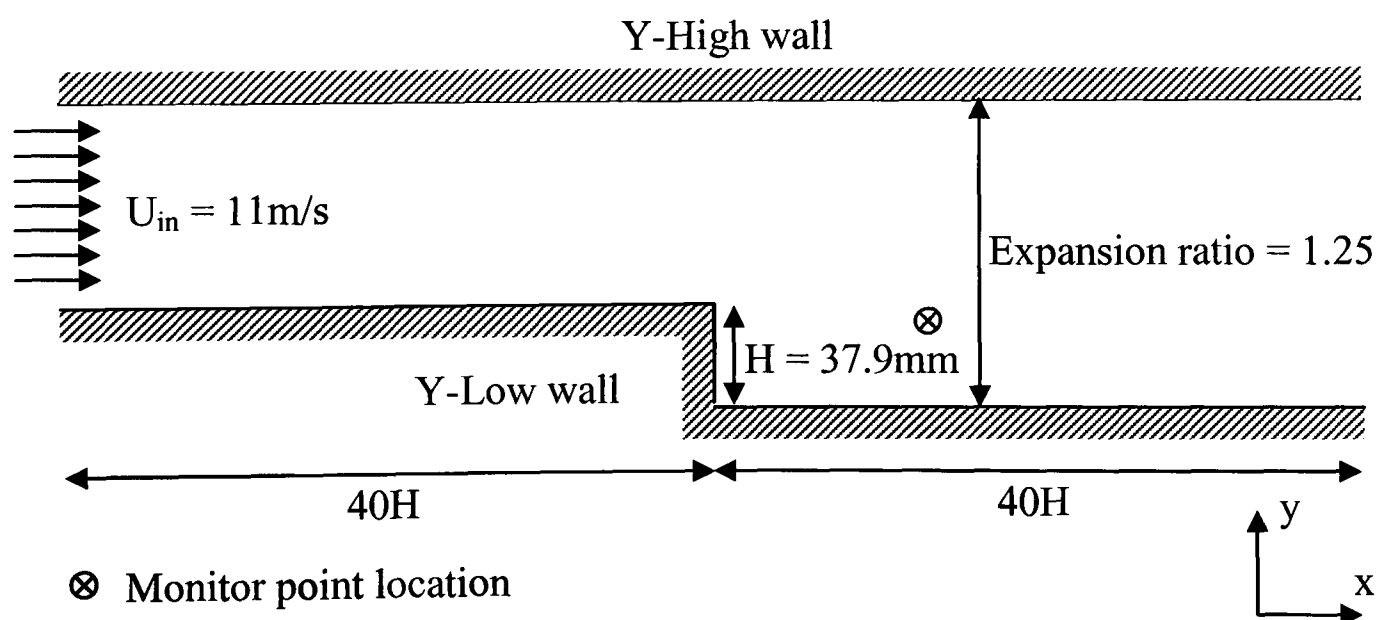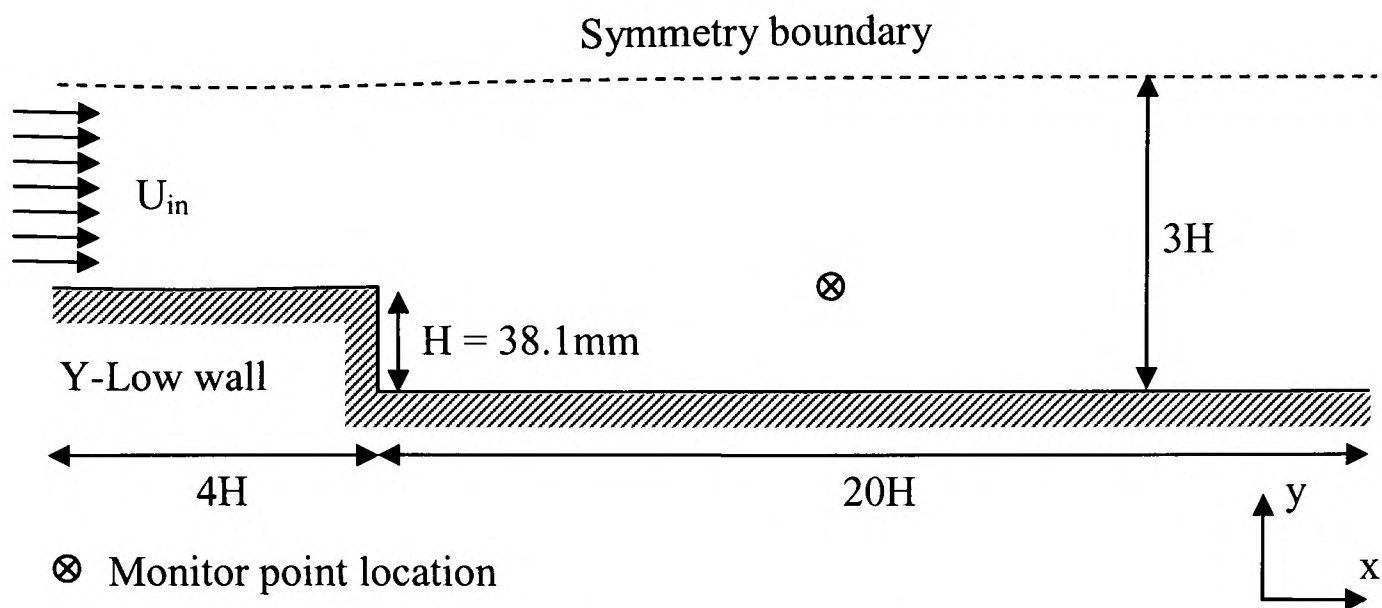**Figure A.9 Backward facing step solution domain Re = 88,000**
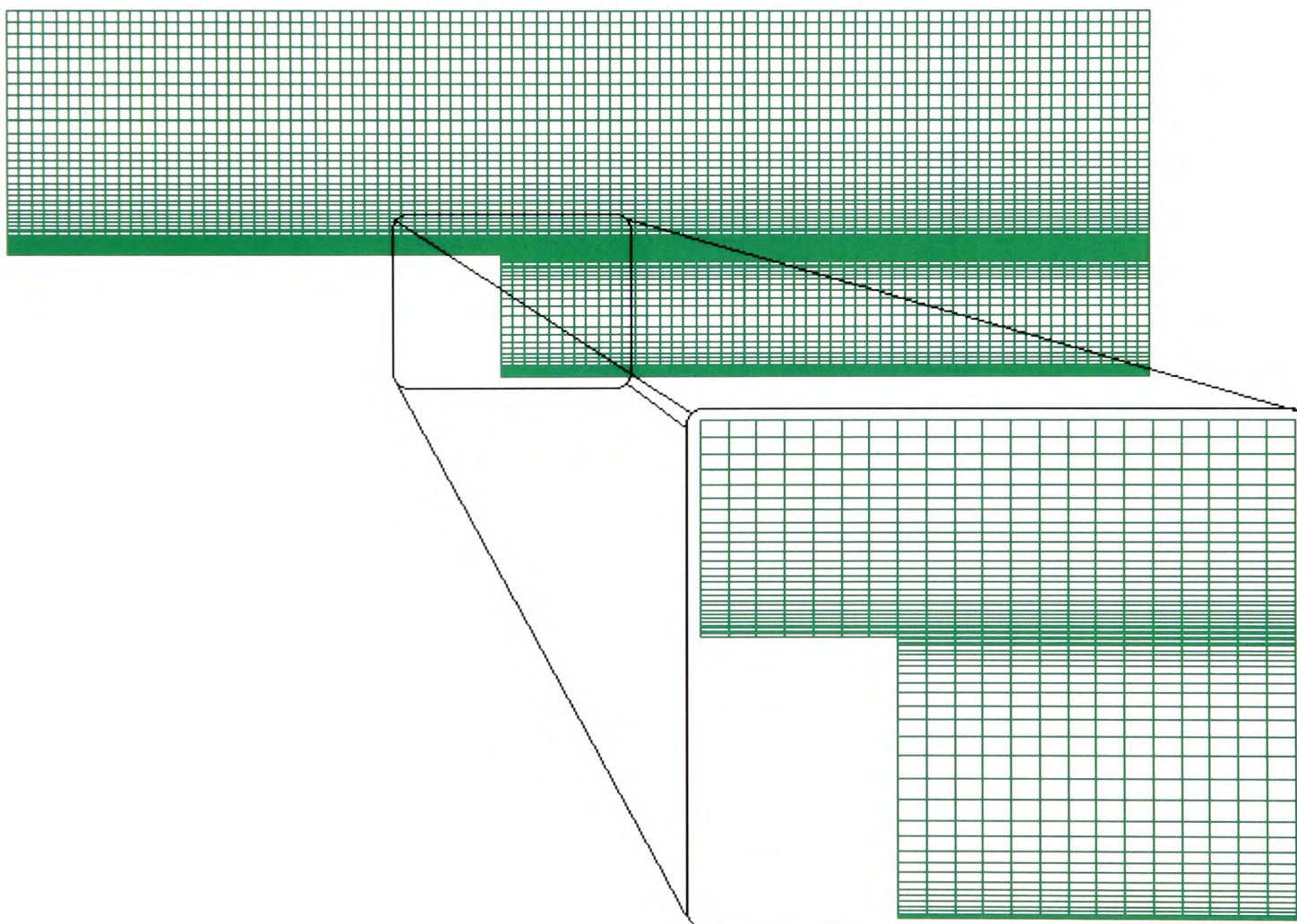
Figure A.10 Mesh density employed for the backward facing step case Re = 88,000

At the inlet boundary the turbulent quantities are estimated using equations (A.17) and (A.18). These boundary condition estimations are identical to the conditions which have been used by Croft.[122]

$$k_{in} = \frac{1}{4} \times 0.018 \times \left(U_{in} \right)^2 \qquad (A.17)$$

$$\varepsilon_{in} = \frac{0.1643 \times \left(k_{in} \right)^{1.5}}{0.09 \times H} \qquad (A.18)$$

The fluid material properties specified for this case use a density of 1.161kg/m^3 and a kinematic viscosity of $1.5586 \times 10^{-5} \text{m}^2/\text{s}$.

A4   Flow over a Heated Rib

This test configuration has been designed to determine if the three CFD codes, FLOTHERM, PHOENICS and PHYSICA use the same thermal equilibrium log-law wall functions when considering heat transfer phenomena. It is noted that when code comparisons are undertaken with all three codes the Upwind differencing scheme is used.

The test geometry has been detailed in Figure A.11. This case has been modelled as a two-dimensional configuration for simplicity as the interest lies in the accurate prediction of the heat dissipated from the rib into the air stream.
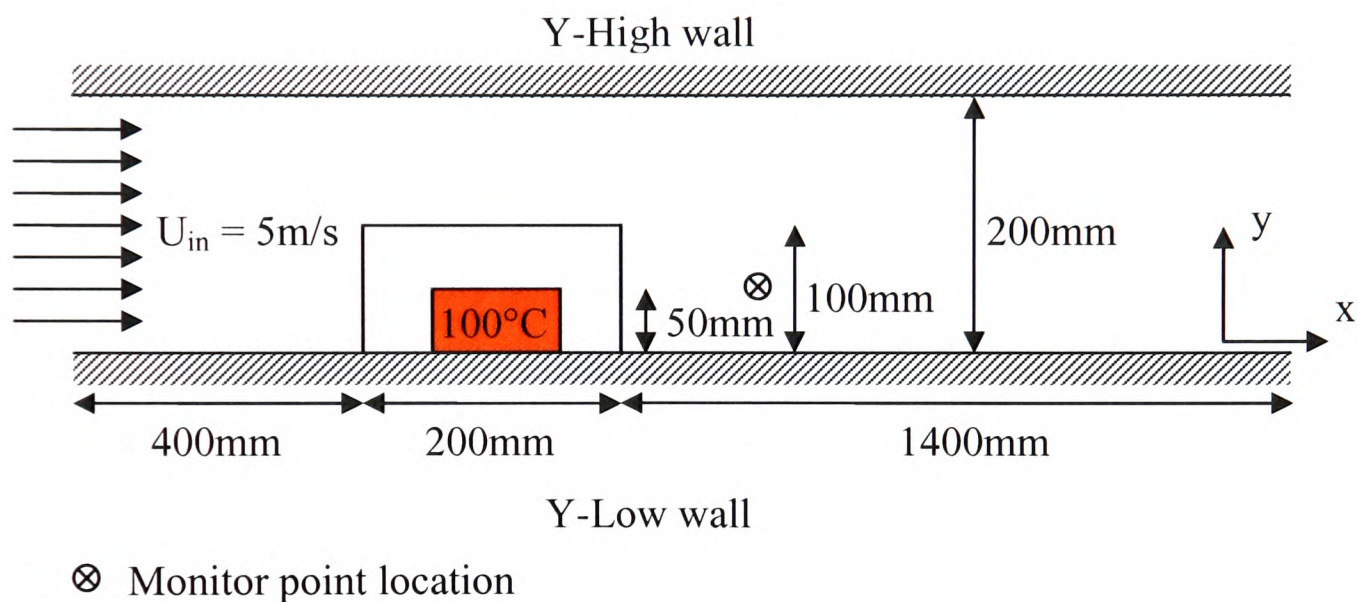
Figure A.11 Two-dimensional flow over a heated rib test geometry

The rib is constructed of two materials. The core of the rib measuring (100 x 50)mm in the x- and y-directions respectively is kept at a constant temperature of 100°C and is made from the high conducting material copper. This copper is then encapsulated by an epoxy resin material of 50mm in thickness for all of the copper surfaces which are exposed to the fluid.

The turbulent inlet quantities have been approximated using equations (A.19) and (A.20).

$$k_{in} = \left(U_{in} \times \text{Turbulent Intensity} \right)^2 \qquad\qquad (A.19)$$

$$\varepsilon_{in} = \frac{\left(k_{in} \right)^{1.5}}{h} \qquad\qquad (A.20)$$

where h is the height of the rib and the turbulent intensity is set to 5%.

The inlet air temperature for the solution domain is set to 20°C. All the material properties are detailed in Table A.1.

	Air @ 20°C	Epoxy @ 27°C	Copper @ 27°C
Density (kg.m^{-3})	1.189	1.900×10^3	8.954×10^3
Kinematic Viscosity (m^2.s^{-1})	1.544×10^{-5}		
Specific Heat (J.kg^{-1}.K^{-1})	1.005×10^3	7.890×10^2	3.830×10^2
Thermal Conductivity (W.m^{-1}.K^{-1})	2.580×10^{-2}	4.000×10^{-1}	3.810×10^2
Thermal Expansion Coefficient (K^{-1})	3.410×10^{-3}		

Table A.1 Material properties adopted for the flow over a heated rib test case

A uniformly distributed mesh density has been employed for this test case of (300 x 30) mesh elements in the x- and y-directions respectively. The mesh concentration in and around the rib has been presented in Figure A.12.
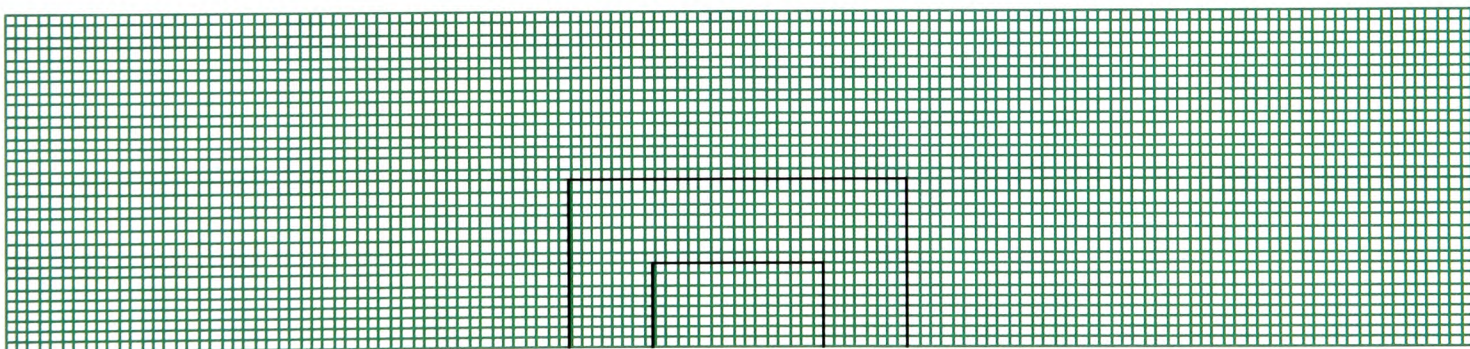
Figure A.12 Mesh density located around the rib region

A5   Martinuzzi High Reynolds Number Single Cube

The study of flow around surface-mounted, sharp-edged obstacles placed in a channel is fundamental to the understanding of the flow mechanisms for complex two- and three-dimensional geometries. There exists a considerable amount of published data for flows over two-dimensional geometries such as ribs and fences. However there are markedly fewer studies in the literature concerned with the flow around three-dimensional obstacles.

The experiments were conducted in a (3900 x 600 x 50)mm (l x w x h) wind tunnel at a Reynolds number of 80,000 based on the channel height. The boundary layer was tripped at the inlet in order to obtain fully-developed conditions at least 5h upstream of the cubes leading edge. The cube of half channel height, $H = h/2$, was mounted at the centreline with the leading edge located 52h downstream of the trip wires. The channel extended approximately 16h downstream of the cubes trailing edge so that the outlet conditions are not expected to affect the wake flow.[21, 22]

The study aimed to provide a general description of the flow around three-dimensional obstacles. This case was used as an ERCOFTAC workshop on Refined Flow Modelling in 1997.[41] The same geometry configuration served as a test case for the Workshop on Large Eddy Simulation of Flows past Bluff Bodies.[66]

The computational domain modelled is presented in Figure A.13. Due to the symmetry of the geometry only half of the flow domain has been modelled.
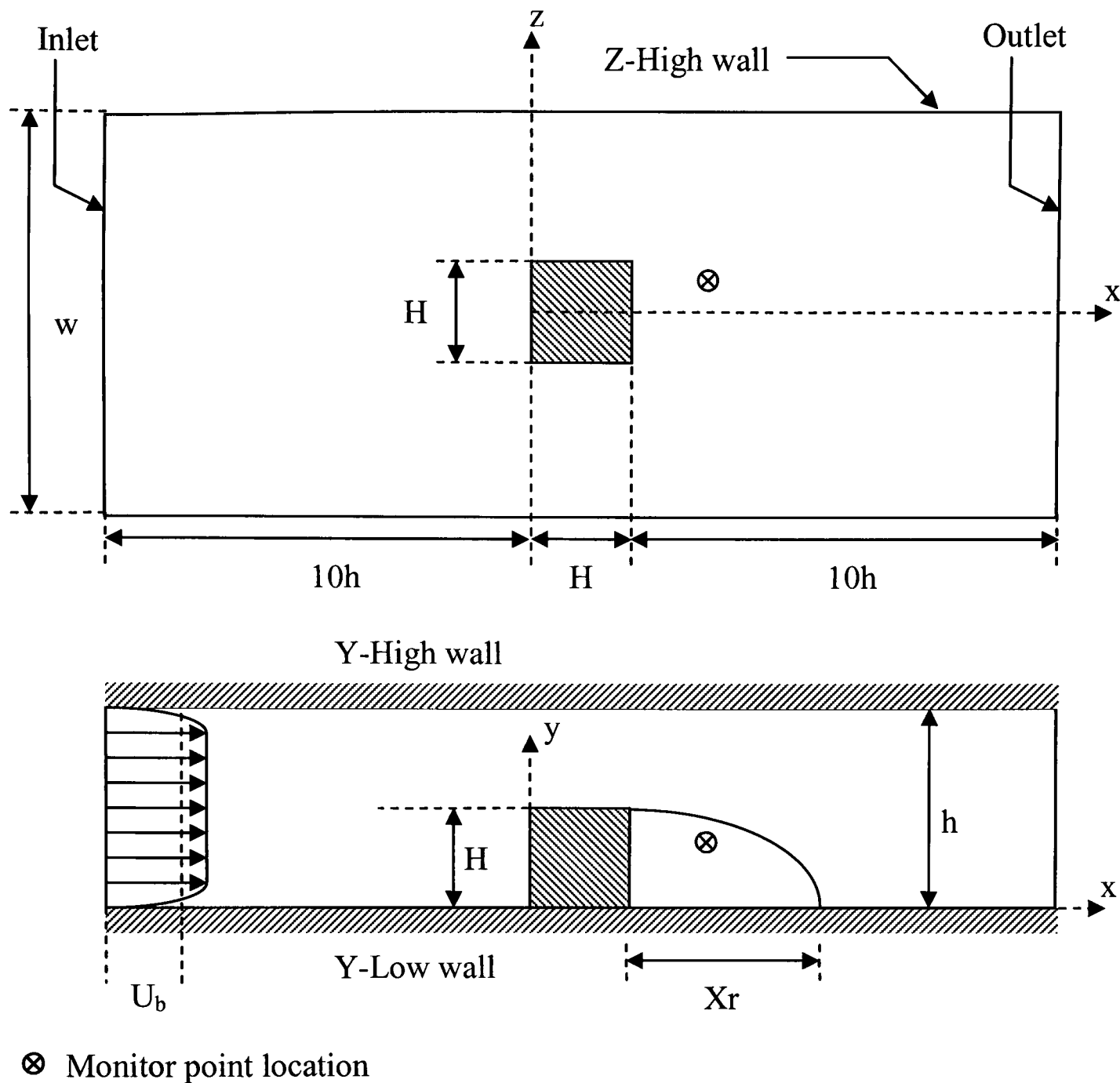
Figure A.13 Martinuzzi single cube configuration

The x- and y-axes are taken in the streamwise and wall-normal directions respectively. The coordinate system originates at the centre of the cubes leading face from the base to the top surface of the channel, Y-Low and Y-High walls respectively as detailed in Figure A.13.

Using material property values associated with air at 20°C and the Reynolds number relationship stated in equation (A.21) an inlet velocity value of 24.176m/s has been calculated.

$$Re_h = \frac{U_b h}{\nu}$$
(A.21)

All computations have been performed using the Upwind differencing scheme and employ a stretched Cartesian mesh with (222 x 51 x 68) mesh cells in the x-, y- and z-directions respectively. On the surface of the cube 26 cells have been applied uniformly in the x- and y-directions with 13 cells distributed in the z-direction. The computational mesh employed can be viewed in Figure A.14.
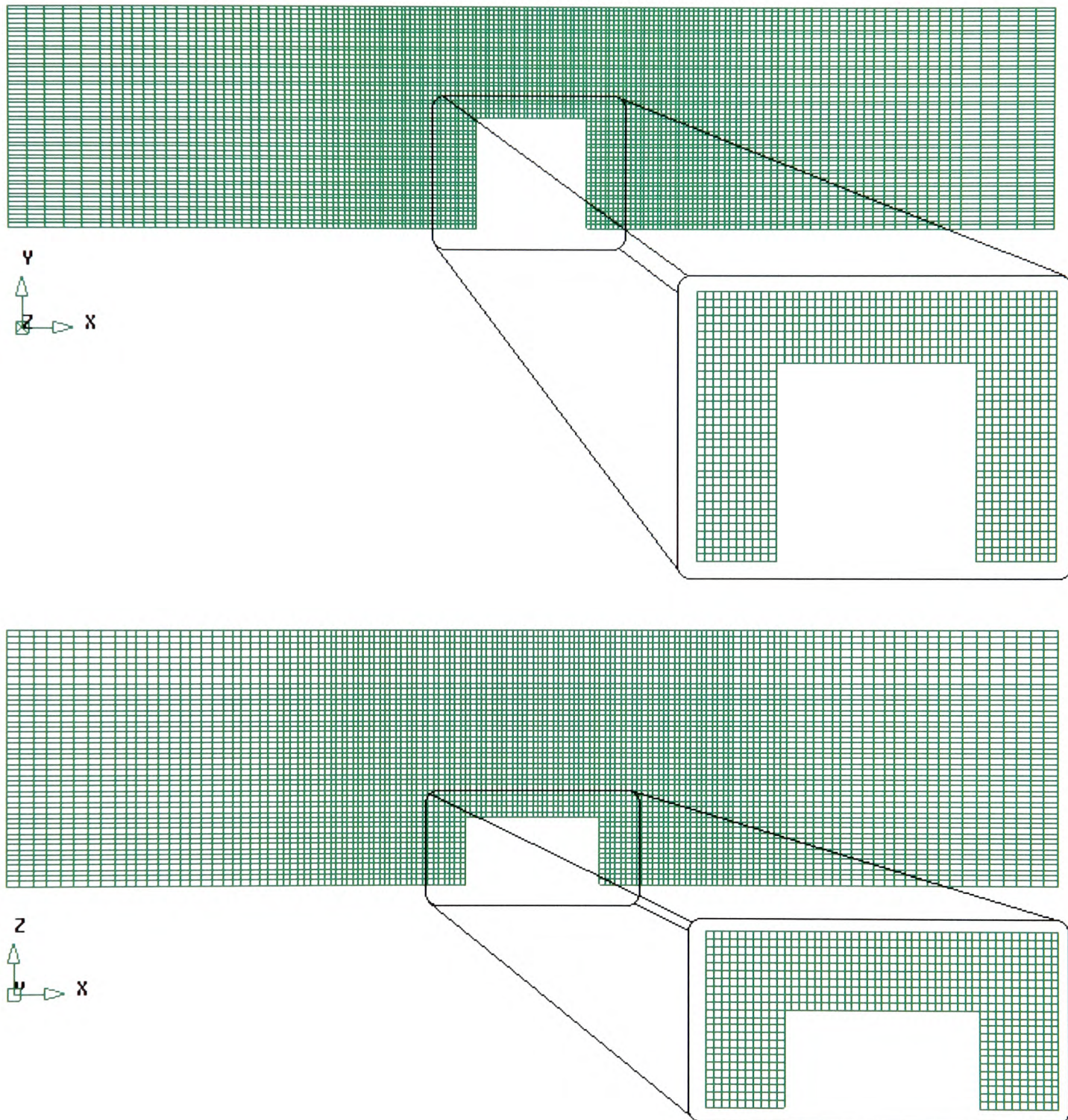
Figure A.14 Mesh density employed for Martinuzzi single cube case study

The mesh density employed for this case is similar to those considered by the participants of the 6th ERCOFTAC workshop where it is noted that the corresponding range of y^+ is 1-5.[125]

In order to set appropriate inlet boundary conditions for the turbulent quantities equations (A.22)-(A.23) are applied.

$$k_{in} = 10^{-3} \times \left(U_{in} \right)^2$$ (A.22)

$$\varepsilon_{in} = \frac{0.1643 \times \left(k_{in} \right)^{1.5}}{l_i}$$ (A.23)

$$l_i = 0.1 \times \left(\text{normal inlet area} \right)^{0.5}$$

A6   Channel Flow

The motivation for this test case is to investigate whether the SST model effectively converts back to the standard $k - \varepsilon$ model when the F_1 blending function, stated in Chapter 8, is equal to zero as reported by Menter et al.[75] as this can not be proven mathematically.

To summarise, the SST model is stated to convert to the standard $k - \varepsilon$ model away from any surfaces when $F_1 = 0.0$ and switches to Wilcox $k - \omega$ when $F_1 = 1.0$ inside the boundary layer. Keeping this in mind the case has been constrained to ensure that the distance to the nearest wall boundary will be such that the standard $k - \varepsilon$ turbulence model is employed.

The case considers a two-dimensional flow channel with an associated fluid temperature of 30°C, therefore resulting in a fluid density of 1.1614kg/m^3 and a kinematic viscosity of $1.5842 \times 10^{-5} \text{m}^2/\text{s}$. The mesh employed has been distributed uniformly which ensures that each mesh element is (1 x 1)m in the x and y-directions respectively. The dimensions of the test geometry have been detailed in Figure A.15.
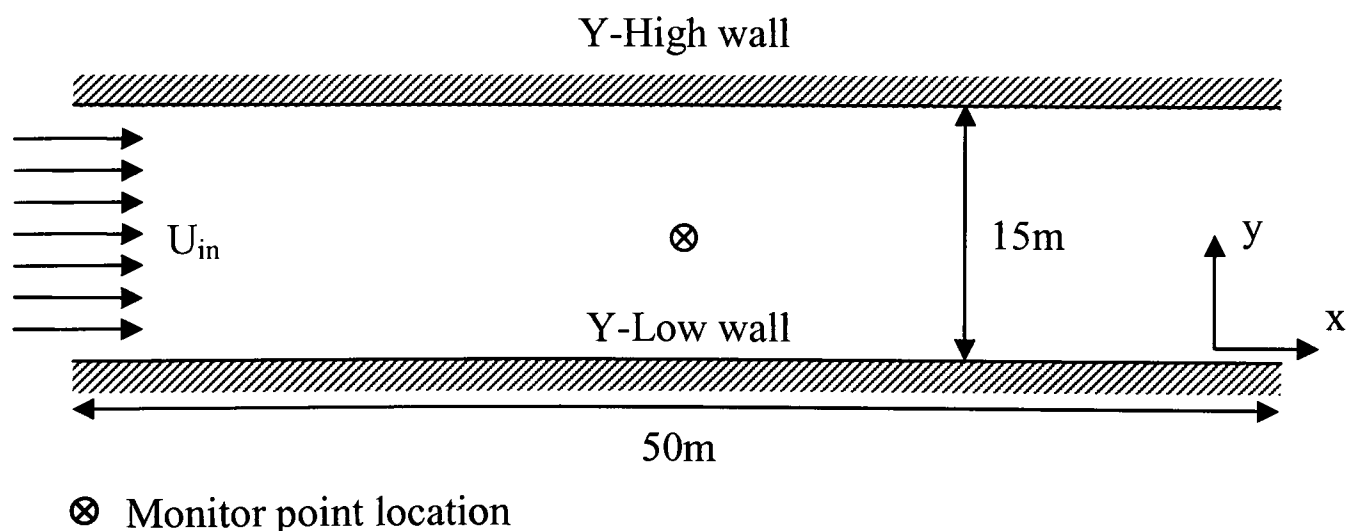
Figure A.15 Channel flow test case geometry

The inlet velocity is calculated to ensure that a Reynolds number of 10,000 is obtained and the turbulent quantities entering the solution domain are estimated using equations (A.24)-(A.26) dependent on the turbulence model being employed.

$$k_{in} = 10^{-3} \times \left(U_{in}\right)^2 \qquad\qquad (A.24)$$

$$\varepsilon_{in} = \frac{0.1643 \times \left(k_{in}\right)^{1.5}}{l_i} \qquad (A.25)$$

$$l_i = 0.1\left(\text{norminal inlet area}\right)^{0.5}$$

$$\omega_{in} = \frac{\varepsilon_{in}}{0.09 \times k_{in}} \qquad (A.26)$$

All simulation work undertaken uses the Hybrid differencing scheme.

A7 Meinders Low Reynolds Number Configurations

Full descriptions of two of the four test configurations investigated by Meinders have been provided. Of these, the Single Cube and Matrix of Cubes configurations were considered most relevant to this project.

The experimental work was conducted in a blowing-type low Reynolds number closed loop wind tunnel. The flow was recirculated by means of two fans. Two heat exchangers were used to thermostat the air to a constant temperature. Honeycombs and fine grids were employed to eliminate the large turbulence scales. Approximately 2m upstream of the test section, the channel contracted to a rectangular channel of height h = 51mm and of 600mm width. Cubes of size H = 15mm were mounted on a base plate which was 10mm in thickness.

Distributions of the time-averaged surface temperature were determined with infrared thermography (IR). This is a commonly used diagnostic measurement technique applied in a broad range of thermo-fluid problems. Flow visualisation was performed with smoke and oil-film visualisation techniques. Detailed documentation of the time-averaged vortex structures and flow dynamics around the cubes was performed with the Laser Doppler Anemometry (LDA) technique. All measurements techniques have been fully discussed in the work performed by Meinders.[31, 158]

All simulation work conducted on these two configurations used the first order accurate Hybrid differencing scheme.

A7.1 Single Cube

For this test case, no thermal and aerodynamic interaction with other heated obstacles is present, which allows for a detailed analysis of the flow structures and the local convective heat transfer. Further, much research has already been devoted to the vortex structures observed in close proximity to a single cube when considering either boundary layer flow or fully developed channel flow phenomena at much higher Reynolds numbers, one such experimental dataset is the work of Martinuzzi and Tropea.[21]

The flow field examined around the single cube contains, broadly speaking, most of the basic features noted for electronic applications, so this case is well suited to study the correlation between surface heat transfer and local flow structure.

The specifications for this low Reynolds number test case have been detailed as a three-dimensional schematic in Figure A.16 with the complete geometry dimensions stated in Figure A.17.
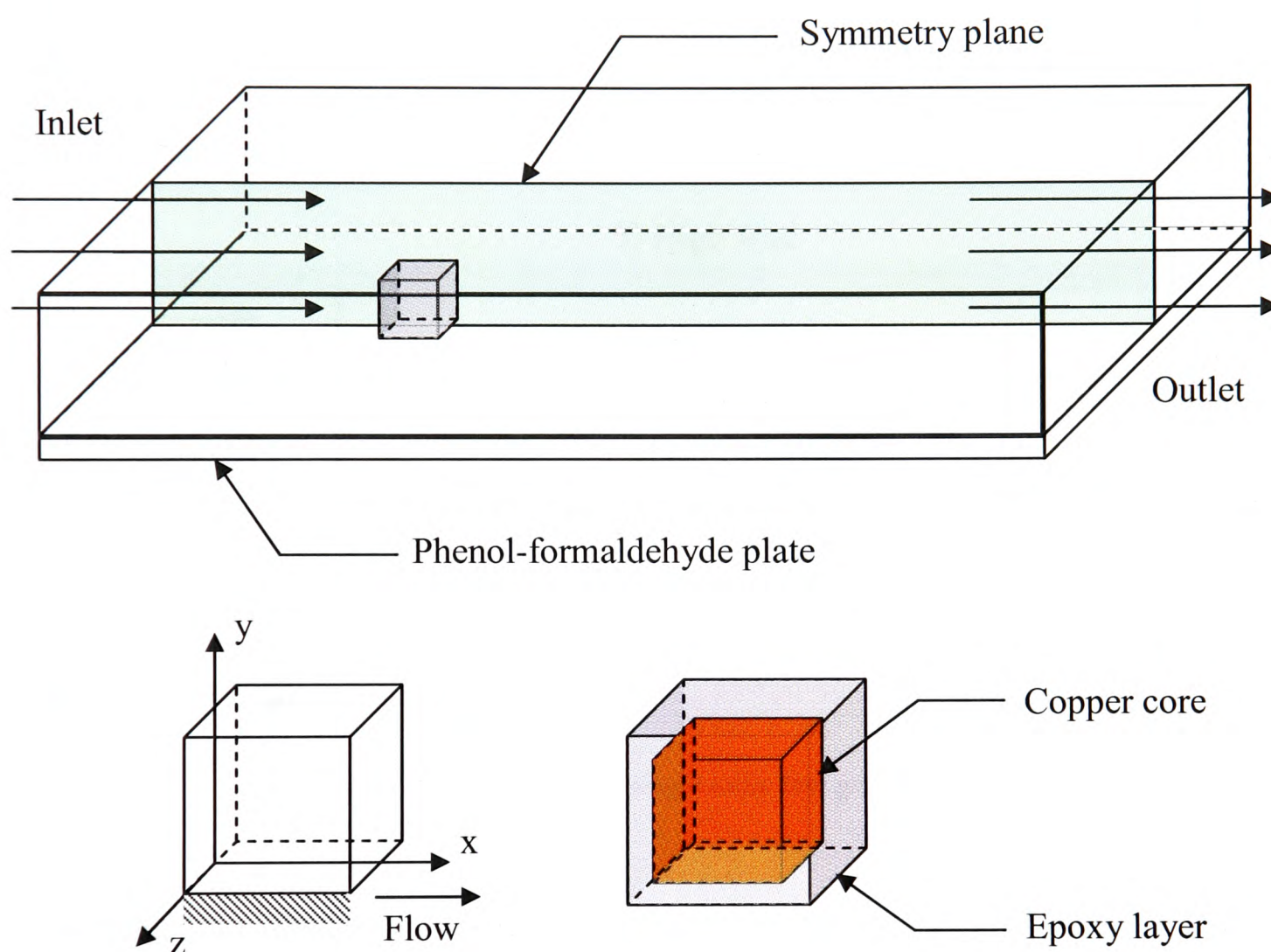
Figure A.16 Three-dimensional schematic representation of the single cube test case

Figure A.17 Meinders single cube test geometry

The test channel has dimensions (1215 x 61 x 600)mm and uses an inlet velocity of 4.47m/s, with the inlet air temperature kept at 20°C, resulting in a Reynolds number based on the cube height, $Re_H = 4440$. The cube of size H = 15mm is mounted x/H = 50 downstream of the inlet boundary on the centreline allowing the use of a symmetry boundary condition in the z-direction.

The test channel base plate is constructed from phenol-formaldehyde which is 10mm in thickness and has a thermal conductivity of 0.33W/mK. The cube is constructed from two materials; the core of the cube measuring 12mm is constructed from copper which is kept at a constant temperature of 75°C. An epoxy resin encapsulates the copper and has a uniform thickness of 1.5mm.

The turbulent inlet boundary conditions have been estimated using equations (A.2)-(A.4) and the material properties used for this test case have been specified in Table A.2.

	Air @ 20°C	Copper	Epoxy	Phenol-Formaldehyde
Density (kg.m^{-3})	1.205	8.930×10^3	1.120×10^3	1.120×10^3
Kinematic Viscosity (m^2.s^{-1})	1.511×10^{-5}			
Specific Heat (J.kg^{-1}.K^{-1})	1.005×10^3	3.850×10^2	1.400×10^3	1.400×10^3
Thermal Conductivity (W.m^{-1}.K^{-1})	2.570×10^{-2}	3.900×10^2	2.400×10^{-1}	3.300×10^{-1}
Thermal Expansion Coefficient (K^{-1})	3.430×10^{-3}	1.700×10^{-5}	6.800×10^{-5}	

Table A.2 Material properties employed for the single cube test case

It is noted that a total of three mesh densities have been undertaken for this test case in order to ensure mesh independence, details of which are provided in Table A.3.

Mesh	Density	y^+ (2dp)
Coarse	(82 x 60 x 41)	3.9
Medium	(102 x 75 x 52)	3.4
Fine	(122 x 90 x 63)	2.2

Table A.3 Computational mesh density information and calculated y^+ values located at the top centre of the cube

The numerical predictions presented in this work employ a stretched Cartesian mesh with 122 x 90 x 63 mesh elements in the x-, y- and z-directions respectively. On the surface of the cube 44 elements in total have been applied in the x- and y- directions with 22 elements distributed in the z-direction. The computational mesh and can be viewed in Figure A.18.

Figure A.18 Computational mesh density employed for the single cube configuration

A7.2 Matrix of Cubes

This in-line matrix array configuration of wall-mounted cubes served as a reference dataset for three ERCOFTAC workshops for the validation of turbulence models and numerical solutions methods held at Delft University of Technology,[41] the University of Manchester[42] and Helsinki University of Technology.[43]

The experimental set-up consists of an equidistantly-spaced matrix array of wall-mounted cubes placed on the base plate of a wind tunnel. The wind tunnel dimensions are specified as having a channel height of 51mm and a width of 600mm. The base plate and the structure of the cubes take the same form as that specified for the single cube. The Reynolds number

based on the bulk velocity, having an inlet temperature of 20°C, and the cube height is calculated to be $Re_H = 3854$. The complete matrix consists of 25 x 10 cubes in the streamwise and spanwise directions respectively which caused periodic turbulent flow far downstream in the matrix. A schematic sub-section of the array is shown in Figure A.19.

x, y, z: Co-ordinate axis

H: Dimensions of cubes = 15mm

h: Channel height = 3.4H

S: Pitch of cubes = 4H

U_b: Bulk velocity = 3.86m/s
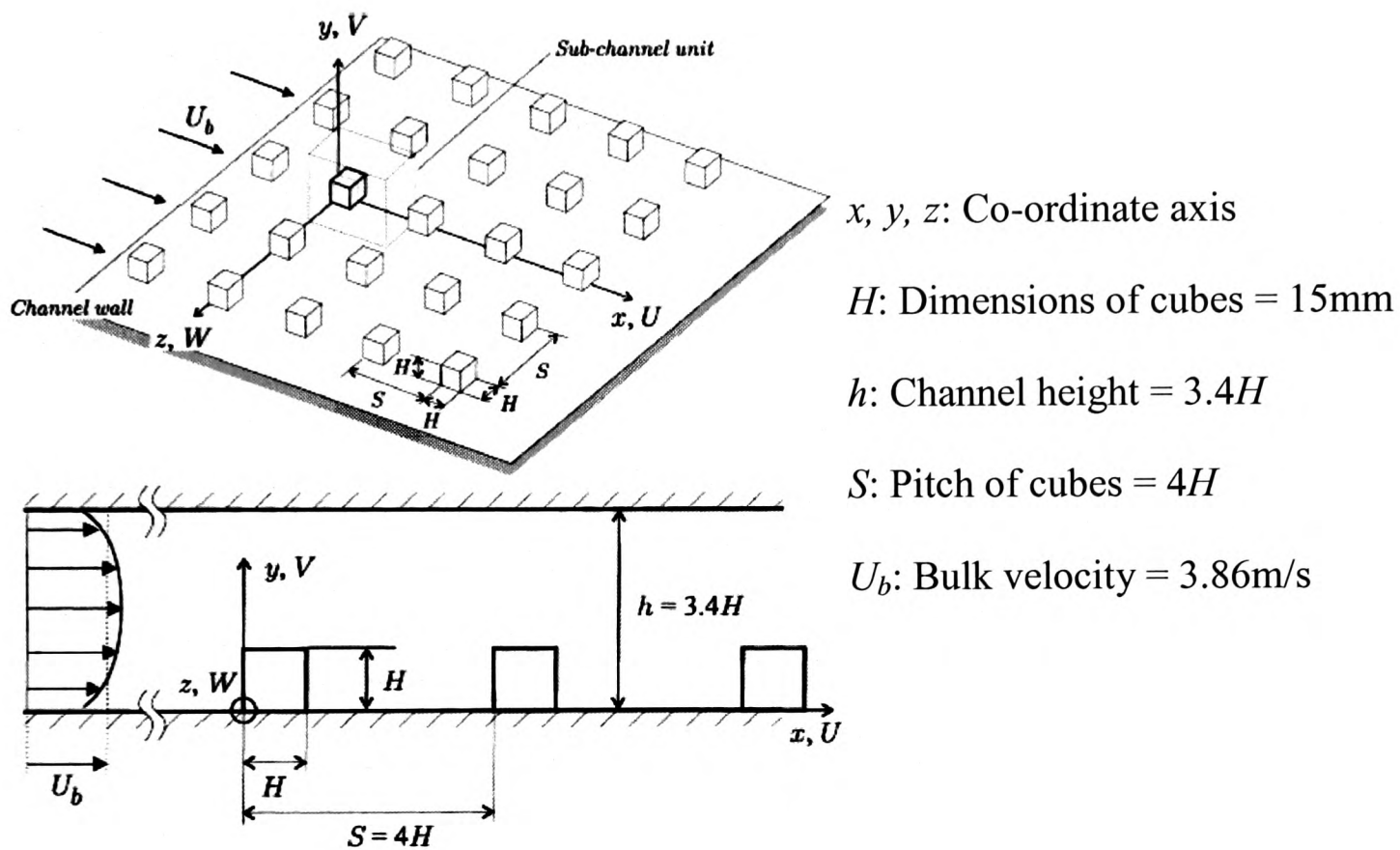
Figure A.19 Three-dimensional representation of the matrix array of cubes on the channel base plate (upper plot) and the side view of the configuration (lower plot). (Meinders[150])

Note that the sub-channel unit shown in Figure A.19 is merely an example for the choice of computational domain and the x- and y-axis have been taken in the streamwise and wall-normal directions respectively with the z-axis denoting the spanwise direction.

Fluid flow and heat transfer measurements have been taken around the 18th row from the inlet, at mid-height of the channel. For this location, the flow was observed to be fully developed in the streamwise direction and symmetric in the spanwise direction which facilitates the use of periodic boundary conditions for the computational work undertaken at the two workshops.

For the simulations work undertaken here both the inlet and outlet domain boundaries did not use periodic conditions due to the addition of heat from the cube to the air stream which would have resulted in a non-periodic thermal field. As an alternative, five upstream cubes and two downstream cubes either side of the heated cube have been modelled with the use of

symmetry boundary conditions on the two spanwise sides of the domain. In the work conducted by Bornoff and Parry[151] this configuration was found to be sufficient to ensure that the flow experienced fully developed conditions at the measurement section.

The computational framework employed for this test case is presented in Figure A.20.

Figure A.20 Modelled flow domain for the matrix of cubes test case

All the cubes for this test case have an identical structure to the cube detailed in the single cube test case. However cubes 1-5 and 7-8 are dummy cubes which are only present as periodic boundary conditions are not employed in the streamwise direction. Only the copper core of cube six is kept at a constant temperature of 75°C. The phenol-formaldehyde base plate is treated as adiabatic.

The estimation of the turbulent quantities entering the solution domain are obtained by using equations (A.2)-(A.4) and the material properties used in this case test are identical to those in the single cube case discussed earlier with the addition of a dummy material for cubes 1-5 and 7-8.

All computations have been performed on a stretched Cartesian mesh with 211 x 80 x 43 mesh elements in the x-, y- and z-directions respectively. On the surface of the cube 34 elements in total have been applied in the x- and y-directions with 17 elements distributed in the z-direction. The computational mesh employed can be viewed in Figure A.21.
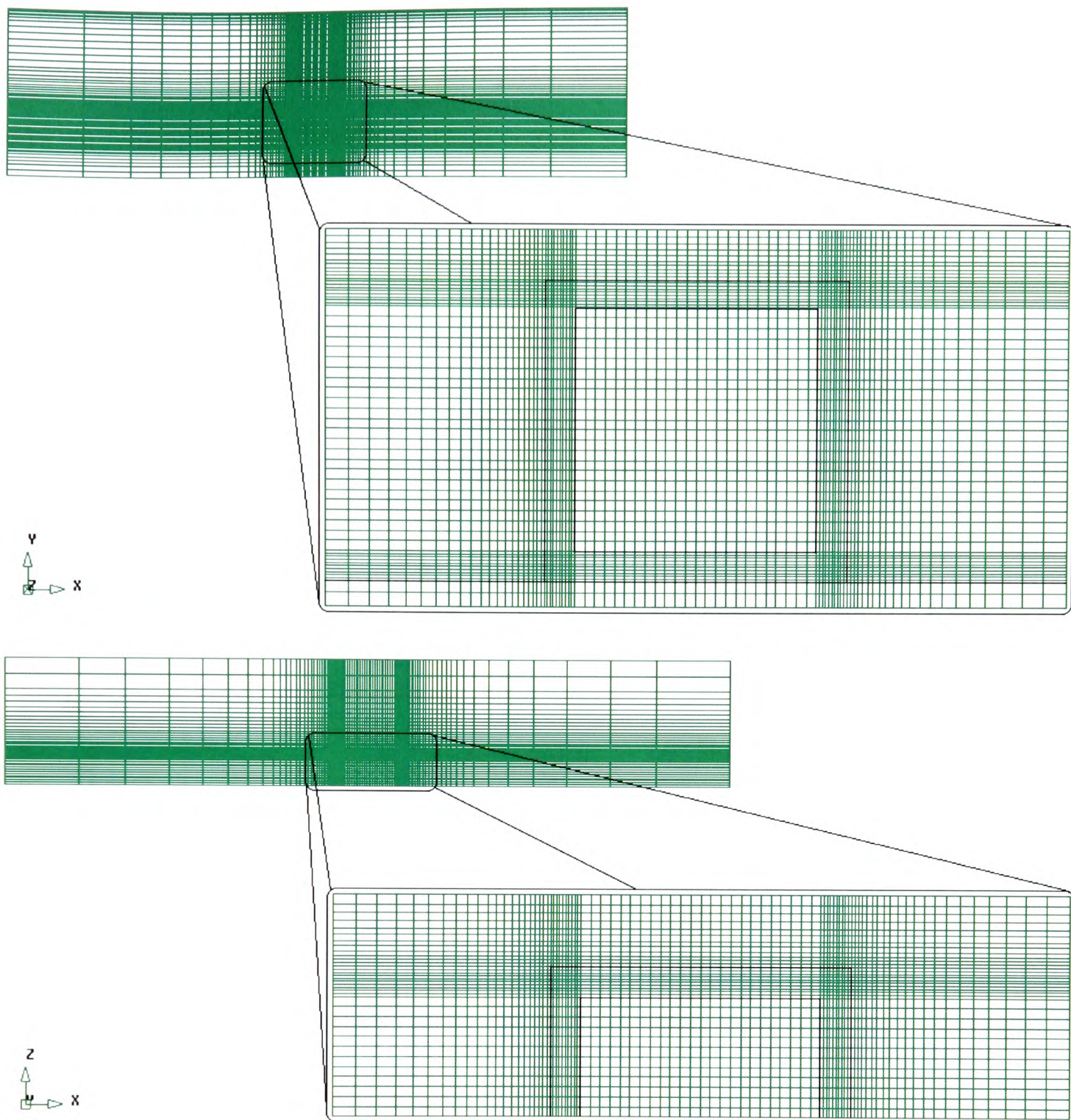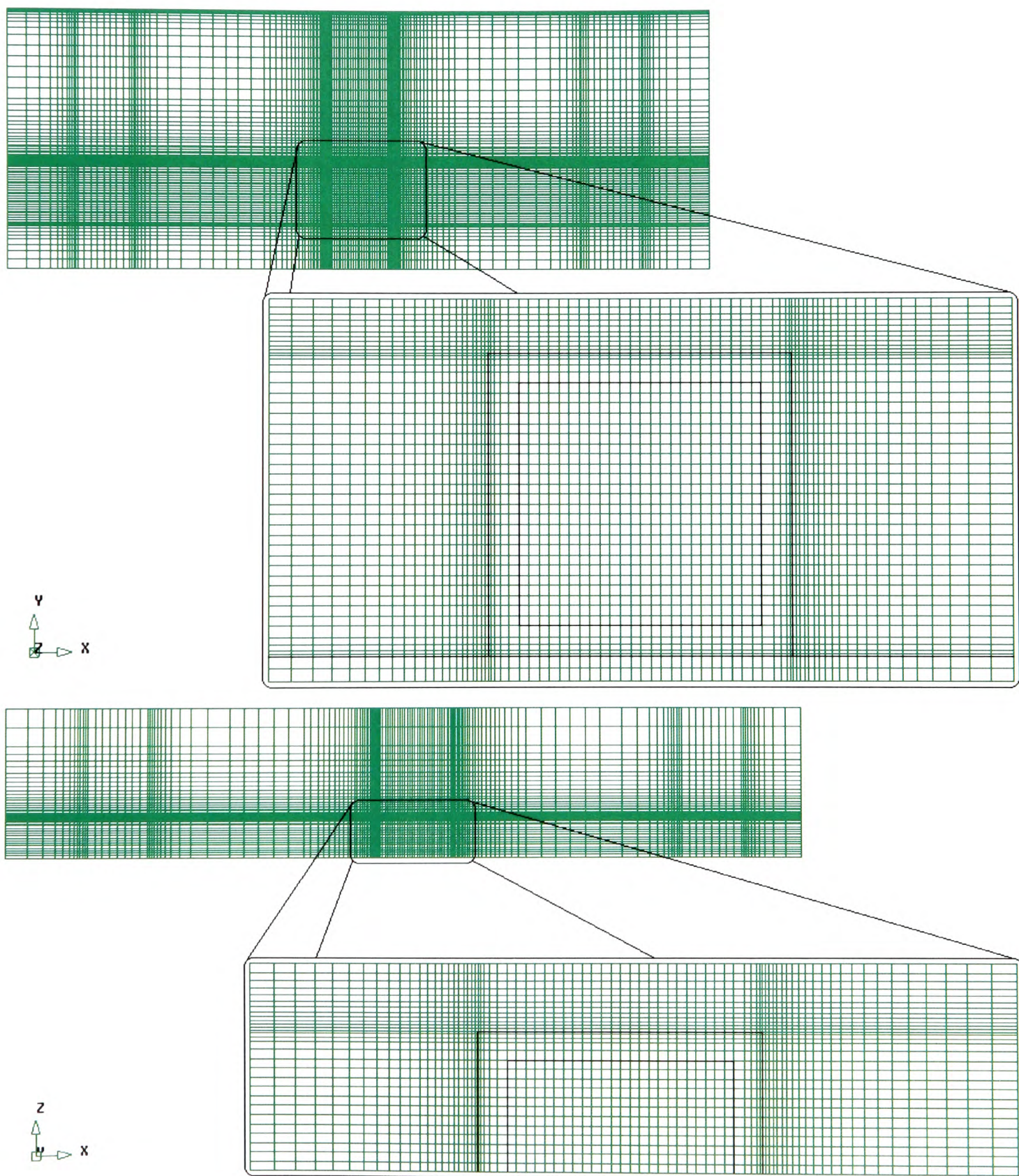

Figure A.21 Computational mesh density employed for the matrix configuration

The mesh density employed for this case is comparable to that used for the single cube configuration, therefore producing similar y^+ values as those reported in the previous section and hence ensuring mesh independent solutions.

The employed mesh density is finer than those run by any of the participants of the 6th ERCOFTAC workshop. Jansson,[152] one of the participants of the workshop who used the standard $k - \varepsilon$ model for the bulk flow and a one-equation model near to the wall, notes that for the mesh located at the near-wall boundaries the approximate y^+ values were within the range 2-5. Similar y^+ values were used by Mathey et al.[153] at the 8th workshop for LES calculations. Furthermore Zhong and Tucker[71, 72] apply comparable y^+ values for their work on this case using a zonal LES/RANS model. Therefore the y^+ values employed in the current study agree well with the mesh densities used by the participants of both ERCOFTAC workshops and others cited in the literature.

B   Flow Profile Derivation

This appendix presents the derivation of both the laminar and turbulent flow profiles used in the Parallel Plates test case to allow for the validation of implemented turbulence models.

B1   Laminar Flow Profile
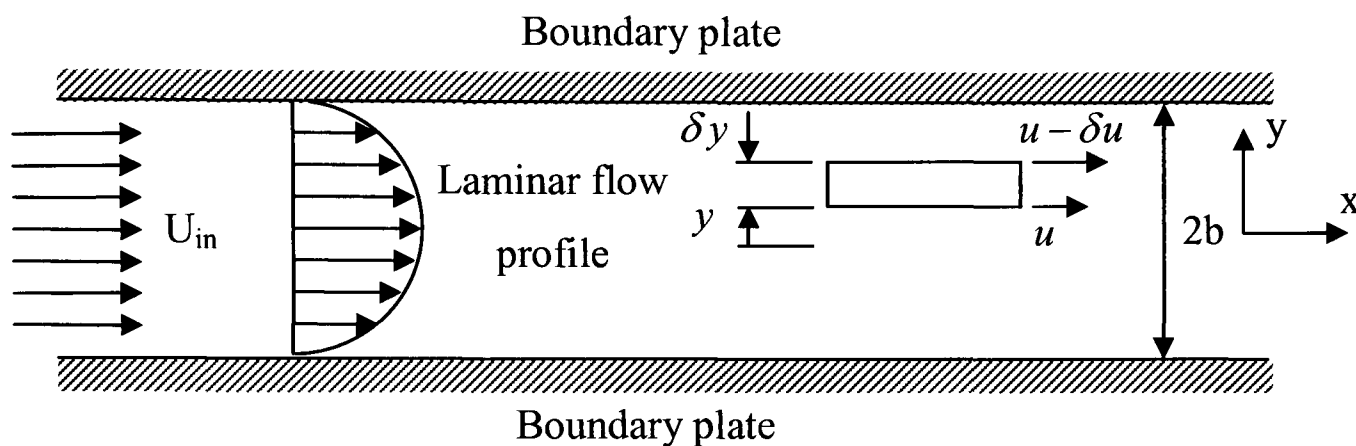
Figure B.1 Schematic representation of laminar flow profile

The smooth boundary plates are assumed to extend out to a great distance in the flow direction and in the direction perpendicular to the page. This assumption is necessary in order to neglect the plate edges having any effect on the flow behaviour of the segment of fluid being considered.

The flow is caused by a difference of pressure between the two ends of the system. As the laminar flow regime is being considered, there is no movement of fluid in any direction perpendicular to the flow, and thus p^* varies only in the direction of flow.

The origin of the coordinate system is located at the centreline of the channel, the flow direction is in the x-axis parallel to the boundary plates and the y-axis is perpendicular to the plate. Let the distance separating the two boundary plates be $2b$.

The requirement of no slip at each boundary produces a variation of velocity in the y-direction. Viscous stresses are set up, and these may be related to the forces due to the

difference of pressure by considering a small rectangular element of the fluid, with sides parallel to the coordinate axes.

Let the south face of the element be a distance y from the origin and here let the velocity be u. At the north face of the element, a distance $y + \delta y$ from the origin, the velocity is $u - \delta u$.

As δu is negative this indicates that the slow-moving fluid just above the north face of the element has a retarding effect on the fluid element. Similarly, the fast-moving fluid adjacent to the south face exerts a forward force on the element. Thus there are stresses of magnitude τ on the north face and $\tau + \delta \tau$, say, on the south face in the directions indicated in the figure below. Also let the pressure be p^* at the west face, and $p^* + \delta p^*$ at the east face.
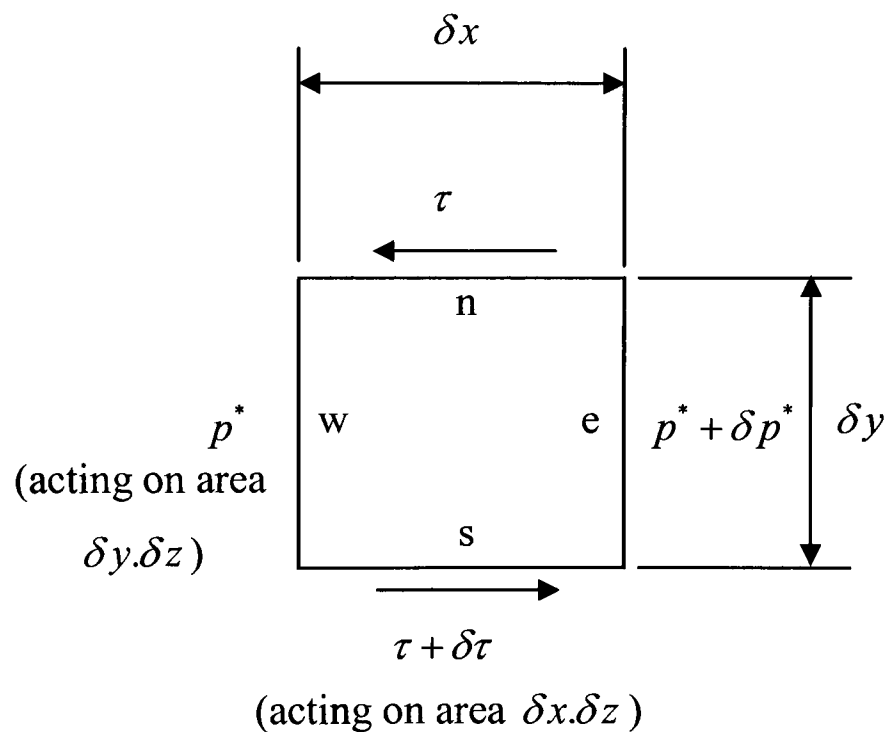
Figure B.2 Stresses acting on element

If the width of the element perpendicular to the page is δz, then the total force acting on the element towards the east direction is formulated to be

$$\left[p^* - \left(p^* + \delta p^* \right) \right] \delta y \delta z + \left[\left(\tau + \delta \tau \right) - \tau \right] \delta x \delta z \qquad \text{(B.1)}$$

However for steady, fully developed flow there is no acceleration and so this total force must be zero.

$$\therefore \ -\delta p^{*}\delta y + \delta\tau\,\delta x = 0 \qquad\qquad (\text{B.2})$$

Dividing by $\delta x\delta y$ and proceeding to the limit $\delta y \to 0$, the following is obtained

$$\frac{\delta p^{*}}{\delta x} = \frac{\partial\tau}{\partial y} \qquad\qquad (\text{B.3})$$

Furthermore for laminar flow of a Newtonian fluid the stress $\tau = \mu\,\partial u/\partial y$. Hence equation (B.3) becomes

$$\frac{\delta p^{*}}{\delta x} = \frac{\partial}{\partial y}\left(\mu\frac{\partial u}{\partial y}\right) \qquad\qquad (\text{B.4})$$

As p^{*} does not vary in the y-direction, $\delta p^{*}/\delta x$ is independent of y and equation (B.4) may be integrated with respect to y

$$\frac{\delta p^{*}}{\delta x}y = \mu\frac{\partial u}{\partial y} + A \qquad\qquad (\text{B.5})$$

If the dynamic viscosity, μ, is constant, a further integration with respect to y can be undertaken to give

$$\left(\frac{\delta p^{*}}{\delta x}\right)\frac{y^{2}}{2} = \mu u + Ay + B \qquad\qquad (\text{B.6})$$

Since the segment of fluid considered is assumed to be at a significantly far distance from the edges of the plates, A and B are constants, independent of both x and z.

In order to determine the constants of integration the boundary conditions must be considered. Given that the origin of the coordinate system is located at the centre of the channel and that the maximum velocity value is also at this location the constant B can first be determined.

Therefore given that at the centreline of the channel $y = 0$ and $u = U_{max}$ substitution of these conditions into equation (B.6) results in the following

$$\left(\frac{\delta p^*}{\delta x}\right)\frac{(0)^2}{2} = \mu\left(U_{max}\right) + A(0) + B \qquad \text{(B.7)}$$

$$\therefore B = -\mu\left(U_{max}\right) \qquad \text{(B.8)}$$

To determine U_{max} it was assumed that the origin of the coordinate system is located at the lower boundary plate which therefore indicates that the velocity u at any distance y from the lower plane can be calculated using

$$U = \frac{1}{2\mu}\left(\frac{\delta p^*}{\delta x}\right)\left(y^2 - 2by\right) \qquad \text{(B.9)}$$

As the velocity profile takes the form of a parabola with its vertex, corresponding to the maximum velocity, mid-way between the plates as is to be expected due to symmetry it can be concluded that the maximum velocity occurs at $y = b$. The substitution of this condition into equation (B.9) defines the maximum velocity as

$$U_{max} = \frac{-b^2}{2\mu}\left(\frac{\delta p^*}{\delta x}\right) \qquad \text{(B.10)}$$

Therefore substituting equation (B.10) into equation (B.8) allows the integration constant B to be stated as

$$B = \frac{b^2}{2}\left(\frac{\delta p^*}{\delta x}\right) \qquad \text{(B.11)}$$

Furthermore as both of the plates are stationary the velocity of the fluid in contact with each plate must be zero so as to satisfy the no slip condition. Therefore with the coordinate system replaced to its original location at the centre of the channel this suggests that at the upper

boundary plate $y = b$ and $u = 0$. The constant of integration A can now be determined by substituting these conditions together with equation (B.11) into equation (B.6).

$$A = 0 \qquad\qquad (B.12)$$

To obtain an expression for the velocity u at any distance from the centreline equations (B.11) and (B.12) are substituted into equation (B.6) to construct the expression

$$U = \frac{1}{2\mu}\left(\frac{\delta p^*}{\delta x}\right)\left(y^2 - b^2\right) \qquad\qquad (B.13)$$

Given that it is reasonable to assume that the mean velocity is equal to the inlet velocity and that it is taken to be $2/3$ of the maximum velocity, the inlet velocity can be stated as

$$U_{in} = \frac{-b^2}{3}\left(\frac{\delta p^*}{\delta x}\right) \qquad\qquad (B.14)$$

Finally after some rearranging U/U_{in} can be shown to be

$$\frac{U}{U_{in}} = \frac{3}{2}\left[1 - \left(\frac{y}{b}\right)^2\right] \qquad\qquad (B.15)$$

For further discussion on the derivation of steady laminar flow between parallel plates see Massey.[159]

B2   Turbulent Flow Profile
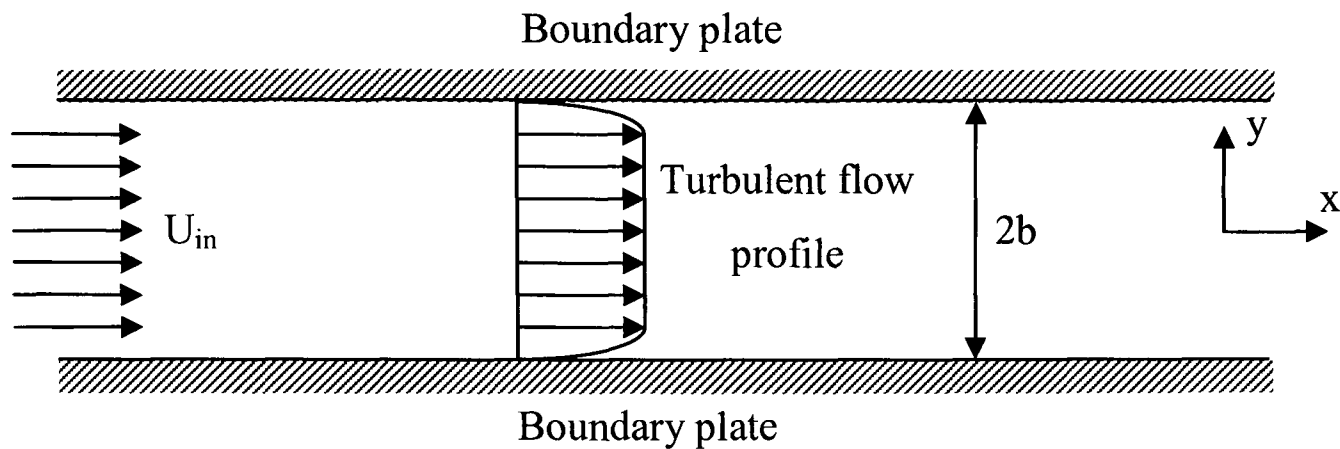
Figure B.3 Schematic representation of turbulent flow profile

To begin the derivation of the turbulent velocity profile the equation describing the velocity distribution in a rectangular channel, as stated in Bird et al.,[160] is utilised.

$$\frac{U_{max} - U}{U_*} = -\frac{1}{\kappa}\left[\ln\left(1 - \left(\frac{y}{b}\right)^{0.5}\right) + \left(\frac{y}{b}\right)^{0.5}\right] \qquad (B.16)$$

The concept of continuity and symmetry is used to determine the relationship between the velocity distribution in the y-direction and the inlet velocity, U_{in}.

$$\int_0^b U \cdot dy = bU_{in} \qquad (B.17)$$

Integrating equation (B.16) between the y limits of zero, at the centreline, and b at the boundary plate is required

$$\int_0^b \frac{U_{max} - U}{U_*} \cdot dy = -\frac{1}{\kappa}\left[\int_0^b \left(\ln\left(1 - \left(\frac{y}{b}\right)^{0.5}\right) + \left(\frac{y}{b}\right)^{0.5}\right)\right] \cdot dy \qquad (B.18)$$

Firstly concentrating on the LHS of equation (B.18):

$$\Rightarrow \int_0^b \frac{U_{max} - U}{U_*} \cdot dy = \left[\frac{U_{max} - U_{in}}{U_*} \right]_0^b = b \left[\frac{U_{max} - U_{in}}{U_*} \right] \qquad \text{(B.19)}$$

Moving onto the first term on the RHS of equation (B.18):

$$\Rightarrow \int_0^b \ln \left(1 - \left(\frac{y}{b} \right)^{0.5} \right) \cdot dy \qquad \text{(B.20)}$$

Using the method of transformation u can be set equal to $(y/b)^{0.5}$, this reduces the limits of the integral from $y = 0 \rightarrow b$ to $u = 0 \rightarrow 1$.

$$u = \left(\frac{y}{b} \right)^{0.5} \qquad \therefore \frac{du}{dy} = \frac{1}{b^{0.5}} \cdot 0.5 y^{-0.5} \equiv \frac{1}{2\sqrt{b}} \cdot y^{-0.5} \qquad \text{(B.21)}$$

Rearranging $u = (y/b)^{0.5}$ to make y the subject allows the following expression to be formulated

$$y^{-0.5} = \frac{1}{u\sqrt{b}} \qquad \text{(B.22)}$$

Substitution of equation (B.22) into equation (B.21) results in the following

$$\frac{du}{dy} = \frac{1}{2u\sqrt{b}\sqrt{b}} = \frac{1}{2ub} \qquad \text{(B.23)}$$

$$\therefore dy = 2ub \cdot du \qquad \text{(B.24)}$$

Constructing new integral to replace equation (B.20)

$$\Rightarrow \int_0^b \ln\left(1 - \left(\frac{y}{b}\right)^{0.5}\right) \cdot dy = \int_0^1 \ln(1-u) \; 2ub \cdot du$$

$$\equiv 2b \int_0^1 u \ln(1-u) \cdot du \qquad (B.25)$$

Again using transformation x can be set to $1 - u$ allowing equation (B.25) to be reformulated

$$\therefore 2b \int_0^1 (1-x) \ln x \cdot dx \qquad (B.26)$$

To permit the solution of equation (B.26) the method of integration by parts is used

$$\int v \frac{ds}{dx} \cdot dx = sv - \int s \frac{dv}{dx} \cdot dx \qquad (B.27)$$

As $\ln x$ can be differentiated but not integrated v is obliged to take the log function. Thus let

$$v = \ln x \qquad \therefore \frac{dv}{dx} = \frac{1}{x}$$

$$\frac{ds}{dx} = 1 - x \qquad \therefore s = x - \frac{x^2}{2} \qquad (B.28)$$

Substituting equation (B.28) into equation (B.27) results in the following

$$\therefore 2b \int_0^1 (1-x) \ln x \cdot dx = 2b\left[\left(x - \frac{x^2}{2}\right)\right]_0^1 - 2b \int_0^1 \left(x - \frac{x^2}{2}\right) \cdot \frac{1}{x} \cdot dx \qquad (B.29)$$

The first term in the RHS of equation (B.29) results in zero at both ends as $\lim_{x \to 0} x \ln x = 0$.

$$\therefore 2b \int_0^1 (1-x) \ln x \cdot dx = -2b \int_0^1 \left(x - \frac{x^2}{2}\right) \cdot \frac{1}{x} \cdot dx = -b\frac{3}{2} \qquad (B.30)$$

Considering the second term on the RHS of equation (B.18):

$$\Rightarrow \int_0^b \ln\left(\frac{y}{b}\right)^{0.5} \cdot dy \equiv \frac{1}{b^{0.5}} \int_0^b y^{0.5} \cdot dy = b\frac{2}{3} \qquad (B.31)$$

Substituting equations (B.19), (B.30) and (B.31) into equation (B.18) gives

$$b\left[\frac{U_{max} - U_{in}}{U_*}\right] = -\frac{1}{\kappa}\left[-b\frac{3}{2} + b\frac{2}{3}\right] = \frac{b}{\kappa} \cdot \frac{5}{6} \qquad (B.32)$$

$$\therefore \frac{U_{max} - U_{in}}{U_*} = \frac{1}{\kappa} \cdot \frac{5}{6} \qquad (B.33)$$

Subtracting equation (B.33) from (B.16) and after some rearrangement gives

$$1 - \frac{U}{U_{in}} = \frac{U_*}{U_{in}}\left(-\frac{1}{\kappa}\left[\frac{5}{6} + \ln\left(1 - \left(\frac{y}{b}\right)^{0.5}\right) + \left(\frac{y}{b}\right)^{0.5}\right]\right) \qquad (B.34)$$

The fraction U_*/U_{in} can be rewritten in the form as a Fanning friction factor, f

$$\frac{U_*}{U_{in}} = \left(\frac{f}{2}\right)^{0.5} \qquad (B.35)$$

Caution must be exercised in the use of tables and formulas involving friction factors as definitions of f vary from text to text. The above definition has been taken from Bird et al.[160]

Substitution of equation (B.35) into equation (B.34) results in the equation for the fully developed turbulent velocity profile

$$\frac{U}{U_{in}} = 1 + \left[\left(\frac{f}{2}\right)^{0.5}/\kappa\right]\left[\frac{5}{6} + \ln\left(1 - \left(\frac{y}{b}\right)^{0.5}\right) + \left(\frac{y}{b}\right)^{0.5}\right] \qquad (B.36)$$

C Equilibrium Log-Law Wall Functions

When dealing with cells located next to a wall boundary empirically derived wall functions are employed. At a significant distance away from the wall the main region of the flow domain adopts high Reynolds number transport equations.

For the most basic wall function, "universal" log laws are adopted for the wall parallel velocity and temperature, and the values of the turbulence parameters are specified at the near wall node, based on local equilibrium assumptions.

C1 Turbulent Heat Transfer Boundary Condition

For the heat transfer at the wall, the flux of the variable T from the wall to the fluid is given by the source expression

$$S_T = \rho \times St \times U_r \times (T_w - T) \times C_p \qquad (C.1)$$

where T denotes the in-cell value of temperature. The calculation of the Stanton number is defined below with equation (C.4) requiring an iterative process to determine s_{turb}.

$$St = \max\left(St_{lam}, St_{turb}\right) \qquad (C.2)$$

$$St_{lam} = \frac{1.0}{Pr_l \times Re} \qquad (C.3)$$

$$St_{turb} = \frac{s_{turb}}{\left(Pr_t \times \left(1.0 + P_m \times \sqrt{s_{turb}}\right)\right)} \qquad (C.4)$$

The dimensionless numbers are defined in equations (C.5)-(C.7).

$$Re = \frac{U_r \times Ldist}{\nu_l} \qquad (C.5)$$

$$Pr_l = \frac{\rho \times v_l \times C_p}{k} \qquad (C.6)$$

$$Pr_t = \frac{\rho \times v_t \times C_p}{k} \qquad (C.7)$$

After reviewing the source code for PHOENICS V3.4 it was found that equation (C.7) has not been implemented which is contrary to what is stated in the reference documentation. Instead Pr_t is simply set to 1.0 which is what has been implemented within PHYSICA. P_m is the smooth wall sub-layer resistance function defined by Jayatillike.[161]

$$P_m = 9.0 \times \left(\left(\frac{Pr_l}{Pr_t} \right) - 1.0 \right) \times \left(\frac{Pr_t}{Pr_l} \right)^{1/4} \qquad (C.8)$$

This P_m function is valid for moderate to high Prandtl number fluids, $Pr_l \geq 0.5$. A P_m function which applies for the whole Pr_l range is stated in equation (C.9).

$$P_m = 11.5 \times \left[\left(\frac{Pr_l}{Pr_t} \right)^{0.72} - 1.0 \right] - \left(\frac{1.0}{k} \right) \times \ln \left\{ \left[1.0 - k \times 11.5 \times \left(\frac{Pr_l}{Pr_t} \right)^{0.72} \right] \Big/ \left(1.0 + k \times \left(y^+ \right) \right) \right\}$$
$$+ \left(\frac{1.0}{k} \right) \times \ln \left[\left(1.0 + k \times \left(y^+ \right) \times \left(\frac{Pr_l}{Pr_t} \right) \right) \Big/ \left(1.0 + k \times \left(y^+ \right) \right) \right] \qquad (C.9)$$

As stated in the reference documentation equation (C.9) has not been implemented within PHOENICS and therefore has not executed within PHYSICA.

D Shear-Stress Transport (FLUENT)

The transport equations used to represent the SST model within the structure of FLUENT V6.1 can be expressed in the following form:

$$\frac{\partial \rho k}{\partial t} + div(\rho \underline{u} k) = div\left[\left(\mu_l + \frac{\mu_t}{\sigma_k}\right) grad\ k\right] + \rho v_t S^2 - \beta^* \rho k \omega \qquad (D.1)$$

$$\frac{\partial \rho \omega}{\partial t} + div(\rho \underline{u} \omega) = div\left[\left(\mu_l + \frac{\mu_t}{\sigma_\omega}\right) grad\ \omega\right] + \alpha_\infty \alpha^* \rho S^2 - \beta_i \rho \omega^2 +$$
$$2(1-F_1)\rho \frac{1}{\sigma_{\omega 2}} \frac{1}{\omega} grad\ k \cdot grad\ \omega \qquad (D.2)$$

Where S is the modulus of the mean rate-of-strain tensor.

The blending functions F_1 and F_2 are defined in a similar form as in the version using the strain rate variable

$$F_1 = \tanh\left\{\left\{\min\left[\max\left(\frac{\sqrt{k}}{\beta^* \omega y}, \frac{500 v_l}{y^2 \omega}\right), \frac{4\rho k}{\sigma_{\omega 2} CD_{k\omega} y^2}\right]\right\}^4\right\} \qquad (D.3)$$

$$F_2 = \tanh\left[\left[\max\left(\frac{2\sqrt{k}}{\beta^* \omega y}, \frac{500 v_l}{y^2 \omega}\right)\right]^2\right] \qquad (D.4)$$

F_1 is equal to zero away from the wall ($k - \varepsilon$) and switches over to one inside the boundary layer ($k - \omega$). The term $CD_{k\omega}$ used in the calculation of the F_1 blending function is defined below:

$$CD_{k\omega} = \max\left(2\rho \frac{1}{\sigma_{\omega 2}} \frac{1}{\omega} grad\ k \cdot grad\ \omega, 10^{-20}\right) \qquad (D.5)$$

with the turbulent eddy viscosity stated as:

$$v_t = \frac{k}{\omega} \frac{1}{\max\left(1/\alpha^*, \Omega F_2/a_1 \omega\right)} \qquad \text{(D.6)}$$

$$\Omega \equiv \sqrt{2\Omega_{ij}\Omega_{ij}} \qquad \text{(D.7)}$$

where Ω_{ij} is the mean rate-of-rotation tensor and α^* takes the same form as stated in the $k - \omega$ model, defined in equation (D.8).

$$\alpha^* = \frac{\alpha_0^* + R_t^*/R_k}{1 + R_t^*/R_k}$$

$$\alpha_0^* = \frac{1}{40}, \quad R_t^* = \frac{k}{\omega v_l}, \quad R_k = 6.0 \qquad \text{(D.8)}$$

The calculation of the model constants are carried out using the following expressions:

$$\alpha_\infty = F_1 \alpha_{\infty 1} + \left(1 - F_1\right)\alpha_{\infty 2} \qquad \text{(D.9)}$$

$$\beta i = F_1 \beta_{i1} + \left(1 - F_1\right)\beta_{i2} \qquad \text{(D.10)}$$

$$\sigma_k = \frac{1}{F_1/\sigma_{k1} + \left(1 - F_1\right)/\sigma_{k2}} \qquad \text{(D.11)}$$

$$\sigma_\omega = \frac{1}{F_1/\sigma_{\omega 1} + \left(1 - F_1\right)/\sigma_{\omega 2}} \qquad \text{(D.12)}$$

where the model constants are defined below:

$$\sigma_{k1} = 1.176, \quad \sigma_{k2} = 1.0, \quad \sigma_{\omega 1} = 2.0, \quad \sigma_{\omega 2} = 1.168$$
$$a_1 = 0.31, \quad \beta_{i1} = 0.075, \quad \beta_{i2} = 0.0828, \quad \kappa = 0.41$$
$$\alpha_{\infty 1} = \frac{\beta_{i1}}{\beta^*} - \frac{\kappa^2}{\sigma_{\omega 1}\sqrt{\beta^*}}, \quad \alpha_{\infty 2} = \frac{\beta_{i2}}{\beta^*} - \frac{\kappa^2}{\sigma_{\omega 2}\sqrt{\beta^*}}$$

E   Shear-Stress Transport Constrained

The constraining of the SST model is detailed in this section. Forcing the SST_V model to reproduce the $k - \varepsilon$ and $k - \omega$ model predictions has not been undertaken as the model is expected to closely replicate the SST model.

E1 F_1 Blending Function = 1.0

It has been stated by Menter et al.[75] that the $k - \omega$ model is recovered when the F_1 function in the SST model tends towards a value of 1.0. In order to prove that this is the case the transport equations of the SST model have been compared against PHYSICA's $k - \omega$ model.

E1.1 k -Transport Equation

Assessment of the k -transport equation has been undertaken to determine if the terms of the equation cancel out or if some form of equation modification is required.

$k - \omega$ model:

$$\frac{\partial \rho k}{\partial t} + div\left(\rho \underline{u} k\right) = div\left(\left[\mu_l + \frac{\rho v_t}{\sigma_k}\right] grad\, k \right) + \rho v_t G - \beta^* \rho \omega k \qquad (E.1)$$

SST model:

$$\frac{\partial \rho k}{\partial t} + div\left(\rho \underline{u} k\right) = div\left(\left[\mu_l + \sigma_k \rho v_t\right] grad\, k \right) + \widetilde{P_k} - \beta^* \rho k \omega \qquad (E.2)$$

The transient and convection terms cancel out between the models.

Diffusion term: the model constant σ_k is set to 2.0 for the $k - \omega$ model. The SST model on the other hand uses equation (E.3) to set the constant.

$$\phi = F_1\phi_1 + (1-F_1)\phi_2$$
$$\therefore \sigma_k = F_1\sigma_{k1} + (1-F_1)\sigma_{k2} \qquad (E.3)$$
$$\sigma_k = 0.85$$

Therefore in order to successfully convert the SST model to the $k-\omega$ model the model constant σ_k requires alteration.

Source term: provided that the $\widetilde{P_k}$ term can be constrained to P_k in the SST model the first half of the source term does not require any modification.

$$P_k = \mu_t \frac{\partial U_i}{\partial x_j}\left(\frac{\partial U_i}{\partial x_j} + \frac{\partial U_j}{\partial x_i}\right) \rightarrow \widetilde{P_k} = \min\left(P_k, 10\cdot\beta^*\rho k\omega\right) \qquad (E.4)$$

$$P_k \equiv \mu_t G \qquad (E.5)$$

The second half of the source term does require a slight modification regarding the model constant β^*. Within the $k-\omega$ model this constant is calculated using equation (E.6).

$$\beta^* = \frac{9}{100}\frac{5/18 + \left(R_t^*/R_\beta\right)^4}{1 + \left(R_t^*/R_\beta\right)^4}, \quad R_\beta = 8.0, \quad R_t^* = \frac{k}{\omega v_l} \qquad (E.6)$$

The SST model on the other hand sets this model constant to 0.09. Therefore the SST model must be altered to use equation (E.6) if the model is to recover the $k-\omega$ model predictions.

E1.2 ω-Transport Equation

Assessment of the ω-transport equation is also required.

$k-\omega$ model:

$$\frac{\partial\rho\omega}{\partial t} + div\left(\rho\underline{u}\omega\right) = div\left(\left[\mu_l + \frac{\rho v_t}{\sigma_\omega}\right]grad\ \omega\right) + \rho\alpha\frac{\omega}{k}G - \beta\omega^2 \qquad (E.7)$$

SST model:

$$\frac{\partial \rho \omega}{\partial t} + div(\rho \underline{u} \omega) = div([\mu_l + \sigma_\omega \rho \nu_t] grad \, \omega) + \alpha \alpha^* \rho S^2 - \beta \rho \omega^2 +$$

$$2(1 - F_1) \rho \sigma_{\omega 2} \frac{1}{\omega} grad \, k \cdot grad \, \omega$$

(E.8)

The transient and convection terms cancel out between the models.

Diffusion term: within the $k - \omega$ model the constant σ_ω is set to 2.0. The SST model alternatively uses equation (E.9) to set the constant.

$$\phi = F_1 \phi_1 + (1 - F_1) \phi_2$$

$$\therefore \sigma_\omega = F_1 \sigma_{\omega 1} + (1 - F_1) \sigma_{\omega 2}$$

$$\sigma_\omega = 0.5$$

(E.9)

Consequently in order to effectively translate the SST model to the $k - \omega$ model the model constant σ_ω requires adjustment as PHYSICA requires the input $1/\sigma_\omega$.

Source term: the model constant α which appears in the first part of the source term requires modification as the $k - \omega$ model calculates this constant using equation (E.10).

$$\alpha = \frac{5}{9} \frac{\alpha_0 + R_t^*/R_w}{1 + R_t^*/R_w} (\alpha^*)^{-1}$$

(E.10)

$$\alpha_0 = \frac{1}{10}, \quad R_w = 2.7, \quad \alpha^* = \frac{\alpha_0^* + R_t^*/R_k}{1 + R_t^*/R_k}, \quad \alpha_0^* = \frac{1}{40}, \quad R_k = 6.0$$

The SST model uses equation (E.11) to set the α constant. Therefore the SST model must be altered to coincide with the $k - \omega$ model.

$$\phi = F_1 \phi_1 + (1 - F_1) \phi_2$$
$$\therefore \alpha = F_1 \alpha_1 + (1 - F_1) \alpha_2 \qquad \text{(E.11)}$$
$$\alpha = \frac{5}{9}$$

E1.3 Turbulent Viscosity Equation

To ensure that the $k - \omega$ model is recovered from SST the equation to calculate the turbulent kinematic viscosity must be consistent between the two models. The standard Wilcox $k - \omega$ expression is utilised and has been stated in equation (E.12).

$$\nu_t = \frac{\alpha^* k}{\omega} \qquad \text{(E.12)}$$

The SST model uses equation (E.13) to calculate the viscosity.

$$\nu_t = \frac{a_1 k}{\max\left((a_1 \omega)/\alpha^*, SF_2\right)} \qquad \text{(E.13)}$$

To ensure that the $k - \omega$ model predictions are obtained the value F_2 must be constrained to 0.0 in equation (E.13).

From the SST validation performed in Chapter 8 it can be concluded that the recovery of the $k - \omega$ model predictions from the SST model was successful.

REFERENCES

[1] FLOTHERM V3.2/4.1, www.flomerics.com

[2] PHOENICS V3.4, www.cham.co.uk

[3] PHYSICA V2.12, www.multi-physis.com

[4] Azar, K. and Morabito, J. (2000) Managing Power Requirements in the Electronics Industry, Electronics Cooling Magazine, Vol. 6, No. 4.

[5] Flomerics http://www.flomerics.com

[6] Flomerics http://www.flomerics.com/floemc/prod_info/

[7] Dyson, J. (1993) FLOTHERM Case Study 1 Laminar and Turbulent Flow and Heat Transfer between Parallel Surfaces, Document No. FLOTHERM/CS1/0293 Issue 1.0, Flomerics Ltd.

[8] PHOENICS Core Library, Channel Flow, Case No. 170.

[9] FEMLAB 3, Model Gallery: Flow Between Two Parallel Plates, http://www.comsol.com/showroom/gallery/232.php

[10] Bird, R. B., Stewart, W. E. and Lightfoot, E. N. (1960) Transport Phenomena, John Wiley & Sons Inc.

[11] Hinze, J. O. (1975) Turbulence, Second Edition, McGraw-Hill Book Company Inc.

[12] Kakac, S., Shah, R. K. and Aung, W. (1987) Handbook of Single-Phase Convective Heat Transfer, John Wiley & Sons Inc.

[13] Vogel, J. C. and Eaton, J. K. (1984) Heat Transfer and Fluid Mechanics Measurements in the Turbulent Reattaching Flow Behind a Backward-Facing Step, Report MD-44, Thermosciences Division, Department of Mechanical Engineering, Stanford University.

[14] Eaton, J. K. and Johnson, J. P. (1980) A Review of Research on Subsonic Turbulent Flow Reattachment, American Institute of Aeronautics and Astronautics (AIAA) Journal, No. AIAA-80-1438.

[15] Kim, J., Kline, S. J. and Johnson, J. P. (1980) Investigation of a Reattaching Turbulent Shear Layer: Flow over a Backward-Facing Step, Transactions of the American Society of Mechanical Engineers (ASME), Vol. 102, pp.302-308.

[16] Mouza, A. A., Pantzali, M. N., Paras, S. V. and Tihon, J. (2005) Experimental and Numerical Study of Backward-Facing Step Flow, Proc. 5th Hellenic Chemical Engineering Conference, Book of Abstracts, pp.1-4.

[17] Nallasamy, M. and Chen, C. P. (1985) Studies on Effects of Boundary Conditions in Confined Turbulent Flow Predictions, Technical Report CR-3929, NASA.

[18] Kline, S. J., Cantwell, B. J and Lilley, G. M., editors, (1980-1981) AFOSR-HTTM-Sanford Conference, Complex Turbulent Flows, Vol. I, II & III.

[19] Schofield, W. H. and Logan, E. (1990) Turbulent Shear Flow over Surface Mounted Obstacles, Journal of Fluid Engineering, Vol. 112, pp. 376-385.

[20] Martinuzzi, R. J. (1992) Experimentelle Untersuchung der Umstroming wandgebundener, rechteckiger, prismatischer Hindernisse, Ph.D. thesis, Erlangen, Germany.

[21] Martinuzzi, R. and Tropea, C. (1993) The Flow Around Surface-Mounted, Prismatic Obstacles Placed in a Fully Developed Channel Flow, Journal of Fluid Engineering, Vol. 115, pp. 85-92.

[22] Martinuzzi, R., Melling, A. and Tropea, C. (1993) Reynolds Stress Field for the Turbulent Flow around a Surface-Mounted Cube placed in a Channel, Proc. 9th Symposium on Turbulent Shear Flows, Kyoto Japan, pp. (13-4-1)-(13-4-6).

[23] Hussein, H. J. and Martinuzzi, R. J. (1996) Energy Balance for Turbulent Flow around a Surface Mounted Cube Placed in a Channel, Physics of Fluids, Vol. 8, pp. 764-780.

[24] AbuOmar, M. and Martinuzzi, R. J. (2003) Experimental Study of the Pressure Field and Flow Structures Around Surface-Mounted Pyramids, Proc. 16th ASCE Engineering Mechanics Conference, University of Washington, Seattle.

[25] Meinders, E. R., Meer, Th.H. van der, Hanjalić, K. and Lasance, C. J. M. (1996) Local 3D Forced Convective Heat Transfer from an Array of Cubical Protruding Components in Vertical Channel Flow, 2nd European Thermal-Sciences and 14th UIT National Heat Transfer Conference, pp. 169-176.

[26] Meinders, E. R., Meer, Th.H. van der, Hanjalić, K. and Lasance, C. J. M. (1997) Application of Infrared Thermography to the Evaluation of Local Convective Heat Transfer on Arrays of Cubical Protrusions, International Journal of Heat and Fluid Flow, Vol. 18, pp. 152-159.

[27] Meinders, E. R, Meer, T. H. van der and Hanjalić, K. (1998) Local Convective Heat Transfer from an Array of Wall-Mounted Cubes, International Journal of Heat and Mass Transfer, Vol. 41, No. 2, pp. 335-346.

[28] Meinders, E. R, Hanjalić, K and Meer, T. H. van der. (1998) Similarity and Dissimilarity between the Surface Heat Transfer and the Flow Structure in Turbulent Flows over Surface-Mounted Cubes, Proc. 11th International Heat Transfer Conference (IHCT), Vol. 3, pp. 51-56.

[29] Meinders, E. R. (1998) Experimental Study of Heat Transfer in Turbulent Flows over Wall-Mounted Cubes, Ph.D. Thesis, Faculty of Applied Science, Delft University of Technology, Delft Netherlands, pp. 163-182.

[30] Meinders, E. R. and Hanjalić, K. (1998) Experimental Evaluation of the Local Convection Heat Transfer from Configurations of Wall-Mounted Cubes in a Channel Flow, Electronics Cooling, Vol. 4, No. 1, pp. 34-39.

[31] Meinders, E. R., van Kempen, G. M. P., van Vliet, L. J. and van der Meer, T. H. (1999) Measurement and Application of an Infrared Image Restoration Filter to Improve the Accuracy of Surface Temperature Measurements of Cubes, Experiments in Fluids, Vol. 26, pp. 86-96.

32 Meinders, E. R. (1998) Experimental Study of Heat Transfer in Turbulent Flows over Wall-Mounted Cubes, Ph.D. Thesis, Faculty of Applied Science, Delft University of Technology, Delft Netherlands, pp. 183-210.

33 Meinders, E. R. and Hanjalić, K. (1998) Distribution of the Local Convective Heat Transfer from a Tandem Arrangement of Wall-Mounted Cubes in a Turbulent Channel Flow, AIAA/ASME Joint Thermophysics and Heat Transfer Conference, Vol. 2, pp. 175-184.

34 Meinders, E. R. and Hanjalić, K. (2002) Experimental Study of the Convective Heat Transfer from In-Line and Staggered Configurations of Two Wall-Mounted Cubes, International Journal of Heat and Mass Transfer, Vol. 45, pp. 465-482.

35 Meinders, E. R. (1998) Experimental Study of Heat Transfer in Turbulent Flows over Wall-Mounted Cubes, Ph.D. Thesis, Faculty of Applied Science, Delft University of Technology, Delft Netherlands, pp. 123-162.

36 Meinders, E. R., Hanjalić, K. and Martinuzzi, R. J. (1999) Experimental Study of the Local Convection Heat Transfer from a Wall-Mounted Cube in Turbulent Channel Flow, Journal of Heat Transfer, Vol. 121, pp. 564-573.

37 Meinders, E. R. and Hanjalić, K. (1999) Vortex Structure and Heat Transfer in Turbulent Flow over a Wall-Mounted Matrix of Cubes, International Journal of Heat and Fluid Flow, Vol. 20, pp. 255-267.

38 Meinders, E. R. (1998) Experimental Study of Heat Transfer in Turbulent Flows over Wall-Mounted Cubes, Ph.D. Thesis, Faculty of Applied Science, Delft University of Technology, Delft Netherlands, pp. 211-233.

39 Ničeno, B. and Hanjalić, K. (2002) Advances in LES of Complex Flows, Kluwer Academic Publishers, pp. 199-216.

40 Ničeno, B., Dronkers, A. D. T. and Hanjalić, K. (2002) Turbulent Heat Transfer from a Multi-Layered Wall-Mounted Cube Matrix: A Large Eddy Simulation, International Journal of Heat and Fluid Flow, Vol. 23, pp. 173-185.

41 Hanjalić, K. and Obi (eds.), (1997) Proc. 6th ERCOFTAC/IAHR/COST Workshop on Refined Flow Modelling, June 6-7, Delft University of Technology, Delft, The Netherlands.

42 Launder, B. and Craft, T. (eds.), (1998) Proc. 7th ERCOFTAC/IAHR/COST Workshop on Refined Turbulence Modelling, May 28-29, UMIST, Manchester, U.K.

43 Hellsten, A. and Rautaheime, P. (eds.), (1999) Proc. 8th ERCOFTAC/IAHR/COST Workshop on Refined Turbulence Modelling, June 17-18, Helsinki University of Technology, Espoo, Finland.

44 Eveloy, V., Rodgers, P. and Lohan, J. (2001) On Numerical Predictive Accuracy for Electronic Component Heat Transfer in Forced Convection, Proc. 7th Thermal Investigations of ICs and Systems (THERMINIC), pp. 36-42, Paris, France.

45 Azar, K. and Rodgers, P. (2001) Visualization of Airflows in Electronic Systems, Electronics Cooling, Vol. 7, No. 2.

46 Eveloy, V., Rodgers, P. and Lohan, J. (2002) Numerical Heat Transfer Predictive Accuracy for an In-Line Array of Board-Mounted PQFP Components in Free

Convection, Proc. 3rd International Conference on Benefiting from Thermal and Mechanical Simulation in Micro-Electronics (EuroSimE), pp. 101-109, Paris, France.

[47] Lohan, J., Eveloy, V. and Rodgers, P. (2002) Visualization of Forced Air Flows over a Populated Printed Circuit Board and Their Impact on Convective Heat Transfer, 8th Intersociety Conference on Thermal and Thermomechanical Phenomena in Electronic Systems (ITHERM), pp. 501-511, San Diego, California, USA.

[48] Eveloy, V., Rodgers P. and Hashmi, M. S. J. (2003) An Experimental Assessment of Computational Fluid Dynamics Predictive Accuracy for Electronic Component Operational Temperature, Proc. American Society of Mechanical Engineers Heat Transfer Conference (ASME), Las Vegas, Nevada, USA, Paper Number HT2003-47282.

[49] Eveloy, V., Rodgers P. and Hashmi, M. S. J. (2003) Numerical Prediction of Electronic Component Heat Transfer: An Industry Perspective, Proc. 19th IEEE Semiconductor Thermal Measurement and Management Symposium (SEMI-THERM), pp. 14-26, San Jose, California, USA.

[50] Rodgers, P. (2003) Prediction of Microelectronics Thermal Behavior in Electronic Equipment: Status, Challenges and Future Requirements, Proc. 4th International Conference on Thermal and Mechanical Simulation and Experiments in Micro-Electronics and Micro-Systems (EuroSimE), pp. 29-39, Aix-en-Provence France.

[51] Rodgers, P. and Eveloy, V. (2004) CFD Prediction of Electronic Component Operational Temperature on PCBs, Electronics Cooling, Vol. 10, No. 2.

[52] Rodgers, P., Eveloy, V. and Hashmi, M. S. J. (2005) An Investigation into the Potential of Low-Reynolds Number Eddy Viscosity Turbulent Flow Models to Predict Electronic Component Operational Temperature, Journal of Electronic Packaging, Vol. 127, No. 1, pp. 67-75.

[53] Spalart, P. R. and Allmaras, S. R. (1992) A One-Equation Model for Aerodynamic Flows, Technical Report AIAA-92-0439.

[54] Menter, F. R. (1994) Two-Equation Eddy Viscosity Turbulence Models for Engineering Applications, AIAA Journal, Vol. 32, No. 8, pp. 1598-1605.

[55] Eveloy, V. (2003) An Experimental Assessment of Computational Fluid Dynamics Predictive Accuracy for Electronic Component Operational Temperature, Ph.D. Thesis, Dublin City University, Dublin, Ireland.

[56] Gardin, P., Brunet, M., Domgin, J. F. and Pericleous, K. (2002) An Experimental and Numerical CFD Study of Turbulence in a Tundish Container, Applied Mathematical Modelling, Vol. 26, pp. 323-336.

[57] Compilation of Experimental Data for Validation of Microscale Dispersion Models (CEDVAL) at Hamburg University, www.mi.uni-hamburg.de/Data_Sets.432.0.html

[58] Heyerichs, K. and Pollard, A. (1996) Heat Transfer in Separated and Impinging Turbulent Flows, International Journal of Heat and Mass Transfer, Vol. 39, No. 12, pp. 2385-2400.

[59] Wilcox, D. C. (1993) The Remarkable Ability of Turbulence Model Equations to Describe Transition, DCW Industries Inc., La Canada, CA.

[60] Wilcox, D. C. (1993) Turbulence Modelling for CFD, DCW Industries Inc., La Canada, CA.

[61] Wilcox, D. C. (2001) Turbulence Modelling: An Overview, AIAA Journal, Paper No. AIAA 2001-0724.

[62] Menter, F. R. (1993) Zonal Two-Equation $k-\omega$ Turbulence Models for Aerodynamic Flows, AIAA Journal, Paper No. AIAA 93-2906.

[63] Driver, D. M. and Seegmiller, H. L. (1985) Features of a Reattaching Turbulent Shear Layer in Divergent Channel Flow, AIAA Journal, Vol. 23, No. 2.

[64] Launder, B. E. and Spalding, D. B. (1974) The Numerical Computation of Turbulent Flows, Computer Methods in Applied Mechanics and Engineering, Vol. 3, pp. 269-289.

[65] Vieser, W., Esch, T. and Menter, F. R. (2002) Heat Transfer Predictions using Advanced Two-Equation Turbulence Models, CFX Technical Memorandum, CFX-VAL10/062.

[66] Workshop on Large Eddy Simulation of Flows past Bluff Bodies, Rottach-Egern, Tegernsee, Germany, June 1995.

[67] Breuer, M., Lakehal, D. and Rodi, W. (1996) Flow around a Surface Mounted Cubical Obstacle: Comparison of LES and RANS-Results, Computation of Three-Dimensional Complex Flows, Notes on Numerical Fluid Mechanics, Vol. 53, pp. 22-30.

[68] Rodi, W. (1991) Experience with Two-Layer Models Combining the $k-\varepsilon$ Model with a One-Equation Model near the Wall, AIAA Technical Paper, No. AIAA-91-0216.

[69] Krajnović, S. and Davidson, L. (2000) Flow around a Three-Dimensional Bluff Body, Proc. 9th International Symposium on Flow Visualisation, Paper No. 177, Heriot-Watt University, Edinburgh.

[70] Krajnović, S. and Davidson, L. (2001) Large Eddy Simulation of the Flow around a Three-Dimensional Bluff Body, AIAA Journal, No. AIAA 2001-0432.

[71] Zhong, B. and Tucker, P. G. (2004) LES and Hybrid LES/RANS Simulations for Turbulent Heat Transfer in Practical Engineering Problems, The Second Conference of the Graduate School, Faculty of Design and Technology.

[72] Zhong, B. and Tucker, P. G. (2004) $k-l$ Based Hybrid LES/RANS Approach and its Application to Heat Transfer Simulation, International Journal for Numerical Methods in Fluids, Vol. 46, pp. 983-1005.

[73] Rautaheimo, P. and Siikonen, T. (1999) Flow in a Matrix of Surface-Mounted Cubes-Description of Numerical Methodology for Test Case 6.2, Proc. 8th ERCOFTAC/IAHR/COST Workshop on Refined Turbulence Modelling, June 17-18, Helsinki University of Technology, Espoo, Finland, pp. 31-36.

[74] Tucker, P. G. and Davidson, L. (2004) Zonal $k-l$ Based Large Eddy Simulations, Computers and Fluid, Vol. 33, pp. 267-287.

[75] Menter, F. R., Kuntz, M. and Langtry, R. (2003) Ten Years of Industrial Experience with the SST Turbulence Model, Proc. 4th International Symposium on Turbulence, Heat and Mass Transfer (ICHMT), pp. 625-632, Antalya, Turkey.

[76] Spalart, P. R., Jou, W. H., Strelets, M. and Allmaras, S. R. (1997) Comments on the Feasibility of LES for Wings and on Hybrid RANS/LES Approach, Proc. 1st AFOSR International Conference on DNS/LES, Ruston, LA.

[77] Spalart, P. and Allmaras, S. (1994) A One-Equation Model for Aerodynamic Flows, La Recherche Aérospatiale, No. 1, pp. 5-21.

[78] Craft, T. J., Gant, S. E., Iacovides, H. and Launder, B. E. (2001) Development and Application of a New Wall Function for Complex Turbulent Flows, European Congress on Computational Methods in Applied Sciences and Engineering (ECCOMAS) Computational Fluid Dynamics Conference, Swansea, Wales.

[79] Craft, T. J., Gant, S. E., Gerasimov, A. V., Iacovides, H. and Launder, B. E. (2002) Wall-Function Strategies for use in Turbulent Flow CFD, Proc. 12th International Heat Transfer Conference, Grenoble, France, pp. 1-12.

[80] Craft, T. J., Gerasimov, A. V., Iacovides, H. and Launder, B. E. (2002) Progress in the Generalization of Wall-Function Treatments, International Journal of Heat and Fluid Flow, Vol. 23, pp. 148-160.

[81] Craft, T. J., Gant, S. E., Iacovides, H. and Launder, B. E. (2004) A New Wall Function Strategy for Complex Turbulent Flows, Numerical Heat Transfer, Vol. 45, Part B, pp. 301-318.

[82] Utyuzhnikov, S. V. (2005) Generalized Wall Functions and their Application for Simulation of Turbulent Flows, International Journal for Numerical Methods in Fluids, Vol. 47, pp. 1323-1328.

[83] Utyuzhnikov, S. V. (2005) Some New Approaches to Building and Implementation of Wall-Functions for Modeling of Near-Wall Turbulent Flow, Computers and Fluids, Vol. 34, pp. 771-784.

[84] Utyuzhnikov, S. V. (2006) The Method of Boundary Condition Transfer in Application to Modeling Near-Wall Turbulent Flows, Computers and Fluids, Article in press.

[85] Patankar, S. V. (1980) Numerical Heat Transfer and Fluid Flow, McGraw-Hill Book Company.

[86] Versteeg, H. K. and Malalasekera, W. (1995) An Introduction to Fluid Dynamics, Pearson Education Limited.

[87] Rhie, C. M. and Chow, W. L. (1983) Numerical Study of the Turbulent Flow Past an Aerofoil with Trailing Edge Separation, AIAA Journal, Vol. 21, pp. 1525-1532.

[88] Leonard, B. P. (1979) A Stable and Accurate Convective Modelling procedure based on Quadratic Upstream Interpolation, Journal of Computer Methods in Applied Mechanics and Engineering, Vol. 19, No. 1, pp. 59-98.

[89] Gaskell, P. H. and Lau, A. C. K. (1988) Curvature-Compensated Convective Transport: SMART, A New Boundedness Preserving Transport Algorithm, International Journal of Numerical Methods in Fluids, Vol. 8, pp. 617-641.

[90] van Leer, B. (1979) Towards the Ultimate Conservative Difference Scheme, V. A Second Order Sequel to Godunov's Method, Journal of Computational Physics, Vol. 32, pp. 101-136.

[91] Schlichting, H. (1968) Boundary-Layer Theory, McGraw-Hill Book Company Inc.

92 Reynolds, O. (1895) On the Dynamical Theory of Incompressible Viscous Fluids and the Determination of the Criterion, Philosophical Transactions of the Royal Society of London, Series A, Vol. 186, pp. 123.

93 Boussinesq, J. (1877) Theorie de l,Ecoulement Tourbillant, Mem. Presentes par Divers Savants Avad. Sci. Inst. Fr., Vol. 23, pp. 46-50.

94 Prandtl, L. (1925) Report on Investigation into Developed Turbulence, Zeitschrift für angewandten Mathematik und Mechanik, Vol. 5, No. 2, pp. 136-139.

95 Prandtl, L. (1945) Uber rein neues Formelsystem fur die ausgebildete Turbulenz, Nacr. Akad. Wiss. Gottingen, Math-Phys. KL. pp. 6-9.

96 Kolmogorov, A. N. (1942) Equations of Turbulent Motion of an Incompressible Fluid, Izvestia Academy of Sciences, USSR, Physics, Vol. 6, Nos. 1-2, pp. 56-58.

97 Rotta, J. C. (1951) Statistische Theorie nichthomogener Turbulenz, Zeitschrift fur Physik, Vol. 129, pp. 547-572.

98 Agonafer, D., Gan-Li, and Spalding, D. B. (1996) The LVEL Turbulence Model for Conjugate Heat Transfer at Low Reynolds Numbers, Application of CAE/CAD Electronic Systems, EEP Proc. American Society of Mechanical Engineers (ASME), Vol. 18.

99 Van Driest, E. R. (1956) On Turbulent Flow Near a Wall, Journal of Aeronautical Sciences, Vol. 23, pp. 1007.

100 Cebeci, T. and Smith, A. M. O. (1974) Analysis of Turbulent Boundary Layers, Ser. In Appl. Math. & Mech., Vol. XV, Academic Press.

101 Baldwin, B. S. and Lomax, H. (1978) Thin-Layer Approximation and Algebraic Model for Separated Turbulent Flows, AIAA Paper 78-257.

102 Dyson, J. (2002) Wall Treatment and Turbulence Models, Flomerics Documentation, No. DEV000057_02.

103 Dyson, J. (2003) Wall Treatment and Turbulence Models in FT/FV 41, Flomerics Documentation, No. DEV000057_02.

104 Baldwin, B. S. and Barth, T. J. (1990) A One-Equation Turbulence Transport Model for High Reynolds Number Wall-Bounded Flows, NASA TM 102847.

105 Chen, H. C. and Patel, V. C. (1988) Near-Wall Turbulence Models for Complex Flows Including Separation, AIAA Journal, Vol. 26, No. 6, pp. 641-648.

106 Wolfshtein, M. (1969) The Velocity and Temperature Distribution in One-Dimensional Flow with Turbulence Augmentation and Pressure Gradient, International Journal of Heat and Mass Transfer, Vol. 12, No. 3, pp. 301-318.

107 Norris, L. H. and Reynolds W. C. (1975) Turbulent Channel Flow with a Moving Wavy Boundary, Report No. FM-10, Stanford University, Mechanical Engineering Department, USA.

108 Launder, B. E. and Spalding, D. B. (1972) Mathematical Models for Turbulence, Academic press, London.

[109] Jones, W. P. and Launder, B. E. (1972) The Prediction of Laminarization with a Two-Equation Model of Turbulence, International Journal of Heat and Mass Transfer, Vol. 15, pp. 301-314.

[110] Jones, W. P. and Launder, B. E. (1973) The Calculation of Low Reynolds Number Phenomena with a Two-Equation Model of Turbulence, International Journal of Heat and Mass Transfer, Vol. 16, pp. 1119-1130.

[111] Lam, C. K. G. and Bremhorst, K. (1981) A Modified Form of the $k - \varepsilon$ Model for Predicting Wall Turbulence, Journal of Fluids Engineering, Vol. 103, pp. 456-460.

[112] Launder, B. E. and Sharma, B. I. (1974) Application of the Energy-Dissipation Model of Turbulence to the Calculation of Flow Near a Spinning Disc, Letters in Heat and Mass Transfer, Vol. 1, pp. 131-138.

[113] Daly, B. J. and Harlow, F. H. (1970) Transport Equations in Turbulence, Physics of Fluids, Vol. 13, No. 11, pp. 2634-2649.

[114] Chen, Y. S. and Kim, S. W. (1987) Computation of Turbulent Flows Using an Extended $k - \varepsilon$ Turbulence Closure Model, NASA CR-179204.

[115] Saffman, P. G. (1970) A Model for Inhomogeneous Turbulent Flow, Proc. Roy. Soc. London, Vol. A317, pp. 417-433.

[116] Spalding, D. B. (1979) Mathematical Models of Turbulent Transport Processes, HTS/79/2, Imperial College, Mechancial Engineering Department.

[117] Patel, V. C., Rodi, W., and Scheuerer, G. (1985) Turbulence Models for Near-Wall and Low Reynolds Number Flows: A Review, AIAA Journal, Vol. 23, No. 9, pp. 1308-1319.

[118] Hughes, W. F. and Brighton, J. A. (1991) Schaum's outline Series: Theory and Problems of Fluid Dynamics, 2nd Edition, McGraw-Hill Inc. pp.117.

[119] Vogel, J. C. and Eaton, J. K. (1985) Combined Heat Transfer and Fluid Dynamics Measurements Downstream of a Backward-Facing Step, Transactions of the American Society of Mechanical Engineers (ASME), Vol. 107, pp. 922-929.

[120] Nallasamy, M. (1987) Turbulence Models and their Applications to the Prediction of Internal Flows: A Review, Journal of Computers and Fluids, Vol. 15, No. 2, pp 151-194.

[121] Vieser, W., Esch, T. and Menter, F. (2002) Heat Transfer Predictions using Advanced Two-Equation Turbulence Models, CFX Technical Memorandum: CFX-VAL10/0602, pp. 25-29.

[122] Croft, T. N. (1998) Unstructured Mesh-Finite Volume Algorithms for Swirling, Turbulent, Reacting Flows, Ph.D. Thesis, University of Greenwich, UK, pp. 142-145.

[123] Malin, M. R. and D. B. Spalding (1995) Turbulence Models in PHOENICS, Documentation Number CHAM/TR/320 Polis Version 2.1.4, CHAM Ltd.

[124] PHOENICS http://www.cham.co.uk/phoenics/d_polis/d_enc/turmod/enc_t321.htm.

[125] Lakehal, D. and Rodi, W. (1997) Proc. 6th ERCOFTAC/IAHR/COST workshop on Refined Flow Modelling, Case 6.2: Fully Developed Flow and Heat Transfer in a Matrix of Surface Mounted Cubes, pp. 152-155, June 6-7, Delft University of Technology, Delft, The Netherlands.

[126] Fackrell, J. E. and Pearce, J. E. (1981) Parameters Affecting Dispersion in the Near Wake of Buildings, CEGB Report No. RD/M/1179/N81.

[127] Logan, E. and Lin, S. H. (1982) Wakes from Arrays of Buildings, NASA Cr-170666.

[128] Breuer, M. (1997) Description of the LES Method and Simulations, Proc. 6th ERCOFTAC/IAHR/COST Workshop on Refined Flow Modelling, June 6-7, Delft University of Technology, Delft, The Netherlands, pp. 137-144.

[129] Camelli, F. E. and Löhner, R. (2002) Combining the Baldwin Lomax and Smagorinsky Turbulence Models to Calculate Flows with Separation Regions, AIAA Technical Paper, AIAA-2002-0426.

[130] Tucker, P. (2001) Computation of Unsteady Internal Flows: Fundamental Methods with Case Studies, Kluwer Academic Publishers.

[131] Tucker, P. G. and Davidson, L. (2003) Zonal $k-l$ Based Large Eddy Simulations, AIAA Technical Paper, AIAA-2003-82.

[132] Tucker, P. G. and Lin, Y. (2005) Contrasting CFD for Electronic Systems Modelling with that for Aerospace, Proc. 6th International Conference on Thermal and Mechanical and Multiphysics Simulation and Experiments in Micro-Electronics and Micro-Systems (EuroSimE), pp.151-158, Berlin Germany.

[133] CFX-5.7 Documentation Turbulence and Wall Function Theory, pp. 69-72.

[134] FLUENT-6.1 Documentation Modeling Turbulence, Chapter 10, pp. 31-35.

[135] Iacovides, H. and Launder, B. E. (1990) Parametric and Numerical Study of Fully-Developed Flow and Heat Transfer in Rotating Rectangular Ducts, ASME Papar 90/GT/24.

[136] Chen, H. C. and Patel, V. C. (1989) Evolution of Axisymmertic Wakes from Attached and Separated Flows, Turbulent Shear Flows 6, pp. 215-231.

[137] Dhinsa, K., Bailey, C. and Pericleous, K. (2004) Investigation into the Performance of Turbulence Models for Fluid Flow and Heat Transfer Phenomena in Electronic Applications, 20th IEEE Semiconductor Thermal Measurement and Management Symposium (SEMI-THERM), pp. 278-285, San Jose California, USA.

[138] Dhinsa, K., Bailey, C. and Pericleous, K. (2004) Low Reynolds Number Turbulence Models for Accurate Thermal Simulations of Electronic Components, Proc. International Conference on Thermal and Mechanical Simulation and Experiments in Micro-Electronics and Micro-Systems (EuroSimE), pp. 483-490, Brussels Belgium.

[139] Dhinsa, K., Bailey, C. and Pericleous, K. (2004) Turbulence Modelling and It's Impact on CFD Predictions for Cooling Electronic Components, Proc. International Conference on Thermal Mechanics Theromomechanical Phenomena in Electronic Systems (ITHERM), pp. 487-494, Las Vegas, Nevada, USA.

[140] Chein, K. Y. (1982) Predictions of Channel and Boundary-Layer Flows with a Low-Reynolds-Number Turbulence Model, AIAA Journal, Vol. 20, pp. 33-38.

[141] Dutoya, D. and Michard, P. (1981) A Program for Calculating Boundary Layers along Compressor and Turbine Blades, Numerical Methods in Heat Transfer, edited by Lewis, R.W., Morgan, K., and Zienkiewicz, O.C, John Wiley & Sons, New York.

[142] Hassid, S. and Poreh, M. (1978) A Turbulent Energy Dissipation Model for Flows with Drag Reduction, Journal of Fluid Engineering, Vol. 100, pp. 107-112.

[143] Hoffmann, G. H. (1975) Improved Form of Low-Reynolds Number $k - \varepsilon$ Turbulence Model, Physics of Fluids, Vol. 18, pp. 309-312.

[144] Reynolds, W. C. (1976) Computation of Turbulence Flows, Annual Review of Fluid Mechanics, Vol. 8, pp. 183-208.

[145] Meinders, E. R. (1998) Experimental Study of Heat Transfer in Turbulent Flows over Wall-Mounted Cubes, Ph.D. Thesis, Faculty of Applied Science, Delft University of Technology, Delft, The Netherlands.

[146] Meinders, E. R. (1998) Experimental Study of Heat Transfer in Turbulent Flows over Wall-Mounted Cubes, Ph.D. Thesis, Faculty of Applied Science, Delft University of Technology, Delft, The Netherlands, pp. 25.

[147] Meinders, E. R. (1998) Experimental Study of Heat Transfer in Turbulent Flows over Wall-Mounted Cubes, Ph.D. Thesis, Faculty of Applied Science, Delft University of Technology, Delft, The Netherlands, pp. 130.

[148] WinDIG Version 2.5, Department of Physical Chemistry, Switzerland.

[149] Meinders, E. R. (1998) Experimental Study of Heat Transfer in Turbulent Flows over Wall-Mounted Cubes, Ph.D. Thesis, Faculty of Applied Science, Delft University of Technology, Delft, The Netherlands, pp. 45.

[150] Meinders, E. R. (1998) Experimental Study of Heat Transfer in Turbulent Flows over Wall-Mounted Cubes, Ph.D. Thesis, Faculty of Applied Science, Delft University of Technology, Delft, The Netherlands, pp. 212.

[151] Bornoff, R. and Parry, J. (1997) Proc. 6th ERCOFTAC/IAHR/COST workshop on Refined Flow Modelling, Case 6.2: Fully Developed Flow and Heat Transfer in a Matrix of Surface Mounted Cubes, pp. 103-105, June 6-7, Delft University of Technology, Delft, The Netherlands.

[152] Jansson, S. (1997) Proc. 6th ERCOFTAC/IAHR/COST workshop on Refined Flow Modelling, Case 6.2: Fully Developed Flow and Heat Transfer in a Matrix of Surface Mounted Cubes, pp. 106-107, June 6-7, Delft University of Technology, Delft, The Netherlands.

[153] Mathey, F., Fröhlich, J. and Rodi, W. (1999) Proc. 8th ERCOFTAC/IAHR/COST workshop on Refined Flow Modelling, Case 6.2: Flow in a Matrix of Surface-Mounted Cubes, pp. 46-49, June 17-18, Helsinki University of Technology, Espoo, Finland.

[154] Meinders, E. R. (1998) Experimental Study of Heat Transfer in Turbulent Flows over Wall-Mounted Cubes, Ph.D. Thesis, Faculty of Applied Science, Delft University of Technology, Delft, The Netherlands, pp. 218.

[155] Schlichting, H. (1968) Boundary-Layer Theory, McGraw-Hill Book Company Inc., pp.575.

[156] Kakac, S., Shah R. K. and Aung, W. (1987) Handbook of Single-Phase Convective Heat Transfer, John Wiley & Sons, Inc., pp. 3.30 & 4.63.

[157] Barber, R. W. and Emerson, D. R. (2001) A Numerical Investigation of Low Reynolds Number Gaseous Slip Flow at the Entrance of Circular and Parallel Plate Micro-

Channels, European Community on Computational Methods in Applied Sciences (ECCOMAS) Computational Fluid Dynamics Conference 4-7 September.

[158] Meinders, E. R. (1998) Experimental Study of Heat Transfer in Turbulent Flows over Wall-Mounted Cubes, Ph.D. Thesis, Faculty of Applied Science, Delft University of Technology, Delft, The Netherlands, pp. 67-120.

[159] Massey, B. S. (1989) Mechanics of Fluids, Chapman and Hall, pp. 160-162.

[160] Bird, R. B., Stewart, W. E. and Lightfoot, E. N. (1960) Transport Phenomena, John Wiley & Sons Inc., pp.175.

[161] Jayatillike, C. L. V. (1969) The Influence of The Prandtl Number and Surface Roughness on The Resistance of The Sublayer to Momentum and Heat Transfer, Prog. in Heat & Mass Transfer, Vol.1, Pergamon Press.